SAPIENZA
UNIVERSITÀ DI ROMA

Risk Assessment from Multiple Hazards in Underground Systems

Emin Alakbarli

Faculty of Civil and Industrial Engineering
Department of Civil, Constructional and Environmental Engineering
Ph.D. Program in Infrastructures and Transport – XXXIX cycle

Supervisor
Guido Gentile

Advisor
Massimo Guarascio

Internal Co-Supervisor
Angelo Libertà
Mara Lombardi

External Co-Supervisor
Marco Andreini
Saverio La Mendola

A dissertation submitted for the attainment of the title of Doctor of Philosophy
(Ph.D.)
in
Sapienza University of Rome
A.Y. 2023-2024

Abstract (ENG)

This dissertation presents a comprehensive framework for multi-hazard risk assessment in underground infrastructures, focusing on the interplay between earthquakes, structural collapse, fire, and evacuation dynamics. A detailed investigation into seismic geostatistics-4D, Incremental Dynamic Analysis (IDA) and structural fragility, fire in confined environment, and the analysis of evacuation conditions is conducted. The analyses consider the probabilities of events that single (earthquake/structural collapse/fire happening on its own) or not mutually exclusive (such as seismic-induced structural collapse, which may or may not lead to a fire), independent (which occur without affecting probabilities of occurrence of others) and non-independent (where one event increases/decrease the probability others). Through the Gu@larp mathematical model, the study offers a refined approach to multi-hazard risk-based design for underground infrastructure. The dissertation is organized into five macro-chapters.

Chapter 1 introduces the need for a comprehensive framework to assess multi-hazard risks in underground infrastructures. These systems, which play an essential role in diverse environments, face increased risks from both natural and human-made hazards, including seismic events, structural collapse, and fires. The study aims to address these vulnerabilities by developing an integrated quantitative risk assessment framework that combines these hazards into a unified approach. The chapter outlines the specific challenges currently faced in multi-hazard risk assessment, such as the absence of methodologies that consider the interactions between multiple hazards and the importance of accurate scenario identification. Through clearly defined objectives, such as advancing risk modelling techniques and understanding in depth human behaviours and transfer it to evacuation analysis, Chapter 1sets the stage for the technical analysis and methodologies that will follow.

Chapter 2 provides an in-depth analysis of the hazards affecting underground infrastructures, focusing on the integration of seismic, structural, fire, and evacuation risks. It begins with an in-depth review of the current state of knowledge with a discussion on seismicity and hazard estimation methods tailored to underground environments, introducing seismic geostatistics-4D analysis as a novel tool for capturing the spatial and temporal complexity of seismic data. The chapter also explores seismic-induced structural collapses. And

fire dynamic is examined through the lens of tenability limits in confined spaces. Evacuation challenges are addressed, focusing on the dynamics of underground environments during fires and earthquakes while dispelling misconceptions about human behaviour in emergencies. The comprehensive risk analysis framework integrates these hazards, providing insights into societal influences on risk perception and advancing methodologies for a multi-hazard risk assessment model that considers both individual risks and their interdependencies to ensure the safety of underground infrastructures.

Chapter 3 focusing on developing a comprehensive multi-hazard risk assessment framework, analysing joint occurrences of different hazards. Theoretical foundations, including the integration of Aristotelian logic and complex systems theory, support scenario identification and modelling for multi-hazard modelling. The ALARP principle is discussed through legal and philosophical perspectives. Incorporating ALARP and Black Swan events into a multi-hazard framework necessitates a broader range of probabilistic concepts, from basic unconditional probabilities to complex multi-conditional probabilities. This broader spectrum provides a foundational basis for probabilistic approaches in analysing hazards within multi-hazard risk assessment. Key four risk indicators are used to evaluate risk exposure, aligning with ethical principles for Gu@larp method, combining scenario quantic-modelling with ALARP, providing a comprehensive framework for multi-hazard risk assessment.

The interest of the dissertation proposed here concerns the improvement of modelling support for the design and assessment of seismic and fire risks for the structural components of underground environments: An example developed and presented in this dissertation is the analysis of the specific seismic actions related to the damage simulated on the blocks in the CERN underground environment, where fires developed either independently or due to falling blocks, with evacuation scenarios based on human behaviour considered during these events. This dissertation in Chapter 4 applies advanced modelling techniques to characterize these scenarios, integrating seismic geostatistical-4D analysis (CoKriging), structural assessment through Incremental Dynamic Analysis (IDA), fire modelling with the Fire Dynamics Simulator (FDS), and evacuation modelling via Performance-Based Design (PBD). All these methods are implemented within the developed Gu@larp quantitative multi-hazard risk assessment framework.

Key conclusions emphasise the importance of understanding multi-hazard scenarios to enhance safety in underground environments in Chapter 5. Lessons learned highlight the integration of multi-hazard risk assessment methodologies with practical design strategies. The study's limitations are acknowledged, along with recommendations for future research directions.

Abstract (ITA)

Questa tesi presenta un quadro complessivo per la valutazione del rischio multi-pericolo nelle infrastrutture sotterranee, concentrandosi sull'interazione tra terremoti, collasso strutturale, incendi e dinamiche di evacuazione. Viene condotta un'analisi dettagliata sulla geostatistica sismica-4D, l'Analisi Dinamica Incrementale (IDA) e la fragilità strutturale, sugli incendi in ambienti confinati e sull'analisi delle condizioni di evacuazione. Le analisi considerano le probabilità di eventi singoli (terremoto/crollo strutturale/incendio che si verificano autonomamente) o non mutuamente esclusivi (come un crollo strutturale indotto da un sisma, che può o meno portare a un incendio), indipendenti (che si verificano senza influenzare le probabilità di altri eventi) e non indipendenti (in cui un evento aumenta o diminuisce la probabilità degli altri). Attraverso il modello matematico Gu@larp, lo studio propone un approccio perfezionato alla progettazione basata sul rischio multi-hazard per le infrastrutture sotterranee. La dissertazione è organizzata in cinque macro-capitoli.

Il Capitolo 1 introduce la necessità di un quadro completo per valutare i rischi multi-hazard nelle infrastrutture sotterranee. Questi sistemi, che svolgono un ruolo essenziale in una varietà di contesti, affrontano rischi crescenti sia naturali che di origine antropica, tra cui eventi sismici, crolli strutturali e incendi. Lo studio mira a rispondere a queste vulnerabilità sviluppando un quadro integrato di valutazione quantitativa del rischio che combina questi pericoli in un approccio unificato. Il capitolo delinea le sfide specifiche attualmente affrontate nella valutazione del rischio multi-hazard, come l'assenza di metodologie che considerano le interazioni tra più pericoli e l'importanza dell'identificazione accurata degli scenari. Attraverso obiettivi chiaramente definiti, come il miglioramento delle tecniche di modellazione del rischio e la comprensione approfondita dei comportamenti umani da trasferire nell'analisi dell'evacuazione, il Capitolo 1 prepara il terreno per le analisi tecniche e le metodologie che seguiranno.

Il Capitolo 2 fornisce un'analisi approfondita dei pericoli che influenzano le infrastrutture sotterranee, concentrandosi sull'integrazione dei rischi sismici, strutturali, di incendio e di evacuazione. Inizia con una revisione dettagliata dello stato attuale delle conoscenze, con una discussione sulla sismicità e i metodi di stima dei rischi specificamente adattati agli ambienti sotterranei, introducendo l'analisi geostatistica sismica 4D come uno strumento innovativo per catturare la

complessità spaziale e temporale dei dati sismici. Il capitolo esplora anche i crolli strutturali indotti dai sismi. La dinamica degli incendi viene esaminata attraverso la lente dei limiti di tenibilità in spazi confinati. Le sfide legate all'evacuazione vengono affrontate, concentrandosi sulle dinamiche degli ambienti sotterranei durante incendi e terremoti, sfatando i preconcetti sul comportamento umano in situazioni di emergenza. Il quadro completo per l'analisi del rischio integra questi pericoli, fornendo approfondimenti sulle influenze sociali nella percezione del rischio e migliorando le metodologie per un modello di valutazione del rischio multi-hazard che considera sia i rischi individuali che le loro interdipendenze, al fine di garantire la sicurezza delle infrastrutture sotterranee.

Il Capitolo 3 si concentra sullo sviluppo di un quadro completo per la valutazione del rischio multi-hazard, analizzando le occorrenze congiunte di diversi pericoli. Le basi teoriche, tra cui l'integrazione della logica aristotelica e della teoria dei sistemi complessi, supportano l'identificazione degli scenari e la modellazione per la valutazione multi-hazard. Il principio ALARP viene discusso attraverso prospettive legali e filosofiche. Integrare il principio ALARP e gli eventi Cigno Nero in un quadro multi-rischio richiede una gamma più ampia di concetti probabilistici, dalle probabilità incondizionate di base alle probabilità multi-condizionali complesse. Questo spettro più ampio fornisce una base per approcci probabilistici nell'analisi dei pericoli all'interno della valutazione del rischio multi-hazard. Vengono utilizzati quattro indicatori chiave del rischio per valutare l'esposizione al rischio, allineandosi ai principi etici del metodo Gu@larp, combinando la modellazione quantistica degli scenari con l'ALARP, fornendo un quadro completo per la valutazione del rischio multi-hazard.

L'interesse della tesi qui proposta riguarda il miglioramento del supporto alla modellazione per la progettazione e la valutazione dei rischi sismici e di incendio per i componenti strutturali degli ambienti sotterranei: Un esempio sviluppato e presentato in questa tesi è l'analisi delle azioni sismiche specifiche legate ai danni simulati sui blocchi nell'ambiente sotterraneo del CERN, dove si sono sviluppati incendi sia indipendentemente sia a causa della caduta dei blocchi, con scenari di evacuazione basati sul comportamento umano considerato durante questi eventi. Questa tesi, nel Capitolo 4 applica tecniche di modellazione avanzate per caratterizzare questi scenari, integrando l'analisi geostatistica sismica 4D (CoKriging), la valutazione strutturale tramite Analisi Dinamica Incrementale (IDA), la modellazione dell'incendio con il Fire Dynamics Simulator (FDS) e la modellazione dell'evacuazione secondo i principi della Performance-Based

Design (PBD). Tutti questi metodi sono implementati all'interno del sviluppato framework di valutazione del rischio multirischio Gu@larp.

Le conclusioni principali sottolineano l'importanza di comprendere gli scenari multi-rischio per migliorare la sicurezza negli ambienti sotterranei nel Capitolo 5. Le lezioni apprese evidenziano l'integrazione di metodologie di valutazione del rischio multi-rischio con strategie di progettazione pratiche. Le limitazioni dello studio vengono riconosciute, insieme a raccomandazioni per future direzioni di ricerca.

Abstract (AZE)

Bu dissertasiya, zəlzələ, struktur çökməsi, yanğın və təxliyə dinamikasının qarşılıqlı təsirinə diqqət yetirərək yeraltı infrastrukturda çoxsaylı təhlükələrin risklərinin qiymətləndirilməsi üçün hərtərəfli çərçivə təqdim edir. Seysmik geostatistika-4D, Artımlı Dinamik Analiz (IDA) və struktur zəifliyi, məhdud məkanda yanğın və təxliyə şəraitinin təhlili üzrə ətraflı tədqiqat aparılmışdır. Təhlillər hadisələrin tək (zəlzələ/struktur çökməsi/yanğın kimi ayrı-ayrı baş verən hadisələr) və ya qarşılıqlı istisna olmayan (məsələn, seysmik səbəbli struktur çökməsi, bu da yanğına səbəb ola bilər və ya olmaya bilər), müstəqil (bir hadisənin digərinin baş vermə ehtimalına təsir etmədən baş verdiyi) və qeyri-müstəqil (bir hadisənin digərinin baş vermə ehtimalını artırması və ya azaltması) xarakterlərini və bu hadisələrin müvafiq ehtimallarını nəzərə alır. Gu@larp vasitəsilə tədqiqat, yeraltı infrastruktur üçün çoxsaylı təhlükələrə əsaslanan risk yönümlü dizayna təkmilləşdirilmiş yanaşma təklif edir. Dissertasiya beş makro-fəsilə bölünmüşdür.

1-ci Fəsil yeraltı infrastrukturda çoxsaylı təhlükələrin risklərinin qiymətləndirilməsi üçün hərtərəfli çərçivənin zəruriliyini təqdim edir. Bu sistemlər, müxtəlif mühitlərdə mühüm rol oynayaraq, zəlzələ, struktur çökməsi və yanğınlar kimi həm təbii, həm də insan mənşəli təhlükələrdən artan risklərlə üzləşirlər. Tədqiqat bu zəifliklər aradan qaldırmaq məqsədi daşıyır və bu təhlükələri vahid yanaşmada birləşdirən inteqrasiya olunmuş kəmiyyət risk qiymətləndirmə çərçivəsi hazırlamağa yönəlmişdir. Fəsil çoxsaylı təhlükələrin risk qiymətləndirilməsində mövcud problemləri, o cümlədən bir neçə təhlükənin qarşılıqlı təsirini nəzərə alan metodologiyaların çatışmazlığını və ssenari müəyyənləşdirmənin dəqiqliyinin əhəmiyyətini vurğulayır. Risk modelləşdirmə texnikalarının təkmilləşdirilməsi və insan davranışlarının dərindən öyrənilməsi kimi aydın şəkildə müəyyən edilmiş məqsədlərlə, və bu məlumatların təxliyə təhlilinə tətbiqi ilə 1-ci Fəsil texniki təhlillər və metodologiyalar üçün əsas yaradır.

2-ci Fəsil yeraltı infrastrukturlara təsir edən təhlükələrin dərin təhlilini təqdim edir və seysmik, struktur, yanğın və təxliyə risklərinin inteqrasiyasına diqqət yetirir. Fəsil yeraltı mühitlərə uyğunlaşdırılmış seysmiklik və təhlükə qiymətləndirmə metodları haqqında müzakirə ilə mövcud biliklərin hərtərəfli icmalı ilə başlayır və seysmik məlumatların məkan və zaman mürəkkəbliyini əks etdirmək üçün yeni alət kimi seysmik geostatistika-4D analizini təqdim edir.

Fəsil həmçinin seysmik səbəbli struktur çökmələrini araşdırır. Yanğın dinamikası məhdud məkanlarda tenabillik həddləri prizmasından araşdırılır. Təxliyə problemləri yanğınlar və zəlzələlər zamanı yeraltı mühitlərin dinamikasına diqqət yetirərək həll olunur və fövqəladə hallarda insan davranışları ilə bağlı yanlış təsəvvürləri aradan qaldırır. Hərtərəfli risk təhlili çərçivəsi bu təhlükələri birləşdirir, risk qavrayışına cəmiyyətin təsirinə dair məlumatlar təqdim edir və yeraltı infrastrukturun təhlükəsizliyini təmin etmək üçün həm fərdi riskləri, həm də onların qarşılıqlı təsirlərini nəzərə alan çoxsaylı təhlükələrin risk qiymətləndirməsi modeli üçün metodologiyaları təkmilləşdirir.

3-cü Fəsil müxtəlif təhlükələrin birgə baş verməsini təhlil edərək çoxsaylı təhlükələrin risk qiymətləndirməsi üçün hərtərəfli çərçivənin hazırlanmasına diqqət yetirir. Aristotel məntiqi və mürəkkəb sistemlər nəzəriyyəsinin inteqrasiyasını əhatə edən nəzəri əsaslar çoxsaylı təhlükələrin modelləşdirilməsi üçün ssenari müəyyənləşdirmə və modelləşdirməni dəstəkləyir. ALARP prinsipi hüquqi və fəlsəfi aspektlərdən müzakirə olunur. ALARP və Qara Qus hadisələrini çoxriskli çərçivəyə daxil etmək, sadə şərtsiz ehtimallardan mürəkkəb çox şərtsiz ehtimallara qədər daha geniş ehtimal anlayışlarını tələb edir. Bu geniş spektr çoxsaylı təhlükələrə əsaslanan risk qiymətləndirməsində təhlükələrin təhlili üçün ehtimal yanaşmalarının əsasını təmin edir. Dörd əsas risk göstəricisi risk məruz qalmasını qiymətləndirmək üçün istifadə olunur və ALARP ilə ssenari kvant-modelləşdirilməsini birləşdirərək Gu@larp metodu üçün etik prinsiplərə uyğunlaşır və çoxsaylı təhlükələrin risk qiymətləndirməsi üçün hərtərəfli çərçivə təmin edir.

Dissertasiyada irəli sürülən maraq sahəsi yeraltı mühitlərin struktur komponentləri üçün seysmik və yanğın risklərinin modelləşdirilməsi dəstəyi ilə bağlıdır: Bu dissertasiyada inkişaf etdirilən və təqdim edilən nümunə CERN yeraltı mühitində bloklarda simulyasiya edilmiş zədələnmə ilə əlaqəli spesifik seysmik hərəkətlərin təhlilidir. Yanğınlar ya müstəqil şəkildə, ya da düşən bloklar nəticəsində inkişaf edir və bu hadisələr zamanı insan davranışına əsaslanan təxliyə ssenariləri nəzərə alınır. Bu dissertasiya, 4-cü Fəsildə bu ssenariləri xarakterizə etmək üçün inkişaf etmiş modelləşdirmə üsullarından istifadə edilir, seysmik geostatistik-4D analizi (CoKriging), Artımlı Dinamik Analiz (IDA) vasitəsilə struktur qiymətləndirməsi, Fire Dynamics Simulator (FDS) ilə yanğın modelləşdirilməsi və Performance-Based Design (PBD) əsasında təxliyə modelleməsi inteqrasiya edilmişdir. Bütün bu metodlar inkişaf etdirilmiş Gu@larp çox-təhlükəli kəmiyyət risk qiymətləndirmə çərçivəsi daxilində həyata keçirilir.

Əsas nəticələr yeraltı mühitlərdə təhlükəsizliyi artırmaq üçün çox təhlükəli ssenariləri anlamaq vacibliyini 5-ci Fəsildə vurğulayır. Öyrənilmiş dərslər çox təhlükəli risklərin qiymətləndirilməsi metodologiyalarının praktiki dizayn strategiyaları ilə inteqrasiyasını vurğulayır. Tədqiqatın məhdudiyyətləri qeyd olunur və gələcək tədqiqat istiqamətləri üçün tövsiyələr təqdim edilir.

Acknowledgements

Embarking on this doctoral journey has been an enlightening and transformative experience. The exploration of Risk Assessment from Multiple Hazards forms the heart of this dissertation, but the soul of this work is the support and encouragement I received from many remarkable individuals and institutions.

This dissertation is not merely a record of my academic efforts but a testament to the collaborative spirit and unwavering dedication of those who have guided, supported, and believed in me throughout this endeavour. The successful development of this dissertation would not have been possible without the invaluable collaboration with Sapienza University of Rome, CERN (HSE-OHS), and Lund University (Division of Fire Safety Engineering), where I had the privilege of working closely with esteemed experts. It is an honour to acknowledge their contributions, which have been instrumental in the completion of this research.

I am profoundly indebted to the distinguished mentor who has guided my intellectual journey from the pursuit of my master's degree to the culmination of my Ph.D. Prof. Massimo Guarascio bestowed upon me not only his invaluable expertise but also imparted a philosophy of rigorous inquiry and relentless pursuit of knowledge.

Dr. Angelo Libertà's meticulous attention to detail and extensive revisions, reflecting his dedication and the significant time he invested, greatly enhanced the quality and scholarly integrity of my dissertation.

At CERN, Dr. Marco Andreini and Dr. Saverio La Mendola went far beyond mere guidance; they meticulously sculpted my work with precision and practical applications, embedding within it a standard of excellence that transcended ordinary expectations.

Under the supervision of Prof. Enrico Ronchi at Lund University, his guidance deeply delved into the intricacies of intellectual exploration. Each critique revealed new layers of thought and encouraged bold inquiries into the field. His profound insights, coupled with meticulous corrections and revisions, urged me to traverse beyond conventional boundaries, significantly enriching my research journey.

I extend my heartfelt appreciation to the distinguished reviewers of this dissertation, Prof. Giulio Sciarra and Prof. Chantal de Fouquet, whose insightful critiques and expert evaluations significantly enhanced the quality of this work. Their feedback was invaluable and successfully implemented to strengthen the dissertation.

I would like to express my sincerest gratitude to all the individuals (listed below in alphabetical order) who provided me with support, help, and protection over the course of my research. I benefited greatly from their expertise and their loyalty. For me, the latter quality is the only one that truly counts.

With the heartfelt friendship, profound affection, and deep appreciation, I thank:

Dr. Marco Andreini – Eng. Brecht Debrouwere

Prof. Håkan Frantzich – Prof. Guido Gentile

Noemi Sara Gentile – Prof. Massimo Guarascio

Prof. Haukur Ingason – Dr. Saverio La Mendola

Dr. Angelo Libertà – Prof. Carla Nardinocchi

Prof. Enrico Ronchi

I am especially grateful to Noemi Sara Gentile, whose unwavering love has accompanied me every step of the way on this journey. Her unwavering support and belief in me have made even the most challenging moments feel surmountable, and this dissertation is as much a reflection of her strength and encouragement as it is of my own efforts.

Lastly, I want to express my deepest gratitude to my family, whose unwavering support has been a constant source of strength and encouragement in all my pursuits.

They have each left an indelible imprint on my work and my character, for which I am eternally grateful. As Albert Einstein once said, "*Creativity is intelligence having fun*". I truly had a lot of fun on this journey. Thank you for all the memorable moments.

Contents

List of Tables

List of Figures

Chapter 1

Introduction

1.1 Introduction

The underground infrastructure, encompassing transportation networks, research centres, and commercial spaces, is a testament to contemporary engineering and infrastructure planning. However, these subterranean complexes are vulnerable to both natural and human-made hazards. Seismic events and fires, in particular, pose significant threats, with the potential to cause catastrophic consequences affecting thousands of lives, incurring substantial economic losses, and disrupting the community.

This dissertation is anchored in the critical need to understand and analyse the risks associated with multi hazards in underground systems. These infrastructures are particularly susceptible to seismic events, fires, toxicity, and complex evacuation challenges. This research is driven by the need to develop an integrated understanding, design for prevention and protection strategies in order to keep these residual risks below the Acceptability Limit curve, and then ensuring the requested level of safety and the proper resilience of these underground infrastructures. It aims to contribute to the safety and resilience of underground systems across various settings by providing a comprehensive framework for quantitative multi-hazard risk assessment in underground systems.

The study of seismic geostatistics is primarily fundamental in assessing the hazard level posed by earthquakes to underground structures, which respond differently to seismic forces than surface buildings. Structural damage like collapse could be new hazard for the risk of the life of the exposed people in underground structures. Understanding the ground motion amplification and induced seismicity is essential for safeguarding these underground systems [1], [2]. One of the main goals of this dissertation work is to calculate the seismic hazard on a specific site with an innovative model based on seismic geostatistical analysis [3], [4].

The rock disturbed zone is unavoidable modification of the physical environment in underground workings, such as mining or civil engineering projects (e.g., the CERN collider, road tunnels). In a seismic environment, seismic action can affect both the rock disturbed zone and structural components. The seismic action must be taken into consideration to analyse both the consequences to users like underground facilities, such as road and rail tunnels or when there is a strategic activity, such as those at CERN, that cannot be disturbed or interrupted.

Mining activity is very similar to the one of construction of underground facilities, e.g., CERN and transport underground metropolitan facilities. To support mining design and planning, seismic geostatistical methodologies have been developed that account for the spatial characteristics of variables in the 4D rock environment, including dynamic effects over time. 4D seismic geostatistics includes the 3D isotropic and anisotropic behaviour of rocks, as well as the dynamic effect related to the time of arrival of PGA in different directions, which is influenced by the anisotropy of the damping and attenuation effects on seismic acceleration. These effects are determined by the varying damping properties of different rock types.

In order to reach maxisum level of PRA as descipred by Paté-Cornell [5], a deep inside is necessary when maximum level of safety is required because of strategic mission of the activity in underground. So, there is a major role of multi-hazard risk scenarios in underground infrastructure with a strategic mission. The most accurate modelling procedure must be used to characterise multi-hazard scenarios, with seismic geostatistical modelling taking into account the anisotropic damping power of the rocks, which affects the perceived stress level in the structure according to the different propagation directions of the seismic waves.

Fire hazards in underground systems also demand critical attention. The confined nature of these spaces, coupled with limited escape routes and the complexity of firefighting, necessitates a detailed exploration of fire dynamics and toxic gas propagation [6], [7].

Effective evacuation strategies are essential in underground systems as well, given the challenges posed by complex layouts and the potential for human behaviour in emergency situations. This research aims to explore and improve evacuation processes, ensuring the safety of individuals during critical accidents [8].

This research intends to bridge the gaps in existing multi-hazard risk assessment methodologies by integrating diverse disciplines. It aims to develop a holistic quantitative approach to multi-hazard risk framework, considering the interrelated nature of seismic, structural collapse and fire, along with evacuation challenges.

In managing these multiple hazards, the ALARP principle is a key concept [9], [10], [11], [12], [13], [14]. And it stands for “As Low As Reasonably Practicable”

and represents a balance in risk management between the severity of risks and the practicality of prevention and protection measures [15]. This principle plays an important role in underground environments, where achieving absolute safety against multiple hazards can be challenging. The application of Gu@larp in this context involves continuous assessment and management of risks to maintain them at a reasonably level.

1.2 Aim of study

How to model multi-hazard risk assessment: natural (seismic) and anthropogenic (structural collapse or fire; structural collapse and fire) hazards for underground system? This is the aim of the present dissertation.

In this dissertation, the term "risk assessment" has transitioned to become the preferred terminology, as it more clearly encompasses both "risk estimation" and "risk evaluation". It is important to note, however, that the foundation of this work lies in "Risk Analysis for Tunnels and Infrastructures from Multiple Hazards", which was developed during my master's degree in Transport Systems Engineering at Sapienza University of Rome (2018–2021), specifically within the course of Safety and Risk Analysis supervised by my tutor and advisor, Prof. Massimo Guarascio.

Over the past three years (2021-2024), my research has taken me through different institutions, starting at Sapienza University, continuing at CERN and at Lund University, each providing unique insights into these interconnected topics within the field of multi-hazard risk assessment. The logical path connecting these hazards must be carefully explained, as the key to effective risk assessment lies not just in measuring probabilities but in accurately identifying the correct scenarios.

Primarily, it is essential to address why seismicity, structural collapse, fire, and human behavior represent the central focus of this research. Seismic hazards pose a fundamental risk to underground facilities, particularly those with strategic missions like CERN, where any interruption can have significant implications. Understanding the interaction between seismic action and structural collapse is important to predicting how these environments will behave under stress. But the risk does not stop at structural failure. The cascading hazards of fire, often triggered by seismic events, and how people behave in these situations are equally important to model.

The core challenge lies in selecting the correct scenarios. The wrong scenario, no matter how accurate the probabilistic model, renders any quantitative risk assessment meaningless. As I progressed through my research from Sapienza to CERN and to Lund University, I repeatedly questioned how to ensure that the scenarios I was working with were the right ones. This realization has led to a fundamental conclusion: Scenario identification is more important than probability calculation. Without the right scenario, even the most precise numbers are meaningless. My journey over the past three years has been shaped by this question: *When can risk truly be measured, and how can we be sure that the numbers and indicators we rely on are not meaningless? This inquiry has significantly shaped my approach, forcing me to reconsider the foundational steps in risk assessment.* This question is at the heart of multi-hazard risk assessment, especially in environments where various hazards are interconnected.

This dissertation, therefore, focuses not only on probabilising hazards but also on ensuring that the scenarios used as the basis for calculations are correct. This is the first and most important step in the process of multi-hazard risk assessment. Without this, all quantitative risk assessments become meaningless.

Chapter 2 presents a state-of-the-art analysis while providing an overview of the key contents. The Chapter is divided into seven subsections whose content is described below.

The first subsection (2.1) examines seismicity, followed by 2.2, which discusses seismic geostatistics-4D analysis, and 2.3 explores structural collapses, including fragility assessments and Incremental Dynamic Analysis (IDA). Subsection 2.4 explores traditional fire safety in tunnels, focusing on factors influencing fire spread, including the role of toxic gases, heat, visibility, and Fractional Effective Dose (FED) in determining tenability limits, as well as the strategies necessary for safe evacuation. Following subsection 2.5 addressing the complexity of human behaviour during emergencies, dispelling misconceptions about panic, focusing on rational decision-making and the role of social identity, while considering the importance of pre-movement and response times in fires and earthquakes. The chapter further in subsection 2.6 delves into the concept of risk, risk analysis and risk assessment, discussing the evolution of risk concepts, societal influences on risk perception, and the ethical considerations involved in assessing and managing risk. Finally, subsection 2.7 explores methods for assessing these multi-hazard scenarios and complexities of multi-hazard risk

assessment, focusing on how interacting hazards can amplify risks. It also addresses the tendency of traditional approaches to underestimate total risk.

The underground environments are very sensible and vulnerable to accidents involving development of fire and structural collapse. And it is of great importance to analyse the risk of joint occurrences of different types of hazards, often referred to as multi-hazard scenarios. The latter Chapter 3 will be the main focus of this study through the theoretical and practical exploration. The mentioned multi-hazard scenarios are the ones that are taken into consideration when dealing with the underground activities. The major difference between civil and mining scenario is the fact that in the civil ones the shape and volume are constant along the time, whereas in the mining environment there is continuously changing scenario starting at time zero to the end of the activities creating the necessity of a dynamic estimation of hazard and risk conditions.

Risk assessment deals with the possible occurring scenarios and their related probabilities, combining the probability of occurrence with the potential consequences, such as fatalities, structural damages, and economic losses. The chapter begins by exploring theoretical aspects, the integration of Aristotelian logic and complex systems theory by Giorgio Parisi, then forming the foundation for scenario identification and modelling for multi-hazard scenarios. The discussion progresses into the application of these theories for mutually exclusive and non-mutually exclusive events, which are essential for accurately modelling physical and probabilistic interdependencies among seismic, structural, and fire-related hazards.

A key focus of the chapter is the ALARP (As Low As Reasonably Practicable) principle, where both philosophical and legal perspectives are considered. Important cases, such as Edwards v. National Coal Board and Marshall v. Gotham Co. Ltd., are analysed to illustrate the practical implications of ALARP.

In order to fully understand and apply the ALARP principle, it is essential to grasp key probabilistic concepts. The chapter introduces these concepts, from basic unconditional probabilities to more advanced concept like multi-conditional probability, which are important for assessing the probability of complex and cascading scenarios. The concept of Black Swan events is integrated into the ALARP framework, addressing the challenges posed by highly improbable but catastrophic risks.

Further, the chapter discusses key risk indicators such as Risk Quantum, Individual Risk, Societal Risk, and Expected Number of Fatalities, which are instrumental in evaluating the level of risk exposure. Risk Quantum, derived from forensic evaluations, is used to assess design scenarios with both deterministic and probabilistic aspects. The Risk Tolerability and Acceptability criteria are modelled according to these indicators, ensuring alignment with ethical principles and societal policy. These four indicators empower Rights-Holders and Duty-Holders to report hazards, prevent disasters, and implement remedial measures. Introduced Gu@larp method, which combines scenario quantic-modelling with the ALARP principle, offering a comprehensive approach to multi-hazard risk assessment framework emphasizing the need for accurate minimum necessary and sufficient scenario identification, and probability estimation.

Chapter 4 applies the multi-hazard risk assessment framework developed in this dissertation to a case study at CERN's TCC2/TDC2 facilities. The chapter begins with an overview of CERN's infrastructure and the unique challenges posed by its underground systems, particularly in relation to seismic gesostatistic-4D, structural, fire, and evacuation risks. It introduces a novel approach; multivariate seismic geostatistical-4D approach to seismic hazard analysis, utilising techniques like CoKriging to estimate seismic hazard curves specific to the region surrounding CERN. Special attention is given to the seismic event of 1 November 2022, where recorded data (Appendix A) is used to refine the hazard models and provide a clearer understanding of the seismic risks at the TDC2/TCC2 facilities.

The chapter continues with an in-depth structural analysis, presenting experimental campaigns, shaking table tests, and model calibration to assess the seismic vulnerability of the TCC2 and TDC2 facilities. This section also explores IDA, which was conducted at CERN to provide insights into structural response, while fragility assessments are performed to evaluate the probability of collapse during seismic events and seismic-induced fires.

Building on this multi-hazard perspective, the chapter then examines independent fire risk at CERN, using data from six FDS analyses conducted as part of the FIRIA methodology at CERN. The minimum necessary and sufficient number of fire scenarios are identified for TDC2 and TCC2, ranging from cable tray fires to compounded vehicle and magnet resin ignition. Given the limitations of historical fire accident data at CERN, fire frequencies are derived from comparable industrial settings to support probabilistic modelling. These selected

cases illustrate how both run and shutdown modes at TDC2 and TCC2 involve distinct ignition probabilities, equipment vulnerabilities and fire propagation pathways.

A detailed evacuation analysis is presented, incorporating performance-based design (PBD) methods to estimate potential fatalities. Human behaviour uncertainties are accounted for in the simulations, exploring the outcomes of different hazard combinations and evaluating safe egress in a multi-hazard context.

By applying the Gu@larp method and multi-hazard event tree analyses, this chapter establishes a holistic multi-hazard risk assessment framework that quantifies hazard progression, integrates human behaviours modelling, and ranks Risk Quantum to support decision-making for CERN's underground infrastructure.

Chapter 5 presents the summary and major conclusions of this dissertation. It also discusses the limitations of the study, highlights key lessons learned, and provides suggestions for future work.

1.3 Problem Statement

I acknowledge that conducting a multi-hazard risk assessment requires expertise in various fields to ensure thorough and rational research. Looking at each component of these fields, such as risk assessment, seismic assessment, structural engineering, fire safety and evacuation engineering, it is evident that there have been significant advancements as well as limitations in each area. The core problem addressed by this dissertation is the need for a comprehensive quantitative multi hazard risk assessment framework for underground systems. Such framework should be capable of addressing multiple hazards within complex systems, which are characterized by intricate interactions and dependencies among various components, leading to emergent behaviours that cannot be understood by analysing each hazard in isolation. Research in the fields mentioned above often treats these hazards in isolation, failing to consider the complex and interconnected nature of risks in underground environments. This oversight can lead to inadequate risk mitigation strategies, potentially compromising the safety and functionality of these crucial infrastructures. The challenges include:

1. Lack of integrated models that consider the compounded effects of seismic and fire hazards in underground systems. Unlike traditional above-ground structures, underground environments have unique spatial constraints.
2. Limited seismic data and site-specific complexities require advanced methodologies, such as geostatistical-4D, to accurately model local seismic hazard. Existing seismic hazard models often assume uniform conditions, which can lead to inaccuracies in highly heterogeneous underground environments like TCC2/TDC2. These complexities highlight the need for improved methods to ensure more precise hazard estimates, providing a reliable foundation for subsequent risk assessments.
3. Traditional seismic analyses often assume monolithic structures and overlook the localized failure modes such as block sliding, rocking, and partial collapse that occur in block-based underground systems like TCC2/TDC2 at CERN. Incorporating these discrete mechanisms into fragility analysis and probabilistic models is challenging, particularly when failures can trigger secondary hazards. This gap highlights the need for advanced discrete-element modelling and IDA-based fragility assessments capable of quantifying the likelihood and cascading potential of multi-hazard events in underground environments.
4. Interactions between multiple hazards are not well understood. For example, a seismic event can cause structural failure, which may lead to fires. The resulting collapse can obstruct evacuation paths, inflict damage on the infrastructure, and the smoke generated from these fires can hinder evacuation efforts and create additional hazards for occupants. This gap in knowledge limits the effectiveness of current risk evaluation strategies.
5. Inadequate evacuation strategies that do not account for the complexities and unique challenges posed by different types of hazards in confined underground environments. The confined spaces, limited escape routes, and potential for high occupant density require tailored approaches to ensure safe and efficient evacuations under multi-hazard conditions. These strategies heavily depend on various physiological and psychological factors. Together, these factors make it challenging to predict how individuals will behave during evacuations in multi-hazard situations like underground environments.
6. The ALARP principle, widely used in risk management, has not been thoroughly explored in the context of multi-hazard environments,

particularly those specific to underground systems. Its application needs to be re-evaluated to ensure that all risks are addressed effectively.

1.4 Objectives

The primary objectives of this research are:

1. To develop an integrated quantitative multi-hazard risk assessment framework for underground systems that considers both isolated and interdependent hazards.
2. To investigate the interaction and compounded effects of these hazards (seismic, structural and fire) on the safety and integrity of underground infrastructures. Employ advanced geostatistical methods for site-specific seismic hazard estimation, leverage IDA data, and integrate fragility-based analyses within a broader probabilistic framework to understand how multiple hazards can escalate into more severe accidents. This includes conducting dynamic simulations to visualize and predict the impact of multiple hazards and their potential to escalate into more severe accidents.
3. To propose and evaluate effective evacuation strategies taking into account human behaviour tailored to the unique challenges of underground environments under different hazard scenarios. This objective will involve the use of human behaviour modelling techniques and evacuation simulation software to develop performance-based design strategies.
4. To enhance the understanding and application of the Gu@larp mathematical model for ALARP principle in the context of multiple hazards in underground systems. Focusing on establishing quantifiable risk Acceptability and Tolerability criteria. This objective will involve utilising the Gu@larp model's methodologies for detailed risk quantification, including Risk Quantum, Individual Risk, Societal Risk, and Expected Number of Fatalities, tailored specifically to underground systems facing multiple hazards. The calculated Risk Design Line, derived from a minimum necessary and sufficient number of simulated probabilised hazard scenarios and impact assessments, acts as a crucial benchmark for determining acceptable, tolerable, and unacceptable levels of risk.

Through empirical research, case study at CERN, and the development of new models and methodologies, this dissertation aims to validate these methods, thereby contributing to the field of underground system safety. The goal is to establish a quantitative multi hazard risk assessment methodology, that is effective and efficient, for the existing and new underground systems to aid in the decision-making of the stakeholders in ensuring a maximum level of safety and minimum risk that are economical and ethical.

Chapter 2

Overview for Seismicity, Seismic Geostatistics-4D, Seismic Structural Collapse, Underground Fire, Underground Evacuation, The Evolution of Risk Concept and Multi Hazard Risk Assessment

2.1 Seismicity

Seismic activity can lead to significant fires, often exacerbated by the structural integrity of buildings and infrastructure. The interplay between seismic forces and structural components plays a significant role in inducing, triggering, developing and propagating these fires.

An earthquake is a natural event with an uncertain site and time of occurrence. The probability of an earthquake can only be measured and estimated as a measure of uncertainty. Primarily caused by the interaction of deep blocks of the Earth's crust (hypocentral zone) known as tectonic plates, an earthquake propagates upward to the ground (epicentral zone) and in the surroundings. These plates, through their extremely slow movements against each other, accumulate significant stress, leading to the build-up of elastic energy in the rocks. When this accumulated energy surpasses the critical resistance threshold of the rocks, sudden and massive movements along faults occur, producing a series of elastic waves called seismic waves (primary or volume waves), which propagate to the surface (R and L waves) and along it [16], [17], [18].

The increasing number of seismic stations established in the early 1900s revealed that earthquakes are not randomly (in the space-time) distributed but tend to occur along well-defined belts with a given return time (Figure 1 and Figure 2). It was not until the 1960s, with the development of plate tectonics theory, that the significance of these belts became evident. Earth’s surface is shaped by the slow movement of rigid tectonic plates, and earthquakes typically occur along plate boundaries where these plates interact, either by spreading apart at mid-oceanic ridges, colliding at trenches and subduction zones, or sliding past one another along strike-slip faults [19]. One of the most active seismic zones is the Pacific Ring of Fire, which surrounds the Pacific Ocean and is known for frequent earthquakes and volcanic activity. This area results from the subduction of oceanic plates beneath lighter continental plates, creating intense seismic and volcanic activities.

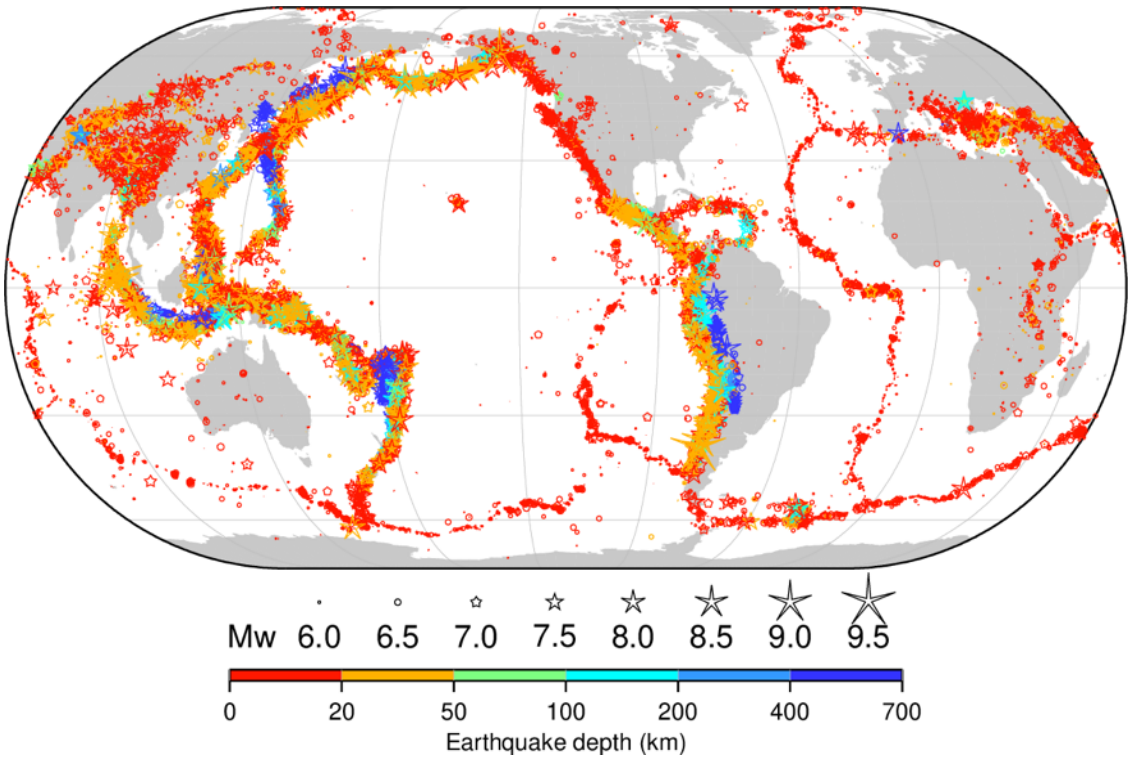

Figure 1: Map showing the distribution of approximately 71,100 earthquakes from 1904 to 2020 as listed in Version 11 of the ISC-GEM Catalogue. The source location for events with depths from 0 to 700 km are shown [20], [21], [22].

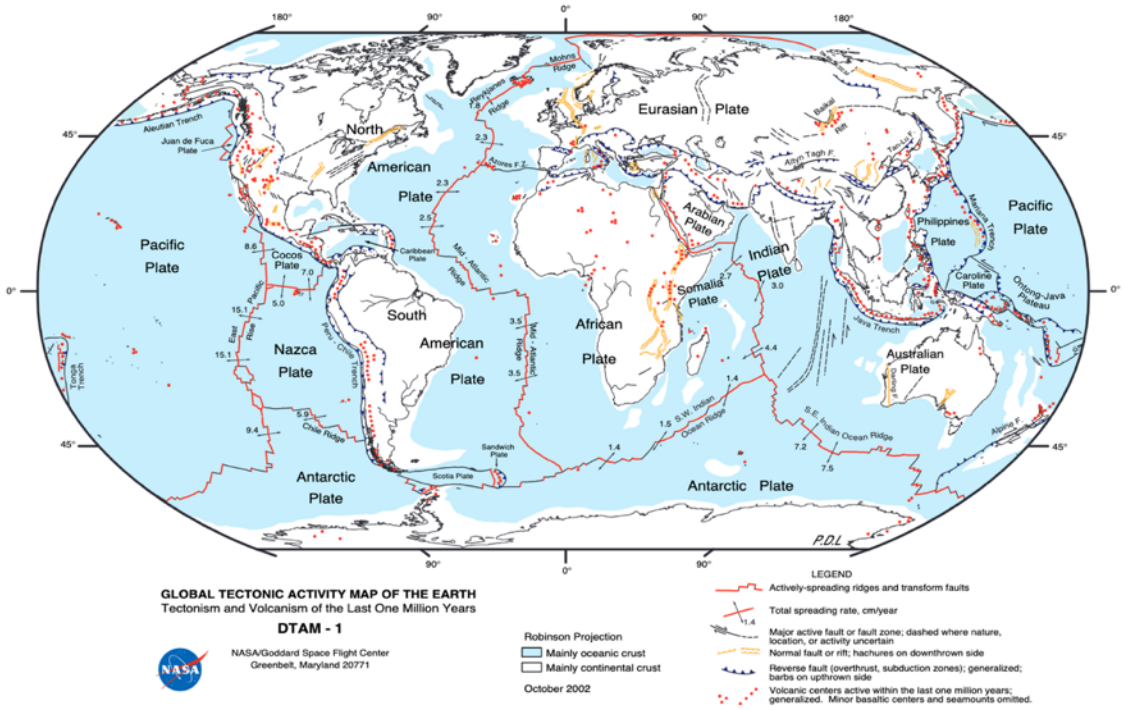

Figure 2: Earth's major tectonic plates. The map shows actively-spreading ridges, transform faults, total spreading rates (cm/year), and major fault zones, distinguishing between normal and reverse faults, as well as volcanic centres active within the last one million years [23], [24], [25].

In Europe, the Alpine-Himalayan Seismic Belt is one of the most significant tectonic regions [26], affecting parts of southern Europe, including the Alps, Apennines and the Mediterranean countries. This zone is characterised by the collision between the African Plate and the Eurasian Plate. The Hellenic Arc, Calabrian Arc and Apennine Mountains in Italy, for example, are key areas of seismic activity related to this plate convergence [27], [28], [29].

Moreover, the North Anatolian Fault in Turkey is one of the most active and well-known strike-slip faults in the world. It stretches across northern Turkey, running roughly 1,200 kilometres from the Aegean Sea in the west to the eastern borders of the country. This fault marks the boundary between the Anatolian Plate and the Eurasian Plate, where the two plates slide past each other in a horizontal motion known as a strike-slip fault [30], [31], [32].

This movement also explains the separation of continents, as first hypothesized by Alfred Wegener in 1912. Wegener proposed the ground-breaking theory of continental drift, which suggested that continents were once joined together in a single supercontinent called Pangaea. Over millions of years, Pangaea gradually broke apart, with its pieces drifting across the Earth's surface to form the continents as they are known today. Wegener's hypothesis was initially controversial, as it lacked a mechanism for how the continents moved, but the later discovery of seafloor spreading and plate tectonics in the 1960s provided the necessary explanation, confirming that tectonic plate movement drives continental drift [33], [34], [35].

As seismic waves travel/propagate through the Earth's layers, their speed of propagation and their directionality change depending on the density, discontinuity and elasticity of the rocks they propagate through. Higher density and elastic properties generally increase wave speed. Discontinuities, low density and poor elasticity create damping and attenuation and directionality change. The transition between layers with different properties can cause the waves to refract or reflect, creating complex wave paths that are not straight but curved. This phenomenon helps seismologists map the internal structure of the Earth.

A fault is a fracture or a zone of fractures between two blocks of rock, along which there has been relative movement (dislocation). This movement may occur suddenly, triggering an earthquake, or it may happen gradually over time, known as creep. When an earthquake occurs, the rock on one side of the fault

shifts (slip) relative to the rock on the other side. The fault surface can be oriented in different ways: it can be horizontal, vertical, or inclined.

To uniquely define a fault plane, two measurements are essential: strike and dip. The strike is the direction of the line formed by the intersection of the fault plane with the horizontal plane, measured as an angle (azimuth) relative to the north. The dip is the angle between the fault plane and the horizontal plane, indicating the steepness of the fault. These measurements are critical for understanding the geometry and kinematics of the fault and for assessing seismic hazards [36].

Faults are classified based on the direction of the relative movement of the rock blocks. According to the direction of the relative displacements occurring on the fault plane, faults can be categorized as dip-slip or strike-slip Figure 3.

- Dip-slip faults involve vertical movement along the fault plane and can be further classified into two types:
    - Normal faults occur in response to extensional stresses, where the hanging wall block moves downward relative to the footwall block. This type of faulting is common in regions undergoing crustal extension, such as rift valleys and mid-ocean ridges.
    - Reverse faults, also known as thrust faults, when the dip angle is shallow, form under compressional stresses. In this case, the hanging wall block moves upward relative to the footwall block. This type of faulting is typically found in regions of crustal compression, such as collision zones between tectonic plates.
- Strike-slip faults involve horizontal movement along the fault plane, parallel to the fault's strike. These faults form in response to shear stresses and can be classified into:
    - In right-lateral strike-slip faults, the block on the opposite side of the fault moves to the right.
    - In left-lateral strike-slip faults, the block on the opposite side of the fault moves to the left [18].

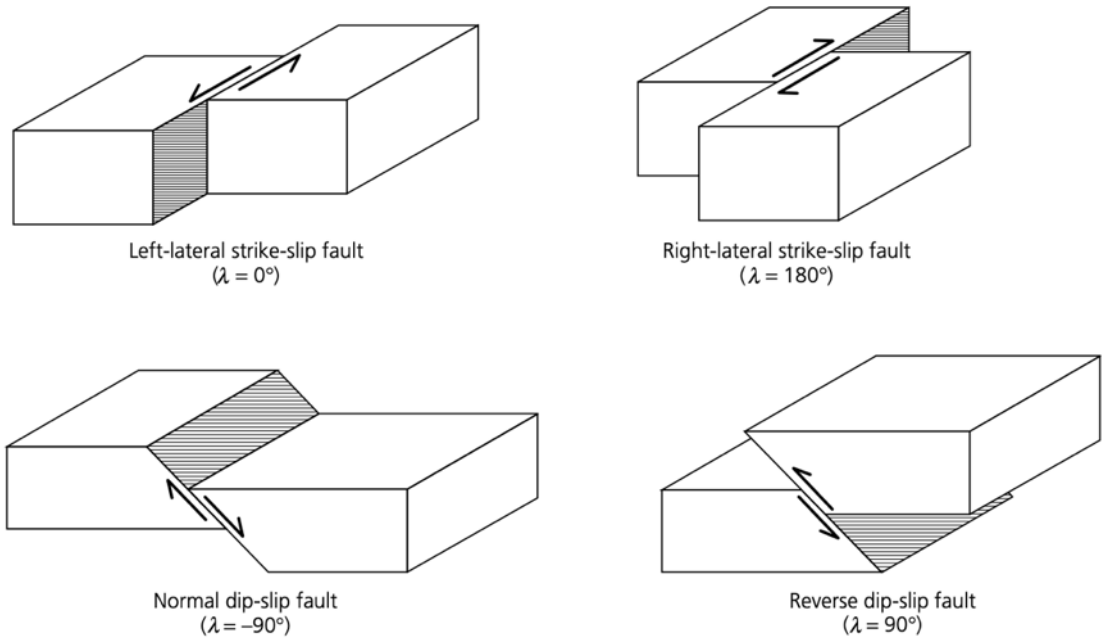

Figure 3: Basic types of faulting. Strike-slip motion can be either right- or left-lateral. Dip-slip faulting can occur as either reverse (thrust) or normal faulting [18].

The hypocentre of an earthquake is typically specified by its latitude, longitude, and depth below the Earth's surface (ground). The epicentre represents the surface projection of the hypocentre's coordinates, while the focal depth denotes the vertical depth below the ground (Figure 4). Seismic energy, released at the hypocentre, propagates as seismic waves through the Earth's layers, eventually reaching and affecting the surface [36]. The degree of energy dissipation during an earthquake is significantly influenced by the depth of the hypocentre. Deep-focus earthquakes, which occur at depths exceeding 300 kilometres, are characterized by the substantial attenuation of seismic wave energy as these waves propagate through the Earth's multiple geological layers. This attenuation process results in the dispersion of seismic energy over a wide area, leading to low-intensity tremors that can be felt across extensive regions. The energy loss in deep-focus earthquakes is attributed to the increased path length and the complex interaction with varying geological structures, which dissipate the seismic energy before it reaches the surface of ground [19].

In contrast, shallow-focus earthquakes, with focal depths of up to 25 kilometres, experience minimal energy dissipation due to the shorter distance and fewer geological obstacles encountered by the seismic waves. As a result, the energy released at the hypocentre cone remains relatively intact as it reaches the ground surface, causing high-intensity tremors confined to smaller, more localized areas. In these areas, the surface waves, originating from the hypocentre/epicentre cone,

are the more relevant component of the seismic action (Figure 4). The minimal attenuation in shallow-focus earthquakes means that the ground shaking is more intense and potentially more damaging, even though the initial energy release may be less than that of deeper earthquakes [18].

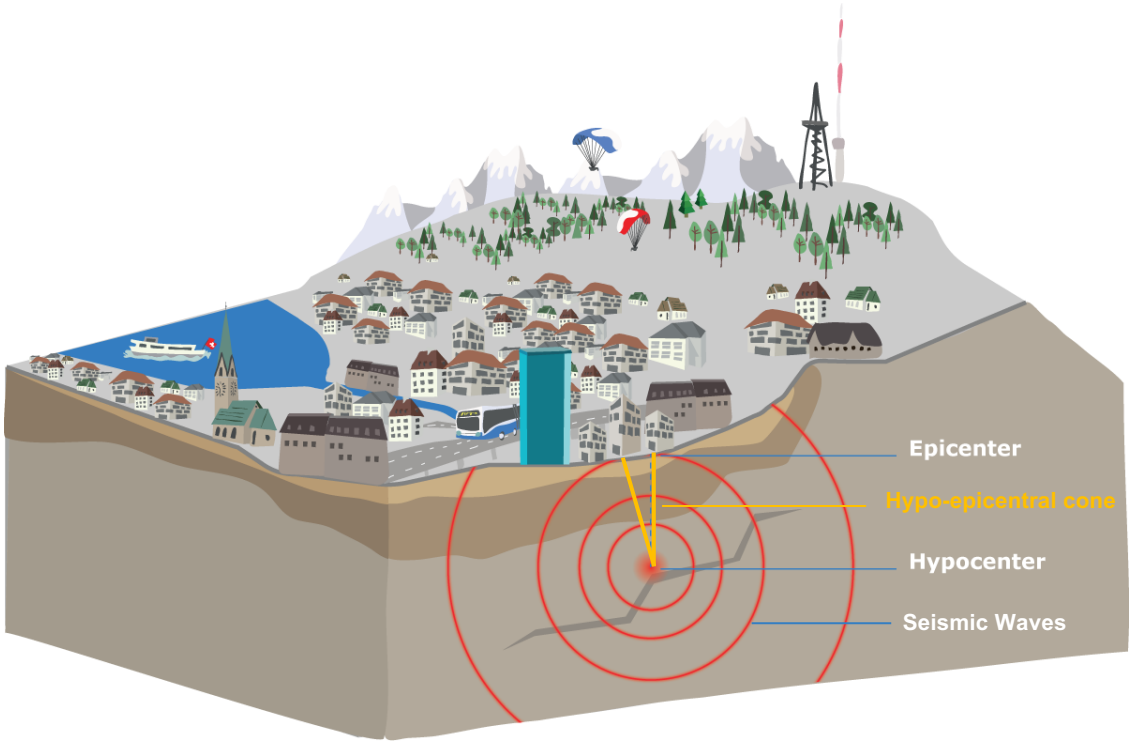

Figure 4: Adapted from ETH, the relationship between the epicentre and hypocentre during an earthquake [37].

With our current level of knowledge, earthquakes remain fundamentally unpredictable phenomena as far as exact location and moment of time occurrence is concerned. Seismogenetic zone is usually defined where return time of the epicentral acceleration is also estimated. While scientific research cannot precisely determine “when” an earthquake will occur, it can identify “where" seismic activity is more likely. Furthermore, it is possible to estimate the potential magnitude of earthquakes in specific regions. Modern building regulations, exemplified by Eurocode 8, are grounded in scientific research and have been demonstrated to effectively mitigate earthquake damage by implementing specific seismic regulations [38], [39].

The propagation of seismic waves from the hypocentre to the surface is influenced by various factors, including the characteristics of the seismic source, the fault rupture process, the stratification, and the geological properties of the ground. These factors determine waves with different characteristics. Seismic waves generated by an earthquake can be classified into two main types: volume

(body) waves, which travel/propagate through the Earth's interior, and surface waves, which travel/propagate along the Earth's surface Figure 5.

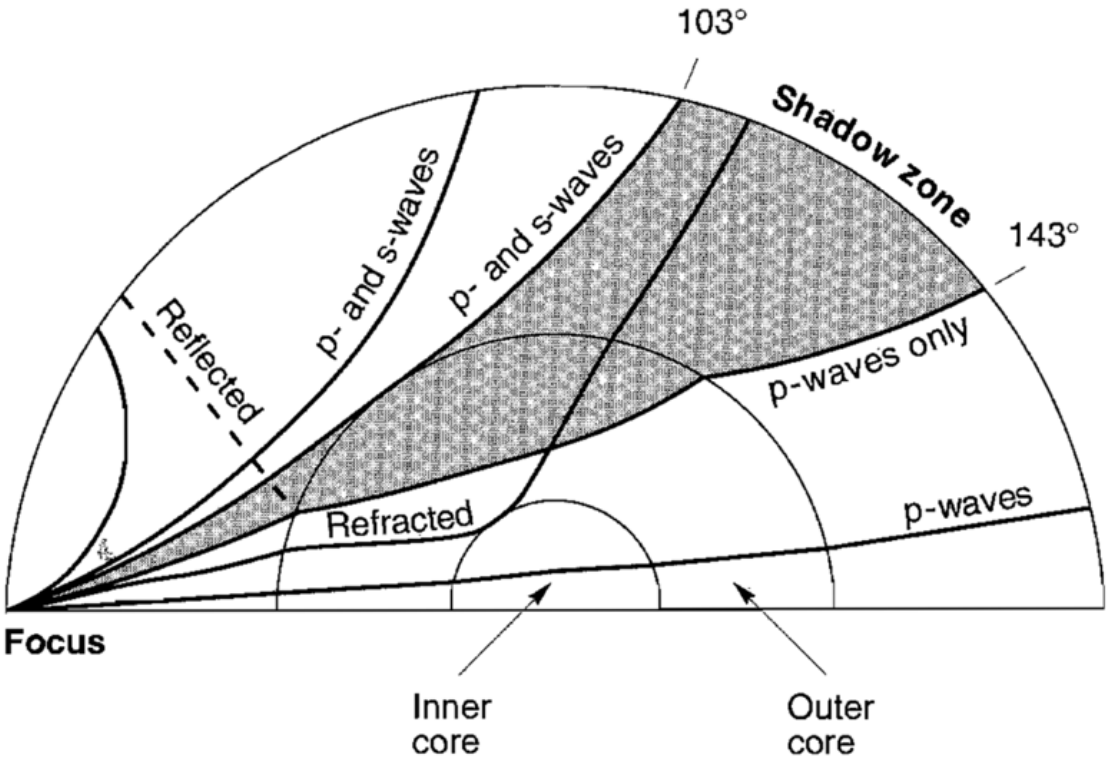

Figure 5: Seismic wave paths illustrating reflection and refraction of seismic waves from the source (focus) of the earthquake by the different layers of the earth. Note that S and P waves can reach the earth's surface between 0 and 103°, but the liquid nature of the outer core allows only P-waves to reach the surface between 143 and 180°. In the shadow zone between angles of 103 and 143°, only paths reflected from the inner core can reach the earth's surface [1].

There are two types of volume (body) waves: primary/pressure waves (P-waves) and secondary/shear waves (S-waves) (Figure 6).

Primary/pressure or longitudinal waves are the fastest type of seismic wave and hence the first to be detected by seismographs. P-waves cause the ground to compress and expand in the direction of travel/propagate, similar to sound waves in air. This compressional motion allows P-waves to travel/propagate through both solid and liquid layers of the Earth. The speed of P-waves varies depending on the density and elastic properties of the medium they travel/propagate through [19], [36].

Secondary/shear or transverse waves follow P-waves and travel at slower speeds. S-wave move the ground perpendicular to the direction of wave propagation, creating shear stress. Unlike P-waves, S-waves can only travel/propagate

through solid materials, as fluids do not support shear stresses. This property helps seismologists to understand the internal structure of the Earth, particularly the liquid outer core [18], [19].

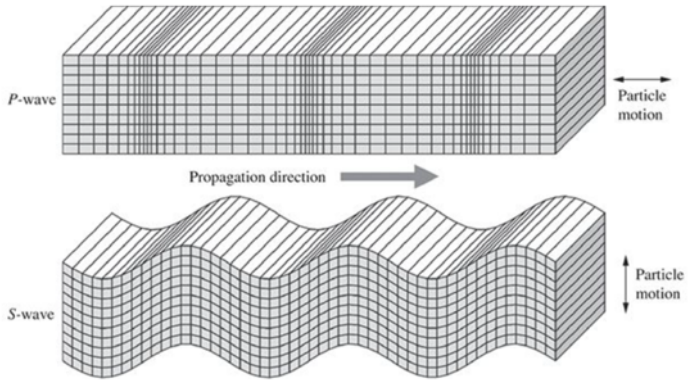

Figure 6: Displacements occurring from a harmonic plane P-wave (top) and S-wave (bottom) traveling horizontally across the page. S-wave propagation is pure shear with no volume change, whereas P waves involve both a volume change and shearing (change in shape) in the material. Strains are highly exaggerated compared to actual seismic strains in the Earth [19].

Surface waves travel along the Earth's surface and typically cause more damage than volume (body) waves due to their larger amplitudes and longer duration. They are slower than volume (body) waves and arrive after the P- and S-waves. There are two main types of surface waves: Rayleigh waves and Love waves (Figure 7).

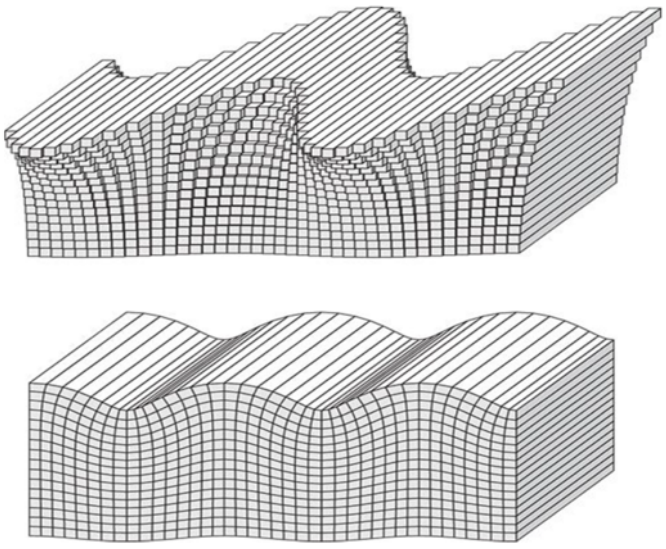

Figure 7: Fundamental Love (top) and Rayleigh (bottom) surface wave displacements (highly exaggerated) for horizontal propagation across the page. Love waves are purely

transverse motion, whereas Rayleigh waves contain both vertical and radial motion. In both cases, the wave amplitude decays strongly with depth [19].

Rayleigh waves roll along the ground in a wave-like motion, causing both vertical and horizontal ground movement in a retrograde elliptical motion. These waves cause the ground to move up and down, and side-to-side (like a ship on the sea wave) in the direction of wave propagation. They are named after Lord Rayleigh, who mathematically predicted their existence in 1885 [40].

Love waves move the ground horizontally, with shear motion perpendicular to the direction of wave propagation. Named after A.E.H. Love, who first described them in 1911, these waves cause horizontal shifting of the Earth's ground surface and are particularly destructive to structures built on the surface [41]. Love waves travel/propagate faster than Rayleigh waves and are the most damaging type of seismic wave [17], [18].

2.1.1 Peak Ground Acceleration

Peak Ground Acceleration (PGA) is the maximum value of ground acceleration measured during an earthquake. It represents the highest recorded value of acceleration (stress) at a specific location, measured in terms of g (acceleration due to gravity). PGA is a critical parameter in earthquake engineering and structural design as it helps define the seismic loads that buildings and infrastructure must withstand in seismic zones.

The importance of PGA in structural design cannot be overstated. It directly influences the seismic design codes and building standards that dictate the construction practices in earthquake-prone areas. By understanding the expected PGA values, engineers can design structures that are more resilient to seismic forces, thereby reducing the risk of structural failure and enhancing public safety [42].

In the literature, various empirical relationships and conversion laws have been developed to relate peak ground acceleration to macroseismic intensity scales. These scales, expressed in degrees using Roman numerals, are determined subjectively by comparing observed damage with predefined descriptions, most notably the 12-degree Mercalli–Cancani–Sieberg (MCS) scale [43], [44].

Seismic hazard is inherently linked to the random nature of earthquakes, the recurrence frequency of these events, and the geological characteristics of the area

where they occur. Assessing seismic hazard involves understanding these factors and quantifying the probability of different levels of ground shaking occurring at a specific location (in a given shaped area) and in a given time period. These two are parameters of Poisson discrete probability law which is applied in the space-time domain.

To this end, the temporal sequence of events that fall within a geographical area and belong to a seismic category (seismic intensity class) is represented by a point Poisson process. This assumption allows us to use the Poisson probability function to calculate the probability of seismic events occurring within any time interval. The statistical inference of the parameters λ of the Poisson distribution is performed for each seismic intensity category using the time series of seismic events. The numerical-statistical modelling of seismic events implies knowledge of the spatio-temporal location and intensity of each earthquake. The measurement of this latter seismic parameter is not always referred to a same intensity scale, i.e., derived from a direct physical measurement of seismic motion. Since 1935, the intensity of earthquakes has been expressed in Richter Magnitude (ML) defined as the ratio between the maximum displacement amplitude (mm) of soil oscillations measured by a standard instrument (seismogram) and the amplitude generated by a sample earthquake [45]. Richter assigns a magnitude 3 (ML = 3) to an earthquake that generates maximum ground amplitude (soil oscillations) of 1.0 mm as recorded by a seismograph located 100 kilometres from the earthquake's epicentre (Figure 8):

$$ML = \log_{10}\left(A/A_0\right) \tag{1}$$

where A is the maximum displacement amplitude of the seismic wave recorded by the seismograph (in millimetres), and A_0 is the maximum displacement of the reference earthquake. This makes the magnitude scale a dimensionless measure, enabling magnitudes calculated from different distances to the epicentre to be comparable [46].

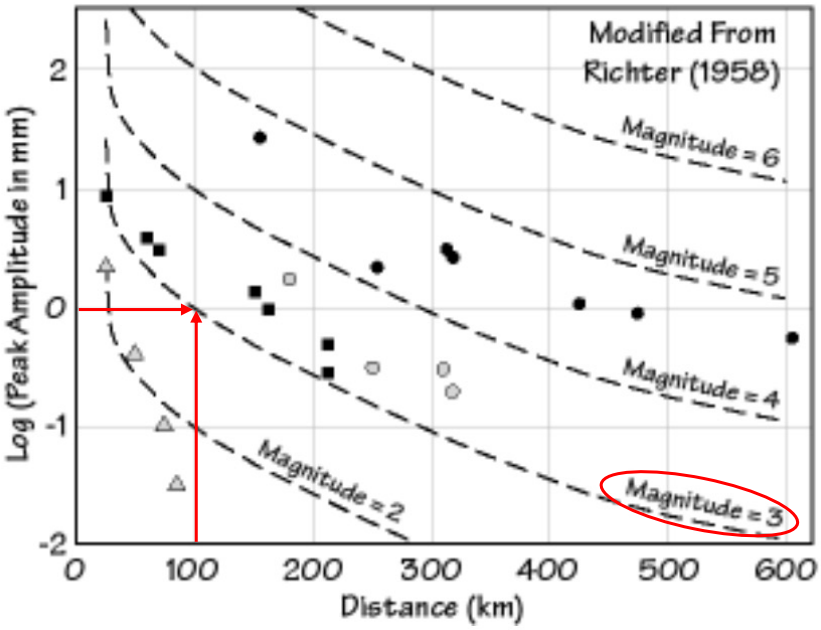

Figure 8: Charles Richter established his magnitude scale using data from observed earthquakes in Southern California in January 1932 [47]. This figure displays peak ground motions, with different symbols representing distinct earthquakes. The dashed lines illustrate how amplitude decreases with increasing distance from the epicentre.

The measurement of ML is not entirely independent of the geographical area, for example, the propagation speed of volume waves (P) and shear waves (S), and the damping of seismic motion at the ground depends on the mechanical characteristics and discontinuities of the rock formations traversed by the seismic waves (Figure 9).

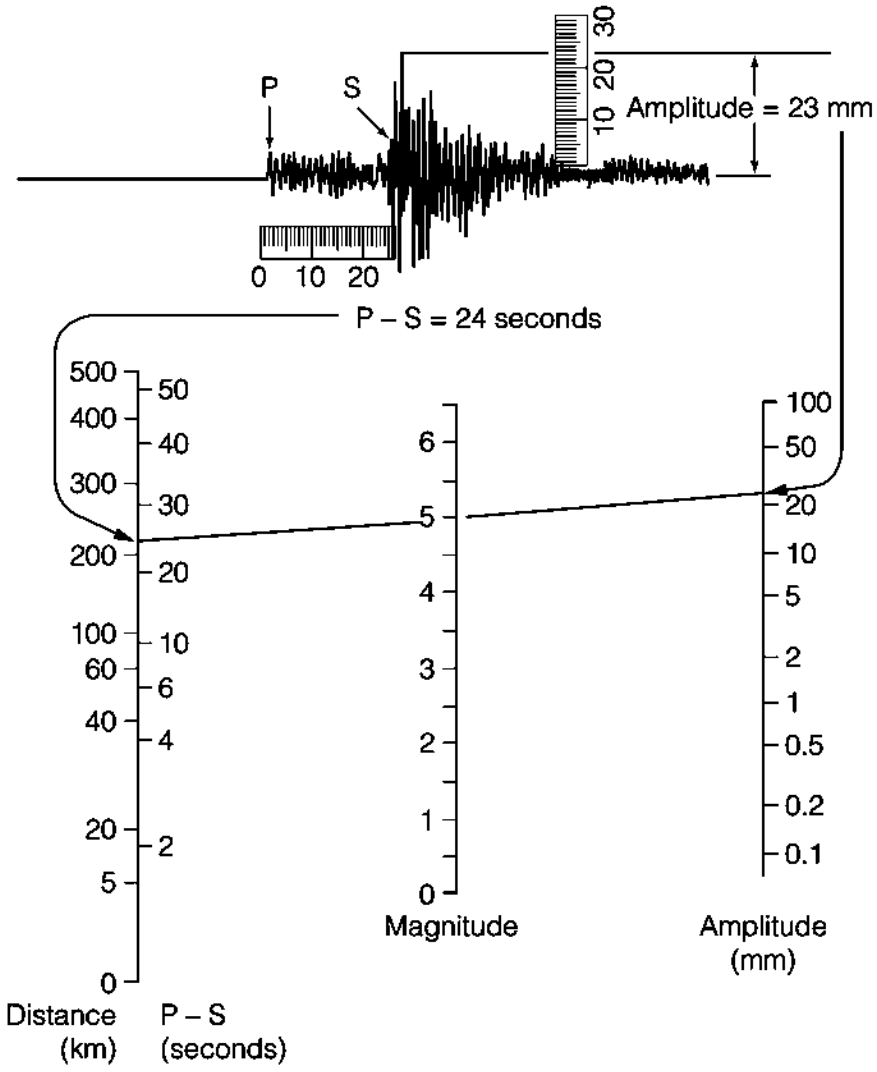

Figure 9: Relationship between earthquake magnitude and intensity. Seismogram demonstrating amplitude measurements used to calculate Richter Magnitude (ML) [48].

Compared to the qualitative assessment of earthquake intensity expressed in degrees of the MCS scale or degrees of the European Macroseismic Scale (EMS 1998) [49], [50], which is based on the assessment of the effects produced by seismic events on people, civil structures (damage to buildings), and the environment (geological and geomorphological effects), Richter Magnitude is a conventional indicator that nevertheless respects the order relations among the seismic ground movements produced by earthquakes. In recent decades, the accelerometric stations of seismic monitoring networks perform a space-time sampling of the ground motion around the epicentral zones of earthquakes. These measurements of the dynamic parameters of ground seismic motion at station points provide a direct measure of earthquake intensity in terms of maximum acceleration (PGA) in the epicentral area of the earthquakes.

PGA is specifically a measure of the maximum ground acceleration induced by an earthquake and recorded by accelerometers. It is a parameter for earthquake-resistant design because it directly correlates with the forces that structures must resist during seismic events [1].

2.1.2 Seismic Hazard Estimation Methods

One of the most famous aspects of PSHA is the ability to relate ground motion parameters like PGA to the probability of exceedance. This process allows decision-makers to assign specific return periods (e.g., a 100, 475-year event) to ground motion estimates, offering a quantifiable basis for seismic design codes. For example, the probability of an earthquake exceeding a certain PGA value in 100 years can be directly calculated through a probabilistic model. The process involves several steps:

Seismic Source Characterization: The first step in PSHA is to identify and characterize the seismic sources (faults or seismogenic zones) in the geographical area. This includes defining the location, geometry, and seismic potential of known fault lines, based on geological, geophysical, and historical data.

Magnitude-Frequency Relationship: The statistical recurrence relationship between earthquake frequency and magnitude is often described by the empirical Gutenberg-Richter law, which is represented as:

$$\log N(M) = a - bM \tag{2}$$

where N(M) is the cumulative number of earthquakes with a magnitude greater than or equal to M, a and b are empirical constants that vary with the tectonic environment.

The actual frequency distribution of seismic events in a specific geographical area is determined by the historical series of earthquakes that have occurred over the past hundreds of years, classified by seismic intensity class (for example, Magnitude or PGA). Seismic historical series are often available on the websites of national geophysical services. For each earthquake, the geographical coordinates and depth of the hypocentre, the date of the seismic event, and the intensity, expressed either in the EMS or the Richter Magnitude scale, are recorded.

Assessment of Seismic Hazard: Poisson model assumes a space-time independent seismic events and that the probability of an earthquake occurring

is stationary, meaning it does not change over space and time. This simplification makes Poisson processes particularly useful for long-term seismic hazard analysis, allowing us to calculate the probability of future seismic events based on past occurrences (seismic time series). The Poisson distribution is used to estimate the likelihood of a given number of earthquakes occurring within a specific period. The seismic hazard rate of a geographic area, defined as the average number of seismic events per year, allows us to calculate the probability of observing n earthquakes in any given year, using the formula (Poisson distribution function):

$$P(n; \lambda) = \frac{(\lambda t)^n}{n!} e^{-\lambda t} \tag{3}$$

where λ is the seismic hazard rate and $P(n; t; \lambda)$ is the probability of n events occurring within time period t. The seismic hazard rate is calculated for each seismic intensity class. The value $1/\lambda$ is the return period of future seismic events (average time interval between occurrences) in the investigated territory.

The λ parameter allows us to calculate the expected value $E(n) = \lambda \cdot t$ and the variance $VAR(n) = \lambda \cdot t$, respectively the average number of earthquakes and the variability in the occurrence of seismic events over time. The expected value gives us an average number of events in a specific time frame, while the variance measures the fluctuation around this average.

The probability $P(n \geq 1; t; \lambda)$ that at least one event will occur within a given period t can be calculated using the Poisson distribution function:

$$P(n \geq 1; \lambda) = 1 - e^{-\lambda t} \tag{4}$$

2.1.2.1 Seismicity Curve of a Territory

The application of the Poisson distribution function to seismic intensity classes defined on the time series of past earthquakes allows us to trace the seismicity curve of a territory:

$$P(PGA) = \sum_k P(PGA_k) = \sum_k (1 - e^{\lambda_k}) \tag{5}$$

where PGA is the epicentral intensity threshold expressed as ground acceleration of seismic motion, and $P(PGA_k)$ is the probability of occurrence at any point in the investigated region of one or more seismic events in the k-th intensity class.

The summation is carried out for all epicentral intensity classes PGA_k. The measurement of the seismicity of a territory can also be expressed as 1/P(PGA), which represents the average return period (in years) of seismic events with epicentral PGA greater than or equal to certain intensity thresholds.

2.1.2.2 Directional Attenuation of Seismic Ground Motion

The heterogeneous rock formations through which seismic waves travel/propagate cause irregular damping of the seismic motion. The different propagation speeds of seismic waves in these rock formations distort the geometry of the wavefronts, resulting in anisotropic directional damping of seismic motion (geometrical attenuation). Moreover, the varying mechanical characteristics of the rock formations generate further irregular local variations in the seismic motion, as part of the energy carried by the seismic waves is continuously and irregularly dissipated due to friction (anelastic damping).

Compared to the isotropic geographical predictive equations proposed and used over the last 40 years to plot seismic ground motion maps around the epicentral zone of an earthquake such as those by Campbell [51], [52], [53], [54], Boore et al.[55], Molas et al. [56], Sabetta et al. [57], Meslem et al. [58], and Irwansyah et al. [59], the multiparametric non-stationary geostatistical estimator proposed by Guarascio, Libertà et al. [4], [60] and Alakbarli et al. [3] introduces the following improvements to better predict seismic ground motion around epicentral zones:

- The directional anisotropy of propagation time and damping of seismic ground motion,
- The error function of the dynamic motion parameters, correlated with the heterogeneity and (undetectable) discontinuities of the rock formations traversed by seismic waves,
- The orography of the Earth's surface,
- The location of accelerometric stations in the seismic monitoring network around each point to be estimated.

The need for a more realistic model for estimating dynamic ground motion parameters (PGA, PGV, etc.) is justified by the presence, as detected in seismic monitoring data from the four largest earthquakes in Central Italy in 2016 [4] as well as the recent earthquake south of CERN on 1 November 2022 [3], [61], [62]:

- Directional anisotropy in the rate of ground motion attenuation,

- A local variability in dynamic ground motion parameters that is not entirely stochastic,
- A non-uniform geographical distribution of accelerometric stations, leading to smaller estimation errors the closer and more numerous the accelerometric stations are to the points being estimated.

The use of the geostatistical estimator implies that both the estimated value (a weighted average of the data recorded at sampling points around the point being estimated) and the variance of the estimation error depend not only on the distance of the point from the epicentral zone but also on:

- The heterogeneity of the rock formations, determined by the error function,
- The number and location of data points around each point to be estimated,
- The local morphology of the Earth's surface.

This represents a further improvement of the geostatistical estimator compared to the multiparametric logarithmic estimator proposed by Campbell [53].

The estimated PGA at the grid nodes is used to plot directional PGA damping profiles as a function of the epicentral distance in various directions. The directional damping profiles are discretized into steps, and the PGA value assigned to each step is calculated as the arithmetic mean of the PGA values of the grid nodes within the circular crowns that have a specified length and angular tolerance relative to the profile direction.

2.1.2.3 Seismic Hazard Curve

The seismicity of the territory (seismicity curve) and the directional attenuation profiles of seismic ground motion are used to trace the seismic hazard curves for any point within the investigated area. These hazard curves show the probabilities of ground motion accelerations perceived at the target site that are greater than or equal to the acceleration thresholds shown on the x-axis (Figure 55c).

It is important to note that variations in territorial seismicity around the target point (regionalization of seismic events) and anisotropic directional damping of seismic motion result in hazard values that depend both on the epicentral distance and direction. In fact, earthquakes of the same epicentral seismic intensity class have a higher probability of occurrence in the areas surrounding

the target point with higher seismicity and generate greater seismic ground motion (perceived PGA) at the target point if located in the direction of lower seismic damping. For operational purposes, the area around the target site is divided into circular cloves (circular sectors), and each clove (sector) is associated with a seismic hazard curve $H_k(PGA)$:

$$H_k(PGA) = \sum_i \frac{a_{k,i}(PGA)}{A_k} P_{k,i} = \sum_i \frac{a_{k,i}(PGA)}{A_k} (1-e^{-\lambda_{k,i}}) \quad (6)$$

where PGA is the perceived ground acceleration threshold at the target site, $a_{k,i}(PGA)$ is the area of the circular crowns with damped ground acceleration greater than or equal to PGA, generated by a seismic event of the i-th intensity class, inside the clove (sector) in the k-th direction. A_k is the area of the entire circular clove (circular sector) in the k-th direction, and $P_{k,i}$ is the probability that one or more seismic events of the i-th epicentral intensity class occur in a year within clove in the k-th direction.

The seismic hazard curve of a site can be used to calculate the probability of exceeding the limit state (P_{LS}) [63] of an infrastructure located at the site:

$$P_{LS} = \sum_k \int_0^{+\infty} P(LS \mid PGA) \frac{dH_k(PGA)}{dPGA} dPGA \quad (7)$$

where $P(LS \mid PGA)$ is the fragility for a certain limit state (LS), representing the probability of exceedance of a certain limit state for a given value of PGA, and $H_k(PGA)$ is the seismic hazard curve of the circular cloves (sectors) in the k-th direction.

A significant aspect of probabilistic methods is their ability to incorporate uncertainty. Uncertainties in seismic hazard analysis are broadly classified into two categories: aleatory and epistemic uncertainties [64].

Aleatory uncertainty refers to the inherent randomness of earthquake processes that cannot be reduced by improving knowledge or data.

Epistemic uncertainty, on the other hand, arises from limited knowledge or data availability and can potentially be reduced by better measurements or models.

Both types of uncertainty are factored into PSHA to produce a hazard curve, which represents the probability of exceeding different levels of ground motion at a site.

2.2 Seismic Geostatistics-4D analysis

Understanding seismic activity requires a comprehensive analysis of spatial and temporal data related to earthquakes. Geostatistics, a branch of statistics focusing on spatial or spatiotemporal datasets, offers valuable tools for such analyses. By applying geostatistical methods to geological and geophysical data, researchers can identify patterns, assess risks, and make predictions about the occurrence and intensity of seismic events.

The range of natural phenomena is extensive, encompassing both simple occurrences that manifest spatially and are characterized by a single variable, and more complex phenomena regulated by numerous variables that interact and are defined in both space and time. This inherent complexity and high variability pose significant challenges for deterministic methods used in characterizing such phenomena. Deterministic methods rely on mathematical models, which are not only intrinsically complex to construct but also require an accurate understanding of every defining parameter of the phenomenon and its spatial distribution. Even if these challenges could be overcome, deterministic methods are limited as they do not provide a means to quantify the error in estimating the value of a parameter outside the measurement points. Consequently, these methods fall short in offering insights into the accuracy of the performed estimations [65].

Conversely, spatial variability of quantities is generally not purely random. Typically, given two measurements at different locations, the closer they are, the more similar they tend to be, indicating a certain degree of correlation. Geostatistical tools capitalize on this spatial correlation, enabling the estimation of a quantity at an unknown measurement point based on the known values from surrounding points and their spatial distribution. When time is integrated into the analysis (4D), the evolution of seismic hazards can be captured, allowing for a dynamic understanding of risk. These tools provide significant improvements over deterministic models by allowing for less complex analysis and the prediction not only of the quantity but also of the associated estimation error at unknown points.

The initial foundations of geostatistical modelling were laid by Danie Krige, a South African mining engineer, in the 1950s. Krige applied statistical techniques to evaluate mineral resources, particularly gold and other metals, in South African deposits [66]. Later, Georges Matheron, another mining engineer and

statistician, formalized Krige's empirical work. Matheron defined the theoretical foundations of geostatistics and named the probabilistic estimation technique of a spatial quantity “krigeage” (translated to “kriging” in English) in honour of his South African colleague [67].

Geostatistics was initially developed for the purpose of estimating mineral deposits [68]. These methods are now widely used in various disciplines such as geology, hydrology, climatology, soil science, hydrogeology, geochemistry, oceanography, environmental hygiene, and agronomy [69], [70], [71]. The fundamental principle underlying geostatistical methodologies is the recognition that certain natural phenomena exhibit spatial continuity and geographic evolution, wherein the states of the phenomena at different locations are correlated based on their spatial proximity. These phenomena are categorized as “regionalized phenomena”, and the variables that describe them are referred to as “regionalized variables” (R.V.) [72]. The Theory of Regionalized Variables, along with probabilistic modelling methods developed by geostatisticians, provides an applicative solution. Guarascio, Libertà et al. [60], applied non-stationary geostatistics to map ground motion around the epicentral zones of the 2016 Central Italy earthquakes and assess the seismic risk of sites in the same geographical area. Similarly, Alakbarli et al. [3] applied the same method for seismic risk assessment at CERN, providing a representative evaluation of ground motion in the investigation domain.

In subsection 4.3.3, Kriging has been applied to estimate the PGA (seismic ground acceleration) at points forming a regular grid covering the entire investigation domain around CERN, providing an accurate and representative assessment of seismic risks.

2.3 Seismic Collapse of Structure

Seismic collapse is a catastrophic event where a structure fails due to the intense forces generated by an earthquake. This collapse can result in significant loss of life and property, and understanding the factors that contribute to such failures is critical for improving building designs and construction practices. Seismic forces result from the sudden release of energy in the Earth's crust, causing ground shaking and displacement. These forces significantly impact the structural response of buildings and infrastructure, influencing their performance during earthquakes. The response of structures to seismic forces is influenced by several factors.

First, the magnitude and duration of seismic events play an important role in determining the level of stress experienced by structures. Larger earthquakes with longer durations generally cause more significant damage due to the sustained and intense shaking they induce. The second factor is the frequency content of seismic waves. The range of frequencies contained in these waves influences how different structures respond. Buildings have natural frequencies, and if the frequencies of the earthquake match these natural frequencies, resonance can occur. Resonance amplifies the structural response, leading to increased stress and potential damage. Finally, the direction of seismic forces is a significant consideration. Seismic waves can impact structures from various directions, and the orientation of the building relative to these forces affects the stress distribution. Depending on the building's design and orientation, different degrees of stress are induced, which can lead to varied damage patterns and structural performance during an earthquake [1], [73], [74].

In recent decades, the seismic performance of underground structures has been a subject of extensive study, with numerous researchers contributing valuable insights [2], [75], [76], [77], [78], [79], [80], [81], [82], [83]. Although these structures generally exhibit superior behaviour compared to surface structures during seismic events, there have been notable instances of severe damage documented in the literature. A particularly significant example is the collapse of the Daikai metro station during the Kobe earthquake in Japan in 1995 (Figure 10). This collapse resulted from the failure of the central columns, which had been designed solely to resist vertical loads [75], [83]

The magnitude 8.0 earthquake that occurred in Wenchuan, China, in 2008, caused extensive damage to many mountain tunnels along the Dujiangyan to Wenchuan highway (Figure 11). The portals of these tunnels, located on steep slopes of weathered rock, were damaged by avalanches and rock falls, rendering some of them impassable. Observed damage included cracking, fracturing, and dislocation of the tunnel lining, as well as heaving and cracking of the invert, leading to transverse fractures of the ground, uplift, tensile fracturing, and bulging. Beyond structural damage, the earthquake had a devastating human toll, with 87,000 deaths and missing persons, and an estimated economic loss of 845 billion Yuan [84].

Figure 10: Collapse of the Daikai subway station during the 1995 Kobe earthquake: (left) settlement of the overlaying roadway caused by the subway collapse, (right) collapse of the central columns of the station [76].

Figure 11: Collapse of the Longxi tunnel during the 2008 Wenchuan earthquake: (left) collapse at the eastern portal of the tunnel, (right) collapse of the lining section at its crossing with a fault [76].

Historical data and research have revealed that the vulnerability of underground structures to seismic events is influenced by various factors, including construction methods and geological conditions. The depth at which an underground structure is built significantly affects its seismic performance [76]. Deep underground structures, typically constructed in rock, benefit from the damping effect of the surrounding rock mass, which reduces the amplitude of seismic waves and lowers the seismic forces acting on the structure. This natural buffer absorbs and attenuates seismic energy, diminishing the intensity of ground motion that reaches the structure. As a result, deep underground structures generally perform better during seismic events compared to their shallow counterparts. In contrast, shallow underground structures, especially those constructed in soft soil, are more vulnerable to seismic activity due to the lack of such damping effects. Additionally, structures built using the cut and

cover method tend to have increased seismic vulnerability. However, some of these shallow structures, when designed with proper seismic design considerations, have demonstrated good behaviour even during strong earthquakes [85]. The stable geological conditions typically found at greater depths further enhance the performance of deep structures, as they are less likely to experience significant ground deformations and instabilities that can exacerbate seismic impacts.

Advancements in seismic design methodologies and tools have enhanced our ability to predict and mitigate seismic damage to structures. One such tool is the development of fragility curves, which represent the probability of reaching or exceeding different damage states given a certain level of seismic intensity (Subsections 2.3.1.1 and 2.3.1.2). These curves are constructed based on empirical data and numerical simulations, providing valuable insights into the expected performance of underground structures under varying seismic conditions. Integrating fragility curves with site-specific seismic hazard data enables engineers to perform probabilistic risk assessments, estimate the likelihood of different damage levels, and make informed decisions about design and retrofitting measures.

2.3.1 Collapse Risk

Collapse risk assessment involves combining information about the seismic hazard at the site with the behaviour of the structure under seismic loading.

Seismic hazard refers to the probability of experiencing earthquake-induced ground shaking at a specific site. This is characterized by a seismic hazard curve, which represents the relationship between the ground motion intensity and its annual exceedance probability. Intensity measures (IM) are parameters used to describe the level of ground motion shaking.

This risk is influenced by various factors, including the structural design, material properties, construction quality, and the characteristics of the seismic event. Assessing collapse risk involves both deterministic and probabilistic approaches to account for uncertainties in seismic demands and structural capacities [86], [87], [88], [89].

Deterministic methods, which focus on the worst-case scenarios, involve numerical modelling of source rupture processes and evaluation of the maximum credible earthquake (MCE) for specific seismic zones. These methods

are useful in situations where infrastructure is designed to withstand extreme seismic events [90].

Probabilistic seismic hazard analysis (PSHA), which is the most widely used method today first introduced by C. Allin Cornell [91], allows for a more comprehensive view of uncertainty. PSHA offers a statistical perspective by associating probabilities with different levels of seismic activity [92].

Conceptually, collapse risk could be assessed by observing a structure over thousands of years and counting the number of collapses, assuming immediate repairs. However, this approach is impractical. Alternatively, creating an analytical model subjected to historical ground motions recorded over a long period is also not feasible due to the limited duration of recorded seismic data. Therefore, practical methodologies involve probabilistic approaches that integrate structural responses to various ground motions with their expected frequencies [93].

A practical approach to collapse risk assessment involves the integration of seismic hazard information with structural behaviour. An IM is typically used to quantify the seismic hazard. The structural response is characterized by conducting IDA on the structure using various ground motions at different intensity levels [94], [95], [96], [97]. By analysing these results, a collapse fragility curve can be developed, showing the probability of collapse as a function of ground motion intensity [98]. The final step in collapse risk assessment involves combining the seismic hazard curve with the collapse fragility curve to compute the annual rate of collapse, which indicates the expected frequency of structural collapse per year [99].

2.3.1.1 Fragility Analysis

Fragility analysis is used to estimate the probability that a structure will reach or exceed a certain damage state given a specific level of seismic intensity. Fragility curves are derived from the statistical evaluation of the results of numerical analyses carried out on structural models. These curves plot the probability of failure against seismic intensity measures, providing a clear visualization of a structure's vulnerability under different seismic conditions. For large-scale fragility analyses, demand and capacity can be determined using analytical methods like IDA [98].

2.3.1.2 Incremental Dynamic Analysis (IDA)

With the accumulation of experience and ongoing efforts of researchers, structural analysis methods have continually developed and improved. These methods have evolved from static analysis to dynamic analysis, and from linear to nonlinear analysis. Currently, the most commonly used analysis methods for the seismic design of structures include the static pushover analysis (SPO) [100] method and the IDA method [94], [95], [97].

IDA is one of the techniques for performing fragility analysis. It involves subjecting a structural model to a suite of ground motions of increasing intensity until the structure reaches collapse. This method provides a detailed understanding of how the structure responds to varying levels of seismic demand. IDA results are used to develop fragility curves, which illustrate the probability of exceeding different damage states, including collapse at various intensity levels.

2.4 Underground Fire

Traditionally, fire safety in underground environments is linked to protective measures such as ventilation, lighting, communication, and evacuation systems, aimed at ensuring visibility and breathability for the time needed for users to reach a safe place. The fire load in these environments is predominantly attributable to various hazards present within the system, including cable trays, equipment, infrastructure components, vehicles and any transported goods or hazardous materials. In this context, attention has been focused on evaluating these hazards as elements of direct-induced hazard and related scenarios.

The dynamics of underground fires involve intricate and powerful interactions between the fire and its surrounding environment, making them uniquely challenging to manage and study [101], [102]. Unlike open fires or compartment fires, where environmental conditions or large spaces may not significantly influence fire behaviour, underground fires are heavily impacted by the underground's physical characteristics and design. These characteristics include the length, cross-sectional geometry, materials used in construction, ventilation systems, protection systems and the presence of hazardous materials [102].

The occurrence of fire in an underground is a rare event, however, its potential severity necessitates thorough investigation. An underground fire can develop

into a critical event characterized by the rapid spread and large size of the fire [101]. Factors influencing the development of such fires include vehicle type, hazardous materials present, airflow conditions within the tunnel, the performance of fire protection systems, and the structural safety features of the tunnel which can contribute to a high heat release rate (HRR).

Materials used in the construction of tunnels, such as concrete, steel, or fire-retardant linings, can impact how heat is absorbed and dissipated. These materials must be chosen carefully to ensure they can withstand high temperatures and provide adequate protection during a fire event. Flashover conditions, as conventionally understood, are rarely met in tunnel environments. The predominant longitudinal dimension of tunnels hinders the traditional build-up of conditions necessary for flashover, due to heat losses through the tunnel walls, the absence of containment for hot gases, and the limited availability of fuel relative to the large volume of the tunnel [102]. Instead, tunnels can find themselves in an under-ventilated situation when there's an excess release of fuel, leading to all available oxygen being consumed, leaving behind a surplus of unburned fuel. The dynamics of ventilation in tunnels revealing that natural ventilation provides sufficient oxygen for a fuel-controlled fire, whereas longitudinal ventilation continually supplies oxygen, supporting ongoing combustion (Figure 12). Experimental findings underscored that under-ventilated situations in tunnels are uncommon.

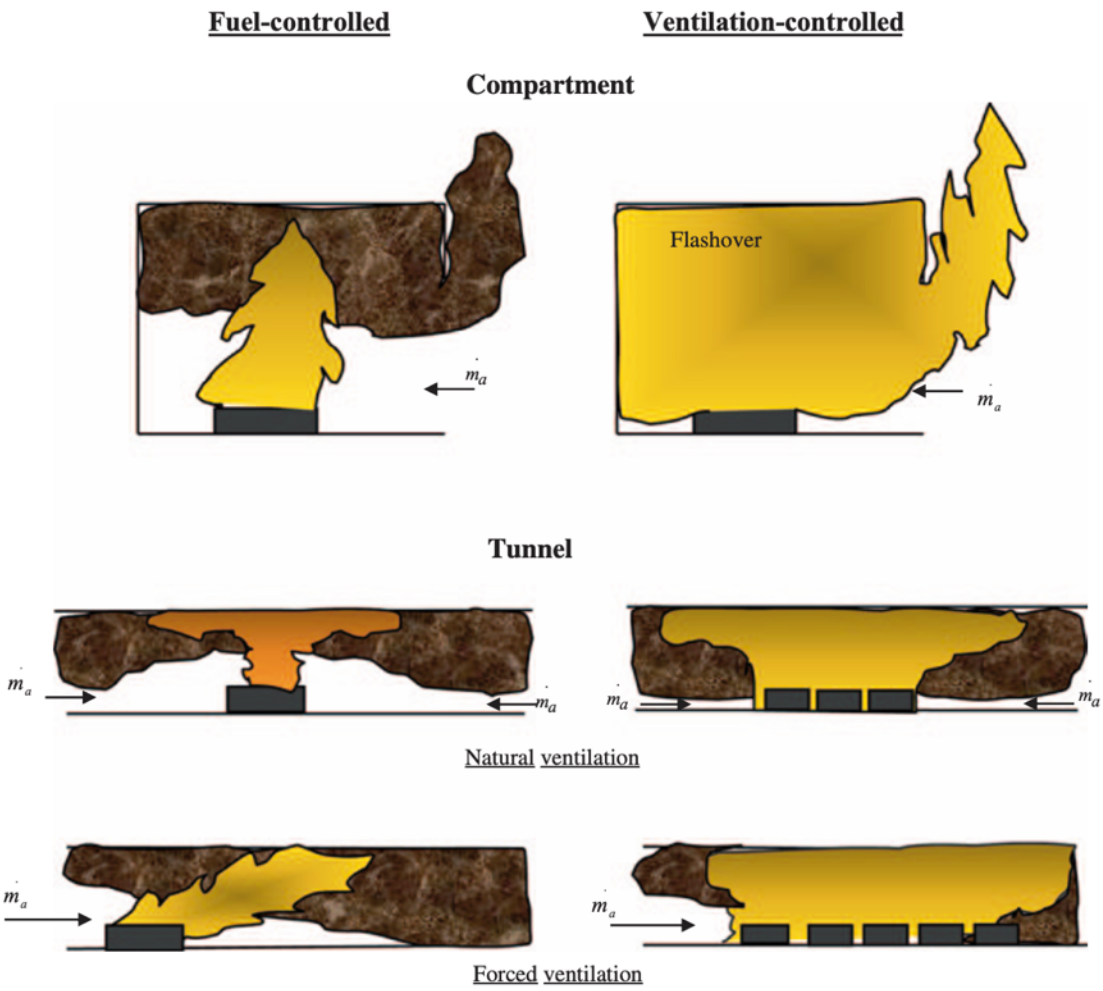

Figure 12: Fuel-controlled (left-side) and ventilation-controlled fires in a compartment and a tunnel (right-side) with natural draught (middle) and forced ventilation (lower), respectively. The arrows indicate the flow of fresh air [102].

Underground fire scenarios can be categorized based on three primary controls: ventilation control, fuel control and vitiation control.

1. Ventilation control occurs when the available oxygen supply limits combustion. These scenarios, often described as under-ventilated, fuel-rich, or oxygen-starved, happen when there is not enough oxygen to combust all the fuel present.
2. Fuel control occurs when the availability of fuel limits combustion. These scenarios are also described as well-ventilated, over-ventilated, oxygen-rich, or fuel-lean. In these cases, there is sufficient oxygen to combust all the available fuel vapours.
3. Vitiation control refers to the depletion of oxygen in a confined space, significantly altering fire dynamics. This situation arises when oxygen

levels are depleted due to the confined nature of the space, which affects how the fire behaves.

Given the intricate relationship between ventilation, fuel and vitiation controls, ventilation plays an important role in determining the spread of smoke, toxic gases, and heat in underground environments.

The dynamics of ventilation in tunnel fires are multifaceted, influenced by a range of factors including the type of ventilation (natural or mechanical), tunnel geometry, fire location, and external environmental conditions. These factors collectively determine the behaviour of smoke and heat, influencing the safety and effectiveness of evacuation and firefighting operations. Ventilation, traditionally defined as the circulation of air, encompasses a range of methods that facilitate the movement of air within an environment. Importantly, this concept is not limited to mechanical interventions such as fans. Natural ventilation, which relies on passive means like pressure differentials and natural airflow, equally qualifies as a form of ventilation. Effective air circulation can be achieved through both mechanical and natural methods.

The impact of ventilation on tunnel fires can be both beneficial and detrimental, depending on how it is managed. Natural ventilation, which relies on ambient pressure differences and wind flow, can inadvertently contribute to the spread of fire if not carefully controlled. For instance, recirculated air can reintroduce oxygen into the fire zone, thereby increasing the HRR (Figure 12). While natural ventilation offers the advantage of lower operational costs and simpler infrastructure, its effectiveness is highly variable and depends on external factors such as wind direction, atmospheric pressure, and temperature gradients.

Conversely, mechanical ventilation systems (Longitudinal, Transverse/Semi-Transverse systems) are specifically designed to control the movement of air and smoke within tunnels. Longitudinal ventilation systems use jet fans or other mechanical means to create a unidirectional flow of air along the length of the tunnel. This is critical in preventing backlayering, a phenomenon where smoke flows against the direction of the intended airflow, moving back toward the fire source. The prevention of backlayering is governed by the concept of critical velocity, which is the minimum airspeed required to stop smoke from reversing its flow direction. Achieving and maintaining this critical velocity is essential for ensuring that smoke is kept away from evacuation routes, thereby protecting

tunnel occupants and allowing emergency responders to operate more effectively.

However, mechanical ventilation systems also present certain challenges. While they are effective in removing smoke and reducing toxicity levels, the introduction of fresh air can disrupt the stratification of smoke layers. Stratification refers to the layering of smoke according to temperature, with hotter, less dense smoke remaining at higher levels while cooler, denser smoke descends. When fresh air is introduced, particularly in the form of high-velocity jets, it can create turbulence that mixes these layers, leading to a more homogenous smoke environment that reduces visibility across the entire tunnel cross-section. This can significantly impair the ability of occupants to find safe evacuation routes and may complicate firefighting efforts.

The behaviour of smoke within tunnels is highly dependent on the velocity of airflow. Depending on the air velocity, smoke can behave in distinct ways, leading to different patterns of stratification (Figure 13):

a) **Very Low Air Velocity (0–0.5 m/s):** In conditions where the airflow in the tunnel is almost non-existent, the smoke from the fire tends to rise due to its heat and lower density compared to the surrounding air. Upon reaching the ceiling, the smoke spreads horizontally, forming a dense layer near the top of the tunnel. Below this layer, the air can remain relatively clear because the smoke is not being forced downward. Near the tunnel exits, pressure differences cause the smoke to swirl and mix as it seeks an escape route. As this dense layer lowers, it can increase the concentration of toxic gases at breathing height, exacerbating the dangers faced by occupants. Additionally, as the smoke recirculates back to the fire, oxygen levels within the tunnel may decrease, leading to vitiation. Although this might initially seem to reduce the fire's intensity, the environment can become increasingly hazardous due to the build-up of unburned fuel gases and other toxic by-products.
b) **Low or No Forced Air Velocity (0–1 m/s):** With slightly higher air velocity, the smoke still rises and accumulates near the ceiling. However, it begins to move slowly along the length of the tunnel. This results in a thick, stratified smoke layer above, with clearer air below. In some cases, a backlayering can occur, where smoke starts to flow back towards the fire source because the airflow is not strong enough to push it all out of the tunnel.

c) **Moderate Forced Air Velocity (1–3 m/s):** At this velocity range, the smoke is actively pushed toward the tunnel's exit. Although it still rises to the ceiling, the airflow carries it forward more rapidly. This leads to a more mixed environment where the smoke is dispersed throughout the tunnel rather than forming distinct layers. Consequently, the stratification is less pronounced, and while the smoke is spread more evenly, it results in a generally smoky atmosphere that is less concentrated near the ceiling.

d) **High Forced Air Velocity (> 3 m/s):** When the airflow is very strong, the typical layering of smoke downstream in the tunnel is eliminated. The fast-moving air prevents the smoke from settling into layers, effectively dispersing it throughout the tunnel. Additionally, backlayering does not occur, meaning the smoke does not flow back toward the fire source. This ensures that the smoke is rapidly moved out of the tunnel, reducing the overall concentration and improving visibility.

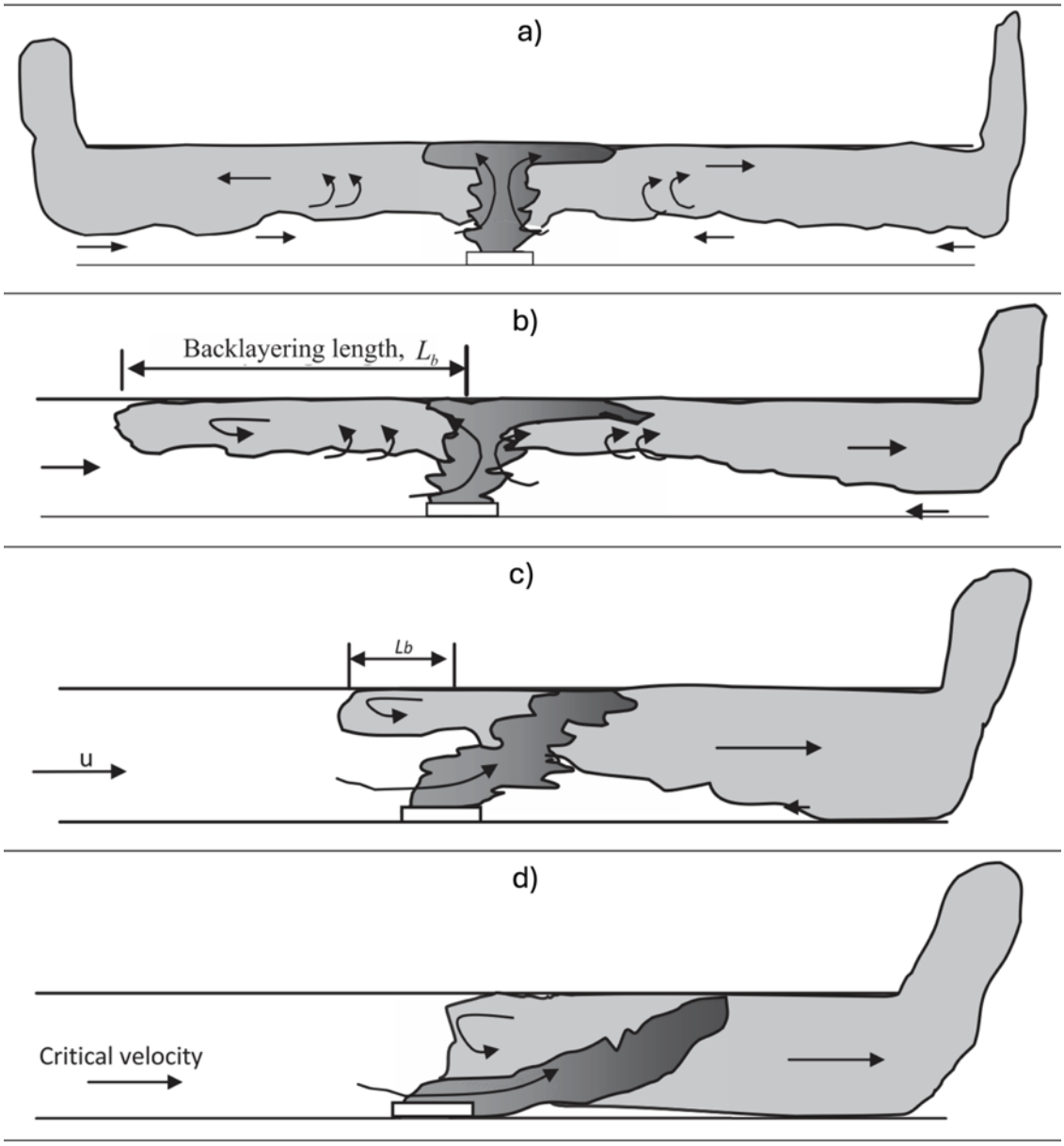

Figure 13: A sketch showing the different types of smoke stratification in a tunnel under various air velocity conditions: (a) Very Low Air Velocity (0–0.5 m/s) with a dense smoke layer near the ceiling; (b) Low Air Velocity (1 m/s) where the smoke layer shows some backlayering toward the fire; (c) Moderate Air Velocity with mixed smoke and reduced layering; and (d) High Air Velocity, where the flow velocity is larger than the critical flow velocity (u_c), resulting in dispersed smoke and preventing layering or backlayering [102].

2.4.1 Tenability Limits

Fire accidents in tunnels are extensively studied by researchers due to their severe consequences on human safety. Without proper emergency strategies, tunnel fires can result in significant loss of life. According to Purser and

McAllister [103], injuries and fatalities due to fires can be categorized into three main types: heat stroke, body surface burns, and respiratory tract burns.

Purser's study [104] specifically highlights the effects of fire products on escape capability in primates and human fire victims. His research identifies two main mechanisms of toxicity: narcosis (asphyxia) and irritancy. Narcotic effects are primarily caused by common asphyxiant gases like CO, HCN, low oxygen levels, and CO2. These effects can be predicted to a reasonable degree using existing knowledge. Irritant effects, caused by a variety of combustion products, impair escape capability by causing severe sensory irritation and respiratory distress. It is important to consider both narcotic and irritant effects when assessing the hazards posed by fire products.

When evaluating the threats to human safety in underground fires, several critical factors must be considered, as they directly influence the severity of the consequences. These factors include high temperature, toxic gases, lack of oxygen, and low visibility. The ability to survive and escape from a tunnel fire depends on whether the environment remains within certain tenability limits.

2.4.1.1 High Temperature

The exposure to high temperatures during a fire poses significant threats to human safety, primarily through mechanisms such as hyperthermia, skin burns, and respiratory tract injuries. The impact of high temperatures on human physiology has been extensively studied, with recent research further elucidating the thresholds at which these injuries occur and their implications for survival in fire environments.

2.4.1.1.1 Hyperthermia

Hyperthermia is a condition characterized by an abnormally high body temperature, typically resulting from prolonged exposure to heat. The human body's thermoregulatory mechanisms can maintain homeostasis up to a core temperature of approximately 38°C, however, exposure to external heat sources in excess of this can lead to hyperthermia, a potentially fatal condition. The hyperthermia begins with symptoms of heat exhaustion such as heavy sweating, tachycardia, dizziness, and confusion which can rapidly progress to heat stroke if the exposure continues.

2.4.1.1.2 Skin Burns

Skin burns are among the most immediate and visible effects of exposure to high temperatures. Burns occur when the skin is exposed to temperatures above 44.8°C, with the severity depending on the duration and intensity of exposure. The threshold for first-degree burns is approximately 48°C, while second-degree burns occur at temperatures around 55°C. These injuries can be caused by radiant heat, convective heat transfer from hot gases, or direct contact with heated surfaces. Radiant heat, in particular, is a major concern in tunnel fires, where the intensity of radiation can reach levels that the human skin cannot tolerate. The exposure limit for radiant heat flux that human skin can withstand is approximately 2.5 kW/m². Convection burns, which occur when skin is exposed to hot gases, are observed at temperatures above 120°C, particularly in scenarios where protective clothing is insufficient or absent. The conduction of heat from heated metals or other surfaces can result in rapid burns, with pain onset occurring within 1 second at 60°C and within 100 milliseconds at 80°C. The long-term effects of thermal injuries are increasingly recognized as critical factors in patient outcomes. Even when immediate survival is achieved, the systemic inflammatory response triggered by severe burns can lead to delayed complications involving vital organs such as the brain, heart, lungs, liver, and kidneys. These complications, which can manifest weeks after the initial injury, contribute to the long-term morbidity and mortality associated with severe burn injuries. The National Institute of Standards and Technology (NIST) provide data on the effects of heat on the human body as summarised in Table 1.

Table 1: Temperature benchmarks and corresponding human responses [105].

Temperature (°C)	Response
37.0	Average normal human oral/body temperature
38	Typical body core temperature for a working firefighter
43	Human body core temperature that may cause death
44	Human skin temperature when pain is felt
48	Human skin temperature causing a first-degree burn injury
54	Hot water causes a scald burn injury with 30 seconds exposure
55	Human skin temperature with blistering and second-degree burn
62	Temperature when burned human tissue becomes numb
72	Human skin temperature at which tissue is instantly destroyed
100	Temperature when water boils and produces steam

250	Temperature when charring of natural cotton begins
> 300	Modern synthetic protective clothing fabrics begin to char
≥ 400	Temperature of gases at the beginning of room flashover
≈ 1000	Temperature inside a room undergoing flashover

2.4.1.1.3 Respiratory Tract Burns

Respiratory tract burns are particularly dangerous due to the potential for severe internal injuries. The severity of these burns is closely related to the temperature and humidity of the inhaled gases. Dry air, which has a lower thermal capacity, generally does not cause thermal burns below the upper airways. Inhalation of steam or hot, humid air at temperatures around 100°C can cause severe burns throughout the respiratory tract. This is due to the high thermal capacity of water vapor and the significant heat transfer that occurs during condensation in the respiratory system.

2.4.2 Toxic Gases and Their Lethal Effects in Fires

Smoke inhalation during fires is particularly hazardous due to the presence of toxic gases, such as carbon monoxide (CO) and (CO2) and hydrogen cyanide (HCN) [106]. These gases can have profound effects on human health, particularly in vulnerable populations such as children, the elderly, and individuals with pre-existing respiratory or cardiovascular conditions. These groups have reduced physiological reserves, making them less able to compensate for the effects of toxic gas exposure.

In fires, carbon monoxide (CO) is the most common asphyxiant, while hydrogen cyanide (HCN) is more toxic but less frequently encountered. Incapacitation limits were initially determined through animal studies. These tests, conducted on juvenile primates such as baboons and cynomolgus monkeys, exposed the subjects to various concentrations of CO and HCN to establish the effects [103], [107].

The severity of toxic gas exposure is determined by two main factors: the concentration of the gases and the duration of exposure. High concentrations of carbon monoxide, for example, can bind to haemoglobin in the blood more effectively than oxygen, leading to hypoxia, or oxygen deprivation at the tissue level. This can result in symptoms ranging from mild (headache, nausea) to severe (loss of consciousness, death) depending on the exposure level and duration. Hydrogen cyanide, on the other hand, interferes with cellular

respiration, preventing cells from using oxygen efficiently, which can lead to rapid onset of symptoms and death in cases of high exposure.

2.4.2.1 Carbon Monoxide

Carbon monoxide (CO) is an especially insidious hazard in fire accidents, as it is completely undetectable by human senses—neither visible, nor detectable by taste or smell [108], [109]. It is only slightly soluble in water, blood serum, and plasma. Within the human body, CO reacts with haemoglobin to form carboxyhaemoglobin (COHb), a compound that significantly impairs the blood's ability to transport oxygen. This reduction in oxygen transport leads to hypoxia, a condition where critical organs, particularly the brain and heart, receive inadequate oxygen.

CO is a leading cause of death in fires, often surpassing other hazards such as carbon dioxide poisoning and oxygen deficiency. The severity of CO exposure is closely linked to the concentration of COHb in the blood. As COHb levels rise, the symptoms intensify from mild effects such as headaches and dizziness at lower concentrations, to severe outcomes including loss of consciousness and death at higher concentrations (Table 2). Typically, a COHb level of ≥ 50% is used to declare CO as the principal cause of death in fire situations. In non-fire accidents, such as suicides involving automobile exhaust or faulty venting of furnaces, the threshold is often set at ≥ 60% COHb. However, fire victims can sometimes have COHb levels below 50% and still succumb to smoke inhalation, as other toxic components of smoke, such as hydrogen cyanide (HCN), may also contribute to their death [110].

Table 2: Symptoms associated with COHb levels in healthy adults and susceptible populations [111].

COHb (%)	**Healthy Adults - Symptoms**	**COHb (%)**	**Susceptible Populations - Symptoms**
≈ 1	Physiologic background concentration	2	Reduced time to onset of angina and ECG signs of myocardial ischemia during physical exertion in individuals with coronary artery disease
5-6	Increase in cardiac arrhythmias in individuals with coronary artery disease	3-8	Background concentration in smokers

10	No appreciable effect, except shortness of breath on vigorous exertion, possible tightness across the forehead, dilation of cutaneous blood vessels	7	Headache, nausea in children
15	Myocardial infarction in individuals with coronary artery disease	13	Cognitive development deficits in children
20	Shortness of breath on moderate exertion, occasional headache with throbbing in temples	25	Syncopes in children
25	Decided headache, irritability, easily fatigued, judgment disturbed, possible dizziness, dimness of vision	25	Stillbirths
40-50	Headache, confusion, collapse, fainting on exertion	-	-
60-70	Unconsciousness, intermittent convulsion, respiratory failure, death if exposure is prolonged	-	-
80	Rapidly fatal	-	-

Fires in underground can generate extremely high concentrations of carbon monoxide, making swift evacuation and access to clean air essential for survival.

2.4.2.2 Carbon Dioxide

Carbon dioxide (CO2) is a by-product of combustion and can be produced in significant quantities during fire accidents. While carbon dioxide itself is less immediately toxic compared to carbon monoxide, its presence at high concentrations poses severe risks, particularly due to its impact on the respiratory system. Exposure to elevated CO2 levels results in hypercapnia, a condition characterized by an increased concentration of carbon dioxide in the bloodstream. At lower concentrations up to 5%, carbon dioxide (CO2) is not toxic, but it strongly stimulates breathing, increasing the rate by a factor of three. Individuals may experience respiratory distress as the body attempts to expel the excess. As the concentration rises above 5%, CO2 itself becomes narcotic. At concentrations between 7 and 10%, unconsciousness can occur within a few minutes [104].

Moreover, carbon dioxide (CO2) contributes significantly to the complexity of fire-related hazards by inducing a condition known as low oxygen hypoxia. While oxygen depletion at head height during fires is often minor when victims are severely affected by CO and HCN, CO2 exacerbates the situation by increasing the rate of uptake of these toxic gases. This accelerated intake is particularly dangerous because the toxic potencies of asphyxiant gases like cyanide are difficult to quantify consistently, especially under varying oxygen levels. In the upper layers of fire effluent plumes, oxygen concentration can drop to dangerously low levels sometimes as low as 1% O2. These conditions, combined with extremely high temperatures, can be lethal. For instance, if a person inhales such an atmosphere, as might occur when opening a door into a fire enclosure, they could collapse unconscious within seconds (Figure 14). This immediate collapse has been observed in some fire accidents, where victims were seen to lose consciousness after inhaling a single breath of smoke [112].

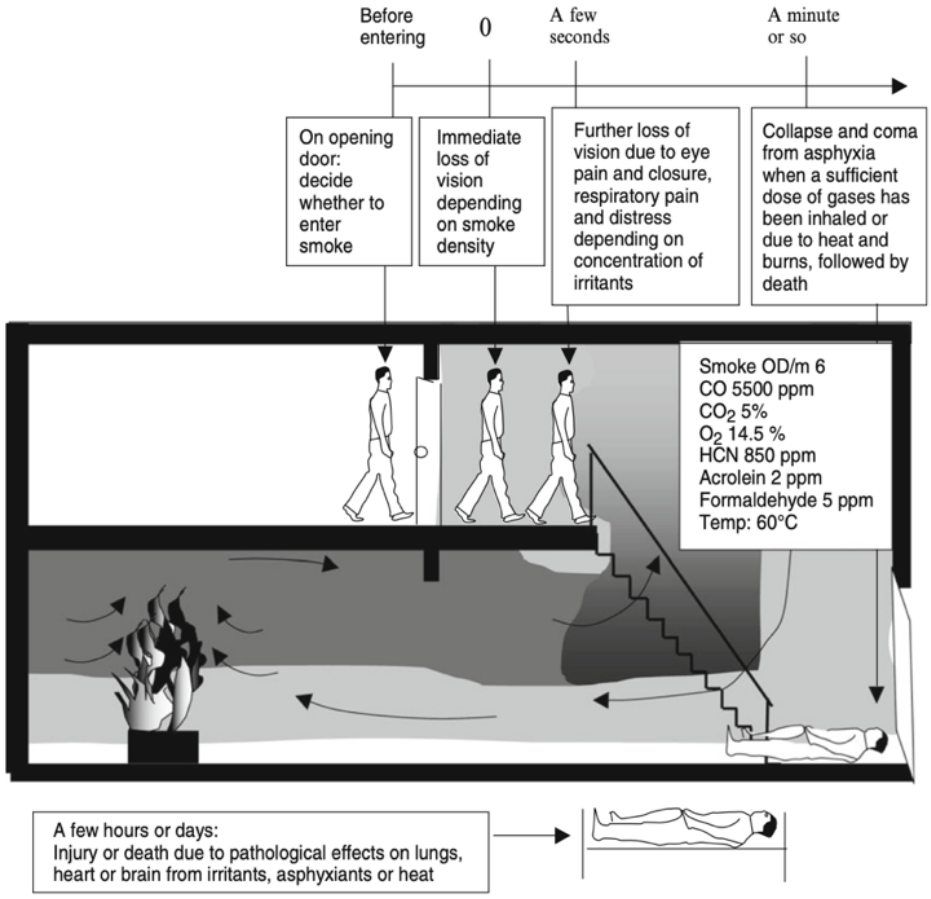

Figure 14: Sequence of toxic effects during a fire. This figure demonstrates the rapid progression of physiological effects when an individual is exposed to smoke and toxic gases after opening a door into a smoke-filled environment. Immediate vision loss is followed by respiratory distress and collapse due to the inhalation of asphyxiant gases such as CO and HCN [103].

2.4.2.3 Oxygen Depletion

Fire consumes oxygen rapidly, and if a tunnel is not adequately ventilated, oxygen levels can drop dramatically, leading to potentially life-threatening conditions for anyone trapped within. As oxygen levels decrease, the human body experiences a range of physiological effects, which can escalate quickly from mild distress to severe incapacitation and death.

The relationship between oxygen concentration and its effects on the human body is well-documented. Under normal atmospheric conditions, oxygen concentration is approximately 20.95%. The impact of low oxygen levels is particularly significant when considering the physiological effects at different altitudes, which can be analogous to oxygen depletion during a fire [103]. As oxygen concentration drops, the body undergoes a range of effects, progressing through different phases, detailed in Table 3.

Table 3: Effects of low oxygen hypoxia at altitude and equivalent sea level reductions in percent oxygen [103].

Altitude Equivalent	**Sea Level O2 Concentration**	**Phase**	**Physiological Effects**
Sea level - 3000 m	20.95% – 14.4%	Indifferent Phase	Minor effects on visual dark adaptation; beginnings of effects on exercise tolerance towards 15% O2.
3000 – 4500 m	14.4% – 11.8%	Compensated Phase	Mild effects: Slightly increased ventilation and heart rate; slight loss of efficiency in complex tasks and short-term memory.
4500 – 6000 m	11.8% – 9.6%	Manifest Hypoxia	Degradation of higher mental processes; loss of critical judgment; increased cardiovascular and respiratory activity.
6000 – 7600 m	< 9.6%	Critical Hypoxia	Rapid deterioration in judgment and comprehension; unconsciousness, followed by cessation of respiration and circulation, leading to death.

2.4.2.4 Visibility and Opacity as Effect of Smoke

There are two different definitions of smoke. One is in the ISO standard ISO 13943:2023 [113] and another is in NFPA 92 [114], [115]. In the ISO standard, smoke is defined as the "visible part of fire effluent", where "fire effluent" is defined as "all gases and aerosols, including suspended particles, created by combustion or pyrolysis and emitted to the environment". The NFPA standard defines smoke as "the airborne solid and liquid particulates and gases evolved when a material undergoes pyrolysis or combustion, together with the quantity of air that is entrained or otherwise mixed into the mass".

The importance of visibility in smoke-filled environments was first recognized in Japan in the mid-20th century by Jin. His experiment involved 31 participants, 14 males and 17 females, navigating a smoke-filled corridor to investigate the effects of smoke on human behaviour. The corridor was filled with white smoke generated by smouldering Japanese cedar crib chips in an electric furnace. The smoke density was carefully controlled, and participants were exposed to varying levels of heat radiation as they moved through the corridor (Figure 15). Cognitive performance, measured by the accuracy of mental arithmetic tasks, served as an indicator of emotional instability under these stressful conditions. Participants initially experienced a significant decline in cognitive performance upon entering the smoke-filled environment, reflecting the immediate physiological and psychological impact of smoke. Although their performance slightly improved as they continued, psychological distress increased, with anxiety and fear persisting and sometimes outweighing physical discomfort. Additionally, heat radiation further impaired cognitive function, with correct answer rates dropping significantly where heat was most intense [116]. The combined physiological and psychological effects of smoke and heat made it increasingly difficult for participants to think clearly and navigate effectively.

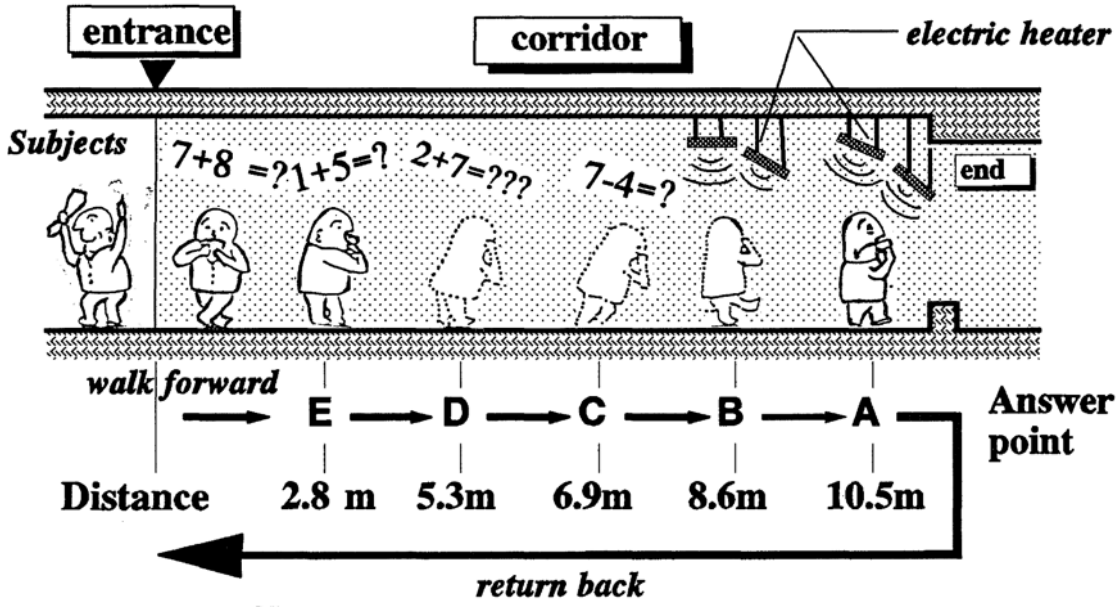

Figure 15: Experimental setup of Jin's study on smoke visibility and cognitive performance, where participants navigated a smoke-filled corridor while performing arithmetic tasks under heat stress [116].

Jin's early studies focused on how different smoke densities and types affected visibility and cognitive performance, establishing the foundational concepts for current models [117]. Then he extended his research to include the irritating effects of smoke on visibility and the psychological impact on evacuees [118], [119].

Visibility is expressed in several ways. The key parameter used to calculate visibility and light obscuration in visibility models is the smoke extinction coefficient C_s, which quantifies the attenuation of light as it passes through smoke. This attenuation is described by the relationship:

$$C_s = \frac{1}{L} \ln\left(\frac{I_0}{I}\right) \tag{8}$$

where I_0 is the incident light intensity (luminosity without smoke (lux)), I is the intensity of the light after passing through smoke (luminosity with smoke (lux)), and L is the path length of the light (m).

This relationship is rooted in Bouguer's law (also known as the Beer-Lambert law), which states that the intensity of light I passing through a medium like smoke decreases exponentially. This law can be expressed as:

$$\frac{I}{I_0} = \exp(-\sigma p_{sm} L) \tag{9}$$

where σ is the mass-specific extinction coefficient (m^2/kg) and p_{sm} is the mass concentration of smoke (kg/m^3). The mass-specific extinction coefficient σ varies depending on the type of combustion, with higher values typically observed in flaming fires compared to smouldering fires [120].

Jin [116] determined that the visibility V_s of signs in smoke-filled environments is influenced by whether the signs are reflecting or illuminated. He recommended specific ranges for the visibility constant K, with values of K = 2 to 4 for reflecting signs and K = 5 to 10 for illuminated (light-emitting) signs [102]. However, a recent study [121] suggested that Jin's visibility constant values may be lower than what more recent experiments indicate. The study observed that light-emitting signs generally outperform reflecting signs under various smoke conditions, and visibility was also affected by the colour of the sign, with red performing better in black smoke and green in white smoke. This variability, particularly in black smoke conditions, suggests that Jin's recommended values may require adjustment for contemporary applications. The visibility can be calculated using the equation:

$$V_s = \frac{K}{C_s} \tag{10}$$

In practical applications, maintaining low smoke obscuration levels is necessary to ensure that visual cues remain visible during an emergency. Specifically, smoke levels should be controlled so that an internally illuminated sign at 80 lux is discernible from 30 metres away, and doors and walls should be visible from 10 metres to facilitate safe evacuation [122].

2.4.3 Available Safe Egress Time (ASET) and Required Safe Egress Time (RSET) in Underground Gatherings

The development of fire safety regulations increasingly relies on performance-based design/risk-based design particularly when assessing egress strategies to ensure the life protection of occupants. Performance-based/risk-based design allows for flexibility, enabling fire safety engineers to go beyond prescriptive rules, provided that the proposed design meets or exceeds the required safety levels/risk Acceptability Limits [123], [124], [125], [126]. This approach requires demonstrating that the fire safety measures implemented are effective in maintaining occupant/exposed safety during evacuation.

In the event of a fire, occupants are exposed to a range of hazardous conditions, including smoke, toxic gases, and high temperatures as discussed in previous subsections. These conditions change dynamically within the environment, both in space and time and must be carefully controlled to ensure safe evacuation. Life safety depends on ensuring that hazardous conditions do not exceed tenability limits along escape routes. Key factors influencing tenability include visibility, gas toxicity, temperature levels, carbon monoxide levels, the FED of toxicants, and radiative heat. Protection systems are multi-component systems designed to mitigate loss of visibility and toxic effects, though they generally do not provide protection against radiative heat in the event of a fire. If the fire can be shown to be extinguished before the development of toxic conditions or excessive temperatures which are factor of the incapacitation during the evacuation [102], then loss of visibility due to smoke may not be the primary life safety criterion [124]. During escape, monitoring these parameters at the height of each occupant's head, typically measured at a conventional human height of 1.8 to 2 metres from the floor to reflect the head height of standing adults, whether they are walking upright or stooping, ensures accurate assessment of their exposure [103], [127], [128].

The evaluation of egress design is fundamentally based on the time each occupant takes to escape from the area where a fire has developed or to reach a safe location. Two critical time parameters are used in this evaluation:

- ASET (Available Safe Egress Time): The time available for occupants to evacuate to a safe location before the onset of untenable conditions.
- RSET (Required Safe Egress Time): The time required for occupants to detect the fire, respond, and evacuate to a safe location.

To this end, fire safety engineering focuses on calculating the ASET based on these tenability limits and comparing it to the RSET. ASET represents the duration during which conditions remain survivable, allowing occupants to escape safely, while RSET is the time required for occupants to detect the fire, respond, and evacuate. For an evacuation to be successful, ASET must exceed RSET, ensuring that occupants have sufficient time to evacuate before conditions become life-threatening. ASET can be calculated using various approaches, including hand calculations [102], [129], zone models available in both 2D and 3D configurations [129], [130], [131], [132], [133], and Computational Fluid Dynamics (CFD) simulations [102], [134].

For a fire safety design to be considered effective, the relationship between ASET and RSET must satisfy the following condition:

$$ASET > RSET \quad (11)$$

The difference between ASET and RSET defines a safety margin (t_{margin}), which ensure that occupants can evacuate safely before conditions become life-threatening.

RSET is composed of several key components:

$$RSET = \Delta t_{det} + \Delta t_a + (\Delta t_{prem} + \Delta t_{trav}) \quad (12)$$

where:

- **Δt_{det} (Detection Time):** The time between fire ignition and detection by an automatic system or an occupant.
- **Δt_a (Alarm Time):** The time from detection to the activation of a general alarm. This can vary depending on the system used, from immediate (0 seconds) to several minutes.
- **Δt_{prem} (Pre-Movement Time):** The time between the occupants becoming aware of the fire and the moment they begin to evacuate. This period includes recognition and response times and may be influenced by occupant behaviour and building layout.
- **Δt_{trav} (Travel Time):** The time required for occupants to reach an exit through the designated egress routes. Travel time can be further broken down into:
    - **$\Delta t_{walking}$:** Average time for an individual to move through the egress routes to the exit.
    - **Δt_{queue} :** Time spent in queue formation at the exit.
    - **Δt_{flow} :** Time taken for occupants to flow through the exit.

RSET calculations must account for a range of factors, including occupant density, the complexity of the building layout or presence of the obstacles (namely vehicles in case of road tunnel), and the effectiveness of the fire detection and alarm systems. The total RSET represents the sum of these components and must be compared against the calculated ASET to ensure that occupants have sufficient time to evacuate safely (Figure 16).

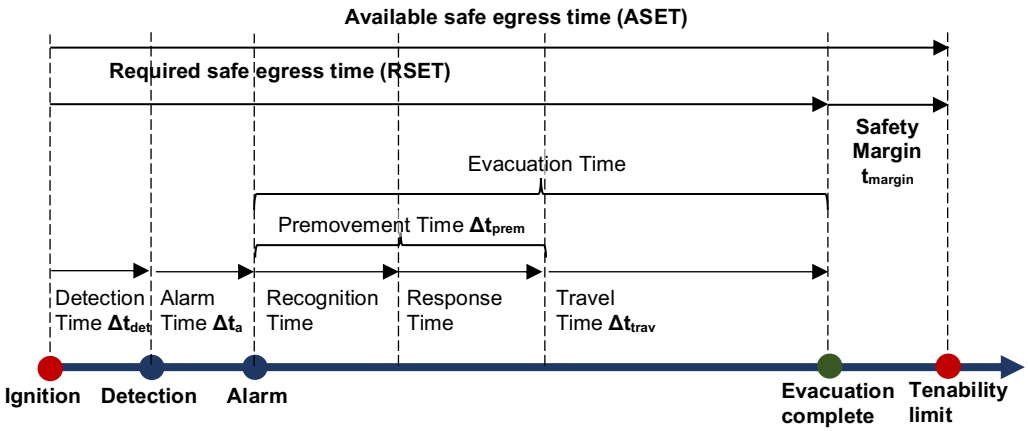

Figure 16: Comparative timeline of ASET and RSET.

Different countries have various requirements for tenability limits. For example, in Sweden (TSFS 2019:93) [135], for tunnels longer than 500 metres where escape routes are more than 200 metres apart, critical conditions must be established and not exceeded during the time needed for evacuation. The specific limits set by this regulation include radiation ≤ 2.5 kW/m², temperature ≤ 80°C, O2 > 15%, CO2 < 5%, CO ≤ 2000 ppm, and visibility ≥ 10 metres. Additionally, a pre-movement time of at least 2 minutes must be assumed.

In Italy, similar stringent measures are in place for fire safety [125]. The ISO 13571 standard [126], which is widely referenced in Italy and other countries, outlines the assessment of life-threatening conditions during a fire (Table 4).

Table 4: Performance thresholds for fire safety calculations [125] .

Model	**Performance**	**Performance threshold**	**Reference**
Obscuration of visibility due to smoke	Minimum visibility of reflective, non-backlit panels, evaluated at a height of 1.80 m from the floor	Occupants: 10 m Occupants in rooms with a gross area < 100m²: 5 m	ISO 13571:2012
		Rescuers: 5 m Rescuers in rooms with a gross area < 100m²: 2.5 m	[*]
Toxic gases	FED, fractional effective dose, and FEC, fractional effective concentration for exposure to toxic and irritant gases, evaluated at a height of 1.80 m from the floor	Occupants: 0.1	ISO 13571:2012, limiting to 1.1% the portion of occupants incapacitated upon reaching the threshold
		Rescuers: no assessment	-
Heat		Occupants: 60°C	ISO 13571:2012

	Maximum exposure temperature	Rescuers: 80°C	[*]
Heat	Maximum thermal radiation from all sources (fire, fire effluents, structure) to which occupants are exposed	Occupants: 2.5 kW/m^2	ISO 13571:2012, for exposures shorter than 30 minutes
		Rescuers: 3 kW/m^2	[*]
[*] For the purposes of this table, rescuers refer to members of company teams who are properly protected and trained for firefighting, the use of respiratory protective devices, and to operate in low visibility conditions. Further guidance can be found, for example, in documents from the Australian Fire Authorities Council (AFAC) for hazardous conditions.			

2.5 Underground Evacuation

The study of human behaviour during evacuations, particularly in high-risk environments such as underground systems, is both complex and critical. Traditional assumptions about evacuation behaviours, often influenced by media representations, have led to misconceptions that can hinder effective emergency planning [136]. These assumptions often overlook the significant variability in human behaviour, which can lead to ineffective or even counterproductive evacuation plans. Understanding this variability is essential because, while human behaviour is something everyone experiences daily, its manifestation in emergency situations is far more diverse and uncertain.

2.5.1 Overview of Evacuation Challenges in Underground Environments

Most underground environments are critical in terms of exit usage, with users often being unfamiliar with the surroundings [137], whether in a road tunnel or the CERN underground. Since people do not typically walk through tunnels on a daily basis, encountering a fire in such a setting may be a first-time experience for most users. Additionally, fires in underground environments are rare, further contributing to a general lack of familiarity with emergency procedures. This unfamiliarity can be significant for the design stage of the evacuation plan and impact the decision-making process during an evacuation.

In such environments, Sime's theory of affiliative behaviour becomes particularly relevant. According to Sime [138], during emergencies, individuals tend to seek out and remain with familiar people, a behaviour driven by a need for social support and reassurance. This affiliative behaviour can influence evacuation

efficiency, as people may delay evacuating to find their companions or follow others without clear knowledge of the escape routes. Incorporating an understanding of these social dynamics is essential for developing evacuation plans for underground settings, ensuring that strategies are effective and consider the natural human tendencies towards social affiliations.

2.5.2 Misconceptions about Human Behaviour during Evacuations

A prevalent misconception, largely perpetuated by media and popular culture, is that individuals tend to panic during emergencies, exhibiting irrational and competitive behaviours [136], [139], [140], [141], [142]. This stereotype, reinforced by media and popular culture, has shaped many evacuation strategies that prioritize managing this presumed panic. However, empirical evidence suggests otherwise. In the aftermath of devastating fires, it has become increasingly important to not only comprehend but also accurately model the actions and decision-making processes of those directly affected by emergency fire scenarios. To achieve this understanding, a series of detailed interviews have been conducted with survivors [136], [140], [143], [144]. A notable revelation from these interactions is that, while the term "panic/disaster shock" is frequently and broadly used by the public and media to describe survivors' responses, it often misrepresents their actual behaviours. Many survivors, when recounting their experiences, detail a series of deliberate and rational decisions made under duress [136]. This disparity between perception and reality underscores the need for a deeper understanding and a more accurate portrayal of human behaviour in emergency situations [145]. Much research has shown that it is time to abandon the overused and often inaccurate terms "panic/disaster shock" and recognise the complexity and rationality behind many of these actions [136], [146], [147], [148].

The concept of panic implies a loss of rationality, characterized by chaotic and competitive behaviour. However, studies have shown that in real-world evacuation scenarios, such behaviours are rare [149]. Instead, what may appear as irrational from an external perspective often has logical explanations when considering the context and the individual's perception of the situation [150].

Contrary to the notion of panic-driven selfishness, research in social psychology, particularly the theory of social identity [151], suggests that people are more likely to exhibit altruistic behaviours. Early theoretical frameworks, such as Social Categorization Theory [152] and the Social Identity Model of crowd

behaviour [153], have shown not only the presence of altruism but also the propensity for self-sacrifice in such situations. When individuals perceive a shared identity with others in a crisis, they are more inclined to help each other, as demonstrated in various studies [142], [144], [154], [155]. For instance, an experiment in the UK revealed that individuals were more likely to assist someone wearing the home football team's shirt outside a stadium than someone wearing a rival team's shirt [156]. This phenomenon extends to larger-scale emergencies, where shared experiences foster communal efforts to ensure collective safety [157].

Historical events, like the World Trade Center attacks [158] and London Underground attack [140], as well as more recent challenges like the COVID-19 pandemic [159], [160], [161], have shown how communities can come together to support each other in times of crisis, reinforcing the importance of social identity in emergency behaviour.

In crowd disasters, what may seem like competitive behaviour is often a result of physical constraints rather than psychological ones [162]. The design of evacuation routes, especially in areas with high foot traffic, can lead to bottlenecks and perceived competition [163], [164]. Most disasters associated with evacuation are linked to poor design, especially in junction areas where there is a high flow of people [165], [166]. It is not about individuals wanting to harm others, but rather about the spatial constraints they face, which can force them into situations where they appear to be acting competitively.

However, while these dynamics are evident in crowd disasters, fire emergencies present a different set of challenges that extend beyond physical constraints alone. Factors such as smoke, heat, reduced visibility, and the presence of combustible materials significantly influence evacuation behaviour and the safety measures required. While spatial limitations can still contribute to bottlenecks, the immediate danger posed by the fire can alter individual and group behaviours. In a tunnel fire, the situation can foster a sense of shared identity among those affected, encouraging cooperative and altruistic behaviour rather than the competitive actions often depicted in media. This cooperative behaviour is evident in real-world observations that challenge the often sensationalised media narratives of panic. During the May 24, 2024, tunnel fire in Boston's Ted Williams Tunnel, while some media outlets described the scene as one of “panic” [167], many drivers acted with a focus on safety. They abandoned their vehicles and walked out of the tunnel to escape the smoke. The situation

demonstrated that, rather than panicking, people generally responded by cooperating, acting rationally with the aim of ensuring safety, and prioritizing their well-being under challenging circumstances. Similarly, during a fire in the Dartford Tunnel, despite media reports of panic [168], many people were seen calmly evacuating and talking with others as they left the tunnel.

These behaviours differ significantly from the panicked scenes often portrayed in the media and movies. Analysing human behaviour in emergency situations allows for the development of effective evacuation strategies. The challenge for evacuation designers is not the concept of panic but rather the opposite where to ensure that individuals recognize the seriousness of the situation and evacuate promptly. In many cases, people do not perceive the threat as imminent and may delay their evacuation [169]. This type of behaviour can be attributed to what is known as “normalcy bias” [170]. This bias leads people to believe that everything is normal, even in the face of clear danger. As a result, individuals may underestimate the severity of a situation, causing them to delay evacuation or engage in routine activities despite the presence of an immediate threat. This behaviour, while seemingly irrational, is not panic but rather a result of underestimating the danger.

2.5.3 Human Behaviour in Earthquake

One of the main questions in earthquake scenarios is identifying the first signs of danger before structural collapse or fire, and understanding how people behave and respond during these early warnings. The way individuals perceive and react to the initial shaking, which is often the earliest indication of an impending disaster, can have a profound impact on survival outcomes. Understanding human behaviour during earthquakes is essential for evacuation analyses, as the decisions made during these moments can significantly influence whether people safely evacuate before collapse or are remain exposed to the hazards that follow.

Research consistently shows that individuals' immediate reactions to earthquake shaking vary widely, influenced by factors such as the intensity of the shaking, their location, and their previous experiences with earthquakes [171], [172], [173]. Social and cultural factors also play a significant role in shaping these responses. In regions with a strong “disaster subculture”, where communities have regularly experienced earthquakes, there tends to be a more coordinated and

effective response. Conversely, in areas with less frequent seismic activity, responses may be less effective due to a lack of ingrained safety practices [174].

Common immediate responses include self-protective actions like "Drop, Cover, and Hold on". Self-protective actions originally developed during the Cold War, "Duck and Cover" was a response to the threat of nuclear attacks. The strategy involved taking cover under desks or sturdy furniture and covering one's head to protect against debris and radiation from nuclear blasts. This method was widely taught in schools across the United States and became a fundamental part of civil defence drills. This drill was widely disseminated through public education campaigns, including the iconic "Bert the Turtle" film [175].

Over time, the principles of "Duck and Cover" were adapted for use in earthquake preparedness. As research into earthquake hazards advanced, it became clear that the most significant threats during an earthquake were from falling objects and structural damage. This led to the development of the "Drop, Cover, and Hold On" principle, which is now widely endorsed as the most effective immediate response during an earthquake [176].

"Drop, Cover, and Hold On" is the most widely recommended safety action for earthquakes (Figure 17).

- **Drop** to their hands and knees to prevent being knocked over by the shaking.
- **Cover** their head and neck under sturdy furniture to protect against falling debris.
- **Hold On** to their shelter until the shaking stops to ensure that the cover stays in place.

Figure 17: Stages of the "Drop, Cover, and Hold On" security position [177].

Another method is Triangle of Life proposed by Doug Copp [178], the "Triangle of Life" suggests that during an earthquake, individuals should lie next to large objects (like furniture) rather than underneath them. The idea is that when a building collapses, voids or "triangles" form near these objects, offering a safe space. This method has been widely criticized by several experts [179] and organizations [180], [181]. Moving during an earthquake also increases the risk of injury. Organizations like the American Red Cross [182], the U.S. Geological Survey [181], the National Emergency Management Agency (New Zealand Government) [183] and Federal Emergency Management Agency (FEMA) [184] have advised using this method in favour of "Drop, Cover, and Hold On".

The decision-making process during an earthquake often involves a brief period of hesitation as individuals assess the situation and seek cues from their environment or others. This period, which can vary from seconds to longer, is critical as it influences whether individuals take actions or attempt [171], [172], [173], [185], [186].

Despite official recommendations to "Drop, Cover, and Hold on", many people instinctively try to evacuate buildings during an earthquake [187]. This instinctive reaction to evacuate immediately is often driven by a fear of being trapped inside a collapsing structure [172]. However, this can be dangerous if not done properly, as rushing outside exposes individuals to falling debris and structural hazards.

In some cases, people may seek out what they perceive to be safer areas within the building, such as standing in doorways or moving next to load-bearing walls. Historically, standing in doorways was recommended, but modern guidance generally advises against this unless no other cover is available, as doorways do not provide sufficient protection from falling objects [188], [189], [190].

There is also a significant portion of people who may freeze or delay their actions during the initial moments of an earthquake. This "freeze" response can increase the risk of injury, as it delays critical protective actions [172], [190]. This "freezing" might not necessarily indicate a paralysis due to shock, but rather a moment where individuals are gathering crucial information and making decisions about the best course of action [190]. Moreover, some individuals might engage in risky behaviours, such as attempting to secure personal belongings [173].

Fundamental component in earthquake evacuation analysis is pre-movement time, [191] which can also be enriched by concepts from fire safety engineering in evacuation analyses and includes recognition time and response time. Recognition time refers to the period from the moment an individual first feels the ground shaking to when they confirm that an earthquake is occurring which normally takes couple of seconds to feel the shaking. This phase can include a delay, particularly if the initial shaking is mild or ambiguous, causing uncertainty about whether the event is indeed an earthquake. This uncertainty can extend the recognition time, delaying the individual's response. For instance, at lower intensities of ground shaking, such as MMI IV, the delay time averages around 22 seconds. This suggests that individuals take longer to recognize the earthquake and decide on a course of action. As the intensity of shaking increases, the delay time decreases significantly. At MMI VIII, the average delay time is reduced to approximately 1.8 seconds, and at MMI IX, it can be as short as 0 second [192]. As the intensity of an earthquake increases, the time individuals take to recognize the event and initiate response actions, referred to as delay time, generally decreases. This reduction occurs because more severe shaking provides a clearer and more immediate indication of danger, leading to quicker recognition and response.

Response time is the duration between this recognition and the initiation of the actions. Individuals display varying of behaviours depending on the intensity of the ground shaking, and these behaviours are influenced by the surrounding environment and the actions of others nearby [173], [188], [190], [191], [192], [193].

In the context of earthquakes, RSET differs significantly from fire emergencies in several keyways. In fire scenarios, recognition time is often longer due to the gradual onset of cues such as smoke or the activation of alarms. Conversely, during an earthquake, the ground shaking is an immediate and unmistakable cue, leading to a typically shorter recognition time.

Response time in an earthquake is heavily influenced by the suddenness and unpredictability of the event. As a fire scenario, also in earthquake scenario can have differ behavioural responses. Unlike fires, where the primary recommended action is immediate evacuation, earthquakes require a different approach. The initial recommended actions during an earthquake are to "Drop, Cover, and Hold On" to protect against falling debris and structural hazards, before considering evacuation if it becomes safe to do so.

The overall RSET for an earthquake scenario can thus be defined as:

$$RSET = \Delta t_{prem} + \Delta t_{trav} \quad (13)$$

where Pre-Movement Time is the sum of Recognition Time and Response Time (Drop, Cover, and Hold) $\Delta t_{prem} = t_{rec} + t_{res}$, and Δt_{trav} represents the duration required to evacuate to a safe location, similar to Travel Time in fire scenarios, which begins once the protective actions have been completed and it is safe to move.

Bernardini et al. [173] identified three key stages of earthquake evacuation: pre-movement, movement towards safety, and post-evacuation. Each stage involves different behaviours, that shape the evacuation process. In line with this, Xiao et al. [194] highlights the second stage (movement towards safety) as the most important, with behaviours such as fleeing the building or gathering with family, where suggests that people often begin evacuating immediately, without waiting for the full pre-movement phase to finish.

2.6 The Evolution of Risk Concept

What is Risk? The concept of risk has evolved significantly over centuries, originating from early philosophical inquiries into the nature of uncertainty and probability. Bernstein [195] provides an overview of how societies have understood and managed risk from ancient times through the modern era, extending through the mathematical formalisations in the Renaissance, and culminating in the complex risk assessment models of today. Special mention must be made of Lord Asquith LJ, who, although neither a mathematician nor a social scientist, was a judge with an intuitive genius to measuring quantum of risk [12], [13], [196]. He viewed risk as the consequence of hazards balanced against efforts for prevention and protection, striving for an equitable equilibrium, as discussed in subsection 3.1.3.1.

Risk analysis does not deal with certainties but with probabilities as measure of uncertainties. As for Aristotle, his approach to science focused on certainties and logical reasoning. In his time, science was primarily concerned with distinguishing between what is true and what is false, and unpredictable or uncertain events were seen as outside the scope of scientific inquiry. Aristotle's philosophy, particularly in his *Metaphysics* [197], emphasized that uncertainty and unexpected events had no place in scientific thought, which aimed at clarity and precision. The integration of uncertainty and the management of risk were

concepts that would only emerge much later, during the Renaissance and Enlightenment periods, when probability theory began to take shape and became an essential part of scientific thinking.

In the pre-modern world, events such as natural disasters or unexpected misfortunes were often attributed to the will of God or fate. Even earlier than Aristotle, Hesiod in his *Works and Days* highlighted the unpredictability of life, reflecting on how human fortunes were shaped by uncontrollable forces of nature [198]. This worldview persisted until the Renaissance and Enlightenment periods, when probability theory and scientific inquiry began to take shape. The integration of uncertainty and the management of risk became essential to scientific thinking, moving away from divine explanations toward natural causes and probabilistic reasoning.

During the Enlightenment, particularly after the 1755 Lisbon earthquake, philosophers such as Voltaire (François-Marie Arouet) and Jean-Jacques Rousseau debated whether such disasters were punishments from God, destiny, or natural occurrences. Voltaire argued that these events were not a result of divine will but natural phenomena, while Rousseau suggested that the severity of the disaster was due to human errors, such as building in unsafe areas or constructing inadequate structures, rather than divine intervention [199].

One might consider the contributions of Hacking [200], explores how the concept of probability itself emerged from philosophical debates and became a tool for statistical thinking and risk management. Hacking's analysis delves into the ways that statistical methods have shaped our understanding of uncertainty and decision-making under conditions of risk.

Daston's [201] work on classical probability provides insight into how Enlightenment thinkers reconciled classical ideas of determinism with the emerging concepts of chance and risk. He discusses how these intellectual shifts influenced legislative, economic, and philosophical thought, setting the stage for modern risk management strategies. Luhmann [202] suggests that modern risk management reflects not only economic and mathematical considerations but also deeply entrenched social and cultural factors that influence how different societies perceive and react to risks.

Risk, fundamentally assessed through probabilities and consequences as per Kaplan & Garrick [203], also involves significant ethical dimensions that transcend numerical analysis. Every risk assessment, whether implicit or explicit,

encompasses value judgments about what constitutes an "acceptable" risk. Decisions about it involve complex value judgments that reflect societal values and individual biases. These judgments not only indicate societal priorities and fears but also engage deeply with ethical considerations and questions of social justice [204], [205].

Decisions on risk thresholds (what risks acceptable/tolerable and who decides) are influenced by cultural norms, economic considerations, political climates, and ethical theories. The concept of "acceptable risk" thus not only pertains to the probability and impact of potential hazards but also to how these probabilities and impacts are perceived and valued by different communities and stakeholders [206]. This decision-making process under uncertainty mirrors the ancient philosophical challenges of predicting future contingents, reminding us that risk assessment is as much about managing unknowns as it is about understanding knowns. Risk involves a dialectic between the knowable and the unknowable, resonating with the ancient philosophical problem of future contingents. As Aristotle pondered whether statements about the future are necessarily true or false [207], [208].

The indeterminate nature of risk challenges risk managers to consider not just the most likely outcomes, but also the less likely ones that could have significant impacts. Ethical risk management involves preparing for extreme events that have low probabilities but high consequences, sometimes referred to as "Black Swan" events by Nassim Nicholas Taleb [209], [210]. It compels organizations to adopt a more nuanced, versatile approach to risk management. By planning for a range of outcomes, businesses and governments can better protect themselves against future uncertainties.

The following table (Table 5) presents a comparison of the definitions of risk as provided by various organizations across different sectors.

Table 5: Definitions of risk by different organizations.

Organization	Definition of Risk	Source	Context and Application
International Organization for Standardization (ISO)	Risk is the effect of uncertainty on objectives.	ISO 31000:2018 [211]	Focuses on the impact of uncertainty in achieving specific goals, highlighting the dual nature of risk (potential losses and gains). Used broadly across various industries.

Society for Risk Analysis (SRA)	Risk is defined in relation to the consequences (effects, implications) of a future activity or event, which could include natural phenomena, the operation of a system, or other scenarios. It focuses on potential negative or undesirable outcomes, often seen in relation to reference values or objectives (such as planned values). The consequences are considered in terms of uncertainty and their severity, with at least one outcome regarded as negative or undesirable.	SRA Glossary [212]	Underlines the prevention of adverse effects, crucial in environmental science and public health.
Project Management Institute (PMI)	An uncertain event or condition that, if it occurs, has a positive or negative effect on a project's objectives.	PMBOK® Guide – Sixth Edition [213], [214]	Highlights the importance of risk in project management, focusing on planning and response strategies to manage project risks.
United States Environmental Protection Agency (EPA)	Risk is the chance of harmful effects to human health or to ecological systems resulting from exposure to an environmental stressor.	EPA Risk Assessment Portal [215]	Focuses on the environmental impacts of risks, essential for regulatory assessments and policymaking to protect ecosystems and public health.
Financial Industry Regulatory Authority (FINRA)	Risk is any uncertainty with respect to your investments that has the potential to negatively impact your financial welfare	FINRA Understanding Risk [216]	Pertains to the financial sector, stressing the uncertainties inherent in financial markets and the importance of economic analysis.
World Health Organization (WHO)	Risk can be defined as a potential uncertain event that could affect the achievement of the WHO's objectives and expected results.	WHO Risk Management Strategy [217]	Frames risk within global health contexts, focusing on the strategic planning needed to mitigate risks associated with diseases and health crises.

United Nations Office for Disaster Risk Reduction (UNDRR)	Risk is the probability of an outcome having a negative effect on people, systems or assets.	UNDRR [218]	Emphasizes disaster preparedness, crucial for managing risks related to catastrophic events and emergency responses.
Institute of Risk Management (IRM)	Risk is a combination of the probability of an event and its consequence. Consequences can range from positive to negative.	IRM Risk Management Standard [219]	Broadens the perspective on risk to include both adverse and beneficial outcomes, key in enterprise risk management.
National Institute of Standards and Technology (NIST)	Risk is a function of the likelihood of a given threat-source's exercising a particular potential vulnerability, and the resulting impact of that adverse event on the organization.	NIST Special Publication 800-30 [220]	Essential in cybersecurity, emphasizing the identification, evaluation, and prioritization of risks based on potential vulnerabilities and threats.
ANAS (Italian National Autonomous Roads Corporation)	RISK: The analytical link between the probability of occurrence of an event and the magnitude of the consequences deriving from it, including the uncertainties related to the estimation of defining magnitudes.	ANAS Condirezione Generale Tecnica, 2009 [221]	Essential in the field road tunnel, especially relevant to road safety. Emphasizes the quantitative assessment of likelihood and impacts of events, alongside acknowledging the estimation uncertainties crucial for infrastructure risk management.

In the simplest terms, risk is the potential for loss or negative outcomes resulting from a hazard. It is quantified typically as the product of the probability of an event occurring and the consequence of that event [203]:

$$\text{Risk} = \text{Probability (of Hazard)} \cdot \text{Consequence (of Hazard)} \quad (14)$$

Where Probability (of Hazard) refers to the likelihood or chance that a hazard will occur, and Consequence (of Hazard) refers to the impact or severity of the hazard if it does occur. This impact could involve financial, environmental, or human losses.

However, this generic definition has limitations as it does not clarify what specific event or scenario the probability is related to. Guarascio's [12], [13], [14], [222], [223] and Alakbarli's [11] works advanced this understanding by introducing the concept of the risk quantum/quantum of risk. A more detailed

discussion on the Risk Quantum can be found in subsection 3.1.10**.** In this approach, risk is tied to a well-defined scenario, where the relationship between different subsystems of scenarios is clarified. Each subsystem or scenario follows a probability path, where mutually exclusive branches represent separate outcomes in a tree diagram, and non-mutually exclusive sub-scenarios represent alternative possibilities. In this framework, risk is viewed as the expected value of the consequence of each scenario multiplied by the probability of the scenario. The probability of a scenario is calculated as the product of the probabilities of each sub-scenario, given that each branch in the tree diagram is mutually exclusive and collectively exhaustive, covering the entire scenario space.

2.6.1 Societal Influences on Risk Perception

Risk perception is not merely a subjective interpretation but is deeply influenced by cultural, social, and educational factors.

Different cultures perceive and tolerate risk in varied ways. For example, some cultures are more risk-averse and prioritize safety over technological or economic gains, while others may accept higher risks for greater benefits. This variation can significantly influence policy-making and risk management strategies at the national and international levels [204]. However, as Laird [224] argues, risk communication cannot be viewed solely as the transmission of technical information. Instead, it operates within a broader political and social framework. The decline of public trust in institutions, a phenomenon Laird terms the "decline of deference", means that risk communication must now also address underlying political alienation and public scepticism. Transparency, inclusivity, and a recognition of public values are important for effective communication and trust-building.

Economic stability shapes how societies handle risks. Wealthier areas can afford comprehensive risk management systems and strict safety standards. In contrast, regions with fewer resources often prioritize immediate needs over long-term safety plans. Balancing the costs and benefits of safety measures is essential for effective risk management. Moreover, the establishment of risk criteria is deeply influenced by the legal and political environment of each area [225], [226], [227], [228].

As noted by Fischhoff [229], effective risk communication must consider the audience's existing beliefs, values, and knowledge, which are significantly shaped by their educational experiences. Education not only influences the

perception of risk by framing the cognitive and affective contexts through which hazards are evaluated [230] but also affects how risk information is received and spread, influencing the social amplification or attenuation of risk perceptions [231].

2.6.2 Risk Analysis and Risk Assessment

This basic equation sets the foundation for more elaborate models that consider various components contributing to risk, especially in complex environments. The articulation of this formula transitions naturally to the domains of risk analysis and risk assessment, key elements in the architecture of effective risk management [232]. These processes are not merely procedural but are fundamental to the strategic assessment and mitigation of risks. Risk analysis and risk assessment processes are multifaceted and can be approached using either qualitative or quantitative methods, depending on the specific objectives and the nature of the risks involved (Figure 22) [233].

- **Qualitative Risk Analysis:** This approach uses non-numerical descriptors to evaluate the likelihood of risk events and the severity of their consequences. Qualitative risk analysis is often used:
    - **As an initial screening tool:** It helps to quickly identify accident scenarios that warrant more detailed analysis.
    - **When time or resources are limited:** If a full quantitative analysis is not justified, qualitative analysis can provide a sufficient basis for decision-making.
    - **When data is insufficient:** In cases where numerical data is scarce or unreliable, qualitative analysis offers an alternative by using expert judgment to assess risks.

In this approach, risks might be categorized as "Low", "Moderate", or "High", with these categories providing a broad indication of which risks are most critical and require further attention.

- **Semi-Quantitative Risk Analysis:** When the need arises for a more detailed analysis than what qualitative methods can offer, but where full quantitative analysis is impractical, semi-quantitative methods are used. In these methods:
    - **Qualitative descriptors are quantified:** Words or descriptive scales are assigned numerical values. For example, a "High" risk might be

given a score of 5, while a "Low" risk might be assigned a score of 1.
    - **Combination of scores:** These scores can be combined in various ways to produce a more nuanced risk picture. For instance, a Risk Priority Number (RPN) might be calculated by multiplying the likelihood, severity, and detectability scores of a risk event.
    - **Purpose:** The objective here is not to generate exact numerical risk values but to create a more refined prioritization than what qualitative methods alone can provide. It allows organizations to focus their resources on the most significant risks, even if the exact probabilities and consequences are not fully quantifiable.
- **Quantitative Risk Analysis (QRA):** In situations where precise risk quantification is essential, Quantitative QRA is employed. This method uses numerical values for probabilities and consequences, often derived from statistical data or simulations. Key features include:
    - **Probabilistic analysis:** This involves calculating the likelihood of different outcomes using statistical models, often based on historical data or theoretical models.
    - **Detailed component analysis:** In a QRA, systems are often broken down into their individual components. By estimating the failure rates of these components and combining them, an overall risk profile is constructed.
    - **Suitability:** QRA is particularly suited for analysing low-probability, high-consequence events, such as nuclear plant accidents or large-scale industrial disasters, where understanding the precise risks is critical.

Various terms are used for QRA depending on the context:

Probabilistic Risk Assessment (PRA): Common in the nuclear and aerospace industries, PRA involves a detailed probabilistic analysis of system reliability and safety.

Process Hazard Analysis (PrHA): Mandated by OSHA for processes involving hazardous chemicals, PrHA focuses on identifying potential hazards in chemical processing.

Formal Safety Assessment (FSA): Used primarily in maritime and offshore industries, FSA involves a structured and formal approach to risk analysis and management.

This initial phase involves a systematic exploration of potential threats. It entails identifying potential hazards, understanding the mechanisms behind each identified risk, assessing the probability of their occurrence, and evaluating their potential impacts. The entire process can be viewed through the lens of three key steps: Causal Analysis, Accidental Event Analysis, and Consequence Analysis (Figure 18). Considering both common and uncommon risk sources. This comprehensive identification and analysis help in preparing for the subsequent phase of risk assessment.

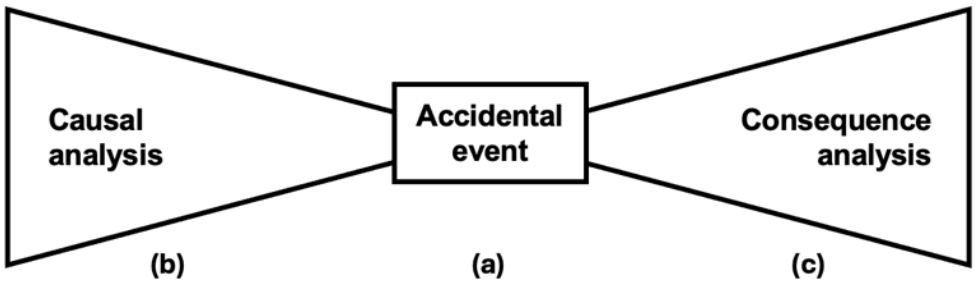

Figure 18: Three key steps in risk analysis [234].

The identification of **Accidental events (a)** is the first critical step in the risk analysis process because it establishes the scope of what the analysis must address. Accidental events are defined as significant deviations from normal operating conditions that can lead to undesired consequences. This definition applies universally across various industries, where any such deviation can have safety, environmental, or operational impacts. Initial identification of these events is critical as it sets the stage for a deeper causal and consequence analysis. Various techniques are employed [233], including:

- **Hazard Log**:
    - **Purpose**: Not a method for identifying hazards but a tool for recording and updating information about identified hazards and hazardous events.
    - **Usage**: Helps maintain an ongoing record of hazards, ensuring that the information is current and accessible throughout the system's lifecycle.
- **Checklist and Brainstorming**:

    - **Purpose**: Useful for starting the hazard identification process by reviewing a list of generic hazards and hazardous events.
    - **Usage**: Aided by brainstorming sessions, a team can decide how and where these generic events might occur in the specific system being analysed.
- **Preliminary Hazard Analysis (PHA)**:
    - **Purpose**: A simple method commonly used during the design phase to identify potential hazards.
    - **Usage**: Called "preliminary" because it is often updated as more detailed risk analyses are conducted. For simpler systems, it might serve as a complete risk analysis. PHA is sometimes referred to as HAZID.
- **Change Analysis**:
    - **Purpose**: Identifies hazards and threats related to planned modifications of a system.
    - **Usage**: Compares the properties of the modified system to a known system to evaluate the impacts of changes. It can also be applied to evaluate changes in operating procedures.
- **Failure Modes, Effects, and Criticality Analysis (FMECA)**:
    - **Purpose**: One of the first methods for system reliability analysis, introduced in 1949.
    - **Usage**: Focuses on identifying potential failure modes of system components, their causes, and the effects these failures might have on the overall system.
- **Hazard and Operability (HAZOP) Study**:
    - **Purpose**: Developed to identify deviations and hazardous situations in process plants.
    - **Usage**: Relies on structured teamwork and brainstorming, guided by specific keywords. It is widely used for risk assessment during the design of process plants and for modifications during later phases. HAZOP can also be adapted to identify hazards in complex work procedures.
- **Structured What-If Technique (SWIFT)**:
    - **Purpose**: A brainstorming method structured around "what-if" questions.
    - **Usage**: Conducted by a group of experts, using a checklist to guide the session. It serves as a simplified version of HAZOP, applicable to similar systems.

- **Master Logic Diagram (MLD)**:
    - **Purpose**: Used to identify hazards in complex systems exposed to various hazards and failure modes.
    - **Usage**: Similar to fault tree analysis but with distinct features. MLD is suitable for systems requiring a broad hazard identification approach.

Following the identification of these accidental events, the Bow-tie model is employed to provide a structured approach to both causal and consequence analysis. This model integrates two traditional methodologies: fault tree analysis (FTA) for examining the causes, and event tree analysis (ETA) for assessing the potential consequences. These models are widely used in industrial settings, where detailed databases on component reliability and failure rates are available. This data allows for precise failure probability assessments and supports the development of flowcharts that represent the operational risks and reliability of complex systems.

In the Bow-tie model, the fault tree's "top event" the central point of failure analysis serves as the pivotal link to the event tree's "initiating event". This visual and conceptual link creates the characteristic bow-tie shape, encapsulating the transition from causative factors to resultant effects (Figure 19). By connecting these two analyses, the Bow-tie model provides a comprehensive view of both the antecedents leading to an accidental event and the potential aftermath of such an event, facilitating a dual exploration of risk that is both retrospective and prospective [235], [236], [237], [238].

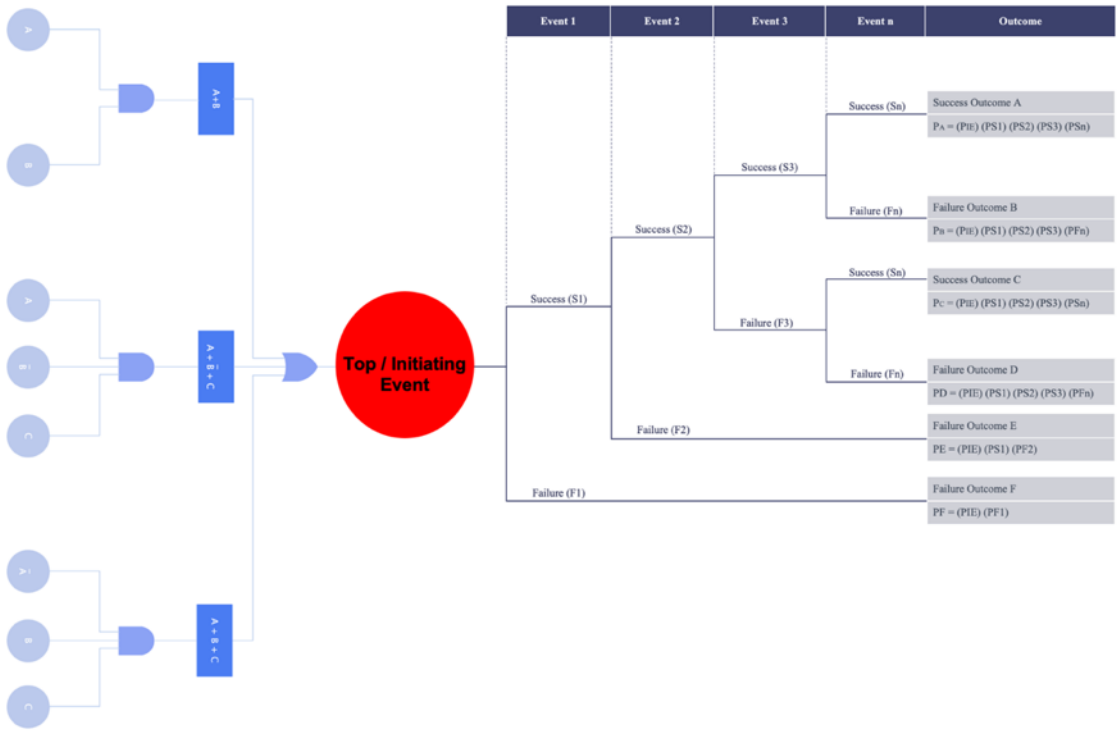

Figure 19: Bow-tie Model Linking Fault Tree's Top Event to Event Tree's Initiating Event.

Causal Analysis (b): Once an accidental event is identified, the potential causes are systematically explored through a causal analysis.

This involves creating a hierarchical structure of main causes and sub-causes, typically represented using a fault tree. The Fault Tree Analysis (FTA) depicted in Figure 20 illustrates how different combinations of basic events, also referred to as elementary causes (Accidental Events), can lead to a specific undesired outcome, known as the Top Event. In the figure, the Top Event is influenced by three different pathways, each representing a combination of Basic Events:

- **Left Branch**: The Top Event will occur if both Event A and Event B happen simultaneously. This is represented by the AND gate, which requires all connected events to occur for the Top Event to be triggered.
- **Middle Branch**: The Top Event will occur if Event A occurs, Event B does not occur (indicated by the line over B), and Event C occurs. This pathway combines events using an AND gate with a NOT condition on Event B.
- **Right Branch**: The Top Event will occur if Event A does not occur (indicated by the line over A), Event B occurs, and Event C occurs. Similar to the middle branch, this pathway also uses an AND gate with a NOT condition, but on Event A.

Each branch in the fault tree uses Boolean logic to show how different combinations of basic events can lead to the Top Event. The AND gates in the figure ensure that the Top Event only happens if all specified conditions within a branch are met. If probability estimates for these basic events are available, they can be used to calculate the likelihood of the Top Event occurring [239], [240].

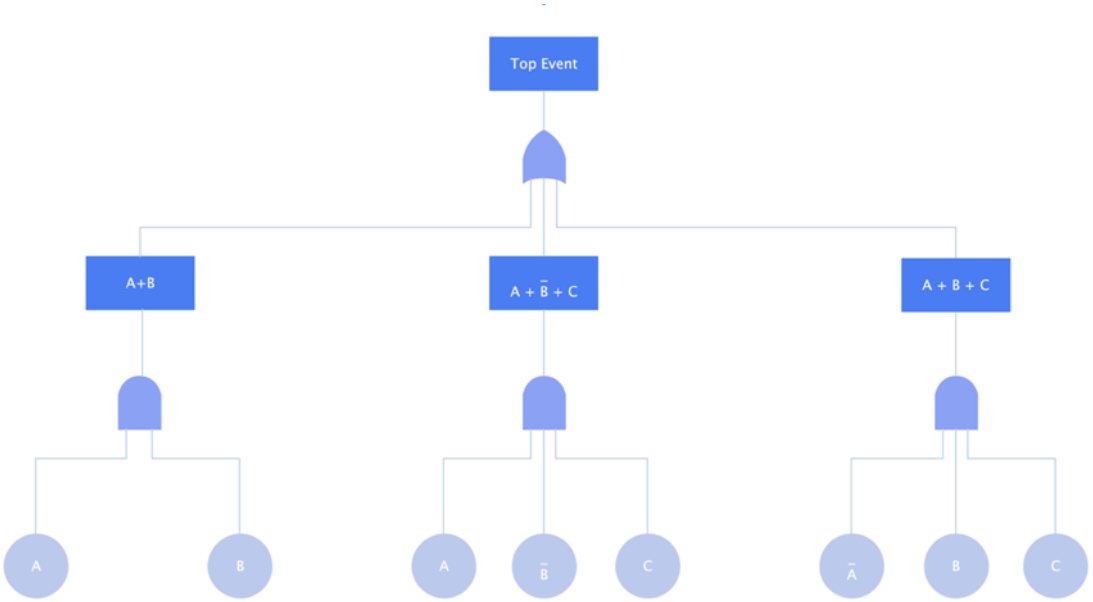

Figure 20: Fault Tree Analysis diagram depicting the relationship between Basic Events and the Top Event.

Consequence Analysis (c): Most systems are designed with various barriers and safety functions intended to mitigate the development or consequences of accidental events. Consequence analysis is conducted to evaluate the effectiveness of these systems, using an event tree analysis (ETA) (Figure 21). The Event Tree employs an inductive approach to explore and highlight accidents sequences triggered by a singular initiating event. It provides a discrete and synthetic representation of all potential evolutionary "scenarios" of the accident, branching from the initiating event based on the occurrence (or non-occurrence) of certain system failures or phenomenological events. This study adopts a logical/probabilistic approach, drastically discretizing reality into macroscopic events, thereby generating alternative accidents sequences that are characterized in probabilistic terms. Consequence (Outcome) analysis may also include the following: simulations of potential scenarios such as fires or system failures; reliability assessments of emergency systems; and evaluations of impacts on human safety, the environment, material assets, and operational continuity [234].

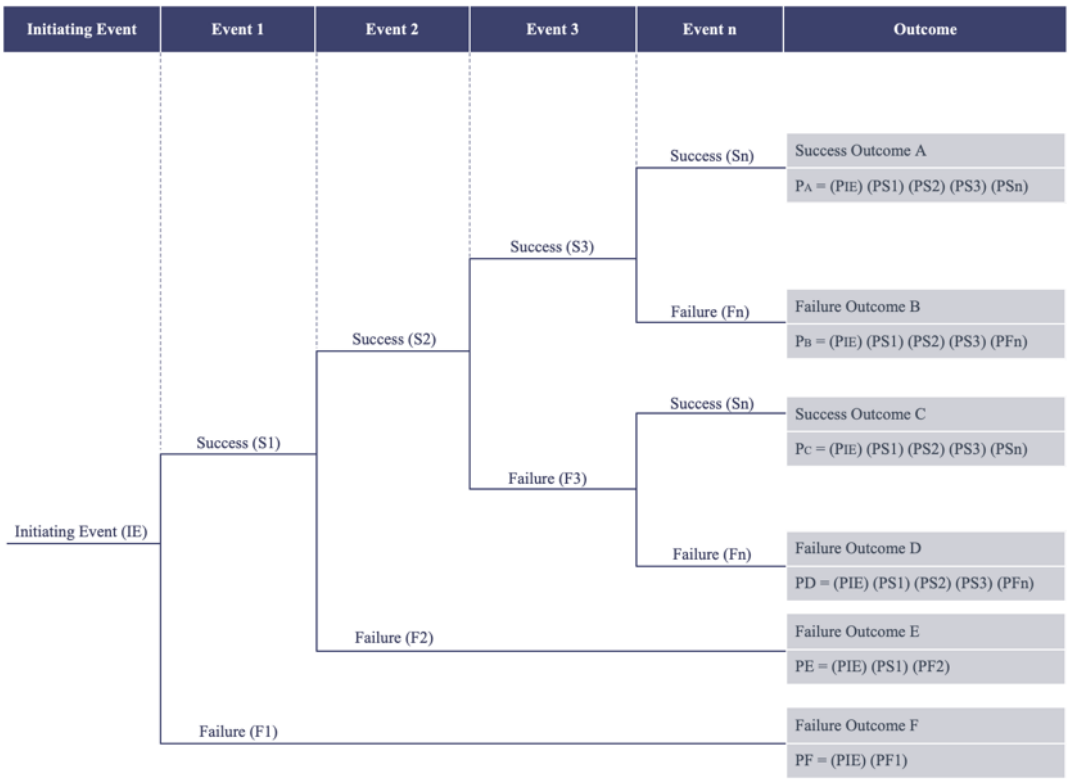

Figure 21: Event Tree Analyses starts from an initiating event and branches into multiple possible outcomes based on successive successes or failures. These branches represent different outcomes and their associated probabilities.

For each necessary and representative event, possible accident sequences are delineated by constructing a logical tree structure. This structure illustrates all potential accident scenarios stemming from the event, based on various evolutionary sequences in which protection and mitigation systems may or may not intervene effectively. This method enables a detailed description of potential accident “scenarios”, each characterized by specific occurrence frequencies and associated damages. Figure 19 illustrates the "Bow-tie diagram" which synthesizes the ensemble of possible accident sequences, categorized by cause types and aggravating factors. The analysis assumes all safety systems function under nominal design conditions, with maintenance plans in place to ensure sustained operation within these parameters.

Before starting an analysis, it is of great importance to pay attention to analysis preparation and system definition. Without considering these two steps previously, the analysis will miss its objective, which certainly makes it hard to focus on where to go and what should and can be achieved. The analysis preparation is aiming at a full understanding of the system under examination and the collection of all necessary data. A definition of the objectives, the

clarification of the applied methods, the procedure, the scope of resources and the precise determination of the object of analysis with its system boundaries are then needed for the system definition.

Once these steps are accomplished, the hazards of the system are identified, and their frequency of occurrence and severity of consequences are determined. For these steps, the already known risk analysis methods are indispensable, approaching the problem successively as well as providing guiding principles and overview. A risk analysis is then completed by depicting the revealed risks of the system in form of graphics in order to present them in a concise way.

Looking at the results of a risk analysis certainly raises the question of meaningful conclusions and resulting consequences for the system. Thus, in order to be able to assess the results, it is necessary to compare them to previously set acceptance criteria. These criteria can either be legal requirements or might well be individual goals defined by the organisation itself. In case the study shows that the risks are above the acceptance criteria, risk reducing measures have to be considered and implemented. The intention of risk management and control is then to observe their implementation and control their consequences and effectiveness upon the system in a repetitive loop.

Building on the foundation laid by risk analysis, this phase focuses on quantifying and prioritizing risks based on their probability and the severity of their potential impacts. It involves advanced statistical tools and modelling techniques to estimate the probability and consequences of identified risks accurately. The insights gained from this phase are for decision-making, enabling organizations to determine which risks are manageable within acceptable thresholds and which require immediate mitigation strategies.

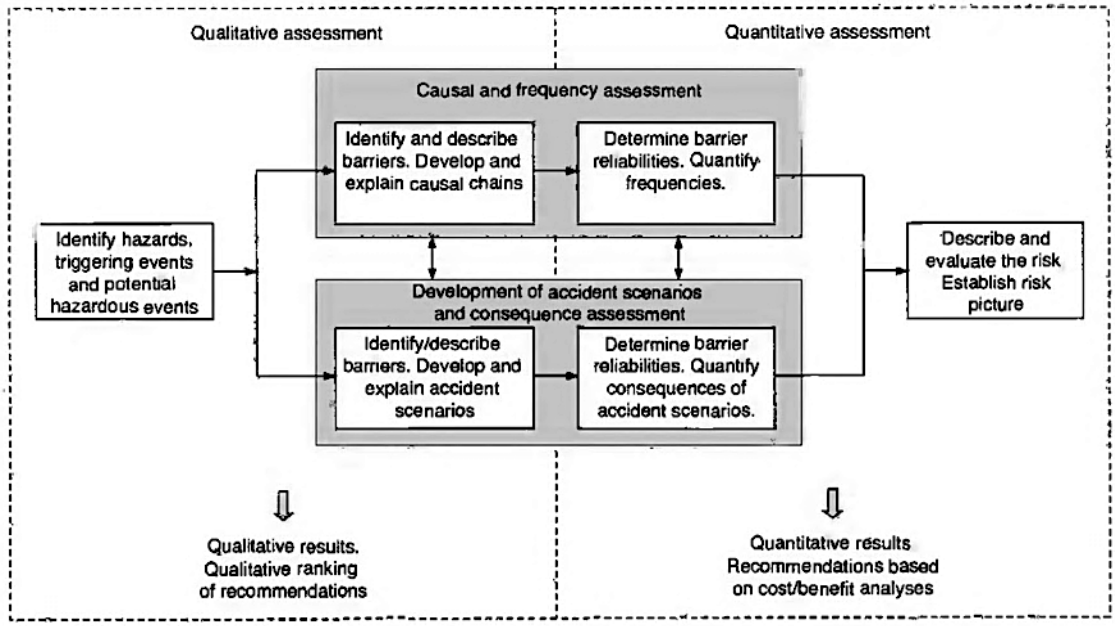

Figure 22: The risk assessment process: qualitative versus quantitative risk assessment [234].

The processes of risk analysis and assessment do not function in isolation but are intricately connected within a comprehensive risk management framework. By systematically identifying and quantifying risks, organizations can implement effective risk management strategies. Table 6 provides a summary of the most widely used risk management standards and frameworks [241].

Table 6: Risk management [241].

Standard/Framework	**Description**	**Reference**
ISO 31000:2018	Guidelines for risk management across all organizations.	International Standards Organization (ISO), 2018 [211]
British Standard BS 31100:2018	Comprehensive approach to effective risk management.	British Standards Institution (BSI), 2018 [242]
COSO ERM Framework: 2017	Structured approach to enterprise risk management.	COSO, 2017 [243]
AS/NZS ISO 31000:2009	Australian/New Zealand version of ISO 31000.	Standards Australia/Standards New Zealand, 2009 [244]
Project Management Institute (PMBOK Guide)	Framework for project management with risk management focus.	PMI 6th edition, 2017 [213]
NIST SP 800-30	Risk management framework for information systems.	NIST, 2012 [220]

2.7 Multi Hazard

2.7.1 Elements of Multiple Hazard Risk Assessment

Multiple hazard assessment is a multifaceted and intricate process. The European Commission in 2010 defines it as the process "to determine the likelihood of occurrence of different hazards either occurring at the same time or shortly following each other, because they are non-independent on one another or because they are caused by the same triggering event or hazard, or merely threatening the same elements at risk without chronological coincidence" [245].

This concept, as defined by the United Nations Office for Disaster Risk Reduction (UNDRR) and United Nations General Assembly, means (1) the selection of multiple major hazards faced by a country, and (2) the specific contexts where hazardous events may occur simultaneously, cascadingly, or cumulatively over time, taking into account their potential interrelated effects [246], [247].

Challenges are known, many regions around the world are exposed to a variety of hazards, broadly categorised as natural or anthropogenic. Natural hazards are environmental events that pose potential threats to human safety, property, and the natural environment [248]. These include geological events like earthquakes and volcanic eruptions, meteorological events such as hurricanes, tornadoes, and ice storms, and hydrological events like floods and tsunamis and others [249]. Anthropogenic, or man-made, hazards are those originating from human activity. They encompass a wide range of accidents, including traffic accidents, industrial disasters, pollution, and acts of terrorism [250].

Such a broad conceptualization permits diverse interpretations and applications within risk assessment frameworks. Various terminologies and concepts have been developed, adding new layers of the multi-hazard concept as described in review by Kappes et all., [251], Jochen Zschau [252], Gill et al., [253] . Generally, the concept of multiple hazards can be approached in two general ways [254], [255]:

1. **Assessing Independent Hazards in a Common Area**: This involves evaluating different hazards that threaten a shared geographical area independently [256], [257]. The goal is to ascertain the individual probability and potential impacts of each hazard [254].
2. **Understanding Interactions and Triggering, Domino, Cascading Effects**: This approach extends beyond evaluating individual hazards [258]. It

delves into the interactions and potential cascading effects [259] between various hazardous events [257], exploring how one event might trigger or exacerbate another, thus leading to compounded risks and impacts.

The occurrence of one type of hazard scenario can amplify the consequences of another hazard scenario of a different nature. This means that the combined effects of multiple hazards are not simply a linear combination of the individual hazards occurring independently. Instead, this reflects the concept of a multi-hazard risk scenario, which must be modelled as a "complex system" that integrates subsystems of different natures. This scenario, where multiple hazards intersect, such as seismic activity and fire in an underground facility, can be understood through the concept of "complex systems" as described by Giorgio Parisi, a Nobel Prize winner for his work on complex phenomena [260]. For instance, during the 2016 Italy earthquake with a magnitude of 6.6, structural collapse in the San Benedetto tunnel caused a minor traffic accident with no fatalities [81]. However, if traffic had been heavier or involved hazardous materials, the number of fatalities and the extent of damage could have been much higher because of the earthquake's effects on traffic conditions. This shows that multi-hazard scenarios involve complex interactions where the combined effects are often far greater than what would be expected from simply considering each hazard on its own.

Parisi explains that complexity is not the same as complication. Complexity refers to the type of relationship between multiple causes and effects, where their interactions behave differently from independent factors. In independent hazard situations, the occurrence of one event does not affect the probability of occurrence of other, but when these hazards occur together, their interactions create compounded risks. Although the same exposed people cannot die twice, it is important to recognize the combination of hazards can exacerbate the overall consequences. Damage to infrastructure and the potential for loss of life are heightened when hazards influence each other, pushing the overall impact beyond what would occur if they were independent.

Consider the interaction between an earthquake and a fire. An earthquake may cause structural collapse, leading to fatalities. Separately, a fire could result in fatalities from toxic gases inhalation. If these events happen independently, the total fatalities would simply be the sum of both events. But in reality, when these hazards occur simultaneously, such as when an earthquake induces a structural collapse, leading to fires their combined effects can multiply the risk. The

interaction between the two hazards creates a scenario where the total impact is not just a sum but an amplification of what each hazard would cause individually. From a mathematical perspective, the relationship between cause and effect in such cases is best described through nonlinear interactions. Physically, the laws governing the effects in a multi-hazard scenario are often different from those governing the hazards when acting independently. Complex systems behave in ways that cannot be easily predicted by analysing individual factors alone; it is the interaction between these factors that leads to unexpected and often amplified outcomes.

Recent advancements in technology and data analytics have led to the development of more sophisticated multi-hazard assessment models [261]. These models use geographic information systems (GIS) [262], remote sensing data [263], and machine learning algorithms [264], [265] to predict and simulate the interactions between different hazards.

Liu, B., Siu, Y. L., and Mitchell, G. [266] developed a systematic hazard interaction classification grounded in the geophysical environment from which natural hazards arise. This environment is segmented into two types of factors: stable factors that set the precondition for natural hazards, and trigger factors determining the frequency and magnitude of hazards. This classification is identifying the relationships between different hazards, including independent, mutex (mutually exclusive), parallel, and series relationships.

Quantitative multi-risk analysis using currently available methodologies poses many challenges as discussed in e.g., [251], [252], [258], [267], [268]. Risks associated with different types of natural disasters, such as earthquakes, landslides, volcanic eruptions, floods and tsunami, are often assessed using different procedures not easily comparable and as a result, individual results are not compared and most of time not possible to relate [258].

Seismic studies [269], [270] show that ground motion damage to partitions and exit systems makes a big difference to common post-earthquake fires, where fire, smoke, and toxic combustion products can spread and prevent fire protection for building occupants [271]. It highlights the inadequacy of computational models, highlighting the need for specific methods to assess and mitigate seismically induced fire risks, and highlights the need to address a significant gap in assessment practices [272].

Moreover, hazard events are often deeply interconnected. For instance, extreme storms can lead to floods and debris flows, while an earthquake might trigger a landslide [273]. A seismic event can also induce secondary hazards like structural collapse and fires, as seen in the 1906 San Francisco earthquake and the 1995 Kobe earthquake, which highlight the significant correlation between seismic activity and subsequent fires. For example, earthquakes can damage electrical [274] and gas lines (San Francisco 1906) [275], creating conditions ripe for fires to ignite and spread [276]. These seismic-induced fires can be particularly devastating, as they compound the impact of the earthquake itself. Additionally, there are scenarios where multiple independent events can occur simultaneously, like hurricanes, floods, and earthquakes, each contributing to an increasingly complex and hazardous situation [277]. However, when considering interaction between different hazards can amplify the overall impact, leading to more severe consequences than if each hazard occurred independently [254].

Solution proposed by Kappes et al. [251] is to shift the focus from multi-hazard to multi-hazard risk. Unlike hazards, risks emerging from different sources are directly comparable, as they quantify potential consequences in terms of loss of life, injuries, and damages.

Work of Gasparini and Aristizabal [278] has emphasized the need for multi-type hazard and risk assessments, particularly in light of past disasters that have demonstrated how natural or man-made events can trigger subsequent hazardous events. This chain reaction often results in a significant increase in fatalities and damages.

Understanding the interdependencies between various hazards for instance, an earthquake can damage infrastructure, leading to gas leaks, which in turn may result in fires. The multi-hazard framework seeks to understand these complex interactions to enhance preparedness and response strategies. Studies have shown that the traditional single-hazard approach may significantly underestimate the multiple risk and impact of disasters when hazards interact [279], [280], [281].

The multi-hazard approach has gained significant implications for policy and planning [282]. Governments and local authorities are increasingly recognizing the importance of integrating risk assessments [281], [283], [284] into spatial planning and building codes to enhance resilience against these scenarios [285]. The Hyogo Framework for Action 2005–2015 (HFA) was the first plan to explain,

describe and detail the work that is required from all different sectors and actors to reduce disaster losses [286]. It was developed and agreed upon by many countries in 2005 in Hyogo, Japan, following the 2004 Indian Ocean tsunami. The HFA outlined five priorities for action and offered guiding principles and practical means for achieving disaster resilience. Its primary goal was to substantially reduce disaster losses by 2015, focusing on saving lives, and reducing the social, economic, and environmental impacts of disasters.

Building on the achievements and lessons of the HFA, the Sendai Framework [287] was adopted in 2015. It provides a more comprehensive approach to disaster risk reduction, expanding the scope beyond natural disasters to include man-made and technological hazards, thereby recognizing the multi-hazard nature of risks. The Sendai Framework sets out four priorities for action and establishes seven global targets, including reducing global disaster mortality, reducing the number of affected people, and reducing economic loss in relation to global GDP by 2030. It emphasizes the importance of understanding disaster risk in all its dimensions of vulnerability, capacity, exposure of persons and assets, hazard characteristics, and the environment.

Latest recherche still highlighted current challenges of multi-Hazard, Ward P.J. et al., [284] discuss the integration and development of disaster risk management strategies to effectively address multi-hazard risks. They recognise the need to consider interconnected hazards and the importance of developing resilience-focused comprehensive management strategies. The EU's Myriad [253] project uses historical data to identify patterns and potential hazard points, focusing on the temporal and spatial correlation of 11 natural hazard events in a 5-pilot area.

The field of multi-hazard risk assessment is rapidly evolving in last 20 years, with ongoing research focusing on improving predictive models and understanding the impacts of multi-hazard scenarios. Future research directions include developing more comprehensive models that can account for interrelation impacts and the increasing interconnectedness of all hazards. But yet detailed analysis of seismic, fire and effect of fire for evacuation and risk analysis of selected scenarios are still gap in the field and lack of research founded in the effect. Due to this the collaborative efforts between governments, academia, and industry are crucial for advancing our understanding with sharing expertise and knowledge in order to managing multi-hazard risks.

Seismic activities can trigger multiple hazards, including fires, leading to complex disaster scenarios. These multi-hazard scenarios often involve an earthquake followed by a fire, as structural damages caused by the seismic event can lead to fire hazards. The severity of these fire hazards depends on the extent of damage to the structures and how long they can withstand the fire post-earthquake [288]. This sequence of earthquake followed by fire is generally considered a sequential hazard Cascading multi-hazards in risk assessment models.

Table 7 presents historical instances of seismic-induced fires. Notable events highlight the significant correlation between seismic activity leading to structural collapses and subsequent fires. In all events, fires caused extensive damage and were major contributors to the overall disaster impact in different phases.

Table 7: Seismic-induced structural collapses, fire outbreaks and fatalities.

Year	Earthquake	Number of Initial Fires	Estimated Fatalities	Estimated Structural Collapses	References
1356	Basel Earthquake	n/a	1000-2000	n/a	[289], [290]
1906	San Francisco Earthquake	50	3000	28000	[291], [292], [293]
1923	Great Kantō Earthquake	129	140000	212000	[291], [294]
1948	Fukui Earthquake	24	n/a	n/a	[291]
1958	Loma Prieta Earthquake	67	65	963	[295], [296], [297]
1971	San Fernando Earthquake	109	n/a	n/a	[291]
1983	Coalinga Earthquake	19	n/a	n/a	[291]
1994	Northridge Earthquake	110	72	n/a	[298], [299]
1995	Kobe Earthquake	293	6437	104906	[294]
2011	Tōhoku Earthquake	330	22152	121776	[294]
2016	Kumamoto Earthquake	15	258	8667	[294]
2024	Noto Peninsula Earthquake	17	245	n/a	[300], [301]

The occurrence of NATECH events [302], [303], where natural hazards trigger technological accidents, is an increasingly significant concern in multi-hazard scenarios [304]. Earthquakes, due to their potential to cause widespread structural damage, are particularly prone to triggering such accidents. These accidents often involve the release of hazardous materials from industrial facilities, leading to additional hazards such as fires, explosions, or chemical spills [305]. The 2011 Tōhoku earthquake in Japan triggered the Fukushima Daiichi nuclear disaster, a severe NATECH event where the earthquake and subsequent tsunami caused nuclear reactor meltdowns, hydrogen explosions, and fires, leading to the release of radioactive materials [297]. Similarly, the 2007 earthquake caused a fire at the Kashiwazaki-Kariwa Nuclear Power Plant, resulting in the leakage of radioactive water into the ocean endure before failure.

The vertical seismic waves associated with the 1995 Hyogo-ken Nanbu (Kobe) earthquake, which led to the failure of the Daikai Underground Station, demonstrate this risk. Seismic activity can cause structural damage to underground systems, leading to a cascade of hazardous events. Broken gas lines in utility tunnels can result in gas leaks, which, in the confined spaces of underground infrastructure, significantly increase the risk of explosions and fires. Similarly, damaged electrical wiring can spark fires, further exacerbating the situation.

In underground systems, the combination of structural damage and potential fires poses a significant risk to public safety and complicates evacuation and rescue efforts.

Seismic activities pose significant risks not only to surface structures but also to underground facilities. However, the response of underground structures to seismic events differs from that of surface structures due to various factors, including the intensity of the earthquake, geological conditions, and specific characteristics of the underground structure itself. General observations on the seismic performance of underground facilities, as summarized by Hashash et al., [75] highlight several critical points (Table 8). While underground structures generally perform better than surface structures during seismic events, cavern tunnels are more vulnerable to seismic forces due to their larger cross-sectional areas and proximity to fault zones. These caverns, excavated from competent rock and reinforced with rock bolts or shotcrete, face increased risks from seismic-induced rock block movement. The dimensions of the cavern often

exceed the spacing between joints in major discontinuities, amplifying the risk of structural damage, particularly in fault fracture zones [80], [306].

Table 8: Key factors influencing the seismic performance of underground structures.

Factor	Description
Reduced Damage for Underground Structures	Underground structures suffer appreciably less damage than surface structures.
Impact of Overburden Depth	Reported damage decreases with increasing overburden depth. Deep tunnels seem to be safer and less vulnerable to earthquake shaking than shallow tunnels.
Vulnerability in Soft Soils	Underground facilities constructed in soils can be expected to suffer more damage compared to openings constructed in competent rock.
Importance of Lining and Grouting	Lined and grouted tunnels are safer than unlined tunnels in rock. Shaking damage can be reduced by stabilizing the ground around the tunnel and by improving the contact between the lining and the surrounding ground through grouting.
Stability Under Symmetric Load	Tunnels are more stable under a symmetric load, which improves ground-lining interaction. Improving the tunnel lining by placing thicker and stiffer sections without stabilizing surrounding poor ground may result in excess seismic forces in the lining. Backfilling with non-cyclically mobile material and rock-stabilizing measures may improve the safety and stability of shallow tunnels.
Damage Correlated with Seismic Parameters	Damage may be related to peak ground acceleration and velocity based on the magnitude and epicentral distance of the affected earthquake.
Importance of Strong-Motion Duration	Duration of strong-motion shaking during earthquakes is of utmost importance because it may cause fatigue failure and therefore, large deformations.
Effect of High Frequency Motions	High-frequency motions may explain the local spalling of rock or concrete along planes of weakness. These frequencies, which rapidly attenuate with distance, may be expected mainly at small distances from the causative fault.

Amplification of Ground Motion Near Tunnels	Ground motion may be amplified upon incidence with a tunnel if wavelengths are between one and four times the tunnel diameter.
Significant Damage Near Tunnel Portals	Damage at and near tunnel portals may be significant due to slope instability.

Why seismic activity is a primary concern for fires in tunnels for our research compared to other natural hazards? Seismic activity is a primary concern for fires in tunnels, particularly in comparison to natural hazards. Earthquakes have a significant impact on underground systems due to their location and construction. As in shown in Table 7 and Table 8. According to a report from Our World in Data, seismic events had a 10.80% effect from 1990 to 2020, with 9,915,286 deaths, second only to droughts and floods [307]. Over the span of two decades from 1998 to 2017, earthquakes accounted for 56% of the total deaths caused by all natural hazards, showing their lethal nature. Economically, earthquakes were responsible for 43% of the total reported losses due to geophysical disasters [308]. Furthermore, from 1900 to 2018, data from the Centre for Research on the Epidemiology of Disasters (CRED) [309] indicate that earthquakes had the highest impact in Europe.

Chapter 3

Multi-Hazard Scenario Modelling and Contextual Risk Assessment

3.1 The Foundation of Aristotelian Logic Integrated by Complex System Logic in Scenario Modelling for Risk Management Purposes

Aristotelian logic, with its methodical approach to reasoning, serves as a foundational framework in the analysis and modelling of complex, multi-hazard scenarios within risk management disciplines. This classical form of logic is articulated through three fundamental types of reasoning: deductive, inductive, and abductive, each essential for dissecting intricate risk configurations and crafting strategic mitigation responses effectively.

1. **Deductive reasoning:** The cornerstone of Aristotelian logic, proceeds from general, universal premises to specific conclusions, providing a structure for necessary inference. For example, the syllogism "All men are mortal; Socrates is a man; therefore, Socrates is mortal", exemplifies deductive reasoning's power to yield incontrovertible conclusions from established truths.

   In scenarios like the Kobe (Japan), San Francisco (USA) and San Benedetto (Italy) tunnel accidents, deductive reasoning helps ascertain definitive outcomes (e.g., earthquake-induced structural failures) from known hazard characteristics and existing safety protocols, ensuring that the risk assessments are sound and predictable on verified data.

2. **Inductive Reasoning:** Contrary to the certainty provided by deduction, inductive reasoning deals with probabilities rather than absolute truths. For instance, observing that "100 swans are white" may lead one to the probable conclusion that "all swans are white", though this is not necessarily a certainty. In the context of multi-hazard scenarios, this reasoning type is invaluable for predicting potential risks based on patterns observed in past events.

   Observing that numerous undergrounds have developed cracks following earthquakes might lead analysts to generalise that seismic activity could likely compromise underground integrity. This inductive process informs decision-making under the ALARP principle, as seen in Edwards v National Coal Board (Subsection 3.1.3) [11], [196].

In this landmark case, the court held that an employer must take all practicable measures to reduce risk, but only to the extent that the cost of those measures is not grossly disproportionate to the level of risk. If inductive reasoning suggests that supported sections of a tunnel show fewer structural issues, one might conclude that supporting the remaining sections could reduce risk. However, under ALARP, the key question is whether the additional cost of reinforcing the entire tunnel is justified. If the cost of reinforcement is disproportionately high relative to the reduction in risk, further action may be unnecessary. Inductive reasoning helps identify the risk patterns, while ALARP ensures a balance between risk reduction and cost-effectiveness. When there is no Acceptability Limit, a sensitivity calculation should be performed to compare the incremental cost of additional measures with the decremental reduction in risk. This process ensures that actions are only taken when they are proportionate to the risk reduction achieved.

3. **Abductive Reasoning:** Abductive reasoning is not directly from Aristotle's works. It was later articulated by American philosopher, logician, and mathematician Charles Sanders Peirce [310]. It involves starting with an incomplete set of observations and proceeding to the likeliest possible explanation. Often considered the inverse of deduction. While abductive reasoning not providing certain truth, it offers a highly probable hypothesis based on available evidence. This approach is particularly useful in complex hazard scenarios where direct causes may not be immediately apparent, allowing for the formulation of plausible risk models based on observed outcomes.

   If a fire breaks out in an underground shortly after an earthquake, and if similar accidents have been previously documented, one might abductively conclude that the earthquake likely caused damage that led to the fire. In a multi-hazard scenario involving an earthquake, structural collapse, and fire, if the tunnel is equipped with the required safety measures (as mandated by law), one might abductively conclude that, given a certain probability, all exposed people will successfully evacuate within the Acceptability Limit boundaries. This ties into the ALARP principle, as risk mitigation measures in the underground must be evaluated to ensure that the residual risks (such as those from multi-hazard events) are reduced to levels that are As Low As Reasonably

Practicable, balancing risk reduction with the cost of additional safety measures.

3.1.1 Application in Multi-Hazard Scenario Modelling

The intricacies of modelling multi-hazard scenarios, such as the sequence of events in underground systems earthquake leading to structural displacement and fire, exemplify the need for a comprehensive approach to risk assessment. By employing Aristotelian logic [311], risk analysts can:

- **Deductive Reasoning:** Validate structural integrity and predictive accuracy of risk models based on established universal principles (e.g., seismic activity's potential to cause structural damage).
- **Inductive Reasoning:** Utilise historical data and observed patterns to probabilistically forecast future hazard scenarios, thereby enhancing preparedness and mitigation strategies.
- **Abductive Reasoning:** Formulate hypotheses regarding unforeseen or complex hazard interactions, adapting risk models to incorporate new evidence or unexpected developments effectively.

As illustrated in Figure 23, the procedure for multi-risk assessment involves several key steps [258]. Effective multi-hazard risk assessment begins with a clear definition of the space-time window, which serves as the foundation for the entire process. The space-time window specifies the geographic area and time period under consideration. The spatial component may encompass a small area, such as a single building, or a larger region, depending on the assessment's objectives. The temporal component defines the time frame, whether short-term for immediate risks or long-term for strategic planning. This definition sets the boundaries for identifying relevant hazards and events.

With the space-time window and an appropriate risk evaluation metric established, the next essential step is to systematically identify all potential hazards and consequent risks that could affect the selected area. The numerical indicator of risk depends on the structural vulnerability and the occupancy level. If a structure is robust against the intensity of an earthquake hazard and no people are present, the risk is effectively null. Conversely, if the structure is weaker than the hazard and there is a large number of exposed individuals, the risk rises significantly. This identification process should be based on a comprehensive analysis of historical data, where inductive reasoning is particularly valuable, providing insights into past events and their impacts. It is

important to consider emerging risks and future scenarios, particularly those that may not have historical precedents but could become significant due to factors such as technological advancements, changes in land use, or increasing complexity in infrastructure networks.

In a multi-hazard risk assessment, particular attention must be given to the interactions among different hazards. These interactions can lead to cascading effects or compound events, where the occurrence of one hazard induces, triggers or amplifies others, resulting in a more severe overall impact. Therefore, it is essential to comprehensively identify and model these hazard interactions, often requiring the application of abductive reasoning to anticipate complex, unforeseen interactions.

The probabilistic assessment of each identified hazard scenario is the next stage, heavily relying on inductive reasoning. This step requires the use of statistical and computational models to estimate the likelihood of different scenarios occurring within the defined space-time window, accounting for the uncertainties inherent in predicting complex natural and anthropogenic processes.

Following this, the vulnerability and exposure of the area to each hazard scenario must be assessed. This assessment considers both the direct impacts of individual hazards, validated through deductive reasoning, and the compounded vulnerability that may arise from the interaction of multiple hazards. For example, an area might be more vulnerable to fire if it has already been weakened by an earthquake or if key infrastructure has been compromised.

The assessment culminates in estimating potential losses and conducting an overall multi-risk assessment. This involves that the probabilities of scenarios are differently conditioned by accidental changes in the vulnerabilities and exposures in the scenario themselves and involves to the order of magnitude of the potential impacts in terms of economic losses, human casualties, and environmental degradation. The multi-risk assessment should provide a holistic view, considering all identified risks and their interactions, to support decision-making processes in emergency management, territorial resilience and sustainability, land-use planning, and other relevant fields.

It is important to recognize that this entire process should be iterative and adaptive, with the flexibility to incorporate new data, evolving risks, and changing societal values. The ultimate goal is to develop a robust and flexible

multi-risk assessment framework that can guide effective risk mitigation and management strategies, tailored to the specific needs of the end-users.

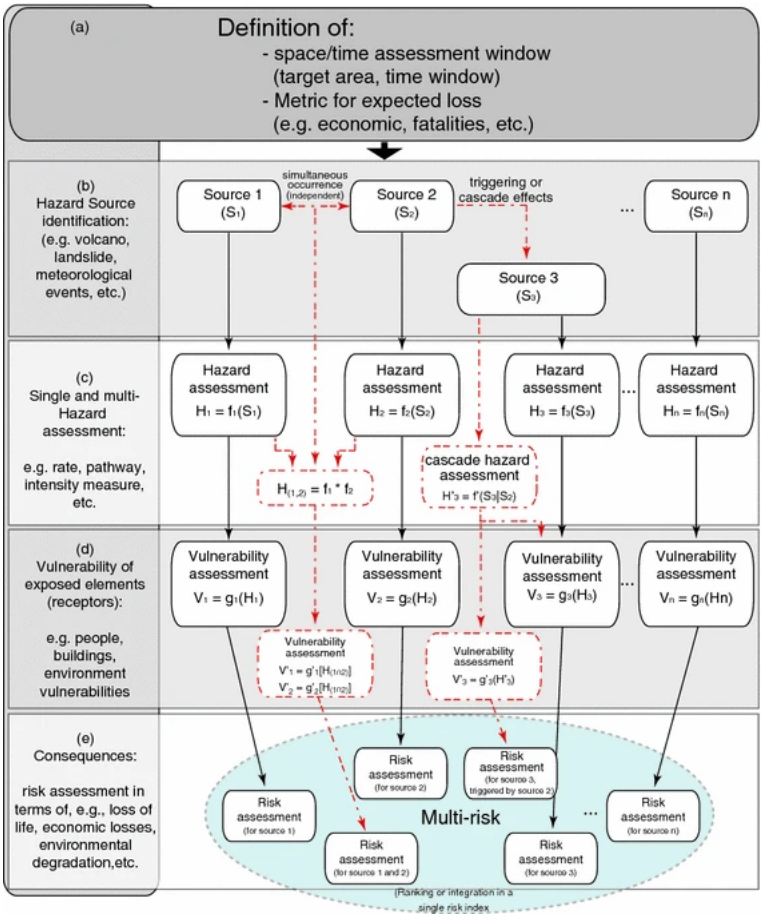

Figure 23: Schematic description of the general procedure followed for the multi-risk evaluation [258].

What there is behind of the definition and modelling of multiple hazard scenario?

There is an example in Figure 24 illustrates independent hazards, as well as a non-independent scenario where seismic action at a specific tunnel location causes the collapse or displacement of a structure, leading to a potential fire hazard involving equipment. Multiple hazards are taken in the sense of the joint action of more than one major hazard occurring in an underground framework. In this specific context possible interrelated potential impacts are taken into consideration when hazardous events creating many possible hazardous scenarios occur simultaneously, gradually or cumulatively over the time. An earthquake can generate different scenarios at various locations due to variations in local conditions. When modelling these events, it is essential to avoid associating one hazard with a single outcome, and instead, multiple possible scenarios must be considered. For instance, one scenario may occur at a specific

location and time, while another might simultaneously occur elsewhere due to variations in factors such as the hypocentre, epicentre, magnitude, local soil conditions and related damping model according to different direction or structural vulnerabilities and others. As the exact scenario that will occur remains uncertain, our assessment must account for a wide range of possible outcomes.

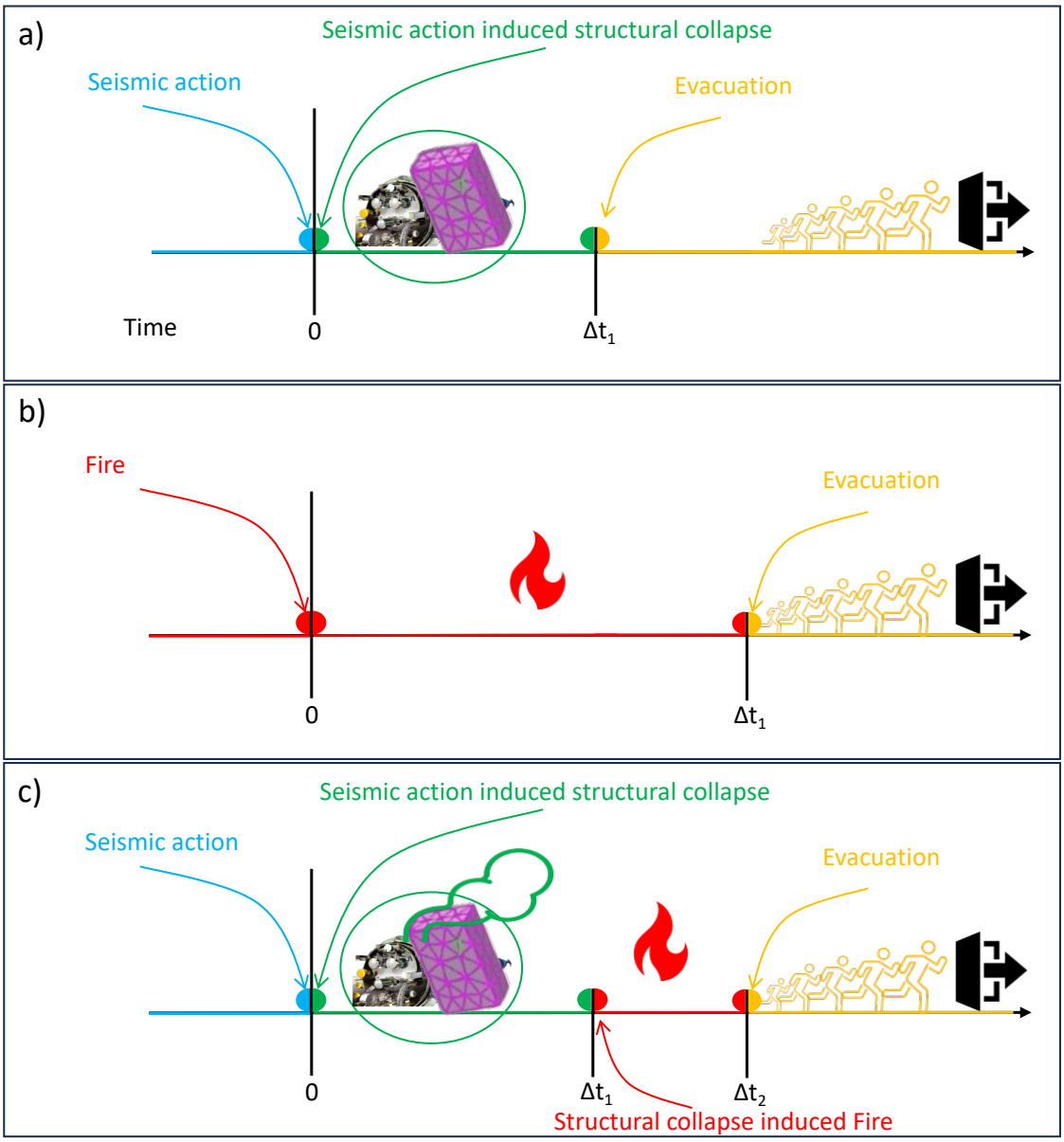

Figure 24: Independent (a; b) and simultaneous (c) in the underground over time. The seismic action and fire events can occur independently, or the fire can be induced by structural collapse triggered by seismic action.

The basic aim of the design process is to identify the necessary and sufficient number of scenario types, as well as the minimum number of scenarios required to validate the risk analysis steps for calculating the suitable key risk indicators [12], [13]. The existence of interactions between different types of hazards presents a significant challenge. These interactions often result in complex chains

of cascading or joint hazards, complicating the analysis [251]. For this reason, each scenario should first be described with its key factors and boundary conditions before undergoing probabilistic evaluation. The prior identification of which scenarios are necessary will condition the probability of the hazard events involved and their intersections. The operating tool used to guarantee that the group of the necessary scenarios identified are "mutually exclusive" are the tree diagrams. The branches of the tree diagrams describe the above defined "mutually exclusive" scenarios. Among branches, there are "mutually exclusive" scenarios, whereas along the branches, non-mutually exclusive sub-scenarios/events are found. These scenarios must then be further analysed and simulated using advanced methods such as incremental dynamic analysis and thermofluid-dynamics to obtain both estimation of structural damage displacement in earthquakes and prediction number of fatalities in fires and earthquakes. When evaluating the evacuation of exposed individuals, human behaviour under these scenarios must also be taken into account (Figure 26).

In this case, the analysis involves three separate event trees (Figure 25):

1. Earthquake events: Representing the potential outcomes of an earthquake, with or without structural collapse.
2. Fire-initiating events: Representing the occurrence of fire initiation independent of any earthquake.
3. Earthquake-induced structural collapse leading to fire events: Where an earthquake causes structural collapse, which subsequently leads to a fire.

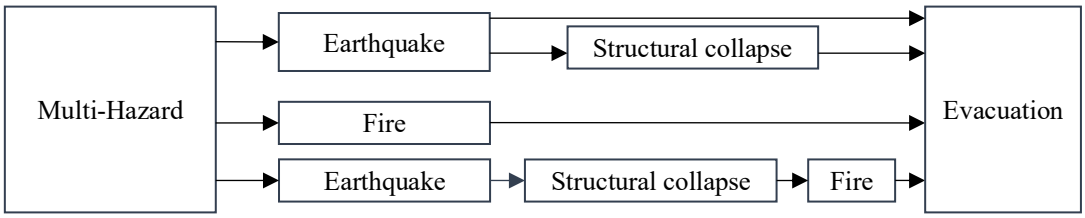

Figure 25: Multi-hazard model for initiating events.

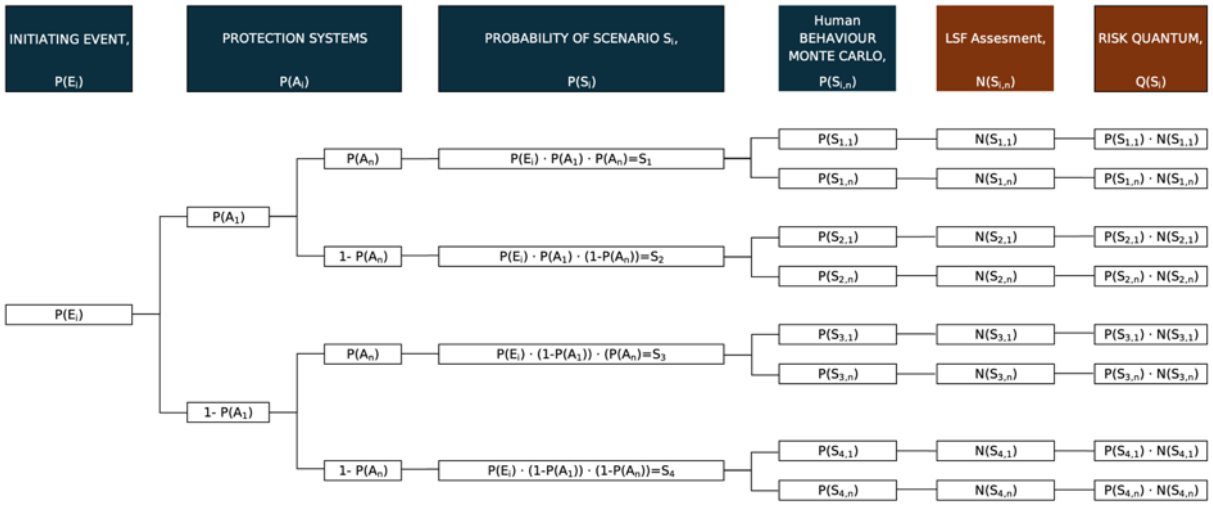

Figure 26: Event tree diagram for initiating (initiator) event.

In multi-hazard risk modelling, understanding how individual events interact and lead to cascading consequences is a key aspect. Voltaire, in *Candide*, used the concept of cause and effect described by the phrase "tout est enchaîné nécessairement, et arrangé pour le mieux" (everything is necessarily chained/linked/connected and arranged for the best) to challenge the deterministic and overly optimistic worldview of philosophers like Leibniz [312], [313]. Leibniz believed that everything happens for the best in the best of all possible worlds. Voltaire's focus was on showing that while events may be interconnected, they often lead to unintended consequences, challenging simplistic views of cause and effect.

3.1.1.1 Qualitative and Quantitative Perspectives in Scenario Selection

From a qualitative perspective, multi-hazard scenario selection involves identifying key risk drivers across various hazards. These drivers must be carefully evaluated to ensure the selection of scenarios that encompass a wide range of potential risks.

Mathematically, the occurrence of improbable events can be viewed through the union of disjoint events. According to probability theory, the probability of any one of several disjoint events occurring is the sum of the individual probabilities of those events. Therefore, while the probability of each specific scenario might be very low, the probability that *one* of the many low-probability events will occur can be surprisingly high.

As Aristotle noted more than 2,000 years ago, "It is probable that improbable things will happen". This principle is well understood in probability calculus [314]. In terms of Black Swan events, these are unexpected, highly impactful accidents that defy normal expectations. A relevant ALARP cases could involve as explained in subsection 3.1.9.

Similarly, in a multi-hazard framework, even if each individual scenario has a very low probability, the overall risk when considering the full range of possible hazard interactions can still be significant. This mathematical understanding helps us recognize the importance of not dismissing low-probability scenarios, as they collectively contribute to the overall risk.

3.1.1.2 Minimum Necessary and Sufficient number of Scenarios: A Mathematical Approach

The key challenge is to determine the minimum necessary and sufficient number of scenarios to represent the risks without overwhelming the analysis. Mathematically, this requires balancing the risk contribution of each scenario, which means how much risk it adds to the overall picture, against the complexity introduced by including more scenarios.

The logic of organizing and selecting minimum necessary and sufficient number of scenarios resembles, in part, the famous riddle of the man going to St. Ives [315]:

"As I was going to St Ives,

I met a man with seven wives,

Each wife had seven sacks,

Each sack had seven cats,

Each cat had seven kits:

Kits, cats, sacks, and wives,

How many were there going to St Ives?"

Just as this riddle requires careful consideration to understand who was actually going to St. Ives, we must carefully examine which scenarios are truly necessary

in our analysis. Despite the apparent complexity, with wives, sacks, cats, and kits, the answer is simple: only "I" was going to St. Ives. Similarly, though there may be countless potential scenarios in risk assessment, the goal is to identify a minimal set of representative scenarios that capture the essential risks without unnecessary redundancy.

At the core of approaches of Kaplan [203], [316], Aven [317], [318] and Hall [319] the idea of grouping scenarios into representative, more manageable scenarios. This concept is widely applied in various risk assessments, including those for fire scenarios in fire risk assessment [320], [321]. The process begins with a complete set of all possible hazard scenarios, which can be denoted as:

$$S = \{S_1, S_2, S_3, \ldots, S_n\} \tag{15}$$

where each element S_i represents a different group of scenarios (e.g., seven scenarios in multi-hazard risk assessment framework). As Kaplan, the set of scenarios $\{S_i\}$ must be complete, meaning that it covers all the possible scenarios, or at least all the important ones.

In this context, the space of events S_A includes both the union of all possible hazard scenarios and its complement, which represents the scenario where no event occurs. Mathematically, this is expressed as:

$$S_A = US_i + \overline{US_i} \tag{16}$$

where US_i is the union of all hazard scenarios, and $\overline{US_i}$ is the complement of those scenarios (i.e., the probability that no accident occurs). The total probability of the event space must sum to 1:

$$P(S_A) = 1 \tag{17}$$

Since analysing all scenarios individually is impractical, these events are organized into manageable subsets. Each set of scenarios for a specific hazard type can be represented as follows:

$$S_i = \{S_{i1}, S_{i2}, S_{i3}, \ldots, S_{im}\} \tag{18}$$

where S_i represents the complete group of scenarios for hazard type i. To further refine the analysis, each scenario S_{ij} can be broken down into smaller sub-scenarios based on additional characteristics.

$$S_{ij} = \{c_{ij1}, c_{ij2}, c_{ij3}, \ldots, c_{ijk}\} \tag{19}$$

These scenario subsets simplify the process by consolidating similar events, allowing for more manageable risk assessment The union of all scenario subsets covers the entire set of possible fire scenario:

$$S = S_1 \cup S_2 \cup S_3 \ldots \cup S_m \tag{20}$$

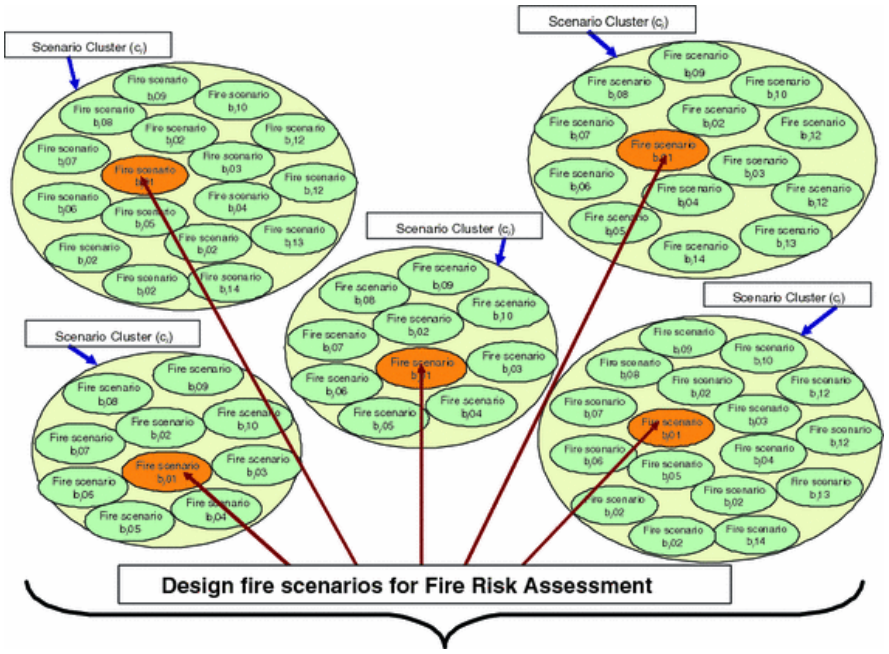

Figure 27: Illustration of fire scenario clusters (subsets) used to represent all possible fire events in a target building. Each cluster contains multiple fire scenarios that share similar characteristics. This grouping simplifies the analysis by reducing the number of fire scenarios to a manageable set for effective risk assessment [319].

This approach shows us that, the scenario set is comprehensive enough to cover all minimum necessary and sufficient scenarios but not so large that it includes negligible or redundant scenarios. For example, when considering fire only scenario ($F \cap \neg SC \cap \neg PGA_i$) (Figure 27) this set S_1 should encompass:

1. One subset $S_{1,1}$ might include high probability,
2. Another subset $S_{1,2}$ might include low probability, high consequence,
3. Another subset $S_{1,3}$ might include different fire origins,
4. Another subset $S_{1,4}$ might include favourable and unfavourable locations.

By organizing scenarios based on key factors (such as probability, origin, or severity), the need for comprehensive risk coverage can be effectively balanced with minimizing the complexity of the analysis. Each subset S_{ij} represents a distinct grouping of scenarios that share certain characteristics, while the further

breakdown into sub-scenarios c_{ijk} allows for more detailed probability calculations based on specific risk factors.

From a mathematical perspective, set theory helps formalise this approach by representing the complete set of fire scenarios and breaking it down into subsets. These subsets S_{ij} form a partition of the risk space S_A, where each scenario S_i satisfies the following conditions:

1. Complete, in the sense that the union of all scenarios $\cup S_i = S_A$, meaning the entire risk space is covered,
2. Finite, ensuring the total number of scenarios $\{S_i\}$ is finite and manageable for analysis $|\{S_i\}| < \infty$,
3. Disjoint, meaning $S_i \cap S_j = \emptyset$ for all $i \neq j$, ensuring no overlap between scenarios.

This partitioning guarantees that each scenario is unique, finite in number, and together they cover the entire risk space comprehensively. By structuring the scenario set in this way, the risk assessment remains both thorough and practical.

To calculate the total probability of a hazardous event across all chosen scenarios, if the scenarios are mutually exclusive (disjoint), the total probability is simply the sum of the probabilities of each scenario:

$$P(S_1) + P(S_2) + \ldots + P(S_n) \tag{21}$$

In this case, the scenarios do not overlap, and the total probability is obtained by summing the individual probabilities. The sufficiency of the scenario set is achieved when the collective risk captured by these probabilities reaches a point where adding further scenarios would contribute negligible risk to the overall analysis.

However, if the scenarios are not mutually exclusive, meaning some scenarios could overlap (e.g., multiple fires starting in the same region or affecting the same equipment), the inclusion-exclusion principle must be applied to avoid overestimating the total risk:

$$P(S_1 \cup S_2 \cup \cdots \cup S_n) = \sum P(S_i) - \sum P(S_i \cap S_j) + \sum P(S_i \cap S_j \cap S_k) - \ldots \tag{22}$$

The sufficiency of the scenario set is achieved when the collective risk captured by these probabilities reaches a point where the addition of further scenarios would contribute negligible risk to the overall analysis.

Mathematically, completeness uncertainty arises because we cannot assign probabilities to events that have not been identified or considered in the analysis. If the scenario set S is incomplete, then the calculated total probability for fire risk P(S) will underestimate the true risk, as unconsidered scenarios are implicitly assigned a probability of zero.

Decision criteria for excluding scenarios should not be based solely on individual probabilities. Instead, they should reflect the aggregate risk of multiple scenarios occurring. This ensures that the overall risk profile remains accurate, even when low-probability events are involved.

To maintain manageability, scenarios that share similar risk drivers can be grouped or categorized to avoid overcomplication. Mathematically, this can be represented as consolidating events in the set S that have similar characteristics. By organizing fire scenarios into scenario subset, it ensures that every possible fire scenario is represented in the risk assessment.

The concept of a scenario in our multi hazard risk assessment serves as a model of what might happen in reality under specific conditions. However, it is important to acknowledge that no matter how detailed or comprehensive a scenario may be, it is highly unlikely that any single modelled scenario will perfectly match a real-world event. This is because the complexity of real-life events often exceeds what can be captured in a controlled, theoretical framework. In fact, when we consider the countless combinations of variables the possible number of scenarios becomes practically infinite. Even if millions of scenarios were constructed, it would still be impossible to account for every possible event. The sheer number of permutations arising from combining different risk factors means an overwhelming amount of data would always be involved. However, this does not undermine the importance of scenarios in risk assessment. On the contrary, despite this infinite complexity, scenarios remain an essential tool for understanding and managing risks.

The goal, then, is not to model every conceivable scenario, but to develop a minimum necessary and sufficient number of representative scenarios that are close enough to cover all potential undesirable events. In this way, scenarios serve as proxies for reality. While they may not capture every detail of what might happen, they provide a structured and actionable framework for identifying and mitigating risks. Even though the exact event that occurs in reality may differ from any one scenario, the carefully chosen representative

scenarios ensure that the assessment remains meaningful and comprehensive. Informed decisions can be made, and better preparation for a wide range of outcomes is possible, even in the face of uncertainty.

3.1.1.3 Independent and Non-Independent Events in Multi-Hazard Scenarios

The interaction between fire, structural collapse, and earthquake reminds us that no event occurs in isolation. Even when hazards appear to be independent, underlying factors often tie them together in ways that might not initially be considered. In complex systems, the lines between events blur, and risks may arise from interactions that were not fully considered in the initial analysis.

This reminds that while hazards are often treated as separate, they are part of a broader, interconnected system. Just as in life, where one action can set off a chain of unforeseen reactions, hazards have dependencies, even when they are not immediately seen. This analysis encourages thinking beyond isolated events and considering that risks are not simply about single occurrences, but about how these events might influence one another, sometimes in ways that are not immediately evident.

To better understand these relationships, Figure 28 uses a Venn diagram to illustrate the complex interdependencies where conditional probability does not equal unconditional probability, and independent occurrences of hazards, where conditional probability equals unconditional probability, in this multi-hazard model. These dynamics are explored through the analysis of 7 distinct scenarios, each representing a unique combination of fire, structural collapse, and earthquake. These represent all valid and distinct combinations of fire, structural collapse, and earthquake, considering mutual exclusivity, independent and non-independent conditions. Building on principles from probability theory [322], [323], [324], [325], [326], [327], the following subsection will delve into each scenario, analysing how these hazards may interact and what risks may arise from these interactions.

3.1.1.3.1 Independent Hazard Scenarios (Mutually Exclusive): Earthquake, Structural Collapse, and Fire

1) Fire only ($F \cap \neg SC \cap \neg PGA_i$): In this scenario, the independent occurrence of fire is examined, independent of both structural collapse and earthquakes (Figure 24b). The focus is on how fire can arise due to internal causes, such as electrical

faults, human error, or spontaneous ignition. A real-world example of such an event is the 1999 Mont Blanc Tunnel fire, where a vehicle fire led to catastrophic consequences, including 39 fatalities [11]. While fire is treated as independent from collapse and earthquakes in this scenario, such events remind us of the potential for fire severity to increase under certain conditions.

From a mutual exclusivity standpoint, fire is assumed to occur without any triggering collapse or earthquake, and the probability of this event is given by:

$$P(F \cap \neg SC \cap \neg PGA_i) = P(F) \cdot P(\neg SC) \cdot P(\neg PGA_i) \quad (23)$$

2) Structural collapse only ($\neg F \cap SC \cap \neg PGA_i$): The structural collapse only scenario represents an event where structural failure occurs independently of both fire and seismic activity. This raises the important question: What factors could lead to a collapse without external forces? Factors such as internal weaknesses, including aging infrastructure, design flaws, corrosion, material fatigue or poor maintenance can cause structural collapse [328], [329], [330], [331], [332] without the involvement of external triggers, as seen in the Morandi Bridge collapse in Genoa, Italy, in 2018, which resulted in 43 fatalities [333], [334]. This makes the collapse independent of fire or earthquakes, yet it prompts us to consider the unseen dependencies that might exist perhaps structural weaknesses also make the system more vulnerable to fire or earthquakes under different circumstances. Although this question is beyond the scope of this research, it provides a direction for future investigation.

As with the previous scenario, non-mutual exclusivity is assumed, meaning the collapse occurs without any fire or earthquake, and the probability is expressed as:

$$P(\neg F \cap SC \cap \neg PGA_i) = P(SC) \cdot P(\neg F) \cdot P(\neg PGA_i) \quad (24)$$

3) Earthquake only ($\neg F \cap \neg SC \cap PGA_i$): The earthquake only scenario describes an earthquake that occurs without causing fire or structural collapse (Figure 24a). Here, the focus is on seismic activity and its isolated impact on the environment. This scenario reflects the independence of earthquakes from fire and collapse. However, this raises a reflective point: Not all earthquakes lead to cascading failures, but does this imply that the risks of structural collapse or fire are entirely absent in every case? In reality, seismic activity may interact with other vulnerabilities even if those do not immediately manifest. Earthquakes often produce aftershocks, which can exacerbate damage to already weakened

structures, eventually leading to collapse even if the initial earthquake did not cause immediate failures [335], [336]. Additionally, cumulative damage can occur [337]. Buildings may experience non-catastrophic damage during a small or moderate earthquake, such as cracks or stress fractures, which, if left unchecked, can increase the risk of collapse or fire in subsequent events, including future earthquakes or even unrelated hazards. Mutual exclusivity is assumed, meaning the earthquake occurs without any fire or structural collapse, and the probability is expressed as:

$$P(\neg F \cap \neg SC \cap PGA_i) = P(\neg SC) \cdot P(\neg F) \cdot P(PGA_i) \tag{25}$$

In each scenario, the events (fire, structural collapse, earthquake) are treated as independent of one another. This allows us to apply the Multiplication Theorem to calculate the probability of the occurrence of one event while others do not occur. Each scenario assumes that the probability of one event does not directly affect the probability of the others.

Each event is mutually exclusive with the other two. In the fire only scenario, neither structural collapse nor earthquake occurs; in the structural collapse only scenario, neither fire nor earthquake occurs; and in the earthquake only scenario, neither fire nor structural collapse occurs. In all scenarios, the simultaneous occurrence of fire, structural collapse, and earthquake is also not possible. This mutual exclusivity is reflected in the following equations:

$$P(F \cap SC) = P(F \cap PGA) = P(SC \cap PGA) = 0 \tag{26}$$

While each scenario is considered in isolation, the Sum Rule allows us to evaluate the total probability of any of these hazards occurring collectively. Since fire, structural collapse, and earthquake are exclusive events (i.e., they cannot occur simultaneously), the total probability is simply the sum of the individual probabilities:

$$P(F \cup SC \cup PGA) = P(F) + P(SC) + P(PGA) \tag{27}$$

3.1.1.3.2 Non-Independent Hazard Scenarios

4) Fire and structural collapse without earthquake ($F \cap SC \cap \neg PGA_i$): In this scenario, both fire and structural collapse occur together, but without the influence of an earthquake. This type of event combination reflects how internal failures whether due to a fire weakening a structure or a structural collapse

causing a fire, can escalate into more significant hazards, even in the absence of seismic activity. This scenario shows the importance of understanding the interaction between different hazards within a system, especially when they occur without external triggers like earthquakes. These dynamics reflect a broader relationship; however, they are not the focus of analysis in this particular case study.

Unlike the previous scenarios, where events were mutually exclusive, fire and structural collapse are non-mutually exclusive in this case. They can occur simultaneously, creating an important question: How do these two events interact, and how does one influence the other?

Fire inducing structural collapse: When fire weakens structural integrity, it may lead to a collapse. In the literature, there are several studies on this topic Jiang & Li, 2019; M. & K.S., 2021; NIST, 2011a; Porcari et al., 2015; Stroup et al., 2004; Torero, 2011). For example, the World Trade Center 7 (WTC 7) in New York City in 2001 [338], [339], [340], [341], where analyses indicated that the building would have collapsed solely due to the effects of the fires, even without debris impact damage. Another example is the Plasco Building in Tehran in 2017 [342], [343], where a fire engulfed the structure, resulting in a complete collapse and numerous fatalities. This introduces conditional dependence, where the probability of structural collapse depends on the presence of fire:

$$P(SC \mid F) \neq P(SC) \tag{28}$$

Structural collapse inducing fire: While specific studies on structural collapse inducing fire may not be as widely documented as fire-induced collapses, the underlying mechanisms can still be logically explained. A significant example of structural collapse-induced fire hazards is the 2012 Sasago Tunnel accident in Japan. The sudden failure of ceiling panels trapped three vehicles beneath the debris, with two vehicles subsequently involved in fires. This event resulted in nine fatalities and two injuries [344], [345]. As in the structural collapse only scenario, structural failure can result from various internal factors. When the collapse occurs, it can damage essential systems or equipment, leading to failures that may initiate a fire, such as electrical wiring, gas pipes, or equipment, creating an environment ripe for ignition. Damaged electrical wires may short-circuit, generating sparks that can easily ignite surrounding materials [346]. Similarly, ruptured gas pipes release flammable gases, creating a highly combustible environment [347], [348], [349], [350]. While gas explosions were once attributed

to “friction sparks”, this term encompasses various mechanical operations, such as grinding, cutting, and impacts, which transform mechanical energy into heat, capable of igniting gas-air mixtures [348]. These factors further increase gas pipes fire risks, especially in debris-filled areas. Additionally, equipment can pose significant fire risks if compromised during a collapse, according to the NFPA, equipment is a common cause of fires in industrial properties [351], [352]. The fire that follows the collapse is conditionally non-independent on the failure of the structure, as it is triggered by the collapse event itself, expressed as:

$$P(F \mid SC) \neq P(F) \tag{29}$$

This differs from an independent fire event, where fire occurs without being causally linked to structural collapse. In this scenario, earthquakes are intentionally excluded, which means we set the probability of fire or structural collapse occurring together with an earthquake to zero. Mathematically,

$$P(F \cap PGA_i) = 0,\ P(SC \cap PGA_i) = 0,\ P(F \cap SC \cap PGA_i) = 0 \tag{30}$$

This implies that, within the scope of the model for this scenario, fire and/or collapse cannot coincide with the earthquake event, making them mutually exclusive with respect to earthquakes. However, mutual exclusivity does not imply independence. Specifically, the occurrence of an earthquake affects the probabilities of fire and structural collapse, and vice versa such that $P(F \cap PGA_i) = 0$ and $P(SC \cap PGA_i) = 0$. Consequently, the probabilities of fire and structural collapse occurring independently of earthquakes are expressed as $P(F \mid \neg PGA_i)$ and $P(SC \mid \neg PGA_i)$, respectively, under the condition that an earthquake does not occur.

For events that are non-independent, like fire and structural collapse, the Multiplication Theorem is applied to calculate their joint probability. The relevant conditional probability must be selected based on the focus of the analysis. For instance, in the case of fire leading to structural collapse, the joint probability can be expressed as:

$$P(F \cap SC \cap \neg PGA_i) = P(F) \cdot P(SC \mid F) \cdot P(\neg PGA_i) \tag{31}$$

Conversely, when considering the scenario where structural collapse leads to fire, the joint probability is represented as:

$$P(F \cap SC \cap \neg PGA_i) = P(SC) \cdot P(F \mid SC) \cdot P(\neg PGA_i) \tag{32}$$

In both cases, the relationship between fire and collapse is modelled conditionally, while the absence of earthquakes is considered.

Given that this scenario specifically addresses fire and structural collapse, the Sum Rule is applicable to these events, allowing us to calculate the probability of at least one occurring. The formula is expressed as follows:

$$P(F \cup SC) = P(F) + P(SC) - P(F \cap SC) \quad (33)$$

This takes into account that fire and structural collapse can happen together (i.e., they are non-mutually exclusive), so the intersection $P(F \cap SC)$ is subtracted to avoid double-counting the overlap. These dynamics reflect a broader relationship; this relationship is not the focus of analysis in this research.

5) Structural collapse due to earthquake without fire ($\neg F \cap SC \cap PGA_i$): In this scenario, structural collapse occurs as a direct consequence of an earthquake, independent of any fire. This shows the potential for seismic activity to compromise structural integrity without necessarily resulting in secondary hazards such as fire (Figure 25). Examples of such events include the 2016 San Benedetto tunnel collapse [4], [81], [353], the 2008 Wenchuan earthquake in China [76], [354], the 1999 Chi-Chi earthquake in Taiwan [353], where seismic activity caused significant structural failure in tunnels without triggering any fires. Here, the relationship between the earthquake and structural collapse is non-mutually exclusive, indicating that the earthquake is a direct cause of the structural failure.

The intensity of the earthquake can significantly influence the probability of structural collapse. The relevant conditional probability in this context is represented as:

$$P(SC \mid PGA_i) \quad (34)$$

Fire is explicitly excluded from this scenario, making it mutually exclusive with both the collapse and the earthquake:

$$P(F \cap SC) = 0,\ P(F \cap PGA_i) = 0,\ P(F \cap SC \cap PGA_i) = 0 \quad (35)$$

This reflects the absence of fire in conjunction with structural collapse or earthquake in this scenario. The Multiplication Theorem is applied to calculate the joint probability of structural collapse occurring due to an earthquake, while fire is excluded:

$$P(\neg F \cap SC \cap PGA_i) = P(PGA_i) \cdot P(SC \mid PGA_i) \cdot P(\neg F) \quad (36)$$

In this scenario, the Sum Rule applies to the earthquake and structural collapse:

$$P(SC \cup PGA_i) = P(SC) + P(PGA_i) - P(SC \cap PGA_i) \quad (37)$$

Here, the intersection $P(SC \cap PGA_i)$ is significant because the collapse is caused by the earthquake. The joint probability must be included to avoid overestimation of the total risk.

6) Fire in the presence of earthquake without structural collapse ($F \cap \neg SC \cap PGA_i$): In this scenario, the occurrence of fire alongside an earthquake is examined, but without structural collapse. In seismic risk assessments, the probability of fire occurring without structural damage is very low, as structural disruption typically creates conditions conducive to ignition. Therefore, the probability of fire occurring directly due to an earthquake, in the absence of structural damage, is considered highly unlikely:

$$P(F \mid PGAi) \approx 0 \quad (38)$$

The assumption is that without structural disruption, the conditions necessary for fire initiation are absent, resulting in an estimated probability close to zero. Since structural collapse is excluded from this scenario, fire is treated as occurring independently of structural failure. However, the relationship between fire and earthquake remains significant. Nevertheless, non-structural components, such as electrical systems, gas lines, equipment, and fire protection materials, can still be damaged during seismic events, even in the absence of structural collapse. This damage can introduce significant fire hazards, as compromised systems and equipment may fail to prevent or even trigger fires. Growing research in the literature has increasingly focused on seismic shaking tests to investigate how non-structural components and equipment respond to earthquakes [269], [270], [355], [356], [357], [358], [359], [360].

Since structural collapse is excluded from the scenario, it is concluded that fire and structural collapse are mutually exclusive in this context:

$$P(F \cap SC) = 0 \quad (39)$$

This means that, under the conditions being analysed, fire cannot coexist with structural collapse. Similarly, the probability of structural collapse resulting from the earthquake is represented as:

$$P(F \cap PGA_i) = 0 \tag{40}$$

This reflects that the earthquake does not lead to structural collapse in this specific context. Given the near-zero probability of fire occurring in the absence of structural damage, we conclude that the joint probability of fire occurring alongside an earthquake, while excluding structural collapse, is approximately zero.

$$P(F \cap \neg SC \cap PGA_i) \approx 0 \tag{41}$$

The Sum Rule can be applied to calculate the total probability of either fire or an earthquake occurring. Since fire is highly unlikely without structural collapse, the primary consideration becomes the earthquake:

$$P(F \cup PGA_i)=P(F) + P(PGA_i) - P(F \cap PGA_i) \tag{42}$$

However, because $P(F \cap PGA_i) \approx 0$, the equation simplifies to:

$$P(F \cup PGA_i) \approx P(PGA_i) \tag{43}$$

This reflects that the earthquake dominates the probability in this case, given the very low likelihood of fire occurring independently.

7) Fire, Structural Collapse, and Earthquake ($F \cap SC \cap PGA_i$): This scenario examines the cascading interaction between fire, structural collapse, and earthquake, which can occur together as part of a multi-hazard risk scenario [361]. Historically, this represents a scenario with a low frequency of occurrence, characterized by the extreme confluence of hazards. Such scenarios are not typically anticipated in routine risk assessments but carry significant potential consequences. Given the complexity, this scenario could be considered a black swan within the scope of the analysis, due to the combination of events and their potential expected severe outcomes (subsection 3.1.9).

Here, an earthquake triggers a structural collapse, which may lead to a fire (Table 7). This empirical data supports the assumptions made in this study and highlights the potential consequences of cascading hazards as represented in Equation (52).

However, alternate sequences, such as the one described in Equation (51), where a fire weakens structural integrity and causes a collapse in the presence of an earthquake, are also theoretically plausible. While historical evidence for this

sequence is limited, its inclusion in the analysis is justified due to the possibility of such interactions under specific conditions. Fire-induced structural weakening has been observed in non-seismic contexts, and similar mechanisms could occur during an earthquake.

The relationships between these events are characterized by their non-independent**,** mutual exclusivity, and conditional probabilities.

The earthquake is an external event, naturally occurring, and is independent of the internal hazards (fire and structural collapse). The probability of the earthquake occurring is independent and a non-conditional probability because the earthquake's occurrence is unaffected by the other events:

$$P(PGA_i) \tag{44}$$

The structural collapse and fire are non-independent events in this scenario. The probability of collapse is conditional on the earthquake's occurrence and intensity:

$$P(SC \mid PGA_i) \tag{45}$$

Conversely, the probability of fire occurring is conditional upon structural collapse, particularly due to damage to the infrastructure:

$$P(F \mid SC) \tag{46}$$

It is important to note that fire can also lead to structural collapse as mentioned in the fire and structural collapse without earthquake ($F \cap SC \cap \neg PGA_i$) scenario which represented:

$$P(SC \mid F) \tag{47}$$

As mentioned earlier, fire occurring during an earthquake without any structural collapse is highly unlikely, as fire often results from the structural damage caused by the earthquake. Thus, fire without collapse during an earthquake is highly improbable:

$$P(F \cap \neg SC \cap PGA_i) \approx 0 \tag{48}$$

Similarly, structural collapse that occurs independently of an earthquake is also unlikely, especially when seismic activity is the primary cause of collapse in our

scenario. Therefore, structural collapse without the earthquake is also highly improbable:

$$P(SC \cap \neg PGA_i) \approx 0 \tag{49}$$

Fire, structural collapse, and earthquake are non-mutually exclusive, meaning they can all happen simultaneously. The earthquake can cause the collapse, and the collapse can result in fire. These events are interconnected and can occur together:

$$P(F \cap SC \cap PGA_i) \tag{50}$$

The Multiplication Theorem is used to calculate the joint probability of non-dependent events in this scenario. Since the order of dependencies between fire, structural collapse, and earthquake can vary, we consider two potential sequences:

In the less common scenario, fire occurs first and causes structural collapse, with the earthquake still present (Earthquake → Fire → Collapse). The joint probability for this sequence is:

$$P(F \cap SC \cap PGA_i) = P(PGA_i) \cdot P(F \mid PGA_i) \cdot P(SC \mid F, PGA_i) \tag{51}$$

Equation (51) calculates the joint probability of an earthquake inducing a fire, and the fire subsequently causing a structural collapse. Here, $P(F \mid PGA_i)$ represents the conditional probability of a fire given an earthquake, and $P(SC \mid F, PGA_i)$ represents the probability of a collapse, conditional on both the earthquake and the fire occurring. This formulation acknowledges that the earthquake's impact on the structure might increase the likelihood of collapse if a fire occurs.

In the more common scenario, the earthquake first causes the structural collapse, and the collapse then triggers a fire (Earthquake → Collapse → Fire) (Figure 24c). The joint probability is calculated as:

$$P(F \cap SC \cap PGA_i) = P(PGA_i) \cdot P(SC \mid PGA_i) \cdot P(F \mid SC) \tag{52}$$

Equation (52) addresses the joint probability where an earthquake causes structural collapse, which then leads to a fire. $P(SC \mid PGA_i)$ calculates the probability of a collapse directly due to the earthquake, while $P(F \mid SC)$ assesses the likelihood of a fire as a consequence of the collapse, not considering additional direct seismic influences on fire initiation.

The formulations of Equations (51) and (52) imply that fire (F) and structural collapse (SC) are independent conditionally on the occurrence of an earthquake (PGA_i).

By focusing on this chain of events, this research seeks to provide a comprehensive understanding of the cascading effects of seismic activity on structural integrity and fire hazards, with implications for multi-hazard risk assessment.

Figure 28: Venn diagram representation of all the relationships among three events: earthquake, structural collapse, and fire.

Based on the seven identified scenarios in this analysis, four key scenarios are the focus of in-depth analysis in the case study (Figure 25).

The current focus is on the most relevant interactions, but as more data becomes available from other scenarios, they could be incorporated in future analyses and

may be included in an expanded model using a similar approach to the current analysis. One approach to this is using Bayesian networks or similar probabilistic models that can integrate different hazard sources and their effects on a structure [254], [272], [362]. The detailed calculations for estimating the probabilities of these chosen scenarios in underground environments are provided in Chapter 4.

3.1.2 What exactly is ALARP?

The essence of ALARP (As Low As Reasonably Practicable) lies not only in its foundational role in risk management but in how it fundamentally reshapes our approach to safety. By shifting the focus from abstract ideals to context-driven decision-making, ALARP emphasizes that safety cannot exist in isolation from the practical realities surrounding it. However, while ALARP is an innovative framework, it is often misunderstood or underutilized by those tasked with implementing it across various sectors. This raises the question: What exactly is ALARP, and why does it matter?

ALARP, a principle deeply embedded in the legal history of England, is far from a theoretical concept. It emerged from the tangible, real-world consequences of court rulings addressing safety in industries such as coal mining, railway construction, and other high-risk sectors. Two landmark rulings, Edwards v. National Coal Board and Marshall v. Gotham Co. Ltd. [363], brought this principle to the forefront. These cases involved the loss of workers' lives due to insufficient safety measures in mines, exposing the dangers of neglecting comprehensive risk assessments.

The severe consequences of these failures in safety regulation led to a watershed moment in legal history: the creation of the Health and Safety at Work Act 1974 [364]. This legislation marked a turning point by introducing a structured approach to safety, one that continues to evolve in response to major accidents. Reflecting on this evolution, it becomes evident that ALARP is not just a static legal requirement but a constantly developing principle that adapts to new risks, technologies, and societal expectations.

Unlike systems of law that rely on abstract principles, the common law tradition of Anglo-Saxon legal systems is uniquely grounded in empirical judgments. These judgments, often emerging from courts, do more than resolve individual cases, they set precedents that shape entire industries. Reflecting on this, it becomes clear that ALARP is not just a legal principle, but a dynamic, evolving framework that continuously responds to new challenges. As seen in the

Edwards and Marshall cases, judicial rulings carry profound weight, often transforming into de facto law that drives industry standards forward.

At its core, ALARP is about more than just minimizing risk. It represents a balanced approach to safety, where decisions are not only guided by the physical and financial feasibility of safety measures but also by their social implications. This creates a framework where safety is ensured within the bounds of what is reasonably practicable and achievable when enough resources are available, and the interests of all stakeholders are favourable. By thinking about ALARP in this way, we can see that it represents a thoughtful, democratic, and collectively oriented approach to safety.

ALARP encourages us to view safety as a collective responsibility, involving all stakeholders such as industry leaders, workers, regulatory bodies, and society at large. This principle challenges us to ask important questions: What is reasonable and what is practicable? What are the limits of what can be achieved in reducing risk, given the available resources? These are not only technical questions but also ethical ones, as they require consideration of the social costs and benefits involved in any safety measure.

3.1.3 Edwards v. National Coal Board and Marshall v. Gotham Co. Ltd.: Impact on the Practical Application of ALARP

The ALARP principle has become a fundamental concept in safety management, not only in mining but across multiple industries such as construction, transportation, and manufacturing, making it a universal principle for workplace safety. Its development, as previously discussed, stemmed from two principal cases: Edwards v. National Coal Board and Marshall v. Gotham Co. Ltd [196], [365]. While these rulings established the legal definition of ALARP, their true significance lies in how they shaped the practical implementation of safety measures in the decades that followed.

3.1.3.1 Edwards v. National Coal Board: Defining Reasonable Practicability

The first case, Edwards v. National Coal Board, represents a significant moment in the legal development of the ALARP principle. This case concerned the tragic death of Mr. Joseph Edwards, who was killed by a falling piece of rock from an unsupported section of a roadway in the National Coal Board's Marine Colliery mine in Wales in 1947. The circumstances leading to this accident revealed that

the National Coal Board had not adhered to proper safety standards, as only half of the mine's roadways had been shored up due to the high cost of securing the entire site. The inevitable outcome of such cost-cutting was the kind of accident that claimed Mr. Edwards' life.

The Court of Appeal's decision in this case, delivered in 1949, marked the introduction of the ALARP principle. Judge Asquith LJ gave a detailed and defining judgment on the standard of duty expected from those responsible for workplace safety, specifically emphasizing the concept of reasonable practicability. In his words:

"*The construction placed by Lord Atkin on the words 'Reasonably practicable' in Coltness Iron Co v Sharp (1938) seems to me, with respect, right. 'Reasonably practicable' is a narrower term than 'physically possible' and seems to me to imply that a computation must be made by the owner, in which the quantum of risk is placed on one scale and the sacrifice involved in the measures necessary for averting the risk (whether in money, time or trouble) is placed in the other; and that, if it be shown that there is a gross disproportion between them – the risk being insignificant in relation to the sacrifice – the defendants discharge the onus on them*".

His judgment established that reasonable practicability does not require the elimination of all possible risks but instead focuses on mitigating risks in proportion to the sacrifices necessary to do so. The sacrifice may take the form of money, time, or effort, but if the cost of averting the risk is grossly disproportionate to the risk itself, it is deemed unreasonable to enforce the safety measure. This approach to risk mitigation provides a balance between worker safety and operational feasibility, guiding industries on how to implement safety standards without imposing excessive burdens. It is important to note that Judge Asquith emphasized that this computation must be made prior to any accident, compelling those responsible for safety to anticipate hazards and not merely react to them. He further explained the specific challenges in predicting the accident that occurred in this case:

"*The questions he has to answer are: (a) What measures are necessary and sufficient to prevent any breach of s 49?; (b) Are these measures reasonably practicable? In the particular type of accident caused by a 'glassy slant', it is admittedly impossible before the event to foresee at all, at what place or in what roadway or in what mine, such an accident would occur*".

In this case, the accident was caused by a "glassy slant", a natural geological feature that could not have been predicted with certainty. This point is of fundamental importance because it illustrates that the law does not require absolute foresight. Industries are not expected to foresee every specific location where a danger may arise. Judge Asquith articulated the unrealistic expectation of predicting the exact site of a potential incident:

"*The argument that the owners could and should have made secure the particular roadway in which, as things fell out, the glassy slant declared its presence, without having to make secure every other roadway in which it might have done so, assumes that the owners could by some process of divination, have predicted that the accident was likely to occur in the particular roadway in which it did, rather than elsewhere. But an owner who is not gifted with second sight can make no such prediction; and without it, security against this peril can only be secured by extending similar security measures to all roadways*".

This insightful passage from Judge Asquith highlights the complexity of risk management. It acknowledges that while specific risks may be unknown, a broad and proactive approach to safety must be taken to ensure that all potential hazards are addressed. This reflects the broader ALARP principle that while it is unreasonable to expect organizations to predict every accident, they must implement comprehensive safety measures that cover all foreseeable risks across their operations.

Furthermore, Judge Asquith remarked on the lack of evidence provided by the National Coal Board to justify its decision not to secure all roadways:

"*So far, I am inclined to agree with the learned judge. But, like my Lord, I do not think any or any sufficient evidence was adduced as to the relative quantum of risk and sacrifice involved, on the basis either that the mines as a whole, or this particular roadway, should be taken as the unit – a necessary prerequisite to any decision that the defendants have proved the necessary measures impracticable. For these reasons I think the appeal should be allowed*".

The National Coal Board was unable to demonstrate that securing the entire mine was impracticable, and thus the court found that the necessary safety precautions should have been taken. The ruling emphasized that when organizations claim that safety measures are too costly or difficult, they must provide clear evidence to support their position. The failure to do so shifts the burden back onto them to take action.

3.1.3.2 Marshall v. Gotham Co. Ltd.: The Balance Between Cost and Risk

The second landmark case that further refined the ALARP principle was Marshall v. Gotham Co. Ltd., which dealt with the tragic death of Mr. George William Marshall, a gypsum miner who was struck and killed by a large piece of the mine's roof. The accident was caused by a geological phenomenon known as a slickenside, a rare and unpredictable condition that had not occurred in the mine for over 25 years. Mrs. Marshall, the widow of George William Marshall, brought the action against Gotham Company Limited in 1952. The case was heard by the House of Lords, where the judges debated whether the company had taken reasonable and practicable precautions to prevent such an accident.

It is important to recognize that the court was faced with a difficult decision. The slickenside was a known hazard, but its occurrence was exceedingly rare. The central question was whether it was reasonable to expect the company to have taken precautionary measures in light of the fact that no similar accident had occurred in over two decades. The House of Lords agreed that the event was indeed an unwonted occurrence, which raised key issues about how far safety measures should go to protect against such rare hazards.

Lord Oaksey, in his ruling, emphasized the importance of balancing the time, effort, and cost of safety precautions against the likelihood of the hazard. He stated:

"*What is 'reasonably practicable' depends upon a consideration whether the time, trouble and expense of the precautions suggested are disproportionate to the risk involved. It is conceded in the present case that it was not reasonably practicable to make the roof secure by timbering, and to have attempted to make it secure by pneumatic props in some places and by leaving it un-mined in others when no slickenside had ever occurred for a period of 20 years was not, in my judgment, reasonably practicable*".

Lord Oaksey's opinion reflects a key point about ALARP: while safety is paramount, it must be achieved within the bounds of what is practically feasible. In this case, the cost and trouble of implementing certain precautions such as timbering the entire roof or installing pneumatic props, was deemed disproportionate to the risk involved, particularly given the rarity of slickensides. This ruling reinforces the idea that industries are not required to take every conceivable precaution but only those that are proportional to the level of risk.

Lord Reid added an important dimension to this ruling, making it clear that even if a precaution is practicable, it must still be judged reasonable in the context of the entire situation:

"*If a precaution is practicable it must be taken unless in the whole circumstances that would be unreasonable. And as men's lives may be at stake it should not lightly be held that to take a practicable precaution is unreasonable*".

This statement adds weight to the responsibility of employers to err on the side of safety when lives are at risk. However, Lord Reid, like Lord Oaksey, acknowledged the disproportionate cost test that had been applied in Edwards v. National Coal Board, reinforcing the idea that safety measures must not impose an unjustified burden on an industry, especially when the danger is both rare and difficult to predict.

Lord Reid's application of the disproportionate cost test provides another layer to the ALARP principle. By recalling this test from the Edwards case, he accepted that even the high cost of safety measures might, in some cases, make certain precautions unreasonable. As he put it:

"*Slickenside was a known danger, but there was no more reason to anticipate it or provide against it at the place of the accident than elsewhere in the mine, and a finding that precautions ought to have been adopted at the place of the accident would imply that they ought also to have been adopted generally. I am of opinion that this was not reasonably practicable, and I base my opinion on these factors. The danger was a very rare one. The trouble and expense involved in the use of the precautions, while not prohibitive, would have been considerable. The precautions would not have afforded anything like complete protection against the danger, and their adoption would have had the disadvantage of giving a false sense of security*".

In this reflection, Lord Reid highlighted several key points about safety management that remain relevant today. First, the rare nature of the danger made it impractical to adopt comprehensive safety measures across the mine. Second, even if the precautions had been implemented, they would not have provided complete protection, raising the issue of diminishing returns when it comes to safety investments. Lastly, he warned that implementing excessive safety measures could create a false sense of security, which might lead workers to believe they are safer than they actually are.

The House of Lords did not deliver a single, unified perspective on the case. Lord Keith, for example, emphasized that there could be no general rule or test that could be universally applied in such cases. He argued that the issue of what constitutes reasonable practicability must always depend on the particular circumstances of each case:

"*There was no general rule or test which could be adopted, and that the issue must depend on the particular circumstances of each case*".

This statement reflects the contextual nature of the ALARP principle, it is not a rigid standard but one that must be applied flexibly based on the specific risks and operational conditions of a given situation. In this way, ALARP allows for adaptation and nuance, recognizing that no two safety situations are exactly alike.

In the end, the ruling of the House of Lords concluded that the Gotham Company had taken reasonably practicable precautions, considering the rarity of the hazard and the disproportionate cost of implementing further safety measures. Lord Tucker and Lord Cohen echoed the sentiment that liability under the statute could not be determined by simply applying the principles of common law negligence, suggesting that statutory obligations must be interpreted through the lens of what is practicable and reasonable within the specific context of the incident [366].

As one can observe, Marshall v. Gotham Co. Ltd. further solidified the disproportionate-cost approach set in Edwards v. National Coal Board. Both cases emphasize that the legal standard for safety is not an absolute mandate, but rather one that is contextual, based on the foreseeability of the risk and the practicality of the measures aimed at mitigating it. This case emphasizes the importance of adopting a balanced approach to safety, ensuring that protective measures are proportionate to the risk and do not incur unreasonable costs. Moreover, it highlights the complexities of risk management, where factors such as the nature of the hazard, the cost of preventive measures, and the potential for harm must all be carefully weighed. The rulings in Marshall v. Gotham Co. Ltd. and Edwards v. National Coal Board offer a clear and comprehensive framework for applying the ALARP principle. They affirm that while industries are obligated to minimize risks, this obligation must be met within the boundaries of what is reasonably practicable, considering both the cost of safety measures and the probability of the hazard [11].

The importance of ALARP was affirmed by the European Court of Justice (ECJ) in a 2007 ruling after nearly a decade of legal proceedings. The European Commission had challenged the UK's application of the "reasonably practicable" standard, arguing that it might not meet the stricter safety requirements set by EU directives. However, the ECJ ruled in favour of the UK, confirming that the ALARP principle was consistent with EU law [367], [368].

3.1.3.2.1 ALARP in UK and in Italy

3.1.3.2.1.1 UK

As previously mentioned, the Health and Safety at Work etc. Act 1974 forms the backbone of the ALARP principle in the UK, placing the concept of reasonably practicable at the centre of workplace safety regulations. The ALARP principle is closely connected to the notion of tolerability of risk, which distinguishes between unacceptable, tolerable, and broadly acceptable risk regions, guiding industries in their risk management decisions. The tolerability of risk framework can be applied to all hazards and provides a structured method for determining what constitutes reasonably practicable measures for managing workplace risks. When choosing safety controls, the adequacy of the chosen option is evaluated in part by considering where the risk lies within the tolerability of risk boundaries. The boundaries between unacceptable, tolerable, and broadly acceptable risk are subject to deliberation and negotiation during policy development. This reflects the value preferences of stakeholders and the practicability of possible solutions. Essentially, ALARP and the tolerability of risk framework function together to ensure that risks are controlled to an acceptable level without imposing disproportionate burdens on employers [15].

To understand the practical application of ALARP, it is important to address the question: What does "reasonably practicable" mean? At its core, the concept requires a balance between the quantum of risk and the cost, time, or effort required to mitigate that risk. This balance ensures that safety measures are proportionate to the risk being managed, avoiding grossly disproportionate sacrifices for minimal risk reduction.

To clarify, the concepts of ALARP and reasonably practicable are essentially two sides of the same coin. Both focus on minimizing workplace risks to the lowest achievable level, as specified in Sections 2 and 3 of the act [364], which oblige employers to take all reasonably practicable steps to prevent accidents and protect employees from harm. The ALARP principle, therefore, demands that

duty holders assess potential hazards and implement proportional safety measures to mitigate them.

In determining whether an employer has violated the ALARP principle, various evaluation criteria come into play. Tolerability in the UK remains flexible, allowing for professional judgment on what constitutes a proportionate response to hazards. These are generally based on current standards and Approved Codes of Practice (ACOP), which serve as essential tools to guide compliance with the law and establish best practices in engineering and safety [369]. For example, if a duty holder is prosecuted for breaching health and safety laws and it is proven that they did not follow the relevant ACOP provisions, the court is likely to find them at fault unless they can demonstrate compliance by alternative means. Conversely, adherence to ACOP provisions demonstrates that the duty holder has implemented the ALARP principle and is compliant with the law.

According to the HSE, the tolerable risk for workers in hazardous industries is 1.0E−03 (Tolerability Limit), while the limit for the public, who may face risks imposed for the wider societal good, is 1.0E−04 (Tolerability Limit) (Figure 29; Table 10; Table 11; and Table 12) [370], [371], [372]. In practice, fatality rates in hazardous industries are often much lower than these limits. For example, in 1999–2000, the fatality rates for agriculture, hunting, forestry, and fishing were 7.7E−05, for construction 4.7E−05, and for mining and quarrying 6.9E−05. In less hazardous sectors like the service industry, the fatality rate was around 2.6E−06, reflecting much lower risk levels. Similarly, the annual risk of death for the public is well below the threshold. For instance, the risk from gas-related incidents (fires, explosions, or carbon monoxide poisoning) between 1994–1995 and 1998–1999 was 6.6E−07. Despite being far below the broadly acceptable risk level, societal concerns about negligence such as landlords failing to conduct safety checks can still generate public alarm, especially where vulnerable groups are involved [15].

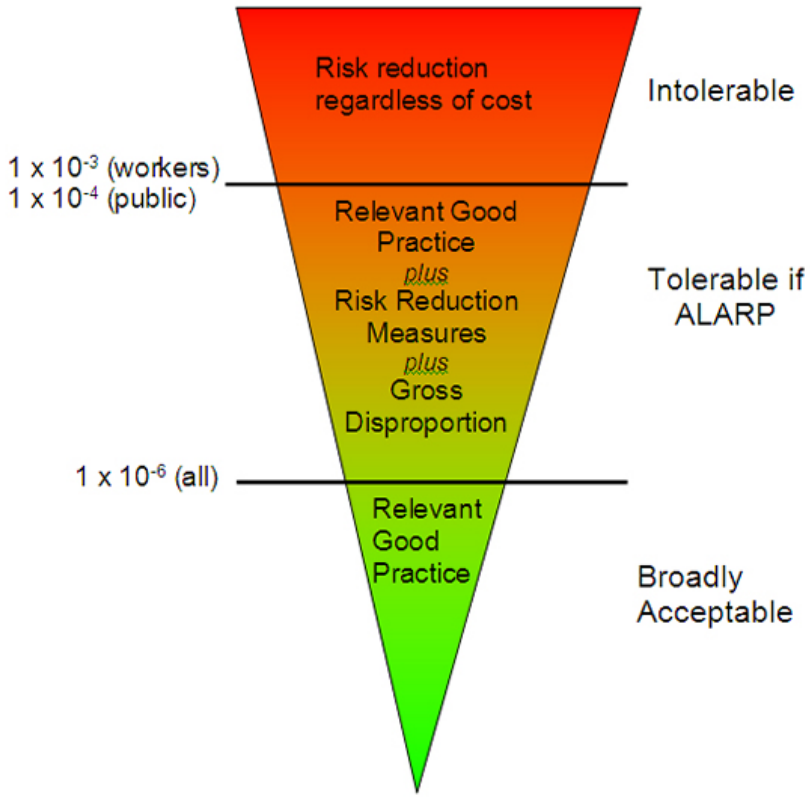

Figure 29: UK HSE Risk Acceptance Criteria: Intolerable, Tolerable (ALARP), and Broadly Acceptable Zones [372].

3.1.3.2.1.2 ALARP in Italy

In Italy, the ALARP principle is incorporated through mandatory criteria for Acceptability and Tolerability of risk for tunnels. The Italian model requires duty holders, who are responsible for ensuring the safety of users in tunnels, to demonstrate that their designs meet the safety levels defined by the Acceptability and Tolerability criteria set in Legislative Decree 05 October 2006, n. 264. According to this regulation, the exceedance probability of one fatality per year must not exceed 1.0E−04 for Acceptability and for 1.0E−01 Tolerability [221], [373], [374]. Italian regulations offer a structured risk-based approach by setting explicit probabilistic limits on fatalities, ensuring that designs meet legally defined safety benchmarks.

Guarascio et al. [12], [222], [375] provided significant insights into the application of the ALARP principle by discussing the three levels of safety, particularly in the context of Italy (Figure 30), drawing on practices from the UK HSE. Their work groups safety levels into three distinct zones: the unacceptable area, the acceptable area, and the intermediate ALARP zone, which requires further deliberation and analysis to ensure that risks are reduced to as low as is

reasonably practicable. In tunnel safety, the number of fatalities (N) must be an integer on the horizontal axis, while the exceedance probability distribution either G(N) or F(N) per year is shown on the vertical axis. Multiple scenarios with the same number of fatalities can occur, and the Risk Line represents both the fatalities and their associated probabilities. Although the fatalities are indicated, the actual scenarios leading to these fatalities are not empirically observable, meaning that these scenarios must be modelled based on probabilistic analysis. Since direct observation of every risk scenario is not feasible, these models serve as the only available tool for measuring risk. They enable us to imagine potential outcomes, assign probabilities to them, and, consequently, calculate risk. This process requires careful consideration of the initial conditions and assumptions, allowing for a comprehensive calculation of the consequences in terms of quantitative data, mathematical models, and probability distributions. The concept of the risk line further illustrates this. It is an irregular, staircase-shaped line, where each step represents a different scenario and its corresponding probability (Figure 39). These steps reflect the varying elevations of risk, the different probabilities of fatal scenarios occurring under different conditions. This irregularity is inherent to the complexity of risk, as each scenario introduces a unique combination of factors that alter the probability distribution. When comparing design curves to the risk model, this visual representation allows engineers and decision-makers to assess whether safety measures are sufficient or require further refinement.

The European Directive 2004/54/EC [376] introduced “minimum level of safety” (Article 1), which were later revised to “minimum sufficient level of safety” (Article 1) in Legislative Decree 05 October 2006, n. 264. This change was significant, as it acknowledged that the mere existence of minimum standards does not guarantee efficiency or effectiveness in safety outcomes. Instead, the measures must be both adequate and proportional to the risks being managed, ensuring that safety interventions lead to meaningful reductions in risk.

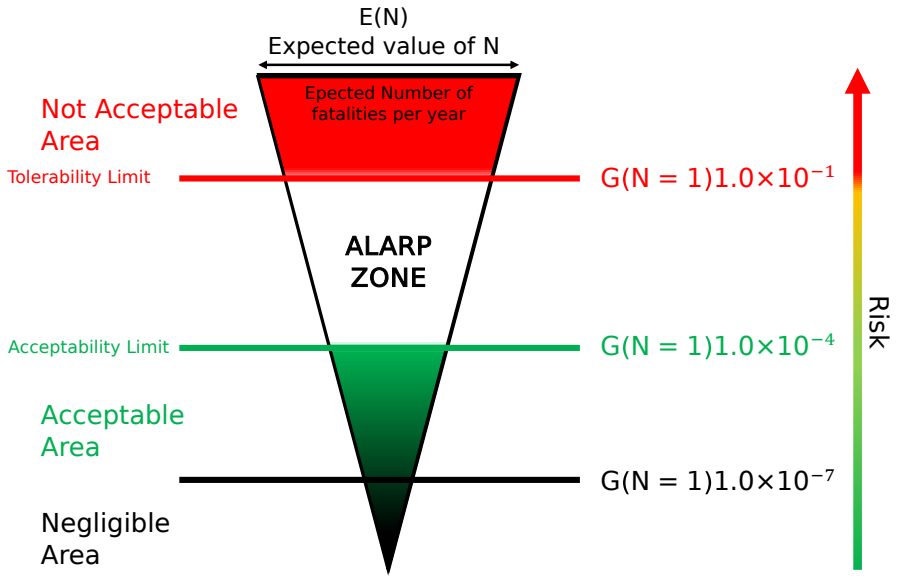

Figure 30: The Tolerability Limit (Gu) for a single fatality (N=1) is set at 1.0×10^{-1}, placing it in the "Not Acceptable Area", where risks are too high to be authorized. In contrast, the Acceptability Limit (Gu) is much lower, at 1.0×10^{-4} fatalities per year, defining the boundary below which risk is considered acceptable without further mitigation. The range between these two limits, known as the ALARP zone, is where further risk reduction is considered, balancing the cost of mitigation against the benefit of reducing risk.

3.1.3.3 Acceptance criteria

The concept of risk tolerability varies significantly across industries and regions, shaped by societal values, regulatory expectations, and historical accident data. In different countries, these thresholds are often represented by two critical parameters: the anchor point (Gu), or baseline probability, and the slope (α), which governs the rate of decay in risk acceptability as the severity of consequences increases [222], [377], [378], [379], [380], [381], [382], [383], [384], [385], [386]. Mathematically, the relationship between these parameters can be expressed as:

$$\alpha = \frac{\ln(\frac{Gu}{G(N)})}{\ln(N)} \tag{53}$$

To derive α, start from the assumed power-law relationship between the exceedance probability G(N), the anchor point Gu, and the number of fatalities N:

$$G(N) = \frac{Gu}{N^{\alpha}} \tag{54}$$

Taking the natural logarithm of both sides linearizes the equation:

$$\ln(G(N)) = \ln(Gu) - \alpha \ln(N) \tag{55}$$

Rearranging the equation to isolate α results in:

$$\ln(Gu) - \ln(G(N)) = \alpha \ln(N) \tag{56}$$

Solving for α yields Equation (53).

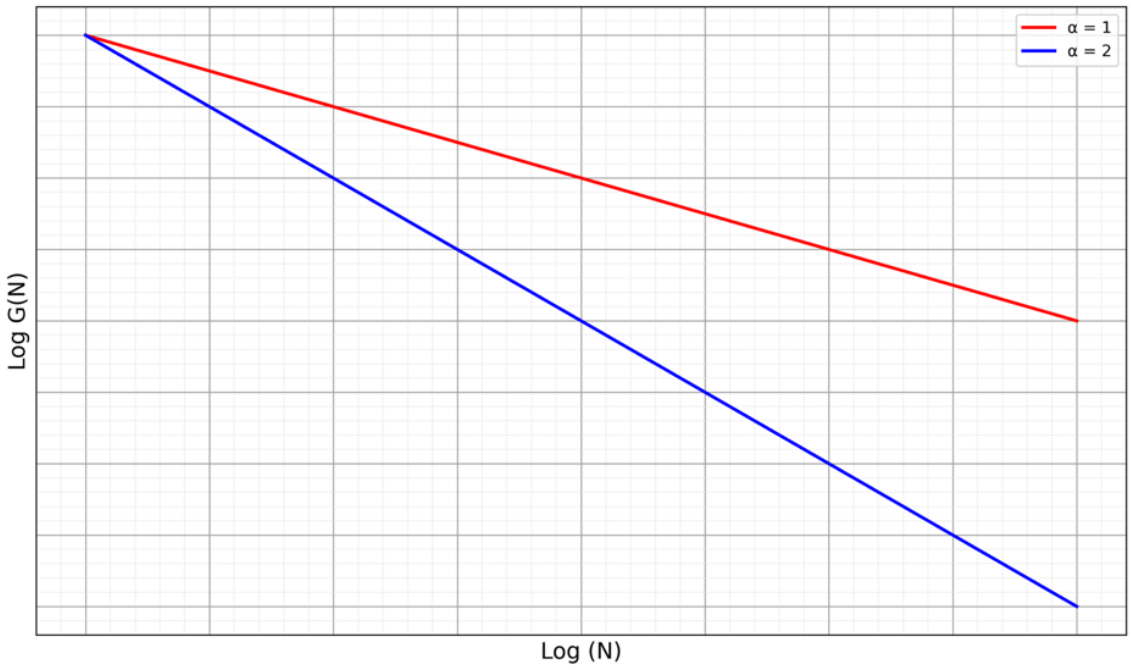

Figure 31: Log-Log representation of Risk Acceptability/Tolerability Curve for different α. The slope of each line corresponds to $-\alpha$, illustrating how the exceedance probability G(N) decreases with increasing fatalities N.

The slope (α) of the risk curve, typically ranging between 1 and 2, serves as a measure of risk aversion. In the log-log plot, a steeper negative slope ($-\alpha$) signifies a higher degree of risk aversion, indicating that the acceptability of risk decreases more rapidly as the severity of consequences increases. A slope of $\alpha = 1$ represents a risk-neutral stance, where risk acceptability decreases proportionally to the severity of the outcome. In contrast, a slope $\alpha > 1$ denotes a risk-averse stance, where larger accidents are weighted more heavily and are accepted only at lower probabilities. As α increases within this range (from 1 up to 2), the degree of risk aversion intensifies, meaning that higher-severity events

are accepted with progressively lower probabilities. For example, both road and rail systems in Italy have specific tolerance levels:

Road Tolerability Limit: For road tunnel in Italy [221], [373], [374], Gu = 1.0E-01 and α = 1 (starting from N = 1). This neutral decay rate reflects moderate risk tolerance, where the probability of exceedance diminishes in direct inverse proportion to N.

Railway Tolerability Limit: For railway tunnel in Italy [387], the values Gu = 2.0E-03 and α = 1.4168 (starting from N = 2) indicate a stricter risk tolerance criterion. The higher decay rate implies a faster reduction in exceedance probability, consistent with a lower tolerance for high-fatality accidents. However, Rail Tolerability Line to start from N = 2 fatalities, the model implicitly avoids single-fatality scenarios compared to road tunnels where N = 1. This suggests that the railway system either assumes inherent control over such events or deems them too improbable to include in risk calculations. While this reflects a high baseline safety expectation in railway systems, it may overlook the importance of addressing lower-severity accidents, which, if unmitigated, could still pose significant operational or reputational risks.

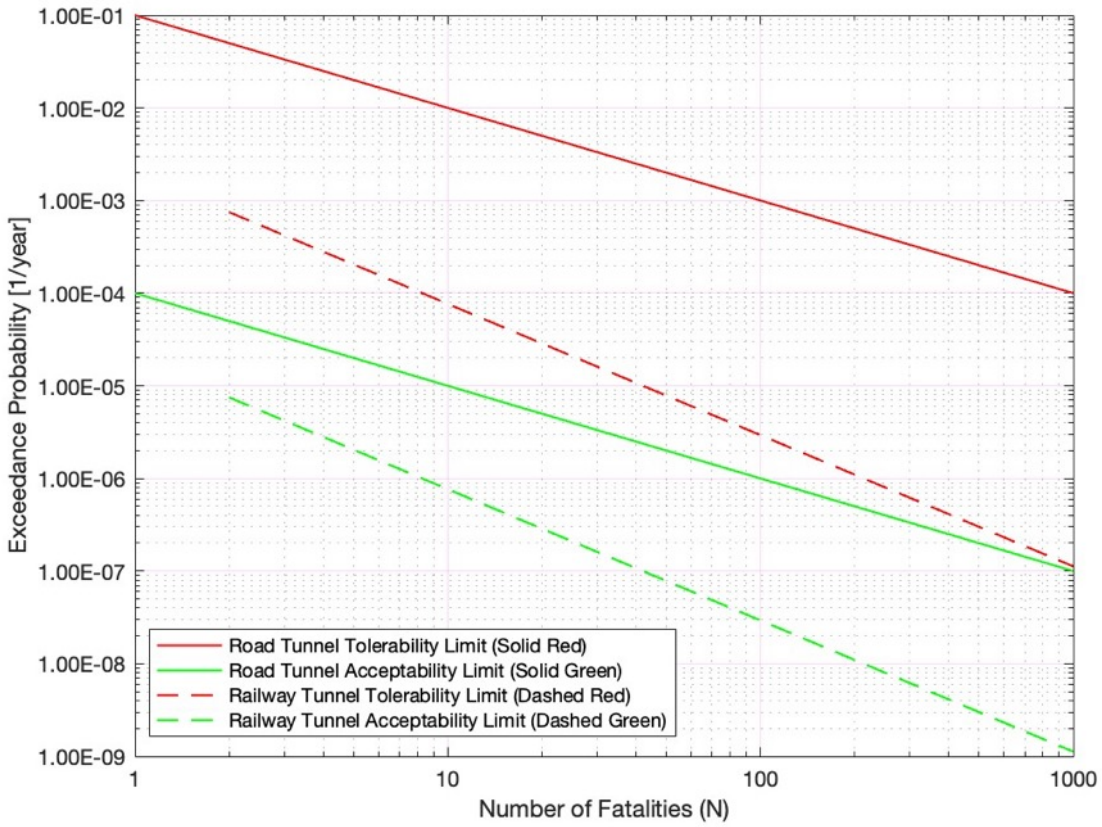

Figure 32: Acceptability and Tolerability Limits for Italian road and railway tunnels.

Another difference we can notice is that the ALARP band for road tunnels encompasses a range of three decades, while for railway tunnels, it is confined to two decades. This broader ALARP band for road tunnels reflects a greater societal tolerability for fire risks, suggesting that road systems are perceived as more manageable or acceptable in the face of potential hazards.

3.1.4 Philosophical and Practical Foundations of ALARP

Concepts from philosophy can be used to better understand and communicate the underlying principles of ALARP. Valuable parallels can be drawn to the Socratic and Galilean methods to deepen the understanding of its principles. The Galilean method emphasizes the importance of empirical observation and experimentation in the pursuit of knowledge [388], [389], [390], [391]. Galileo, often credited with laying the groundwork for modern scientific inquiry, insisted that conclusions should be based on evidence gathered through direct observation and experimentation rather than on speculation or adherence to traditional beliefs. His approach revolutionized science by introducing systematic experimentation and the use of mathematical analysis to interpret

results, fundamentally changing how knowledge was pursued in natural sciences. In a similar vein, ALARP encourages a rigorous, data-driven approach to risk management, where decisions are made based on the best available evidence, and where assumptions are only used when they are supported by existing knowledge and subject to continual revision as new data becomes available. Similarly, the Socratic method [392], [393], [394], [395], [396], known for its emphasis on ethical inquiry and questioning assumptions, can help frame the ethical considerations within ALARP. The principle challenges consideration of not just the technical feasibility of safety measures, but also their broader impact on society and the individuals affected.

ALARP can be understood through four key profiles, each offering a distinct yet interconnected perspective on its application:

1. **Social-Ethical Profile**: This profile reflects the Socratic tradition, focusing on the ethical implications of safety decisions and the responsibilities of individuals and organizations within society. It posits that safety is not merely a technical or legal obligation but a moral one, where decision-makers must consider the broader impact of their actions on society as a whole. This profile challenges the need to weigh the justice and equity of safety measures, ensuring that the risks and benefits are distributed fairly.
2. **Forensic and Legal Profile**: This profile examines how ALARP is applied within legal contexts, particularly in determining responsibility for safety failures. It delves into the judicial process of determining "who is really right and what is true" when safety measures are questioned or challenged. The forensic aspect involves analysing evidence to determine causality and liability in cases of accidents or safety breaches. Courts rely on this evidence to establish whether the actions taken were "reasonably practicable" under the circumstances, making this profile valuable for understanding how legal standards and precedents shape the application of ALARP.
3. **Mathematical Profile**: The mathematical profile deals with the quantification of risk and uncertainty, reflecting the Socratic acknowledgment that "I know that I do not know". However, as Socrates pointed out, the real problem is not just recognizing ignorance but understanding "how much I know I do not know". In the context of ALARP, this means assessing whether knowledge is generic or if there is acute awareness of specific gaps in understanding that force the establishment of criteria for Acceptability. The key challenge is not just

recognizing ignorance but measuring it, quantifying the unknowns to the extent possible. Probabilistic methods are employed to assess risks and measure uncertainty.

4. **Engineering, Regulatory, and Technical Profile**: This profile is where the ALARP principle directly meets practical implementation. Engineers and regulators are the ones responsible for applying ALARP in the real world, often dealing with the complexities of ensuring that safety measures are effective within the constraints of available resources. This profile focuses on the practical challenges of designing, implementing, and regulating systems that are not only safe but also feasible and sustainable for the community. Engineers must ensure that the systems they design are robust enough to protect people while being adaptable to evolving circumstances and technological advancements. The role of the regulatory bodies is to ensure that these systems comply with ALARP standards, balancing safety with practicality and cost-effectiveness.

At its core lies a mathematical inquiry: What constitutes the ALARP diagram? Why do experts refer to this as an ALARP curve or, at times, an ALARP straight line? These terms are not merely semantic choices but reflect the underlying complexities of risk representation. This line arises from the nature of the variables plotted along the abscissa, the horizontal axis. These variables, which typically represent people or potential victims, are integer values because ALARP's primary focus is the safeguarding of human life, which cannot be fractionally quantified. Among the risk indicators is the Expected Number of Fatalities E(N), a location parameter that exists on the real number line. This expected number can indeed be a real number, sometimes smaller than one, representing the weighted average of outcomes across all scenarios. However, the individual scenarios involve integer fatality counts, and the expected number serves as a "centre of gravity" for these values, offering a meaningful way to assess risk while maintaining integer-based measures for each possible outcome.

The origin of the ALARP framework is deeply rooted in the need to balance the imperatives of safety against the constraints of economic viability. This balance is articulated through a criterion known as the maximum acceptable expenditure. Expenditure, within this framework, is treated as a variable measured in the smallest units of currency, such as euro cents, where granularity is essential. Below the cent, no currency exists, making it the fundamental unit for economic assessments within ALARP. In discussions of economic impact, whole numbers typically represent euros, with cents forming the second decimal place. This

precision in financial terms contrasts sharply with the approach to human impacts, where the idea of half a victim is, of course, nonsensical. Therefore, while financial calculations might extend into thousandths or beyond, they remain distinctly separate from the human-centred approach that deals only with whole, indivisible numbers.

In practical applications of ALARP, such as scenario simulations, the outcomes are often evaluated in terms of the number of victims relative to the number of people exposed to a particular risk. These simulations are designed to estimate potential impacts. This approach is critical for maintaining clarity and precision in how risks are quantified and communicated. It reflects a deeper principle within ALARP: that all counting methods employed must function with integer values, ensuring that the assessments remain firmly grounded in reality.

The ALARP diagram, therefore, might initially appear to be a simple collection of discrete points, each corresponding to a specific integer value. For example, points on this plane might represent 27, 28, or 29 individuals. However, this interpretation, while useful, does not capture the full complexity of the ALARP curve. The curve also incorporates probabilistic elements that complicate the seemingly straightforward relationship between these points.

Central to this complexity is the concept of exceedance probability, or backward probability. On the ordinate, the vertical axis, this backward probability is plotted, representing the likelihood that a specific risk threshold will be exceeded. The backward probability is not merely a static measure but one that has significant implications both graphically and numerically. Between any two points on this axis lies a deeper understanding of how risks accumulate or diminish, depending on the scenarios being considered.

The calculation of this probability involves a process known as retro-cumulative addition. This method constructs the curve by summing exceedance probabilities from the highest value down to the smaller ones. This retro-cumulative process is more than just a numerical procedure; it represents the fundamental structure of the ALARP curve. Selecting a point on this curve reveals the probability of exceeding a given risk threshold, thus providing a clear, albeit complex, picture of risk distribution. Interestingly, the direction in which this probability is assessed is counterintuitive, it moves backward, highlighting how risks that are higher in severity are assessed before those of lower magnitude. This reverse

analysis offers crucial insights into how risks are managed over time and across different potential scenarios.

Moreover, this approach to risk assessment within the ALARP framework is not limited to theoretical models. It has practical applications across various industries, including nuclear energy, aviation, and chemical manufacturing, where understanding the balance between risk and expenditure is essential. In these contexts, the ALARP curve serves as an important tool for decision-makers, helping them determine when additional risk mitigation is justified and when it may no longer be reasonable given the associated costs.

In reflecting on the ALARP diagram, it becomes evident that this is not just a mathematical construct but a comprehensive framework that encapsulates the intricate balance between human safety and economic realities. The ALARP curve, with its integration of discrete and continuous variables, represents the complex nature of risk management in modern industries. It forces decision-makers to grapple with the difficult trade-offs between ensuring the safety of individuals and managing the financial implications of risk reduction.

This reflective process is essential because it underscores the ethical dimensions of risk management. While the ALARP principle is grounded in practicality, it also implicitly requires a moral calculus—deciding when it is justifiable to cease additional safety measures because they would require disproportionate resources. This decision is never taken lightly, and the ALARP curve provides the analytical tools necessary to make these judgments with confidence and precision.

3.1.5 Introduction to Probability in Risk Assessment

In the evolution of risk assessment, probability serves as a foundational concept, particularly in fields such as engineering, natural/anthropogenic hazard prediction, and decision-making under uncertainty. Throughout history, probability theory has evolved into several distinct interpretations, each contributing a unique perspective to how we assess risk and uncertainty. In probability theory, we primarily distinguish between two broad categories: unconditional (or absolute) probabilities and conditional probabilities [397]. Unconditional probabilities provide the likelihood of an event occurring independently of other events, while conditional probabilities account for the dependence between events, where the occurrence of one event affects the probability of another. This distinction allows us to quantify not only

independent risks but also non-independent hazards. For example, while the unconditional probability might assess the likelihood of an earthquake, conditional probability would determine the likelihood of a structural collapse and subsequent fire, given that the earthquake has already occurred, as these events are interdependent.

When formalizing the notion of probability, a key conceptual choice arises: should conditional probability be defined in terms of unconditional probability, or vice versa? This choice influences how we frame risk, particularly in fields like engineering and hazard analysis, where multiple events are often interdependent. This conceptual choice is important because it influences how multi-hazard risks are modelled. If risk is defined in terms of conditional probability, the focus is on how one event (e.g., fire) is triggered by another event (e.g., structural collapse), helping to analyse cascading risks. If unconditional probabilities are used, events are treated as independent, which may oversimplify real-world scenarios where multiple events are often interdependent.

3.1.6 Different Types of Unconditional Probability

In probability theory, there are various interpretations of unconditional probability, each providing a different way of understanding how an event occurs without reference to any other event. Four primary types of unconditional probability serve as the foundation for this study: classical probability (a priori), frequentist or statistical probability (a posteriori), subjective probability, and axiomatic probability.

3.1.6.1 Classical (A Priori) Probability:

Classical probability is a deductive approach based on reasoning before any experimentation or observation takes place, relying on theoretical assumptions. It assumes that all outcomes are equally likely [201]. If there are N possible outcomes and n favourable ones, the probability P(E) of an event E occurring is:

$$P(E) = \frac{\text{Favorable outcomes}}{\text{Total possibili outcomes}} = \frac{n}{N} \tag{57}$$

This form of probability is often applied in well-defined, controlled scenarios, such as games of chance (e.g., rolling a fair die or flipping a coin).

3.1.6.2 Frequentist (A Posteriori) Probability:

Frequentist probability, also known as empirical probability, is inductive and based on observations or experiments. It calculates the probability of an event by looking at how frequently it occurs over a large number of trials. This is often referred to as a posteriori because it is derived after experiments or data collection [398].

$$P(E) = \frac{\text{Number of times event E occurs}}{\text{Total number of trials}} = \frac{n}{N} \tag{58}$$

In some cases, the distinction between classical (a priori) probability and frequentist (a posteriori) probability can blur. For instance, when calculating the probability of rolling a 6 on a fair die, one might start with the classical assumption that the probability is 1/6, but a frequentist might verify this assumption by rolling the die many times and observing how often a 6 appears.

3.1.6.3 Subjective Probability

Subjective probability reflects an individual's personal belief or degree of confidence that an event will occur [399]. Unlike classical and frequentist probabilities, which are based on objective calculations, subjective probability is inherently opinion-based [400]. It varies from person to person, as it represents an individual's judgment based on available information, intuition, or prior experiences.

This type of probability is frequently used in areas where uncertainty is high, such as expert judgments in engineering, particularly in risk assessments of complex systems under uncertainty conditions. While subjective probabilities can be useful, they are not as mathematically rigorous as classical or frequentist approaches. However, its main limitation is the lack of objectivity, as personal biases can influence the assigned probabilities. Nonetheless, Bayesian statistics often incorporates subjective probabilities, blending personal beliefs with observed data to update likelihood estimates.

3.1.6.4 Axiomatic Probability

Axiomatic probability, introduced by Andrey Kolmogorov in 1933, is a formal mathematical framework that provides a set of rules or axioms to define probability in a consistent and abstract manner [401], [402], [403]. It is built on a set of three fundamental axioms that all probabilities must adhere to:

Axiom 1: (Non-negativity) The probability of any event P(E) must be greater than or equal to 0.

$$P(E) \geq 0 \tag{59}$$

Axiom 2: (Certainty) The probability of a certain event is 1.

$$P(\Omega) = 1 \tag{60}$$

Where Ω is the sample space of all possible outcomes.

Axiom 3: (Additivity) If two events E_1 and E_2 are mutually exclusive, the probability of their union is the sum of their individual probabilities.

$$P(E_1 \cup E_2) = P(E_1) + P(E_2) \text{ if } E_1 \cap E_2 = \emptyset \tag{61}$$

These axioms ensure that probabilities behave in a logical, consistent manner. The axiomatic approach is widely used in theoretical probability and underpins much of modern probability theory and statistics.

3.1.7 Alternative Theories of Probability

While classical, frequentist, subjective, and axiomatic probabilities are widely used in risk assessment, other formal theories of probability exist, each proposing alternative methods of defining probabilities that extend beyond the conventional range of 0 to 1. These alternative frameworks challenge traditional notions of probability and open up new ways of thinking about uncertainty.

Some examples include probabilities involving negative numbers [404], imaginary numbers [405], unbounded numbers [406], and frameworks such as the Dempster-Shafer theory [407], fuzzy sets [408], and possibility theory [409], among others. These models push the boundaries of probability theory by offering tools to deal with ambiguity, vagueness, or uncertainty that cannot be adequately handled by classical methods [397].

Kolmogorov's axiomatic system remains the most widely accepted formal foundation of probability, but it is not the only valid framework. Kolmogorov's axioms define how probabilities should behave: they must be non-negative, sum to one for certain events, and obey the additivity rule for mutually exclusive events. However, this formalism only tells us how probabilities should behave, not necessarily what probabilities represent.

There are many systems and quantities that satisfy the Kolmogorov axioms but are not necessarily probabilities in the traditional sense. For instance, the areas of regions on a tabletop could satisfy Kolmogorov's axioms since areas are non-negative, can sum to 1 when covering the entire table, and can be additive for disjoint regions, yet we would not call these areas "probabilities". This observation shows the importance of not conflating mathematical behaviour with philosophical meaning.

The question then arises: What do probabilities represent? Are they objective features of reality, such as frequencies or propensities, or are they subjective degrees of belief held by individuals or systems? As the exploration of probabilistic modelling in complex systems progresses, especially in areas like quantitative risk assessment, it becomes essential to reflect on whether the understanding of probability is complete, or whether these alternative frameworks might offer deeper insights into uncertainty and decision-making under risk.

3.1.8 Introducing Conditional Probability

While the above mentioned four types of probability fall under unconditional probability, a separate and equally important concept in probability theory is conditional probability. This describes the probability of an event occurring given that another related event has already occurred. It is calculated using the formula [410]:

$$P(A \mid B) = \left(\frac{P(A \cap B)}{P(B)}\right) \tag{62}$$

where $P(A \mid B)$ is the probability of event A given that event B has occurred. $P(A \cap B)$ is the joint probability of events A and B occurring together, and $P(B)$ is the probability of event B occurring.

3.1.8.1 Bayesian probability

The idea of conditional probability naturally leads into Bayesian probability, where prior beliefs are updated based on new evidence.

Bayesian probability has a rich and fascinating history that dates back to the 18th century. It is named after Reverend Thomas Bayes, an English Presbyterian minister and mathematician, who developed what is now known as Bayes' theorem. In his work, *An Essay towards Solving a Problem in the Doctrine of Chances*

(published posthumously in 1763) [411], Bayes sought to provide a method for updating the probability of a hypothesis in light of new evidence.

While Bayes' work initially received little attention, it was rediscovered and developed further by Pierre-Simon Laplace, a French mathematician and astronomer, who independently derived the theorem in the late 18th century. Laplace extended Bayes' ideas, applying them to various fields such as astronomy, physics, and statistics [412]. He is often credited with laying the foundations for what would later become Bayesian inference.

For much of the 19th and early 20th centuries, Bayesian probability was overshadowed by the rise of frequentist statistics, which dominated the academic landscape. The frequentist approach, led by figures like Ronald Fisher and Jerzy Neyman, focused on probability as the long-run frequency of events, and this perspective was favoured in scientific and statistical methods [399]. However, in the mid-20th century, Bayesian methods began to gain prominence again, particularly in areas where prior knowledge and uncertainty play important roles [413]. The resurgence was fuelled by advancements in computational techniques and the realization that Bayesian approaches offer flexible and powerful tools for updating probabilities in real-time as new data becomes available.

Bayesian probability uses Bayes' Theorem, which is stated as:

$$P(A \mid B)=\left(\frac{P(B \mid A) \cdot P(A)}{P(B)}\right) \tag{63}$$

where P(A | B) is the posterior probability: the probability of event A given that B has occurred. P(B | A) is the likelihood: the probability of event B assuming A is true. P(A) is the prior probability: the initial probability of A before observing B. P(B) is the evidence: the total probability of observing B under all possible hypotheses.

To further explore the role of probability in risk assessment and decision-making, understanding a simple yet profound example from classical physics is essential: the probability of heads in a coin toss (Appendix B).

3.1.9 ALARP and Black Swan

Deductive reasoning supports the application of the ALARP principle by confirming that if risk reduction measures are known and established to

significantly mitigate risk without disproportionate cost, then they must be applied. For instance, if it is universally accepted (general premise) that certain safety protocols drastically reduce the likelihood of accidents, and these protocols are cost-effective (specific premise), then logically (conclusion), they should be implemented to satisfy the ALARP criterion.

Conversely, inductive reasoning allows for the formulation of general rules based on the observation of specific instances where safety measures have effectively reduced risks. This form of reasoning is important when dealing with scenarios where data on accidents are limited but critical for making informed decisions about safety measures. By observing the outcomes of risk reduction strategies across various cases (specific instances), analysts can generalize that similar strategies will likely be effective in comparable scenarios (probable conclusion), thus supporting ALARP's "reasonably practicable" standard.

The case of Mr. Marshall's slickenside event stands as a poignant example of a "Black Swan" event in the field of underground coal mines. This accident, characterised by a fatal rock failure, is an exemplary scenario where the unexpected happened despite the perceived rarity of such events. The ALARP principle, employed in various industries, aims to reduce risks to a level that is "as low as reasonably practicable". However, this case illustrates the limitations of conventional risk assessment models in predicting and mitigating rare, high-consequence events. In Mr. Edward's case, the accident resulted in one fatality for one exposed unit. Despite its low probability, the severity of the outcome was significant (most severe death of individual) – a characteristic feature of "Black Swan" events.

In his book "The Black Swan", Nassim Taleb introduces the concept of extremely improbable events with enormous implications, events that are so rare that they are outside the usual expectations. The theory, focused on economic and financial systems. To prepare for multi-hazard, a phenomenon that shares characteristics with Taleb's Black Swans: rarity, extreme impact, and retrospective predictability.

These events align with abductive reasoning from Aristotelian logic, where one starts with an observation (a rare, high-impact event) and works backwards to find the most likely explanation. This form of reasoning shows the importance in risk management, especially for predicting the occurrence of Black Swan events

that conventional models fail to anticipate due to their reliance on empirical data and historical frequencies.

Seismic-induced structural collapse leading to fire can be considered an example of “Black Swan” events in the field of multi hazard assessment. As history has shown with examples such as Table 7, these fires can have devastating, albeit rare, consequences. The challenge in here is the unpredictability and lack of historical data for underground facilities that renders standard probabilistic risk assessments inadequate.

Taleb distinguishes between “Mediocristan“ and “Extremistan“ based on the statistical properties of randomness. While many hazards, including earthquakes and fires, are often considered to belong to “Mediocristan“, where occurrences follow well-documented patterns, seismic-induced structural collapse and the fires it triggers, due to their cascading effects and complexity, align more closely with “Extremistan“. In “Extremistan“, events are scalable, exhibit a vast range of potential outcomes, and defy conventional predictive models.

Nassim Taleb's “Black Swan” theory complements the ALARP principle by highlighting the limitations of predicting rare, high-consequence events. Taleb argues that conventional risk assessment models, which often rely on Gaussian distributions, are ill-equipped to account for the “fat tails” - the low-probability, high-impact outcomes [210], [267], [279], [414]. This perspective challenges the adequacy of standard risk management approaches, particularly when attempting to capture the full spectrum of potential disasters, such as seismic-induced structural collapse leading to fires.

Applying the principles from this case to the context of seismic-induced fires, it can be argued that while such events might be rare and unpredictable (“Black Swan” events), there is a duty to take all reasonable measures to mitigate their impact. Risk assessments should be made that consider even low-probability, high-impact events.

The choice of seismic-induced structural collapse leading to fire in this context recognizes that, even in the face of inherently rare events, reasonable steps must be taken to mitigate the associated risks. This aligns with Taleb's “Black Swan” theory and Lord Asquith's judgment, both of which advocate for measuring the quantum of risk in the presence of rare and high-impact events.

Integrating the Black Swan concept with the ALARP principle suggests a need for a more cautious approach to risk management. It calls for a paradigm shift from conventional probability-based models to strategies that emphasize resilience and robustness, preparing for the unforeseen, and acknowledging the limitations of predictive models in capturing the full spectrum of risks, especially those in the "Extremistan" of natural and man-made hazards.

To apply the concept of rare conjunctions of known phenomena, such as seismic-induced structural collapse leading to fire, probabilistic methods are typically applied [262], [279], [415], [416], [417], [418].

3.1.10 Methodology of Gu@larp for Multi-Hazard Risk Assessment

In the domain of underground safety, multi-hazard risks are the fusion and synthesis of two fundamental but complementary concepts: the unexpected and the undesirable side of possible joint hazardous occurrences also not independent. In particular, an appropriate number of scenarios must be identified, which is both necessary and sufficient for multi hazard risk analysis purposes. Scenarios are not observable entities. In risk-based safety design practice, scenarios are identified according to basic hypotheses or conjectures. Risk indicators are important forerunners of undesirable or unexpected underground events that may have a detrimental impact on users, governments and duty-holders.

Building on the research work of Guarascio, we define here the equations of the four basic risk indicators, the Scenario Risk Quantum, allows us to obtain the others [12], [13], [222], [223], [375].

1. **Scenario Risk Quantum:**

The Risk Quantum $Q(S_i)$ is the product of the probability of each scenario $P(S_i)$ times the number of fatalities in the same scenario $N(S_i) = N_i$.

$$Q(S_i) = P(S_i) \cdot N(S_i) \tag{64}$$

Just like measuring the risk for fatalities, the risk for property damage can also be assessed. This is done by multiplying the probability of the scenario by the amount of property structural damage $D(S_i)$ in a conventional scale it could cause:

$$Q(SD_i) = P(S_i) \cdot D(S_i) \tag{65}$$

2. Exceedance Probability (Societal Risk):

Exceedance probability $F(N_i)$, also named Societal Risk, represents the cumulative probability of observing at least i fatalities. It is calculated by summing the probabilities $P(S_k)$ of all scenarios S_k where the number of fatalities $N(S_k)$ is greater than or equal to i [419], [420], [421], [422]:

$$F(N_i) = \sum_{\substack{k \\ N(S_k) \geq i}} P(S_k) \tag{66}$$

The exceedance probability $F(SD_i)$ represents the probability that the property damage (SD) will exceed a given threshold i. It is calculated as the sum of the probabilities of all scenarios S_k where the property damage $SD(S_k)$ is greater than or equal to the threshold i:

$$F(SD_i) = \sum_{\substack{k \\ SD(S_k) \geq i}} P(S_k) \tag{67}$$

3. Individual Risk:

Individual Risk $q(N_i/Exp)$ is the probability that an individual will lose their life in an underground accident (scenario) if exposed once a year corresponding to the Risk Quantum of the above scenario divided by exposed people units in the considered scenario itself.

$$q\left(\frac{N_i}{Nexposed}\right) = \frac{\text{Risk Quantum } Q(S_i)}{\text{Exposed units in } S_i} = \frac{P(S_i) \cdot N(S_i)}{\text{Exposed units in } S_i} \tag{68}$$

While the concept of individual risk is traditionally used to assess the probability of personal harm, such as injury or fatality, it does not directly apply to property damage. Property damage typically affects a broader scope, impacting multiple assets or structures rather than just one individual. Therefore, property damage is more appropriately evaluated through collective risk measures, such as expected loss or exceedance probabilities, which consider the potential impact on all affected properties within a given scenario.

4. Expected Number of Fatalities and Property Damage

Expected Number of Fatalities E(N) in the Union of all the Design Scenarios corresponding to the sum of the Risk Quantum of the above union.

This indicator represents the total anticipated number of fatalities across all possible scenarios. It is calculated by summing up the risk quanta of fatalities for each scenario. This sum gives a single value that represents the Expected Number of Fatalities due to all considered scenarios:

$$E(N) = \sum_i Q(S_i) = \sum_i [P(S_i) \cdot N(S_i)] \tag{69}$$

In the same way, the Expected Property Damage is determined by adding up the risk quanta for property damage across all scenarios. This provides a total figure for the anticipated economic loss due to potential incidents:

$$E(SD) = \sum_i Q(SD_i) = \sum_i [P(S_i) \cdot D(S_i)] \tag{70}$$

The four definitions and equations described above provide the fundamental numerical risk indicators for all purposes of risk analysis. They are effective for both single hazards and when considering multiple hazards together. In a multi-hazard assessment, these indicators are adjusted to assess the combined impact and probability of different hazards occurring simultaneously.

3.1.11 The ALARP Framework: A Semantic and Mathematical Approach

Among the various criteria used to evaluate risk, the ALARP concept is in agreement with a lot of good properties for risk management in many sectors of civil and industrial engineering systems. The ALARP principle essentially "involves weighing a risk against the trouble, time, and money needed to control it". A decision as to whether the use of risk reduction strategies is grossly disproportionate to the benefits achieved by the risk reduction must be made. The concept is natural and symmetrical between duty holders and rights holders.

A schematic representation of Lord Asquith's judgment is presented in Figure 33. In this judgment, Lord Asquith introduced the term "quantum of risk" to emphasize the need for a specific, quantifiable measure of risk. This measurable degree of risk is crucial for making a computation in which the risk is weighed against the sacrifice involved in averting it. The use of "Quantum" underscores the necessity of an objective assessment, ensuring that decisions are made based

on concrete evaluations rather than vague perceptions. This approach ensures that risks are managed to achieve the ALARP conditions [423].

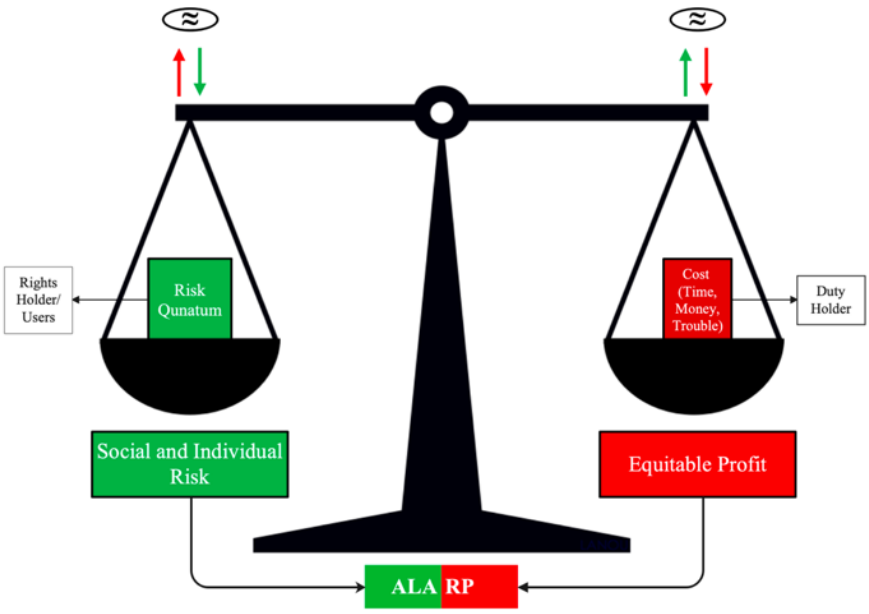

Figure 33: Schematic representation of the ALARP concept when considering the risk and cost of the risk reduction.

Risk is an abstract concept that traditionally involves a deterministic term measuring the number of fatalities on one scale and the probabilities of occurrence of scenarios involving the above number of fatalities on another scale. However, in a more comprehensive multi-hazard risk analysis, it is essential to also consider property damage alongside fatalities. This means evaluating the potential economic losses due to various hazardous events in addition to the loss of life.

While cost-benefit analyses are employed to identify the ALARP point, the process is not purely objective; it involves careful judgment from duty holders. The ALARP point serves as a critical threshold, where the reduction in risk is balanced against the cost (time, money, trouble) required. Beyond this point, any additional reduction in risk would necessitate a disproportionately high cost, which is generally considered unreasonable [424], [425]. This relationship is effectively illustrated in Figure 34. The figure shows that, as we move along the x-axis to the right, risk levels decrease, but the associated costs and efforts rise sharply.

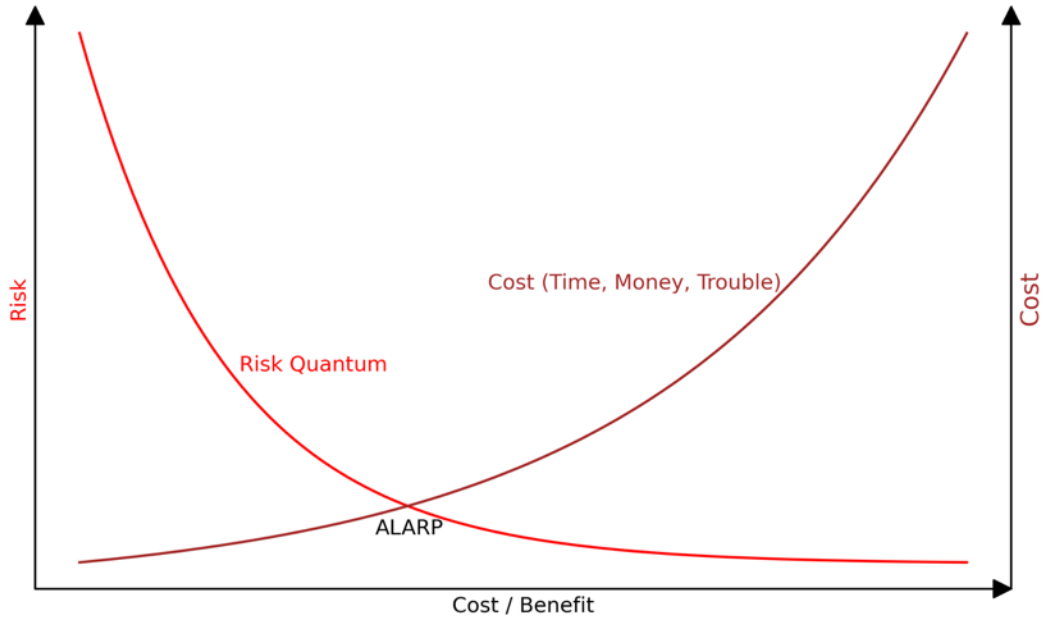

Figure 34: The ALARP point where risk reduction and cost curves intersect.

3.1.11.1 Equilibrium Strategies

Furthermore, when analysing multi-hazard scenarios, where multiple risks such as earthquakes, structural failures and fires may occur simultaneously or sequentially, decision-making becomes increasingly complex. In such case, a balance must be achieved between two key groups: the rights holders, who aim to minimize risk, and the duty holders, who are responsible for ensuring that risk reduction is reasonably practicable. The interactions between these groups can be understood through the framework of Game Theory, particularly concepts like Nash Equilibrium [426], and Pareto Optimality [427], [428].

The strategies available to each party can be understood as follows: the duty holder, responsible for implementing risk mitigation, can either invest in safety measures, which reduces risk but may impact profitability, or refrain from additional safety investments, maintaining profitability but leaving risks higher. The rights holders, concerned with their exposure to hazards, can either advocate for risk reduction, demanding further mitigation efforts, or accept the current risk levels without pressing for further action.

The outcomes of these strategic decisions are reflected in the trade-offs between risk and profit. If both parties push for safety through the duty holder's investment and the rights holders' advocacy, risk will likely be reduced, though with some cost to the duty holder's profits. Conversely, if neither side pushes for further action, the risk remains higher, but the duty holder preserves

profitability. This interaction can lead to different equilibria, where the players no longer have an incentive to change their strategies.

This framing aligns with Nash's model of a non-cooperative game, where equilibrium is reached when neither party benefits from altering their strategy unilaterally. For example, if the duty holder does not invest in safety while the rights holders push for protection, an unstable equilibrium arises, prompting potential adjustments from either side. A stable equilibrium occurs when both parties' strategies align, ensuring that neither benefits from further deviation, balancing risk and cost.

Table 9: Strategic payoff matrix for rights holders and duty holders in risk mitigation.

Duty Holders / **Rights Holders**	**Strategy 1**	**Strategy 2**
Strategy 1	Profit (+1) / Low Risk (+1)	No Profit (0) / Low Risk (+1)
Strategy 2	Profit (+1) / High Risk (0)	No Profit (0) / High Risk (0)

In Case 1, both parties win: the duty holder invests in safety, reducing risk, and the rights holders advocate for risk reduction, achieving low risk. This is a stable equilibrium, where neither party benefits from changing their strategy.

In Case 2, the duty holder invests in safety, but the rights holders accept the current risk. While this is an equilibrium, it is not ideal for the rights holders, who may push for lower risk.

In Case 3, the duty holder does not invest in safety, but the rights holders advocate for risk reduction. This results in high profit for the duty holder but high risk for the rights holders, making this equilibrium unstable.

In Case 4, neither party pushes for action: the duty holder maintains profitability, while the rights holders face high risk. This could escalate if the rights holders eventually demand change, making this situation a non-equilibrium state, as it incentivizes strategy alterations.

In real-world scenarios, the relationship between duty holders and rights holders is not always symmetrical. The duty holder typically has more resources, knowledge, and control, while the rights holders rely on regulations and advocacy to protect their interests. Nash Equilibrium assumes all players are rational with equal capability, but in reality, the duty holder often holds an

inherent advantage due to financial and decision-making power. This imbalance needs to be considered when applying Nash Equilibrium.

Pareto Optimality provides a complementary framework. In the context of risk management, Pareto Optimality refers to a situation where no party can be made better off without making the other party worse off. In other words, the optimal balance between safety investments and risk reduction is achieved when neither the duty holder nor the rights holders can improve their position without negatively impacting the other. In this optimal solution, the duty holder cannot reduce safety measures without increasing risk for the rights holders, while the rights holders cannot push for more safety measures without creating unsustainable costs for the duty holder.

Pareto Optimality ensures fairness and efficiency in decision-making by guaranteeing that risk mitigation strategies are implemented without disproportionately favouring one party over the other. By balancing the interests of both groups, it helps achieve a solution that both sides can accept without compromising their positions.

In such cases, the role of a neutral decision-maker, such as regulators or policymakers, becomes crucial. They ensure that both parties benefit from a balanced outcome. If biased toward the duty holder, the decision-maker risks exposing the rights holders to unmitigated hazards. On the other hand, if the decision-maker overly favours the rights holders, the duty holder may face unsustainable costs, threatening the long-term viability of the risk mitigation strategy.

The recommended Disaster Risk Reduction (DRR) strategies within the ALARP framework allow for the implementation of risk mitigation measures, provided they are reasonably proportionate to the efforts required for risk reduction and are not excessively burdensome. To express Lord Asquith's idea in probabilistic and quantitative terms, we can articulate it as follows:

$$\text{ALARP} = \min(\text{Risk} \mid \text{Equitable Cost}) = \min(\text{Cost} \mid \text{Acceptable Risk}) \tag{71}$$

The ALARP principle can be expressed in words as minimizing risk given an equitable cost or, equivalently, minimizing cost given an acceptable level of risk. The above principle can be described quantitatively with a relationship similar to the spirit of Bayes' theorem:

$$P(R \mid EC) \cdot P(EC) = P(C \mid AR) \cdot P(AR) \tag{72}$$

Here, EC stands for Equitable Cost, AR for Acceptable Risk, R for Risk, and C for Cost. This equation can be interpreted as balancing the probability of (acceptable) risk under an equitable cost, and conversely, the probability of an equitable cost under acceptable risk.

This leads us to the Bayes' theorem condition:

$$P(EC \cap AR) = P(EC) \cdot P(R \mid EC) = P(AR) \cdot P(C \mid AR) \tag{73}$$

or equivalently,

$$P(EC \cap AR) = P(R \mid EC) \cdot \ P(EC) = P(C \mid AR) \cdot P(AR) \tag{74}$$

If these two products describe the same intersection EC ∩ AR, setting them equal implies both perspectives (risk-focused vs. cost-focused) must converge on the same balanced outcome. This requirement forms the foundation of the ALARP principle: risk is reduced "as low as reasonably practicable," yet cost remains equitable and not overly burdensome. Consequently, an optimization must be performed within the common domain of "Equitable Cost" and "Acceptable Risk" to ensure that risk reduction efforts align with proportionate cost expenditures.

3.2 Gu@larp Model

The probabilities of the single S_i are indicated in the Gu@larp model as $g(N_i(S_i))$ or shortly $g(N_i)$. The corresponding exceedance probability is $G(N_i) = Gu/N_i$, where Gu is equal to $G(N_i) = 1$. This function is a real staircase-type function, monotonically decreasing, where the variable (N) assumes only the integer values. The related exceedance probabilities are defined as $G(N_i) = \sum_{N(S_k) \geq i}^{k} g(S_k)$. The related probability of a scenario (S_i) can be described as $g(N_i) = G(N_i) - G(N_i + 1)$.

The parent functions in the continuous number domain are the equations of the equilateral hyperbola functions, namely $G(x) = Gu \cdot x^{-1}$, where Gu plays the role of parameter. The corresponding density function is:

$$\begin{cases} g(x) = Gu \cdot x^{-2} & \text{where } x \geq 1 \\ g(x=0) = 1 - Gu & \text{(Dirac } \eth \text{ type)} \\ g(x) = 0 & \text{elsewhere} \end{cases} \tag{75}$$

In practice for representative descriptions of reality, the density function is truncated at an appropriate value $x = x_{max}$. The above assumption does render the expected value E(x) a limited one. To achieve this result, an acceptable approximation is to locate a Heaviside step function in the point $x = x_{max}$ equal to $G(x_{max}) = Gu/x_{max}$. Consequently, the finite expected value is $E(x) = Gu(\text{Log}\, x_{max} + 1)$. Figure 35 below presents three examples of exceedance probability models.

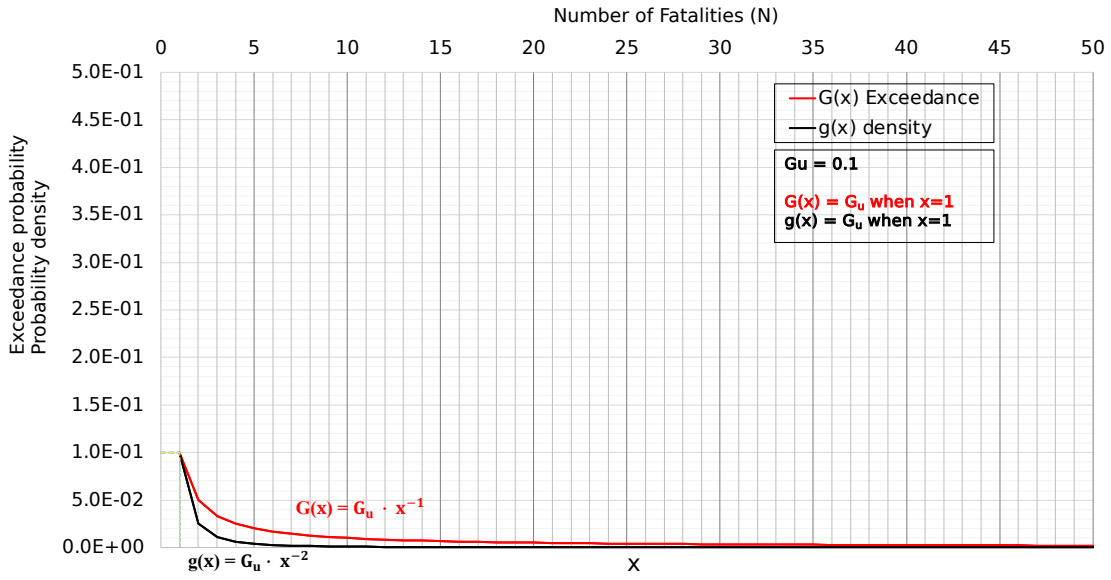

(a)

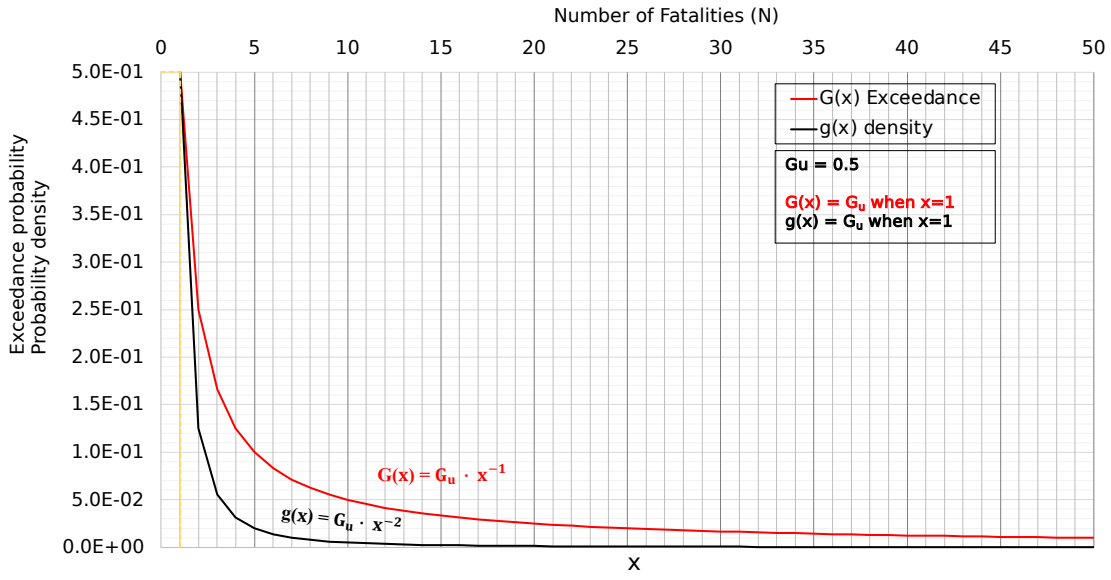

(b)

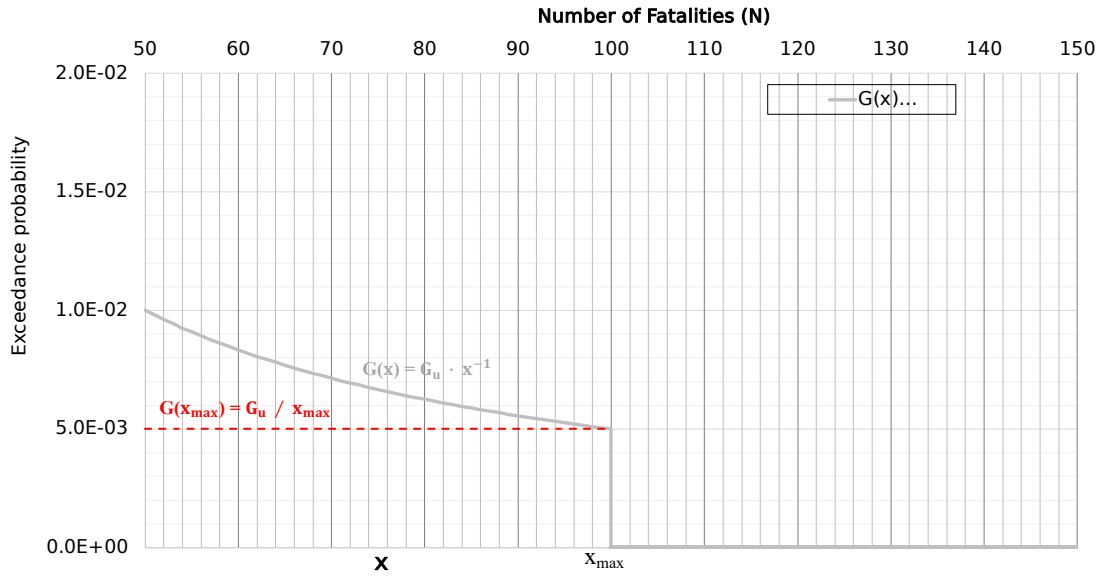

(c)

Figure 35: Exceedance probability model assuming: (**a**) Gu = 0.5; (**b**) Gu = 0.1; (**c**) Gu = 0.5 and $G(x_{max}) = Gu/x_{max}$ for $x \geq x_{max}$ values. The red dotted line emphasises the coordinates of the truncation point, which is important for practical applications [13].

The numerical models of the scenario probability as g(N) functions and related exceedance probability G(N) are usually represented in a diagram on a logarithmic scale where on the horizontal axis, there are integer values of the number of fatalities (N) of the scenarios, and on the vertical axis, there is the probability of exceedance of the integer threshold values (Figure 36a).

The above probability of exceedance is nothing other than the probability of the union of the scenarios with the number of fatalities greater than the threshold value. The relation between the number of fatalities and exceedance probability on an arithmetic scale is also shown in Figure 36b.

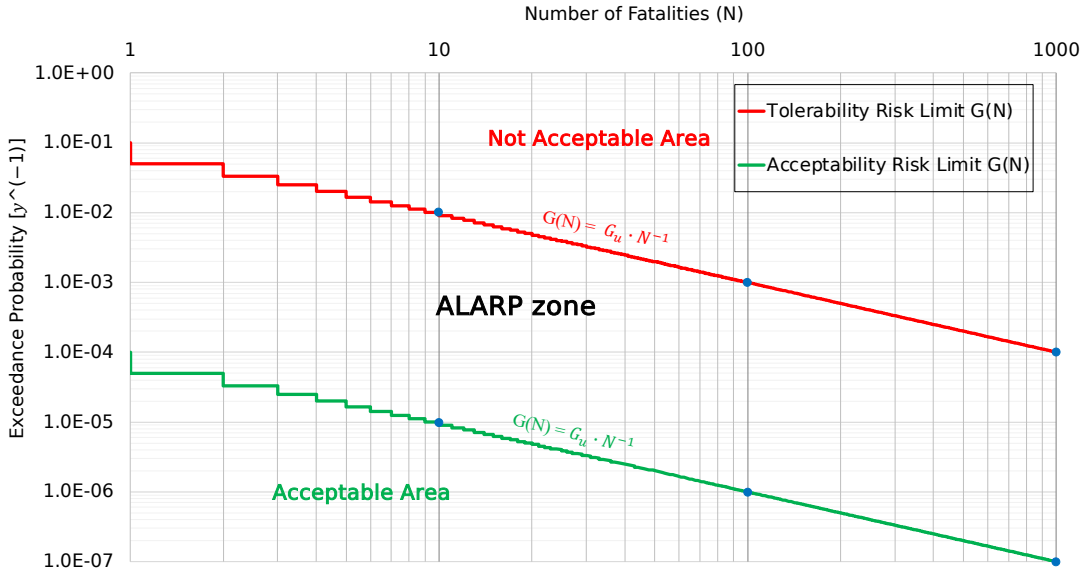

(a)

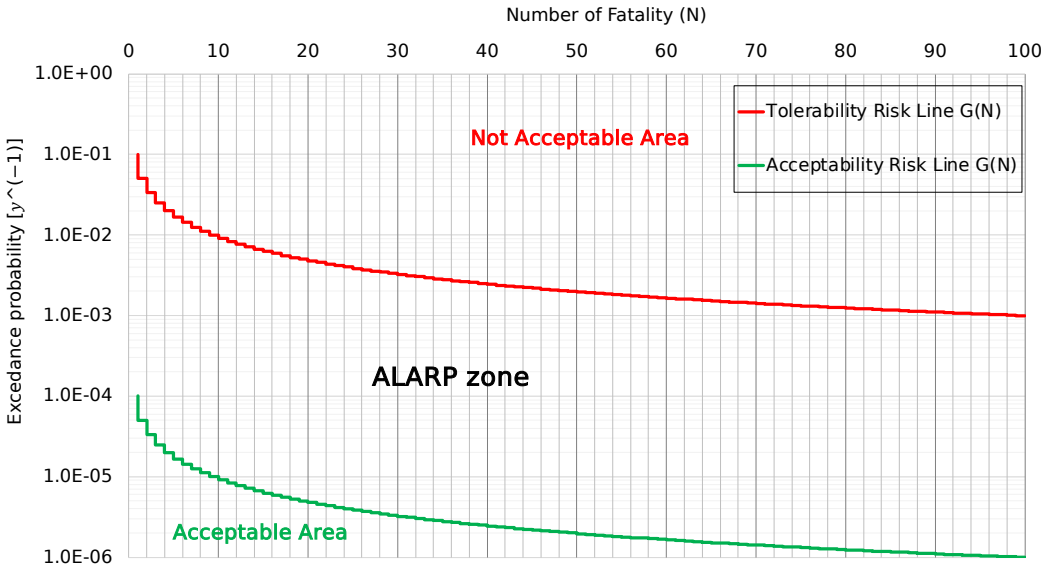

(b)

Figure 36: Gu@larp (Italian Legislative Decree No. 264/2006) models on logarithmic (a); and arithmetic (b) scales.

The risk function has to be a staircase type in order to describe and calculate properly the Risk Quantum of the single scenarios, defined below for the purpose of a serious and accurate design objective. Once all of the above quantities are

estimated, risk indicators could be immediately obtained for all possible hazards and hazardous events on one hand, and protection systems and fatality scenarios on the other hand.

The approach, named the Gu@larp model, relates to the ALARP principle adopted in the Italian Legislative Decree No. 264/2006 [374] in agreement with the Directive 2004/54/EC [376]. Table 10, Table 11, Table 12 and provide examples of numerical values characterising the Tolerability and Acceptability Limits curves adopted in Italian law and by the UK HSE.

Table 10: Maximum individual risk indicator in the Tolerability and Acceptability Limit curves models that corresponds to the case of one fatality when there is one exposed unit only in the scenario.

Limit criteria	**Tolerability Limit (Italy road tunnel)**	**Acceptability Limit (Italy road tunnel)**	**Tolerability Limit (UK-HSE Worker)**	**Acceptability Limit** (UK-HSE All)
(Gu)	1.0E−1	1.0E−4	1.0E−3	1.0E−06

Table 11: Examples of numerical limit values of Societal Risk (exceedance probability) with the Tolerability and Acceptability Limit curves models.

Fatalities	**Tolerability Limit (Gu) (Italy road tunnel) per Year**	**Acceptability Limit (Gu) (Italy road tunnel) per Year**	**Tolerability Limit (Gu) (UK-HSE Worker) per Year**	**Acceptability Limit Gu) (UK-HSE All) per Year**
1	1.0E−1	1.0E−4	1.0E−03	1.0E−06
10	1.0E−2	1.0E−5	1.0E−4	1.0E−7
50	2.0E−03	2.0E−06	2.0E−05	2.0E−08
100	1.0E−3	1.0E−6	1.0E−5	1.0E−8

Individual Risk exists and differs depending on the number of exposed individuals. Individual Risk refers to the risk of an individual becoming a fatality in a single accident. The Individual Risk changes depending on the number of exposed individuals and the number of fatalities. For example, if one person is exposed and there is one fatality, or if 10 people are exposed and there is only

one fatality, the Individual Risk changes accordingly as below Table 12 and Figure 37.

Table 12: Examples of numerical limit values of the probability of scenarios with the Tolerability and Acceptability Limit curves models (rise of the staircase-type curve of the corresponding scenario).

Fatalities	Tolerability Limit (Italy Road Tunnel, Gu) per Year	Acceptability Limit (Italy Road Tunnel, Gu) per Year	Tolerability Limit (Gu) (UK-HSE Worker) per Year	Acceptability Limit Gu) (UK-HSE All) per Year
1	5.0E−02	5.0E−05	5.0E−04	5.0E−07
10	5.0E−03	5.0E−06	5.0E−05	5.0E−08

Figure 37a and b consider the number of fatality intervals from 0 to 10 with reference points given in Table 10. The Individual Risk is taken into account, and its behaviour is observable when considering the number of exposed people, parameterised by the number of fatalities, represented in different coloured lines. The Individual Risks show hyperbolic-type behaviour vs. exposed units, where the highest value corresponds to the minimum number of exposure units, which decreases monotonically as the number of exposed units increases.

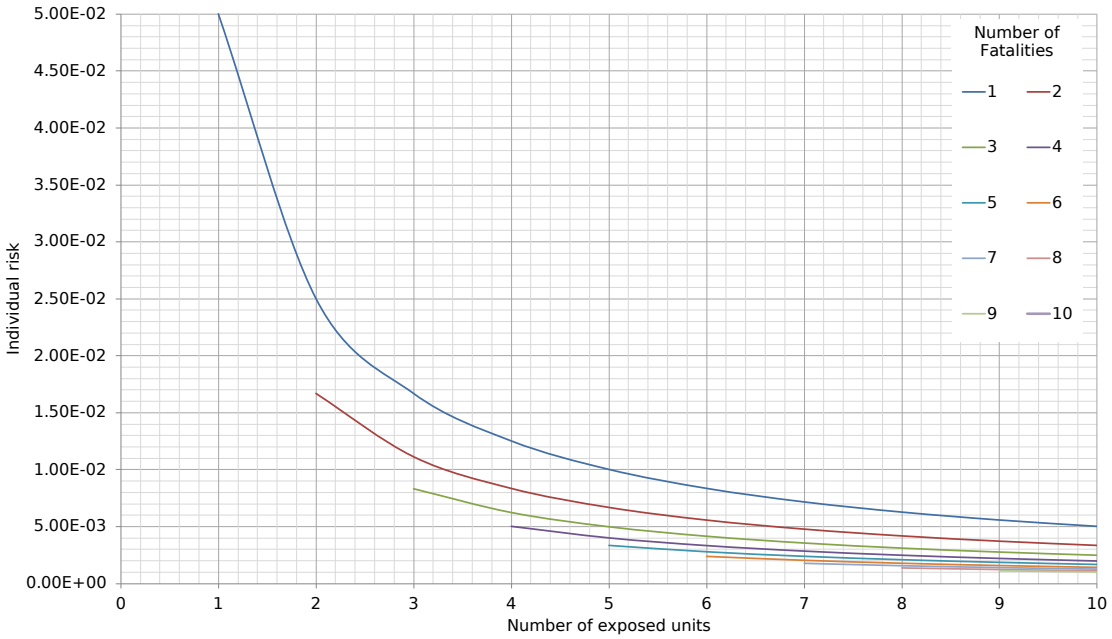

a)

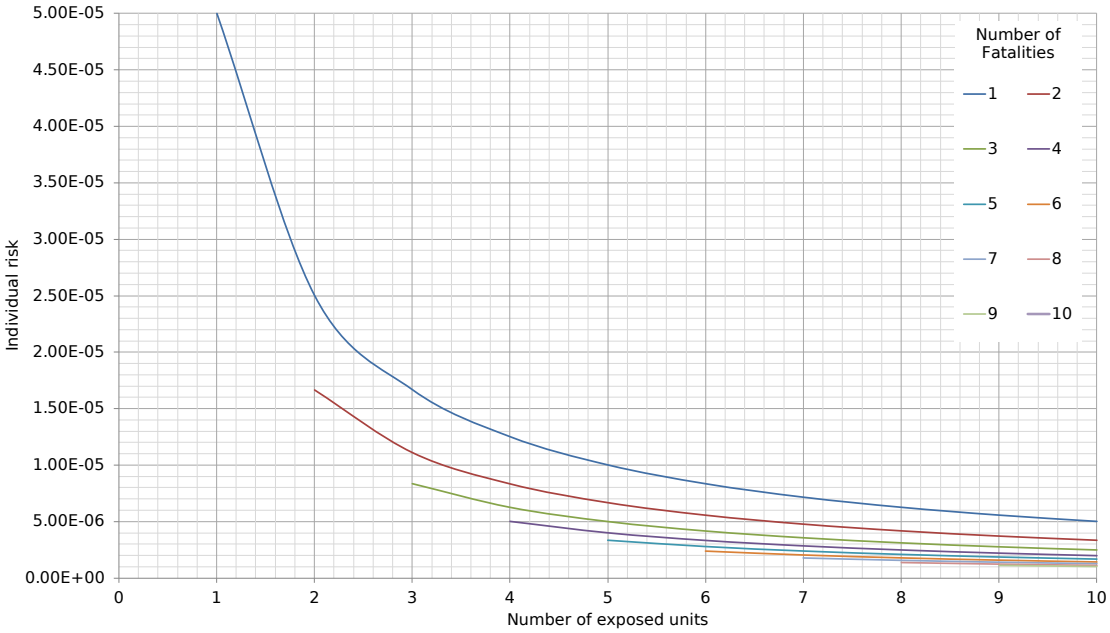

b)

Figure 37: Behaviour of the Individual Risk with respect to number of exposed units, on an arithmetic scale for different values of Gu and with the number of fatalities as parameters in coloured lines: (a) Gu = 1.0E−01; and (b) Gu = 1.0E−04.

In Figure 38, it can be appreciated how much, for a given value of the Risk Quantum in a scenario, the number of fatalities can range in a wide interval, increasing as the value of the Risk Quantum itself increases and the corresponding Individual Risk will vary accordingly.

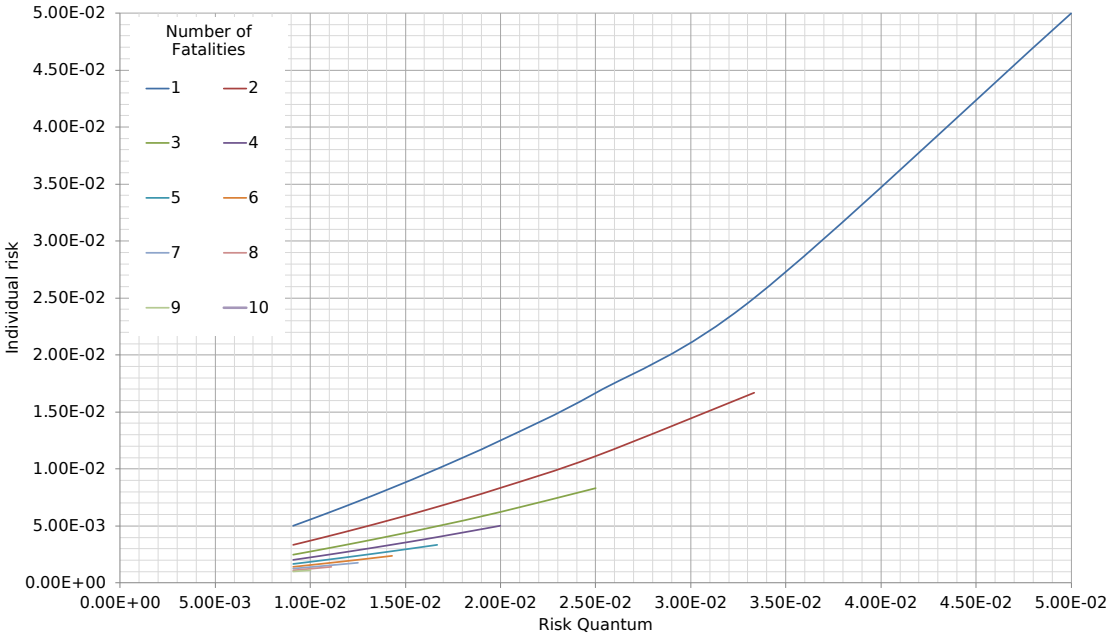

a)

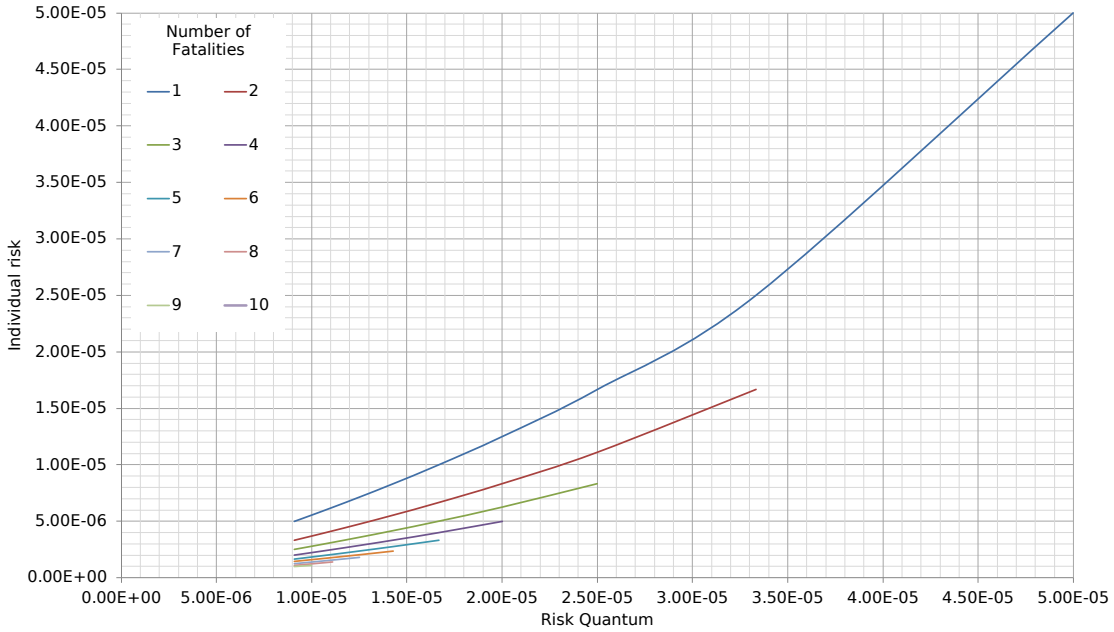

b)

Figure 38: Pattern of the Individual Risk versus the Risk Quantum, on an arithmetic scale. Different numbers of fatalities are represented by different coloured lines: (a) Gu = 1.0E−01; and (b) Gu = 1.0E−04.

Figure 39 demonstrates the Gu@larp risk-time-unit model within a framework of Tolerability and Acceptability criteria, used to evaluate the risk design line. Fatalities, represented as integer values from 0 up to the total number of individuals in the underground, are evaluated in steps where each $\Delta N = 1$ symbolizes one "run". The exceedance probability $G(N_i) / F(N_i)$, associated with a specific threshold N, is calculated as the cumulative probability of all scenarios S_k where the number of fatalities $N(S_k) \geq N$. Each scenario is represented by a rectangle, and the quantum of risk, based on the number of fatalities, forms part of the staircase on the exceedance axis.

Each N_i corresponds to a specific "rise" $g(N_i)$, calculated by subtracting the exceedance probability $G(N_i + 1)$ from $G(N_i)$. On the graph, the "run" and "rise" are depicted by the points with coordinates (N, G(N)). The line descends monotonically, meaning the rise values decrease accordingly. These rises are determined by the probabilities g(N) for each fatality threshold N. When multiplying g(N) by N, the rectangle's area under the curve (with N as the base and g(N) as the height) represents the Risk Quantum, $Q(S_i)$, interpreted as probabilised fatalities. The Individual Risk in each scenario is different, and it is represented by the rise of the rectangle in the staircase. The Risk Quantum for a given number of fatalities forms part of the stair in the exceedance probability

axis. A single stair step may encompass more than one scenario, so we might have different strips representing the same number of fatalities, but with different probabilities for each scenario.

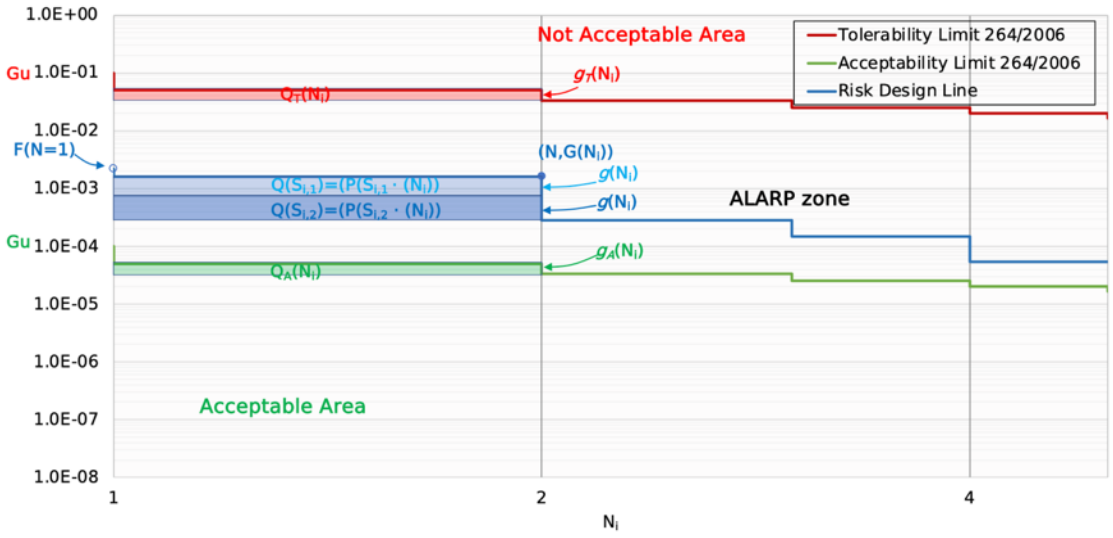

Figure 39: Risk Design Line vs Acceptability and Tolerability Limit curves in Gu@larp risk-time-unit.

The Tolerability/Acceptability Limit curves are nothing else but the exceedance probability curves corresponding to the limit tolerated and limit accepted scenarios. The risk curve characterizing the safety design is obtained by connecting the number of fatalities obtained by the simulation of deterministic scenarios, and the estimated probabilities of the equivalent scenarios. If there are more than one scenario with the same number of fatalities N, these scenarios will be combined and analysed as a single group of scenarios with probability equal to the sum of their probabilities.

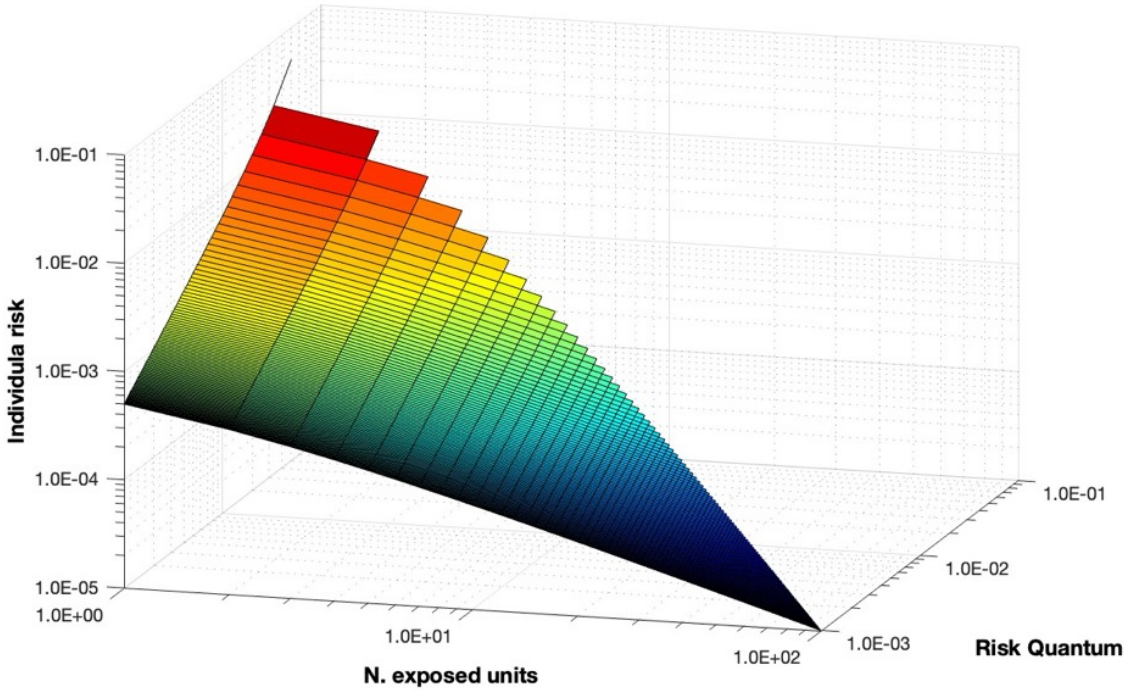

Figure 40**:** Three-dimensional view of $Q(S_i)$, $q(N_i/Nexposed)$, and Nexposed on a logarithmic scale, (Gu = 1.0E−01).

In Figure 40, a 3D view of the relationship in a given Gu@larp model for the assumption of Gu = 1.0E−01 is shown, illustrating the relationship between the Risk Quantum $Q(S_i)$, the Individual Risk $q(N_i/Nexposed)$ and the Number of Exposed units Nexposed. For a scenario with a given Risk Quantum, the corresponding Individual Risk shows a relationship inversely proportional to the number of exposed units.

The procedure adopted for the quantitative multi-hazard risk assessment is illustrated in Figure 41.

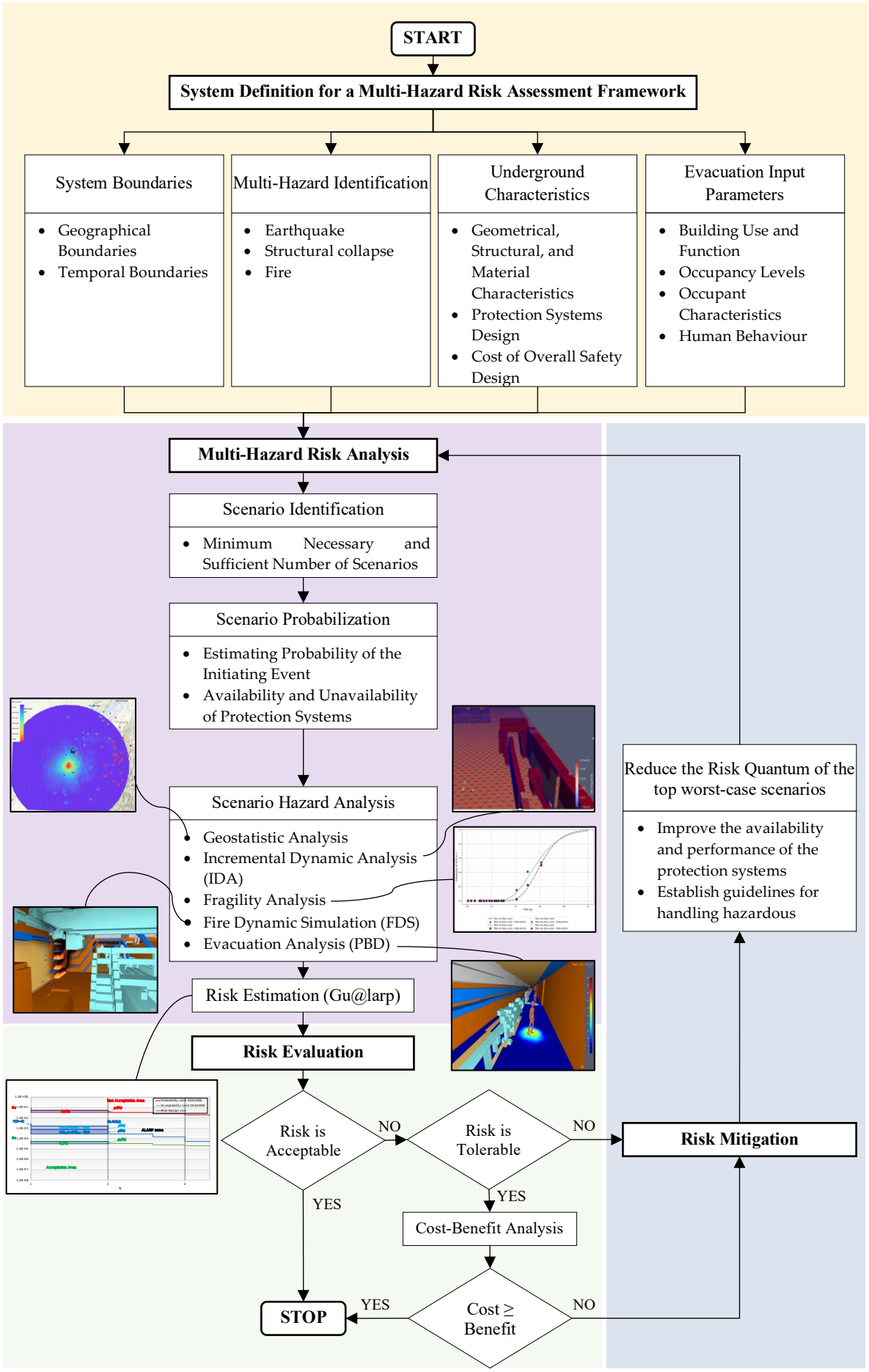

Figure 41: Multi-hazard Risk-Based Design Methodology Framework.

Chapter 4

Multi-Hazard Risk Assessment: CERN Case Study

4.1 What is CERN?

The European Centre for Nuclear Research, also known as CERN, stands as the world's leading particle physics laboratory, encompassing both extensive surface facilities and more than 83 kilometres of underground infrastructure (Figure 42) [429], [430], each with its own research objectives and associated risks. Located at the Franco-Swiss border near Geneva, at the base of the Jura mountains, it was established in 1954 and has since grown to include 24 member nations [431]. The organization supports a vast community of over 13,000 scientific users, who contribute to its mission from more than 950 institutions across over 80 countries. In 2023, a diverse global community of more than 17,000 colleagues from around the world engaged in the laboratory's activities, contributing to various research projects [432].

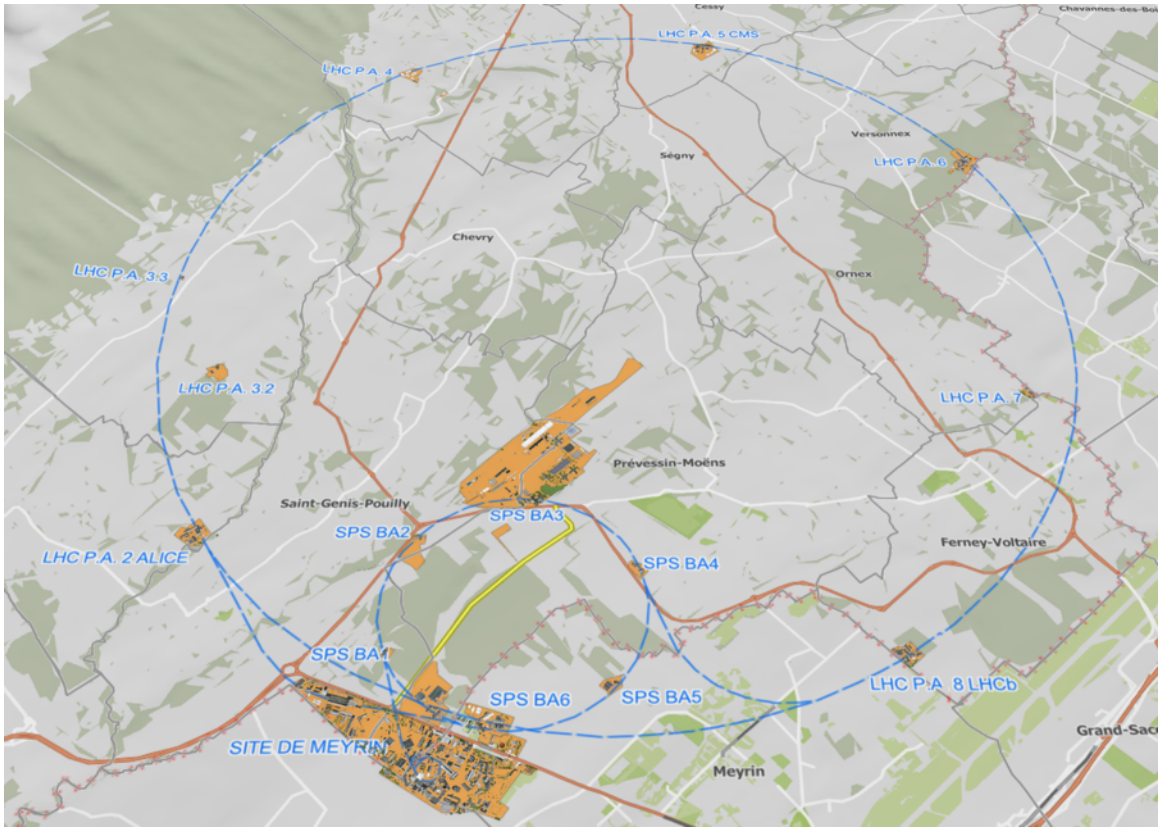

Figure 42: Layout of the CERN complex: surface and underground and infrastructures [433].

CERN's primary focus is on particle physics, commonly referred to as High Energy Physics (HEP), which involves rigorous analysis and experimentation on the fundamental constituents of matter at the subatomic level. Significant advancements in particle physics were achieved throughout the 20th century, including the discoveries of the electron and the atomic nucleus, alongside the

development of transformative theories such as special relativity and quantum mechanics.

CERN replicates the high-energy conditions of the early universe. These experiments provide insights into the universe's evolution and the fundamental forces at play during its formation. The LHC, in particular, is designed for high luminosity and energy, facilitating detailed observations of rare particle interactions. The advanced operations have been key in validating the existence of the Higgs boson, confirming the process by which elementary particles acquire mass.

The Super Proton Synchrotron (SPS) is CERN's second-largest accelerator, with a circumference of nearly 7 kilometres, operational since 1976. The SPS facilitates the acceleration of protons and heavy ions to energies up to 450 GeV, serving as a critical pre-accelerator to the Large Hadron Collider (LHC) by providing the necessary beam intensity for further acceleration (Figure 43). The SPS also supports a variety of fixed-target experiments, including SHINE, NA62, COMPASS, NA64, NA65, AWAKE all of which delve into various aspects of particle physics, such as the study of quark-gluon plasma, particle interactions, and the search for rare processes that could reveal new physics beyond the Standard Model [434], [435].

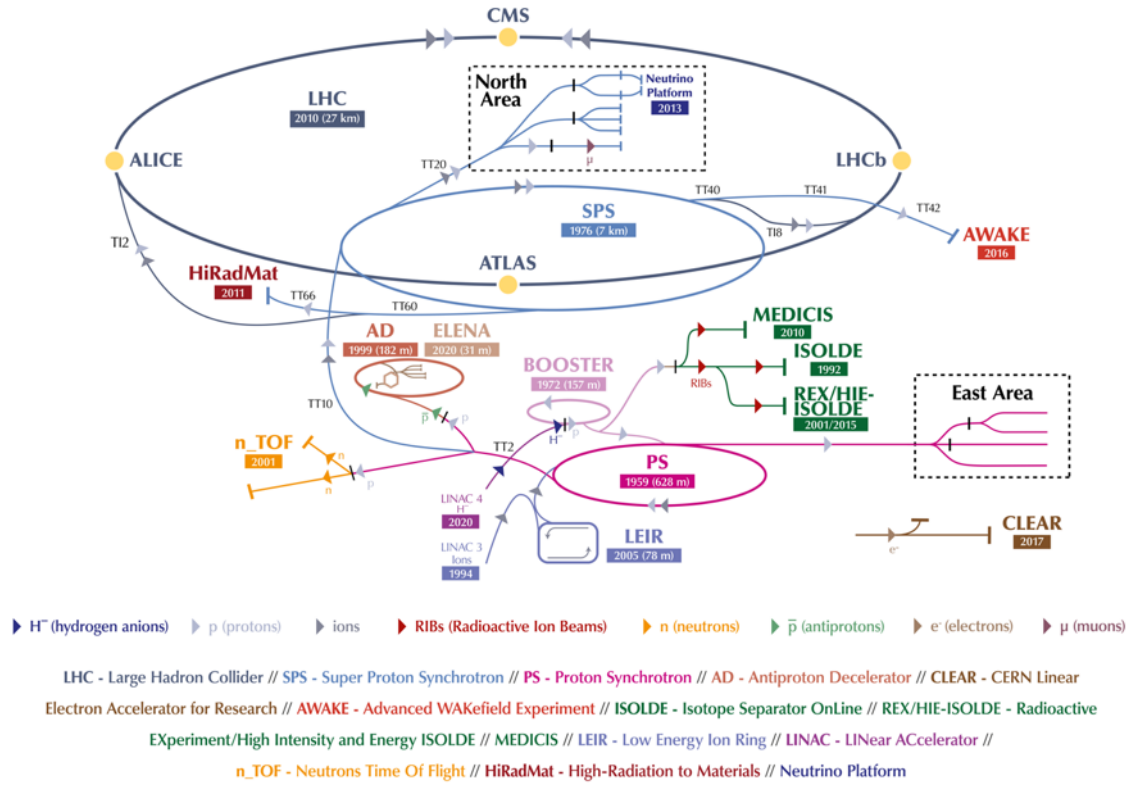

Figure 43: Schematic of the CERN accelerator complex and beamline connections [436].

The SPS supplies particle beams through 6 kilometres of beamlines connected to CERN's North Area, supporting both experimental and research development. Since its inception, the SPS has contributed to several key discoveries, including the identification of the W and Z bosons, deepening our understanding of the weak force. The facility remains essential for ongoing and future experiments, particularly under the Physics Beyond Colliders (PBC) initiative, which aims to explore new physics phenomena and drive technological advancements [437].

The North Area of CERN is a dedicated experimental zone where high-energy proton beams, extracted from the SPS, are processed and delivered to multiple experimental stations. This area comprises three key experimental buildings: EHN1, EHN2, and ECN3, each supporting a range of physics experiments and research activities. The primary proton beam, after being extracted from the SPS, is directed into the TT20 tunnel. Within the TDC2 cavern, this beam is split into three beams, hitting the target stations T2, T4, and T6. These stations are the initiation points of the TCC2 cavern, which generate secondary beams. These secondary beams are then routed to the experimental buildings EHN1, EHN2, and ECN3 (Figure 44) [438], [439].

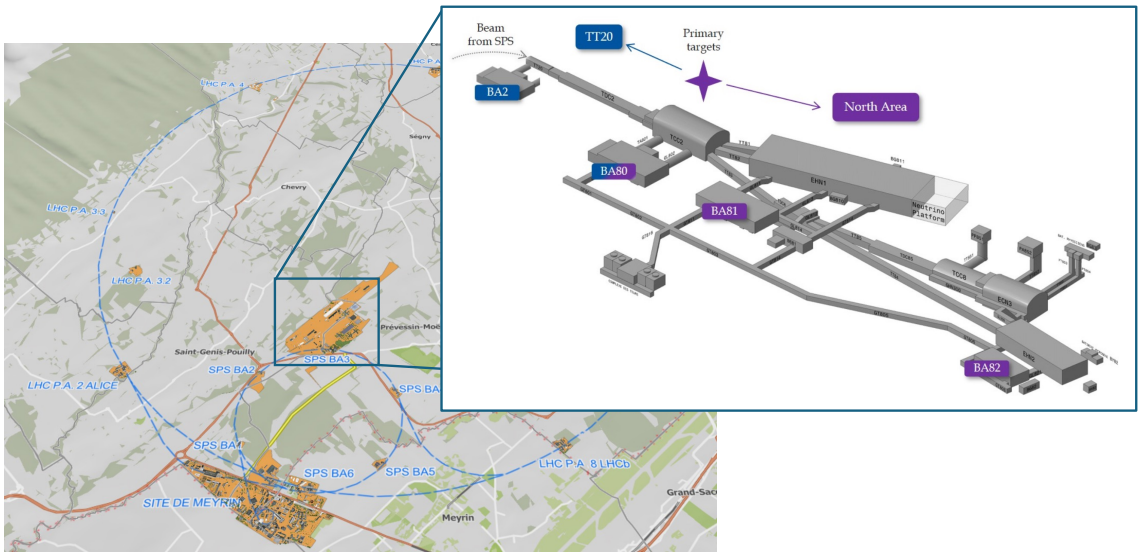

Figure 44: TT20 and North Area facilities [440].

4.2 Multi-Hazard Risk Assessment of the TDC2/TCC2 CERN Facility

CERN was selected as a case study for the application of the proposed method. This diverse structure offers a rich context to validate the flexibility and

adaptability of the method. Each building within the CERN complex presents different challenges that need to be addressed individually. These challenges arise from the unique nature of the research being conducted, the layout of the facilities, the type and number of occupants, and the special environmental and hazardous conditions associated with high-level physics experiments.

This case study is dedicated to a comprehensive examination of the multi-hazard risks associated with the TCC2 and TDC2 caverns at CERN particularly focusing on seismic risks, structural integrity, and systemic interactions that could lead to catastrophic events. The operational environment within these caverns is characterized by conditions that amplify the potential for diverse hazards. Challenges such as seismic activity, the possibility of structural compromise, falling blocks, and resultant fires are not merely hypothetical but represent tangible risks that could severely impact both safety and operational continuity.

Figure 45: TDC2 (left) and TCC2 (right) tunnels [441], [442].

The analysis method integrates multiple hazard scenarios, taking into account both independent and cascading effects [443]. By considering these effects, a comprehensive quantitative multi-hazard risk analysis is employed that not only quantifies the probability of each hazard but also assesses the potential consequences on the exposed elements (people, buildings, lifelines, economy, environment, etc.). Considering both independent and cascading effects moves beyond isolated assessments. Independent effects look at the direct consequences of single hazards acting alone. The direct impact of each identified hazard is examined by assessing the potential damage specific events, such as a fire or an earthquake, could cause to the caverns' infrastructure, equipment, and personnel.

Cascading effects, on the other hand, explore how one hazard could trigger another, creating a chain of events that might amplify the overall risk. For example, an earthquake could cause structural damage that leads to a collapse, which might then ignite a fire if the present hazards are compromised. This interconnected view helps anticipate complex scenarios where the total impact of combined hazards is greater than the sum of their individual effects.

The commitment to a comprehensive quantitative multi-hazard risk analysis is driven by the need to not only quantify the probability and impact of these hazards but also to develop a robust framework for managing them. By employing quantitative methods such as statistical analysis, probabilistic modelling, and several simulations, the aim is to measure these risks with precision.

4.3 Seismic Hazard Analysis for the TDC2/TCC2 facility at CERN: A Multivariate Geostatistical-4D Approach

A comprehensive seismic hazard analysis was performed at CERN to assess the potential of earthquake-induced ground motions and their impact on the site's structures and facilities. This study focuses on the underground facilities TCC2 and TDC2, critical components of the SPS complex. Accurate seismic hazard analysis is relevant for the overall multi hazard risk assessment, also ensuring the operation of SPS. Seismic data from recording stations located in Switzerland, France, and Italy were collected within a 150-km radius area centred in the TCC2. The collected raw data were then filtered to obtain specific frequency ranges of interest, enabling efficient processing and analysis for accurate seismic hazard analysis of the TCC2 and TDC2. This research proposes an innovative model that integrates multivariate statistical analysis methodologies with geostatistical ones, addressing three critical aspects of seismic modelling: directional anisotropy of the value and the arrival time of the PGA, geographical continuity in terms of space correlation function describing the apparently irregular variations between data pairs. The experimental validation of a geostatistical estimator accuracy is carried on checking the estimation errors in all the location points of the recording stations. In these points, the recorded values and estimated ones are both known. This model allows a more complete seismic assessment of critical facilities like the TCC2 and TDC2 to ensure SPS operation and safety of personnel, by providing more accurate seismic analysis [3].

As the foundational step in the multi-hazard risk assessment for the TCC2 cavern at CERN, a seismic hazard analysis was performed to establish the probability distribution of seismic events. This analysis provides important input for subsequent stages of risk assessment, such as structural collapse analysis. Within the broader context of multi-hazard risk assessment, this seismic hazard analysis offers initial probability estimates for different PGA levels. By establishing these probabilities, the assessment follows a data-driven approach to quantify the likelihood of seismic events and their potential impact. These probabilities serve as the foundation for simulations such as IDA, which model how the TCC2 blocks behave under various seismic intensities, identifying which blocks are likely to fall. This integrated approach enables the estimation of structural failure risk based on both seismic probabilities and simulated block behaviour.

4.3.1 Seismic Hazard Curve Estimation Using Geostatistical Modelling for the TDC2/TCC2 Facility

The structural design standards bind the assessment and verification of the dynamic stability of the load-bearing elements of a building or industrial infrastructure to the seismic hazard of a certain site. The validity of the design largely depends on level of representativeness of the seismic hazard curves and, more precisely, on the local representativeness of the damping profiles of the ground motion variables estimated using the data recorded by a seismic monitoring accelerometer station network. The accuracy of the local estimate depends on the ratio between the number of information collected and the amount of information necessary to describe, with a given accuracy, the phenomenon of propagation of seismic motion in rock formations. Consequently, a first step to reduce the overall uncertainty of the estimate is the availability of a seismic monitoring network coupled with the information that takes into account the position of active faults capable of generating earthquakes, the geomorphological characteristics of rocks and the lithological features of the ground [444].

However, at the same time, it is necessary to develop and validate an efficient numerical estimation methodology [57]. Guarascio et al. [4], [60] tested a non-stationary geostatistical estimator to estimate and validate the PGA numerical values and arrival time at the nodes of a predefined grid around the epicentral zones of the earthquakes that occurred in Italy in 2016.

In this subchapter the same non-stationary geostatistical model has been used to estimate the PGA components (North-South, and vertical) and the related arrival time of the earthquake which occurred approximately 30 km South-West of the CERN area on 1 November 2022, having Local Magnitude (ML) of 3.4. The estimation values of the PGA at the nodes of 1 km space grid were used to determine the directional damping profiles of the seismic motion with the epicentral directional distances. Finally, the seismic hazard curve was drawn at a point in proximity of the TDC2/TCC2 facility for seismic events located in the area in the azimuthal sector of greatest seismicity around the CERN area that is the 135° azimuth sector South-West to East.

4.3.2 Seismicity of the Territory Around CERN

To assess the seismicity of the territory in the surrounding of CERN, earthquake lists from the past 323 years within a 100-km radius were obtained from the websites of the national geophysical services of Switzerland, France, and Italy, all members of the Federation of Digital Seismograph Networks (FDSN). The ObsPy library was used for processing seismic waveforms, metadata, and catalogues [445]. Initially, a dataset of 15,000 data points was collected from these sources: ETH, RESIF, and INGV. Through a data cleaning process, duplicates resulting from overlapping network records were removed, yielding a refined dataset of 10,020 data points with magnitudes of 1.0 or higher (Figure 46).

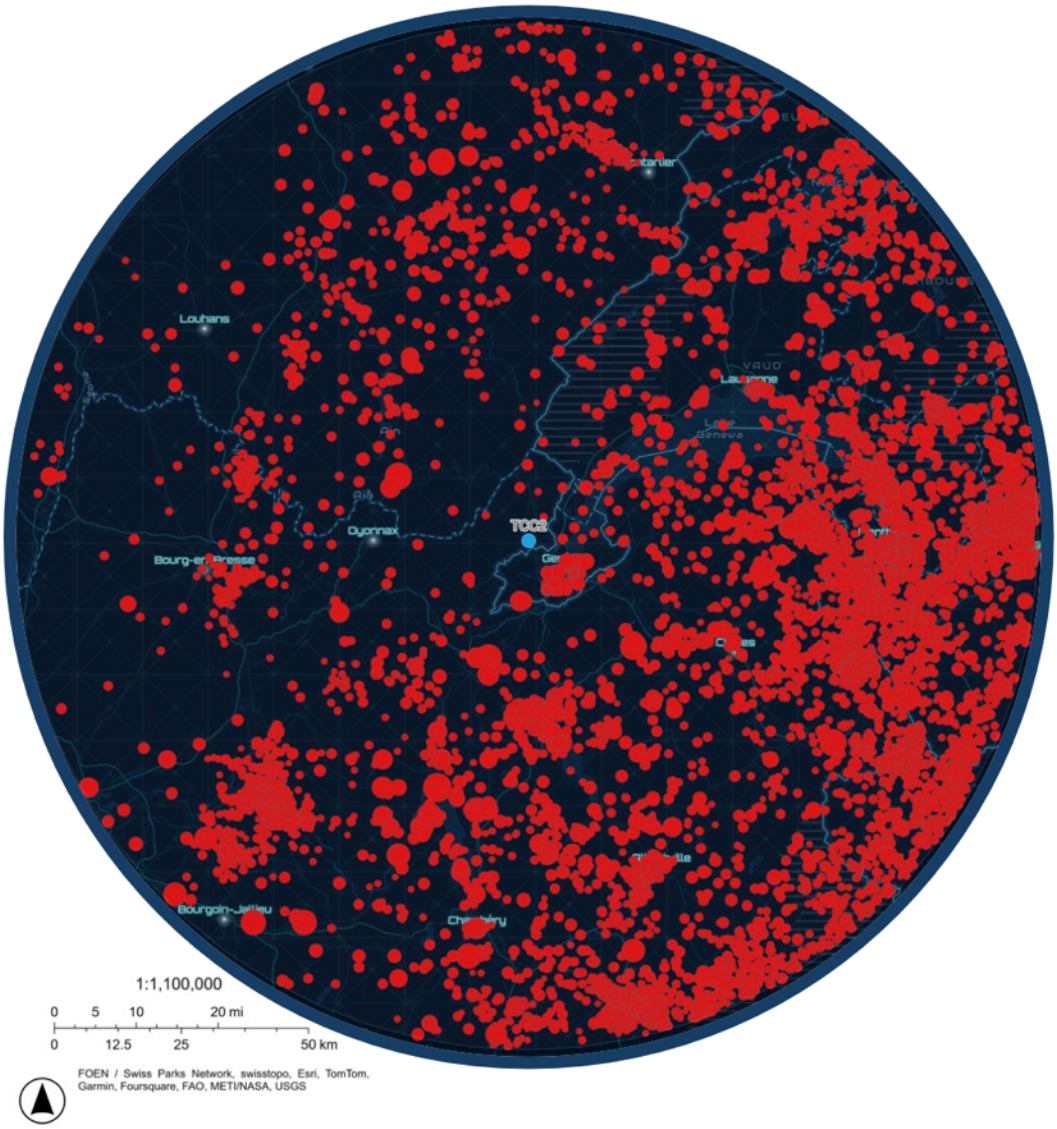

Figure 46: Earthquake occurrences (10,020 events, Magnitude 1.0 or higher) in the CERN region since 1155.

The data reduction phase focused on extracting key seismic intensity measures relevant to the study. Bandpass filtration was applied to the data to isolate specific frequency ranges of interest, reducing noise and improving signal clarity. The filtered data was then cross-referenced with national databases to ensure accuracy, including a comparison with results from the Swiss seismological centre [446] (Figure 47). For each earthquake, the geographical coordinates of the epicentre and the intensity, expressed either in EMS or Richter Magnitude scale, were collected. The empirical relationships proposed by Camassi and Stucchi [447] and Gomez et al. [448] were used to estimate the epicentral PGA from the earthquake EMS intensity and Richter magnitude values. Below the intensity of seismic events is expressed by the epicentral PGA. Figure 48 and Figure 49

display the historical series of earthquakes that occurred around the CERN area from 1700 and 1850 to 2022.

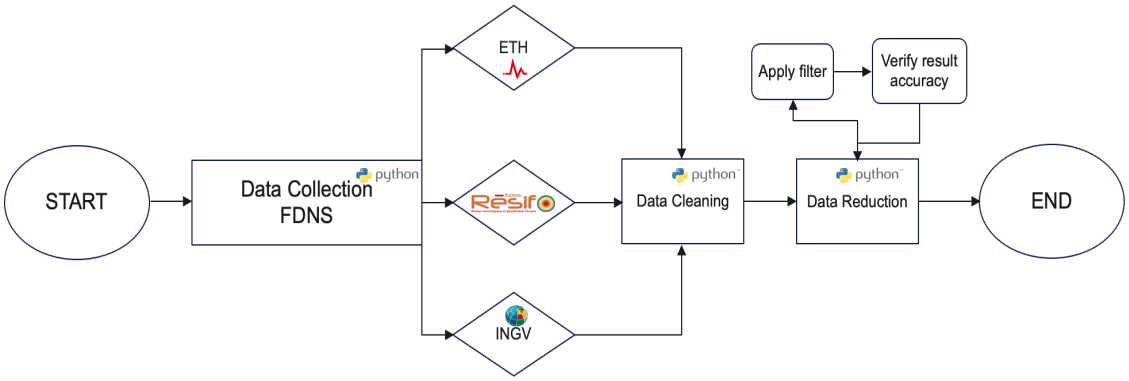

Figure 47: Flowchart of seismic data collection and processing.

The analysis focused on the last 323 years because data from earlier periods is less reliable. Historical records become systematically available starting from the 17th century, providing a more consistent and accurate dataset for analysis.

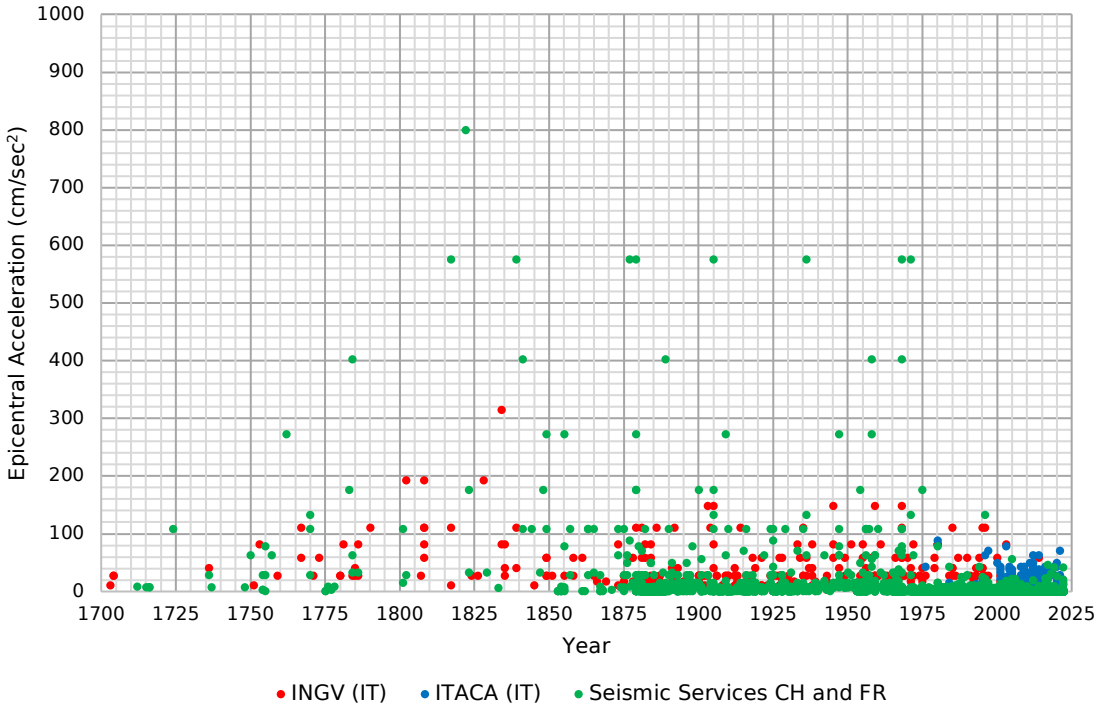

Figure 48: Time series of earthquakes that occurred over the past 323 years in the vicinity of the CERN area.

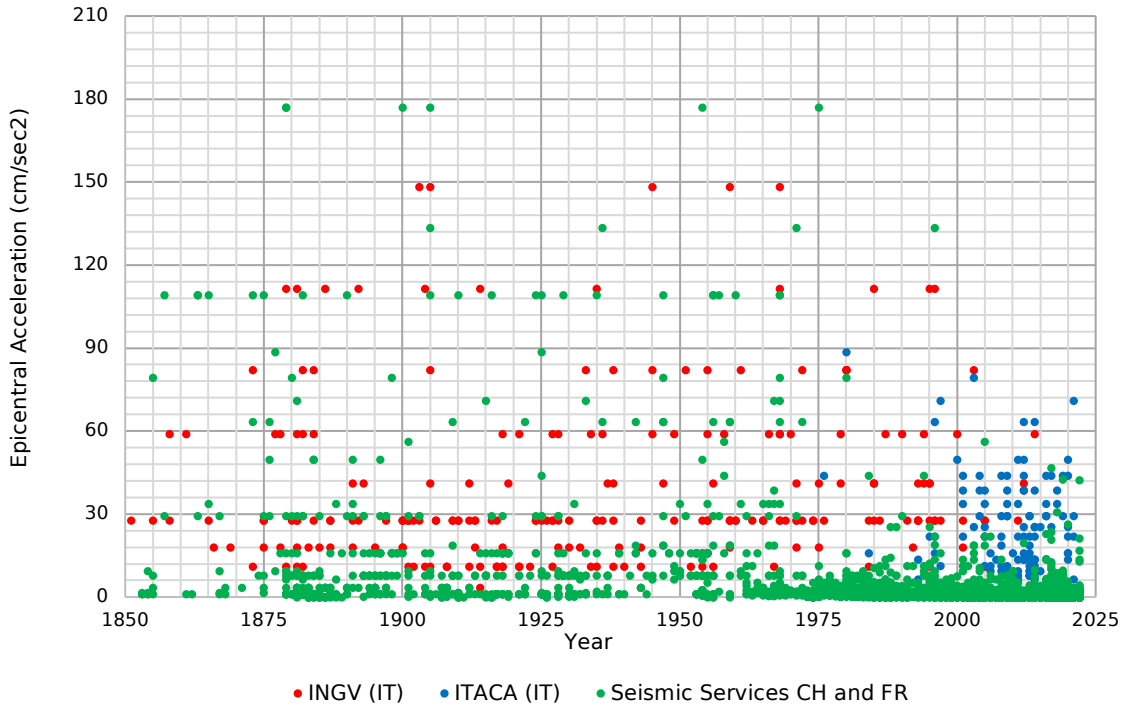

Figure 49: Time series of earthquakes that occurred over the past 173 years in the vicinity of the CERN area.

Figure 48 and Figure 49 illustrates the higher occurrence of low-intensity earthquakes (PGA < 60 cm/sec²) detected in the last 150 years. This differential sampling led to the estimation of the parameter for the Poisson probability distribution for low-intensity seismic events over two-time intervals shorter than 323 years.

The geographical distribution of earthquakes in the mentioned area is not uniform. The majority of earthquakes and events with the highest epicentral intensity (PGA > 400 cm/sec²) are predominantly located to the South and South-East of CERN facilities. Of particular note is the earthquake that occurred in 1822 to the North of Lake Le Bourget, roughly 50 km southwest of Geneva [449]. This earthquake was estimated to have a magnitude between VII and VIII on the Richter scale, corresponding to an epicentral PGA of approximately 800 cm/sec². The Le Bourget earthquake aligns to the North with an event from 1971 with an epicentral PGA of approximately 600 cm/sec², and to the North-East with five events of the same intensity that occurred in the sequence of 1839, 1877, 1879, 1936, and 1968. Figure 50 shows the positions of these earthquakes, having a PGA greater than 400 cm/sec² with a distance less than 65 km from the TDC2/TCC2 facility. Table 13 shows the number of earthquakes that occurred over the past 323 years within the 8 circular sectors of 45° width, where ° indicates sexagesimal degrees, and centred in the TDC2/TCC2 facility; the events are categorized by

their epicentral PGA. For some PGA ranges, it was calculated the parameter λ of the Poisson distribution function, representing the probability of occurrence for a seismic event within that range in a given year. The inverse of the parameter λ provides an estimate of the average time interval between two seismic events having a PGA in the same range.

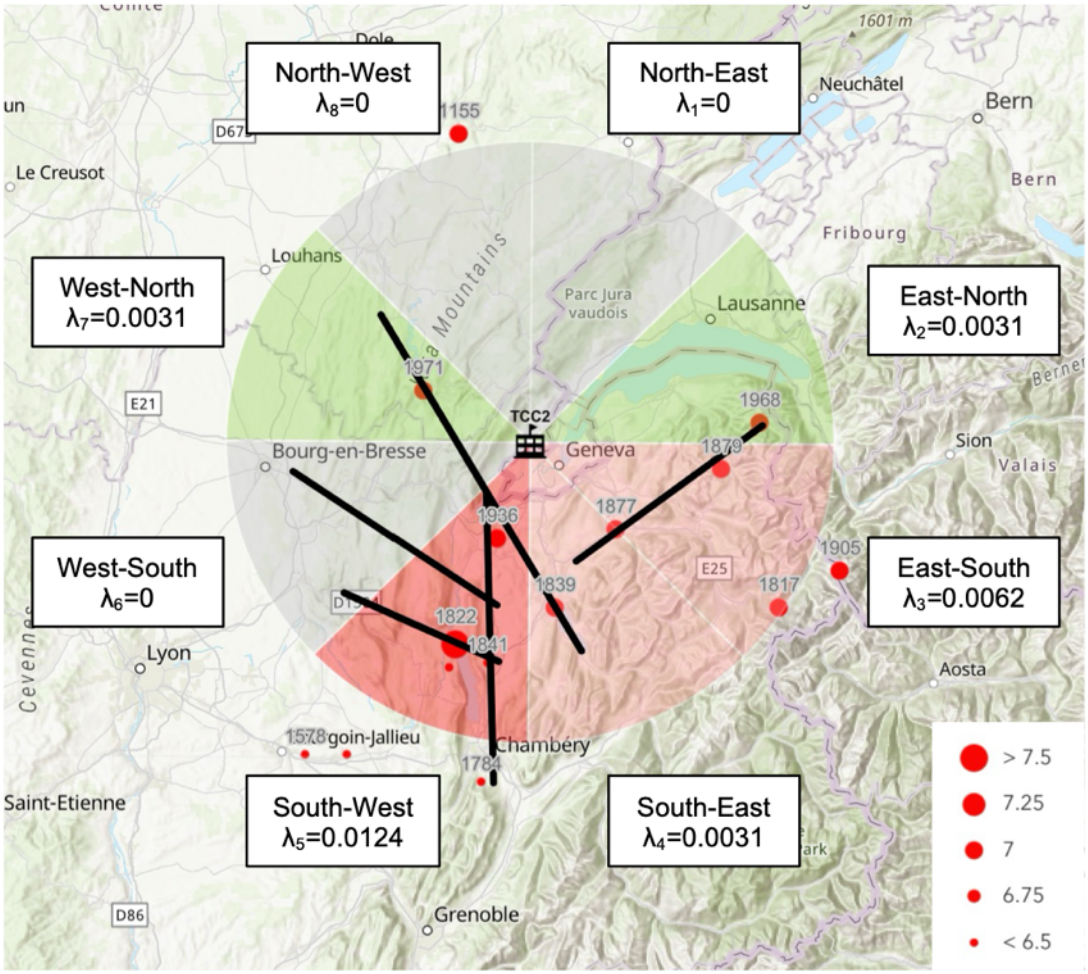

Figure 50: The map shows earthquakes from 1155 to 2022, with magnitudes from 6.5 to 7.5. It also illustrates the fault lines associated with the most intense earthquakes (PGA ≥ 400 cm/sec²) and the 8 circular cloves (sectors) centred around the TDC2/TCC2 facility. The parameter λ of the Poisson distribution represents the ratio between the number of earthquakes with PGA ≥ 400 cm/sec² and the observation period of 323 years (1700–2022).

From the data presented in Table 13 , the seismicity of the mentioned 8 circular sectors was estimated (Figure 50). The measurement of the seismicity of this territory is defined as the probability of occurrence of seismic events; this level of seismicity can also be expressed as the average return period of seismic events with epicentral PGA greater than certain intensity thresholds.

Table 13: Number of detected earthquakes around TDC2/TCC2 facility in the last 323 years, used for the Hazard Rate (λ) estimation and the corresponding Return Period (1/λ) of future seismic events in the 8 circular sectors investigated.

Range of Estimated Epicentral Accelerations (cm/sec²)	Direction	Number of Years	Number of Events (*)	Return Period (Years)
5 ≤ PGA < 30	East-North	47	35	1.34
	North-East		12	3.92
	North-West		8	5.88
	West-North		4	11.75
	West-South		6	7.83
	South-West		13	3.62
	South-East		34	1.38
	East-South		26	1.81
30 ≤ PGA < 60	East-North	147	3	49.00
	North-East		1	147.00
	North-West		0	-
	West-North		0	-
	West-South		0	-
	South-West		4	36.75
	South-East		6	24.50
	East-South		2	73.50
60 ≤ PGA < 100	East-North	323	2	161.50
	North-East		1	323.00
	North-West		2	161.50
	West-North		0	-
	West-South		0	-
	South-West		3	107.67
	South-East		4	80.75
	East-South		2	161.50
100 ≤ PGA < 200	East-North	323	1	323.00
	North-East		0	-
	North-West		2	161.50
	West-North		1	323.00
	West-South		1	323.00
	South-West		11	29.36
	South-East		3	107.67
	East-South		6	53.83
200 ≤ PGA < 400	East-North	323	0	-
	North-East		0	-
	North-West		0	-

	West-North		0	-
	West-South		0	-
	South-West		1	323.00
	South-East		0	-
	East-South		1	323.00
400 ≤ PGA < 600	East-North	323	1	323.00
	North-East		0	-
	North-West		0	-
	West-North		1	323.00
	West-South		0	-
	South-West		3	107.67
	South-East		2	161.50
	East-South		2	161.50
PGA ≥ 600	East-North	323	0	-
	North-East		0	-
	North-West		0	-
	West-North		0	-
	West-South		0	-
	South-West		1	323.00
	South-East		0	-
	East-South		0	-
(*) Earthquakes with a maximum distance from CERN of 65 km				

4.3.3 Universal CoKriging Geostatistical Estimator of the Seismic Variables

4.3.3.1 Preliminary Considerations

A first spatial trend of the damping of the seismic variables' (peak displacement, velocity and acceleration) with the distance from the epicentral zone is obtained from the physical theory of propagation of elastic waves, radially emitted by a point source in a homogeneous and isotropic material. The theoretical result shows a damping law of elastic oscillations (geometric attenuation), inversely proportional with the distance from the source that can be described by the Equation $f(r) = a\, r^{-c}$, where $f(\cdot)$ is a function of the distance r of a generic point from the epicentre providing the generic seismic variable (i.e., peak displacement, velocity or acceleration) and a is a constant depending on the seismic variable of interest. The exponent c is equal to 1 for volume waves while is equal to 0.5 for surface ones.

The values recorded by the accelerometer stations deviate from the values predicted by physical theory due to the heterogeneity and discontinuity of the rock formations crossed by seismic waves. Indeed, the different propagation speeds of the seismic waves in the rock formations deform the geometry of the surface waves with consequent irregular and anisotropic variations of the geometric attenuation; furthermore, irregular local variations of the seismic motions are a consequence of the different anelastic behaviour of the rock formations. A part of the energy carried by seismic waves is continuously and irregularly dissipated by friction in an anelastic damping mechanism.

Despite this, the data recorded over distances of tens of kilometres from the epicentral zone by the accelerometer stations show good consistency with the mentioned surface wave attenuation equation and the motion anelastic dissipation, which follows an exponential law from the epicentre such as $e^{-b\,r}$, where b is a constant depending on the rock damping properties. The accelerograms recorded by the stations of the seismic monitoring network represent a spatio-temporal sampling of the phenomenon of propagation of the ground seismic motion in the neighbourhood of the epicentral zone for a certain earthquake.

4.3.3.2 Definition of the Geostatistical Estimator for the Seismic Variables

The geostatistical estimator is defined as an application of random functions of variables defined on a certain Euclidean space of a rock-like medium [450], [451], [452]. For the analysis purposes, the Universal CoKriging (UCoK) with external drift was chosen, as it allows for the integration of: i) the physical law of damping of anelastic waves, referred to in the following as the Seismic First-Guess (SFG); ii) the morphology of the topographic surface; iii) the position of the relevant accelerometer stations and iv) the geographical continuity of the seismic variables, which can be described by a variogram and a cross-variogram model [72].

Let $Z=\{Z(\mathbf{x}): \mathbf{x} \in D \subseteq \mathbb{R}^2\}$, where $\mathbf{x}$ is the 2-dimensional coordinate vector of a generic point, be a non-stationary random field defined on the investigated continuous domain D of the Euclidean space $\mathbb{R}^2$ and reflecting the defining seismic variable at the altitude of the earth's surface (seismic ground motions). The random function of Z is then considered as described by the following Equation:

$$Z(\mathbf{x}) = m(\mathbf{x}) + \sigma(\mathbf{x})Y(\mathbf{x}), \quad \forall\, \mathbf{x} \in D \tag{76}$$

where $m(\mathbf{x}) : \mathbb{R}^2 \to \mathbb{R}$ is an unknown continuous function that captures the large-scale geographic pattern of the seismic variable on the topographic surface. This function represents the SFG, which approximates the underlying physical processes governing seismic behaviour.

$\sigma(\mathbf{x}) : \mathbb{R}^2 \to \mathbb{R}^+$ is an unknown continuous function that describes the local standard deviation, representing the variability of the seismic residual relative to the geographic trend encapsulated by $m(\mathbf{x})$.

$Y(\mathbf{x})$ is a quasi-stationary random field with zero mean and a variogram $\gamma(\mathbf{h})$, where $\mathbf{h}$ is the distance vector between two points $\mathbf{x}_1$ and $\mathbf{x}_2$. The variogram $\gamma(\mathbf{h})$, quantifies the spatial correlation of seismic residuals, depending solely on the separation between these points, and is independent of any specific origin [453], as defined by Chilés and Delfiner [450].

From this model, the first two moments of the increments of the random fields $Z(\mathbf{x})$ and $Y(\mathbf{x})$ offer valuable insights into the structure and behaviour of the seismic field.

First Moment (Expectation):

$$\mathrm{E}[Z(\mathbf{x}_1) - Z(\mathbf{x}_2)] = m(\mathbf{x}_1) - m(\mathbf{x}_2) \tag{77}$$

This equation shows that the expectation of the difference between the seismic variable at two points is determined solely by the deterministic component $m(\mathbf{x})$, which reflects the large-scale spatial trend. This trend, captured by the SFG, approximates the geographical variation of seismic ground motions. The first moment, therefore, emphasizes how the broad geographic pattern in seismic behaviour is governed by physical and topographic factors, which are essential to understanding the deterministic structure of the seismic field.

Second Moment (Variance):

$$\mathrm{Var}[Z(\mathbf{x}_1) - Z(\mathbf{x}_2)] = \mathrm{Var}[Z(\mathbf{x}_2) - Z(\mathbf{x}_1)] = 2\sigma(\mathbf{x}_1)\sigma(\mathbf{x}_2)\gamma(\mathbf{x}_2 - \mathbf{x}_1) \tag{78}$$

The second moment, represented by the variance, captures the local variability of the seismic field, primarily driven by the residual field $Y(\mathbf{x})$. Here, $\sigma(\mathbf{x})$ represents the local scaling factors (i.e., the pointwise standard deviations), while $\gamma(\mathbf{h})$ models the spatial correlation of the normalized residuals (see Subsection

4.3.4.2) as a function of the distance between points. The variogram $\gamma(\mathbf{h})$, central to geostatistics, encapsulates the decay of spatial correlation as distance increases. Thus, this formulation reveals how seismic variability at the local scale is influenced by both the geographic position and the distance between measurement points.

Quasi-Stationary Nature of Residuals:

$$E[Y(\mathbf{x}_1) - Y(\mathbf{x}_2)] = 0 \tag{79}$$

The residual field $Y(\mathbf{x})$, being quasi-stationary with zero mean (the local mean of the residuals shows a slight and continuous variation much lower than the spatial variability of the residuals themselves), ensures that the second-order structure of the field, governed by the variogram, remains independent of the absolute location but depends on the relative distance between points. This property is critical in characterizing the spatial continuity of seismic residuals and in enabling robust interpolation across the domain D.

The non-stationary behaviour of the random field $Z(\mathbf{x})$ is characterized by the non-stationary parameters $m(\mathbf{x})$ and, $\sigma(\mathbf{x})$, which vary continuously across the domain D. These parameters capture both the broad geographic patterns (through $m(\mathbf{x})$) and the local variability ($\sigma(\mathbf{x})$), thus offering a comprehensive depiction of how seismic ground motions change across space. The variogram function $\gamma(\mathbf{h})$ provides a means to quantify the spatial dependence of the residuals $Y(\mathbf{x})$, reflecting the local correlation structure and thereby ensuring that both large-scale and small-scale features of the seismic field are adequately modelled.

To calculate both the value and the arrival time of PGA, the Universal CoKriging (UCoK) method was used. Indeed, the UcoK estimator is herein considered as an estimation $Z^*(\mathbf{x})$ at a point of coordinates $\mathbf{x}$ of the seismic variable Z, which can be either the PGA value or the related arrival time. It can be obtained as a linear combination of the data Z_0 of the variable to be estimated (iv=0) and the data Z_1 of the auxiliary variable (iv=1) around the point of interest:

$$Z_0^*(\mathbf{x}) = \sum_{k=0}^{1} \sum_{i=1}^{n} \lambda_{k,i} \, Z_k(\mathbf{x}_i) \tag{80}$$

where $\lambda_{0,i}$ are the weight coefficients for the target variable Z_0, and $\lambda_{k,i}$,i (where $k > 0$) are the coefficients for the auxiliary variable Z_k. The coordinates $\mathbf{x}_i$ denote

the observation points where data for both variables have been collected. The coordinates $\mathbf{x}_i$ denote the n observation points, where the pair of metric coordinates $\mathbf{x}_i$ is necessary to locate the i-th point in the geographic domain. The inclusion of the PGA arrival time as an auxiliary variable improves the accuracy of the PGA estimation (seismic parameter of engineering interest) because it captures additional information; some features of the propagation around the epicentral zone of the seismic movement are better represented by the variable "PGA propagation time". Therefore, in estimating the PGA value, the arrival time of the acceleration peak is considered as the auxiliary variable, and vice versa.

The coefficients $\lambda_{0,\,i}$ and $\lambda_{1,\,i}$ are determined by solving a system of linear equations. For each node in the grid, the following system is solved:

$$\begin{aligned} &\sum_{jv=0}^{1} -\boldsymbol{\Gamma}_{iv,jv}\ \boldsymbol{\lambda}_{jv} + \ \mathbf{F}_{iv}\ \boldsymbol{\mu}_{iv} \ = \ -\boldsymbol{\Gamma}_{iv,0} \qquad\qquad iv = 0,\,1 \\ &\mathbf{F}_{iv}^{T}\ \boldsymbol{\lambda}_{iv} \ = \ \mathbf{f}_{iv,0}\ \delta_{iv,1} \qquad\qquad iv = 0,\,1 \end{aligned} \tag{81}$$

where, $\boldsymbol{\Gamma}_{i,j}$ represents the n × n matrices of variograms or cross-variograms between pairs of observation points, capturing the spatial correlation between the target and auxiliary variables. F_{iv} is the n × L matrix containing the values of the SFG functions at the observation points. $\Gamma_{i,0}$ are the vectors of variograms and cross-variograms between the point to be estimated and the observation points. $f_{l,0}\ \delta_{i,l}$ represents the values of the SFG for the target variable at the observation points, with these values set to zero for the auxiliary variable, ensuring unbiasedness for the auxiliary variable as well.

Once the weight coefficients $\lambda_{k,\,i}$ are obtained, they must satisfy two key conditions for ensuring that the estimation is both unbiased and optimal:

The **mean estimation error** of the target variable must be zero, ensuring that the estimator is unbiased. This is imposed by the following equations present in the above system:

$$\mathbf{F}_{iv}^{T}\ \boldsymbol{\lambda}_{iv} \ = \ \mathbf{f}_{iv,0}\ \delta_{iv,1} \qquad\qquad iv = 0,\,1 \tag{82}$$

The **variance of the estimation error** (estimation variance) must be minimized, providing an optimal estimate with minimal uncertainty.

$$\sigma^2_{CK} = \sum_{iv=0}^{1} \boldsymbol{\lambda}_{iv}^T \, \boldsymbol{\Gamma}_{iv,0} + \boldsymbol{\mu}_0^T \, \mathbf{f}_{0,0} \tag{83}$$

Here, $\boldsymbol{\lambda}_{iv}$ and $\boldsymbol{\mu}_{iv}$ are the vectors of weight coefficients and Lagrange parameters, respectively; the matrix $\boldsymbol{\Gamma}_{iv,0}$ contains the variograms and cross-variograms between the observation points and the point to be estimated and $\mathbf{f}_{0,0}$. Thus, the estimation variance depends on several factors, including the number and geometry of the observation points, their position relative to the point being estimated, and the local variability of the seismic variables being treated.

4.3.3.3 SFG Equation for the Seismic Variables

SFG equation for both PGA values and the related arrival time are herein presented.

The systematic decrease of PGA with distance from the epicentral zone was modelled as a product of the mentioned geometric attenuation of the PGA and the anelastic dissipation laws. The effect of the earth's surface morphology on the seismic ground motion is also modelled. The SFG for the PGA is herein indicated as m_{PGA} and can be defined as:

$$m_{PGA}(\mathbf{x}) = c_{0,PGA} + c_{1,PGA} q(\mathbf{x}) + c_{2,PGA} \frac{1}{\sqrt{\bar{d}_s(\mathbf{x},\mathbf{x}_0)}} e^{-b\,\bar{d}_s(\mathbf{x},\mathbf{x}_0)} \tag{84}$$

where $\mathbf{x}_0$ identifies the coordinates of the centre of the earthquake epicentral zone (circle of radius 3.5 km), $q(\mathbf{x}) : \mathbb{R}^2 \rightarrow \mathbb{R}$ is its elevation on the earth surface, $\bar{d}_s(\mathbf{x},\mathbf{x}_0) : \mathbb{R}^2 \rightarrow \mathbb{R}^+$ is the directional anisotropic proximity distance of the point $\mathbf{x}$ from the epicentral zone centred at the point $\mathbf{x}_0$ (non-Euclidean mean distance), b is the coefficient of the anelastic dissipation law and $c_{0,PGA}$, $c_{1,PGA}$ and $c_{2,PGA}$ are three real coefficients.

The SFG for the PGA arrival time m_t increases with distance from the epicentral zone and the related equation is defined in a similar way, such as:

$$m_t(\mathbf{x}) = c_{0,t} + c_{1,t} q(\mathbf{x}) + c_{2,t} \bar{d}_s(\mathbf{x},\mathbf{x}_0) \tag{85}$$

with akin meaning of the symbols used in Equation (84).

The measurement of seismic proximity from the epicentral zone is represented by a non-Euclidean mean distance between the point x and the circle of radius 3.5 km centred at the point x_0 (which is the epicentral zone of the earthquake).

The non-Euclidean distance between two points is defined as follows:

$$d_s(\mathbf{x}_1,\mathbf{x}_2) = \sqrt{(\mathbf{x}_1 - \mathbf{x}_2)^{\mathrm{T}}\mathbf{M}(\mathbf{x}_1 - \mathbf{x}_2)},\ \ \forall(\mathbf{x}_1,\mathbf{x}_2) \in D\times D \tag{86}$$

where $\mathbf{M}$ is the metric tensor in $\mathbb{R}^2$ introduced to model the directional anisotropy observed on the seismic variables.

4.3.4 Seismic Survey of the Earthquake Event of 1 November 2022

The accelerograms recorded by 58 accelerometer stations during the earthquake on 1 November 2022 (epicentral zone about 30 km South-West from CERN) were processed to determine the directional attenuation profiles of the seismic motion in the rock formations around the CERN area. This seismic event was chosen because it is the most recent earthquake near the CERN area with the greatest intensity since the previous significant event occurred in Frangy on 29th May 1975, which consisted of a shallow main shock followed by two aftershocks [454]. The seismic variables (PGA value and arrival time) around 60 km from the TDC2/TCC2 facility were estimated at the nodes of a 1 km space grid using the recorded data from the 56 surface accelerometer stations belonging to the seismic monitoring networks of Switzerland, France and Italy (Appendix A).

4.3.4.1 SFG equation of the seismic variables

The maximum 3D-oscillation component PGAs during the earthquake of 1 November 2022 were recorded by the station with the code SAVIG. This station was found to be the closest to the epicentre of this seismic event. The oscillation component PGAs recorded by this station are 3.474 cm/sec² in the North-South direction (PGA_{NS}), 3.224 cm/sec² in the East-West direction (PGA_{EW}) and 1.541 cm/sec² vertically (PGA_{Vert}) (Figure 51 and Table 14). In particular, the CERNS station, located at 23 km North of the SAVIG station, recorded the following oscillation component PGAs: 0.865 cm/sec² in the North-South direction, 0.690 cm/sec² in the East-West direction and 0.413 cm/sec² vertically. Further considerations on the interpretation of the data recorded by the CERN underground and surface accelerometer stations are presented in Figure 56.

Table 14: Percentiles of the oscillation component PGAs in the North-South, East-West and Vertical directions recorded in the 58 station points during the earthquake of 1 November 2022 (Appendix A).

Seismic variable	Number of station points	25-th percentile	50-th percentile	90-th percentile	Maximum value
PGA_{N-S}	58	0.0818	0.1928	0.7848	3.4736
PGA_{E-W}	58	0.0799	0.2169	0.7686	3.2243
PGA_{Vert}	58	0.0609	0.1609	0.5661	1.5410

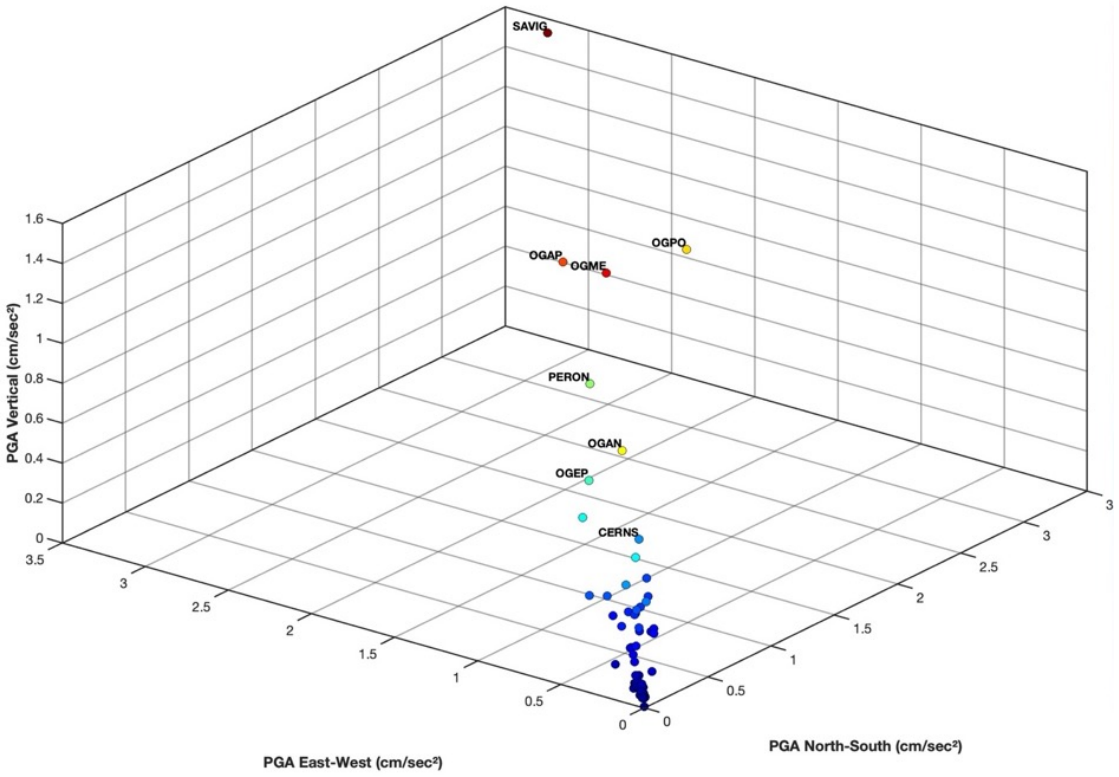

Figure 51: 3D scatter diagram of PGA North-South, East-West, and Vertical ground seismic oscillations.

The scatter plot in Figure 52 shows the damping in function of the distance from the epicentral zone for the PGA_{NS} values recorded at the station points. This graph shows a lower attenuation of the PGA_{NS} at the station points aligned in the East-West direction with an angular tolerance of ±25° compared to the station points located on the North-South direction with the same tolerance of ±25°. This anisotropic damping of the seismic ground motion between the 2 geographical directions is detectable only for distances greater than 60 km. The same damping anisotropy was detected on the two components PGA_{EW} and PGA_{Vert}.

The coordinates of the centre of the epicentral zone and the coefficients of the SFG, Equation (84), for the PGA_{NS} and PGA_{Vert} were calculated using Markov Chain Monte Carlo (MCMC) simulations to solve the following minimization problem:

$$\mathbf{C}(\mathbf{x}) = \min_{\boldsymbol{\theta}(\mathbf{x})\in\Theta}\left\{\sum [z_{PGA}(\mathbf{x}_i) - m_{PGA}(\mathbf{x}_i)]^2\right\} \tag{87}$$

where $z_{PGA}(\mathbf{x}_i)$ stands for the PGA value recorded in the station having coordinates $\mathbf{x}_i$, $\boldsymbol{\theta}(\mathbf{x})$ is the 2-component vector consisting of the anelastic damping parameter and the diagonal elements of the metric tensor matrix normalized to the value for the North-South geographical direction, and $\mathbf{C}(\mathbf{x})$ is the vector of the coefficients of the related SFG equations. Both vectors were referenced to the grid nodes' coordinates.

In particular, for each grid node (1000x1000 m^2), samples of N pairs of values for the anelastic damping parameter and of the diagonal elements of metric tensor matrix were randomly generated within a predefined range of variation. These sample pairs describe the seismic damping law around each grid node. Each sample pairs differ from the previously generated one for a small random variation. The sample pair values are accepted or rejected in the MCMC process on the basis of the Root Mean Squared Error (RMSE) calculated on the recorded data at the station points. The epicentral zone is centred on the grid node with the lowest RMSE. The SFG equations for the seismic variables are calculated for this grid node as well. The coefficients of the two SFG equations are estimated by linear regressions using the observed data from 56 surface station points (Figure 52).

The coefficients of the PGA seismic attenuation law are accepted if the Root Mean Square Error (RMSE) index, calculated on the errors committed in the station points $z_{PGA}(x_i) = z_{PGA}(x_i) - m_{PGA}(x_i)$ of the k-th sampling, is lower than the RMSE indices of all the previous samplings; otherwise the solution is rejected and the new sampling is generated starting from the last accepted sampling. Randomly, 25% of the time, the k-th sampling is still used to generate the next sampling. In each sampling of the anelastic damping coefficient and the ratio between the diagonal elements of the metric tensor the coefficients of the PGA first-guess equation are calculated using the data at the station points $z_{PGA}(x_i)$: $c_{k,PGA} = \sum_{i=1}^{n} w_{k,i}\, z_{k,PGA}(x_i)$; $k = 0, 1, 2$.

The epicentral area is centred on the grid node with the lowest RMSE index. The first-guess equation of the PGA arrival time refers to this same node and the coefficients of the equation are calculated using the data of PGA arrival time at the station points.

4.3.4.2 Cross-Validation of the UCoK Unbiased Estimator

Geostatistical estimators are poorly accurate if the number of sampled data is low and if the spatial variability depends on a complex physical phenomenon. This explains the choice of the UCoK estimator with external drift which allows to integrate the data recorded by the accelerometric stations to the SFG equations (derived from the physical model of seismic wave propagation in a material medium) for a representative prediction of the seismic motion on the ground even in areas without or with a low number of accelerometric stations. Where there are a sufficient number of accelerometric stations, the UCoK with external drift estimator performs a more accurate prediction of the seismic motion than the prediction provided by the SFG equations.

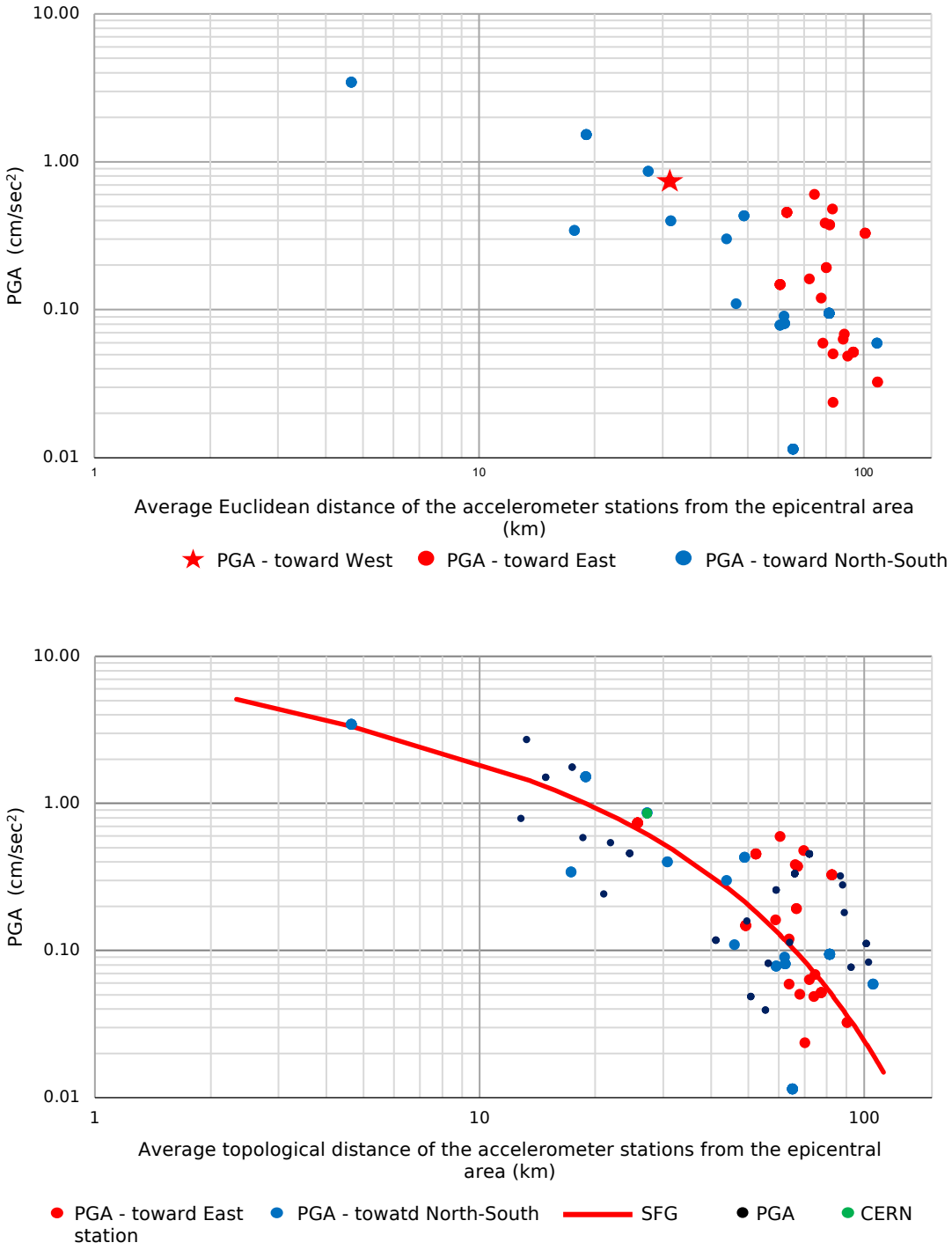

Figure 52: Earthquake of 1 November 2022 (ML=3.4) – North-South component PGA. In the graph on the up is the scatter-diagram of the PGA at the station points in the East-West direction (red dots) around epicentral zone that are mainly arranged in the upper part of the point cloud. In the East-West direction, the accelerometer stations located East of the epicentral area (±25° East) have a distance greater than 60 km, while only one station is located West of the epicentral area (red star); in the graph on the down is the same scatter-diagram with the seismic proximity distance on the horizontal axis.

UcoK estimator at any point of the investigated domain, where the seismic variable must be estimated, is given as a weighted average of the data of the PGA values and the PGA arrival times recorded at station points located in the related neighbourhood. The estimation of the weighting coefficients in Equation (80) and the variance of the estimation error of each seismic variable depend on the local variability of the ground motion, which is at its maximum near the earthquake's epicentral zone and decreases with distance.

For this reason, the experimental variogram $\gamma_{PGA}(\mathbf{h})$ was calculated using the normalized residuals of the PGAs recorded at the station points: $y'_{PGA}(\mathbf{x}) = [y_{PGA}(\mathbf{x}) - m_{PGA}(\mathbf{x})]/\sigma(\mathbf{x})$; $\gamma_{PGA}(\mathbf{h})$ was then calculated as the average of the squared difference between the pairs of station points, which were grouped by distance and direction classes; the hypothesis of local stationarity of the normalized residues was assumed [450].

The local standard deviation $\sigma_{PGA}(\mathbf{x})$ of the residuals $y_{PGA}(\mathbf{x})$ is expressed as a function of $m(\mathbf{x})$ (SFG of the PGA field): $\sigma_{PGA}(\mathbf{x}) = c_0 + c_1[1 - e^{c_2\, m_{PGA}(\mathbf{x})}]$. The three coefficients of this function were calculated by minimizing the square differences between the experimental standard deviation value around each station point and the $\sigma_{PGA}(\mathbf{x})$ value at the same point. For this purpose, the experimental standard deviations were calculated on the $y_{PGA}(\mathbf{x_1})$ values at the station points within a radius of 15 km from each station point.

In geostatistics, the functional relationship between $\sigma(\mathbf{x})$ and $m(\mathbf{x})$ is defined as a proportional effect [450], [455]. The PGA normalized residuals were used also to calculate the cross-variogram between PGA values and PGA arrival time.

The experimental variograms of the PGA normalized residuals and PGA arrival times are fitted by spherical models with a range of 25 km and 30 km, respectively. Both seismic variables present a greater variability in the East-West direction (zonal anisotropy) characterized by a continuous growth of the PGA arrival time variability between 0 and 30 km, while 70% of the PGA normalized residual variability is located near the origin of the variogram (1 km). The geographic correlation between PGA normalized residuals and PGA arrival times is 0.10 in the North-South direction and -0.10 in the East-West direction; the correlation is zero for distances greater than 15 km.

Once the coefficients of the SFG equations have been calculated and the variograms and cross-variogram of the seismic variables have been modelled, the

whole estimation process for all grid nodes can be implemented as a sequence of numerical calculations well tested in practice. The cross-validation phase of the selected estimator is carried out in order to verify the coherence between the modelling of the geographical pattern of the seismic ground motion, as described by the SFG equations and by the variogram and cross-variogram models, and the data recorded at the station points around the epicentral zone of the 1 November 2022 earthquake [3], [455].

The UCoK estimator with external drift was applied to estimate the seismic variables at all station points, without considering the data in the station point where the variables are estimated. This way the following information is available for the 56 surface station points: i) the recorded data during the seismic event; ii) the UCoK estimations; iii) the committed estimation error, calculated as the difference between estimated value and recorded data; and iv) the variance of the estimation error calculated by the UCoK estimator.

From the cross-validation results it is revealed that for the two seismic variables: i) the average of the estimation errors at the station points is close to zero; and ii) the dispersion variance of the same estimation errors is close to the average value of the estimation variances predicted by the UCoK estimator in the station points (Table 15). Figure 53 compares the estimated PGA values with the PGA recorded from the 56 station points.

Table 15: Statistical parameters of the seismic variables calculated from the recorded data, the estimate errors and the estimate variances predicted by the UCoK estimator.

Seismic variable	**Number of station points**	**Data Average**	**Data Minimum**	**Data Maximum**	**Average error**	**Variance error**	**CoKriging Variance**
$PGA_{N\text{-}S}$	56	0.4219	0.0115	3.4736	0.0195	0.1197	0.1199
$PGA_{N\text{-}S}$ Arrival Time	56	82.78	64.1	109.22	0.08	19.87	19.47

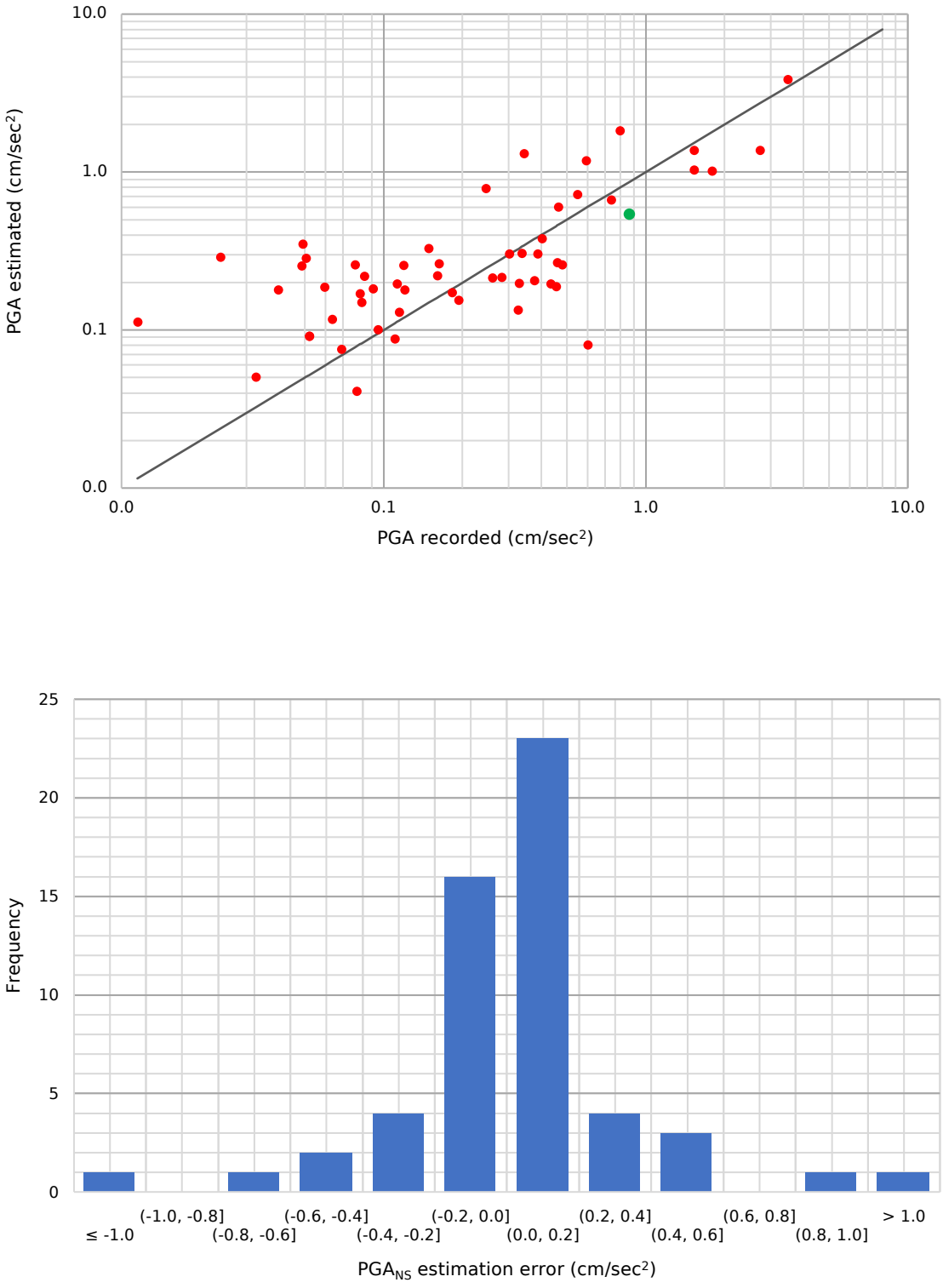

Figure 53: Earthquake of 1 November 2022 (ML=3.4) – North-South component PGA. In the graph on the up is the scatter-diagram of the estimated PGA_{NS} values at the station points versus the data recorded by the accelerometer stations. The green dot represents the PGA_{NS} estimated at the location point of the CERNS station. The graph on the down shows the histogram of the PGA_{NS} estimation errors in the 56 station points, from which it is visible how the UCoK estimator be unbiased as the error distribution mean tends to zero and the shape is symmetrical.

4.3.4.3 Damping PGA Profiles' Modelling

The seismic variables of the ground motion were reconstructed around the epicentral area of the earthquake of 1 November 2022. The PGA values and the respective arrival time of the two oscillation components were estimated at the nodes of a 1 km space grid using the UCoK estimator.

A dynamic search algorithm was used to select the stations in the estimation neighbourhood of each grid node. Such an algorithm selects the two closest stations for each of the 8 circular sectors of 45° angular width and centred in the node to be estimated. If there is no data in more contiguous circular sectors, the algorithm increases the data of the other circular sectors, searching the nearest station to the first selected pair of stations. A grid node is not estimated if it does not have at least 6 stations in the node neighbourhood. Figure 54 shows the PGA_{NS} map around the epicentral zone of the earthquake of 1 November 2022.

The estimated PGA at the grid nodes were used to plot the directional PGA damping profiles in function of the epicentral distance towards the East (0° East), North (90° East), West (180° East) and South (270° East). The directional damping profiles were discretized into 2.5 km steps and the PGA value assigned to each step was calculated as the arithmetic means of the PGA values of the grid nodes inside the circular crowns having 2.5 km length and angular width ± 22.5° with respect to the profile direction (Figure 54).

4.3.5 Seismic Hazard Curve at the Location of the TDC2/TCC2 Facility

As mentioned, the level of seismicity of the territory is not uniform in the various sectors around the CERN area. The probability of occurrence of earthquakes with an epicentral PGA greater than 100 cm/sec^2 in the South to East sector (approximately 5000 km^2) is 4.3 time higher than the probability of occurrence of earthquakes of the same intensity level located in the Northern zone from East to South-West of the CERN area (8200 km^2). This result has suggested to concentrate focusing the investigation for modelling the corresponding seismic hazard curve for the 135° circular sector between South-West and East directions (Figure 50).

The seismic propensity of a given identified area, or more accurately, the seismicity observed within a specific time and shaped located area, can be estimated as the average number of earthquakes expected annually. This is

referred to as the seismic hazard rate for the corresponding territory, expressed as a yearly and area unit.

Instead, the seismic hazard functions at a target point describe the azimuthal perceived ground actions (e.g. PGA), originating from the directional propagation azimuths corresponding to different epicentral location and distances. The epicentral PGA value and the relative distance from the target points of the same facility influence different damping profile models.

Geostructural features refer to faults that generate earthquakes and act as barriers to wave propagation, while lithological features relate to material characteristics, specifically impedance strength, which affects resistance to wave propagation through different rock layers. Together, these geostructural faults and lithological features significantly influence the azimuthal characterization, through the damping effect, of hazard functions at well-identified target points. The crowns and cloves methodology allows for the inclusion of these different azimuthal damping profiles, including limit distances for perceivability for a given azimuth. The limit distance helps define the seismic hazard rate/Poisson parameter of each crown/clove, which varies based on the number of square kilometres within the crown's area, thereby impacting the value of λ. This variation in λ affects the probability of perceived values at the target point and, consequently, the location of the corresponding hazard curve.

It is incorrect to calculate the perceived value without considering the different damping profiles associated with azimuths. Thus, averaging the damping effect based on a typical damping profile is a physical error because it is not additive. In contrast, seismicity is additive; if separate calculations of λ are performed, the result aligns with the average value over 360 degrees. From a seismicity perspective, the rate of all crowns together equals the sum of the different λ values for each crown. When counting the number of earthquakes over 360 degrees, they are the same. However, if earthquakes are subdivided into 6 or 8 crowns, different λ values emerge. The total λ is merely the sum of the λ values for each crown because it is additive.

The problem arises because damping profiles differ, so the perceived values of acceleration vary across different crowns. A weighted average with damping effects must be used, which renders the approach of averaging damping effects from a simple average incorrect. The average value of the damping gradient is not linear; thus, damping cannot be averaged first before calculating perceived values. Instead, perceived acceleration should be calculated crown by crown

separately, and afterward, the hazard curve can be calculated considering the different perceived values, each with a different probability depending on the limit length and distance of each crown.

Guiding the concept from the physical phenomenon, there are two primary phases: the first phase is the seismic generation at the hypocentre, which depends on faults, and the second phase is the propagation of seismic waves, which is influenced by the material of rocks, types of layering, and discontinuities, and is characterized as damping. The hazard model function includes both the probability of the genesis of the phenomenon at the first phase and deterministic damping during the second phase, coupled with the probabilistic occurrence of earthquakes. Initially, the earthquake is generated at the hypocentre, and subsequently, the seismic waves travel along the Earth as volume waves and on the surface as surface waves.

The PGA damped models for the events belonging to the 7 seismic intensity ranges (Table 13) were drawn up by rescaling the PGA damping profile in the North direction of the seismic event of 1 November 2022 (epicentral PGA equal to 4.7 cm/sec^2) (Figure 55). The 7 damped models discretize the territory into concentric circular crowns of width 2.5 km (Figure 56) and a seismic event in a circular crown generates at the TDC2/TCC2 facility an acceleration equal to the PGA of the damping model crown of the event intensity range. Assuming a constant seismic hazard rate in the South to East cloves (5000 km^2), the probability that the TDC2/TCC2 facility perceives a PGA greater than the threshold value (PGA_k) is proportional to the sum of the areas of the circular crowns whose damped PGA is greater than or equal to the threshold value. Then, the probability that an earthquake of seismic intensity E_i, of the seismic intensity range shown in Table 13 , will cause at the target point a peak acceleration greater than PGA_k is (Figure 55):

$$P\left(E_i, PGA_k\right) = \frac{a(E_i, PGA_k)}{A} P(E_i) \tag{88}$$

where $a(E_i, PGA_k)$ is the sum of the areas of the circular crowns with damped ground acceleration greater than PGA_k generated by a seismic event of intensity in the range E_i, A is the area of the South-West to East cloves (5000 km^2) and $P(E_i)$ is the probability that one or more seismic events of intensity in the range E_i occur in the area A in a year: $P(E_i)=1/T_{rp},(E_i)$, where $T_{rp}(E_i)$ is the return period of seismic events of intensity in the range E_i.

The probability of the seismic scenario PGA_k is obtained as the sum of the probabilities of perceiving accelerations greater than or equal to PGA_k at the target point (Equation (88) for any earthquake with seismic intensity epicentral acceleration (Table 13) greater than or equal to PGA_k.

The variances of the estimation error of the PGA values at the grid nodes, predicted by the UCoK estimator, were used to calculate the variation range of the PGA damping profiles. The seismic hazard curves were then drawn by repeating the calculation of $P(PGA_k)$ first with the minimum PGA damping profile and then with the maximum one (Figure 55b).

From the seismic hazard curves shown in Figure 55b, the PGA values for return period of 475 years and 975 years have been identified, as they are used in design of structures respectively for the life-safety and collapse limit states [38], which are used to determine seismic actions for design and dynamic stability verification of buildings and infrastructures. Specifically, at the point in correspondence of TDC2/TCC2 facility, the PGA values for return periods of 475 years and 975 years are respectively 185 cm/sec^2 (confidence range from 113 to 224 cm/sec^2) and 248 cm/sec^2 (confidence range from 203 to 313 cm/sec^2), respectively.

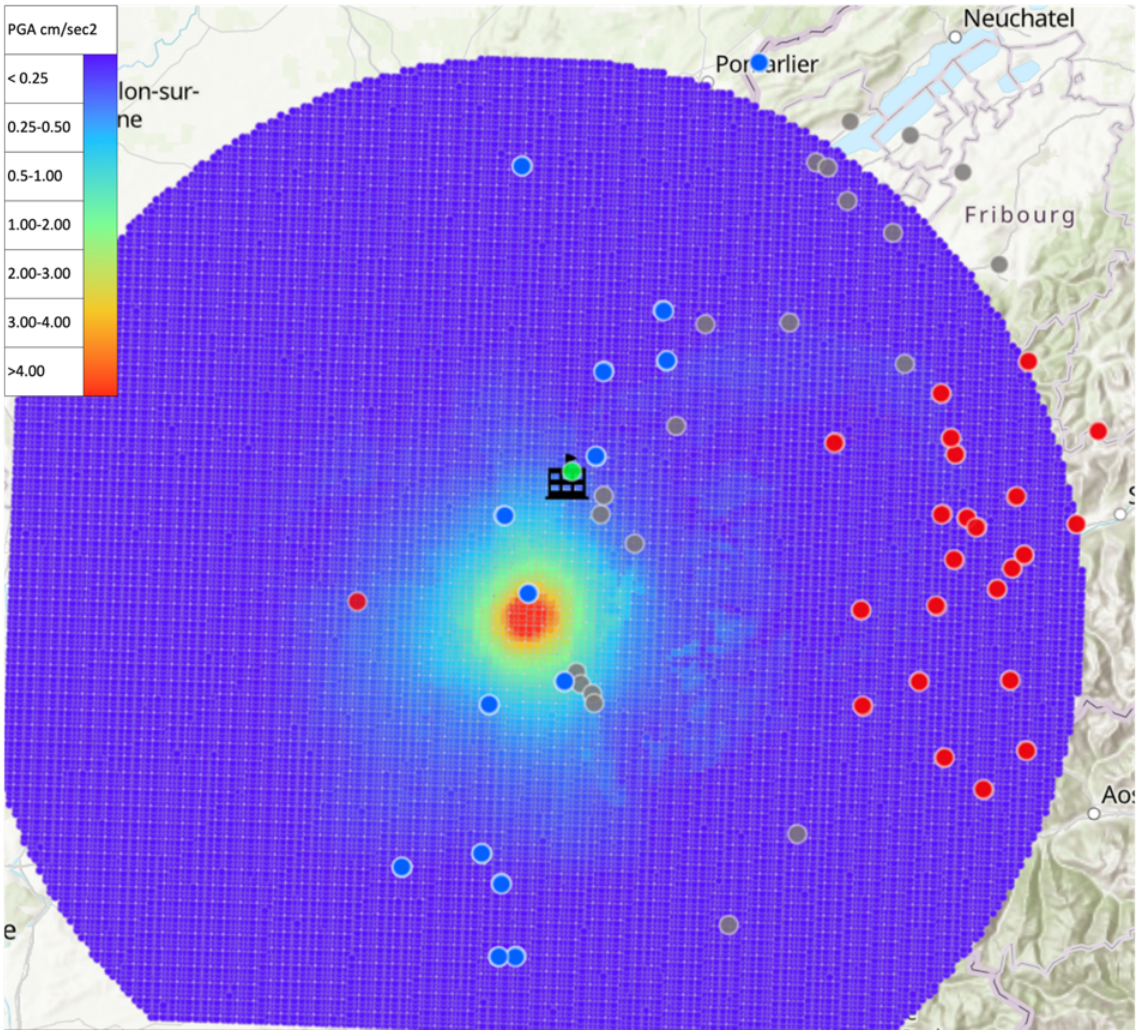

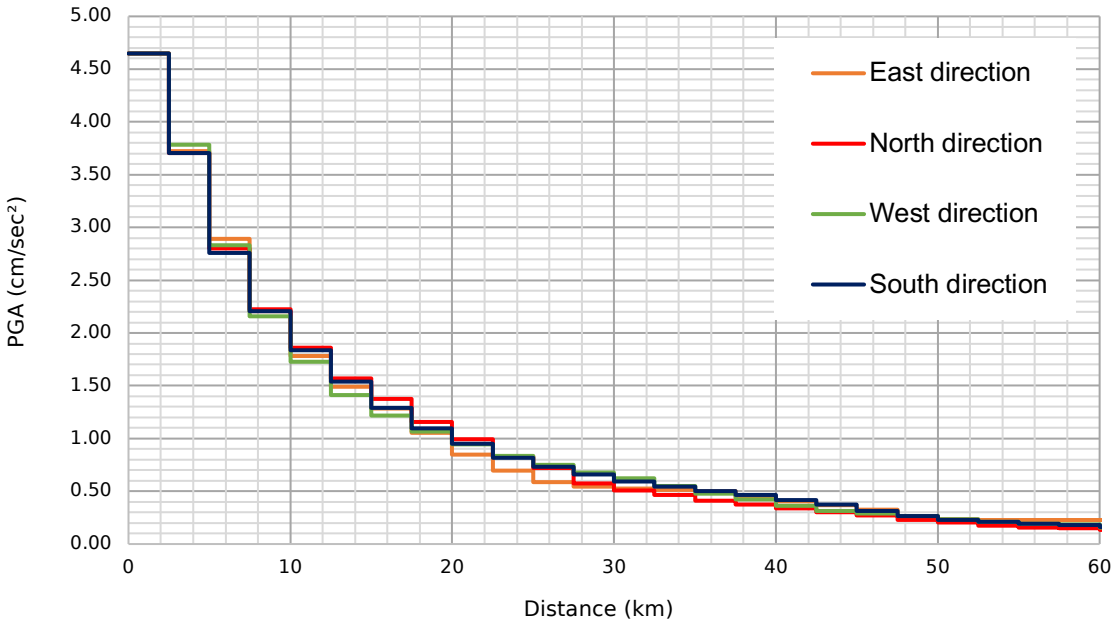

Figure 54: The map on the up represents the areal damping pattern of the PGA North-South component of the 1 November 2022 earthquake reconstructed at the nodes of a 1-km space grid. The estimated values of the PGA at the grid nodes are everywhere

consistent with the physical theory of propagation of the oscillatory movement in a homogeneous medium with radial anisotropy, as described by the SFG. Locally, the seismic data recorded at the station points, containing information on the lithological heterogeneity of the rocks, return a PGA value more consistent with the local lithological and mechanical characteristics of the subsoil (seismic micromodelling zoning). The UCoK estimator made it possible to integrate the physical damping law of seismic motion and the sampled seismic data, returning a spatial model of the PGA. The PGA values given by such a spatial model are consistent with a rock model whose lithological characteristics are a spatial average of those related to the real rock volumes crossed from seismic waves, that converge to the most representative values where the data are present. These are the zones in which the variance of the estimation error is lower. The graph on the down shows the PGA damping profiles of the PGA North-South oscillation component, according to the four main propagation directions, in function of the epicentral distance, for each geographical direction.

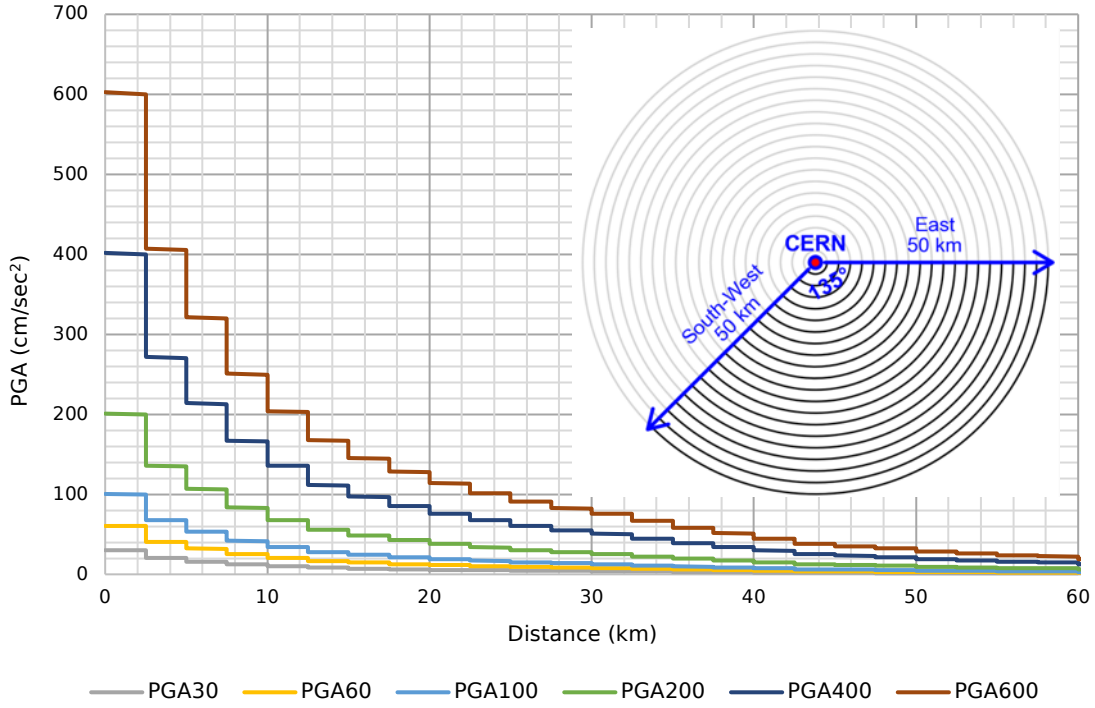

a)

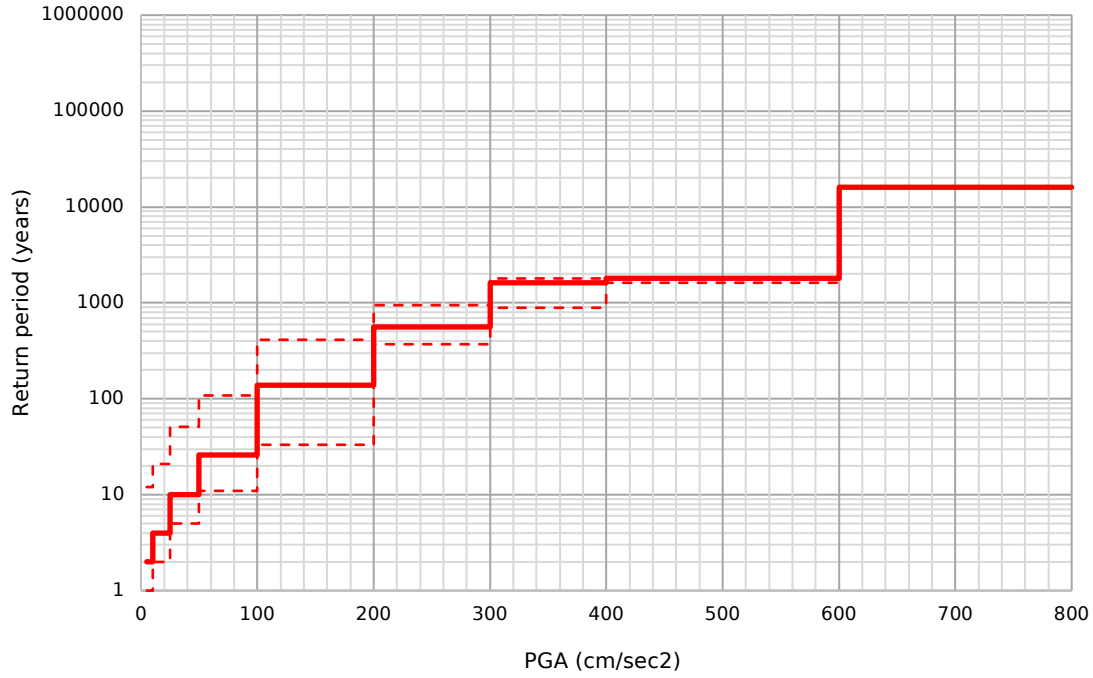

b)

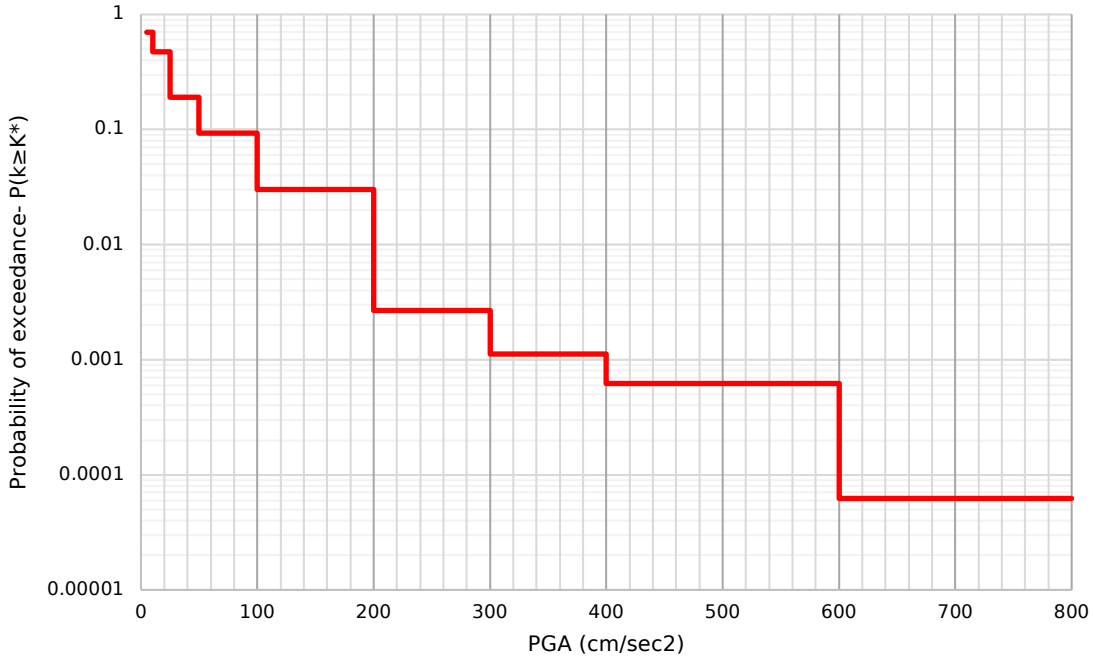

c)

Figure 55: a) PGA Damping Profiles Models for the North-South oscillation component in function of the epicentral distance. The Models are staircase-type curves where the runs of each step describe circular crowns of 2.5 km width at various distances from the centre (CERN point). In the vertical axis are the values of PGA in the epicentral area, ranged from 30 to 600 cm/sec^2. b) Seismic hazard curve at the TDC2/TCC2 facility for earthquakes in the South-West to East sector. The graph also shows the range of variation due to the PGA estimation error. c) Seismic hazard curve showing the

probability of exceeding specific ground accelerations for earthquakes in the South-West to East sector (clove).

Different hazard curves from various crowns, when associated with distinct damping profiles, cannot be averaged. Instead, they must be presented and utilized separately. Although risks can be cumulated because the events are mutually exclusive, the probability of the union is the sum of the probabilities of each event that shares the same perceived value. However, the same perceived value corresponds to different distances from the target points across different crowns due to the damping effect. The risk is a union of events with the same perceived acceleration. Probabilities can be summed, but these must be events with the same perceived values, albeit not the same epicentral distances nor the same damping effects.

The perceived acceleration depends on three factors: acceleration at the epicentre, the distance of the crown from the target points, and the perceived value itself. The distance influences the probability since it determines the area of the crown, which in turn propagates to the probability. Therefore, the probability depends on the distance, and the damping effect also varies by distance but differs for each crown. The aforementioned crowns, positioned at the same distance but belonging to different cloves with distinct damping profiles, produce different perceived values while maintaining the same probabilities.

Due to these variations, hazards must be assessed separately for each crown. At the conclusion of the analysis, the same perceived values can be summed up despite differing probabilities, allowing for the creation of a unique hazard curve that considers each crown separately. This methodology reveals different hazards for crowns and enables the summation of probabilities for all events that share the same perceived values.

Furthermore, it is important to calculate these aspects separately and to highlight the crown with the maximum contribution in terms of propagation direction. This is particularly important from a structural perspective if the structure is not isotropic and possesses a non-circular symmetry, such as the elongated structures at CERN. Different geometries in structural constraints affect propagation differently. For instance, if propagation originates from the south and the structure is oriented in a specific manner, the impact will differ from that of the same intensity but from an orthogonal propagation direction. Our methodology provides this information and can also be valuable for structural analysis because the geometry of the structure influences the stress according to

the propagation direction, which is a significant factor in the type of stress experienced. These factors should also be considered for further structural analysis.

4.3.6 Further Considerations on the Interpretation of the Data Recorded by the CERN Underground and Surface Accelerometer Stations

The dynamic ground motion seismic variables in the epicentral zone are quasi-stationary without precise and detectable location definition; the ground motion generate new types of seismic waves, such as the surface waves, which propagate radially only in the most superficial layers of the geostratigraphic system. Out of the epicentral zone, the ground seismic motion is the combination of the vibrational movements related to the surface waves and the vibrational movements related to the volume ones rising from the deeper layers of the geo-stratigraphic configuration. Moving away from the epicentral zone i) the amplitudes of the surface waves become predominant compared to the amplitude of the longitudinal (P) and transversal (S) volume waves, and ii) the ground motion tends to dampen.

The experimental evidence offered by the accelerograms recorded by the 5 surface stations (SAVIG, PERON, CERNS, COLLE and LADOL, as named in the Swiss accelerometer network) and the 2 underground stations of CERN (i.e., CERN1 and CERN5) aligned in the 75° East direction, from SAVIG station (epicentral distance 4.66 km) to LADOL station (epicentral distance 46.62 km), during the 1 November 2022 earthquake, shows (Figure 56):

- the linear dependence on the distance from the epicentral zone of both the onset time of the ground motion, generated by the volume waves rising from the deeper layers of the geo-stratigraphic configuration (P and S waves), and the PGA arrival time generated by the surface waves (Rayleigh and Love waves),
- the presence of an increase in the acceleration of the seismic motion recorded by the CERN5 underground station about 5 seconds after the arrival time of the volume waves respect to the accelerogram of the CERN1 underground station, which is closest to the epicentral area of about 8.33 km. This second movement is probably generated by the propagation phenomena of wall waves in the LHC tunnel,

- the perfect match of the PGA values recorded by the 5 surface stations with the geometric attenuation law of surface waves, which are inversely proportional to the square root of the distance from the epicentral zone,
- the perfect match of the acceleration peaks in the first second of the seismic motion recorded by the underground stations CERN1 (83.7 m depth) and CERN5 (90.2 m depth) with the geometric attenuation law of volume waves, which appear as inversely proportional to the distance from the hypocentral zone,
- the acceleration peak (0.1193 cm/sec^2) recorded by the CERN1 underground station in the first second of the seismic motion is the maximum of the entire recording. A similar acceleration value (0.1122 cm/sec^2) was recorded by the CERN1 station about 5 seconds after the first peak. On the contrary, the acceleration peaks recorded by the CERNS surface station and the CERN5 underground station are respectively 0.8650 cm/sec^2 and 0.2483 cm/sec^2 and are greater than the accelerations recorded during the first second of the seismic motion, as shown in Table 16. These maximum values of the accelerogram have a delay of about 5 seconds from the acceleration peak recorded during the first second of seismic motion. The order of recording of the above mentioned acceleration peaks suggests that: i) the seismic motion recorded by the CERN1 station can be due only to the volume waves while ii) the acceleration peaks recorded in the other two CERN stations can be attributed to the seismic motion generated by waves, as triggered by volume waves respectively in the surface layer of the geo-stratigraphic configuration and in the rocks around the LHC tunnel,
- the perfect matches between the peak acceleration values recorded by the 3 CERN stations during the first second of the seismic motion and the damping law of the volume waves and between the PGA values recorded by the 5 surface stations and the damping law of the surface waves demonstrate that i) the damping law of the volume waves is not representative of the PGA geographical pattern around the epicentral zone and ii) the PGA values recorded by the surface stations cannot be referred to the deep rock formations (bed-rock).

Table 16: Seismic data referred to the stations aligned in the 75° East direction, from SAVIG station (epicentral distance 4.66 km) to LADOL station (epicentral distance 46.62 km), in occasion of the 1 November 2022 earthquake.

Station Code	Elevation	Epicentral distance	Direction	Onset time of the seismic motion	Peak acceleration in first second	Speed between pairs of stations	PGA arrival time	PGA	Speed between pairs of stations	PGA damping compared to epicentral PGA
	(m)	(km)	°East	(sec)	(cm/sec^2)	(km/sec)	(sec)	(cm/sec^2)	(km/sec)	(%)
SAVIG	529	4.6603	89.3	61.93	1.4645		64.105	3.4736		73.91
PERON	708	18.9876	103.7	63.205	0.776	11.24	66.345	1.5262	6.40	32.47
CERNS	463	27.5897	73.00	65.268	0.1539	4.17	69.956	0.865	2.38	18.40
COLLE	447	31.578	66.9	65.96	0.201	5.76	71.215	0.4013	3.17	8.54
LADOL	1455	46.6157	72.8	68.66	0.026	5.57	80.595	0.1105	1.60	2.35
CERN1	356	24.03	73.00	64.70	0.1193		65.376	0.1193		
CERN5	418	32.36	73.00	65.88	0.0873	7.06	71.208	0.2483	1.43	

a)

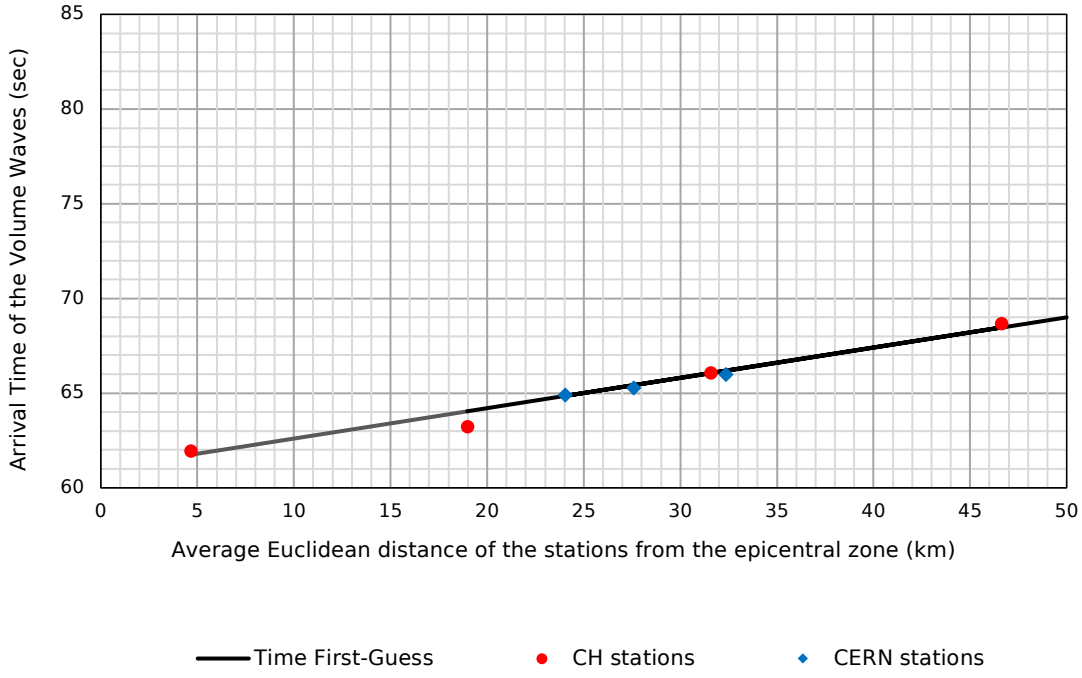

b)

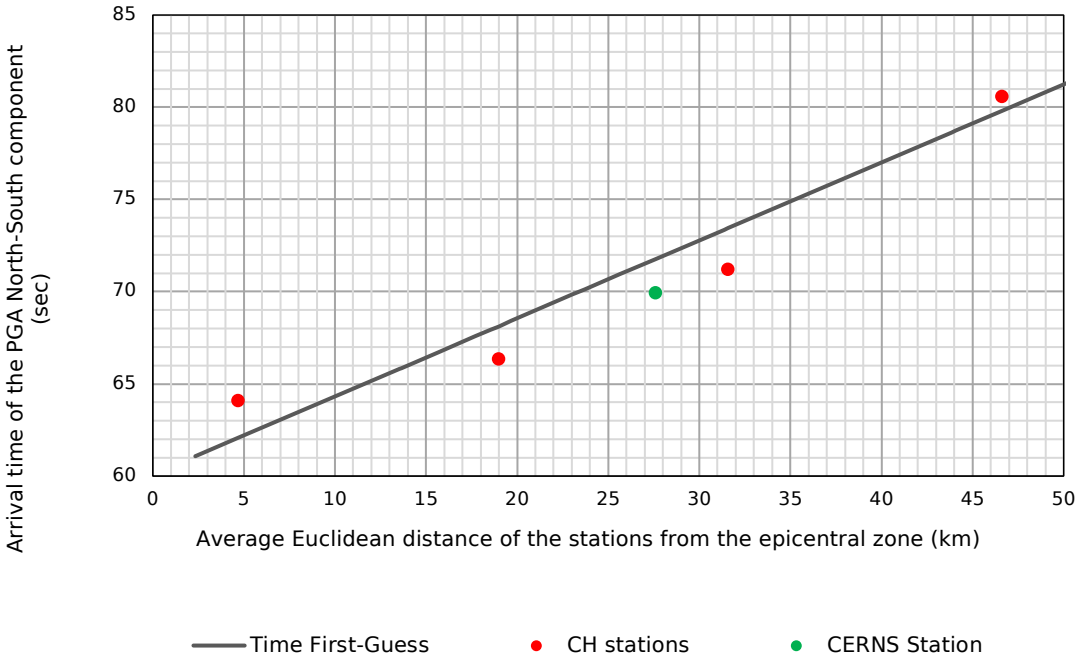
Arrival time of the PGA North-South component (sec)
85
80
75
70
65
60
0
5
10
15
20
25
30
35
40
45
50
Average Euclidean distance of the stations from the epicentral zone (km)
Time First-Guess
CH stations
CERNS Station

c)

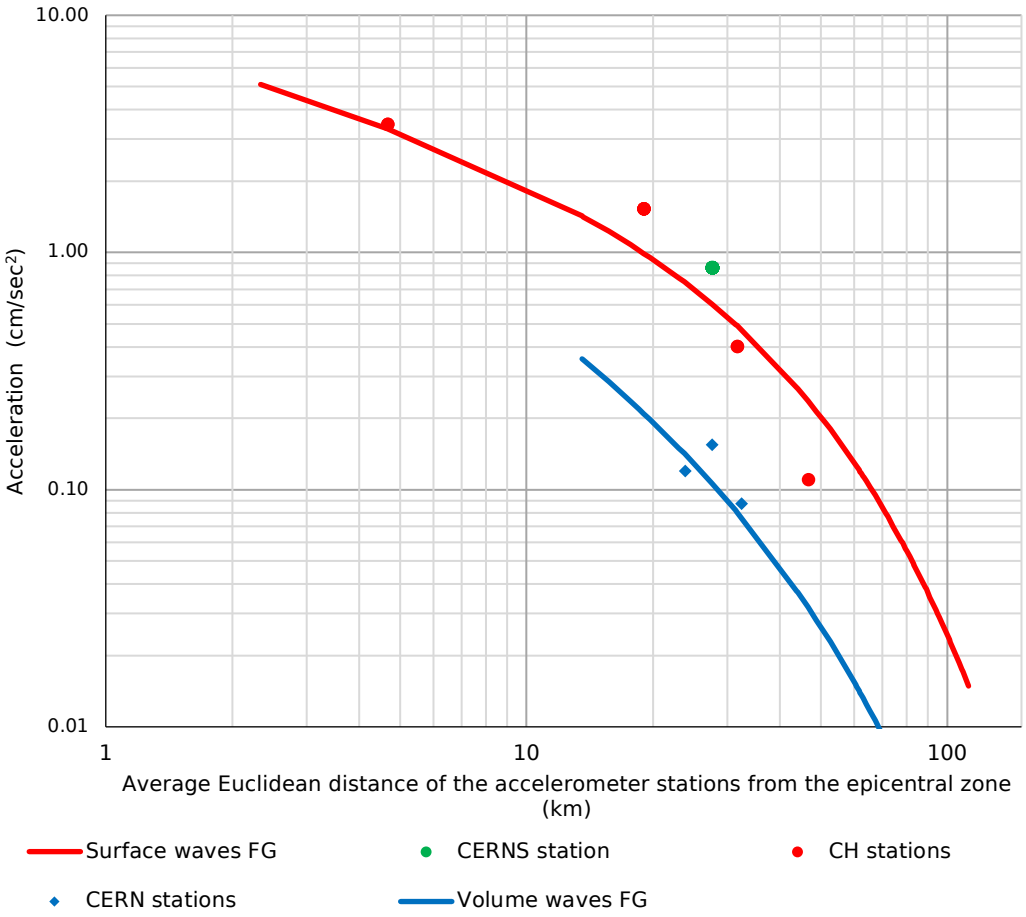
Acceleration (cm/sec²)
10.00
1.00
0.10
0.01
1
10
100
Average Euclidean distance of the accelerometer stations from the epicentral zone (km)
Surface waves FG
CERNS station
CH stations
CERN stations
Volume waves FG

d)

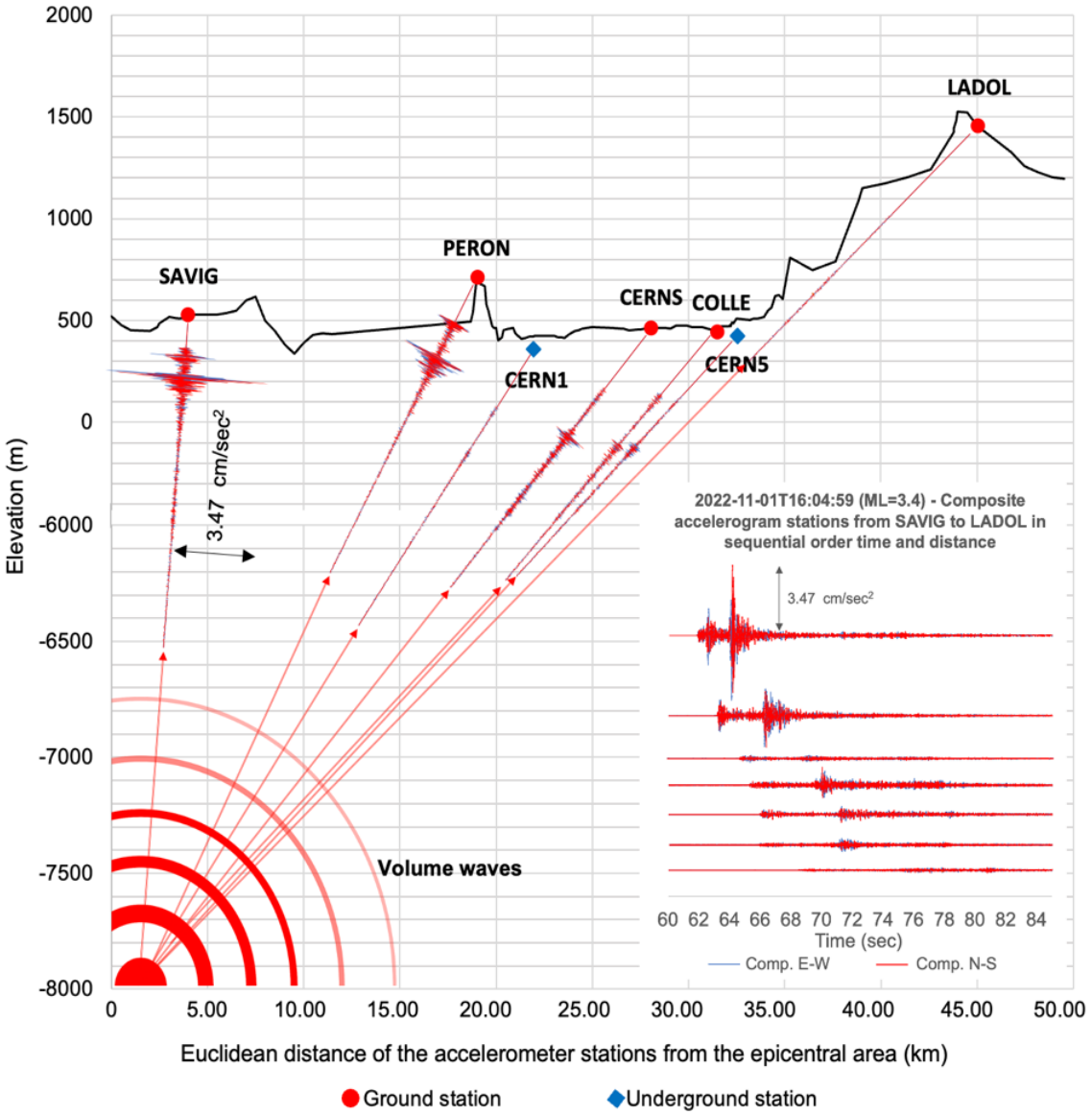

Figure 56: Plots of the seismic data referred to 7 stations aligned in the 75° East direction, from SAVIG to LADOL station, in occasion of the 1 November 2022 earthquake: Function of the distance from the epicentral zone for the a) arrival time of the volume waves, b) arrival time of the PGA North-South component, and c) North-South component of the maximum acceleration of the sole volume waves recorded in the first second in CERN stations (blue) and the PGA recorded in surface stations (red). d) Ground vertical section indicating the recorded accelerograms.

The study highlights how the use of geostatistical estimated seismic variables at grid points does properly and effectively represent the seismic phenomena, across the entire geographical domain, considering the use for engineering purposes, namely the damping and point hazard curve characterization. The local information data lack is compensated by assuming the SFG as a physical

model representing elastic and anelastic damping in the rocks. Such a compensation is also quantified in the modelling of the related variogram and the cross-variogram. The variogram and cross-variogram models characterize the type of geographical continuity of the seismic variables presented herein in 2-dimensions and then adding a third dimension by considering the PGA arrival time also. The observed data have supported the identification of a physical model and representativeness of the variograms and cross-variogram models for taking into account the geological conditions including discontinuities, heterogeneities and anisotropies.

The UCoK estimator has been applied taking advantage from the recorded data by the seismic stations around each node of a 1 km space grid providing, together with the seismic variable estimated values, the indicator of accuracy of the estimation itself (UCoK standard deviation of the estimation errors). The above estimated values have been cross-validated at the point of the accelerometric stations where both the recorded data and estimated ones are available. The results of the above cross-validation procedure have been reasonably satisfactory and then the presented seismic hazard curve obtained at the point in correspondence of CERN TDC2/TCC2 facility can be considered with a high level of confidence.

As a future development, the use of the data recorded in the underground stations of CERN will permit to have a better understanding of the phenomena tied to the wall wave propagation in the CERN Large Hadron Collider (LHC) circular tunnel. Indeed, the accelerograms recorded in such underground stations show an increase of the acceleration in proximity of the points farer from the epicentral zone [3].

In the analysis, the focus was on calculating the probability of events within three of the eight circular cloves (sectors) around the TCC2/TDC2 caverns, ranging from the South-West to the East. For future analyses, new seismic surveys should include all cloves of territory surrounding the target site.

To the South and South-East of CERN, an active fault system has generated numerous seismic events with magnitudes greater than 5 over the last 300 years. These fault systems are absent to the North of CERN, which explains the lower seismicity and the absence of magnitude 5 or higher seismic events in the same period. An additional factor influencing seismic risk is the location of an earthquake's epicentre and the anisotropic directional damping of seismic

motion, which is affected by the heterogeneity of rock formations. This directional damping effect was observed in ground motion data recorded by accelerometer stations during two recent earthquakes near CERN: the 2022 earthquake of magnitude 3.4 to the South and the 2019 earthquake of magnitude 4.0 to the East.

In the approach to calculating seismic hazard, the area surrounding CERN is divided into cloves (sectoral divisions) and crowns (concentric circular areas). The North azimuth is set to zero, with cloves spaced at 45-degree intervals. The crowns represent circular areas within each clove and are distinguished by their distance from the centre. Each crown covers an area measured in square kilometres, with the area increasing as the distance from the centre grows.

Consequently, the probability is proportional to the area, meaning that the probability of an earthquake occurring in the most peripheral crowns is higher due to the greater surface area of the circular crown, but the intensity of the seismic motion perceived by the site is lower.

The damping effect is different in each azimuthal clove due to the anisotropic damping of seismic motion detected in the around of the CERN area. Therefore, it is not correct to use the average damping curve of the azimuthal cloves around the target site to calculate the seismic hazard of the site. It is necessary to calculate separately the seismic hazard for the seismic events that fall in each clove, thus obtaining the probability of the acceleration value perceived by the target site and then add the probabilities (sum of the probabilities of mutually incompatible events). Otherwise, one would use an average damping curve that is not representative of any clove. The average damping curve is only an arithmetic concept, not a physical reality, and it is a mistake to use it as a physical characteristic of rock formations.

Therefore, to calculate the probability of the perceived value, each clove's attenuation must be assessed separately. Only after this can the hazards be combined, as the probabilities of mutually exclusive events can be summed. This combined sum provides the perceived value according to the hazard curve calculation procedure. It is essential, however, to sum probabilities rather than attenuations, since attenuations differ based on epicentral values even though they lead to the same perceived value at CERN.

For example, the perceived value in clove South-West (5) differs from the epicentral value in clove South-East (4) (Figure 50); however, we can still sum the

probabilities for the same perceived value. This is because different damping effects produce different accelerations at varying distances, resulting in the same perceived value at the CERN point due to the physics of seismic wave propagation.

The exceedance probability of seismic acceleration thresholds is not equal in all cloves around CERN's TCC2/TDC2 caverns because each clove has an own seismicity profile and damping characteristics. For each perceived acceleration threshold, the exceedance probability (seismic hazard curve) is obtained by summing the exceedance probabilities across each clove for that same threshold at the target site.

Building on the seismic data, the subsequent subchapter (4.4) examined how the TCC2/TDC2 caverns' structures, particularly the blocks in the TCC2 cavern, responded to seismic forces as indicated by the seismic hazard curves. This analysis focused on:

- **Structural Vulnerability**: Assessing the integrity of the caverns and identifying weak points susceptible to seismic forces.
- **Response Modelling**: Using PGA data, the analysis simulated structural responses during seismic events, which clarified the potential damage scenarios within the TCC2/TDC2 caverns.

Throughout this analysis, the interplay between seismic exposure and structural response was explored, particularly how structural failures could lead to secondary hazards like fires.

4.4 Structural Analyses

Natural disasters, particularly earthquakes, pose significant risks to both structural integrity and safety due to the potential for cascading failures. One critical aspect of such disasters is the probability of structural collapse and the subsequent risk of fire induced by these collapses. This analysis aims to provide a probabilistic framework for assessing these risks, focusing on structural collapse and fire induction in the event of an earthquake.

In the multi-hazard risk assessment for the TCC2 caverns at CERN, seismic hazard analysis serves as the foundational step. By determining the probability distribution of seismic events through PGA values, this analysis provides critical input for subsequent structural collapse assessments. The seismic hazard curve

informs the IDA and the development of fragility functions, enabling a data-driven approach to quantify failure risks at various seismic intensities.

To analyse the mechanical behaviour of the structures, IDA conducted by CERN, was utilised to simulate the dynamic response of concrete blocks used for shielding against ionizing radiation. CERN developed discrete-element models (DEM) such as LMGC90 and LS-DEM to overcome the impracticality of large-scale shake table testing for complex structures [456]. Simplified block configurations were tested and benchmarked against these models. By incrementally scaling the PGA values, the structure was pushed through elastic instability until it reached global dynamic instability and collapsed, helping to identify the critical thresholds for structural failure. To evaluate failure mechanisms, this study adopts a local, block-by-block displacement criterion. This choice allows for early detection of instability at individual block interfaces and reflects the complexity of discrete block assemblies like TCC2.

Following the seismic analysis and structural assessments, the concrete blocks were subjected to a fire scenario, introduced as a secondary risk triggered by earthquake-induced structural collapse. This multi-hazard approach highlights the cascading risks where structural collapse could lead to fire, demonstrating the need for a probabilistic assessment to fully understand the probability and consequences of these combined hazards.

4.4.1 Experimental Campaigns and Shaking Table Tests

In 2019, CERN conducted a significant experimental campaign at the Eucentre Foundation in Italy [457], [458], [459], [460]. This campaign involved seismic tests on four different concrete block configurations, designed to investigate their dynamic response under seismic excitation. These experiments aimed to:

1. **Capture Sliding and Rocking Dynamics**: Block sliding and rocking are critical failure modes during seismic events. The experiments were designed to measure these dynamics as blocks moved under varying seismic excitations.
2. **Evaluate Frictional Contact Behaviour**: The friction between concrete-concrete and steel-concrete interfaces plays a significant role in the stability of block structures. By varying these interfaces, the experiments aimed to understand how different friction coefficients influence seismic performance.

3. **Observe Displacement and Block Interaction**: Displacement data was gathered to observe how individual blocks moved relative to each other, especially at the points of contact.

The experimental setup consisted of precast concrete blocks, the primary materials used for shielding are precast concrete blocks, with occasional use of steel and lead at CERN. These concrete blocks, the most commonly used, measure 2.40 x 1.60 x 0.80 metres and weigh 77 kN. They have been designed in compliance with EN 206-1 and Eurocode 2 standards. Notably, these blocks have been designed to meet specific characteristics, including a concrete quality of C40/50 and an exposure class of XC4-XD3-XF3. The design also includes a maximum aggregate diameter of 32 mm, a chloride content of 0.20%, and the use of metallic formwork type IV. With edge chamfers of 2 cm and reinforced with steel grade B500B, these blocks have been configured to meet the diverse requirements of installations across CERN sites, including the TCC2 facility.

Each block configuration was tested under several seismic scenarios, allowing to observe the sliding and rocking mechanisms between the blocks. The data collected included:

- **Relative Displacements**: The movement of blocks relative to each other was tracked using high-precision measurement instruments.
- **Contact Forces**: Sensors placed at key contact points measured the forces between blocks during seismic excitation.
- **Rotational Movements**: Rotational effects caused by rocking behaviour were monitored, as they can contribute significantly to overall block displacement during seismic events.

The seismic tests revealed several important characteristics about the dynamic behaviour of concrete blocks under seismic loads:

1. **Sliding Dominated at Lower Friction Values**: In tests where friction coefficients between the concrete blocks were reduced, sliding dominated the block movement. This confirmed that lower friction interfaces are more prone to failure during seismic events.
2. **Rocking Increased with Higher Friction**: As the friction coefficient between blocks increased, rocking became the dominant form of movement. The blocks tended to pivot around the contact points, with less sliding.

3. **Displacement Patterns**: The experiments showed a clear correlation between the intensity of seismic excitation and the magnitude of displacement. Blocks subjected to higher-intensity earthquakes exhibited greater displacements, indicating increased instability.
4. **Non-Linear Contact Dynamics**: The contact behaviour between blocks was non-linear, with larger displacements at higher excitation levels.

4.4.2 Model Calibration

The results from these full-scale tests provided the necessary empirical data to calibrate the numerical models. Specifically, the calibration process involved tuning input variables for the discrete-element models such as:

- **Friction Coefficients**: Friction values between concrete-concrete, steel-concrete, and steel-steel interfaces were adjusted to match the experimental results.
- **Material Densities**: The concrete density was modified based on the physical properties of the tested blocks.
- **Moduli of Elasticity**: The stiffness of the blocks was fine-tuned to reflect the observed behaviour under seismic excitation.

Based on the test results, both LS-DEM and LMGC90 were employed to simulate block behaviour under seismic conditions, with LS-DEM focusing on deformable systems and LMGC90 on rigid block systems.

The LMGC90, developed at the University of Montpellier, is designed to simulate non-smooth contact dynamics (NSCD), making it suitable for modelling the rigid blocks used at CERN. The calibration of the LMGC90 model involved a semi-probabilistic approach. Geometrical variables were treated as deterministic, while mechanical variables, which inherently show variability as outlined earlier such as friction coefficients for concrete-concrete and concrete-steel contacts, were treated as random and described by log-normal distributions based on the variability documented in technical literature. Table 17 below presents the key distribution models and calibrated parameters for the mechanical properties used in LMGC90 simulations. A Correlation Controlled Latin Hypercube Sampling (LHS) technique was chosen for sampling the mechanical variables' distributions. LHS was used because of its efficiency and precision when handling small sample sizes. In the preliminary analysis, it was observed that 20 samples were sufficient to achieve an appropriate level of accuracy in calibrating the model. The calibration process involved adjusting the distribution

parameters of the mechanical variables, such as mean, standard deviation (SD), and coefficient of variation (C.o.V.), to ensure that the numerical model's predicted maximum and minimum block displacements closely matched the experimental data from the four tested configurations.

The distribution of samples obtained through the LHS method for these mechanical properties is shown in Figure 57, demonstrating the LHS technique's efficiency in generating statistically representative samples with minimal computational effort.

Table 17: Model variables' distributions and related parameters obtained after the calibration process [459].

Variable	**Distribution Model**	**Mean**	**SD**	**C.o.V.**
Friction Concrete/Concrete [-]	Log-normal	0.75	0.075	0.1
Friction Concrete/Foundation [-]	Log-normal	0.75	0.075	0.1
Friction Steel/Concrete [-]	Log-normal	0.3	0.03	0.1
Concrete Density [kg/m³]	Log-normal	2400	96	0.04
Concrete Young's Modulus [Pa]	Log-normal	3.45E+10	5.175E+09	0.15
Concrete Viscous Modulus [Pa]	Log-normal	1.5E+08	2.25E+07	0.15
Steel Density [kg/m³]	Log-normal	7700	77	0.01
Steel Young's Modulus [Pa]	Log-normal	0.21E+12	6.3E+09	0.03
Steel Viscous Modulus [Pa]	Log-normal	0.21E+10	6.3E+07	0.03

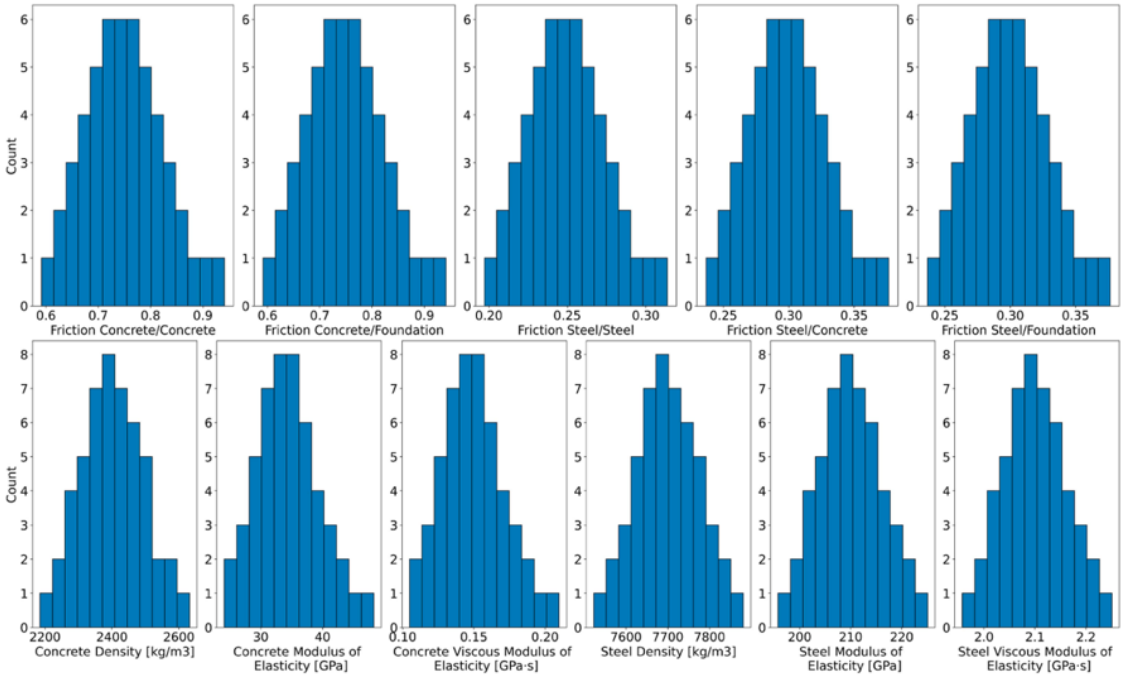

Figure 57: Histograms of the samples obtained by the LHS technique [457].

Once calibrated, the model allowed CERN to simulate both current and future concrete block configurations under a range of seismic load conditions. These simulations accounted for cascading failures, where the collapse of one block alters the contact forces and support conditions for adjacent blocks. Through iterative time-stepping, the model dynamically captures these interactions, ensuring that secondary failures caused by loss of support are included in the analysis. This modelling approach is highly effective in probing the seismic performance of different configurations, ensuring that CERN's infrastructure remains resilient to seismic events. Key aspects of the seismic simulation included:

- Mesh size for block structures: 0.2 metres, ensuring fine-grained detail in the simulations.
- Time step used: 0.001 seconds, selected to capture high-frequency seismic interactions between blocks.
- The model simulated both rigid and deformable blocks (elastic and viscoelastic), allowing for comparisons in behaviour under the same seismic conditions.

The calibration process highlighted several key findings that influenced the choice of behaviour for the final simulations [457]. One significant finding was the importance parameter across all behaviours (rigid, elastic, and viscoelastic) of the chamfer on the blocks. It played a crucial role in ensuring the accuracy of

the LMGC90 calibration, particularly in the contact dynamics between blocks. Among these, rigid behaviour emerged as the most effective at replicating real-world conditions, especially when high friction coefficients between the concrete blocks were applied, making it the most suitable for simulations. The elastic behaviour was appropriate for configurations 1 and 2 but proved inadequate for configurations 3 and 4, where the dynamics were more complex. Viscoelastic behaviour, though the most accurate for all configurations, required significantly longer computational times, making it less practical for large-scale simulations on CERN's cluster. Ultimately, rigid behaviour was chosen as the optimal balance between accuracy and computational efficiency.

In this chapter, the LMGC90 model was adopted and calibrated based on the methodology established by CERN. The model calibration process, carried out by CERN, aimed to simulate realistic block behaviour under seismic loads, particularly focusing on the TCC2 caverns. The geometrical model of TCC2 was developed using CATIA software [461], with both a .step file and Bill of Materials (BOM) exported to ensure accurate input for the LMGC90 simulations (Figure 58).

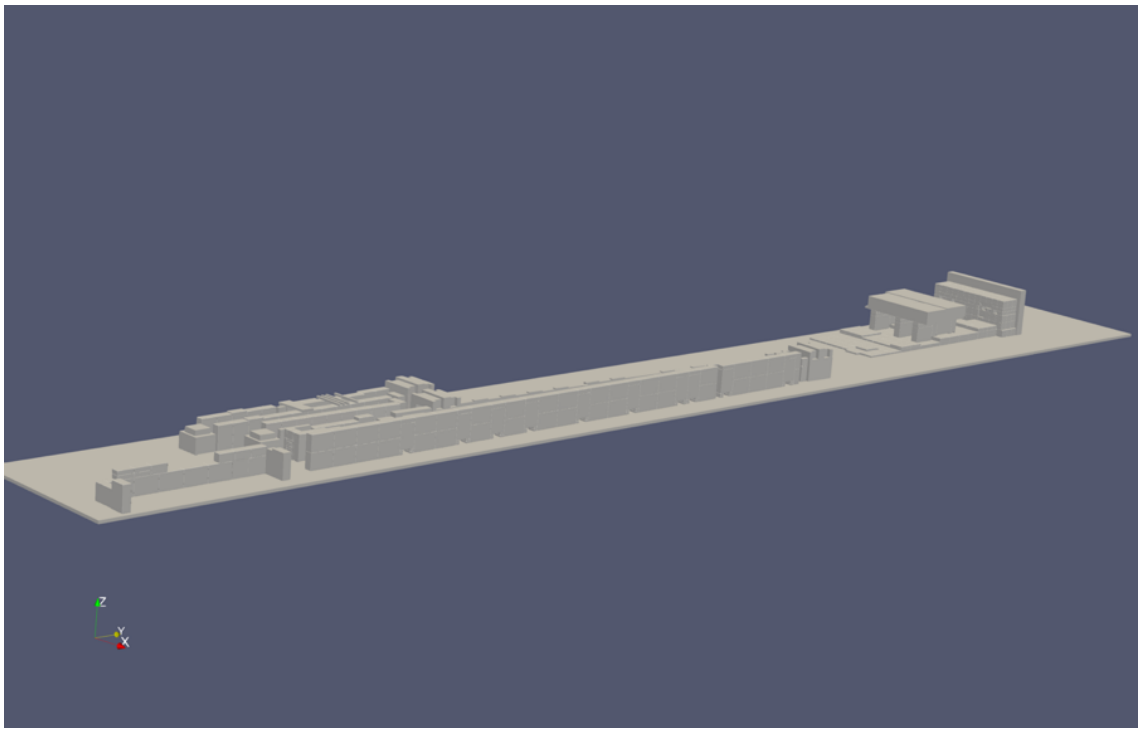

a)

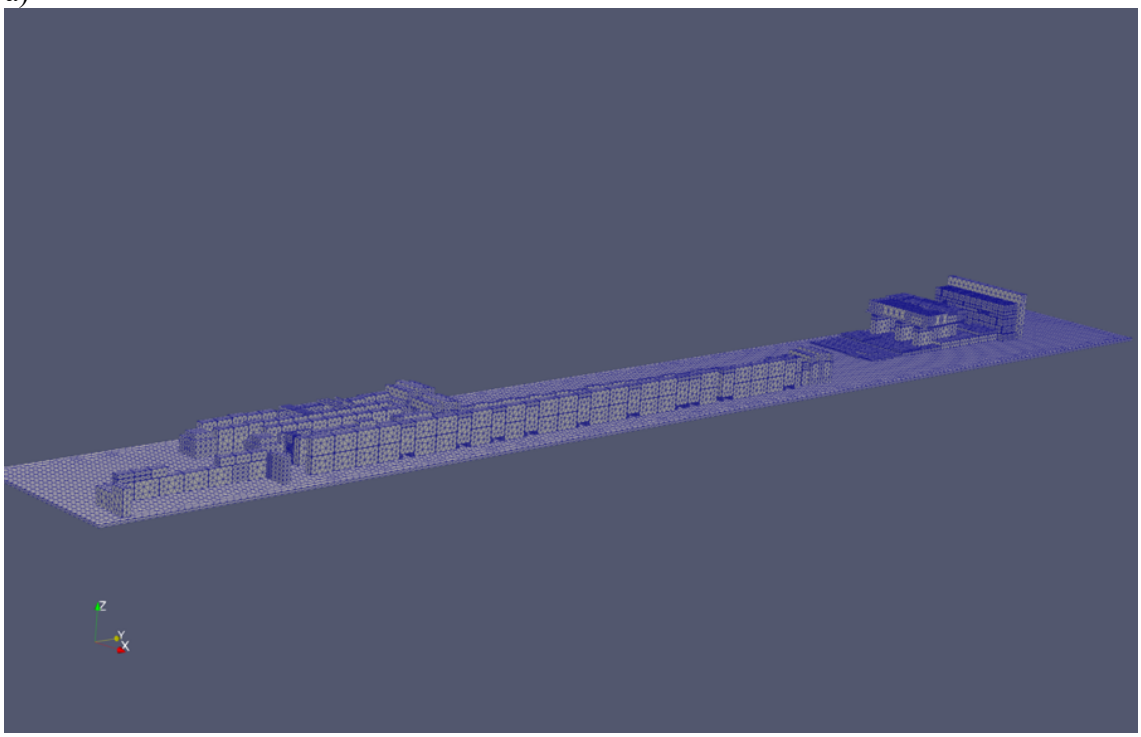

b)

Figure 58: CATIA 3D geometrical model (a) and LMGC90 mechanical model (b) of the TCC2 configuration.

4.4.3 Seismic Vulnerability Assessment

Assessing seismic vulnerability is necessary to understand how structures respond to earthquake forces, particularly in high-risk facilities like CERN's TCC2 caverns. Following the calibration of the LMGC90 model, IDA was employed by CERN to evaluate the seismic behaviour of the TCC2 block structures. IDA, a well-established method for assessing structural performance under increasing seismic intensity, allows for a detailed examination of how the blocks respond to various seismic conditions, identifying specific failure thresholds and response patterns. With the calibrated LMGC90 model accurately reflecting the mechanical properties and behaviour of the TCC2 blocks, IDA simulations were conducted using a series of scaled seismic accelerograms. By gradually increasing seismic loads, the analysis reveals when and how failure mechanisms such as sliding, rocking, and collapse occur.

4.4.3.1 IDA Methodology Applied

The process of conducting IDA on the TCC2 block structures followed a detailed procedure to ensure a thorough evaluation of seismic performance. This approach is based on the methodology used at CERN, as previously described in

the subsections, which involves nine key stages to assess the seismic vulnerability of the block configurations:

1. **Identify Blocks to Monitor**: The first step was to identify the blocks most representative of the probable failure mechanisms, such as sliding, rocking, or collapse. These blocks were selected based on their location and configuration within the structure, as well as their susceptibility to seismic forces.
2. **Select a 3-Component Accelerogram**: Seven sets of 3-component accelerograms (2 horizontal and 1 vertical) were selected from the European Strong Motion (ESM) database (Table 18), ensuring compatibility with the elastic response spectra for the TCC2 site. Each accelerogram provided a realistic representation of the seismic ground motions likely to occur at CERN, forming the basis for the dynamic analysis.

Table 18: Selected 3-component accelerograms from the European Strong Motion Database (ESM) for the TCC2 Site.

No.	Event Location	Year	Reference
1	Poggio di Roio, Italy	2009	[462]
2	Accumoli, Italy	2016	[463]
3	Castelsantangelo sul Nera, Italy	2016	[464]
4	Agia Thekli, Greece	2014	[465]
5	Castelsantangelo sul Nera, Italy	2016	[466]
6	Castelsantangelo sul Nera, Italy	2016	[467]
7	Friuli Venezia Giulia, Italy	1976	[468]

3. **Normalize the Accelerogram**: The chosen accelerogram was normalized to the PGA of the main horizontal component, ensuring consistency across different seismic intensities. Normalizing the accelerogram to the PGA allowed for the application of varying seismic intensities in the subsequent steps.
4. **Create a Range of Scale Factors (SCFs)**: A series of 17 Scale Factors (SCFs) was created to represent different levels of seismic intensity, ranging from 0.005 g to 0.612 g. For each SCF, a corresponding set of scaled 3-component accelerograms was generated, covering a wide range of earthquake intensities from minor tremors to extreme events.
5. **Run Non-Linear Dynamic Analysis**: A non-linear dynamic analysis was conducted on the 20 sample models generated from the mechanical

variable distributions (as described in subsection 4.4.2). These models were subjected to the full range of scaled accelerograms created in Step 4. This non-linear analysis provided a detailed understanding of how each model responded to different levels of seismic excitation. During the simulations, displacements were continuously monitored at each time step of 0.001 seconds, providing a detailed time-history of block movements. This approach ensures that any exceedance of the defined threshold (0.2 meters) is captured precisely when it occurs. While the threshold defines collapse, intermediate displacements approaching this limit are also analysed to understand progressive failure mechanisms and near-collapse behaviour.

6. **Collect Damage Measure (DM) Results**: The results of each simulation were measured in terms of Damage Measure (DM), which was calculated based on maximum relative and residual displacements between blocks. The DM provided a quantitative measure of the extent of damage the blocks experienced under each seismic intensity.
7. **Plot IDA Curves**: After collecting the DM results for each model, IDA curves were generated by plotting the DM against the (IM), which in this case was the PGA. The IDA curves illustrate how the block structures respond to increasing seismic intensity, showing the transition from minor displacements to severe damage or failure.
8. **Calculate Median and Percentiles**: For each level of seismic intensity, the median DM and relevant percentiles were calculated (Figure 59). This provided a statistical representation of the block performance across different models, offering insights into the general trends and variabilities in block behaviour under seismic loads.
9. **Repeat for Remaining Accelerograms**: The entire procedure was repeated for each of the remaining six accelerograms to ensure accuracy in the results. By running the IDA on multiple accelerograms, the study captured a wide range of potential earthquake scenarios, providing a thorough assessment of the seismic vulnerability of the TCC2 blocks.

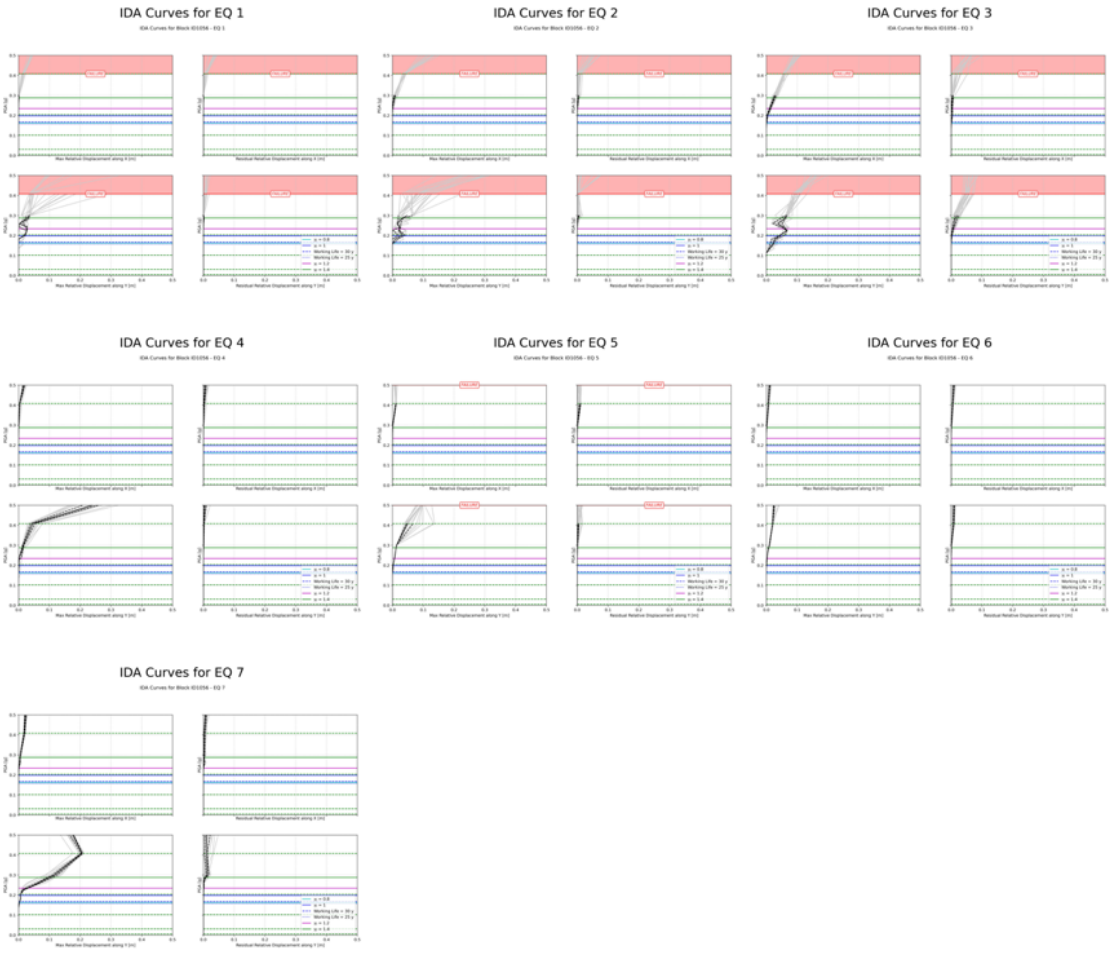

Figure 59: IDA curves for Block ID 1056 under seven earthquake events.

This comprehensive process of applying IDA enabled the study to evaluate the seismic performance of the TCC2 block structures across a spectrum of seismic intensities. By simulating different levels of seismic excitation and monitoring the resulting displacements and damage, the study was able to identify the points at which the blocks would fail and the most likely failure modes under various earthquake scenarios.

The IDA involves subjecting a structural model to a suite of earthquake ground motion records, with the intensity of these records being incrementally increased until the structure reaches a predefined limit state, such as collapse. This process provides a detailed picture of the TDC2/TCC2 performance under varying levels of seismic demand. For each PGA level, IDA results were used to identify blocks that exceed a displacement of 0.2 meters (in any direction). Any block experiencing displacements equal to or exceeding 0.2 meters is considered to have collapsed, reflecting a condition where the structural configuration and intended functionality are no longer maintained.

4.4.3.2 Seismic Fragility Curves

Following the completion of the IDA, seismic fragility curves were developed to further quantify the vulnerability of the TCC2 blocks. Fragility curves provide a probabilistic measure of failure, showing the likelihood of block failure as a function of seismic intensity, typically expressed as PGA.

1. **Fragility Curve Development**: Fragility curves were developed by plotting the probability of block failure against PGA. Each curve represented a specific failure mode, such as sliding or collapse, and was generated by analysing the results from the IDA simulations. These curves allowed the study to quantify the risk of failure at different seismic intensities.
2. **Probability of Failure**: The fragility curves indicated that the probability of sliding failure increased sharply at moderate PGAs, while the probability of collapse remained low until higher-intensity seismic events. This information is critical for understanding the seismic resilience of the block structures and for determining the seismic intensity thresholds that would require intervention.
3. **Application to TCC2**: By overlaying the seismic hazard data for the TCC2 site, the study was able to estimate the probability of failure for the block structures under different earthquake scenarios.

Figure 62 illustrates the fragility curves generated for the TCC2 blocks, showing the relationship between PGA and the probability of block failure:

4.4.3.3 Cascading Risks and Multi-Hazard Analysis

In addition to direct seismic impacts, the potential for cascading risks must also be considered. In the event of seismic-induced block failure, secondary hazards such as fire may be triggered. For example, if block displacement causes structural damage, critical systems like electrical or mechanical equipment could be compromised, increasing the likelihood of fire. This makes it essential to view the seismic vulnerability assessment within the broader context of a multi-hazard risk assessment, where interactions between various hazard types are evaluated to create a more comprehensive risk profile for the TCC2 site.

4.4.4 Structural Model and Analysis

The structural model of TCC2, consisting of 1250 blocks, was analysed to assess its dynamic response to scaled earthquake records. The analysis focused on maximum relative displacements along the x and y axes, which represent the movement between blocks during the seismic event, and maximum residual displacements, indicating the permanent shift that remained afterward. A simulation period of 29.900 milliseconds was selected to capture the full time-history of the structural responses along the x and y axes.

4.4.4.1 Demand Capacity Ratio

The DCR is a metric used to evaluate the likelihood of structural failure under seismic loading. It compares the demand imposed on a structural component by earthquake-induced forces and displacements to the component's capacity to withstand those forces and displacements without failing. This ratio is widely used in performance-based seismic design and assessment to quantify the vulnerability of structural components.

4.4.4.1.1 Definition and Significance

The DCR is defined as the ratio of the demand displacement to the limit displacement for a given structural component. It provides a normalized measure of how close the component is to failure:

$$\mathrm{DCR} = \min\left(\frac{\Delta_n}{\Delta_{limit}}, 1\right) \tag{89}$$

where Δ_n is the demand displacement in a given direction (e.g., x-axis, y-axis, rotation) for a specific ground motion level. Δ_{limit} is the limit displacement, representing the maximum displacement the component can endure before failure.

The significance of DCR lies in its ability to quantify the vulnerability of structural components. A higher DCR indicates a higher probability of failure, whereas a lower DCR indicates a greater margin of safety. The use of DCR is well-documented in seismic design guidelines and standards, such as FEMA 356 [469], [470], ASCE/SEI 41-17 [470], and FEMA P-58 [471], which provide detailed procedures for calculating and interpreting DCR in the context of seismic rehabilitation and performance assessment. The calculation of DCR involves the following steps:

4.4.4.1.1.1 Determine Demand Displacements (Δ_n)

Perform IDA to obtain the demand displacements for various PGA levels. These displacements are recorded for different directions and rotations, specifically (Figure 60):

Δ_x: Relative displacement along the x-axis.

Δ_y: Relative displacement along the y-axis.

Δ_{rx}: Residual displacement along the x-axis after shaking.

Δ_{ry}: Residual displacement along the y-axis after shaking.

4.4.4.1.1.2 Establish Limit Displacements (Δ_{limit})

The limit displacements were established based on the results from the IDA and the performance criteria defined for the TCC2 blocks. The limit displacements are defined by two key factors: ensuring the safety of personnel working at CERN, while also protecting sensitive equipment and experiments from damage.

In this study, a 0.2 meters threshold was established for both maximum relative and residual displacements, representing a final collapse condition at the block level rather than an earlier (e.g., serviceability) limit state. This choice arises from engineering judgment, prior experimental data on block-stability under seismic loading, and the practical requirement to safeguard personnel and equipment.

Given the discrete nature of TCC2's precast blocks, a local (block-by-block) failure criterion is adopted, whereby any block exceeding a displacement of 0.2 meters (in either the x or y direction) is classified as collapsed. Although this is a local measure, inter-block interactions are inherently captured by LMGC90's contact algorithms: if one block's large displacement alters forces on a neighbouring block, that neighbour may also exceed the 0.20 meters threshold, creating a cascading failure. A purely global collapse mechanism (as used in monolithic or fully interconnected structures) is less suitable here, since each block can individually fail without compromising the entire configuration—at least until multiple adjacent blocks exceed their respective thresholds.

The DCR for each direction and rotation is calculated using the following formula:

$$\mathrm{DCR} = \min\left(\frac{\Delta_x}{\Delta_{limit}}, \frac{\Delta_y}{\Delta_{limit}}, \frac{\Delta_{rx}}{\Delta_{limit}}, \frac{\Delta_{ry}}{\Delta_{limit}}, 1\right) \tag{90}$$

The minimum function ensures that the DCR does not exceed 1, indicating certain failure if the demand exceeds the capacity.

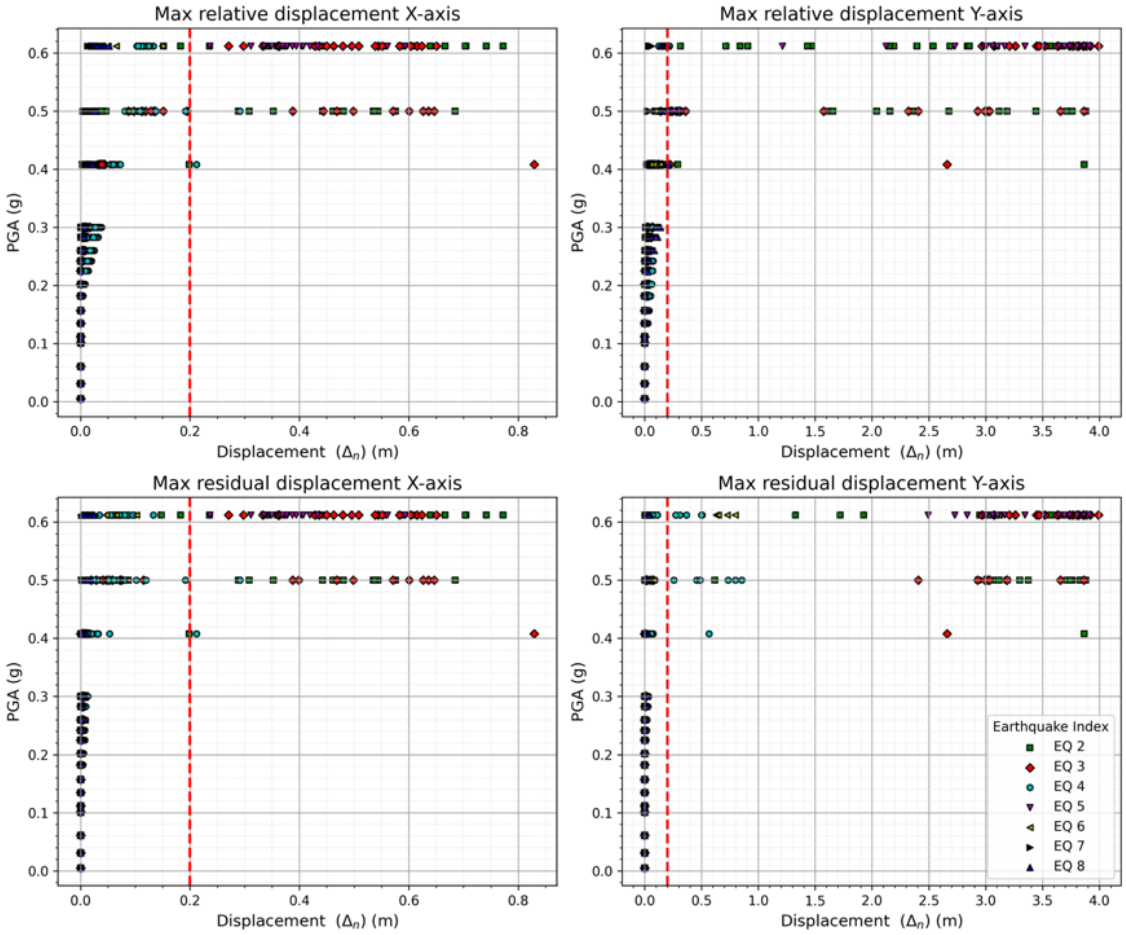

Figure 60: Relative and residual displacements (x and y axes) for Block ID 1056 across seven earthquake events. The red dashed line indicates the displacement limit (Δ_{limit} = 0.2 meters), beyond which the block is considered to have reached its failure threshold.

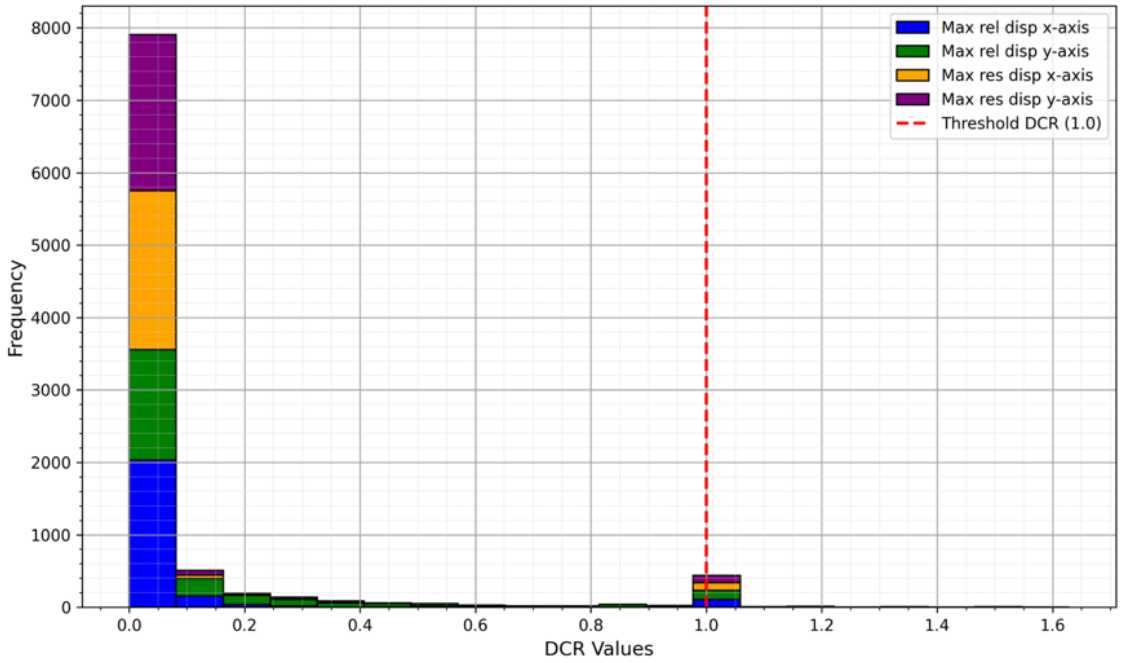

Figure 61: This histogram illustrates the distribution of DCR values for Block ID 1056, categorized by maximum relative and residual displacements along the x and y axes. The red dashed line represents the DCR threshold of 1.0, signifying the onset of structural failure.

The DCR values are used to assess the probability of failure for each structural component. The relationship between DCR and the probability of failure is as follows (Figure 61):

- **If DCR ≥ 1**, The probability of failure for that direction is 1 (certain failure). This indicates that the demand has exceeded the component's capacity.
- **If DCR < 1**, The probability of failure is proportional to the DCR value. This means that as the DCR approaches 1, the probability of failure increases but will always be less than 1.

By calculating the DCR for each direction and rotation, a comprehensive understanding of the component's vulnerability under seismic loading is obtained. These DCR values are then used to determine the joint probability of structural failure, which considers the combined effects of displacements in all directions and rotations.

4.4.4.2 Estimation of Fragility Functions

The DCR values derived from IDA are important inputs for developing fragility functions. Fragility functions describe the probability of exceeding a certain damage state (e.g., collapse) given a specific seismic intensity (e.g., PGA). To

accurately capture the probability of structural failure, it is essential to use fragility functions. Fragility functions quantify the probability of reaching or exceeding a certain level of structural damage given a specific intensity of ground shaking. Baker, J. W. [98] provides a detailed methodology for estimating these fragility functions.

This approach involves scaling each ground motion until it causes collapse (SC), thereby identifying the PGA_i level at which each motion causes failure. The fragility function parameters can be estimated using the lognormal distribution, defined as:

$$P(DCR \geq 1 \mid PGA_i) = \Phi\left(\frac{\ln\left(\frac{PGA_i}{\theta}\right)}{\beta}\right) \tag{91}$$

where Φ is the standard normal cumulative distribution function (CDF), θ is the median of the fragility function (the PGA_i level with a 50% probability of collapse), and β is the standard deviation of (PGA_i) (sometimes referred to as the dispersion of PGA).

4.4.4.2.1 Maximum Likelihood Estimation (MLE).

To fit fragility functions using data from the DCR values derived from IDA, the Maximum Likelihood Estimation (MLE) method is employed. This method maximizes the likelihood of the observed data given the candidate fragility function.

For each intensity level PGA_i, the number of ground motions that result in collapse and those that do not is observed. The likelihood function for the observed data is given by:

$$\text{Likelihood} = \prod_{i=1}^{m} \binom{n_i}{z_i} p_j^{z_j}(1 - p_i)^{n_i - z_i} \tag{92}$$

where z_j is the number of ground motions at PGA_i level. z_i is the number of ground motions causing collapse. p_i is the probability of collapse at PGA_i, given by the fragility function $p_j = \Phi\left(\frac{\ln\left(\frac{PGA_i}{\theta}\right)}{\beta}\right)$.

To make the fragility parameters θ and β explicit in the likelihood function, we substitute p_i with the fragility function:

$$\text{Likelihood} = \prod_{i=1}^{m} \binom{n_i}{z_i} \Phi\left(\frac{\ln\left(\frac{PGA_i}{\theta}\right)}{\beta}\right)^{z_i} \left(1 - \Phi\left(\frac{\ln\left(\frac{PGA_i}{\theta}\right)}{\beta}\right)^{z_i}\right)^{n_i - z_i} \quad (93)$$

Here, the probability of collapse for each ground motion level $PGA_i$is modelled by the fragility function. The goal of MLE is to find the values of θ and β that maximize the likelihood of observing the data.

Because maximizing the likelihood function directly is often complex, it is typically easier to maximize the logarithm of the likelihood function. The log-likelihood function is:

$$\ln(\text{Likelihood}) = \sum_{i=1}^{m} \left(z_i \ln\Phi\left(\frac{\ln\left(\frac{PGA_i}{\theta}\right)}{\beta}\right) + (n_i - z_i) \ln\left(1 - \Phi\left(\frac{\ln\left(\frac{PGA_i}{\theta}\right)}{\beta}\right)\right)\right) \quad (94)$$

By maximizing this log-likelihood function, the parameters θ (the median PGA at which collapse is equally likely) and β (the dispersion of the lognormal distribution) are estimated. This ensures that the fragility function provides the best fit to the observed collapse data [98].

After obtaining the fragility functions, according to exceeding probability in terms of the intensity measures for the different damage states, the fragility curve is available to plot (Figure 62).

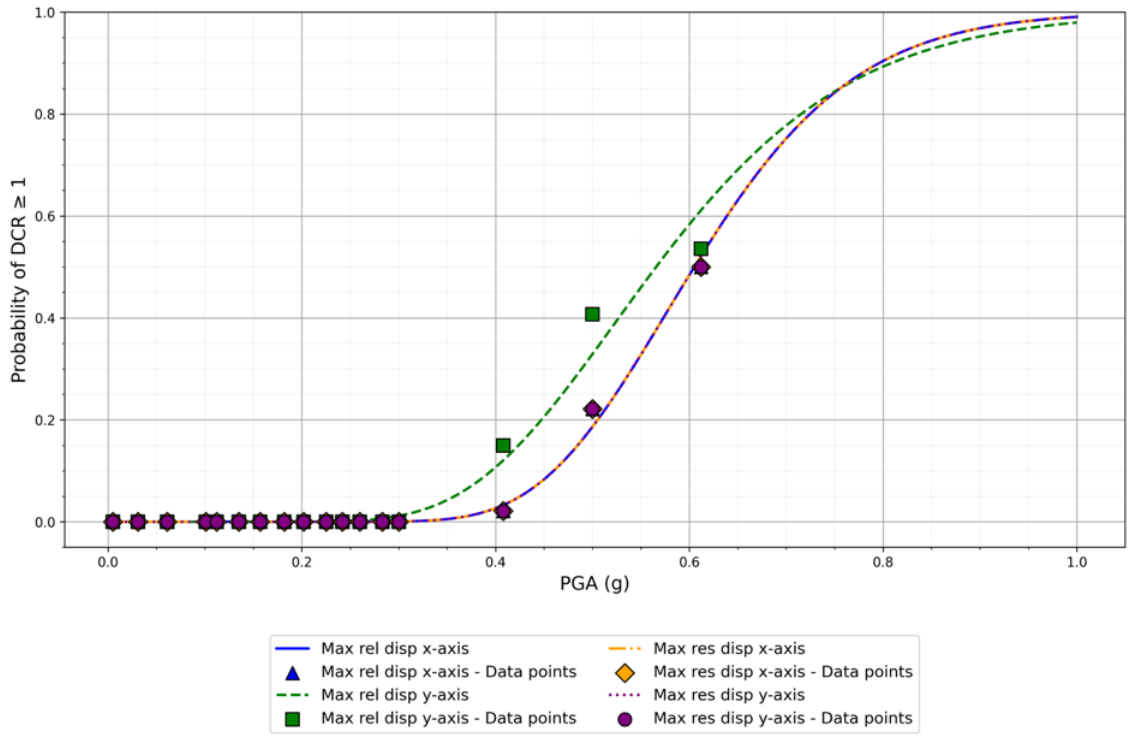

Figure 62: Fragility curves for chosen area: Block ID 1056 showing the probability of DCR ≥ 1 as a function of PGA (g), based on relative and residual displacements along the x and y axes.

4.4.4.3 Joint Probability of Structural Failure

Since the fragility curves of any given block provide different probabilities of failure for each type of displacement (relative and residual) along both directions (x- and y-axes), the joint probability of structural failure at a given PGA level n can be calculated as:

$$P(SC_b \mid PGA_i) = P(SC_x \mid PGA_i) \cdot P(SC_y \mid PGA_i) \cdot P(SC_{rx} \mid PGA_i) \cdot \cdot P(SC_{ry} \mid PGA_i) \quad (95)$$

where SC_b is DCR ≥ 1, then $P(SC_x \mid PGA_i)$ is the probability of failure of Maximum relative displacement along the x-axis. $P(SC_y \mid PGA_i)$ is the probability of failure of Maximum relative displacement along the y-axis. $P(SC_{rx} \mid PGA_i)$ is the probability failure of Maximum residual relative displacement along the x-axis. $P(SC_{ry} \mid PGA_i)$ is the probability of failure of Maximum residual relative displacement along the y-axis.

4.4.5 Convolution of Hazard and Fragility Curves

Convolution of hazard and fragility curves, the annual probability or rate of collapse, obtained by integrating (or summing) the product of the hazard and fragility curves.

Once the joint probability of failure for a chosen block has been established for each PGA level, the annual probability of collapse is determined by convolving the joint fragility function with the hazard curve. This convolution reflects the integration of the structure's vulnerability across various PGA levels (as described by the fragility curve in subsection 4.4.4) with the annual exceedance probability (as described by the hazard curve in subsection 4.3.5).

The most general form of convolution is expressed as, where a continuous seismic hazard function is present, the convolution process is expressed in continuous form as:

$$P_c = \int_0^{+\infty} P(SC_b \mid PGA) \frac{dH(PGA)}{dPGA} dPGA \tag{96}$$

P_c is the total annual probability of collapse for each block b. $P(SC_b \mid PGA)$ is the joint fragility function, representing the conditional probability of collapse for block b given a specific PGA value, and $dH(PGA)$ is the seismic hazard curve.

The seismic hazard curve is fundamental to this analysis because it describes how often different levels of ground shaking are expected to occur at a given site. Importantly, this curve reflects the site-specific seismic risk.

$$P(PGA \geq 0) = 1 \tag{97}$$

This implies that any seismic event results in some level of ground motion, an essential consideration when analysing any structural response. Even minor ground accelerations, while not catastrophic, contribute to the overall risk profile.

As we move forward, the probability that the PGA exceeds a given threshold x_i provides more information about the intensity of shaking that might be expected:

$$P(PGA \geq x_i) \tag{98}$$

This part of the hazard curve guides the understanding of how likely it is for the ground shaking to exceed critical thresholds that may compromise structural integrity.

A more specific focus arises when examining the probability that PGA falls within a particular range:

$$P(x_i \leq PGA \leq x_{i+1}) = |H(x_{i+1}) - H(x_i)| \tag{99}$$

This helps focus on the intensity range where structural damage or collapse is most likely to occur. Reflecting on this, it is recognized how hazard curves provide a framework not just for predicting extreme events but for examining the intermediate seismic risks that, over time, contribute significantly to structural wear or damage.

Additionally, the probability that PGA remains below a certain threshold can be examined:

$$P(0 \leq PGA \leq x_i) = |H(x_i) - 1| \tag{100}$$

This brings attention to events that fall short of causing major damage but still present risks, prompting consideration of whether even smaller events can be ignored when evaluating long-term structural vulnerability.

In more complex cases, such as at CERN, where seismic analyses are divided into multiple cloves (8 circular sectors) around the target site, each clove (sector) can have a distinct hazard curve.

$$P_c = P\left(_{collapse,block_b}\right) = \sum_{k=1}^{m} \int P(SC_b \mid PGA) \frac{dH_k(PGA_i))}{dPGA} dPGA \tag{101}$$

The summation is over m cloves (sectors), with each sector having its own seismic hazard curve $H_k(PGA)$. This equation allows summing across discrete cloves (sectors) around the target site, each with its own hazard curve. As mentioned above, this approach is particularly useful in sites where each sector has its own seismic hazard curve.

However, in many practical situations, hazard data is only available at discrete PGA values, and the seismic hazard curve is represented by specific exceedance rates at those PGA values (Figure 63). In cases where the area is divided into

cloves (sectors), as in this study at CERN, each clove (sector) has its own hazard curve. For instance, the hazard curve for the South-West clove (sector) may differ from that of the East clove (sector). When working with discrete data, the seismic hazard curves for each clove (sector) are summed to compute the total collapse probability of block b-th as:

$$P_c = \sum_{k=1}^{m} \sum_{i} |H_k(PGA_{i+1}) - H_k(PGA_i)| \int_{PGA_i}^{PGA_{i+1}} P(SC_b \mid PGA) dPGA \quad (102)$$

where $|H_k(PGA_{i+1}) - H_k(PGA_i)|$ is the difference between two consecutive PGA values of the seismic hazard curve, representing the probability of PGA lying within that interval. This means that the contribution from each clove's (sector's) hazard curve is included in the final probability calculation.

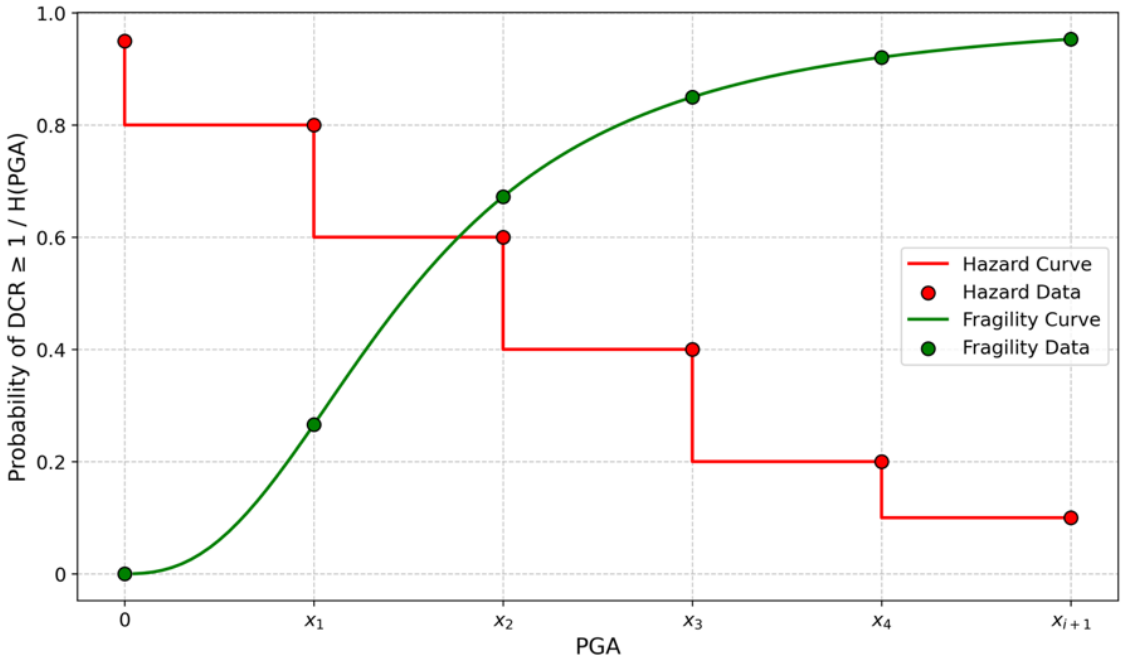

Figure 63: The stepwise seismic hazard curve and the fragility function in terms of PGA.

The choice between continuous and discrete forms of convolution reflects the availability and nature of the seismic data. In theory, the continuous form provides the most precise calculation, as it integrates over all possible ground motion intensities.

Once calculated the collapse probability for each block, combine the probabilities for all blocks using the following formula:

$$P_{cc} = 1 - \prod_{b=1}^{n} (1 - P(\text{collapse,block}_b)) \quad (103)$$

However, in practice, the discrete form is often more applicable because the seismic data available are not numerous and do not allow a continuous statistically representative reconstruction of both the seismicity of an area and the attenuation of seismic ground motion.

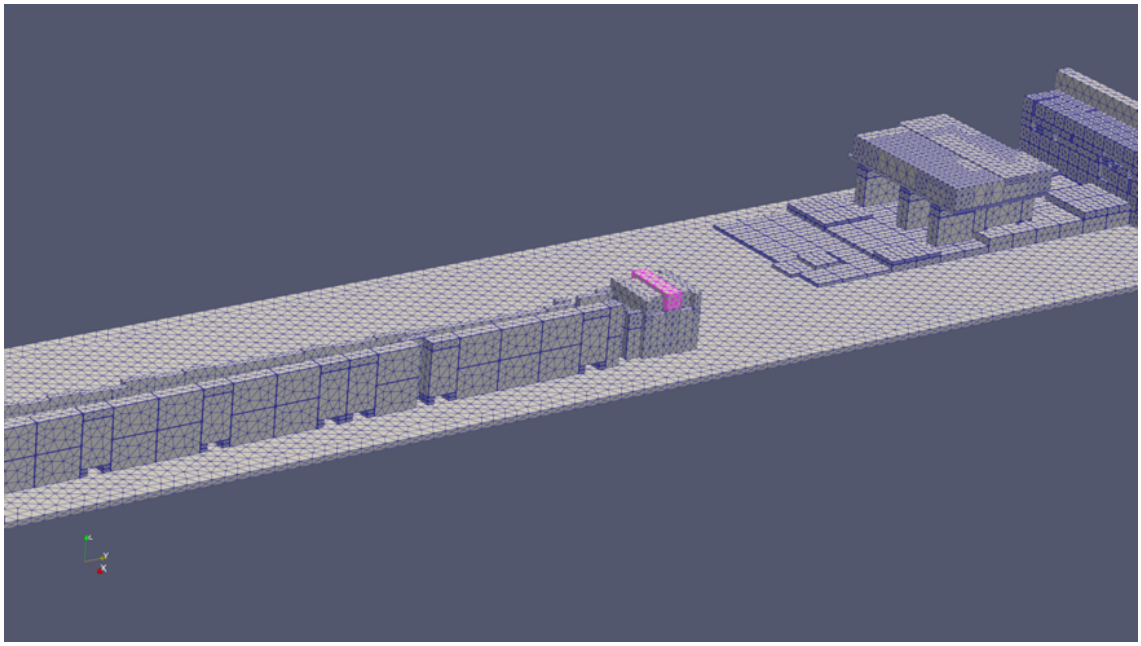

Figure 64: Location of block ID 1056.

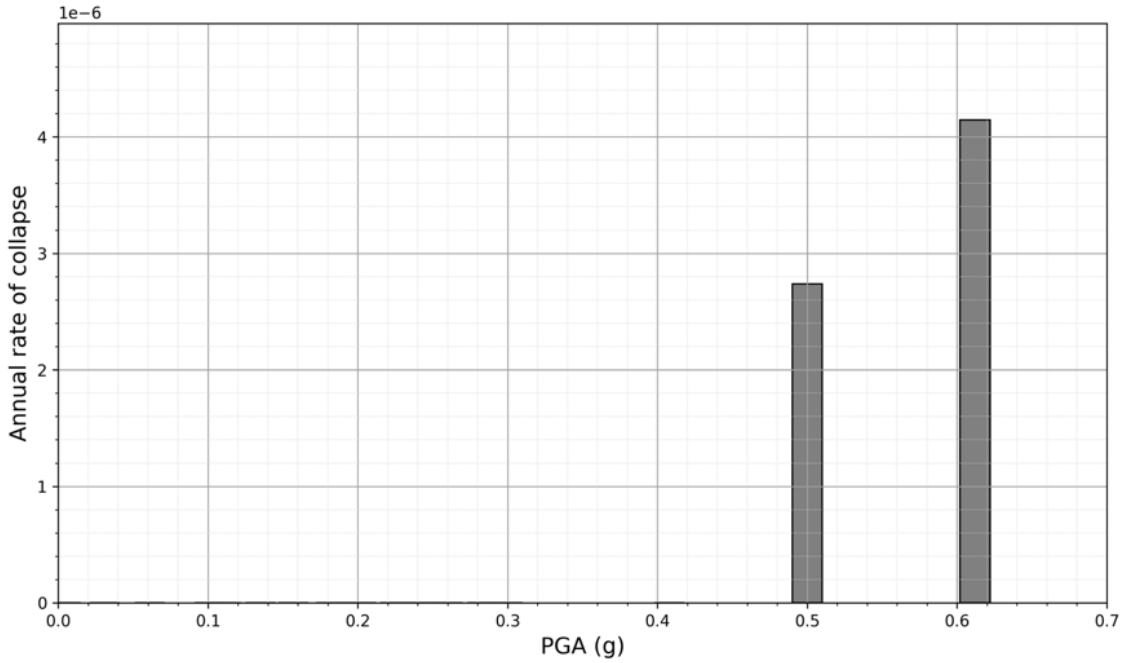

Figure 65: The figure demonstrates how the hazard curve for the sector between the South-West and East of the CERN area is combined with the joint probability fragility

function of Block ID 1056. The convolution of these two components yields the total probability of collapse of Block ID 1056.

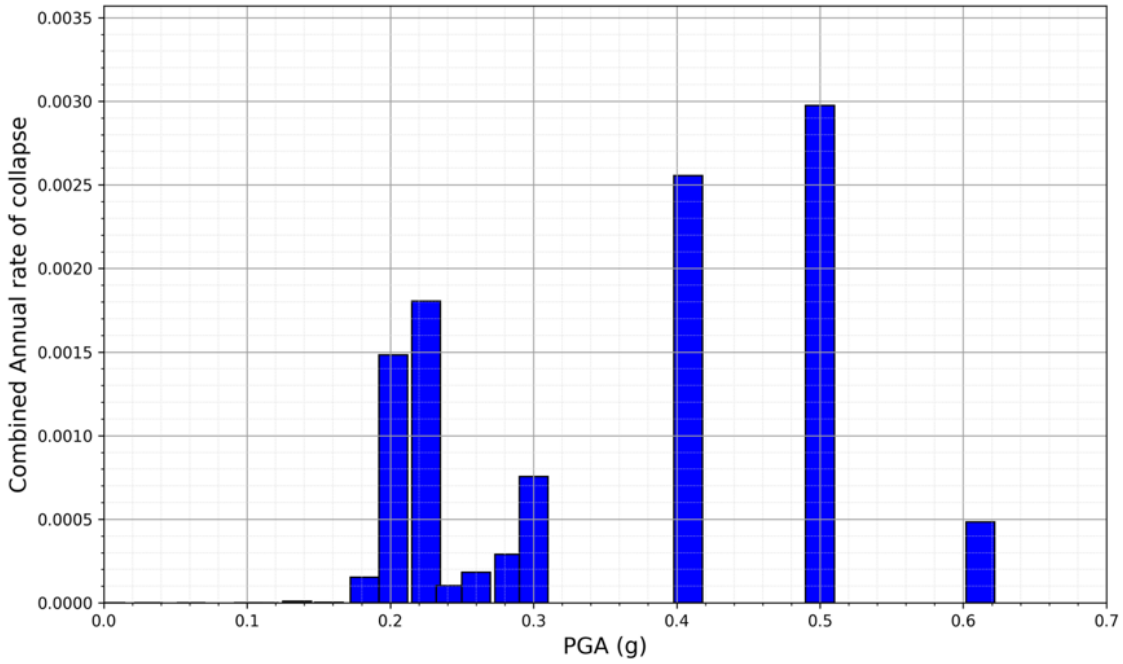

Figure 66: Building on the approach shown in Figure 65 for Block 1056, this figure extends the process to all blocks (1250). It illustrates how the hazard curves for the relevant sectors and the joint probability fragility functions for each block are used to determine the overall collapse probability for the entire TCC2.

Once the overall probability of collapse is determined (Figure 66), this information becomes important for guiding broader risk assessment, such as assessing the seismic-induced fire probability.

Table 19: Seismic Hazard, Fragility, and Collapse Probability Data for Block ID 1056 and Overall Collapse Probability of All Blocks in TCC2.

PGA (g)	**$P(SC_{1056} \mid PGA)$**	**$H_{South\text{-}West\ to\ East}(PGA)$**	**$P\ (_{collapse\ 1056})$**	**P_{CC}**
0.005	0.00E+00	7.01E-01	0.00E+00	0.00E+00
0.031	0.00E+00	4.71E-01	0.00E+00	0.00E+00
0.061	0.00E+00	1.90E-01	0.00E+00	0.00E+00
0.101	0.00E+00	9.30E-02	0.00E+00	0.00E+00
0.112	0.00E+00	9.30E-02	0.00E+00	0.00E+00
0.135	0.00E+00	9.30E-02	0.00E+00	9.61E-06
0.157	0.00E+00	3.02E-02	0.00E+00	3.66E-06
0.182	0.00E+00	3.02E-02	0.00E+00	1.54E-04
0.202	0.00E+00	3.02E-02	0.00E+00	1.48E-03
0.225	0.00E+00	3.02E-02	0.00E+00	1.80E-03
0.242	0.00E+00	2.69E-03	0.00E+00	1.03E-04

0.26	0.00E+00	2.69E-03	0.00E+00	1.83E-04
0.283	0.00E+00	2.69E-03	0.00E+00	2.90E-04
0.3	0.00E+00	2.69E-03	0.00E+00	7.56E-04
0.408	1.48E-06	1.12E-03	1.66E-09	2.56E-03
0.5	4.42E-03	6.19E-04	2.74E-06	2.98E-03
0.612	6.70E-02	6.19E-05	4.15E-06	4.83E-04

4.4.6 Identify Fire-Prone Blocks

The fire-prone blocks are particularly important because their collapse has cascading consequences beyond structural damage. In practice, determining which blocks are fire-prone requires both engineering judgment and empirical evidence from simulations. In this case, based on the results from the IDA simulations, blocks located in particularly vulnerable areas are identified, where the infrastructure is highly susceptible to both collapse and fire.

These failure modes—sliding, rocking, and collapse—can significantly increase the likelihood of fire due to the interaction between structural components and potentially hazardous materials in TCC2. The presence of magnetite devices, cable trays, and forklifts increases the fire risk. Failure modes can displace or damage these systems, potentially causing electrical fires or other hazardous interactions. For instance, sliding can dislodge cable trays or destabilize magnetite devices, while rocking motions can interfere with forklifts and other equipment.

For each fire-prone block, it was initially assumed that if the block collapses, it would almost certainly induce a fire, represented as $P(F \mid SC_b) = 1$. This assumption simplifies the analysis but introduces a degree of uncertainty. While simulation data indicates that certain blocks are located in highly vulnerable areas where collapse could interact with critical equipment, such as magnetite devices, cable trays, or forklifts, the actual probability of fire occurring upon block failure is less definitive.

The uncertainty arises from several factors. First, block failure modes can differ significantly depending on the direction and magnitude of displacement, as well as whether the failure involves sliding, rocking, or complete collapse. These different failure mechanisms may interact with equipment in varying ways, making it difficult to predict the precise likelihood of fire. For example, a sliding block might dislodge cable trays, potentially sparking an electrical fire, while a rocking block might destabilize a forklift, with no direct ignition source involved.

Secondly, while the structural failure of blocks can be modeled with a high degree of accuracy, there is no comprehensive literature or empirical evidence specific to CERN's infrastructure that quantifies how such block failures interact with magnetite devices, cable trays, or forklifts to cause a fire. It depends heavily on the unique interactions between structural movements and electrical or mechanical systems, for which there is limited data.

Given these complexities, it may be more realistic to assign a range of conditional probabilities for fire occurrence upon collapse, rather than assuming $P(F \mid SC_b) = 1$. Depending on the block's location, failure mode, and proximity to sensitive equipment, this probability could vary rather than being an absolute certainty. The decision to model the conditional probability of fire as a range, rather than a certainty, reflects the inherent uncertainty in the interaction between block failure and fire risk in CERN's specific context. By considering P(fire, block $_i$) as variable, a better account can be made for the different failure modes and the lack of empirical data on fire ignition in these types of environments. This reflects the practical challenges faced in multi hazard risk assessments, where secondary hazards like fire are often difficult to quantify precisely. Furthermore, future research could focus on gathering more data on how equipment like cable trays or magnetite devices respond to structural impacts, helping to refine these probabilities further.

The probability that each block will induce a fire if it collapses is calculated:

$$P(\text{fire}, \text{block}_b) = P(\text{collapse}, \text{block}_b) \cdot P(F \mid SC_b) \quad (104)$$

Here, the probability of fire occurring for block b is the product of the probability of failure modes (sliding, rocking, and collapse) and the conditional probability that a fire will be triggered by the failure modes. This equation shows the interdependence of seismic-induced collapses and fire risk. By focusing on specific fire-prone blocks, we can tailor our analysis to areas where the cascading effects of structural failure are most likely to be catastrophic.

4.4.6.1 Non-Independent Fire Risk Between Blocks

It is important to recognize that the fire risk across blocks within a single location is non-independent. This interdependency arises from the fact that if any one block collapses and induces a fire, the fire risk from other blocks in that area becomes redundant. This is an important consideration when modelling fire risk

in shared environments such as CERN's facilities, where multiple blocks are situated near critical equipment.

Treating the fire risks for each block independently would lead to an overestimation of the total fire probability. If the individual fire probabilities were summed across all blocks directly, the result would inaccurately suggest that multiple fires could occur simultaneously in a single area, which conflicts with the reality that only one fire event is needed to damage the shared equipment.

To address this, the probability of fire in each location is modelled using the "at least one fire" approach. This method ensures that the fact that only one block's failure is sufficient to induce a fire is accounted for, avoiding the error of counting multiple fire occurrences in the same area. The probability of at least one fire in a location is given by:

$$P(\text{at least one fire in location}) = 1 - \prod_{b=1}^{Nf} (1 - P(\text{fire}, \text{block}_b)) \quad (105)$$

where Nf is the total number of fire-prone blocks in that location. This equation captures the reality that once a fire has been triggered, additional block collapses in the same location do not further increase the fire risk.

In this area, there are 67 fire-prone blocks (Figure 67). For each block, the collapse probability has been calculated. To determine the probability that at least one block induces a fire, the probability that no block causes a fire is first computed. Based on the collapse probabilities of the 67 blocks, the final probability of at least one fire occurring in this location is shown in Table 20 for different PGA levels.

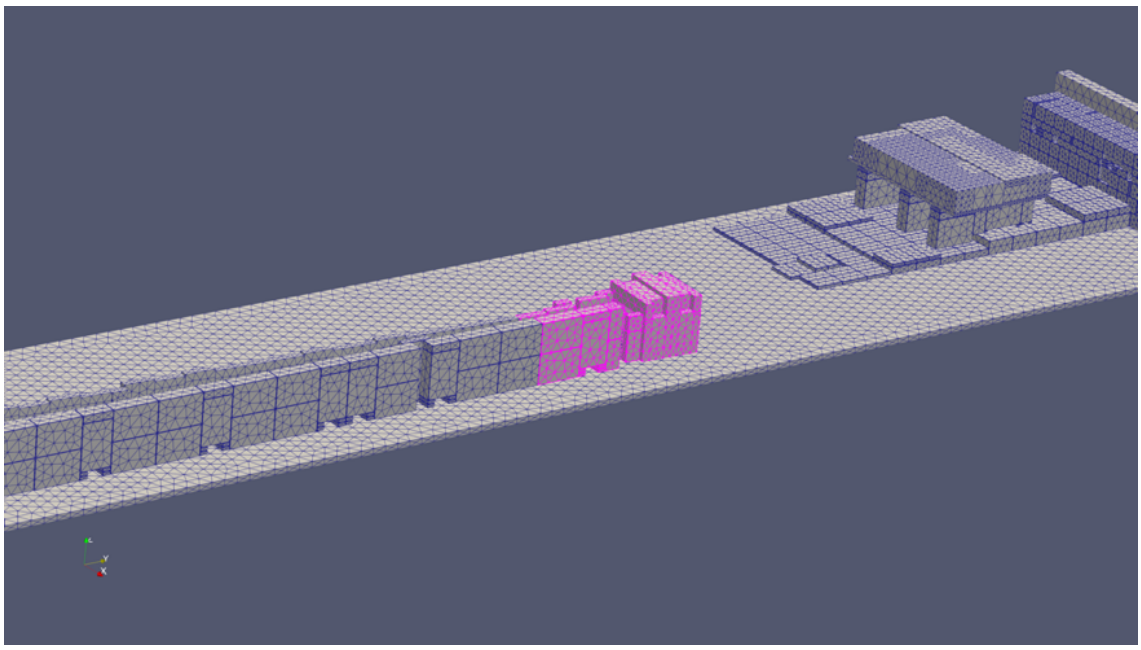

Figure 67: Fire-prone blocks for fire scenarios CFS2, 3 and 5 (Figure 68), showing the fire scenario zone where the collapse of any of the selected 67 blocks could induce a fire.

Table 20: Probability of structural collapse-induced fire for Block ID 1056 and across 67 blocks (Figure 67).

PGA (g)	**$P(_{fire,\ block\ 1056})$**	**Probability of at least one fire across 67 blocks**
0.005	0.00E+00	0.00E+00
0.031	0.00E+00	0.00E+00
0.061	0.00E+00	0.00E+00
0.101	0.00E+00	0.00E+00
0.112	0.00E+00	0.00E+00
0.135	0.00E+00	9.30E-06
0.157	0.00E+00	6.20E-07
0.182	0.00E+00	9.53E-05
0.202	0.00E+00	3.11E-04
0.225	0.00E+00	3.95E-04
0.242	0.00E+00	2.75E-05
0.26	0.00E+00	4.14E-05
0.283	0.00E+00	3.58E-05
0.3	0.00E+00	6.19E-05
0.408	1.66E-09	1.22E-04
0.5	2.74E-06	1.07E-04
0.612	4.15E-06	3.56E-05

4.5 Independent Risk Fire

In reviewing the history of fires at CERN, it is evident that while several accidents have been documented, the primary focus of this record-keeping has not been on detailed risk analysis. Fires at CERN have occurred over the years, with some causing significant damage to equipment and operations [472], [473]. However, the systematic registration of these accidents was not originally designed for the purpose of informing fire risk assessments. As a result, the available data on fire frequency and causes remains insufficient to predict future risks accurately.

However, to address the limitations in fire risk documentation and improve the ability to perform quantitative fire risk assessments, CERN has developed a new methodology known as FIRIA (Fire-Induced Radiological Integrated Assessment) [474], [475]. The FIRIA project was initially launched in 2018, with phase 1 (2018–2021) focused on the development of tools and methodologies for conducting quantitative fire risk assessments. These methodology aim to quantify fire risks based on factors such as fire frequency, potential consequences, and the performance of fire safety systems. However, transitioning to phase 2 (2022–2025), known as the "production phase", CERN is now applying the developed methodologies to several of its facilities, including TDC2/TCC2. This production phase aims to refine and implement these methodologies on a larger scale.

Despite the advancements made by the FIRIA project, probabilistic quantitative risk assessment remains challenging, particularly due to the need for systematic and high-quality data. For probabilistic models to be effective, they require detailed information on past fire accidents, equipment failures data, and environmental conditions. However, the historical fire data at CERN, as previously noted, lacks the consistency and comprehensiveness necessary for precise risk analysis. Even though FIRIA provides a quantitative framework for assessing fire risks, the ability to model fire scenarios probabilistically is limited until more complete and systematic data can be gathered.

Given the limitations of the available historical fire data at CERN, it is not feasible to directly use this information for probabilistic risk assessments. The data lacks the systematic detail required for accurately modelling fire frequency, particularly in complex and aging facilities like TDC2/TCC2. As a result, to develop fire scenarios and determine probabilities, it is necessary to refer to similar fire frequencies documented in the literature. This can be particularly

challenging when analysing a unique facility like CERN. However, comparisons can be drawn with other industries and environments that share characteristics with CERN's underground experimental facilities, such as high-tech laboratories, industrial plants, or power generation facilities, where fire risks are similarly driven by chosen scenarios. By adopting fire frequency data from comparable environments, a more credible basis for estimating the probability of fire events in the selected scenarios can be established, providing a more reliable foundation for risk analysis.

4.5.1 Minimum Necessary and Sufficient Number of Scenarios

The selection of fire scenarios is the initial step in conducting a credible risk assessment for the fire only scenario. The goal is to capture a range of potential fire events that reflect the real risks within a facility like CERN's TDC2/TCC2 cavern, without overwhelming the analysis with unnecessary complexity. Determining the minimum necessary and sufficient number of scenarios requires balancing comprehensiveness with practicality, ensuring that the scenarios chosen represent the key risks without diluting focus through overly detailed or redundant cases (Subsection 3.1.1.2).

4.5.1.1 Fire scenarios in TCC2/TDC2

In the case of the TCC2/TDC2 facility at CERN, an underground experimental facility presents a range of fire hazards due to the presence of combustible materials, complex equipment, and hazardous substances. Since its construction in 1974, the facility has aged over 50 years, with several parts and installations deteriorating, and some components remaining from its initial build. The facility is divided into two operational modes:

- Run mode (when the beam is active and access is restricted): During this phase, the facility is shut down, and no personnel are allowed, except for emergency interventions.
- Shutdown mode (when supervised access is allowed for maintenance and other activities): During technical stops, supervised access is granted under strict protocols.

The facility's design, age, and specific components lead to multiple fire risks that must be accounted for in any risk assessment. Given the complexity and the varied fire hazards, a minimum necessary and sufficient number of fire scenarios must be chosen.

TCC2: A 130m long, 16m wide cavern with a maximum height of 10m and a total area of 2,080m².

TDC2: A 228m long tunnel, 6 to 10m wide, with an average height of 4m and a total area of 1,908m².

The minimum necessary and sufficient number of fire scenarios are selected and presented in Table 21 followed the rationality as described in Subsection 3.1.1.2.

Fire Origin	Location	Description
Electrical	Junction area of TCC2 (near TA801); Blocking	A fire in 13 cable trays located in the junction area between TCC2 and TDC2. The fire could spread both upwards and downwards due to the arrangement of
Electrical	Central section of TCC2; Blocking Exit Door 3	A fire involving the exposed resin in a quadrupole magnet. Assumes no melting, with only the exposed part of the resin burning.
Electrical	Central section of TCC2; Blocking Exit Door 3	Assumes that the resin has melted and forms a pool fire over a 9 m² area. This is a conservative worst-case scenario.
Mechanical	Junction area of TCC2 (near TA801); Blocking	A fire involving a transport vehicle such as a forklift during technical shutdowns. Could block evacuation paths.
Electrical + Combined	Central section of TCC2; Blocking Exit Door 3	A compounded fire where a magnet resin fire propagates to nearby cables, leading to a combined fire.
Electrical + Mechanical	TDC2; Blocking Exit Door 1	A compounded fire where a vehicle fire leads to magnet resin ignition, which spreads to cable type trays mentied above.

Table 21: Summary of Selected Fire Scenarios

Scenario ID	Fire Source	Maximum HRR	Probability	
			Run	Shutdown
CFS1	Cable Trays	15 MW	1.56E-03	2.91E-03
CFS2	Small Magnet Resin	0.09 MW	9.78E-06	4.82E-06
CFS3	Large Magnet Resin	2.75 MW	9.78E-06	4.82E-06
CFS4	Transport Vehicle	0.8 MW	0.00E+00	9.90E-06
CFS5	Cable Tray + Magnet Resin	3.7 MW	2.28E-08	4.25E-08
CFS6	Cable Tray + Magnet Resin + Vehicle	4.4 MW	0.00E+00	4.90E-12

The TCC2/TDC2 facility contains a wide variety of fire hazards due to its diverse infrastructure, including warm dipole and quadrupole magnets, cable trays, targets, XTAX (Target Attenuator eXperimental areas, a mobile dump collimator used to dump or control beam acceptance) [476] and TCSC (Splitter collimator) [477]. Significant beam losses on components such as the TCSC separation septum and the presence of secondary beam production targets also make this area one of the most radioactive at CERN. Fire hazards in this context include combustible cables**,** magnet resin in the magnets, and transient fuel loads such as transport vehicles and pallets, which are generally not present during run mode but appear during maintenance activities.

The facility operates an aspiration fire detection system; however, there are several deficiencies in the overall fire safety measures, particularly given the presence of hazardous materials and equipment.

The fire scenarios were modelled and analysed by CERN using the Fire Dynamics Simulator (FDS) to simulate fire spread, HRRs, and the response of fire safety systems, and as outlined in the FIRIA report [478]. To better understand the spatial distribution and fire scenarios within the TCC2/TDC2 facility, Figure 68 below presents an overview of the identified fire scenario locations. The evacuation exits, fire hazards, and the locations where fire accident could occur. For a detailed FDS analysis, HRR curves for each fire scenario are presented in Figure 69, Figure 70, Figure 71 and Figure 72. HRR data were derived from sources such as the CHRISTIFIRE model [479], studies from Lund University on cable materials on the behaviour of magnet resin under heat flux [480], [481]. Vehicle fire data were provided from the FENWICK E15Z-02 experimental forklift fire test [482]. These simulations were conducted to evaluate fire behaviour within the TDC2/TCC2 facility [478].

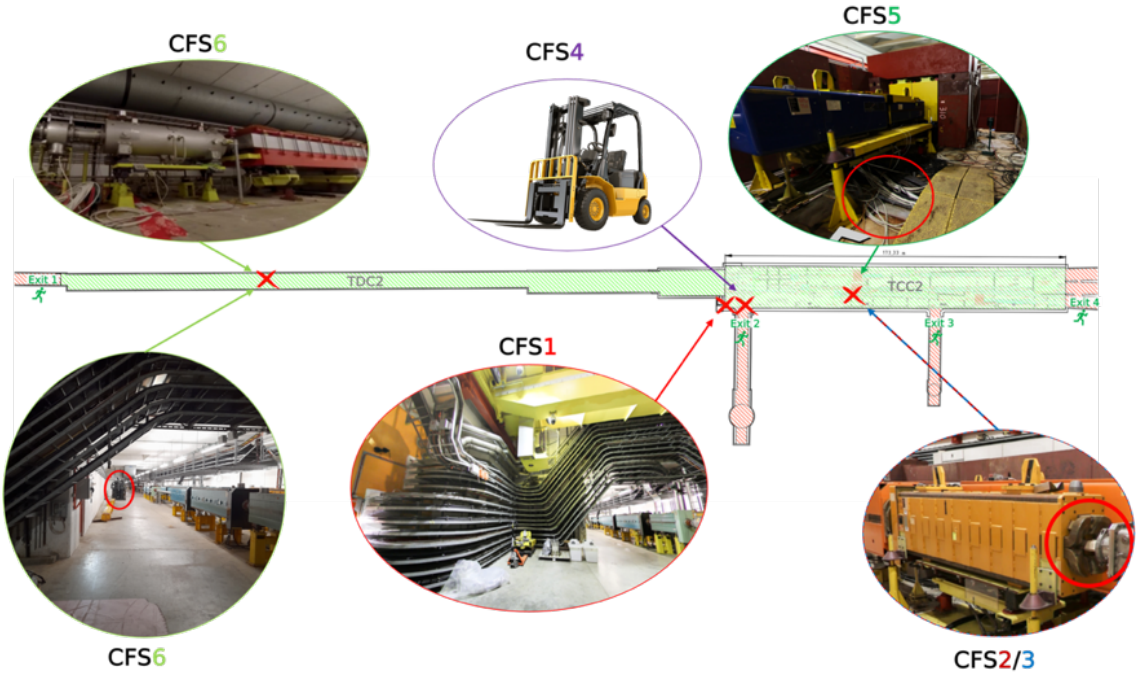

Figure 68: Fire scenario locations (CFS1, CFS2, CFS3, CFS4, CFS5, and CFS6) and Exit locations (Exits 1, 2, 3 and 4) within the TCC2/TDC2 facility.

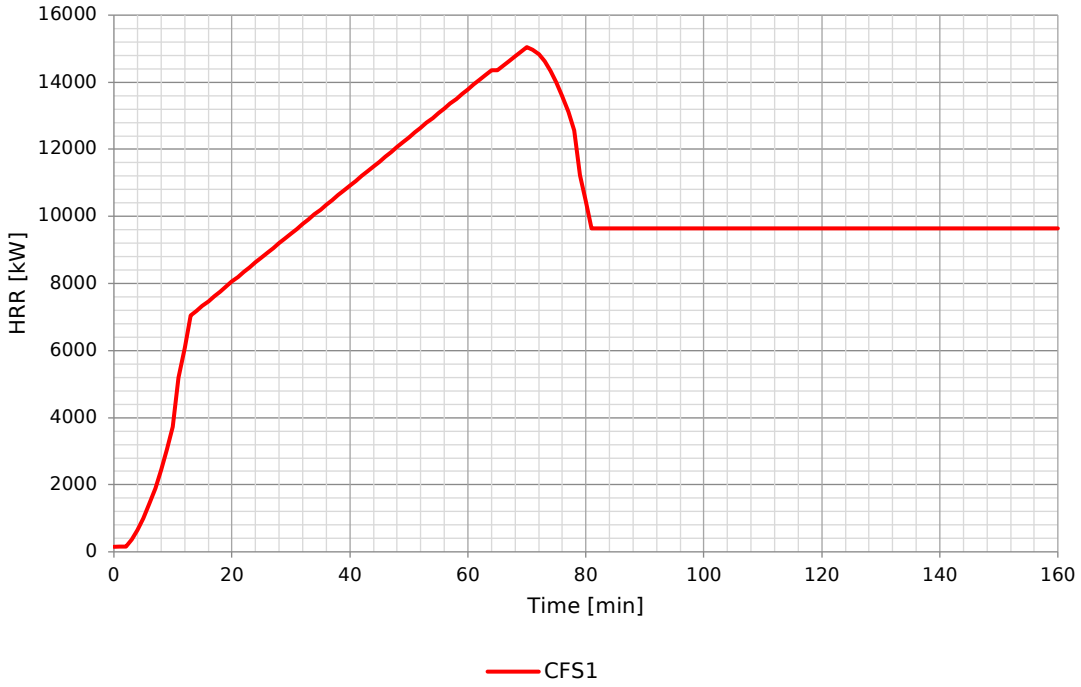

Figure 69: CFS1 (Cable Tray Fire)-A fire scenario involving 13 vertically stacked cable trays located in the junction area between TCC2 and TDC2. The HRR for this scenario reaches 15 MW after a growth phase of 68 minutes.

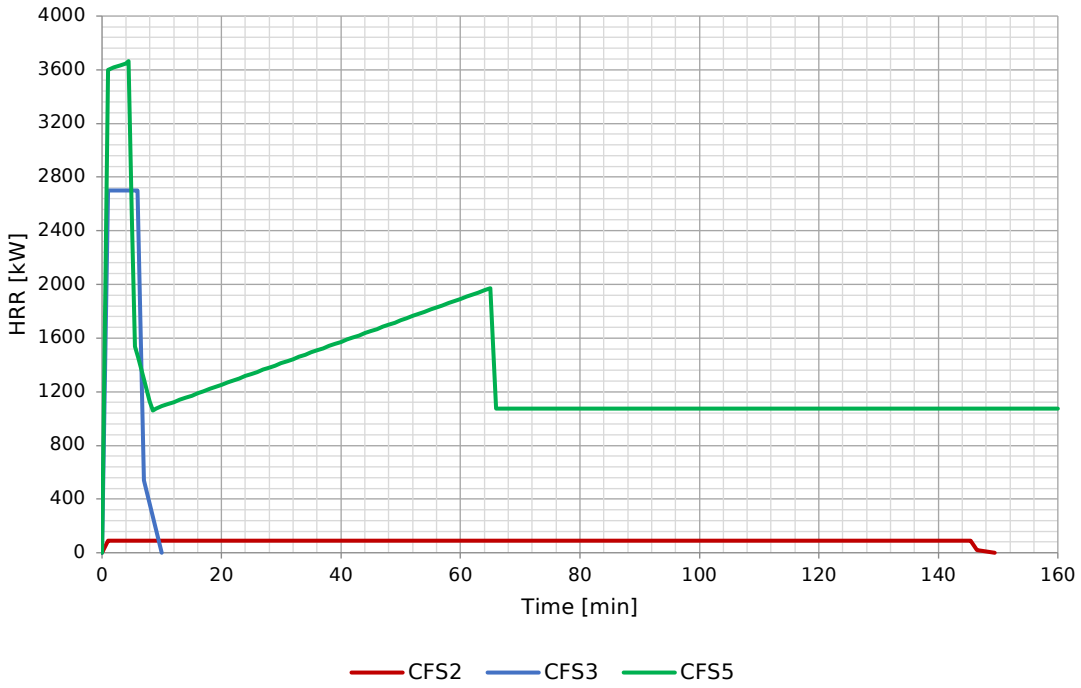

Figure 70: Fire scenarios occurring near beamline T6 within the TCC2 complex: CFS2 (Magnet Resin Fire)-A fire originating from thermosetting resin, peaking at an HRR of 0.09 MW; CFS3 (Magnet Resin Pool Fire)-A scenario where thermoplastic resin melts, forming a pool fire with a peak HRR of 2.75 MW; CFS5 (Combined Magnet Resin and Cable Tray Fire). This compounded scenario involves fire spreading between magnet resin and cable trays, with the fire reaching a peak HRR of 3.7 MW.

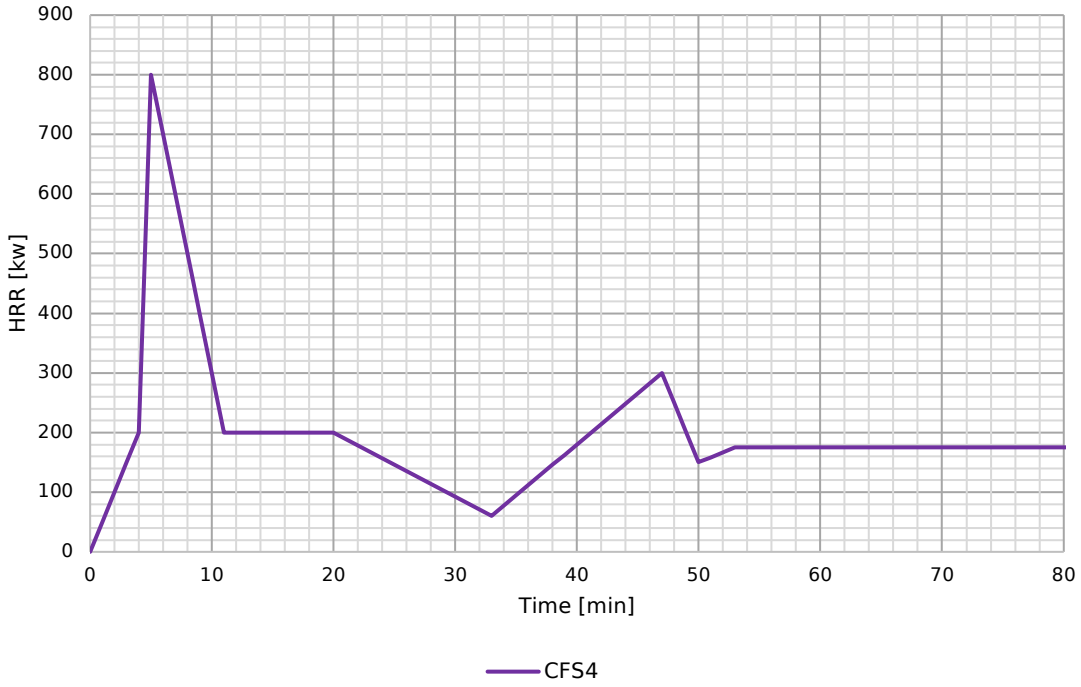

Figure 71: CFS4 (Transport Vehicle Fire)-A fire scenario involving a transport vehicle, such as a forklift truck, located in the TCC2/TDC2 complex during a technical shutdown. The fire could originate from a malfunctioning machine (e.g., short circuit, electrical failure) or an incident where the operator loses control and crashes into powered equipment. The peak HRR for this scenario is 800 kW.

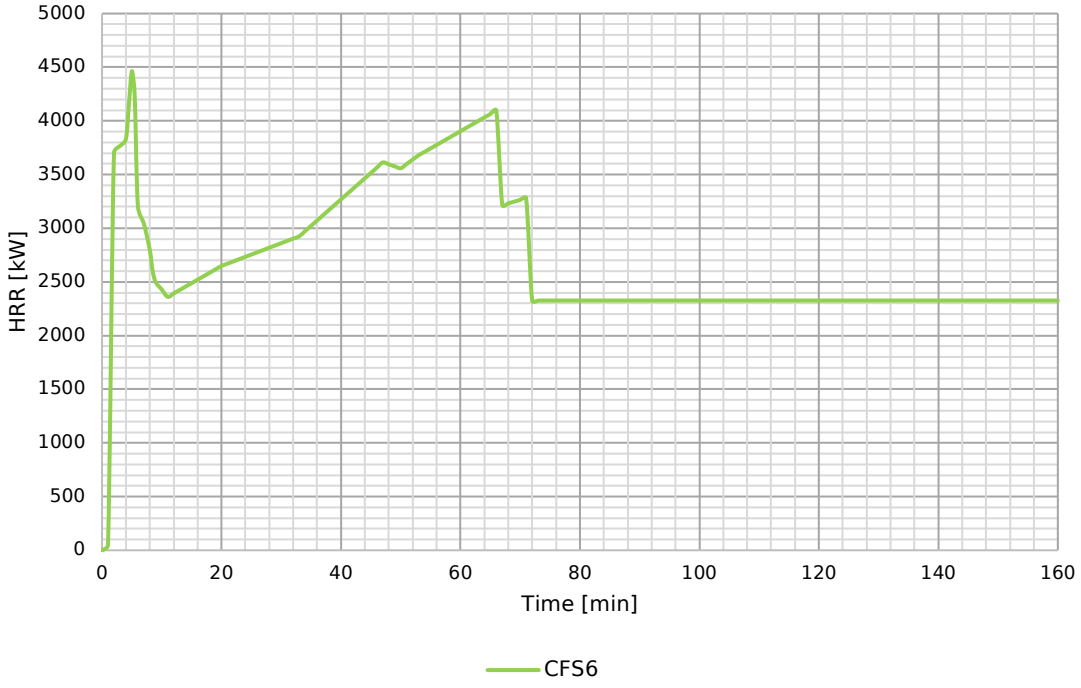

Figure 72: CFS6 (Compounded Transport Vehicle, Magnet Resin, and Cable Tray Fire)-A compounded fire scenario starts with a transport vehicle fire in TDC2, near the beamline, which subsequently ignites nearby fuel packages such as magnet resin and cable trays. The fire escalates as the transport vehicle fire spreads to the magnet resin,

and then to the cable trays located overhead. The peak HRR for this compounded fire is 4.4 MW.

4.5.2 Estimated Probabilities for Chosen Fire Scenarios

In the risk assessment of the TDC2/TCC2 facilities, it is essential to estimate fire probabilities for operational equipment, both during run and shutdown modes. The primary goal is to assess the probability of different fire scenarios based on the identified ignition sources, such as cable trays, magnet equipment and forklifts. Once the initiation probabilities are estimated, event tree analysis is used to calculate the probabilities for each branch of the fire scenario outcomes.

4.5.2.1 Fire Probabilities for Cable Tray and Magnet Equipment

Following the methodology developed by Funk [483] and applied in various facilities at CERN [484], a structured approach is applied to estimate the probability of cable fire initiation in the TCC2 facility. This method, while data-intensive, ensures that key fire risks are identified and quantified with reasonable accuracy. The seven steps of the methodology used in the analysis are outlined below.

4.5.2.1.1 Step 1: Fire Hazards Walkdown

The first step involves identifying potential ignition sources and cable targets within the TCC2 and TDC2 facilities. Based on GIS data [485], magnet equipment units are located in both areas, presenting a significant fire risk due to their electrical activity. The primary targets are the cable trays, which are distributed across the following compartments:

- Compartment A: 2 cable trays, each running 130 metres.
- Compartment B: 5 cable trays, each running 130 metres.
- Compartment C: 13 cable trays, each running 16 metres.
- Compartment D: Equivalent to 2.5 cable trays running along the floor for 130 metres.
- Compartment E: Equivalent to 4 cable trays running along the cavern for 228 metres.

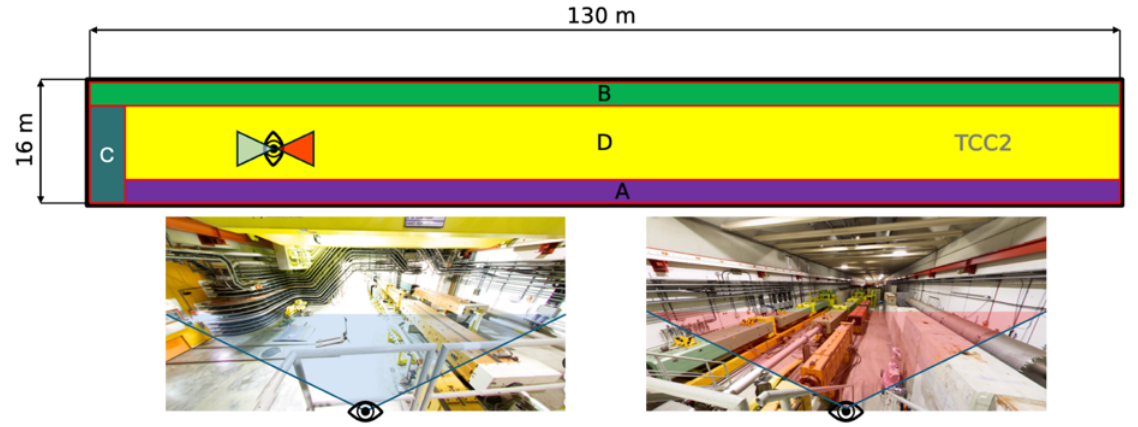

a)

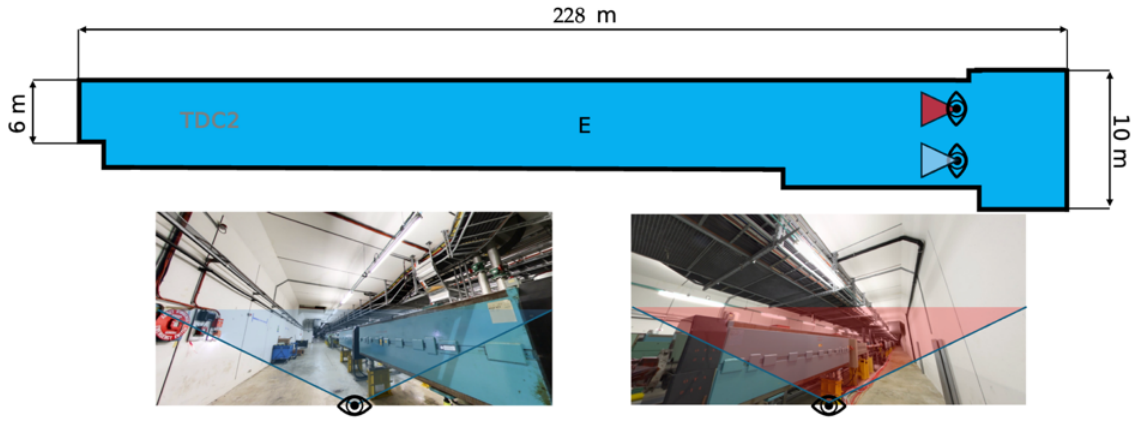

b)

Figure 73: Cable Tray Zones of (a) TCC2 and (b) TDC2 shows the spatial layout of the facility, highlighting different compartments (A, B, C, D, and E) where cable trays and magnet equipment are located. The views at the bottom of each figures (a) and (b) show how the cable trays are arranged across the compartments: A (Purple): Running along the lower part of the layout, this wall has cable trays running along its length; B (Green): Located on the top side of the schematic, showing another set of cable trays; C (Dark Blue): On the left side, housing multiple vertically arranged cable trays; D (Yellow): In the middle of the tunnel, where cables are laid on the floor, with magnet equipment placed centrally; E (Light Blue): In TDC2, cable trays continue along the cavern.

4.5.2.1.2 Step 2: Data Compilation and Boundary Conditions

In this step, data was compiled, and compartments (A, B, C, D and E) were defined based on the layout of the TCC2 and TDC2 facilities. The analysis considers two operating modes:

- Run mode (67% of the time): All equipment is energized, presenting both external and self-ignited fire risks.
- Shutdown mode (33% of the time): Equipment is de-energized, reducing the likelihood of fire, particularly self-ignited fires.

The bin count for magnet equipment is 137 units for TCC2 and 108 units for TDC2, which are assumed to be distributed uniformly across the compartments [486], [487], [488]. All cable trays remain energized during Run mode and are de-energized during Shutdown mode.

4.5.2.1.3 Step 3: Zone of Influence (ZOI) Matrix

In this step, the influence of magnet equipment on the cable trays in each compartment is assessed based on proximity. A Zone of Influence (ZOI) matrix is employed to determine the likelihood of a fire affecting the cable trays due to their exposure to the magnet equipment. The ZOI factor represents the level of exposure. For simplicity, a ZOI factor of 1 is assigned to all compartments, reflecting equal influence across the area (Figure 77 and Figure 78).

4.5.2.1.4 Step 4: External Cable Fire Calculation

In this step, the external cable fire frequency for each compartment is calculated. The calculation is based on several key assumptions:

- Baseline Fire Frequency for magnet unit: 2.00E-03 per year (chosen as a conservative estimate due to the lack of specific data in the literature).
- Total Units: TCC2 has 137 magnet units, and TDC2 has 108 magnet units.
- ZOI Factor: 1.0 for all compartments (as determined in Step 3).
- Operating Mode Fractions: 0.67 for Run mode (67% of the time) and 0.33 for Shutdown mode (33% of the time).

The external fire frequency for each compartment can be calculated using the following formulas:

Run mode (33%):

$$F_{external} = \left(\frac{\text{Baseline Frequency}}{\text{Total Units}}\right) \cdot \text{Units in Compartment} \cdot \text{ZOI Factor} \cdot 0.67 \quad (106)$$

Shutdown mode (33%):

$$F_{external} = \left(\frac{\text{Baseline Frequency}}{\text{Total Units}}\right) \cdot \text{Units in Compartment} \cdot \text{ZOI Factor} \cdot 0.33 \quad (107)$$

TCC2 EXTERNAL CABLE FIRE (SHUTDOWN)						
Bin ID	Count	Function	$Freq_{ind}$	$Freq_{comp}$	ZOI	Bin Totals
Magnet	0	N	1.46E-05	0.00E+00	1	0.00E+00
Weld/Cut	1	Y	2.77E-04	2.77E-04	1	2.77E-04
Transients	1	Y	4.28E-03	4.28E-03	1	4.28E-03
Maintenance	1	Y	4.28E-03	4.28E-03	1	4.28E-03
					TOTAL	**8.83E-03**
TCC2 EXTERNAL CABLE FIRE (RUN)						
Bin ID	Count	Function	$Freq_{ind}$	$Freq_{comp}$	ZOI	Bin Totals
Magnet	137	Y	1.46E-05	2.00E-03	1	2.00E-03
Weld/Cut	0	N	2.77E-04	0.00E+00	1	0.00E+00
Transients	0.05	Y	4.28E-03	2.14E-04	1	2.14E-04
Maintenance	0	N	4.28E-03	0.00E+00	1	0.00E+00
					TOTAL	**2.21E-03**

TDC2 EXTERNAL CABLE FIRE (SHUTDOWN)						
Bin ID	Count	Function	$Freq_{ind}$	$Freq_{comp}$	ZOI	Bin Totals
Magnet	0	N	0.00E+00	0.00E+00	1	0.00E+00
Weld/Cut	1	Y	2.77E-04	2.77E-04	1	2.77E-04
Transients	1	Y	4.28E-03	4.28E-03	1	4.28E-03
Maintenance	1	Y	4.28E-03	4.28E-03	1	4.28E-03
					TOTAL	**8.83E-03**
TDC2 EXTERNAL CABLE FIRE (RUN)						
Bin ID	Count	Function	$Freq_{ind}$	$Freq_{comp}$	ZOI	Bin Totals
Magnet	108	Y	1.85E-05	2.00E-03	1	2.00E-03
Weld/Cut	0	N	2.77E-04	0.00E+00	1	0.00E+00
Transients	0.05	Y	4.28E-03	2.14E-04	1	2.14E-04
Maintenance	0	N	4.28E-03	0.00E+00	1	0.00E+00
					TOTAL	**2.21E-03**

Figure 74: Analysis of External Cable Fire for TDC2 and TCC2 in Shutdown and Run modes.

4.5.2.1.5 Step 5: Self-Ignited Cable Fire Calculation

The self-ignited cable fire frequency is calculated based on the distribution of cable types in each compartment and the baseline frequency for self-ignited fires. For the TDC2/TCC2 facility, the breakdown of self-ignited cable fire frequencies is taken from Table 22. The self-ignited cable fire frequency is calculated based on the distribution of cable types in each compartment, using baseline fire frequencies provided in NUREG-2169 [489] . Although these values were initially developed for nuclear facilities, the methodology has been adapted for the specific conditions at CERN. The frequencies have been adjusted by dividing the plant-wide probabilities from NUREG-2169 by the number of relevant items at CERN to derive the individual ignition source probabilities for each bin.

Further refinements to the NUREG-2169 methodology are made by addressing specific hazards present at CERN, including transient fire risks and compartmentalised analysis. While the original nuclear industry methodology utilises a generalised bin for self-ignited cable fires, this analysis implements more tailored parameters that consider the characteristics of the circuits specific to CERN. The refined breakdown of self-ignited cable fire frequencies is

presented in from Table 22, illustrating the customized approach to the facility's cable configurations.

Table 22: Breakdown of Self-Ignited Cable Fire Basic Event Frequencies [483].

Bin Description	**Mean**
Self-ignited cable fires (plant wide)	7.02E-4
Self-ignited cable fires – Control power	7.02E-5
Self-ignited cable fires – 400 V power	2.81E-4
Self-ignited cable fires – 18 kV power	3.51E-4
400 V Power circuit breaker failure (60)	1.53E-1
18 kV Power circuit breaker failure (20)	5.10E-2
Molded case circuit breaker (80)	4.08E-1
18 kV overcurrent challenge	1.35E-1
400 V overcurrent challenge	1.20E-2
Control power overcurrent challenge	4.22E-4

Three types of cables are considered: Control Power, 400 V Power, and 18 kV Power. Each of these has different baseline fire frequencies due to varying dimensions, insulation properties, and materials. For more accurate estimations, the calculation is based on known cable tray lengths and standard weights per meter for each cable type.

The weight of each type of cable is approximated using manufacturer data [490], [491], [492], [493], with Control Power cables weighing around 0.4 kg/m, 400 V Power cables weighing approximately 1.2 kg/m, and 18 kV Power cables at around 3.0 kg/m. These weights are applied to the cable tray lengths in the TDC2/TCC2 facility, which vary across different compartments.

The total weight of cables is calculated as:

$$\text{Weight}_{\text{Cable Type}} = \text{Weight per Meter} \cdot \text{Length of Cable} \tag{108}$$

And then the fraction of each cable type per tray:

$$\text{Fraction}_{\text{Cable Type}} = \frac{\text{Weight}_{\text{Cable Type}}}{\text{Total Weight}} \tag{109}$$

Table 23: Estimated cable weights and fractions for each compartment in TDC2/TCC2 facility.

Compartment	Control Power Weight (kg)	400 V Power Weight (kg)	18 kV Power Weight (kg)	Total Weight (kg)	Control Power Fraction	400 V Power Fraction	18 kV Power Fraction
A	104	312	780	1196	0.087	0.261	0.652
B	260	780	1950	2990	0.087	0.261	0.652
C	52	156	390	588	0.087	0.261	0.652
D	130	390	375	1495	0.087	0.261	0.652
E	364.8	1094.4	2736	41952	0.087	0.261	0.652

In each compartment, the cable fractions are calculated based on the total weight of cables (Table 23). Since the same baseline assumptions for cable types are used across all compartments, the proportions of cable types in each sector are identical, leading to consistent fire frequency calculations across compartments. Due to the complexity and limitations in the available data on cables, it was not possible to obtain the observed values directly from the facility.

In order to calculate the self-ignited fire frequency for each cable type, the cable fractions derived from the total cable weight in each compartment are used (Table 23). The formula for the self-ignited fire frequency of a specific cable type is as follows:

$$\text{Freq}_{\text{self-ignited, Cable Type}} = \text{Freq\_site} \cdot \text{Fraction}_{\text{Cable Type}} \cdot \lambda_{\text{breaker}} \cdot \lambda_{\text{protection}} \quad (110)$$

To calculate the total frequency of self-ignited fires, the frequencies for each cable type are summed.

TCC2 SELF-IGNITED CABLE FIRES COMPARTMENT A (RUN)							
Circuit Class	Fraction	Energized	$Freq_{site}$	$Freq_{comp}$	$\lambda_{breaker}$	$\lambda_{protection}$	SI Totals
Control Power	9%	Y	7.02E-05	6.10E-06	4.08E-01	1.66E-01	1.02E-06
400 V Power	26%	Y	2.81E-04	7.33E-05	1.53E-01	2.34E-02	1.72E-06
18 kV Power	65%	Y	3.51E-04	2.29E-04	5.10E-02	2.60E-03	5.95E-07
						TOTAL	**3.33E-06**
TCC2 SELF-IGNITED CABLE FIRES COMPARTMENT B (RUN)							
Circuit Class	Fraction	Energized	$Freq_{site}$	$Freq_{comp}$	$\lambda_{breaker}$	$\lambda_{protection}$	SI Totals
Control Power	9%	Y	7.02E-05	6.10E-06	4.08E-01	1.66E-01	1.02E-06
400 V Power	26%	Y	2.81E-04	7.33E-05	1.53E-01	2.34E-02	1.72E-06
18 kV Power	65%	Y	3.51E-04	2.29E-04	5.10E-02	2.60E-03	5.95E-07
						TOTAL	**3.33E-06**
TCC2 SELF-IGNITED CABLE FIRES COMPARTMENT C (RUN)							
Circuit Class	Fraction	Energized	$Freq_{site}$	$Freq_{comp}$	$\lambda_{breaker}$	$\lambda_{protection}$	SI Totals
Control Power	9%	Y	7.02E-05	6.10E-06	4.08E-01	1.66E-01	1.02E-06
400 V Power	26%	Y	2.81E-04	7.33E-05	1.53E-01	2.34E-02	1.72E-06
18 kV Power	65%	Y	3.51E-04	2.29E-04	5.10E-02	2.60E-03	5.95E-07
						TOTAL	**3.33E-06**
TCC2 SELF-IGNITED CABLE FIRES COMPARTMENT D (RUN)							
Circuit Class	Fraction	Energized	$Freq_{site}$	$Freq_{comp}$	$\lambda_{breaker}$	$\lambda_{protection}$	SI Totals
Control Power	9%	Y	7.02E-05	6.10E-06	4.08E-01	1.66E-01	1.02E-06
400 V Power	26%	Y	2.81E-04	7.33E-05	1.53E-01	2.34E-02	1.72E-06
18 kV Power	65%	Y	3.51E-04	2.29E-04	5.10E-02	2.60E-03	5.95E-07
						TOTAL	**3.33E-06**
TDC2 SELF-IGNITED CABLE FIRES COMPARTMENT E (RUN)							
Circuit Class	Fraction	Energized	$Freq_{site}$	$Freq_{comp}$	$\lambda_{breaker}$	$\lambda_{protection}$	SI Totals
Control Power	9%	Y	7.02E-05	6.10E-06	4.08E-01	1.66E-01	1.02E-06
400 V Power	26%	Y	2.81E-04	7.33E-05	1.53E-01	2.34E-02	1.72E-06
18 kV Power	65%	Y	3.51E-04	2.29E-04	5.10E-02	2.60E-03	5.95E-07
N/A=1; Y=1; N=0						**TOTAL**	**3.33E-06**

Figure 75: Self-Ignited Cable Fire Analysis for components A, B, C, and D of TCC2 and component E of TDC2 during Run mode.

TCC2 SELF-IGNITED CABLE FIRES COMPARTMENT A (SHUTDOWN)							
Circuit Class	Fraction	Energized	$Freq_{site}$	$Freq_{comp}$	$\lambda_{breaker}$	$\lambda_{protection}$	SI Totals
Control Power	9%	N	7.02E-05	6.10E-06	4.08E-01	1.66E-01	0.00E+00
400 V Power	26%	N	2.81E-04	7.33E-05	1.53E-01	2.34E-02	0.00E+00
18 kV Power	65%	N/A	3.51E-04	2.29E-04	5.10E-02	2.60E-03	5.95E-07
						TOTAL	**5.95E-07**
TCC2 SELF-IGNITED CABLE FIRES COMPARTMENT B (SHUTDOWN)							
Circuit Class	Fraction	Energized	$Freq_{site}$	$Freq_{comp}$	$\lambda_{breaker}$	$\lambda_{protection}$	SI Totals
Control Power	9%	N	7.02E-05	6.10E-06	4.08E-01	1.66E-01	0.00E+00
400 V Power	26%	N	2.81E-04	7.33E-05	1.53E-01	2.34E-02	0.00E+00
18 kV Power	65%	N/A	3.51E-04	2.29E-04	5.10E-02	2.60E-03	5.95E-07
						TOTAL	**5.95E-07**
TCC2 SELF-IGNITED CABLE FIRES COMPARTMENT C (SHUTDOWN)							
Circuit Class	Fraction	Energized	$Freq_{site}$	$Freq_{comp}$	$\lambda_{breaker}$	$\lambda_{protection}$	SI Totals
Control Power	9%	N	7.02E-05	6.10E-06	4.08E-01	1.66E-01	0.00E+00
400 V Power	26%	N	2.81E-04	7.33E-05	1.53E-01	2.34E-02	0.00E+00
18 kV Power	65%	N/A	3.51E-04	2.29E-04	5.10E-02	2.60E-03	5.95E-07
						TOTAL	**5.95E-07**
TCC2 SELF-IGNITED CABLE FIRES COMPARTMENT D (SHUTDOWN)							
Circuit Class	Fraction	Energized	$Freq_{site}$	$Freq_{comp}$	$\lambda_{breaker}$	$\lambda_{protection}$	SI Totals
Control Power	9%	N	7.02E-05	6.10E-06	4.08E-01	1.66E-01	0.00E+00
400 V Power	26%	N	2.81E-04	7.33E-05	1.53E-01	2.34E-02	0.00E+00
18 kV Power	65%	N/A	3.51E-04	2.29E-04	5.10E-02	2.60E-03	5.95E-07
						TOTAL	**5.95E-07**
TDC2 SELF-IGNITED CABLE FIRES COMPARTMENT E (SHUTDOWN)							
Circuit Class	Fraction	Energized	$Freq_{site}$	$Freq_{comp}$	$\lambda_{breaker}$	$\lambda_{protection}$	SI Totals
Control Power	9%	N	7.02E-05	6.10E-06	4.08E-01	1.66E-01	0.00E+00
400 V Power	26%	N	2.81E-04	7.33E-05	1.53E-01	2.34E-02	0.00E+00
18 kV Power	65%	N/A	3.51E-04	2.29E-04	5.10E-02	2.60E-03	5.95E-07
N/A=1; Y=1; N=0						**TOTAL**	**5.95E-07**

Figure 76: Self-Ignited Cable Fire analysis for components A, B, C, and D of TCC2 and component E of TDC2 during Shutdown mode.

4.5.2.1.6 Step 6: Termination Equipment Fire Calculation

The fire risk for termination equipment fires is calculated by considering the probability of fire propagation along cables connected to the magnet equipment (termination points). This calculation depends on whether the cables are protected (e.g., sealed conduits or flexible conduits) and the assigned propagation factor.

Key assumptions include the following: Magnet equipment is connected to cable trays via non-sealed wireways or flexible conduits, increasing the likelihood of fire propagation. A propagation factor of 1 is assumed for non-sealed wireways, indicating full fire propagation. For High-Energy Arcing Fault (HEAF) equipment, such as 400 V and 18 kV power systems, the propagation factor is reduced to 0.7 based on relevant research [483], [484].

TCC2 ZONE OF INFLUENCE MATRIX (RUN/SHUTDOWN)					
IS/Target	A	B	C	D	Consolidated
Magnet	1	1	1	1	1
Weld/Cut	1	1	1	1	1
Transients	1	1	1	1	1
Maintenance	1	1	1	1	1

TCC2 TERMINATION FIRE - HEAF (SHUTDOWN)					
HEAF EQ ID	Energized	Volt Class	$Freq_{ind}$	Prop Factor	$Freq_{comp}$
Power Pnl (LV)	N	400 V	1.52E-04	7.00E-01	0.00E+00
				TOTAL	**0.00E+00**

TCC2 TERMINATION FIRE - HEAF (Run)					
HEAF EQ ID	Energized	Volt Class	$Freq_{ind}$	Prop Factor	$Freq_{comp}$
Power Pnl (LV)	Y	400 V	1.52E-04	7.00E-01	1.06E-04
				TOTAL	**1.06E-04**

TCC2 TERMINATION FIRE - PROPAGATION (SHUTDOWN)			
IS/Target	$Freq_{ind}$	Prop Factor	$Freq_{comp}$
Magnet	1.46E-05	0	0.00
		TOTAL	**0.00E+00**

TCC2 TERMINATION FIRE - PROPAGATION (RUN)			
IS/Target	$Freq_{ind}$	Prop Factor	$Freq_{comp}$
Magnet	1.46E-05	0	0.00
		TOTAL	**0.00E+00**

Figure 77: Zone of Influence Assessment and Terminal Equipment Cable Fire analysis for TCC2 during Run and Shutdown modes.

TDC2 ZONE OF INFLUENCE MATRIX (RUN/SHUTDOWN)					
IS/Target	A	B	C	D	Consolidated
Magnet	1	1	1	1	1
Weld/Cut	1	1	1	1	1
Transients	1	1	1	1	1
Maintenance	1	1	1	1	1

TDC2 TERMINATION FIRE - HEAF (SHUTDOWN)					
HEAF EQ ID	Energized	Volt Class	$Freq_{ind}$	Prop Factor	$Freq_{comp}$
Power Pnl (LV)	N	400 V	1.52E-04	7.00E-01	0.00E+00
				TOTAL	**0.00E+00**

TDC2 TERMINATION FIRE - HEAF (RUN)					
HEAF EQ ID	Energized	Volt Class	$Freq_{ind}$	Prop Factor	$Freq_{comp}$
Power Pnl (LV)	Y	400 V	1.52E-04	7.00E-01	1.06E-04
				TOTAL	**1.06E-04**

TDC2 TERMINATION FIRE - PROPAGATION (SHUTDOWN)			
IS/Target	$Freq_{ind}$	Prop Factor	$Freq_{comp}$
Magnet	1.46E-05	0	0.00
		TOTAL	**0.00E+00**

TDC2 TERMINATION FIRE - PROPAGATION (RUN)			
IS/Target	$Freq_{ind}$	Prop Factor	$Freq_{comp}$
Magnet	1.46E-05	0	0.00
		TOTAL	**0.00E+00**

Figure 78: Zone of Influence Assessment and Terminal Equipment Cable Fire analysis for TDC2 during Run and Shutdown modes.

4.5.2.1.7 Step 7: Total Fire Risk Calculation

In final step, the calculated fire frequencies for external fires (Figure 74), self-ignited fires (Figure 75 and Figure 76), and termination fires (Figure 77 and Figure 78) are combined to determine the total fire risk for each compartment (A, B, C, D and E) within the TDC2/TCC2 facility in both Run (Figure 80) and Shutdown (Figure 79) modes.

CABLE FIRE IGNITION SOURCE & TARGET INVENTORY

TDC2 and TCC2 Shutdown Scenario Description

Ignition Source	Calculated Frequency	Per Shutdown (33 % per year)
TCC2 EXTERNAL CABLE FIRE	8.83E-03	2.91E-03
TDC2 EXTERNAL CABLE FIRE	8.83E-03	2.91E-03
TCC2 TERMINATION FIRE - PROPAGATION	0.00E+00	0.00E+00
TDC2 TERMINATION FIRE - PROPAGATION	0.00E+00	0.00E+00
TCC2 TERMINATION FIRE - HEAF	0.00E+00	0.00E+00
TDC2 TERMINATION FIRE - HEAF	0.00E+00	0.00E+00
SELF-IGNITED CABLE FIRES		
Compartment A	5.95E-07	1.96E-07
Compartment B	5.95E-07	1.96E-07
Compartment C	5.95E-07	1.96E-07
Compartment D	5.95E-07	1.96E-07
Compartment E	5.95E-07	1.96E-07

TCC2 Total Cable Fire Frequency	**8.83E-03**	**Total Cable Fire Frequency During Shutdown (33% of the year)**	**2.91E-03**
TDC2 Total Cable Fire Frequency	**8.83E-03**	**Total Cable Fire Frequency During Shutdown (33% of the year)**	**2.91E-03**

Ignition Source Inventory

Bin ID	Energized
Magnet	N
Magnet	N
Power Pnl (LV)	N
Welding/Cutting	Y
Transients	Y
Maintenance Activity	Y

Ignition Source Frequency (Events/year)

Bin ID	Bin Count	$Freq_{base}$	$Freq_{ind}$
Magnet TCC2	137	2.00E-03	1.46E-05
Magnet TDC2	108	2.00E-03	1.85E-05
Power Pnl (LV)	Unknown	1.52E-04	1.52E-04
Weld/Cut	Unknown	2.77E-04	2.77E-04
Transients	Unknown	4.28E-03	4.28E-03
Maintenance	Unknown	4.28E-03	4.28E-03

Targets

Raceway	Type	Function	Energized
A	Tray	*N/A	Y
B	Tray	*N/A	Y
C	Tray	*N/A	Y
D	Tray	*N/A	Y
E	Tray	*N/A	Y

*N/A indicates that the specific function of the cable trays (whether they are Control Power, Control, Power, or Signal) is not known at this time.

Figure 79: Calculated probabilities for TCC2 and TDC2 Shutdown scenarios: Ignition Source Frequency, Ignition Source Inventory, and Compartment Targets.

CABLE FIRE IGNITION SOURCE & TARGET INVENTORY			
TDC2 and TCC2 Run Scenario Description			
Ignition Source		Calculated Frequency	Per Run (67 % per year)
TCC2 EXTERNAL CABLE FIRE		2.21E-03	1.48E-03
TDC2 EXTERNAL CABLE FIRE		2.21E-03	1.48E-03
TCC2 TERMINATION FIRE - PROPAGATION		0.00E+00	0.00E+00
TDC2 TERMINATION FIRE - PROPAGATION		0.00E+00	0.00E+00
TCC2 TERMINATION FIRE - HEAF		1.06E-04	7.13E-05
TDC2 TERMINATION FIRE - HEAF		1.06E-04	7.13E-05
SELF-IGNITED CABLE FIRES			
Compartment	A	3.33E-06	2.23E-06
	B	3.33E-06	2.23E-06
	C	3.33E-06	2.23E-06
	D	3.33E-06	2.23E-06
	E	3.33E-06	2.23E-06

TCC2 Total Cable Fire Frequency	**2.33E-03**	**Total Cable Fire Frequency During Run (67% of the year)**	**1.56E-03**
TDC2 Total Cable Fire Frequency	**2.32E-03**	**Total Cable Fire Frequency During Run (67% of the year)**	**1.56E-03**

Ignition Source Inventory	
Bin ID	Energized
Magnet	Y
Magnet	Y
Power Pnl (LV)	Y
Welding/Cutting	N
Transients	Y
Maintenance Activity	N

Ignition Source Frequency (Events/year)			
Bin ID	Bin Count	$Freq_{base}$	$Freq_{ind}$
Magnet TCC2	137	2.00E-03	1.46E-05
Magnet TDC2	108	2.00E-03	1.85E-05
Power Pnl (LV)	Unknown	1.52E-04	1.52E-04
Weld/Cut	Unknown	2.77E-04	2.77E-04
Transients	Unknown	4.28E-03	4.28E-03
Maintenance	Unknown	4.28E-03	4.28E-03

Targets			
Raceway	Type	Function	Energized
A	Tray	*N/A	Y
B	Tray	*N/A	Y
C	Tray	*N/A	Y
D	Tray	*N/A	Y
E	Tray	*N/A	Y

*N/A indicates that the specific function of the cable trays (whether they are Control Power, Control, Power, or Signal) is not known at this time.

Figure 80: Calculated probabilities for TCC2 and TDC2 Run scenarios: Ignition Source Frequency, Ignition Source Inventory, and Compartment Targets.

4.5.2.2 Fire Probability for Forklift

In the TDC2/TCC2 facility, where forklifts are present in shutdown mode, it is essential to consider the fire probabilities associated with these vehicles. Based on industrial data reviewed by Cadwallader [494], forklifts and other equipment entering facilities can present a fire hazard, with potential causes ranging from hot exhaust lines to engine malfunctions. For electric-driven forklifts, which are commonly used indoors, the fire frequency is estimated to be around 3.0E-05 per year. In contrast, diesel-driven forklifts have a fire frequency approximately an order of magnitude higher, and propane-driven forklifts are expected to have similar fire risks unless more specific data is available. Since the forklifts operate only during shutdown mode, which constitutes 33% of the year, the fire

frequency for electric-driven forklifts is adjusted to 9.9E-06 per year in this analysis.

4.6 Performance-Based Design in Underground System

Assessment of emergency evacuation design from confined environment [495] involves a comprehensive review of used procedures and a suitable specific development of protocols to ensure a validated level of safety during hazard scenarios.

Design-scenario definition process includes the identification of potential hazard-exposure scenarios, infrastructure capacity, layout [496], [497], representative human behaviour model under smoke [103], [498], protection systems [499], development of straightforward communication, [500], [501] and evacuation trainings [502]. In the context of fire-related accidents in underground systems [102], [503], [504], [505], the confined space and limited exits significantly affect evacuation success [506]. Historical accidents in tunnels [507], [508] and mines [509] have demonstrated the devastating outcomes.

Nowadays, Performance-Based Design (PBD) approaches [510], [511], [512], [513], [514] enable designers to identify right models to predict the effectiveness of evacuation plans under various conditions [515]. The reliability of evacuation models is often scrutinized due to the complexity of human behaviour in emergency situations, particularly in road tunnels [516]. The literature also offers several PBD case studies in different framework such as for high-rise building [517], [518], hospital [519], [520], school [521] and ship [522].

The concept of PBD marks a significant progression toward customising the design of infrastructures to fulfil specified performance benchmarks during fire accidents [523]. The evacuation models help designers clarify evacuation dynamics and improving effectiveness of evacuation plan. The work of Ronchi et al. [524], has contributed significantly to the improvement of developments of modelling. However, one of the key challenges in this field is the uncertainty of human behaviour during evacuation [525]. This concept encompasses a variety of factors [526] that are difficult to accurately predict and model, such as the location, actions of occupants, and physical characteristics, all of which affect movement speed and behaviour.

Numerous studies have been conducted to address the uncertainty of human behaviour during evacuations [527], aiming to appreciate and model behavioural

variability which is not directly observable in the accidental scenarios. Babrauskas et al. [528] effectively analyse the RSET/ASET model for its oversimplification of human behaviours, which are likened to "robotic actions" as they described. Thus, undermining the complexity of actual human behaviour in emergency situations. They assert, "these priorities should be reversed—to improve fire safety, it is much more important to study the failures than the successes", challenging the prevailing focus and advocating for a more detailed appreciation of human behaviour's role in evacuation processes. A thorough understanding of such behaviours, especially by analysing failures of egress as well as successes, is fundamental for improving evacuation design. Kobes et al. [529] discussed that fire safety measures and building designs should take into account the interplay between human behaviour and building characteristics. It implies that current design standards may not sufficiently consider this interaction, particularly the psychological aspects of human behaviour in emergency fire situations. Recent study of Haghani et al. [530], incorporating behavioural understanding into engineering practices, allow us to advocate for informed, PBD that better accommodate human behaviour and decisions during fire scenarios. All the above research explores the role of human behaviour in PBD, providing strategies assuring more realistic human behaviour models rather than robotic actions.

Study of Tinaburri discusses evacuation simulation complexities for individuals needing assistance, highlighting the importance of accurate, inclusive modelling and Monte Carlo methods to randomise behavioural variabilities for PBD [520]. These studies aim to generate a variety of evacuation outcomes based on diverse inputs, capturing the uncertainty inherent in human behaviour during emergencies. Such simulations yield a spectrum of evacuation outcomes, enabling researchers to derive statistical measures. Statistical analysis in evacuation studies is for interpreting the vast amounts of data generated during evacuation simulations [531], drills [8] and unannounced evacuation experiments [532]. It helps in understanding patterns, identifying anomalies, and making informed predictions.

In the context of evacuation, the LSF could analogously represent the successful or unsuccessful evacuation of individuals over time, considering various factors such as egress (non-egress), gas toxicity, temperature, structural collapse and other conditions impacting survivability. Here, the LSF would depict whether an individual has not yet evacuated (or has 'survived in place') at different points after the initiation of an evacuation order.

For each primary scenario (S_1), the event tree diagram branches into sub-scenarios $N(S_{1,1})$, $N(S_{1,2})$, …, $N(S_{1,n})$, reflecting various behavioural responses during evacuations with given LSF (Figure 26). We determine the necessary number of simulation runs after the convergence analyses for each scenario based on predefined conditions, ensuring that all relevant behavioural variations are captured across multiple runs (Run 1, Run 2, ..., Run n).

In evacuation assessment, deterministic models preferentially focus on worst-case scenarios, as highlighted by Averill [533]; these models often fail to capture the stochastic nature of human behaviour in evacuations, by rather providing structured but inflexible responses. Probabilistic models incorporate randomness by using pseudo-random sampling from stochastic variables and statistical distributions, offering a more dynamic understanding of human behaviour [534]. This significantly improves our comprehension of evacuation dynamics by factoring in behavioural uncertainty.

The above model should be complemented with both system reliability and total survival criteria. These ensure that the impacts of hazards such as toxic exposure, heat, and reduced visibility on evacuation processes are fully considered [103], [112]. System reliability determines how well evacuation systems (such as alarms or lighting) function under stress, directly influencing the progression of hazards and the success of evacuation efforts. Total survival criteria, governed by the LSF, define the threshold conditions for successful or unsuccessful evacuation, helping to optimize evacuation strategies and improve the chances of safe evacuation.

This study proposes a design optimization approach that accounts for uncertainty and randomness, representing more than just the worst-case scenario but what can realistically occur. By randomizing human behaviour in the model, a credible range of possibilities is properly considered. The rationale for this study arises from the need to improve PBD in response to the dynamic and complex nature of multi-hazard scenarios.

4.6.1 PBD Approach for Multi-Hazard Evacuation

In this subsection of evacuation analysis, an approach to performance-based design (PBD) is presented, integrating techniques from various engineering disciplines, including fire safety engineering and structural analysis. This methodology evaluates egress (or non-egress) and limit state values in each hazard scenarios, identifying potential areas of failure across a range of human

behaviours in multi-hazard scenarios. The process is described in a multi-stage diagram with 4 phases (Figure 82) as illustrated below.

4.6.1.1 Phase 1: Preliminary Assessment

The Preliminary Assessment phase is based on combination of empirical observations, recent data, simulation outcomes, and expert judgment tailored to the individual underground characteristics [497]. The initial phases of analysis focus on the chosen hazard scenarios. Potential hazard scenarios are identified through minimum necessary and sufficient number of scenarios (Subsection 3.1.1.2). Occupant loads are extrapolated from recorded usage statistics, reflecting both average and peak conditions. Occupant characteristics, important for personalising evacuation planning, are profiled using demographic surveys. The underground design is thoroughly reviewed, with the floor plans are translated into a graphical model, where various areas within the facility are representing potential evacuation routes like exits, obstacles, staircases, and corridors. Environmental conditions providing an accurate representation of factors influencing occupant mobility. The reliability and coverage of communication and detection systems are assessed to determine their guaranteed level of performance and availability during each evacuation path. Adaptive by design, this phase integrates new variables (X) as necessary, accommodating the evolving nature of risk and technological advancements [496], [497], [535], [536], [537].

4.6.1.1.1 Step 1: Multi-hazard Scenarios

Let multi hazards scenarios be the defined representative set $\{S_1, S_2, \ldots, S_n\}$ of all possible scenarios for all practical safety purposes. Each scenario S_i is defined by a distinct set of parameters able to identify and describe the scenarios as a set of mutually exclusive ones. The identified group is then representative sample space of the universe (Subsection 3.1.1.2) [538]. These parameters detail both the hazard aspect — the source of danger — and the risk of life for exposed people, which includes the probability and severity of potential consequences for individuals, such as risk of injury or death. Having an exposure map describing a location of a given number of people when a hazard occurs, a measure of the risk to life of exposed people is assessed based on the probability of such events occurring and their consequences. However, in order to calculate the absolute risk, we need to estimate the probability of occurrence of hazard (Subsections 4.3,

4.4.4 and 4.5.2) [539], combine this with the probabilities of the various outcomes associated with each scenario.

4.6.1.1.2 Step 2: Occupant Loads

Define a matrix of occupant loads, where each element o_{ij} represents the occupancy level at location i at time j. The estimation process is hierarchical, utilising the most accurate data available as follows:

$$o_{ij} = \begin{cases} \text{Real time management}^{a}, & \text{if available;} \\ \text{Historical data-derived estimates}^{b}, & \text{if real time data is absent;} \\ \text{MC Simulations } (o_{ij} \mid \text{Parameters})^{c}, & \text{otherwise.} \end{cases} \quad (111)$$

[a][540], [541]; [b][542], [543]; [c][544], [545], [546]

Here, parameters encapsulate any known variability patterns, occupancy limits, and other relevant information guiding the simulations [547].

4.6.1.1.3 Step 3: Occupant Characteristics

Represent the characteristics of occupants as vectors in a multidimensional space Occupant Characteristic = $\{\vec{c}_1, \vec{c}_2, \ldots, \vec{c}_k\}$, with each vector $\vec{c}_k$ corresponding to a set of individual or group traits. These components correspond to distinct attributes, including age, mobility, familiarity with the facility layout and other relevant factors (Table 24). This representation allows a detailed analysis of how specific characteristics may influence the behaviour and effectiveness of the evacuation design procedure [548], [549], [550].

4.6.1.1.4 Step 4: Impact of Facility Design

In this step, the effectiveness of the proposed design process is investigated to identify the desired optimum solution for a given layout. The process begins with the creation of a basic visual map that identifies all critical areas, including rooms, halls, stairs, lifts and exits. This map will be of upmost importance for understanding and evaluating how people move through the facility and identifying potential bottleneck points that could impede evacuation [500], [548], [551], [552], [553].

4.6.1.1.5 Step 5: Environmental Conditions

Environmental conditions are represented by a set, where each element corresponds to a particular environmental factor such as visibility or lighting conditions, which are known to affect evacuation behaviours and speeds [137], [549], [554], [555], [556], [557], [558], [559], [560].

4.6.1.1.6 Communication Plans and Detection Systems

Communication and detection systems are represented by a description of how effective communication (such as alarms and announcements) is at different times and locations within the facility. [137], [561], [562].

The phase presented here is adaptive in nature, designed to encompass additional variables required by the complexity and evolution of the scenario analysed. The basic structure allows for the seamless integration of additional factors should they become relevant during the progress of the modelling work. For instance, if needs arise to cover more detailed aspects of the operational characteristics of the facility or to assimilate new emergency response protocols, these can be encapsulated as a set of new variables, $X = \{x_1, x_2, \ldots, x_m\}$ increases the set of available variables.

4.6.1.2 Phase 2: Modelling

Here, data from Phase 1 is summarized to construct independent and non-independent evacuation scenario models, integrating stochastic elements to account for the uncertainty of real-life emergencies.

4.6.1.2.1 Step 1: Identification of Emergency Type Locations

The knowledge of hazard scenarios from Phase 1 is applied to identify the potential minimum necessary number of locations L within the facility where such hazards could occur [497], [563]. This identification considers the facility's usage patterns and design vulnerabilities identified in the previous phase.

4.6.1.2.2 Step 2: Earthquake and Fire Modelling

For each potential independent and non-independent hazard's location $l_i \in L$, the fire models (FDS) must be developed to simulate the ignition, growth and spread of fire (Subsection 4.5) [102]. As well as structural analysis (IDA) must be

performed to assess structural collapse under different scenarios (Subsection 4.4). These models incorporate the facility's design features, allowing for projections of how independent and dependent hazards could evolve. IDA specifically helps determine in which areas structural collapse occurs under given PGA scenarios.

4.6.1.2.3 Step 3: Evacuation Modelling

The evacuation model is constructed by defining navigation meshes. Once the evacuation model was established, the outputs from the fire (FDS) models were imported, and the identified structural collapse zones from the IDA models were integrated into the evacuation model. This model simulates the movement of evacuees (pre-evacuation and travel times) [564] within the facility [547], [565], taking into account behaviours, collapse zones (which might block the exit path), environmental conditions, including constrains, and communication plans, detection systems and new variables (X).

4.6.1.2.4 Step 4: Randomisation of Human Behaviour in Scenarios

To introduce the randomness observed in real-life emergencies, integrate pseudo-random sampling from statistical distributions is integrated. This enhances the stochastic model's realism by accounting for the identified uncertainties in people's locations, actions, and physical characteristics during an evacuation.

As highlighted by Tavares and Ronchi [566], uncertainties in evacuation modelling can significantly impact the accuracy of simulation results. By employing stochastic simulations using pseudo-random sampling and conducting convergence analyses, these uncertainties are addressed, ensuring that the models more accurately reflect the range of possible human behaviors during emergencies.

In computational simulations, "pseudo-random sampling" refers to the generation of numbers using deterministic algorithms known as pseudo-random number generators (PRNGs). These algorithms produce sequences of numbers that approximate the properties of random sequences. The term "Monte Carlo" simulation is often used broadly to describe methods that rely on repeated random sampling; however, for precision and clarity, we refer to our methods as stochastic simulations using pseudo-random sampling.

Through this process, a range of possible outcomes for each hazard scenario is generated, which are then analysed to assess the reliability of different evacuation plans.

4.6.1.3 Phase 3: Convergence and Validation

In this phase, the accuracy of the evacuation design simulation is validated through a convergence analysis process [525]. Specifically, pseudo-random sampling from statistical distributions is employed to approximate human behaviour stochastically in the simulations. his process includes statistical criteria and computational checks to ensure the stability and reliability of the design simulation outputs, which are influenced by the stochastic elements introduced through the randomisation of human behaviour.

4.6.1.3.1 Step 1: Convergence Analysis

Upon completion of Phase 2 design simulation, n simulations are generated using a pseudo-random sampling method. Each simulation is denoted as SA_1, SA_2 ..., SA_n and the output of the i-th simulation is represented by $M(SA_i)$. The model's convergence is assessed [525] by performing a statistical test to analyse the outputs across these simulations.

4.6.1.3.2 Step 2: Convergence threshold and consecutive runs

A convergence threshold τ is defined, and with a sequence of consecutive runs b, where b is initially set to a predefined value b_0. Convergence for the initial set of simulations is determined using the following criterion:

$$\frac{1}{b}\sum_{i=1}^{b}\left|M(SA_i) - M(SA_{i-1})\right| < \tau \tag{112}$$

indicating that the average change in outputs over b consecutive simulations is below the threshold τ. If this criterion is met, the model is considered to have converged, and no further simulations are required. Otherwise, the iterative refinement process described in Step 3 is initiated.

4.6.1.3.3 Step 3: Iterative Convergence Refinement

If the convergence criterion defined in Equation (112) is not met— indicating that the average change in outputs over *b* consecutive simulations exceed τ— the total number of simulations is increased from n to n′. The newly added simulations are denoted as SA_{n+1}, SA_{n+2}..., SA_{n}, where n+1 represents the first simulation in the new batch.

To ensure continuity between the original and additional simulations, the convergence criterion is re-evaluated for the newly added simulations and their immediate predecessor (SA_n) using the following formula:

$$\frac{1}{b}\sum_{i=n+1}^{n'} \left|M(SA_i) - M(SA_{i-1})\right| < \tau \tag{113}$$

here, i = n + 1 marks the start of the evaluation for the additional simulations, ensuring that the changes between consecutive outputs are consistently calculated across the expanded sequence of simulations. If the above criterion is satisfied, the model is deemed to have converged. If not, further simulations are added (n′ → n″) and the process is repeated.

4.6.1.3.4 Step 4: Adjusting Convergence Parameters

Should the model fail to converge after an increase in simulation runs in the randomisation of human behaviour method, we refine our approach by either increasing the convergence threshold τ to τ′ or by adjusting the value of b downward, reflecting a more relaxed convergence criterion or a reduced stringency in consecutive run analysis, respectively. The process is formalised as:

$$\tau' > \tau \tag{114}$$

or

$$b' < b \tag{115}$$

The iterative process of adjusting n, τ, and b continues until the convergence criteria are satisfied, or until the model's variability is within acceptable limits, ensuring the reliability of the model for further validation.

4.6.1.3.5 Phase 4: Limit State Function (LSF) Assessment

After achieving convergence with the random sampling method for each hazard scenario S_i, the number of runs n is determined. For each scenario run $S_{i,n}$ (where i represents the scenario and n represents the specific run), the hazard conditions (such as visibility, toxic gases, temperature, or structural collapse) are compared against critical thresholds defined by the Limit State Function (LSF). Once the hazard conditions are evaluated in each scenario run, the potential for incapacitation or fatalities is determined. If any condition exceeds a predefined threshold, the system is considered to have failed, leading to potential fatalities (Figure 81).

The LSF compares the conditions experienced by each individual during the evacuation process with critical thresholds. These thresholds, while not explicitly defined for every condition, represent the point at which the environment becomes life-threatening. If the conditions experienced by any individual exceed the critical limit defined by the LSF, fatalities are recorded.

The number of fatalities in each simulation run is determined using the following generalised equation:

$$N_{i,n} = \sum_{k=1}^{O_{i,n}} 1(C_k(t) \text{violates LSF } (C_{crit})) \tag{116}$$

where $N_{i,n}$ is the number of fatalities for scenario S_i in the n-th simulation run. $O_{i,n}$ represents the total number of occupants in the danger zone during the n-th simulation run of scenario S_i. Ck(t) refers to the general critical condition experienced by occupant k over time, such as temperature, visibility, toxic gas exposure or structural collapse. LSF(C_{crit}) is the LSF, which incorporates the generalized critical threshold for the hazardous condition. 1(C_k(t) violates LSF is an indicator function that equals 1 if occupant k's exposure violates the LSF, resulting in fatality.

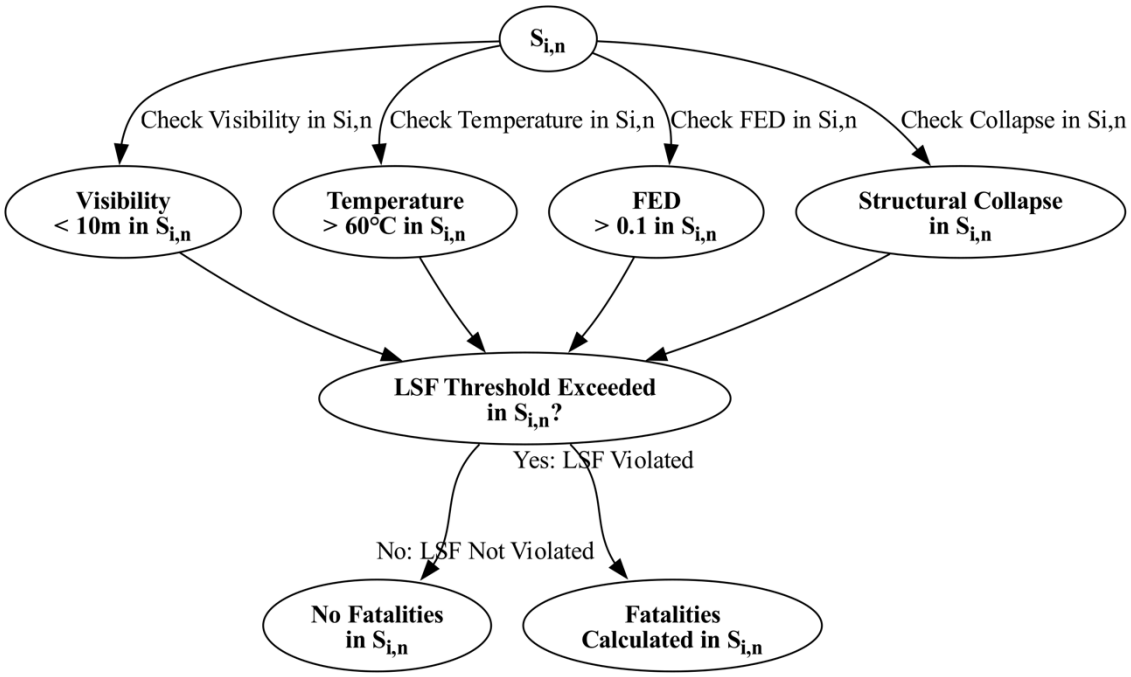

Figure 81: LSF assessment framework for fatality determination.

This framework ensures that various hazards can be modelled without specifying each threshold, providing flexibility in determining when conditions exceed the critical limit and lead to fatalities.

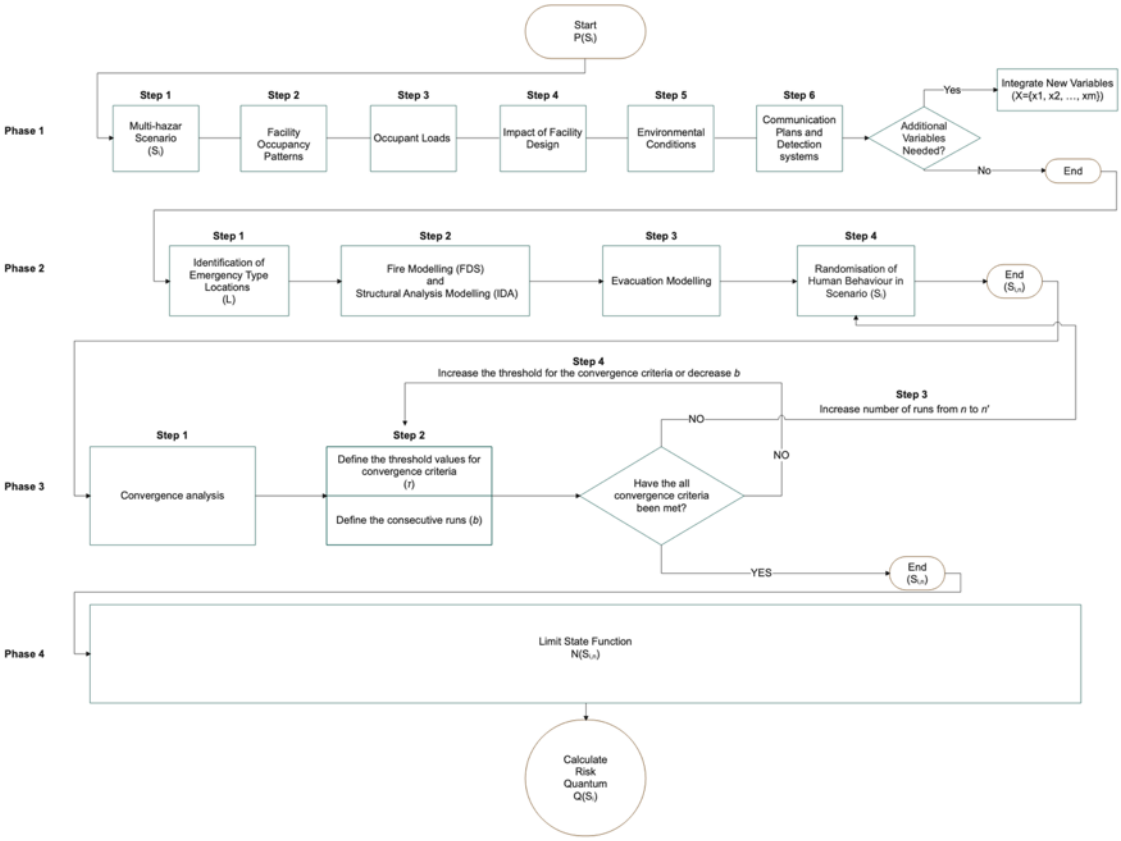

Figure 82: Flowchart of the multi-stage process for the PBD methodology for multi-hazard scenarios.

4.6.2 Evacuation analyses in chosen scenarios for multi-hazard risk assessment

Hazards in underground environments can have rapid and uncertain development, exacerbated by the presence of hazardous materials. Evacuations should therefore include strategies for rapid response in the event of multi-hazard scenarios, taking into account the complex layout of the facility and the presence of hazardous materials [495], [567], [568], [569], [570], [571], [572].

4.6.2.1 Phase 1: Preliminary Assessment of CERN's TDC2/TCC2 facility

The TDC2/TCC2 cavern is located approximately 10.5 metres below the surface, with the surface at 461 metres above sea level and the tunnel entrance at 450.95 metres. Access to the TDC2/TCC2 area is facilitated by the BA80 building with an access point, located on the Prévessin (France) site. The BA80's infrastructure includes a lift in the PA80 that leads to the TA801 corridor, which directly connects to the TCC2 area, as indicated in Figure 68. Moreover, the GT802 tunnel

serves as an emergency exit, with stairs in the PGT802 shaft providing a route to the surface, as well as the TT20 and TT83 tunnels, also serving as emergency exits. This underground, equipped with a total of 4 emergency doors, ensures a dual-route system for the swift and safe evacuation of personnel in emergency fire scenarios.

4.6.2.1.1 Step 1: Multi-hazard Scenarios

For the TDC2/TCC2 underground facility, the representative set of scenarios is defined based on Table 19, Table 20 and Table 21, HRR: S = { CFS1, CFS2, CFS3, CFS4, CFS5, CFS6, E1ISC-E17ISC, E1ISCIF- E17ISCIF }. This set includes independent fire scenarios CFS1 to CFS6, seismic events induced structural collapse scenarios E1ISC to E17ISC, and seismic-induced structural collapse scenarios that trigger fire CFS5, with corresponding fire-induced collapse scenarios E1ISCIF to E17ISCIF. Each scenario is characterized by distinct parameters, as described in subsections 4.2, 4.4 and 4.5, providing a comprehensive framework for assessing multiple hazards.

4.6.2.1.1.1 Step 2: Facility Occupant Loads (Identification of users and their characteristics of CERN TDC2/TCC2 facility)

TDC2/TCC2 is characterised by its stringent access control due to the presence of radiation and the need for close supervision. The architecture of this subterranean structure is designed with a singular focus on the safety and security required for high-level research involving radiological materials. Despite its underground system, TCD2/TCC2's design ensures all safety protocols are seamlessly integrated, providing a safety environment for its sanctioned users [442]. Data for identifying users and their characteristics are collected from the access control system. This system records each person's entry and exit times, providing detailed information about occupant loads. During 2023, the maximum recorded occupancy was 38 users during shutdown mode (no one is permitted to be present in run mode) (Figure 83). The access control system logs occupancy data but ceases to track individuals beyond the PAD/MAD point YDPZ01=BA80 in building BA80 [573].

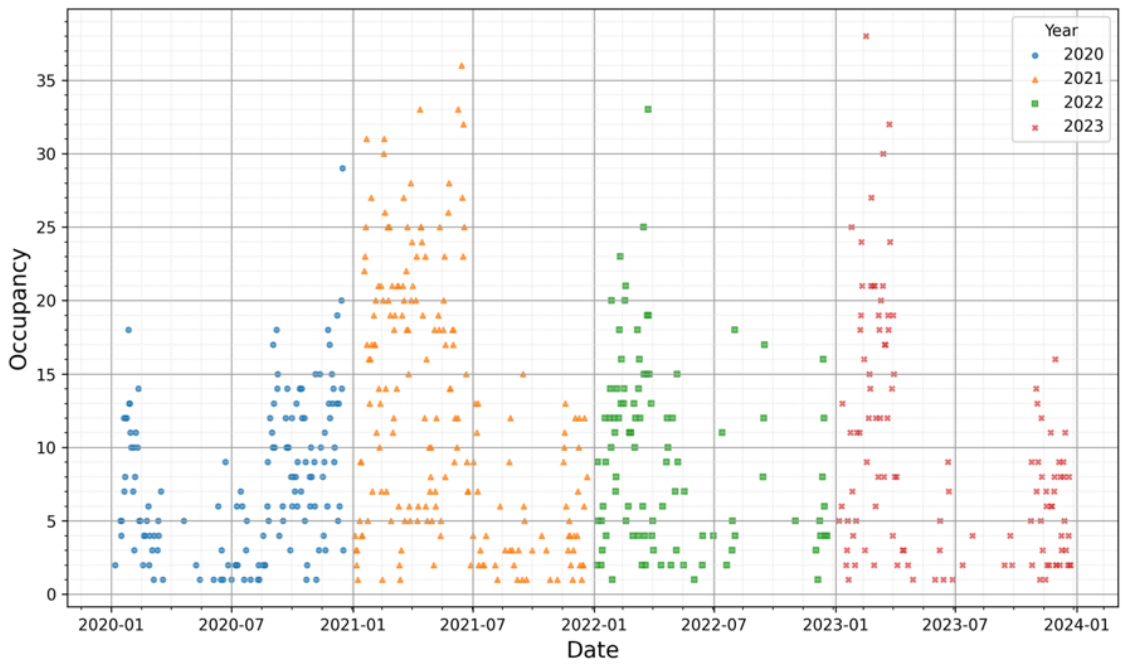

Figure 83: User occupant loads at TDC2/TCC2 from 2020 to 2023.

Occupants are only present during specific periods (Shutdown mode), such as Year-End Technical Stops (YETS) or technical stops, and their access is regulated through the PAD/MAD system. This system requires that users undergo comprehensive training, have an approved IMPACT assessment, and wear personal protective equipment (PPE), such as safety shoes, helmets, and dosimeters.

4.6.2.1.2 Step 3: Occupant Characteristics for TDC2/TCC2

The occupant characteristics for TDC2/TCC2, based on area information [442], [478] and CERN regulations [574], [575] are provided in Table 24. These individuals, primarily composed of technical staff or contractors (no visitors allowed), were required to undergo comprehensive safety training, including radiation protection and emergency response, before gaining access to the facility.

Table 24: Occupant profile TDC2/TCC2.

User	Gender	Age Group	Safety Training	Access Authorization	Social Groupings	Vulnerabilities & Restrictions	Cognitive/ Mobility	Familiarity Status
Staff/Contractor	Mix	18-67	Required	Supervised	Individua/ Team	None; No heart condition/ pregnancy	None	Unknown

4.6.2.1.3 Step 4: Impact of Facility Design

In Step 4, the building layout, GIS data, and 3D panoramic views are used to build both the PyroSim 2023.3.1312 fire simulation model and the Pathfinder 2023.3.1206 evacuation model, which accurately map and visualize the existing layout of the TDC2/TCC2 facility (Figure 84).

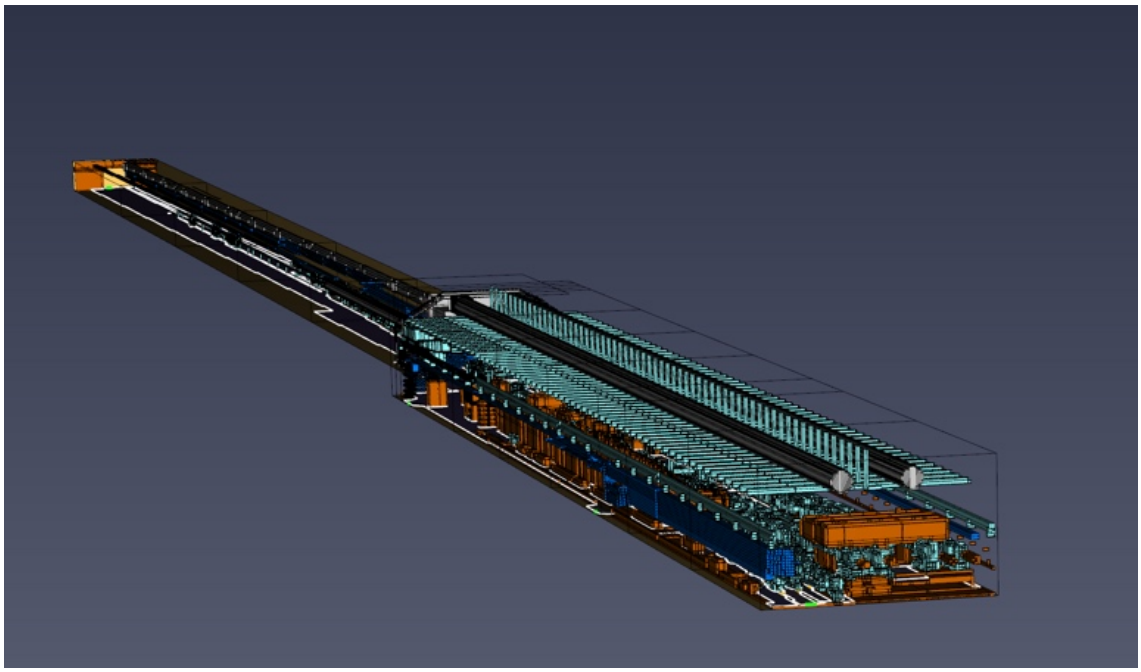

Figure 84: Detailed TDC2/TCC2 layout visualization (Pathfinder 2023.3.1206).

4.6.2.1.4 Step 5: Environmental Conditions

The facility is equipped with emergency lighting, exit signs, fire detection, and an alarm system. However, there is no smoke ventilation system, sprinkler or extinguishing systems, and no handheld fire extinguishers [478].

4.6.2.1.5 Step 6: Communication Plan and Detection Systems

The existing fire detection system can take up to 360 seconds to activate the alarm. While the facility is equipped with an evacuation alarm that is triggered upon detection, it also sends a signal to the fire brigade. The estimated arrival time for the fire brigade is 30 minutes [478].

4.6.2.2 Phase 2: Modelling

4.6.2.2.1 Step 1: Identification of Multi-Hazard Scenarios and Step 2: Subsequent Modelling

Using data synthesised from Phase 1, critical points within the facility most likely to experience hazards were identified. These locations were pinpointed based on identified vulnerabilities, forming the basis for our subsequent modelling Figure 67 and Figure 68.

For each potential hazard location, models built using PyroSim (Figure 84) and IDA (Figure 58) were used. These models simulated various fire scenarios (Table 21) and structural collapse scenarios (Table 19 and Table 20)

4.6.2.2.2 Step 3: Evacuation Modelling

The evacuation model constructed in Pathfinder 2023.3.1206, starting with the construction of navigation meshes based on the facility layout. Once the fire model simulations were completed, outputs such as visibility reduction, smoke spread, temperature changes and FED values were imported into the evacuation model to assess their impact on occupant evacuation dynamics. After defining collapsing blocks from structural collapse scenarios (Figure 85), several key changes added to the evacuation simulation such as the collapsing blocks physically blocking certain evacuation paths, reducing available exits (e.g., Exit Door GT802 in structural collapse with PGA 0.5 g). These simulations accounted for the movement dynamics of people, influenced by a combination of individual behaviours (Table 25) and physical characteristics that affect speed, environmental factors, and the facility's design. Importantly, the starting locations of individuals were randomly assigned to reflect the variability in initial positioning during an emergency.

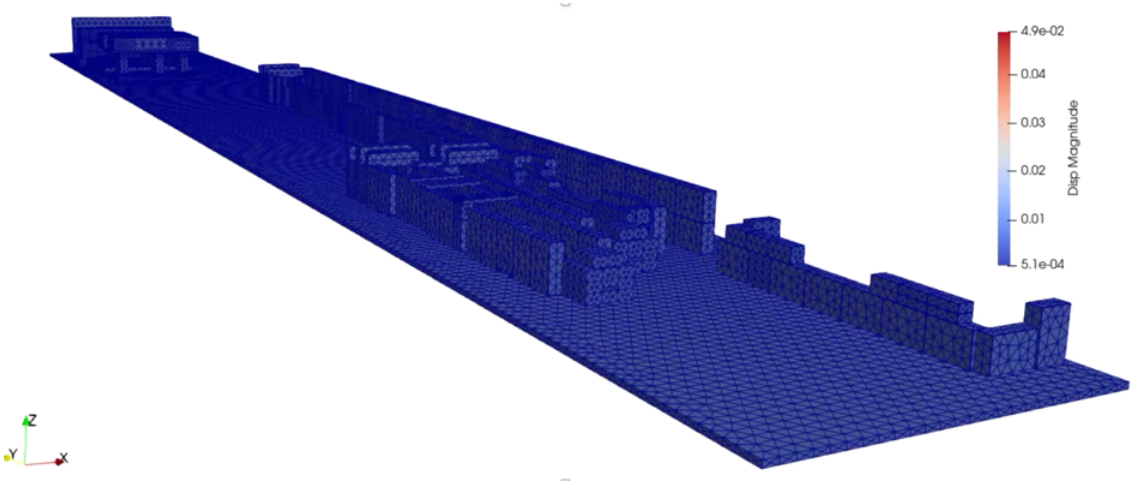

a)

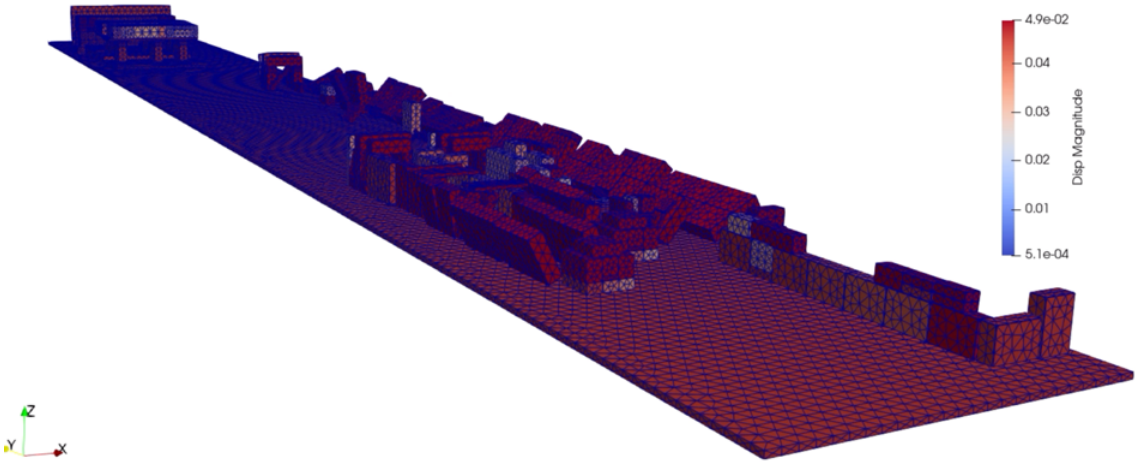

b)

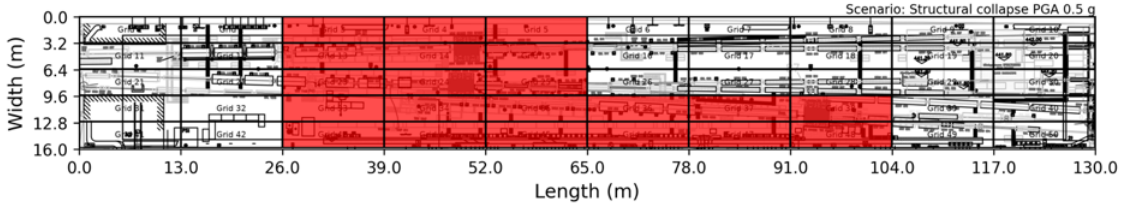

c)

Figure 85: TCC2 under a PGA of 0.5 g earthquake scenario (corresponding to either E16IS/Shutdown or E16ISIF/Shutdown scenarios in the multi-hazard analysis), where red highlighted grids (c) indicate collapse areas of blocks (a: at 0 seconds, when the earthquake begins, and b: at 10 seconds, showing the progression of collapse). Any individual located in the red-highlighted grids is considered a fatality in the evacuation simulation (each grid measuring 13m × 3.2m, with an area of 41.6m²).

Walking speed, under the normal lighting conditions (illuminated conditions, (L)) is assumed to vary with a normal distribution of ±1.25 m/s [576]. For risk assessment purposes, in the event of lighting failure (no illumination (NL)), walking speed is assumed ranges from 0.24 to 0.88 m/s, with a mean value of 0.49 m/s, reflecting the conditions observed in the study of completely darkened full-scale tunnel experiments [577]. The assumption about human body dynamics highlights those physical characteristics [578] influence walking speed, particularly when navigating obstacles or moving through crowded environments.

The recognition time for fire scenarios is triggered by the fire alarm, with a detection time set at 360 seconds. In the event of alarm failure, occupants will trigger the alarm themselves at 360 seconds, as smoke becomes visible to them at that point in the simulation. It is important to note that in earthquake scenarios, detection time does not equate to alarm time, as there is no early warning system in TDC2/TCC2 facility. Instead, individuals typically feel the shaking within a few seconds, leading to recognition times that can range from 2 to 50 seconds, depending on the intensity of the earthquake [194], [579], [580], [581], [582]. This pre-movement time includes a delay in recognition, particularly for lower intensities of shaking, such as MMI IV, where the delay can extend significantly. For our simulations, a 50-second shaking duration was selected, assuming that individuals follow the "Drop, Cover, and Hold on" procedure, representing their response time. After the shaking ceases, travel time begins as individuals initiate movement toward a safe location (Subsection 2.5.3).

In this case study of the TDC2/TCC2 facility, alignment is made with the environmental factors impacting evacuation as delineated in Frantzich's study (see Table 64.8 in the SFPE Handbook) [548], [583]. These factors, which exhibit a high degree of correspondence with those identified in the study. For the purposes of the fire model, these pre-evacuation times are represented using a lognormal distribution, due to social influence and the variability in human behaviour during evacuation. The parameters have been collated in Table 25, which serves as an essential input for the pre-evacuation time modelling component (Figure 86).

Table 25: Input for pre-evacuation time during fire scenarios.

Distribution type	**Mean (sec)**	**Min (sec)**	**Max (sec)**	**Standard deviation (σ) ***
Lognormal	97	30	217	0.50

(σ)* is calculated on the log-transformed scale.

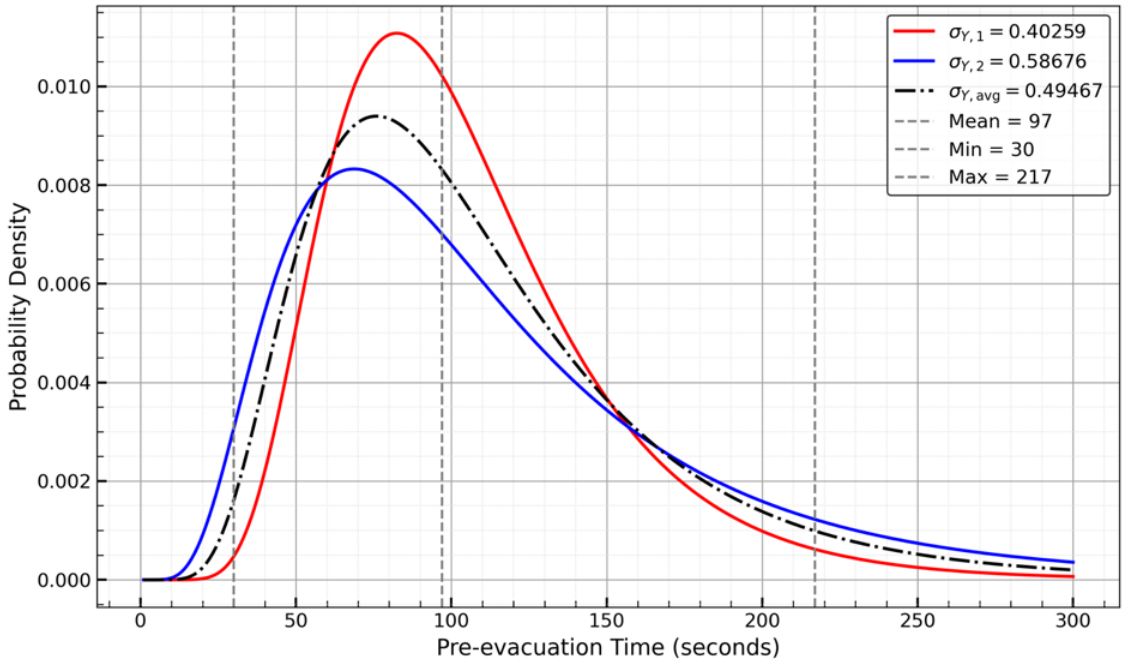

Figure 86: Estimated lognormal probability density functions.

4.6.2.2.3 Step 4: Randomisation of Human Behaviour in Scenarios

Stochastic simulations using pseudo-random sampling were integrated into the evacuation modelling to account for the variability and uncertainties in human behaviour during emergencies. Using the predefined outputs from Step 3, numerous evacuation scenarios were generated for both independent and non-independent hazards in the context of multi-hazard analysis.

Using Pathfinder's Monte Carlo simulation capabilities [584], pseudo-random sampling from specified statistical distributions (such as pre-evacuation times, walking speeds, and initial positions) is employed to model human behaviour stochastically. This process allows for simulating the diverse locations, responses and movements of individuals during an evacuation. Each simulation run reflects different combinations of behaviours, speeds and starting positions, providing a comprehensive analysis of possible scenarios.

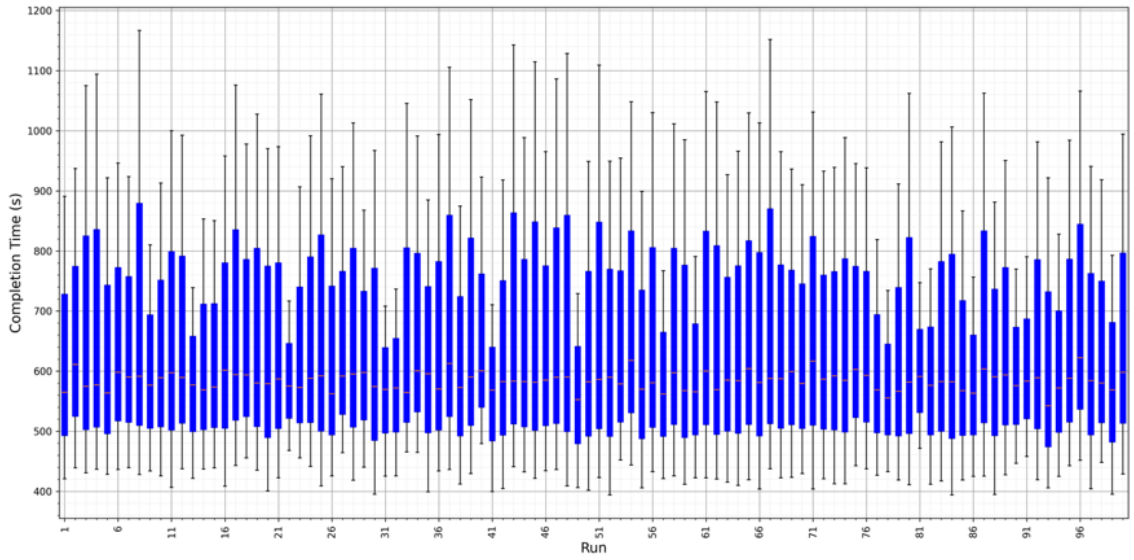

Figure 87: Box plot of completion times for all occupants across 100 runs in CFS1 scenario.

Figure 87 box plot presents the range of completion times (minimum, average, and maximum) for all occupants over 100 simulation runs in the CFS1 scenario.

4.6.2.3 Phase 3: Convergence and Validation

This study applied convergence analysis methodologies from Ronchi's study [525], described through five specific equations. It established specific convergence thresholds for each equation, ensuring that each metric met its threshold in 10 consecutive runs from the simulations, as depicted Figure 88 and Table 26 [585].

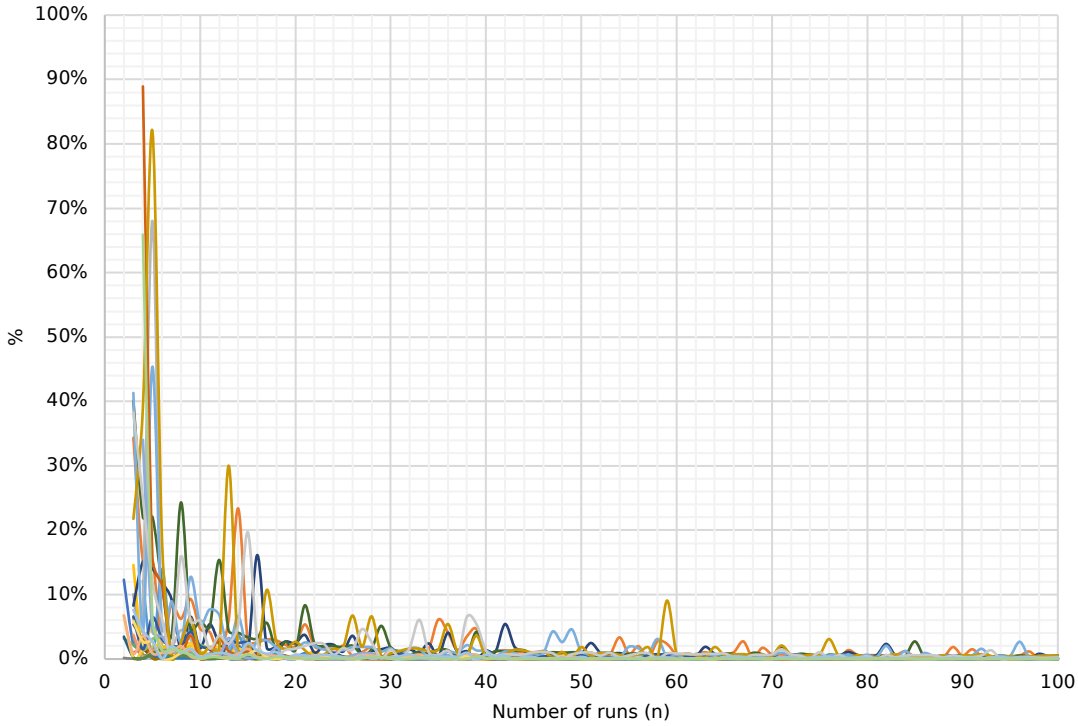

Figure 88: Convergence analysis of only fire scenario evacuations.

Table 26: Convergence analysis of fire-only scenarios and structural collapse-induced fire scenario evacuations.

Scenario	**TET**	**SD**	**ERD**	**EPC**	**SC**
	(Run)	**(Run)**	**(Run)**	**(Run)**	**(Run)**
Threshold	0.005	0.015	0.005	0.005	0.005
CFS1L	31	49	32	47	31
CFS1NL	47	47	31	42	27
CFS2L	14	61	14	14	26
CFS2NL	21	58	12	13	23
CFS3L	22	49	23	31	28
CFS3NL	33	47	27	33	24
CFS4L	40	68	28	41	25
CFS4NL	49	65	27	37	22
CFS5L	23	49	15	27	46
CFS5NL	28	54	24	22	45
CFS6L	49	49	33	52	25
CFS6NL	51	43	38	49	27
E1ISCIFL	51	51	49	52	22
E1ISCIFNL	46	59	55	56	26
E1ISCL	51	51	49	52	22
E1ISCNL	46	59	55	56	26

….					
E17ISCL	51	51	49	52	22
E17ISCNL	46	59	55	56	26
E17ISCIFL	51	51	49	52	22
E17ISCIFNL	46	59	55	56	26

The convergence analysis of structural collapse-induced fire scenarios is identical because all scenarios (E1ISCIFL to E17ISCIFL and E1ISCIFNL to E17ISCIFNL) are derived from the sole fire scenario CFS5. Similarly, for earthquake-induced structural collapse scenarios (E1ISCL to E17ISCL and E1ISCNL to E17ISCNL), the same parameters were used.

This approach allowed for accurately determine the necessary number of sub-scenarios ($S_{i,n}$) for each scenario (S_i), preventing the need for excessive simulations that could otherwise require an impractically large number of runs. The thresholds were carefully selected based on established convergence procedures, ensuring efficiency and precision.

This optimization focused on minimizing the number of runs while maintaining the required level of accuracy, ensuring that the number of simulations performed was sufficient but not arbitrarily large.

4.6.2.4 Phase 4: Reliability Analysis

After achieving convergence with the runs (Table 26) from the simulation for each scenario the data is ready for the calculation of the limit state function (e.g., FED, visibility, and temperature, and area of collapse during seismic event), can be selected based on the relevant codes and guidelines. There are well-established FED thresholds for both incapacitation and lethality due to exposure to fire effluents. The time to loss of tenability from the effects of smoke, toxic gases, or heat is calculated when the FED reaches a value of 1.0 (Table 4). At this threshold, the exposure level is sufficient to cause incapacitation in most individuals, rendering the environment untenable for safe egress. Approximately 90% of the population is considered susceptible at an FED below 1.3 [103]. A tenability limit of 0.3 is recommended as a conservative measure to ensure safety, allowing occupants more time to escape before conditions become life-threatening [6] (ISO 13571:2012). Furthermore, for sensitive populations, it is advisable to adopt an even stricter limit of 0.1 [586]. This limit accounts for the increased vulnerability of these groups, ensuring that nearly all exposed individuals have a safe opportunity to evacuate.

In scenarios involving earthquakes where structural collapse occurs, individuals near the collapse area are considered fatalities due to severe injuries. In our analysis, when heavy blocks weighing 77 kN fall on a person, surviving and escaping without immediate help is assumed to be nearly impossible. These zones were identified based on the results of the structural analyses (Subsection 4.4).

The chosen FED value (Table 27) represents the cumulative exposure level beyond which it is deemed unsafe for individuals to remain in the environment.

Table 27: Ranking: Occupants with highest FED values at 360 seconds alarm time.

Scenario (Si)	Scenario Type	Run ID (Si,n)	Occupant ID	FED received	Collapse	Time (s)
CFS6	Fire	4	24	0.311396		1067.65
CFS6	Fire	14	12	0.270867		1071.075
CFS6	Fire	11	24	0.269776		1014.525
CFS6	Fire	71	24	0.250372		1046.075
CFS6	Fire	13	19	0.243447		1001.95

4.6.3 Evaluation of Evacuation Analysis and Risk Quantification for Multi-Hazard Scenarios

The concept is PBD for a series of hazard scenarios related to the number of choices in terms of evacuation design when preparing an emergency plan. The objective is to ensure the safety of all [587] exposed units within a given time frame, similar to Vision ZERO [588], [589]. This is the target, within a specified time, a design parameter is checked with the simulation to guarantee that all exposed units are safe within a given time with a fixed margin of safety. This is a deliberate design alternative, not a random check. It is important to acknowledge that this approach assumes uniform vulnerability across all individuals, as detailed in Table 24, which does not report specific vulnerabilities any group within the TDC2/TCC2. Therefore, the safety measures are designed with a fixed margin of safety for a homogeneous group. The idea here is the randomisation of human behaviour to ensure the designed solution can be guaranteed. What remains is the choice of randomising human behaviour to cover all scenarios. In practical terms, it is not feasible to account for every instance where exposed individuals might become fatalities due to unforeseen accidents; these cannot be included in the simulation of evacuation for emergency purposes. This is the

margin that remains outside our calculations and is not considered. In risk mitigation step in order to reduce highest Risk Quantum scenarios we must design conditions such that the possibility of rescue allows everyone to be safe, acknowledging that evacuation involves risk and emergency conditions. Simulation and randomisation of human behaviour are needed because it is a major source of uncertainty. This approach involves very sophisticated and controllable PBD. The reason for these sophisticated probabilistic scenarios is that all possible behaviours need to be accounted for to identify the most favourable and unfavourable outcomes. So, the only way forward is to randomise human behaviour in simulations, taking into consideration all possible (location, action, physical characteristic of human), and then to probabilise. This approach allows conclusions to be drawn after the numerical simulation with randomisation, transforming these numerical observations into support for multi-hazard quantitative risk assessment.

The quality of the computation can also be assessed in a synthetic way to demonstrate quantitative improvements. As combinations are designed and initial conditions modified, relationships between results and initial conditions can also be created and these scenarios ranked (Table 27). This will help designers better communicate with stakeholders, illustrating the problems and solutions.

At this juncture, it is critical to introduce a nuanced understanding of risk assessment, particularly concerning fatalities in independent and non-independent scenarios. The risk of fatalities—success and failures—where failures correspond to fatalities, represent countable integers in unsuccessful egress scenarios. The probabilisation of these scenarios allows for a quantifiable estimation of the risk associated with each. Specifically, probabilisation provides the possibility for a quantitative assessment of a scenario's real-number probability, as described mathematically in work of Guarascio et al. [13] and subsection 3.1.10 which encompasses unsuccessful evacuation egress, implying fatalities. The tally of fatalities, when related to their probabilities, provides a quantic estimation of the Risk Quantum. With a comprehensive set of scenarios both necessary and sufficient, the expected value of unsuccessful evacuation egress can be measured, enhancing our understanding and communication of risk.

In road tunnels, there is an Acceptability level that can be checked against the ALARP principle [11], aiming to minimize cost while ensuring a minimum level of safety [13]. However, in cases where there is no Acceptability level of risk, no

fatalities are tolerated, designing for zero fatalities. It becomes common that choices are sometimes shaped by "collegial political" [590] decision-making processes as Alvarez et al. discuss, reflect the collaborative nature of stakeholder engagements in defining acceptable levels of risk and safety. Where it denotes the consensus-building process among diverse stakeholders, where factors like cost, community values, and political could influence the adoption of safety measures as much as, if not more than, technical assessments.

A probabilistic approach helps to recognise the uncertainty and facilitates a more realistic and flexible process. Traditional deterministic [591] and probabilistic [550], [592], [593] approaches in evacuation models [594] help calculating the RSET [528] are widely recognised in the fire safety field. These concepts are valuable for establishing baseline safety standards, while probabilistic models are designed to account for the uncertainty of initial conditions of human behaviour. Researchers commonly follow Averill's [595] recommendation to employ cumulative distribution functions (CDF) in evacuation analysis [543], [596]. The exceedance probability provides an inverse perspective to the CDF by showing the probability of an evacuation not being completed by a certain time. Analogously, longer exposure (times) correspond to a higher risk of death [586], [597], [598]. Similarly, the longer the distance of evacuation, the longer the exposure is [599]. Consequently, a lower probability of successful evacuation within the critical time window indicates a higher risk of death and unsuccessful egress.

In this section, the proposed PBD approach is optimized and distinct from a basic prescriptive approach because it takes into account suitable randomisation of human behaviour and calculation of egress time, FED and fatalities in collapse area. A prescriptive approach provides instructions for evacuation based on experiences in best practices, whereas a PBD includes tools to ensure the design meets commitments and performance standards including random human behaviour and limit state values. This includes ensuring that evacuees are informed, trained, and constrained to respect the evacuation parameters for a successful evacuation. To achieve this, it is necessary to provide individuals with training and information to ensure they can evacuate within the given number of seconds. Designers have to provide the necessary tools, information, and training they need to implement an effective evacuation plan that adheres to the time constraints. This study's scenario assumptions account for the random nature of human behaviour but in a framework of consistent patterns.

To integrate the results of scenario occurrence from randomised human behaviour, how can this data be transferred into the risk of death? In the process of assessing the risk of fatalities, a PBD approach was applied to evaluate the consequences of the evacuation process. In risk assessment as discussed previous chapters, it is important to estimate the initiating event's probability $P(E_i)$ and the performance of protection systems $P(A_n)$. The event tree model represents the primary branches, such as the availability or failure of protection systems, which form the first level of bifurcations in our analysis.

When the probability of scenario occurrence is known, it is still necessary to understand how to transfer the result of the output to fatalities, considering the inherent randomness in human behaviour. Taking into consideration the assumed random model in human behavior, along with the availability/unavailability of protection performance, the probability of death can be estimated given the knowledge of scenario occurrence probability.

However, these primary branches alone do not capture the full complexity of the situation. Each scenario then leads to sub-branches that reflect the variability in human behaviour, particularly under hazard conditions (Figure 26). In line with PBD principles, stochastic simulations are used to model these uncertainties, generating multiple evacuation outcomes, represented by $(S_{i,n})$, where n refers to the number of simulation runs. Each run captures different behavioural outcomes under the same scenario, reflecting the range of possible initial position, speed and actions during an evacuation. The procedures currently enable the establishment, at given number of runs for each scenario, if the design and performance are as according to the plan.

After performing convergence analysis, the sufficient number of simulation runs n, needed for each scenario S_i can be determined. Once convergence is achieved, the limit state functions are established within the PBD framework to define what constitutes a fatality (Figure 81). The application of the limit state then identifies the point at which a fatality occurs for each run of each occupant. As the event tree progresses, these sub-branches, informed by $N(S_{i,n})$, help capture how small behavioural variations can significantly influence final outcomes. Based on the outcomes, the Risk Quantum $Q(S_i)$, representing the probability of fatalities or incapacitations, is calculated by integrating the scenario probabilities $P(S_{i,n})$ with the outcomes of the with LSF-based stochastic simulations $N(S_{i,n})$. In this way that the variability in human behaviour is accounted for across multiple runs, while

the limit state determines when a scenario results in fatalities, allowing for an accurate risk assessment in multi-hazard framework.

4.7 Gu@larp Analysis in Multi-Hazard Scenarios

4.7.1 Introduction to Event Tree Diagrams

The scenario tree diagrams of initiating events act as essential computational tools, helping to quantify risk in multi-hazard framework by evaluating the progression of each hazard and the performance of protective systems. Each tree encapsulates a range of mutually exclusive events, all originating from a single initiating event, such as a fire, earthquake, earthquake induced structural collapse, earthquake-induced structural collapse that leads to a subsequent fire. The probability of each outcome $P(S_{i,n})$ (sub-scenarios) is calculated as the product of the probability of the initiating event $P(E_i)$, and the availability of protection systems, and the time slot and place of the accident within the tunnel, which is considered as the space-time unit.

One important consideration is how the level performance of systems such as emergency illumination, directly influences the evolution of these hazards. In particular, scenarios involving reduced visibility and slower evacuation speeds. This complexity grows when structural collapse blocks exit paths or impedes evacuation routes, creating potential fatality risks, especially in scenarios where fires follow an earthquake-induced structural collapse.

The challenge in these analyses lies not only in the direct impacts of structural collapse or fire but also in accounting for human behaviour under uncertainty. To address this, a randomised approach is adopted that models a range of human responses, reflecting the variability of evacuation behaviours. By simulating these responses, it becomes possible to estimate the fatalities associated with each hazard pathway, drawing from a more comprehensive understanding of risk (Subsection 4.6.3).

The event tree approach provides a structured framework for quantifying the impact of different initiating events $P(E_i)$ on the progression of hazards, both in space and time, and for estimating the probability of specific scenarios $P(S_i)$. Each branch of the tree represents a possible path, determined by the performance of protection systems $P(A_i)$ and their potential failures. By assigning probabilities to these branches, the probability of each scenario $P(S_i)$ can be calculated, which

combines the probability of the initiating event with the availability/effectiveness of protective measures.

To evaluate the Risk Quantum $Q(S_i)$, human behaviour is further integrated into the model using Monte Carlo simulations $P(S_{i,n})$. These simulations account for variability in human responses under different conditions, such as structural collapse-induced fires or impaired evacuation due to blocked exits. The Risk Quantum for each path $Q(S_i)$ is then calculated as the product of the scenario probability $P(S_{i,n})$ and the number of people affected $N(S_{i,n})$, which is estimated through simulations (e.g., Pathfinder). The number of people affected $N(S_{i,n})$, when compared with the number of exposed units at the initial time of the same scenario, allows for the numerical calculation of individual risk coupled with that scenario.

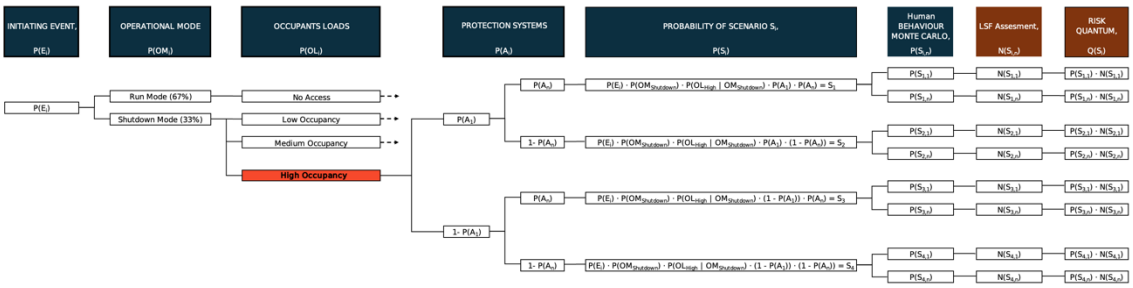

Figure 89: A schematic representation of an event tree showing how initiating events (e.g., earthquake, structural collapse, fire, and structural-collapse-induced fire) progress under different operational modes and occupant loads, with the performance of protective systems determining the probability of various outcomes.

However, this methodology does raise further questions. For instance, what assumptions are being made regarding the reliability of protective systems, and how do these assumptions influence the results? Given the lack of comprehensive data, used subjective probability to estimate the reliability of protective systems (Subsection 3.1.6.3), for the availability and performance of the illumination system based on engineering judgment and the safety documentation available for TDC2/TCC2 [442], [478]. This subjective approach reflects our best understanding under current constraints, but it also prompts further reflection: How sensitive are the results to this assumption, and what might the consequences be if real-world reliability differs from our estimate? In the protection systems for example: the failure of the emergency lighting during an earthquake can occur independently due to an autonomous failure of the

electrical supply or a defect in the lamp, or it can be conditioned by the earthquake through damage caused by structural collapse or fire. These aspects should be further explored, as the inherent uncertainty in using subjective probabilities necessitates caution when interpreting the outcomes of such analyses. Future research should focus on validating these estimates with more comprehensive data to reduce uncertainty in the risk evaluation.

Ultimately, the simulations aim to provide a deterministic estimate of fatalities based on different hazard conditions. However, the real challenge lies in interpreting these results within the broader context of multi-hazard risk analysis. For instance, how can the different fatality across scenarios be reconciled? And how does this inform the design of mitigation measures within underground facilities like TDC2/TCC2?

By reflecting on these considerations, a better understanding is gained of how scenario tree diagrams and risk quantification techniques contribute to the overall safety strategy in multi-hazard environments. In doing so, a deeper insight is gained into the exposed units, specifically the individuals within the area of influence, who face varying levels of risk from earthquakes, structural collapse, and fire. A total of 4,024 scenarios were derived from main scenarios, including 6 fire scenarios, 17 earthquake scenarios with varying PGAs inducing structural collapse, and earthquake scenarios with varying PGAs inducing structural collapse which induced fire CFS5. Among the fire scenarios, CFS5 was selected for a more detailed assessment because it encompasses the combined effects of structural collapse and subsequent fire, representing a critical hazard pathway in TDC2/TCC2 and occurring in a location particularly prone to such events. However, for this study, the focus was placed on the maximum occupant load (38 persons) in Shutdown mode, as it represents a critical condition for initial analysis, with other occupant load scenarios left for future analyses. For each scenario, Monte Carlo simulations were conducted to model human behaviour, yielding approximately 50 sub-scenarios after convergence in each event tree diagram.

4.7.2 Gu@larp Model for Multi-Hazard Assessment

Following the analysis of the event tree, which identifies various scenarios and their associated probabilities, these outcomes can be evaluated against regulatory safety limits. Incorporate these scenario probabilities as described in the Risk

Design line and assess whether they comply with the Tolerability and Acceptability Limit curves.

Given the unique architectural, operational and political environment of CERN, there are no established Tolerability or Acceptability Limit curves at CERN. While the ALARA (As Low As Reasonably Achievable) principle [600] is adopted and currently applied to radiation safety at CERN [601], [602], [603], it is specific to radiation hazards and does not extend to other risks, such as fire or structural collapse. In this multi-hazard risk assessment, different safety criteria are applied according to who is being protected. The Italian road tunnels criteria are used for scenarios involving the general public, such as civilian tunnels. These criteria aim to protect individuals who use these spaces regularly but may not be aware of the inherent risks or have specific safety training. On the other hand, the UK-HSE standards focus on ensuring the safety of workers in occupational settings. These standards are designed to mitigate workplace hazards that employees may encounter due to their specific job roles.

The Tolerability and Acceptability Limit curves for Italian road tunnels (based on the Italian Decree 264/2006) and the UK-HSE Tolerability and Acceptability Limit curves are distributed according to the Gu@larp model. As defined in subsection 3.2, the exceedance probability $G(N_i)$ corresponding to a given threshold N_i is the probability of the union of scenarios with fatalities $\geq N_i$, where the reference values of the Tolerability and Acceptability Limit curves at N = 1 are Gu = 1.0E−1, Gu = 1.0E−4 for Italian road tunnels, and for the UK-HSE Tolerability and Acceptability Limit curves, the values are Gu = 1.0E−3 and Gu = 1.0E−6, respectively (Table 10). It can also be noted that the exceedance probabilities of the curves decrease monotonically, meaning that as N increases, the probability of exceedance decreases. While the rate of decrease diminishes on an arithmetic scale, the relationship follows a constant slope of $-\alpha$ on a bi-logarithmic scale, where $\alpha = 1$ indicates inverse proportionality between G(N) and N. By applying the Tolerability and Acceptability Limit curves, the exceedance probability curve resulting from the design of a specific underground facility can be evaluated for compliance with these criteria, as illustrated in the Gu@larp model applied in the context of CERN (Figure 90).

In 2023, the maximum exposure scenario at CERN, where 38 persons were present (Figure 83) [573], occurred only once during the shutdown mode. With the shutdown mode accounting for approximately 120 days annually, or 33% of the year, the daily probability of this scenario involving 38 persons occurring

during the shutdown mode is calculated to be 0.97% (High Occupancy Load) (Figure 89). Figure 90 represent the upper envelope of the exceedance probability, highlighting it as one of the worst-case exposure scenarios under typical shutdown conditions.

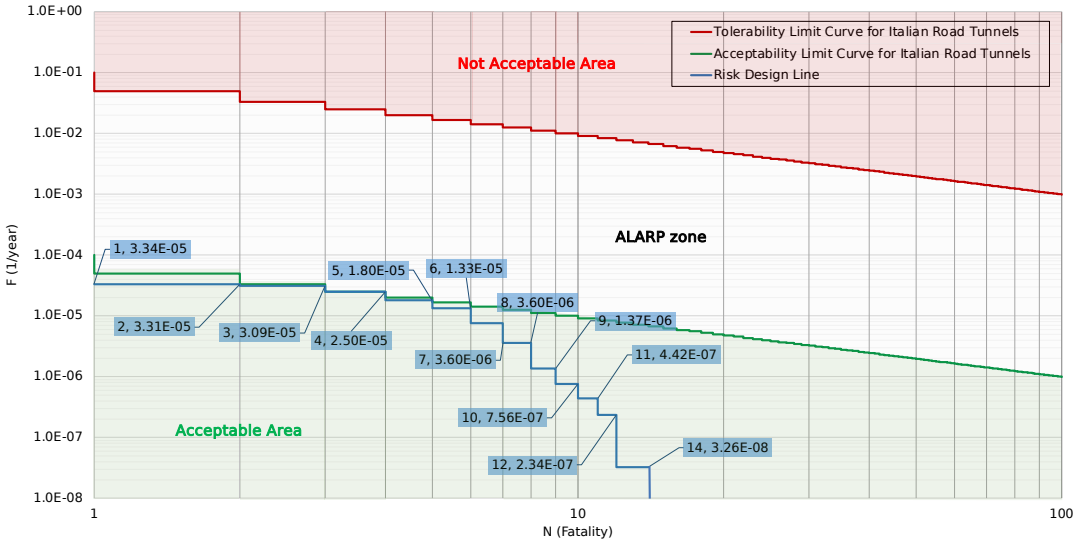

a)

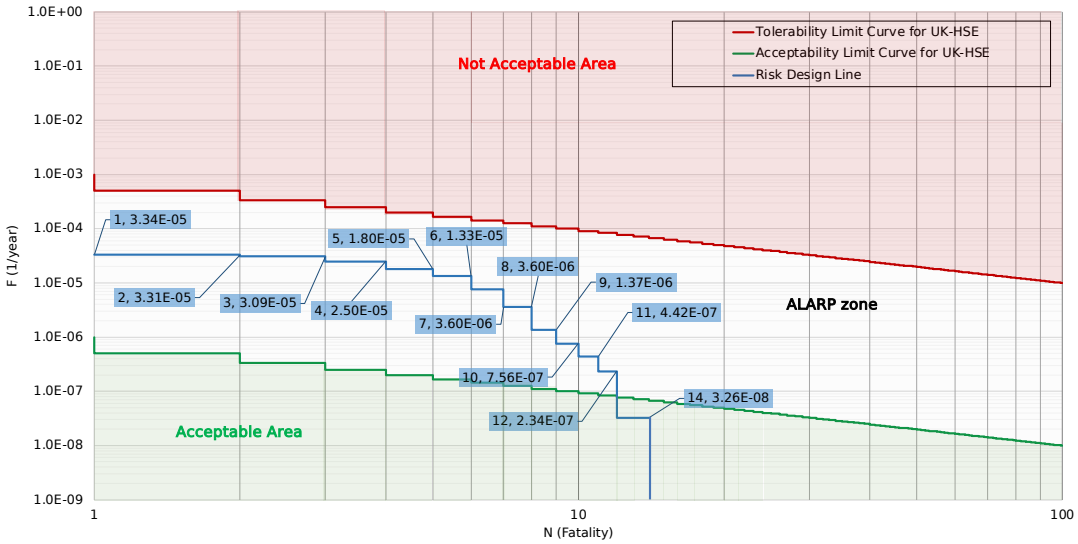

b)

Figure 90: ALARP, Tolerability, and Acceptability Limit Curves for Italian Road Tunnels (a) and UK-HSE (b) (The carrot diagram (Figure 29) has been transformed to represent exceedance probability). An example of the staircase-type envelope is the designed Exceedance Probability Curve for the TDC2/TCC2 with calculated Risk Design Line (Gu@larp Model). The staircase is subdivided into discrete "steps" along the horizontal axis, which in this case represents the potential number of fatalities (N) (1 to 100). The height of each step corresponds to the probability P(S) of a scenario producing exactly

that number of fatalities, and thus the area of each step (or "strip") reflects the quantum of risk contributed by that particular scenario.

In other words, each step on the horizontal axis corresponds to an integer number of potential fatalities (N) for a given scenario, while the height of the step represents P(S), the probability that the scenario will result in that exact number of fatalities. The area of each step (calculated as width multiplied by height) reflects the quantum of risk associated with that scenario.

Furthermore, if the number of people exposed in a scenario is known, one may calculate the individual risk immediately from the probability of the scenario or from the quantum of risk associated with that scenario. For instance, in the scenario "E16IS/Shutdown/Light/n38", the probability of the scenario is 1.56E−7, and 12 fatalities out of 38 exposed individuals. The individual risk for a single person can be calculated as the probability of the scenario multiplied by the ratio of fatalities to the total number of exposed individuals. This calculation yields an individual risk of 4.92E−8.

Alternatively, the same result can be obtained using the quantum of risk, which represents the total fatalities for the scenario. The quantum of risk is calculated as the product of the scenario probability and the number of fatalities, giving 1.87E−06. Dividing this value by the total number of exposed individuals, 38, again yields an individual risk of 4.92E−8.

Both methods confirm that, for the "E16IS/Shutdown/Light/n38" scenario at CERN, the individual risk for an individual exposed person is 4.92E−8.

For the Italian road tunnel criteria, the Risk Design Line shows that all scenarios are positioned below the Acceptability Limit curve, placing them in the Acceptable Area. Thus, no further action is required. However, periodic monitoring and review should be conducted to ensure that risks remain within acceptable limits over time. This positioning suggests that the current risk management measures are adequate, meeting safety standards without the need for additional interventions.

According to UK-HSE criteria, the Risk Design Line indicates that all scenarios, with the exception of the one involving 14 fatalities, which falls into the Acceptable Area, remain within the ALARP zone.

The 14-fatality scenarios cumulatively have a total probability of 3.26E−8 per year, corresponding to a return period of around 30.7 million years. This extremely low probability places the scenario within the Acceptable Area and ensures it does not drive the overall risk beyond acceptable limits. This probability arises from the combined probabilities of four specific scenarios as shown in Table 28.

Table 28: Ranked 14-Fatality Scenarios by Quantum of Risk with Probabilities and Individual Risk.

Rank №	Scenario, (Si)	Probability Scenario, P(Si,n)	Fatality, N((Si,n))	Risk Quantum, Q(Si)	Individual Risk
118	E17IS/Shutdown/Light/n38	2.42E-08	14	3.39E-07	8.91E-09
381	E17IS/Shutdown/NoLight/n38	6.05E-09	14	8.47E-08	2.23E-09
746	E17ISIF/Shutdown/Light/n38	1.86E-09	14	2.60E-08	6.85E-10
1253	E17ISIF/Shutdown/NoLight/n38	4.65E-10	14	6.51E-09	1.71E-10

In contrast, scenarios with other fatality counts have relatively higher probabilities than the 14-fatality scenarios, placing them in the ALARP zone and necessitating prioritized risk-reduction measures. This suggests that while they meet basic safety standards, there is still room for further risk reduction. In the ALARP zone, it is expected that all reasonable measures should be taken to reduce risk further if it is cost-effective and feasible to do so. The ranking presented in the following subsection provides detailed information on the measures required to achieve effective risk reduction.

4.7.3 Prioritization of Risk Reduction Strategies through Ranking of Scenarios by Risk Quantum

Table 29 presents a ranking of Risk Quantum scenarios based on risk levels. Since a long list of optimization strategies could be exhaustive and time-consuming, a new approach using the Risk Quantum can be applied in identifying the effective strategies. Through the ranking of the quantum, the scenario with the highest risk can be located and consequently identify the risk-contributing factors, and so makes it possible to determine the appropriate strategies that could offer the highest contribution in the improvement of the TDC2/TCC2 safety design.

Table 29: Top 20 ranked scenarios for risk reduction strategy for TDC2/TCC2 (out of 4,024 total risk quantum scenarios).

Rank №	Scenario, (Si)	Probability Scenario, P(Si,n)	Fatality, N((Si,n))	Risk Quantum, Q(Si)	Individual Risk	∑(Q), %	Expected Number of Fatalities E(N)
1	E16IS/Shutdown/Light/n38	1.56E-07	12	1.87E-06	4.92E-08	**1.11%**	**1.68E-04**
2	E15IS/Shutdown/Light/n38	1.34E-07	11	1.47E-06	3.87E-08	0.88%	
3	E16IS/Shutdown/Light/n9	1.56E-07	9	1.40E-06	3.69E-08	0.84%	
4	E16IS/Shutdown/Light/n3	1.56E-07	8	1.25E-06	3.28E-08	0.74%	
5	E16IS/Shutdown/Light/n12	1.56E-07	8	1.25E-06	3.28E-08	0.74%	
6	E16IS/Shutdown/Light/n17	1.56E-07	8	1.25E-06	3.28E-08	0.74%	
7	E16IS/Shutdown/Light/n20	1.56E-07	8	1.25E-06	3.28E-08	0.74%	
8	E16IS/Shutdown/Light/n25	1.56E-07	8	1.25E-06	3.28E-08	0.74%	
9	E16IS/Shutdown/Light/n33	1.56E-07	8	1.25E-06	3.28E-08	0.74%	
10	E16IS/Shutdown/Light/n42	1.56E-07	8	1.25E-06	3.28E-08	0.74%	
11	E16IS/Shutdown/Light/n45	1.56E-07	8	1.25E-06	3.28E-08	0.74%	
12	E16IS/Shutdown/Light/n1	1.56E-07	7	1.09E-06	2.87E-08	0.65%	
13	E16IS/Shutdown/Light/n13	1.56E-07	7	1.09E-06	2.87E-08	0.65%	
14	E16IS/Shutdown/Light/n19	1.56E-07	7	1.09E-06	2.87E-08	0.65%	
15	E16IS/Shutdown/Light/n21	1.56E-07	7	1.09E-06	2.87E-08	0.65%	
16	E16IS/Shutdown/Light/n24	1.56E-07	7	1.09E-06	2.87E-08	0.65%	
17	E16IS/Shutdown/Light/n26	1.56E-07	7	1.09E-06	2.87E-08	0.65%	
18	E16IS/Shutdown/Light/n28	1.56E-07	7	1.09E-06	2.87E-08	0.65%	
19	E16IS/Shutdown/Light/n29	1.56E-07	7	1.09E-06	2.87E-08	0.65%	
20	E16IS/Shutdown/Light/n37	1.56E-07	7	1.09E-06	2.87E-08	0.65%	

*EIS/Shutdown/Light/Run: Earthquake-induced structural collapse at a specific PGA level, with lighting on during shutdown, for a simulation run.
EISIF/Shutdown/NoLight/Run: Earthquake-induced structural collapse including fire at a specific PGA level, without lighting during shutdown, for a simulation run.

For instance, certain scenarios in Table 29 involve eight potential fatalities. These scenarios originate from the main scenario "E16IS/Shutdown/Light" but are further subdivided into multiple sub-scenarios, symbolized as "E16IS/Shutdown/Light/n", to account for randomised human behaviour. As a result, each sub-scenario is assigned a proportional probability derived from the initial event probability. Consequently, scenarios with eight fatalities, which arise from this structured branching process, share the same base probability and thus exhibit identical quantum of risk and individual risk, despite differences in behavioural assumptions across sub-scenarios.

The location of scenarios within the ALARP zone reflects their respective probabilities and quantum of risk. The 14-fatality scenario falls within the Acceptable region due to its extremely low probability, as defined by the Acceptability Limit Curve for UK-HSE criteria. In contrast, the ranking highlights that the 12-fatality scenario, with a much higher Risk Quantum, demands immediate attention. This higher quantum suggests the need to investigate the factors contributing to its elevated risk.

The ranking all scenarios serves as an important tool for prioritizing interventions. It provides insights into which scenarios demand immediate attention and identifies solutions that are both effective and feasible. For example, for scenario E16IS/Shutdown/Light (Figure 85), which involves

structural collapse, structural reinforcements are essential. These measures directly address the root cause by strengthening weak points in the collapsed blocks and reducing the probability of future collapses. Reinforcements targeting the highest Risk Quantum scenario not only mitigate the specific scenario in question but also address the root causes of related structural collapse scenarios, thereby reducing the total risk across multiple scenarios. While these measures often involve higher costs, they provide a measurable and reliable reduction in risk.

Effective risk reduction requires a calibrated approach. To address these risks effectively, it is essential to identify the appropriate reinforcement measures, including where, why, and how they should be implemented. This requires a careful and intelligent approach, as scenarios are designed to reveal weak points within the system. For Structural collapses often result in fatalities due to the proximity of individuals to collapse zones, highlighting the importance of identifying and reinforcing these areas. Similarly, fire scenarios lead to fatalities due to toxic smoke exposure, due to longer alarm times. Identifying the time zones and locations of these weaknesses allows for targeted reinforcement solutions. Combining this information with an understanding of human behaviour can help reduce risks to levels within the acceptable region.

In evaluating the benefits of this approach, focusing on probabilised fatalities, or the Risk Quantum becomes essential. By summing the Risk Quantum across all 4,024 scenarios, the Expected Number of Fatalities (E) is determined to be 1.68E−04, numerically representing the overall risk of the system. While this expected value captures a comprehensive picture of system risk, it may not be the most effective parameter in cost-benefit analysis. The reason lies in its inclusion of the entire scenario space, which requires calculating and simulating every possible scenario and strategy. This approach differs from the aim of this project, which is to optimize resources by reducing the number of simulations as much as possible.

When a high quantum is observed, it reveals significant potential for optimization, particularly in relation to the performance and availability of protection systems, as well as improvements to the current design. As illustrated in Table 29, main scenarios contribute substantially to the overall system risk, primarily due to large variations in scenario probabilities. This observation suggests that it may not be necessary to simulate every scenario to assess a strategy's impact; rather, focusing on high-quantum scenarios provides a

streamlined and cost-effective path to refining the design while maintaining safety objectives.

The concept of the Risk Quantum allows for ranking the scenarios, and then quantitatively appreciate the comparative contribution of every single scenario to the overall Expected Number of Fatalities.

The design capability provided by Gu@larp and the ranking system offers a unique framework for approaching decision-making and optimization in safety design. These tools integrate human reasoning with numerical support, allowing solutions to be grounded in both rational thought and quantifiable data. By analysing the probabilities of events, associated fatalities, their quantum, and various engineering factors, this process establishes a foundation for thoughtful evaluation of safety measures.

One of the key insights from this approach lies in its ability to provide an immediate understanding of the scale and cost of potential solutions. Structural reinforcement, for instance, is a clear yet often costly intervention. It requires consideration not only of the material and labour involved but also of the broader implications, such as the disruption caused during implementation. Alarm systems, on the other hand, may represent a less expensive and more straightforward improvement, yet their success depends heavily on human factors, such as response times and situational awareness. Similarly, education and training programs, although cost-effective, must address the challenge of ensuring consistent behavioural changes under high-stress conditions.

What emerges from these analyses is a broader understanding of the balance between cost, feasibility, and effectiveness. Structural reinforcement directly addresses risks related to collapse, but its high cost and scope make it a targeted solution. Education and alarm improvements, in contrast, tackle behavioural and procedural gaps, complementing engineering measures by addressing the human dimension of risk.

The ranking system supports this thought process by justifying choices that prioritize ease of implementation, cost efficiency, and overall impact. This reflective approach emphasizes the importance of selecting measures that not only reduce risk but also align with practical constraints. Ultimately, the goal is to achieve risk minimization in line with established criteria while optimizing safety outcomes through a careful balance of cost and benefit. The interplay of

technical, social, and economic considerations is what shapes a well-rounded and effective safety design strategy.

Chapter 5

Conclusion and Future Directions

5.1 Conclusion and Future Directions

Underground systems present unique challenges due to their confined conditions and often complex, sometimes linear, configurations. These environments escalate the level of hazard in cases of structural collapse, fire, smoke, explosions, and radiation emissions, among others. The confined and elongated nature of these environments can accelerate the horizontal spread of smoke and heat during a fire, especially in the absence of effective protection systems. This rapid propagation can degrade conditions even hundreds of metres from the source, endangering those who have not evacuated. Structural collapses can similarly obstruct escape routes with debris, further impeding evacuation. The layout of vulnerable units within these environments, along with limited access points and pathways, intensifies mobility constraints, making evacuation and rescue operations exceptionally challenging. Similar challenges have been observed in underground mining, which is closely tied to the origins of the ALARP principle in the UK in 1949 [196], [365]. Tragic events in underground transport systems, such as the Balvano train disaster in the Armi railway tunnel in 1944 [604], the Baku Metro fire in 1995 [605], the Mont Blanc Tunnel fire in 1999, and the Gotthard Tunnel fire in 2001 [508], are just a few examples that highlight the diverse and complex risks inherent to confined environments.

The field of risk assessment has evolved to encompass not only traditional approaches but also quantitative assessments of multi-hazard scenarios. This represents a significant theoretical advancement in multi-hazard risk assessment in underground systems. Looking back at key milestones, 75 years have passed since Lord Justice Asquith's 1949 statement, made in response to a mining accident, in which he emphasized that the quantum of risk must be measured and kept "as low as reasonably practicable" for an individual. We now have the tools to provide risk indicators for each scenario, fulfilling his vision by being able to measure the Risk Quantum of any single scenario and related Individual Risk.

Within the ALARP framework, it is possible to evaluate risk mathematically, and by integrating capital and operational costs, further research can identify potential cost distortions, providing a clearer view of where risk mitigation is financially balanced or imbalanced. The Gu@larp model serves as both a mathematical and graphical tool, allowing us to translate the abstract concept of risk into something more solid both theoretically and practically. Through graphical representations such as the Risk Design Line and the Acceptability and

Tolerability Limit curves it is possible to visualize the order of magnitude and subtleties of risk. Without these tools, risk would remain an abstract concept, challenging to fully comprehend and apply in practical situations.

The Gu@larp model can also be applied in a purely social context, aiming to minimize fatalities and optimize public investment toward saving lives. Within the ALARP framework, this is visualized using a balance scale with two pans—the first pan representing risk (Expected Number of Fatalities) and the second pan representing cost (capital investment) (Figure 33). The Acceptability Limit curve and the "second pan" help us weigh proportionality because incremental capital and operating costs (CapEx) lead to proportional decrements in fatalities, thereby decreasing the rate of fatalities. This demonstrates that investing public or private funds into safety measures can effectively reduce the risk to human life following rational ALARP criteria.

In the generalized spirit of ALARP, we acknowledge our limitations, recognizing that we are not omnipotent. Yet, we strive toward two objectives: when we can prevent accidents, we have a responsibility to do so; when prevention is not feasible, we must accept that some risks are unavoidable. However, accidents that could be avoided through well-justified investments, whether public or private, should be addressed. Therefore, the unit measure of risk encompasses both human life and socioeconomic impact quantified in terms of public money. By achieving a balance between the two pans (Figure 33), safety investments are both effective and economically justified, aligning public expenditure with the societal value placed on human life.

Multi-hazard risk assessment begins by identifying scenarios that comprehensively represent potential events within the tunnel environment. These scenarios include different type of relationships:

- **Mutually Exclusive Events**: These are events that cannot occur simultaneously, such as an earthquake, structural collapse, or fire happening on its own. It is possible for an earthquake to occur without causing structural collapse. However, the propensity and relationship with the fragility curve suggests that structural collapse becomes more likely at higher levels of PGA. Nevertheless, analysing structural collapse and fire as practical approaches allows us to use the concept of Non-Mutually Exclusive Events to determine whether these events are independent or non-independent.

- **Non-Mutually Exclusive Events**: These events may occur together or in sequence, such as a seismic-induced structural collapse that may or may not lead to a fire. Here, the events are not mutually exclusive, meaning they can co-occur without one necessarily affecting the probability of the other.
- **Independent Events**: Events that occur without influencing the probabilities of other events. For example, a fire occurring in isolation does not affect the likelihood of an earthquake or structural collapse elsewhere within the tunnel.
- **Non-Independent Events**: In these cases, the occurrence of one event directly alters the probability of another. For instance, an earthquake causing structural instability may increase the probability of a collapse, creating a dependency between these events.

By theoretically categorizing events in this way, one can more accurately model the complex interactions between different hazards and their combined impact on risk levels.

The methodology of the quantitative multi-hazard risk assessment and the criteria for risk Acceptability and Tolerability are addressed, acknowledging that CERN is a unique place without established criteria like those in road tunnels or as used by the UK-HSE. For each multi-hazard scenario, a minimum necessary and sufficient number of scenarios is defined to enable advanced simulations that deterministically assess their consequences, particularly in terms of potential fatalities within specified tenability limits and conditions for structural collapse. Multi-hazard risk assessment initiates with the design of initiating (initiator) events, including earthquake-induced structural collapse, fire accidents caused by structural collapse and independent fires. Tools such as IDA, FDS, and Pathfinder support the proposed methodology, making it suitable for both existing and new tunnels. The methodology incorporates seismic geostatistics-4D technique (CoKriging) to model spatial and temporal variations in seismic hazards. The selected hazard-initiator must be mutually exclusive among themselves, their union covers a representative sample of all possible initiators. Separate Event Tree Diagrams are developed for each initiator, where each branch represents an intersection of non-mutually exclusive events along the path. However, each complete branch sequence is mutually exclusive from the others. These scenarios are included by earthquake-induced structural collapse at specific PGAs as well as by both independent and non-independent fires, with their estimated probabilities calculated based on the operational state (run or

shutdown) of the TDC2/TCC2 facilities. A quantitative multi-hazard risk assessment is conducted for the initial tunnel configuration. The Risk Design Line related to the current configurations remains below the Tolerability Limit Curve for both Italian road tunnels and UK-HSE criteria. For the UK-HSE criteria, the Risk Design Line is positioned within the ALARP zone, indicating a need for further risk reduction efforts where reasonably practicable. Additionally, the Expected Number of Fatalities and Individual Risk are calculated.

Hazard scenarios incorporate an exposure map that details the locations of structural collapses, fires, safety exits, and the initial actions and movements of occupants within the tunnel, based on the defined initiator events. Each scenario is analysed using event tree diagrams, which detail both the availability and performance of protection systems, adjusting or fine-tuning each scenario's characteristics in order to increase representativeness itself, with a defined probability of occurrence. Following this, Monte Carlo simulations are performed for each scenario, generating multiple runs to account for uncertainties in human behaviour under the constrained hazard conditions, with convergence achieved within these simulations. Lethality models are then applied to determine the severity of consequences in terms of fatalities. The Risk Quantum, a critical parameter derived from the product of scenario probability and its related consequences, aids in interpreting the risk level of each scenario and the overall system. The availability of the Risk Quantum for all scenarios, when properly identified, described, and probabilised, allows for the immediate calculation of remaining required risk indicator values (Societal Risk; Expected Number of Fatalities; and Individual Risk) in the multi-hazard risk assessment framework.

The process then involves evaluations to determine scenario probabilities and detailed design descriptions, culminating in the calculation and ranking of these designs based on their Risk Quantum. The identification of the most adverse scenarios facilitates the optimisation of their Risk Design Line, ensuring that alternative configurations are quantitatively assessed to manage risk levels effectively. While sensitivity analyses were not performed in this study, they are recommended for future work to evaluate how variations in key parameters influence scenario probabilities, Risk Quantum, and the placement of the Risk Design Line, particularly when the current Risk Design Line lies within the ALARP zone. Integrating economic evaluations of different protection systems of the alternative configurations to ensure cost-effective safety solutions. Later on, Cost-benefit versus risk analysis is also possible in the ALARP spirit.

It emerges that current design practice for multi-hazard risk assessment is not homogeneous and is sometimes oriented toward a quick assessment that does not merit the appellation of quantitative risk assessment. Considering all the uncertainties affecting the real underground system and its representation in terms of sub-systems, which form the basis for Fault Tree Analysis and Event Tree Analysis, it should at least be verified that the adopted numerical procedure yields conservative results. The need for a comprehensive approach, supported by reliable and accurate numerical tools able to quantify the effect of selected measures in terms of risk indicators, directs attention to seismic, structural collapse, fire, and evacuation models in these scenarios. These are considered advanced tools according to the state of the art in their respective fields because they allow for detailed descriptions of seismic and structural collapse dynamics, fire dynamics, and evacuation patterns.

The details of how to conduct multi-hazard scenario probabilities and consequence analyses for the numerical estimation of risk indicators are not included in existing literature or guidelines for either surface or underground environments. This is addressed explicitly in the dissertation, which offers a detailed procedure for multi-hazard risk assessment. The methodology includes estimation of probabilities alongside advanced deterministic simulations for fire and structural collapse, providing a basis for selecting the minimum necessary and sufficient number of scenarios for life safety verifications.

The results from the TCC2/TDC2 case study are specific to this context and cannot be generalized. In each case study, particular attention must be given to ensuring that a minimum necessary and sufficient number of scenarios are conducted to address the specific multi-hazards present in the environment. However, these results demonstrate that the methodology is effective for quantitatively evaluating current risk levels and also provides a means to check how certain measures may improve or worsen safety conditions and overall risk within an underground system. The methodology combines seismic geostatistics-4D, using CoKriging to model spatial and temporal variations in seismic hazards, along with IDA to assess structural response and potential collapse under seismic loads. The FDS models fire spread, while PBD is specifically applied to analyse evacuation processes within the chosen scenarios, considering the impacts of both structural collapse and fire on occupant safety. Recognizing the inherent uncertainties in human behaviour during such conditions, the PBD approach also accounts for variability in occupant responses, which can significantly affect evacuation outcomes. The application of

geostatistics in this context is not a retrospective justification of the method but a deliberate tool for constructing hazard curves, which quantify the likelihood of hazard intensities over space and time. This output is integrated with structural fragility analyses, fire dynamics, and evacuation models within a comprehensive multi-hazard risk assessment framework, providing insights previously unavailable. For designers, this approach provides a solid foundation, both theoretically and practically for proposing and evaluating both current and alternative safety measures. For jurisdictional authorities, it offers an insightful framework to balance risk reduction and cost-effectiveness in their assessments. This raises broader questions about how our understanding and management of multi-hazard scenarios can inform safer, more resilient infrastructure.

Most countries and industries apply tolerability limits within the ALARP framework, though with varying levels which depends on slope and Gu (anchor point) based on specific industry requirements and national safety standards. But what about CERN? Establishing appropriate limits here raises critical questions: what constitutes an acceptable or tolerable risk level, and how should risk reduction decisions be approached in light of varying stakeholder perspectives? The process is often complex, as the diverse interests of stakeholders introduce layers of consideration that can both shape and challenge consensus. This dissertation offers a solution to those questions through quantitative multi-hazard assessment, offering a structured framework with numerical and graphical illustrations of Risk Design Line for TDC2/TCC2 cavern, based on its present configuration and operational conditions. This framework can offer guides a rational understanding of risk, benchmarking against different Acceptability and Tolerability Limit curves such as Italian road and UK-HSE.

Understanding these tolerability limits also brings attention to their practical implications. In this context, the investments in CERN's installations translate into both time and productivity. Money invested in this installation represents potential time lost if the installation becomes unavailable. Time effectively measures the productive use, or fruition, of the installation. Any interruption can disrupt research at CERN, impacting both scientific productivity and potential financial support. Stakeholders may therefore use unavailability as a criterion for assessing research performance, as downtime directly impacts scientific output and operational efficiency.

The ranking of the Risk Quantum demonstrates that both structural collapse and structural collapse-induced fire led to similar fatality outcomes, though with

different probabilities. The primary cause of death in both cases is the collapse itself. When the collapse occurs, most fatalities are immediate, and for the remaining occupants, there is often enough time to evacuate through the available exits. This is because fires, though dangerous, typically take time to escalate and create life-threatening conditions.

However, an important question arises regarding the intervention of emergency services. In fire scenarios, it is estimated that firefighters will arrive at the scene in approximately 30 minutes [478].

This observation raises important questions about the timing of emergency services interventions. For fire scenarios, the estimated response time is around 30 minutes. But can one realistically expect this in a multi-hazard situation? From past earthquake events worldwide, it is known that large-scale disasters rarely impact just one building. Multiple structures are often hit simultaneously, complicating the response effort.

In cases where structural collapse occurs without fire, it might still be possible to rescue individuals trapped under debris. The survival time for individuals trapped under debris can vary widely depending on factors such as the severity of injuries, access to air, temperature, hydration, and available space. In general, people can survive for several hours to days, with many cases showing survivors being rescued after 72 hours or more. This critical window is often referred to as the "Golden 72 Hours" [606], where the survival rate is highest. After this period, the chances of survival decrease significantly, particularly if there is no access to water or if medical conditions worsen. However, in scenarios where collapse is followed by fire, the dynamics change dramatically. Fire not only adds complexity to the rescue efforts in collapsed structures but also reduces the chances of survival for anyone trapped.

This brings us to an important area for future research. How should emergency response strategies be adapted and optimized for multi-hazard event? How can lessons learned from past global disasters shape more effective response strategies? These are pressing questions that need to be addressed to improve survival rates in multi-hazard disaster scenarios.

Like all risk assessments, multi-hazard risk assessments face significant challenges due to the lack of reliable data.

One promising approach to gather more reliable data on occupant behaviour is to schedule unannounced evacuation drills and record video of what transpires. By closely examining how occupants behave during these simulations, researchers can capture essential details such as the time required for evacuation in a specific area, the routes individuals choose, and how varying occupancy loads throughout the day or year influence movement. These insights form a critical basis for refining risk assessments and developing more accurate evacuation models.

This process is already underway at CERN, where systematic data collection from evacuation drills is expected to provide valuable insights into human behaviour. Such data collection is particularly relevant in environments where multiple hazards may be present ranging from potential structural failures, fires, or even radiation risks, such as at CERN or in similarly complex facilities. These video recordings and performance metrics can then be integrated into a multi-hazard risk assessment framework, one that can address not only conventional safety threats but also more complex hazards. It is worth noting that, the collected video recordings and performance metrics serve as valuable tools for the validation and verification of simulation results, providing benchmarks to ensure consistency and reliability in representing observed behaviours and outcomes.

When radiation is a concern, adhering to the principle of ALARA is essential to minimize exposure. Meanwhile, the broader safety concept of ALARP is equally relevant for managing other significant risks, including those that may trigger or exacerbate radiation hazards. Different zones may experience variable radiation levels depending on the time of day or year, and some areas might exhibit higher radiation only during specific operations or events. In such cases, careful planning is required to protect both workers and the surrounding environment. Indeed, hazard scenarios such as structural collapse or fire can induce radiation accidents, potentially escalating into broader public-safety challenges if contamination spreads. This can result in large-scale damage to the facility infrastructure, local economies, and the environment.

Another significant impact and innovative aspect of this study lies in its focus on quantifying risk for exposed individuals at CERN, a dimension previously unavailable. This study addresses two key components: the need for detailed quantitative risk assessments alongside existing safety policies and the application of probabilistic frameworks for evaluating hazards, exposures, and evacuations in underground environments.

While CERN has historically implemented safety measures based on worst-case scenarios to develop engineering protections and organisational measures, these efforts were not supported by comprehensive probabilistic quantitative analyses. Although the ALARA principle has been widely applied to radiation hazards, including fire risks, it has not yet been extended probabilistically to other risks such as earthquakes, fires, or structural collapses. This work bridges this gap by introducing a robust methodology that links fatalities to structural collapses, fires, and the cascading effects of earthquake-induced structural collapses, which in turn induce fires and exacerbate evacuation challenges. This represents a major advancement in multi-hazard risk assessment, integrating external hazards, structural failures, and fire events within a unified probabilistic framework.

This research provides CERN with a probabilistic framework for evaluating hazards and exposures. While radiation hazards were excluded from this analysis due to the scope of the study being cantered on seismic geostatistics, structural risks, fire hazards and evacuation. The study focuses on developing scenarios tailored to underground environments. These scenarios are evaluated using acceptability and tolerability criteria from Italy and the UK that have been transformed to represent exceedance probability within the Gu@larp mathematical model.

Since CERN does not have specific tolerability and acceptability limits, comparisons were drawn using the Risk Design Line in similar contexts, such as private tunnel mobility in Italy and workplace environments in the UK, providing valuable insights. In Italy, the ALARP principle is primarily applied to private mobility in tunnels, while in the UK, it focuses on workplace environments where duty holders bear responsibility for risk mitigation. This makes the UK model more applicable to CERN's underground work environments where workers operate in underground environments exposed to natural risks such as earthquakes and fires. It is the duty of CERN to evaluate the impacts of hazards (earthquakes, fires, structural collapses, etc.) on operations and personnel. CERN conducts structural collapse and fire analyses; however, this study is the first to connect these hazards with quantitative probabilistic scenario-building for exposed individuals.

The duty holder is responsible for conducting quantitative analyses, a role that marks a significant advancement in knowledge and awareness. Previously, CERN lacked a practical framework that integrated quantitative measures with the necessary accuracy for comprehensive risk assessment. The introduction of

methods to formulate and simulate risk scenarios has driven substantial progress. While geostatistics and seismic hazard analyses contribute empirical, accurate, and quantitatively robust data helped to identifying the appropriate number of scenarios and estimating probabilities necessitates the integration of diverse disciplines to establish rational criteria that were previously unavailable. By addressing these gaps, this research lays a foundation for improved decision-making, providing methods and tools that had not been accessible at CERN before.

Estimated initiating probabilities, as estimated in Chapter 4 can be updated or refined using the proposed methods as new data becomes available, and technological advancements offer opportunities for further refinement. Yet, the question remains: how much can we mitigate uncertainties, and to what extent will technological improvements reduce the limitations inherent in every field of study? It is worth considering how ongoing developments may gradually address these gaps.

In this study, time constraints and limited available literature led to a focus on four of the seven main multi-hazard scenarios (Subsection 3.1.1.3), leaving room for future exploration of the remaining ones. While the Gu@larp calculations are based on estimated fatalities, there is still potential to expand the scope to include damage assessments, as presented through the equations in subsection 3.1.10. Moreover, using the risk indicators proposed in this dissertation, combined with available financial data, economic losses resulting from fatalities and damage can be calculated. The quantitative approach outlined here for multi-hazard scenarios offers new insights and efficiencies over conventional models.

Additionally, other hazards can be integrated into the model based on geographic area analysis and independent quantitative hazard assessments. Although this introduces more complex interactions, it is possible to manage these complexities in a rational manner, supported by global experiences that have begun to reveal the intricacies of multi-hazard risk assessment.

5.2 Lessons Learned

Building upon the results obtained through the multi-hazard risk assessment at CERN's TDC2/TCC2 facility, several practical insights have emerged that extend beyond theoretical modelling. These insights represent one of the major merits of

this study. The lessons learned are presented in the chronological order of the study:

1) **Directional Damping and Seismic Hazard:** The geostatistical seismic analysis (using CoKriging) demonstrated that adopting directional damping profiles for each azimuthal sector yields a more reliable hazard curve than relying on simplified, averaged attenuation functions. In practice, this granular approach enabled the design and verification of more robust structural protection measures for underground caverns where isotropic assumptions would have underestimated or overlooked localized high-risk zones. Finally, geostatistics is a necessary tool allowing the correct and representative model of seismic stress.
2) **Sector-Specific Hazard Curves for Targeted Mitigation**: The integration of directional hazard curves for discrete cloves (sectors) around TDC2/TCC2 highlights that seismic demand varies with epicentral direction. This information helps identify specific areas where targeted seismic retrofits, such as additional bracing or friction enhancement measures, may be most beneficial.
3) **Block-Level Thresholds and Cascading Effects**: By adopting a local failure criterion (0.2 m displacement) rather than a global collapse limit, the study demonstrated that partial failures could cascade and compromise adjacent blocks. This approach is already consistent with CERN's existing practices.
4) **Refined Estimation of Collapse-Related Fire Risk**: Even moderate seismic events could trigger block displacements sufficient to affect cable trays or magnetite devices, posing ignition sources for post-seismic fires. While the assumption $P(F|SC) = 1$ is conservative, the work highlights a real need to define more accurate probabilities for fire ignition during block failure scenarios, leading to improved fire-segmentation strategies.
5) **Convolution of Hazard and Fragility Curves for Risk Assessment**: The convolution of fragility curves with hazard curves, done separately for each block and then combined, provides transparency into which blocks, or block groups drive the greatest share of overall collapse probability. This insight is important for managing assets in TCC2, as it allows for prioritising blocks where the risk is significantly higher than acceptable levels.
6) **Realistic Modelling of Human Behaviour**: Through stochastic modelling, the study demonstrated that small variations in factors such as reaction times, body characteristics that influence speed, and occupant locations

within the facility can lead to significant differences in evacuation outcomes. This highlights the importance of using pseudo-random sampling to accurately represent occupant heterogeneity and to prevent an overly optimistic assessment of tunnel safety.

7) **Convergence Analysis to Avoid Misrepresentation**: The simulations showed that early runs can misrepresent the actual distribution of evacuation outcomes. The simulations revealed that early runs often fail to represent the true distribution of evacuation outcomes. Increasing the number of runs until convergence thresholds were achieved ensured the results reflected genuine occupant behavior, free from computational artifacts. This process provides clarity on the critical question of how many simulation runs are sufficient to ensure stable and representative outcomes.
8) **Relative Impact of Collapse vs. Fire:** The analysis showed that the largest contribution to immediate fatalities derived from structural collapse triggered by seismic action, while fire though devastating in the longer term, generally allows more time for occupant evacuation.
9) **Human Behaviour Modelling and the Value of Empirical Validation**: While simulations provide detailed "what-if" landscapes, actual evacuation drills and real accident data are essential for verifying assumptions about human behaviour in TDC2/TCC2. Incorporating data from unannounced evacuation drills or similar areas within CERN tunnels can significantly improve the realism of human behaviour modelling. Tools such as video analysis and detailed measurements, including reaction times, pre-evacuation delays, and overall evacuation times, offer valuable benchmarks for calibrating egress simulations. By capturing a broader range of human behaviour dynamics, these methods ensure that model parameters remain anchored in reality and allow for more accurate evacuation process modelling. Facilities with similar underground infrastructures can benefit from this approach, as design changes, signage placement, and other mitigation strategies can be tested virtually before implementation.
10) **Scenario Granularity Improves Accuracy:** By considering specific variations, such as different levels of hazard intensity, protection-system performance, and occupant behaviour under various conditions, dividing initiating events into smaller sub-scenarios increased the fidelity of the overall risk picture. Although this approach produced thousands of scenarios, it pinpointed critical combinations of these factors. For example,

event-tree diagrams and subsequent Monte Carlo simulations revealed that failures of protective systems, such as emergency lighting, can significantly alter occupant behaviour, while structural collapses may block exits, compounding risks. These findings underscore the interconnected nature of technical systems and human decision-making during emergency situations, further justifying the need for detailed scenario granularity.

11) **Criteria for Quantitative Assessment and Comparative Analysis of ALARP in Italian Road Tunnels and UK-HSE within the Gu@larp model:** The quantitative assessment and comparative analysis of ALARP applications between Italian road tunnels and UK-HSE highlight significant differences in how acceptability and tolerability criteria are defined. The ALARP philosophy has evolved to address the complexities of underground workplaces and mobility systems. Acceptability and tolerability thresholds are integral components of this philosophy, making it particularly effective for multi-hazard risk assessments at CERN. The Gu@larp mehtod facilitates the adaptation and comparison of ALARP principles under different conditions, such as underground workplaces and underground mobility. This approach enhances knowledge, awareness, and the practical application of ALARP at CERN for managing risks associated with multiple hazards.
12) **Ranking by Quantum of Risk is Efficient**: Employing the Risk Quantum ranking (rather than analysing every single scenario equally), once the minimum necessary and sufficient number of scenarios is identified, proved highly effective for highlighting which events drive the greatest share of the total system risk. Focusing on scenarios at the top of the ranked list enables targeted interventions that achieve the most substantial overall risk reduction in risk-based design.
13) **Gu@larp's Role in ALARP and Risk-Based Fatality Judgments:** Gu@larp's basic equation is not the same as Bayes' theorem; instead, ALARP is expressed using Bayesian methods. By numerically determining the exposed units in a scenario and focusing on the key factors concerning those units, individual risk can be calculated scenario by scenario. In an example from CERN, the calculated individual risk aligns with the ALARP principle. The risk in the Lord Asquith case was considered individual risk. Each fatality represents a separate judgment based on the specific scenario. When evaluating multiple fatalities, each fatality is assessed based on its specific circumstances. If all fatalities occur

under the same conditions, with the same responsibilities and effects, then an identical judgment applies to each. However, not all fatalities share identical circumstances or responsibilities. The Gu@larp method addresses each fatality individually by providing a single judgment for each sub-scenario, since it provides both numerically individual risk and the quantum of risk for each. This approach establishes a legal basis for understanding the cause-and-effect relationships involved in every decision.

14) **Applicability Beyond TDC2/TCC2**: The multi-hazard risk assessment framework developed for and applied at CERN's TCC2/TDC2 unique tunnel environment, including CoKriging, IDA, FDS, PBD, the Gu@larp model, event trees, and Risk Quantum ranking, can be transferred to other underground systems such as road tunnels, metros, or mines. This adaptability requires proper calibration of local hazard data and occupant profiles to ensure accurate and relevant application in different contexts.

Overall, the results and methodologies presented in this dissertation demonstrate that a structured, quantitative multi-hazard risk assessment framework is both feasible and practically implementable. It can be applied to different types of underground environments, such as road and rail tunnels, underground malls, mining operations, among others. This dissertation successfully applied and validated the framework in the highly complex underground infrastructure of CERN, showcasing its effectiveness for similar environments with appropriate local calibration of occupant data and hazard profiles. Furthermore, the potential application of this framework to future projects like CERN's FCC highlights its versatility in addressing the unique safety challenges posed by large-scale, state-of-the-art underground facilities. The TDC2/TCC2 experience has shown that occupant behaviour modelling, once established, is not static. As facilities evolve with new technology, staffing levels, or hazard mitigation features, ongoing recalibrations of the model ensure that it reflects current reality. In urbanized or high-occupancy areas, where both human behaviour and complex infrastructure intersect, these findings are especially important enables more robust safety measures that can help prevent or reduce harm from multi-hazards.

Appendix A: Supplementary Material for Seismic Accelerogram Data of the 1 November 2022 Earthquake

This appendix outlines the methodology used to analyse seismic accelerogram data recorded by 58 available stations (surface and underground) in Switzerland, France, and Italy during the earthquake that occurred on 1 November 2022. The FDSN (Federation of Digital Seismograph Networks) was used to retrieve relevant earthquake catalogues, and the stations involved in recording the events were identified. The search parameters were set to retrieve stations within a 150 km radius of the 1 November 2022 earthquake, taking into account both spatial proximity to the earthquake and the specific event time.

Seismic data were recorded by a network of stations distributed across the region, with each station measuring ground motion in three components: North-South, East-West, and Vertical. The data capture covered a duration of 180 seconds following the initial tremor, ensuring comprehensive coverage of the earthquake's ground motion. A standardised workflow was applied to process and analyse the data, utilising the ObsPy library for accessing and handling the waveforms, station metadata, and catalogues.

Waveform data were initially retrieved from the relevant seismic networks (ETH, RESIF, and INGV) for the specified time window, beginning at 16:04:00 UTC and spanning 180 seconds from the earthquake's onset. The instrument responses of each station were removed to convert the raw waveform data into physical ground motion values in acceleration (m/s^2). This step ensured that the data were corrected for instrument-specific characteristics, allowing for consistent analysis across all stations.

To reduce noise and isolate relevant seismic signals, a bandpass filter was applied to the processed data.

The calculation of PGA involved extracting the acceleration time series for each seismic component at every station. The maximum absolute value in each time series was identified, representing the highest ground acceleration recorded during the event. This process was repeated for the North-South, East-West, and

Vertical components at all 58 stations, resulting in a comprehensive dataset of PGA values.

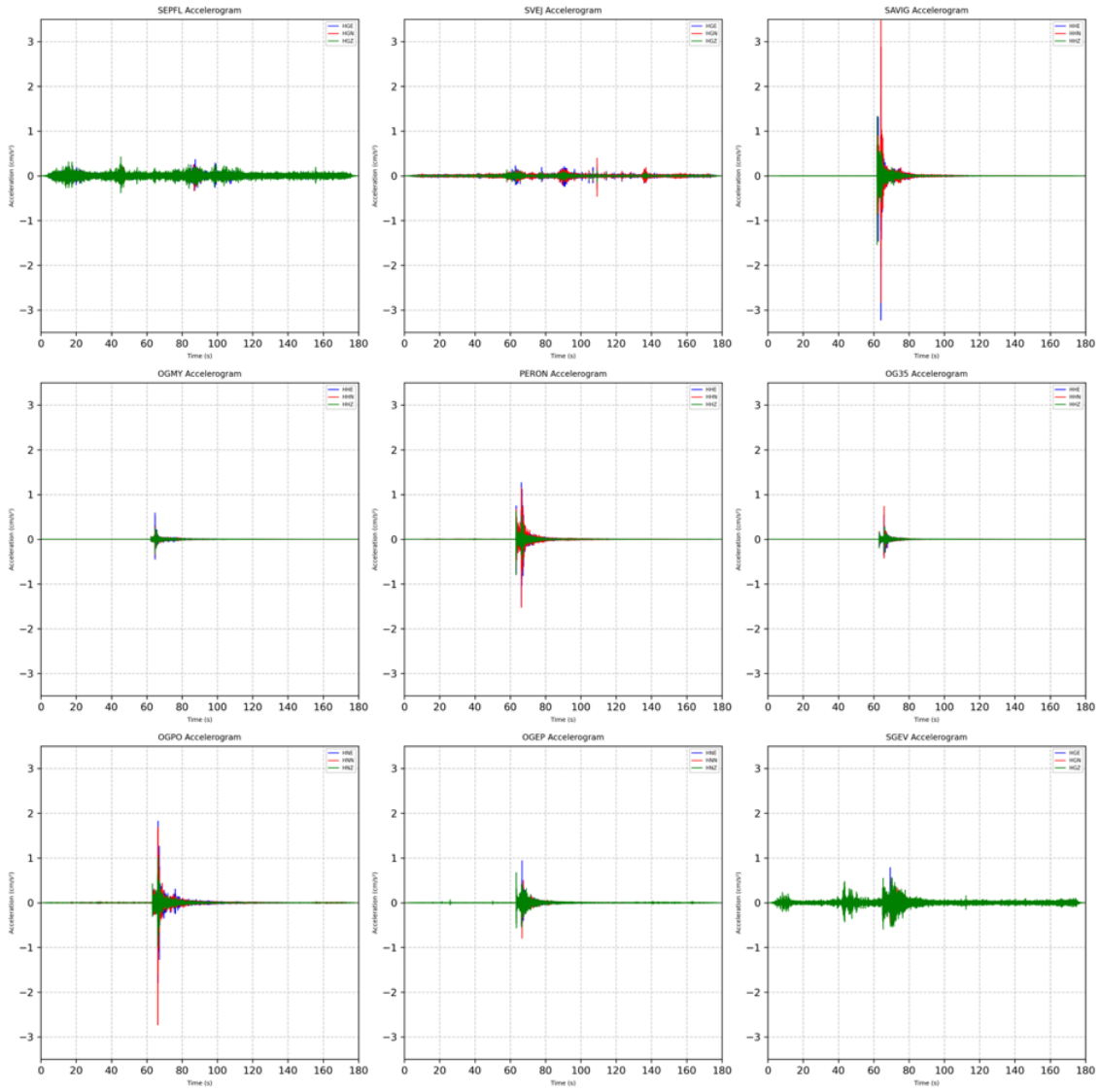

Figure 91: Acceleration time histories for the three components of motion recorded at the stations SEPFL, SVEJ, SAVIG, OGMY, PERON, OG35, OGPO, OGEP, SGEV.

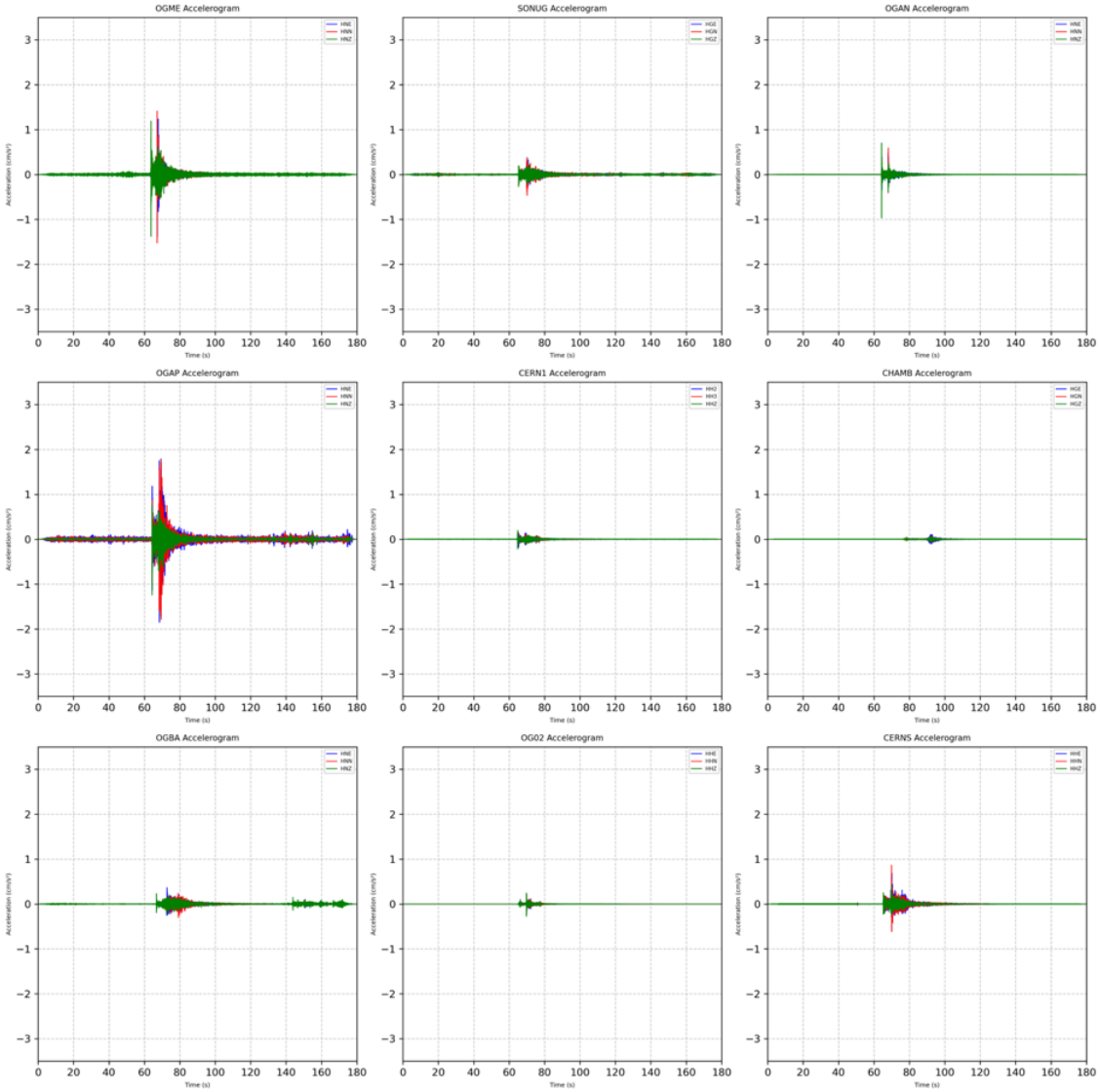

Figure 92: Acceleration time histories for the three components of motion recorded at the stations OGME, SONUG, OGAN, OGAP, CERN1, CHAMB, OGBA, OG02, CERNS.

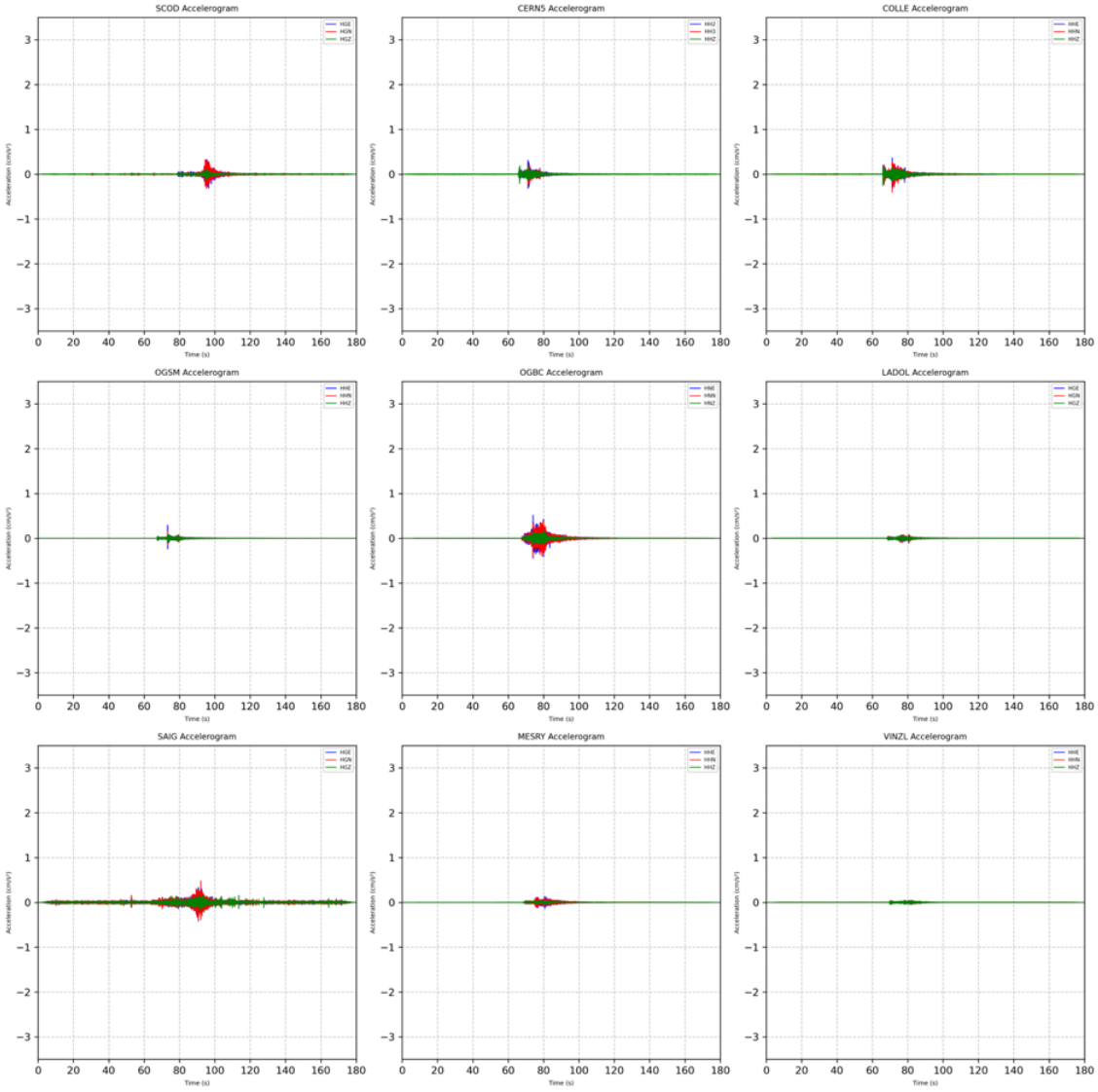

Figure 93: Acceleration time histories for the three components of motion recorded at the stations SCOD, CERN5, COLLE, OGSM, OGBC, LADOL, SAIG, MESRY, VINZL.

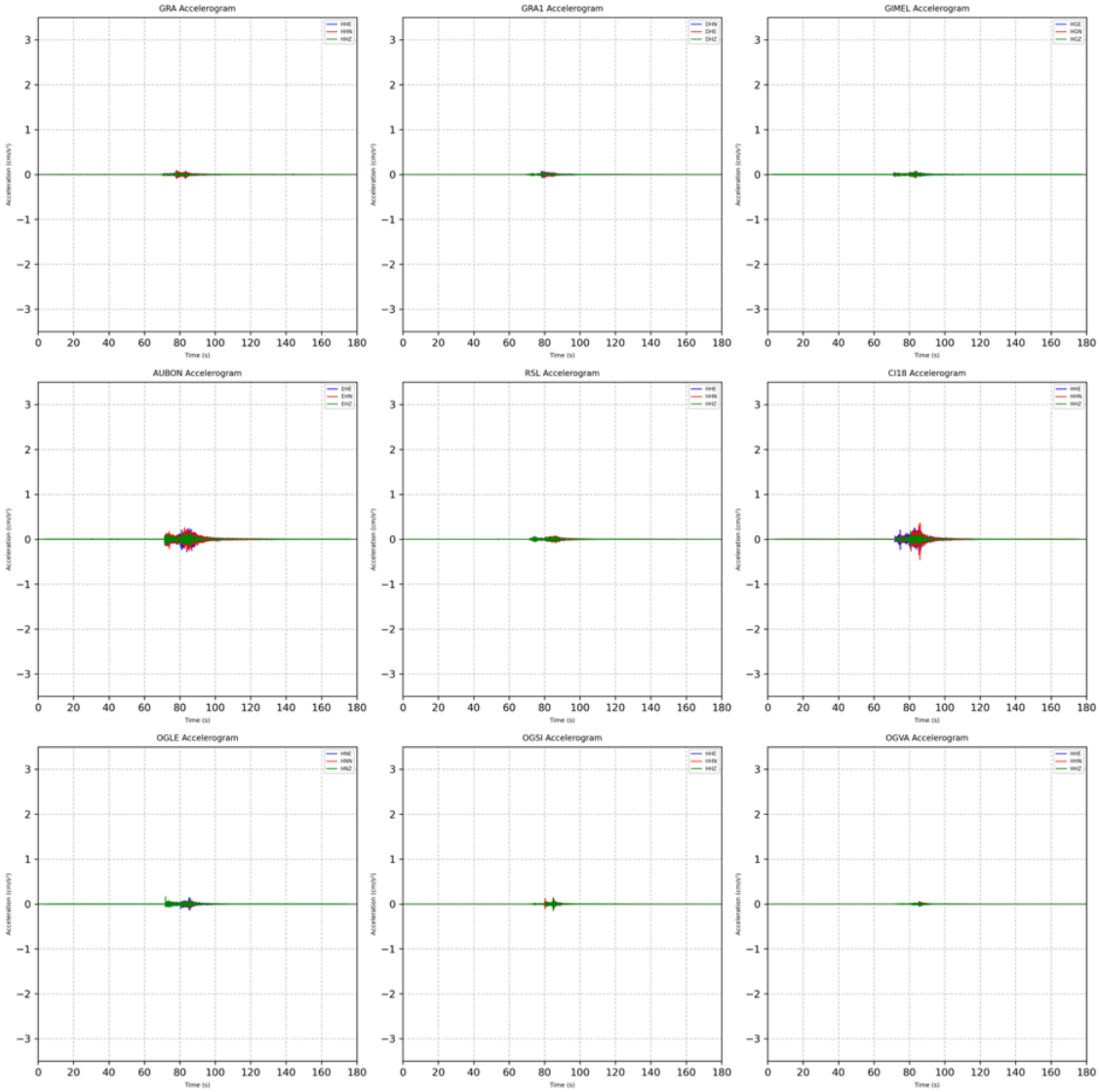

Figure 94: Acceleration time histories for the three components of motion recorded at the stations GRA, GRA1, GIMEL, AUBON, RSL, CI18, OGLE, OGSI, OGVA.

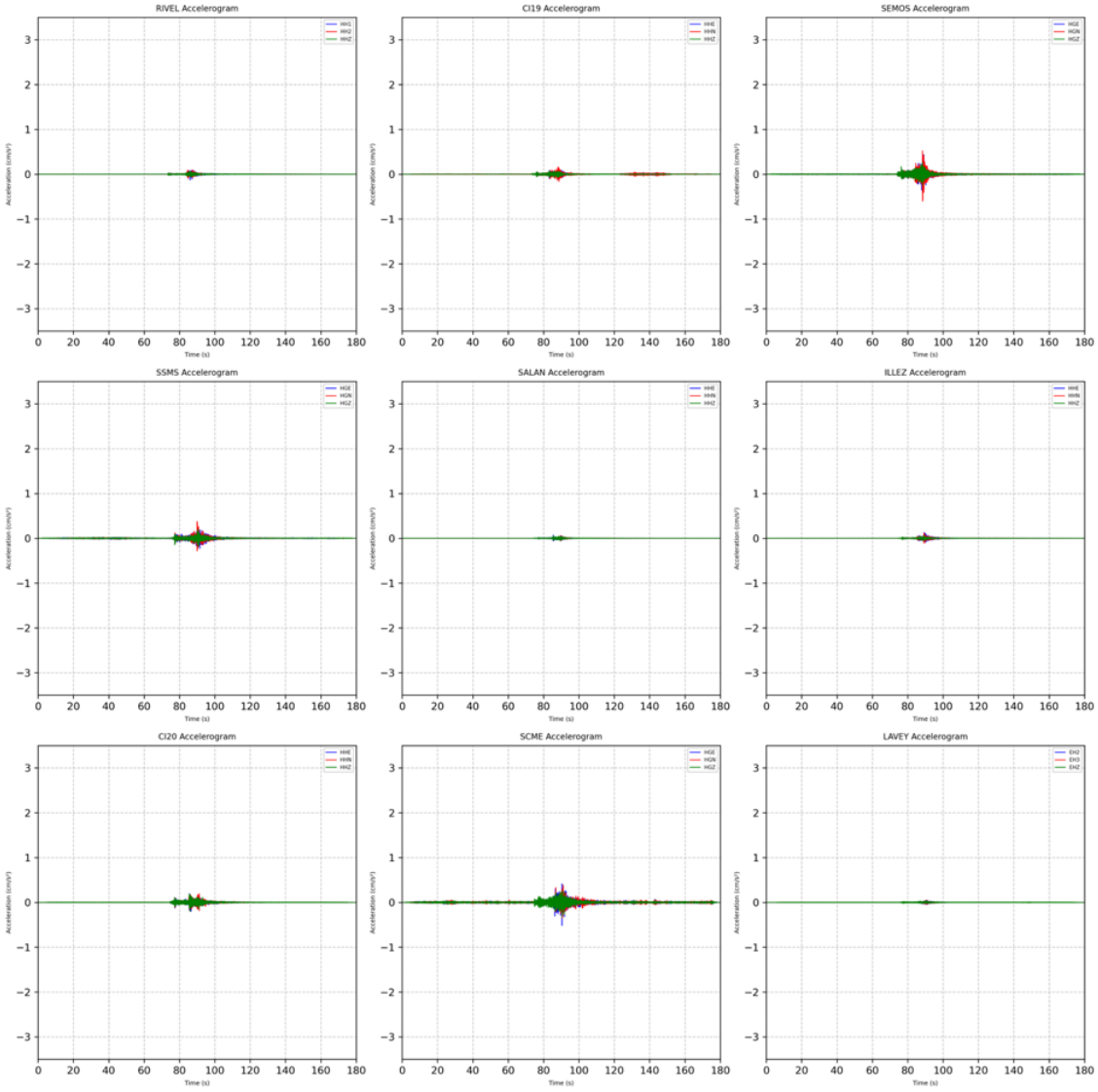

Figure 95: Acceleration time histories for the three components of motion recorded at the stations RIVEL, CI19, SEMOS, SSMS, SALAN, ILLEZ, CI20, SCME, LAVEY.

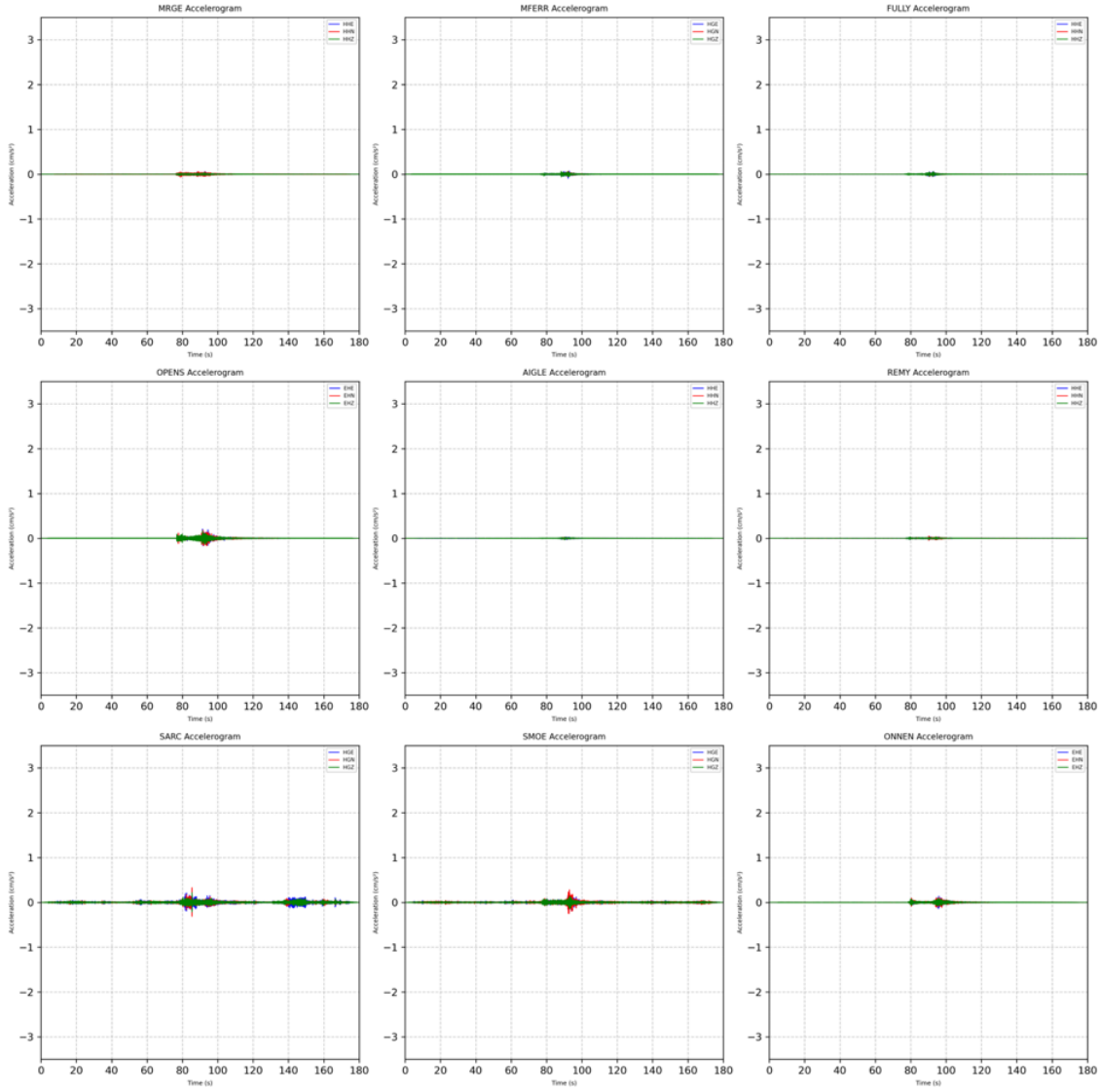

Figure 96: Acceleration time histories for the three components of motion recorded at the stations MRGE, MFERR, FULLY, OPENS, AIGLE, REMY, SARC, SMOE, ONNEN.

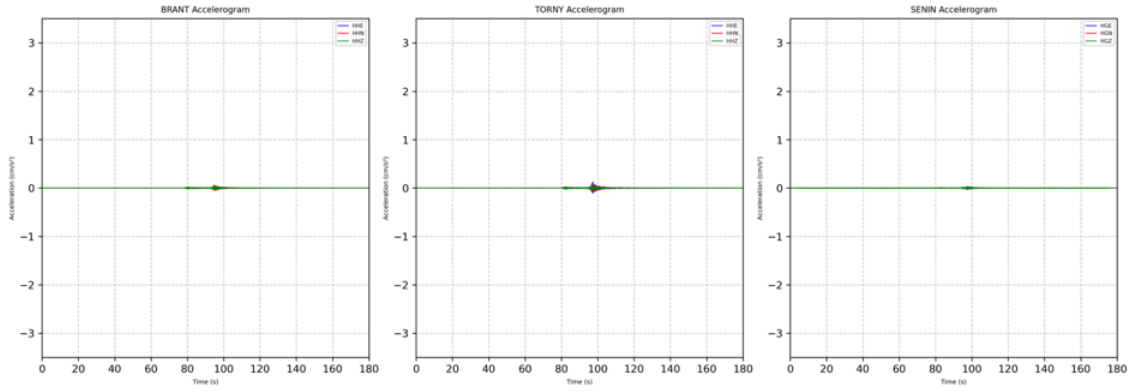

Figure 97: Acceleration time histories for the three components of motion recorded at the stations BRANT, TORNY, SENIN.

Appendix B: From Theory to Practice: The Coin Toss Example

The seemingly simple act of tossing a coin raises intriguing questions about randomness and predictability. Why is the outcome of a coin toss regarded as random, even though it is governed by the deterministic laws of physics? If the process is random, why is a specific probability associated with each possible outcome? Moreover, how can this probability be calculated given the initial conditions? Joseph B. Keller's work provides significant insights into these questions, showing how the physical dynamics of a coin toss can be analysed, while practical uncertainty still leads to randomness [607]. To address these questions, the dynamics of a coin toss, a classical physics problem, offer profound insights into the nature of probability.

A closer look at the motion of a coin, specifically a circular coin with a defined radius and negligible thickness. The coin's center of gravity is assumed to be located at its geometric center. To understand its movement, the height of this center of gravity over time is tracked and denoted as y(t).

According to Newton's laws of motion, the vertical movement of the coin's centre of gravity is influenced by gravity. This relationship can be described using the following differential equation:

$$\frac{d^2y(t)}{dt^2} = -g \tag{117}$$

Here, g represents the constant acceleration due to gravity, a familiar force that pulls objects downward. To complete the description of the coin's motion, initial conditions must be set. At the starting time t = 0, the coin's center is assumed to be at a certain height a, moving upward with an initial velocity u. These conditions are expressed as:

$$y(0) = a \ \left(\text{initial height}\right), \ \frac{dy(0)}{dt} = u \text{ (initial upward velocity)} \tag{118}$$

These two components, the differential equation (117) and the initial conditions (Equations (118)), work together to determine how the height y(t) changes over time. Choosing $y(0) = a$ provides an initial condition that simplifies the calculations. However, the starting height can be adjusted depending on the

specific scenario being considered. This approach facilitates a clearer analysis of the coin's motion over time. This choice helps simplify the calculations that follow and makes it easier to understand how the coin behaves as it moves.

Rotational Motion of the Coin

The coin's motion is not limited to its vertical trajectory; it also undergoes rotation about a horizontal axis that runs through its diameter. For clarity, this axis of rotation is aligned with the z-axis. The angular position of the coin at any given time t can be described by the angle $\theta(t)$. This angle is defined as the measure between the positive y-axis and the normal to the side of the coin marked heads, with both lying in the xy-plane, as illustrated in the figure below (Figure 98).

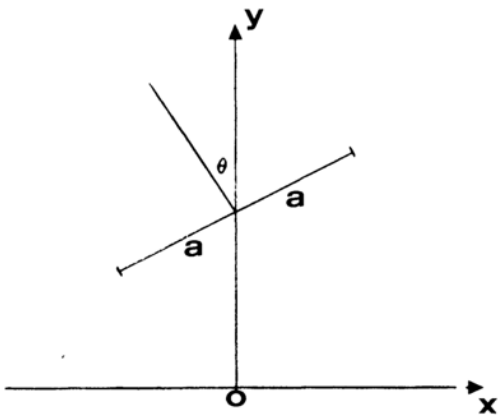

Figure 98: The angular position $\theta(t)$ of the coin in the xy-plane [607].

The rotational dynamics of the coin can be captured by a simple equation, which states:

$$\frac{d^2\theta(t)}{dt^2} = 0 \tag{119}$$

This equation indicates that the angular velocity is constant, provided no external torques act on the coin. At the initial time $t = 0$, the coin is assumed to be oriented horizontally with the heads side facing upward, corresponding to $\theta(0)=0$. Additionally, the coin begins with an initial angular velocity ω. These initial conditions are expressed as:

$$\theta(0) = 0 \ (\text{initial angular position}), \quad \frac{d\theta(0)}{dt} = \omega \ (\text{initial angular velocity}) \tag{120}$$

In the analysis, a different initial value for $\theta(0) = 0$ could have been chosen, but selecting this specific value simplifies the subsequent calculations. This initial condition aligns the coin horizontally at the start, making it easier to track its rotational motion over time.

Solutions to the Differential Equations

The solutions to the differential equations governing both the vertical motion y(t) (Equation (117) and the rotational motion $\theta(t)$ (Equation (119), given the initial conditions for velocity u and angular velocity ω (Equations (118 and (120) are:

For vertical motion:

$$y(t) = ut - \frac{1}{2}gt^2 + a \tag{121}$$

For rotational motion:

$$\theta(t) = \omega t \tag{122}$$

These equations describe the behaviour of the coin from the initial time t=0 until the moment $t_0 > 0$ when the coin makes contact with a surface, assumed to be the plane y = 0. At this moment, the side of the coin facing upwards remains unchanged if the coin lands on a surface such as sand or mud, which absorbs the impact. However, if the coin lands on a hard surface, it might bounce or roll, potentially altering its final orientation.

The coin will settle with the heads side up if, at the moment of impact, the angular position $\theta(t_0)$ satisfies the following inequality:

$$2n\pi - \frac{1}{2} < \theta(t_0) < 2n\pi + \frac{\pi}{2}, \quad n = 0, 1, 2, \ldots \tag{123}$$

This inequality defines the range of angles within which the coin will land heads up. The angle $\theta(t_0)$ must lie within $\frac{\pi}{2}$ radians on either side of an even multiple of 2π. If the angle falls outside this range, the coin will land tails up.

Determining the Landing Time t_0

To determine the exact time t_0 when the coin lands, it is necessary to examine the lowest point of the coin at time t. This position is given by:

$$y(t) - a\,|\sin\theta(t)| \tag{124}$$

At the moment the coin makes contact with the ground, the vertical position $y(t_0)$ must equal the lowest point, which corresponds to the plane y = 0. Therefore, the time t_0 can be found as the smallest positive root of the following equation:

$$y(t_0) - a|\sin\theta(t_0)| = 0 \tag{125}$$

Determining Heads or Tails

With t_0 determined, equations (123) and (125) can be analysed to check whether the coin will land heads up or tails up by substituting t_0 back into the expression for $\theta(t_0) = \omega t_0$. The solution to this will allow us to determine if the coin's final orientation falls within the specified angular range for heads-up landing.

The analysis of equations (123) and (125) will determine if the coin lands heads up for given values of the initial velocity *u* and the initial angular velocity ω. The set of all pairs u, ω of nonnegative values for which it ends up heads will be called the pre-image of heads in the u, ω plane, and denoted as H. First, the end points of the intervals in equation (123) which are given by $\theta(t_0) = \left(2n \pm \frac{1}{2}\right)\pi$ will be considered. At these points, equation (122) yields:

$$\omega(t_0) = \left(2n \pm \frac{1}{2}\right)\pi \tag{126}$$

Now, since equation (125) $y(t_0) – a = 0$. becomes. When equation (121) is used in this equation $\sin(\theta(t0)) = \pm 1$, equation (125) becomes:

$$ut_0 - \frac{gt_0^2}{2} = 0 \tag{127}$$

The positive solution of equation (127) is $t_0 = \frac{2u}{g}$. Then this result in equation (126) to obtain:

$$\omega = \left(2n \pm \frac{1}{2}\right)\frac{\pi g}{2u},\ n = 0, 1, 2 \ldots \tag{128}$$

Pre-image of Heads in the u, ω Plane

The relation equation (128) corresponds to the endpoints of the intervals in equation (123), and therefore it determines the boundaries of the region H in the u, ω plane. This relation is graphed below for many values of n. Each curve is a

hyperbola. On the axis ω=0, heads remain up throughout the toss, so this axis and the adjacent strip lie in H. The next strip lies in T, the pre-image of tails, and the successive strips alternate between H and T, as seen by examining equation (123) (Figure 99).

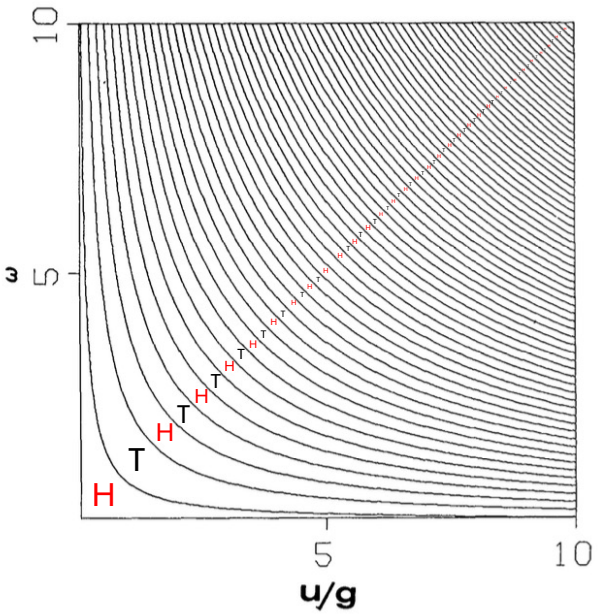

Figure 99: Regions of Heads (H) and Tails (T) outcomes in the u/g vs. ω plane, adapted from B. Keller [607].

In considering these factors, both u/g and ω play significant roles in influencing the probability of whether the coin lands heads-up or tails-up. The normalized initial velocity u/g and the angular velocity ω, around the axis that passes through the coin's centre of gravity, govern the coin's motion. As these factors increase, the vertical separation between the head and tail zones decreases. This suggests that the probability of the coin landing heads-up becomes more conditioned by these two factors, as the zones become closer with increasing values of u/g and ω.

Probability of Heads

So far, the sets H and T in the u, ω plane, which are the pre-images of heads and tails respectively, have been determined. Now suppose that the initial condition u, ω is a random variable with a continuous probability density p(u, ω) with support in the region u > 0, ω > 0. Then the probability of heads P_H is given by:

$$P_H = \int\int_H p(u,\omega)du\, d\omega \tag{129}$$

Thus, the outcome is random because the initial conditions are assumed to be random. This the answer to the first question asked at the beginning. For any value P_H in the interval [0,1], there are densities p for which the integral in equation (129) has that value.

When considering this scenario, it is interesting to reflect on how, despite the equations governing the motion being deterministic (meaning they should predict exactly what happens), real-life coin tosses often feel unpredictable. This is because tiny differences in the initial conditions, which are hard to measure or control exactly, can lead to different outcomes. This unpredictability introduces an element of probability into what might otherwise seem like a straightforward situation, much like the behaviour of complex systems in multi-hazard scenarios.

REFERENCES

[1] S. L. Kramer, *Geotechnical earthquake engineering*, vol. 653. Prentice Hall, 1996.

[2] C. H. Dowding and A. Rozan, 'Damage to Rock Tunnels from Earthquake Shaking', *Journal of the Geotechnical Engineering Division*, vol. 104, no. 2, pp. 175–191, Feb. 1978, doi: 10.1061/AJGEB6.0000580.

[3] E. Alakbarli, M. Andreini, Y. Kadi, S. La Mendola, A. Libertà, and M. Guarascio, 'SEISMIC HAZARD ANALYSIS FOR THE TDC2/TCC2 FACILITY AT CERN: A MULTIVARIATE GEOSTATISTICAL APPROACH', in *Proceedings of the 18th World Conference on Earthquake Engineering (WCEE 2024)*, 2024.

[4] M. Guarascio, A. Libertà, D. Berardi, E. Alakbarli, and M. Lombardi, 'Geostatistical Modeling of Seismic Actions on the Structural Components of The San Benedetto Road Tunnel, Italy', Dec. 2022, pp. 27–38. doi: 10.2495/SSR220021.

[5] M. E. Paté-Cornell, 'Uncertainties in risk analysis: Six levels of treatment', *Reliab Eng Syst Saf*, vol. 54, no. 2–3, pp. 95–111, Nov. 1996, doi: 10.1016/S0951-8320(96)00067-1.

[6] National Fire Protection Association (NFPA), *NFPA 130: Standard for Fixed Guideway Transit and Passenger Rail Systems*. National Fire Protection Association, 2023.

[7] H. Ingason and A. Lönnermark, 'Heat release rates from heavy goods vehicle trailer fires in tunnels', *Fire Saf J*, vol. 40, no. 7, pp. 646–668, Oct. 2005, doi: 10.1016/j.firesaf.2005.06.002.

[8] G. Proulx, 'Evacuation time and movement in apartment buildings', *Fire Saf J*, vol. 24, no. 3, pp. 229–246, Jan. 1995, doi: 10.1016/0379-7112(95)00023-M.

[9] Y. Lee *et al.*, 'Quantitative risk assessment of offshore carbon dioxide injection system considering seismic effects', *International Journal of Greenhouse Gas Control*, vol. 77, pp. 1–13, Oct. 2018, doi: 10.1016/j.ijggc.2018.07.010.

[10] C. Li, L. Ding, Q. Fang, K. Chen, and D. Castro-Lacouture, 'Risk-informed knowledge-based design for road infrastructure in an extreme environment', *Knowl Based Syst*, vol. 216, p. 106741, Mar. 2021, doi: 10.1016/j.knosys.2021.106741.

[11] E. Alakbarli, N. S. Gentile, and M. Guarascio, 'Juridical Side of ALARP: The Monte Bianco Tunnel', in *Proceeding of the 33rd European Safety and Reliability Conference*, Singapore: Research Publishing Services, 2023, pp. 2007–2014. doi: 10.3850/978-981-18-8071-1_P043-cd.

[12] M. Guarascio, E. Alakbarli, C. Despabeladera, A. Ghasemichamazkoti, N. Darabi, and V. Cardinale, 'Acceptability Model of Risk in Italian Tunnels', in *The 10th International Workshop on Applied Probability, IWAP2023*, 2023, p. 66.

[13] M. Guarascio, E. Alakbarli, C. Despabeladera, V. Cardinale, A. Ghasemichamazkoti, and N. Darabi, 'Assessing Risk Acceptability and Tolerability in Italian Tunnels with the Quantum Gu@larp Model', *Entropy*, vol. 26, no. 1, p. 40, Dec. 2023, doi: 10.3390/e26010040.

[14] M. Guarascio *et al.*, 'Road Tunnel Risk-Based Safety Design Methodology by GU@LARP Quantum Risk Model', Dec. 2022, pp. 39–50. doi: 10.2495/SSR220031.

[15] Health and Safety Executive (HSE), *Reducing Risks, Protecting People (R2P2)*. Health and Safety Executive, 2001. [Online]. Available: https://www.hse.gov.uk/enforce/expert/r2p2.htm
[16] C. H. Scholz, *The mechanics of earthquakes and faulting*. Cambridge university press, 2019.
[17] K. Aki and P. G. Richards, *Quantitative seismology*. 2002.
[18] S. Stein and M. Wysession, *An introduction to seismology, earthquakes, and earth structure*. John Wiley & Sons, 2009.
[19] P. M. Shearer, *Introduction to seismology*. Cambridge university press, 2019.
[20] International Seismological Centre (ISC), 'ISC-GEM Earthquake Catalogue'. Accessed: Oct. 29, 2024. [Online]. Available: https://doi.org/10.31905/d808b825
[21] I. Bondár, E. R. Engdahl, A. Villaseñor, J. Harris, and D. Storchak, 'ISC-GEM: Global Instrumental Earthquake Catalogue (1900–2009), II. Location and seismicity patterns', *Physics of the Earth and Planetary Interiors*, vol. 239, pp. 2–13, Feb. 2015, doi: 10.1016/j.pepi.2014.06.002.
[22] D. Di Giacomo, E. R. Engdahl, and D. A. Storchak, 'The ISC-GEM Earthquake Catalogue (1904–2014): status after the Extension Project', *Earth Syst Sci Data*, vol. 10, no. 4, pp. 1877–1899, Oct. 2018, doi: 10.5194/essd-10-1877-2018.
[23] P. Lowman, J. Yates, P. Masuoka, B. Montgomery, J. O'Leary, and D. Salisbury, 'A Digital Tectonic Activity Map of the Earth', *Journal of Geoscience Education*, vol. 47, no. 5, pp. 428–437, Nov. 1999, doi: 10.5408/1089-9995-47.5.428.
[24] ReliefWeb, 'Global Tectonic Activity Map: Earth'. Accessed: Oct. 29, 2024. [Online]. Available: https://reliefweb.int/map/world/global-tectonic-activity-map-earth
[25] The National Aeronautics and Space Administration (NASA), 'Digital Tectonic Activity Map'. Accessed: Oct. 06, 2024. [Online]. Available: https://visibleearth.nasa.gov/images/88415/digital-tectonic-activity-map/88415t
[26] I. Koulakov, S. Tychkov, N. Bushenkova, and A. Vasilevsky, 'Structure and dynamics of the upper mantle beneath the Alpine–Himalayan orogenic belt, from teleseismic tomography', *Tectonophysics*, vol. 358, no. 1–4, pp. 77–96, Nov. 2002, doi: 10.1016/S0040-1951(02)00418-3.
[27] M. Boccaletti, R. Nicolich, and L. Tortorici, 'The Calabrian Arc and the Ionian Sea in the dynamic evolution of the Central Mediterranean', *Mar Geol*, vol. 55, no. 3–4, pp. 219–245, Mar. 1984, doi: 10.1016/0025-3227(84)90070-7.
[28] L. Tortorici, C. Monaco, C. Tansi, and O. Cocina, 'Recent and active tectonics in the Calabrian arc (Southern Italy)', *Tectonophysics*, vol. 243, no. 1–2, pp. 37–55, Mar. 1995, doi: 10.1016/0040-1951(94)00190-K.
[29] A. H. Stride, R. H. Belderson, and N. H. Kenyon, 'Evolving miogeanticlines of the East Mediterranean (Hellenic, Calabrian and Cyprus outer ridges)', *Philosophical Transactions of the Royal Society of London. Series A, Mathematical and Physical Sciences*, vol. 284, no. 1322, pp. 255–285, Feb. 1977, doi: 10.1098/rsta.1977.0010.
[30] A. I. Okay, A. Kaşlılar-Özcan, C. İmren, A. Boztepe-Güney, E. Demirbağ, and İ. Kuşçu, 'Active faults and evolving strike-slip basins in the Marmara Sea, northwest Turkey: a multichannel seismic reflection study', *Tectonophysics*, vol. 321, no. 2, pp. 189–218, May 2000, doi: 10.1016/S0040-1951(00)00046-9.
[31] A. M. C. Şengör *et al.*, 'The North Anatolian fault: A New Look', *Annu Rev Earth Planet Sci*, vol. 33, no. 1, pp. 37–112, May 2005, doi: 10.1146/annurev.earth.32.101802.120415.
[32] A. M. C. Şengör and N. Canitez, 'The North Anatolian fault', 1982, pp. 205–216. doi: 10.1029/GD007p0205.

[33] H. R. Frankel, *The continental drift controversy*, vol. 2. Cambridge University Press, 2012.
[34] A. Wegener, *The origin of continents and oceans*. Courier Corporation, 1966.
[35] A. Hallam, 'Alfred Wegener and the hypothesis of continental drift', *Sci Am*, vol. 232, no. 2, pp. 88–97, 1975.
[36] T. Lay and T. C. Wallace, *Modern global seismology*. Elsevier, 1995.
[37] Z. ETH, 'FAQ - Things to Know About Seismology'. Accessed: Oct. 29, 2024. [Online]. Available: http://www.seismo.ethz.ch/en/knowledge/things-to-know/faq/
[38] European Committee for Standardization (CEN), *Eurocode 8: Design of structures for earthquake resistance - Part 1: General rules, seismic actions and rules for buildings (EN 1998-1:2004)*. Brussels, Belgium: CEN, 2004.
[39] Ministero delle Infrastrutture e dei Trasporti, *D.M. 17/01/2018: Aggiornamento delle "Norme Tecniche per le costruzioni" (NTC2018)*. Gazzetta Ufficiale, Serie Generale n.42 del 20-02-2018 - Suppl. Ordinario n. 8, 2018. Accessed: Oct. 29, 2024. [Online]. Available: https://www.gazzettaufficiale.it/eli/id/2018/2/20/18A00716/sg
[40] Lord Rayleigh, 'On waves propagated along the plane surface of an elastic solid', *Proceedings of the London mathematical Society*, vol. 1, no. 1, pp. 4–11, 1885.
[41] A. E. H. Love, *Some Problems of Geodynamics: Being an Essay to which the Adams Prize in the University of Cambridge was Adjudged in 1911*. University Press, 1911.
[42] D. M. Boore, W. B. Joyner, and T. E. Fumal, 'Equations for Estimating Horizontal Response Spectra and Peak Acceleration from Western North American Earthquakes: A Summary of Recent Work', *Seismological Research Letters*, vol. 68, no. 1, pp. 128–153, Jan. 1997, doi: 10.1785/gssrl.68.1.128.
[43] R. M. W. Musson, G. Grünthal, and M. Stucchi, 'The comparison of macroseismic intensity scales', *J Seismol*, vol. 14, pp. 413–428, 2010.
[44] S. Floridia, *Progettare le strutture in legno*. Flaccovio Dario, 2006.
[45] C. F. Richter, 'An instrumental earthquake magnitude scale', *Bulletin of the seismological society of America*, vol. 25, no. 1, pp. 1–32, 1935.
[46] C. F. Richter, 'ELEMENTARY SEISMOLOGY..', 1958.
[47] F. Romanelli, 'Seismic Sources 4: Earthquake Size'.
[48] D. Hyndman and D. Hyndman, *Natural Hazards and Disasters*. Cengage Learning, 2010.
[49] G. Grünthal, 'European macroseismic scale 1998 (EMS-98)', 1998.
[50] A. S. Elnashai and L. Di Sarno, *Fundamentals of earthquake engineering: from source to fragility*. John Wiley & Sons, 2015.
[51] K. W. Campbell, 'Updated Near-Source Ground-Motion (Attenuation) Relations for the Horizontal and Vertical Components of Peak Ground Acceleration and Acceleration Response Spectra', *Bulletin of the Seismological Society of America*, vol. 93, no. 1, pp. 314–331, Feb. 2003, doi: 10.1785/0120020029.
[52] K. W. Campbell, 'Prediction of Strong Ground Motion Using the Hybrid Empirical Method and Its Use in the Development of Ground-Motion (Attenuation) Relations in Eastern North America', *Bulletin of the Seismological Society of America*, vol. 93, no. 3, pp. 1012–1033, Jun. 2003, doi: 10.1785/0120020002.
[53] K. W. Campbell, 'Strong Motion Attenuation Relations: A Ten-Year Perspective', *Earthquake Spectra*, vol. 1, no. 4, pp. 759–804, Aug. 1985, doi: 10.1193/1.1585292.
[54] K. W. Campbell, '60 Strong-motion attenuation relations', 2003, pp. 1003–1012. doi: 10.1016/S0074-6142(03)80174-2.

[55] D. M. Boore, W. B. Joyner, and T. E. Fumal, ‘Estimation of response spectra and peak accelerations from western North American earthquakes; an interim report’, US Geological Survey, 1993.
[56] G. L. Molas and F. Yamazaki, ‘Attenuation of earthquake ground motion in Japan including deep focus events’, *Bulletin of the Seismological Society of America*, vol. 85, no. 5, pp. 1343–1358, Oct. 1995, doi: 10.1785/BSSA0850051343.
[57] F. Sabetta and A. Pugliese, ‘Estimation of response spectra and simulation of nonstationary earthquake ground motions’, *Bulletin of the Seismological Society of America*, vol. 86, no. 2, pp. 337–352, Apr. 1996, doi: 10.1785/BSSA0860020337.
[58] A. Meslem, F. Yamazaki, Y. Maruyama, D. Benouar, and N. Laouami, ‘Strong motion distribution and microtremor observation following the 21 May 2003 Boumerdes, Algeria earthquake’, in *Proc. 14th World Conf. on Earthquake Engineering*, 2008.
[59] E. Irwansyah, E. Winarko, Z. E. Rasjid, and R. D. Bekti, ‘Earthquake hazard zonation using peak ground acceleration (PGA) approach’, *J Phys Conf Ser*, vol. 423, p. 012067, Apr. 2013, doi: 10.1088/1742-6596/423/1/012067.
[60] M. Guarascio, A. Libertà, and D. Berardi, ‘Application of Seismic Geostatistics to Improve the Territorial Infrastructure Resilience and Sustainability’, 2022.
[61] E. T. H. Zurich, ‘Earthquake Event Page - 1 November 2022’. Accessed: Oct. 29, 2024. [Online]. Available: http://www.seismo.ethz.ch/en/earthquakes/switzerland/eventpage.html?originId=%27c21pOmNoLmV0aHouc2VkL3NjMjBhZy9PcmlnaW4vTkxMLjIwMjIxMTEyMjMzNzE3LjUzNjkxNi43OTY4OQ==%27&magnitude=3.4
[62] E. T. H. Zurich, ‘Strong Motion Portal Event Detail - 1 November 2022 - 1 November 2022’. Accessed: Oct. 29, 2024. [Online]. Available: https://strongmotionportal.seismo.ethz.ch/select-events/results/event-detail/index.html?eventid=472967348
[63] F. Bonnes, A. Miano, A. Fiorillo, A. Prota, M. Andreini, and R. Jacobsson, ‘Seismic Risk of Non-Conforming Steel Structures - Preliminary Assessment of the Ship Decay Vessel at CERN’, in *Proceedings of the 18th World Conference on Earthquake Engineering (WCEE 2024)*, Milan, Italy, 2024.
[64] M. Dolce *et al.*, ‘Seismic risk assessment of residential buildings in Italy’, *Bulletin of Earthquake Engineering*, vol. 19, no. 8, pp. 2999–3032, Jun. 2021, doi: 10.1007/s10518-020-01009-5.
[65] E. H. Isaaks and R. M. Srivastava, ‘Applied geostatistics’, 1989.
[66] D. G. Krige, ‘A statistical approach to some basic mine valuation problems on the Witwatersrand’, *J South Afr Inst Min Metall*, vol. 52, no. 6, pp. 119–139, 1951.
[67] G. Matheron, ‘Principles of geostatistics’, *Economic geology*, vol. 58, no. 8, pp. 1246–1266, 1963.
[68] M. Guarascio, C. J. Huybrechts, and M. David, *Advanced geostatistics in the mining industry: proceedings of the NATO Advanced Study Institute held at the Istituto di Geologia Applicata of the University of Rome, Italy, 13–25 October 1975*, vol. 24. Springer Science & Business Media, 2012.
[69] A. Marechal, ‘The practice of transfer functions: Numerical methods and their application’, in *Advanced Geostatistics in the Mining Industry: Proceedings of the NATO Advanced Study Institute held at the Istituto di Geologia Applicata of the University of Rome, Italy, 13–25 October 1975*, Springer, 1976, pp. 253–276.
[70] P. Goovaerts, *Geostatistics for natural resources evaluation*. Oxford University Press, USA, 1997.

[71] A. G. Journel and C. J. Huijbregts, ‘Mining geostatistics’, 1976.
[72] G. Matheron, ‘The Theory of Regionalized Variables and Its Applications’, *Les Cahiers duCentrede Morphologie Mathematique de Fontainebleau*, no. 5, 1971.
[73] T. Paulay and M. J. N. Priestley, *Seismic design of reinforced concrete and masonry buildings*, vol. 768. Wiley New York, 1992.
[74] A. K. Chopra, *Dynamics of structures*. Pearson Education India, 2007.
[75] Y. M. A. Hashash, J. J. Hook, B. Schmidt, and J. I-Chiang Yao, ‘Seismic design and analysis of underground structures’, *Tunnelling and Underground Space Technology*, vol. 16, no. 4, pp. 247–293, Oct. 2001, doi: 10.1016/S0886-7798(01)00051-7.
[76] G. Tsinidis *et al.*, ‘Seismic behaviour of tunnels: From experiments to analysis’, *Tunnelling and Underground Space Technology*, vol. 99, p. 103334, May 2020, doi: 10.1016/j.tust.2020.103334.
[77] J. Patil, R. Gosavi, and P. Minde, ‘A comprehensive review of seismic response of cast-in-place and prefabricated underground metro station buildings’, *Asian Journal of Civil Engineering*, vol. 25, no. 2, pp. 1877–1898, Feb. 2024, doi: 10.1007/s42107-023-00883-z.
[78] S. Kontoe, L. Zdravkovic, D. M. Potts, and C. O. Menkiti, ‘Case study on seismic tunnel response’, *Canadian Geotechnical Journal*, vol. 45, no. 12, pp. 1743–1764, Dec. 2008, doi: 10.1139/T08-087.
[79] S. Sharma and W. R. Judd, ‘Underground opening damage from earthquakes’, *Eng Geol*, vol. 30, no. 3–4, pp. 263–276, Jun. 1991, doi: 10.1016/0013-7952(91)90063-Q.
[80] G. N. Owen and R. E. Scholl, ‘Earthquake engineering of large underground structures’, 1981.
[81] P. Galli, A. Galderisi, M. Martino, G. S. Mugnozza, and F. Bozzano, ‘The coseismic faulting of the San Benedetto tunnel (2016, Mw 6.6 central Italy earthquake)’, in *Tunnels and Underground Cities: Engineering and Innovation Meet Archaeology, Architecture and Art*, CRC Press, 2020, pp. 805–811.
[82] C. L. Xin *et al.*, ‘Seismic response mechanisms of casing-shape composite tunnel lining: Theoretical analysis and shaking table test verification’, *Soil Dynamics and Earthquake Engineering*, vol. 162, p. 107440, Nov. 2022, doi: 10.1016/j.soildyn.2022.107440.
[83] G. Yan, Z. Zhang, C. Xu, K. Iqbal, P. Dou, and X. Du, ‘Centrifuge shaking table tests on a subway station structure in liquefiable interlayer site’, *Acta Geotech*, vol. 19, no. 4, pp. 1687–1706, Apr. 2024, doi: 10.1007/s11440-023-02005-0.
[84] T. Li, ‘Damage to mountain tunnels related to the Wenchuan earthquake and some suggestions for aseismic tunnel construction’, *Bulletin of Engineering Geology and the Environment*, vol. 71, no. 2, pp. 297–308, May 2012, doi: 10.1007/s10064-011-0367-6.
[85] G. Gazetas, N. Gerolymos, and I. Anastasopoulos, ‘Response of three Athens metro underground structures in the 1999 Parnitha earthquake’, *Soil Dynamics and Earthquake Engineering*, vol. 25, no. 7–10, pp. 617–633, Aug. 2005, doi: 10.1016/j.soildyn.2004.11.006.
[86] E. L. Krinitzsky, ‘Deterministic versus probabilistic seismic hazard analysis for critical structures’, *Eng Geol*, vol. 40, no. 1–2, pp. 1–7, Nov. 1995, doi: 10.1016/0013-7952(95)00031-3.
[87] J. J. Bommer, ‘DETERMINISTIC VS. PROBABILISTIC SEISMIC HAZARD ASSESSMENT: AN EXAGGERATED AND OBSTRUCTIVE DICHOTOMY’, *Journal of Earthquake Engineering*, vol. 6, no. Special Issue 1, p. 43, 2002, doi: 10.1142/S1363246902000644.
[88] B. Bradley, ‘Structure-specific probabilistic seismic risk assessment’, 2009.

[89] J. Baker, B. Bradley, and P. Stafford, *Seismic Hazard and Risk Analysis*. Cambridge University Press, 2021. doi: 10.1017/9781108425056.
[90] L. Mualchin, 'History of Modern Earthquake Hazard Mapping and Assessment in California Using a Deterministic or Scenario Approach', *Pure Appl Geophys*, vol. 168, no. 3–4, pp. 383–407, Mar. 2011, doi: 10.1007/s00024-010-0121-1.
[91] C. A. Cornell, 'Engineering seismic risk analysis', *Bulletin of the Seismological Society of America*, vol. 58, no. 5, pp. 1583–1606, Oct. 1968, doi: 10.1785/BSSA0580051583.
[92] S. L. Kramer and S. B. Paulsen, 'Seismic performance evaluation of reinforced slopes', *Geosynth Int*, vol. 11, no. 6, pp. 429–438, Dec. 2004, doi: 10.1680/gein.2004.11.6.429.
[93] L. Eads, *SEISMIC COLLAPSE RISK ASSESSMENT OF BUILDINGS: EFFECTS OF INTENSITY MEASURE SELECTION AND COMPUTATIONAL APPROACH*. STANFORD UNIVERSITY, 2013.
[94] P. P. Cordova, G. G. Deierlein, S. S. F. Mehanny, and C. A. Cornell, 'Development of a two-parameter seismic intensity measure and probabilistic assessment procedure', in *The second US-Japan workshop on performance-based earthquake engineering methodology for reinforced concrete building structures*, Pacific Earthquake Engineering Research Center, University of California …, 2000, p. 0.
[95] D. Vamvatsikos and C. A. Cornell, 'Incremental dynamic analysis', *Earthq Eng Struct Dyn*, vol. 31, no. 3, pp. 491–514, Mar. 2002, doi: 10.1002/eqe.141.
[96] D. Vamvatsikos and C. Allin Cornell, 'Direct estimation of the seismic demand and capacity of oscillators with multi-linear static pushovers through IDA', *Earthq Eng Struct Dyn*, vol. 35, no. 9, pp. 1097–1117, Jul. 2006, doi: 10.1002/eqe.573.
[97] D. Vamvatsikos and M. Fragiadakis, 'Incremental dynamic analysis for estimating seismic performance sensitivity and uncertainty', *Earthq Eng Struct Dyn*, vol. 39, no. 2, pp. 141–163, 2010.
[98] J. W. Baker, 'Efficient Analytical Fragility Function Fitting Using Dynamic Structural Analysis', *Earthquake Spectra*, vol. 31, no. 1, pp. 579–599, Feb. 2015, doi: 10.1193/021113EQS025M.
[99] J. J. Bommer, 'Earthquake hazard and risk analysis for natural and induced seismicity: towards objective assessments in the face of uncertainty', *Bulletin of Earthquake Engineering*, vol. 20, no. 6, pp. 2825–3069, Apr. 2022, doi: 10.1007/s10518-022-01357-4.
[100] Federal Emergency Management Agency (FEMA), '440, Improvement of nonlinear static seismic analysis procedures', *FEMA-440, Redwood City*, vol. 7, no. 9, p. 11, 2005.
[101] A. Beard and R. Carvel, *Handbook of tunnel fire safety*. ICE publishing, 2012.
[102] H. Ingason, Y. Z. Li, and A. Lönnermark, *Tunnel Fire Dynamics*. New York, NY: Springer New York, 2015. doi: 10.1007/978-1-4939-2199-7.
[103] D. A. Purser and J. L. McAllister, 'Assessment of Hazards to Occupants from Smoke, Toxic Gases, and Heat', in *SFPE Handbook of Fire Protection Engineering*, New York, NY: Springer New York, 2016, pp. 2308–2428. doi: 10.1007/978-1-4939-2565-0_63.
[104] D. A. Purser, 'The effects of fire products on escape capability in primates and human fire victims', *International Association of Fire Safety Science*, vol. 1, pp. 1101–1110, 1986.
[105] National Institute of Standards and Technology (NIST), 'Fire Dynamics'. Accessed: Oct. 29, 2024. [Online]. Available: https://www.nist.gov/el/fire-research-division-73300/firegov-fire-service/fire-dynamics

[106] A. A. Stec, ‘Fire toxicity – The elephant in the room?’, *Fire Saf J*, vol. 91, pp. 79–90, Jul. 2017, doi: 10.1016/j.firesaf.2017.05.003.
[107] H. L. Kaplan, A. F. Grand, W. G. Switzer, D. S. Mitchell, W. R. Rogers, and G. E. Hartzell, ‘Effects of Combustion Gases On Escape Performance of the Baboon and the Rat’, *J Fire Sci*, vol. 3, no. 4, pp. 228–244, Jul. 1985, doi: 10.1177/073490418500300401.
[108] D. Penney, V. Benignus, S. Kephalopoulos, D. Kotzias, M. Kleinman, and A. Verrier, ‘Carbon monoxide’, in *WHO guidelines for indoor air quality: selected pollutants*, World Health Organization, 2010.
[109] C. Tomaszewski, ‘Carbon monoxide’, *Goldfrank’s toxicologic emergencies. 7th edition. New York: McGraw-Hill*, pp. 1478–1497, 2002.
[110] Y. Alarie, ‘Toxicity of Fire Smoke’, *Crit Rev Toxicol*, vol. 32, no. 4, pp. 259–289, Jan. 2002, doi: 10.1080/20024091064246.
[111] National Research Council and Committee on Acute Exposure Guideline Levels, ‘Carbon monoxide acute exposure guideline levels’, in *Acute Exposure Guideline Levels for Selected Airborne Chemicals: Volume 8*, National Academies Press (US), 2010.
[112] D. A. Purser, ‘Combustion Toxicity’, in *SFPE Handbook of Fire Protection Engineering*, New York, NY: Springer New York, 2016, pp. 2207–2307. doi: 10.1007/978-1-4939-2565-0_62.
[113] International Organization for Standardization (ISO), *ISO 13943:2023: Fire safety — Vocabulary*. Geneva, Switzerland: International Organization for Standardization, 2023.
[114] National Fire Protection Association (NFPA), *NFPA 92B: Standard for Smoke Management Systems in Malls, Atria, and Large Spaces*. Quincy, MA: National Fire Protection Association, 2009.
[115] National Fire Protection Association (NFPA), ‘NFPA 92: Standard for Smoke Control Systems’, NFPA, 2024. [Online]. Available: https://www.nfpa.org/codes-and-standards/nfpa-92-standard-development/92
[116] T. Jin, ‘Studies on human behavior and tenability in fire smoke’, *Fire Safety Science*, vol. 5, pp. 3–21, 1997, doi: 10.3801/IAFSS.FSS.5-3.
[117] T. Jin, ‘Visibility Through Fire Smoke.’, 1978.
[118] T. Jin, ‘Studies of emotional instability in smoke from fires’, 1981.
[119] T. Jin and T. Yamada, ‘Irritating effects of fire smoke on visibility’, *Fire Science and Technology*, vol. 5, no. 1, pp. 79–90, 1985.
[120] G. W. Mulholland and C. Croarkin, ‘Specific extinction coefficient of flame generated smoke’, *Fire Mater*, vol. 24, no. 5, pp. 227–230, Sep. 2000, doi: 10.1002/1099-1018(200009/10)24:5<227::AID-FAM742>3.0.CO;2-9.
[121] Elhokayem Lea, ‘Visibility in Smoke With Different Extinction Coefficients’, 2022.
[122] I. Y. Maevski, *Design Fires in Road Tunnels*. Washington, D.C.: National Academies Press, 2011. doi: 10.17226/14562.
[123] International Organization for Standardization (ISO), *ISO/TR 16738:2009 Fire-safety engineering - Technical information on methods for evaluating behaviour and movement of people*. Geneva, Switzerland: International Organization for Standardization, 2009.
[124] British Standards Institution (BSI), ‘7974 Application of Fire Safety Engineering Principles to the Design of Buildings-Code of Practice’, *British Standards Institution, UK*, 2001.
[125] Dipartimento dei Vigili del fuoco del Soccorso pubblico e della Difesa civile, ‘Codice di Prevenzione Incendi’, Ministero dell’Interno, 2021. Accessed: Oct.

29, 2024. [Online]. Available: https://www.vigilfuoco.it/sites/default/files/2022-10/COORD_DM_03_08_2015_Codice_Prevenzione_Incendi.pdf
[126] International Organization for Standardization (ISO), *ISO 13571:2012 Life-threatening components of fire - Guidelines for the estimation of time to compromised tenability in fires*. Geneva, Switzerland: International Organization for Standardization, 2012.
[127] Society of Fire Safety NSW Chapter (SFS), 'Practice Note for Tenability Criteria in Building Fires', Engineers Australia, 2014. Accessed: Oct. 29, 2024. [Online]. Available: https://www.engineersaustralia.org.au/sites/default/files/2024-01/tenability-criteria-practice-note_0.pdf
[128] National Fire Protection Association (NFPA), *NFPA 101: Life Safety Code*. Quincy, MA: National Fire Protection Association, 2024.
[129] D. Drysdale, *An Introduction to Fire Dynamics*. Wiley, 2011. doi: 10.1002/9781119975465.
[130] R. D. Peacock, P. A. Reneke, and G. P. Forney, 'CFAST – Consolidated Model of Fire Growth and Smoke Transport (Version 7) Volume 2: User's Guide', Gaithersburg, MD, Dec. 2015. doi: 10.6028/NIST.TN.1889v2.
[131] N. Johansson, 'Evaluation of a zone model for fire safety engineering in large spaces', *Fire Saf J*, vol. 120, p. 103122, Mar. 2021, doi: 10.1016/j.firesaf.2020.103122.
[132] N. Johansson, E. Ronchi, R. Scozzari, and M. Fronterrè, 'The use of multi-zone modelling for tunnel fires', *Tunnelling and Underground Space Technology*, vol. 134, p. 104996, Apr. 2023, doi: 10.1016/j.tust.2023.104996.
[133] N. Johansson, E. Ronchi, R. Scozzari, and M. Fronterrè, 'The use of multi-zone modelling for tunnel fire risk analysis', 2021.
[134] K. B. McGrattan and G. P. Forney, 'Fire dynamics simulator (version 4) ':, Gaithersburg, MD, 2004. doi: 10.6028/NIST.SP.1019.
[135] Transportstyrelsen (Swedish Transport Agency), 'TSFS 2019:93 Transportstyrelsens föreskrifter om trafiksäkerhetssystem för spårfordon', 2019, Accessed: Oct. 29, 2024. [Online]. Available: https://www.transportstyrelsen.se/sv/Regler/ts-foreskrifter-i-nummerordning/2019/details?RuleNumber=2019:93&ruleprefix=TSFS
[136] R. F. Fahy, G. Proulx, and L. Aiman, 'Panic or not in fire: Clarifying the misconception', *Fire Mater*, vol. 36, no. 5–6, pp. 328–338, Aug. 2012, doi: 10.1002/fam.1083.
[137] K. Fridolf, E. Ronchi, D. Nilsson, and H. Frantzich, 'Movement speed and exit choice in smoke-filled rail tunnels', *Fire Saf J*, vol. 59, pp. 8–21, Jul. 2013, doi: 10.1016/J.FIRESAF.2013.03.007.
[138] J. D. Sime, 'Affiliative behaviour during escape to building exits', *J Environ Psychol*, vol. 3, no. 1, pp. 21–41, Mar. 1983, doi: 10.1016/S0272-4944(83)80019-X.
[139] A. R. Mawson, 'Understanding Mass Panic and Other Collective Responses to Threat and Disaster', *Psychiatry: Interpersonal and Biological Processes*, vol. 68, no. 2, pp. 95–113, Jun. 2005, doi: 10.1521/psyc.2005.68.2.95.
[140] J. Drury, C. Cocking, and S. Reicher, 'The Nature of Collective Resilience: Survivor Reactions to the 2005 London Bombings', *Int J Mass Emerg Disasters*, vol. 27, no. 1, pp. 66–95, Mar. 2009, doi: 10.1177/028072700902700104.
[141] J. Drury and S. D. Reicher, 'Crowd Control', *Sci Am Mind*, vol. 21, no. 5, pp. 58–65, Nov. 2010, doi: 10.1038/scientificamericanmind1110-58.
[142] J. Drury, 'The role of social identity processes in mass emergency behaviour: An integrative review', *Eur Rev Soc Psychol*, vol. 29, no. 1, pp. 38–81, Jan. 2018, doi: 10.1080/10463283.2018.1471948.

[143] R. F. Fahy and G. Proulx, ‘Human behavior in the world trade center evacuation’, in *International Association for Fire Safety Science, Fifth International Symposium*, 1997, pp. 713–724.
[144] J. Drury, C. Cocking, and S. Reicher, ‘Everyone for themselves? A comparative study of crowd solidarity among emergency survivors’, *British Journal of Social Psychology*, vol. 48, no. 3, pp. 487–506, Sep. 2009, doi: 10.1348/014466608X357893.
[145] E. D. Kuligowski, ‘Human Behavior in Fire’, in *SFPE Handbook of Fire Protection Engineering*, New York, NY: Springer New York, 2016, pp. 2070–2114. doi: 10.1007/978-1-4939-2565-0_58.
[146] P. J. DiNenno, *SFPE handbook of fire protection engineering*. 2002.
[147] J. L. Bryan, *SFPE handbook of fire protection engineering 2*. 2002.
[148] H. W. Fischer, *Response to disaster: Fact versus fiction & its perpetuation: The sociology of disaster*. University press of America, 1998.
[149] P. Gantt and R. Gantt, ‘Disaster psychology: Dispelling the myths of panic’, *Prof Saf*, vol. 57, no. 08, pp. 42–49, 2012.
[150] E. L. Quarantelli, ‘The nature and conditions of panic’, *American Journal of Sociology*, vol. 60, no. 3, pp. 267–275, 1954.
[151] J. Drury and S. Reicher, ‘Collective Psychological Empowerment as a Model of Social Change: Researching Crowds and Power’, *Journal of Social Issues*, vol. 65, no. 4, pp. 707–725, Dec. 2009, doi: 10.1111/j.1540-4560.2009.01622.x.
[152] H. Tajfel and Turner John, ‘An integrative theory of intergroup conflict’, *The social psychology of intergroup relations/Brooks/Cole*, 1979.
[153] S. D. Reicher, ‘Crowd behaviour as social action’, *Rediscovering the social group: A self-categorization theory*, vol. 10, 1987.
[154] M. Gerges, S. Penn, D. Moore, C. Boothman, and C. Liyanage, ‘Multi-storey residential buildings and occupant’s behaviour during fire evacuation in the UK’, *International Journal of Building Pathology and Adaptation*, vol. 36, no. 3, pp. 234–253, Jun. 2018, doi: 10.1108/IJBPA-08-2017-0033.
[155] J. Drury, ‘The role of social identity processes in mass emergency behaviour: An integrative review’, *Eur Rev Soc Psychol*, vol. 29, no. 1, pp. 38–81, Jan. 2018, doi: 10.1080/10463283.2018.1471948.
[156] M. Levine, A. Prosser, D. Evans, and S. Reicher, ‘Identity and Emergency Intervention: How Social Group Membership and Inclusiveness of Group Boundaries Shape Helping Behavior’, *Pers Soc Psychol Bull*, vol. 31, no. 4, pp. 443–453, Apr. 2005, doi: 10.1177/0146167204271651.
[157] M. Haghani, ‘Empirical methods in pedestrian, crowd and evacuation dynamics: Part I. Experimental methods and emerging topics’, *Saf Sci*, vol. 129, p. 104743, Sep. 2020, doi: 10.1016/j.ssci.2020.104743.
[158] G. Proulx and R. F. Fahy, ‘Evacuation of the World Trade Center: what went right’, *CIB REPORT*, pp. 27–34, 2003.
[159] J. B. Vieira, S. Pierzchajlo, S. Jangard, A. A. Marsh, and A. Olsson, ‘Acute anxiety during the COVID-19 pandemic was associated with higher levels of everyday altruism’, *Sci Rep*, vol. 12, no. 1, p. 18619, Nov. 2022, doi: 10.1038/s41598-022-23415-2.
[160] E. Haller *et al.*, ‘To Help or Not to Help? Prosocial Behavior, Its Association With Well-Being, and Predictors of Prosocial Behavior During the Coronavirus Disease Pandemic’, *Front Psychol*, vol. 12, Feb. 2022, doi: 10.3389/fpsyg.2021.775032.
[161] S. Tekin, M. Sager, A. Bushey, Y. Deng, and Ö. M. Uluğ, ‘How do people support each other in emergencies? A qualitative exploration of altruistic and prosocial behaviours during the COVID-19 pandemic’, *Analyses of Social Issues*

and Public Policy, vol. 21, no. 1, pp. 1113–1140, Dec. 2021, doi: 10.1111/asap.12277.
[162] N. R. Johnson, 'Panic at "The Who Concert Stampede": An Empirical Assessment', *Soc Probl*, vol. 34, no. 4, pp. 362–373, Oct. 1987, doi: 10.2307/800813.
[163] R. C. Hidalgo, D. R. Parisi, and I. Zuriguel, 'Simulating competitive egress of noncircular pedestrians', *Phys Rev E*, vol. 95, no. 4, p. 042319, Apr. 2017, doi: 10.1103/PhysRevE.95.042319.
[164] M. Haghani, E. Cristiani, N. W. F. Bode, M. Boltes, and A. Corbetta, 'Panic, Irrationality, and Herding: Three Ambiguous Terms in Crowd Dynamics Research', *J Adv Transp*, vol. 2019, pp. 1–58, Aug. 2019, doi: 10.1155/2019/9267643.
[165] P. J. Harding, M. Amos, and S. M. V. Gwynne, 'Mutual Information for the Detection of Crush', in *Pedestrian and Evacuation Dynamics*, Boston, MA: Springer US, 2011, pp. 779–784. doi: 10.1007/978-1-4419-9725-8_73.
[166] G. K. Still, *Crowd dynamics*. University of Warwick UK, 2000.
[167] WCVB Channel 5 Boston, 'Panic inside Boston tunnel after multiple vehicles catch fire, people abandon vehicles'. Accessed: Aug. 19, 2024. [Online]. Available: https://www.youtube.com/watch?v=M_HA7inroRg
[168] Daily Mail, 'Drivers flee their cars in panic after vehicle bursts into flames in the Dartford Tunnel'. Accessed: Aug. 19, 2024. [Online]. Available: https://www.dailymail.co.uk/news/article-3671685/Drivers-flee-cars-panic-vehicle-bursts-flames-Dartford-Tunnel.html
[169] G. Proulx, 'Response to fire alarms', *Fire Protection Engineering*, vol. 33, p. 8, 2007.
[170] M. T. Kinateder, E. D. Kuligowski, P. A. Reneke, and R. D. Peacock, 'Risk perception in fire evacuation behavior revisited: definitions, related concepts, and empirical evidence', *Fire Sci Rev*, vol. 4, no. 1, p. 1, Dec. 2015, doi: 10.1186/s40038-014-0005-z.
[171] J. D. Goltz and L. B. Bourque, 'Earthquakes and human behavior: A sociological perspective', *International Journal of Disaster Risk Reduction*, vol. 21, pp. 251–265, Mar. 2017, doi: 10.1016/J.IJDRR.2016.12.007.
[172] M. K. Lindell *et al.*, 'Immediate behavioural responses to earthquakes in Christchurch, New Zealand, and Hitachi, Japan', *Disasters*, vol. 40, no. 1, pp. 85–111, 2016.
[173] G. Bernardini, R. Lovreglio, and E. Quagliarini, 'Proposing behavior-oriented strategies for earthquake emergency evacuation: A behavioral data analysis from New Zealand, Italy and Japan', *Saf Sci*, vol. 116, pp. 295–309, Jul. 2019, doi: 10.1016/J.SSCI.2019.03.023.
[174] D. E. Wenger and J. M. Weller, 'Disaster subcultures: The cultural residues of community disasters', 1973.
[175] A. M. Winkler, 'The" atom" and American life', *Hist Teacher*, vol. 26, no. 3, pp. 317–337, 1993.
[176] S. K. McBride, J. S. Becker, and D. M. Johnston, 'Exploring the barriers for people taking protective actions during the 2012 and 2015 New Zealand ShakeOut drills', *International Journal of Disaster Risk Reduction*, vol. 37, p. 101150, Jul. 2019, doi: 10.1016/J.IJDRR.2019.101150.
[177] Earthquake Country Alliance (ECA), 'Earthquake Country Alliance'. Accessed: Oct. 29, 2024. [Online]. Available: http://www.earthquakecountry.org
[178] D. Copp, 'Triangle of life', *Translated by Alireza Yasrebi, Mashal Azadi Publications*, 2006.

[179] S. Arlikatti, S. HuANg, C.-H. Yu, and C. Hua, ‘‘Drop, cover and hold on’or ‘Triangle of life’attributes of information sources influencing earthquake protective actions’, *International Journal of Safety and Security Engineering*, vol. 9, no. 3, pp. 213–224, 2019.
[180] Earthquake Country Alliance (Earthquake Country Alliance (ECA)), ‘How to protect yourself during an earthquake’. Accessed: Oct. 29, 2024. [Online]. Available: http://earthquakecountry.org/dropcoverholdon/
[181] United States Geological Survey (USGS), *What is the triangle of life and is it legitimate?* 2018. Accessed: Oct. 29, 2024. [Online]. Available: https://usgs.gov/faqs/what-triangle-life-and-it-legitimate?qt-news_science_products=0#qt-news_science_products
[182] American Red Cross, ‘How to Prepare for Earthquakes’. Accessed: Oct. 29, 2024. [Online]. Available: https://www.redcross.org/get-help/how-to-prepare-for-emergencies/types-of-emergencies/earthquake.html
[183] National Emergency Management Agency New Zealand Government, ‘Drop, Cover, and Hold On: The Right Action During an Earthquake’, 2015. Accessed: Oct. 29, 2024. [Online]. Available: https://getready.govt.nz/assets/Uploads/documents/earthquake/drop-cover-hold/drop-cover-right-action-fact-en-apr15.pdf
[184] Federal Emergency Management Agency (FEMA), ‘Earthquake Early Warning System: Drop, Cover, and Hold On’. Accessed: Oct. 29, 2024. [Online]. Available: https://community.fema.gov/ProtectiveActions/s/article/Earthquake-Earthquake-Early-Warning-System-Drop-Cover-and-Hold-On
[185] J. D. Goltz, H. Park, G. Nakano, and K. Yamori, ‘Earthquake ground motion and human behavior: Using DYFI data to assess behavioral response to earthquakes’, *Earthquake Spectra*, vol. 36, no. 3, pp. 1231–1253, Aug. 2020, doi: 10.1177/8755293019899958.
[186] M. K. Lindell, C. S. Prater, and D. H. House, ‘Cascadia Subduction Zone Residents’ Tsunami Evacuation Expectations’, *Geosciences (Basel)*, vol. 12, no. 5, p. 189, Apr. 2022, doi: 10.3390/geosciences12050189.
[187] M. D’Orazio, L. Spalazzi, E. Quagliarini, and G. Bernardini, ‘Agent-based model for earthquake pedestrians’ evacuation in urban outdoor scenarios: Behavioural patterns definition and evacuation paths choice’, *Saf Sci*, vol. 62, pp. 450–465, Feb. 2014, doi: 10.1016/J.SSCI.2013.09.014.
[188] Z. Feng *et al.*, ‘How people make decisions during earthquakes and post-earthquake evacuation: Using Verbal Protocol Analysis in Immersive Virtual Reality’, *Saf Sci*, vol. 129, p. 104837, Sep. 2020, doi: 10.1016/J.SSCI.2020.104837.
[189] J. D. Goltz, L. A. Russell, and L. B. Bourque, ‘Initial behavioral response to a rapid onset disaster: A case study of the October 1, 1987 Whittier Narrows earthquake’, *Int J Mass Emerg Disasters*, vol. 10, no. 1, pp. 43–69, 1992.
[190] L. J. Vinnell, P. Inch, D. M. Johnston, and N. Horspool, ‘Behavioral responses to earthquake shaking: Video footage analysis of the 2016 kaikōura earthquake in wellington, aotearoa new zealand’, *Earthquake Spectra*, vol. 38, no. 3, pp. 1636–1660, 2022.
[191] G. Bernardini, E. Quagliarini, and M. D’Orazio, ‘Towards creating a combined database for earthquake pedestrians’ evacuation models’, *Saf Sci*, vol. 82, pp. 77–94, Feb. 2016, doi: 10.1016/J.SSCI.2015.09.001.
[192] J. D. Goltz, H. Park, V. Quitoriano, and D. J. Wald, ‘Human Behavioral Response in the 2019 Ridgecrest, California, Earthquakes: Assessing Immediate Actions Based on Data from “Did You Feel It?”’, *Bulletin of the Seismological Society of America*, Jul. 2020, doi: 10.1785/0120200159.

[193] E. Lambie *et al.*, 'Human behaviour during and immediately following earthquake shaking: developing a methodological approach for analysing video footage', *Natural Hazards*, vol. 80, no. 1, pp. 249–283, Jan. 2016, doi: 10.1007/s11069-015-1967-4.
[194] M. Xiao *et al.*, 'Estimation of earthquake safety escape time and casualties in Chinese masonry buildings', *Geomatics, Natural Hazards and Risk*, vol. 14, no. 1, Dec. 2023, doi: 10.1080/19475705.2023.2225690.
[195] P. L. Bernstein and P. L. Bernstein, *Against the gods: The remarkable story of risk*. Wiley New York, 1996.
[196] Court of Appeal (CA), *Edwards v National Coal Board*, vol. 743. 1949.
[197] Aristotle, *Metaphysics*, vol. 1. Harvard University Press Cambridge, MA, 1933.
[198] H. G. Hesiod, *Hesiod: The Homeric Hymns and Homerica (Loeb Classical Library# 57)*. Loeb Classical Library, 1932.
[199] R. R. Dynes, 'The dialogue between Voltaire and Rousseau on the Lisbon earthquake: The emergence of a social science view', *Int J Mass Emerg Disasters*, vol. 18, no. 1, pp. 97–115, 2000.
[200] I. Hacking, *The emergence of probability: A philosophical study of early ideas about probability, induction and statistical inference*. Cambridge University Press, 2006.
[201] L. Daston, *Classical Probability in the Enlightenment*. Princeton University Press, 2023.
[202] N. Luhmann, *Risk: a sociological theory*. Routledge, 2017.
[203] S. Kaplan and B. J. Garrick, 'On the quantitative definition of risk', *Risk analysis*, vol. 1, no. 1, pp. 11–27, 1981.
[204] M. Douglas and A. Wildavsky, *Risk and culture: An essay on the selection of technological and environmental dangers*. Univ of California Press, 1983.
[205] C. R. Sunstein, *Laws of fear: beyond the precautionary principle.* Cambridge University Press, 2005.
[206] U. Beck, *Risk society: Towards a new modernity*, vol. 17. sage, 1992.
[207] D. Frede, 'The sea-battle reconsidered: A defense of the traditional interpretation', *Oxf Stud Anc Philos*, vol. 3, 1985.
[208] C. W. A. Whitaker, *Aristotle's De interpretatione: contradiction and dialectic*. Oxford University Press, 1996.
[209] E. Lybeck, *An Analysis of Nassim Nicholas Taleb's The Black Swan: The Impact of the Highly Improbable*. Macat Library, 2017.
[210] N. Nicholas, 'The black swan: the impact of the highly improbable', *Journal of the Management Training Institut*, vol. 36, no. 3, p. 56, 2008.
[211] International Organization for Standardization (ISO), 'ISO 31000: Risk management – Guidelines', International Organization for Standardization, Geneva, 2018. [Online]. Available: https://www.iso.org/standard/65694.html
[212] Society for Risk Analysis (SRA), 'SRA Glossary', Society for Risk Analysis (SRA), 2020. Accessed: Feb. 04, 2025. [Online]. Available: https://www.sra.org/risk-analysis-introduction/risk-analysis-glossary/
[213] Project Management Institute, *A Guide to the Project Management Body of Knowledge (PMBOK Guide)*, 6th ed. Project Management Institute, 2017.
[214] Project Management Institute (PMI), 'PMBOK Risk Management Guide', Project Management Institute (PMI), 2018. Accessed: Feb. 04, 2025. [Online]. Available: https://www.pmi-centralitaly.org/wp-content/uploads/2019/06/PMBoK_Risk_03072018.pdf
[215] United States Environmental Protection Agency (EPA), 'About Risk Assessment'. Accessed: Feb. 04, 2025. [Online]. Available: https://www.epa.gov/risk/about-risk-assessment

[216] Financial Industry Regulatory Authority (FINRA), ‘Risk’. Accessed: Feb. 04, 2025. [Online]. Available: https://www.finra.org/investors/investing/investing-basics/risk
[217] World Health Organization (WHO), ‘Risk Management Strategy’, World Health Organization, 2023. Accessed: Feb. 04, 2025. [Online]. Available: https://www.who.int/publications/m/item/risk-management-strategy
[218] United Nations Office for Disaster Risk Reduction (UNDRR), ‘Understanding Risk’. Accessed: Feb. 04, 2025. [Online]. Available: https://www.undrr.org/building-risk-knowledge/understanding-risk
[219] Institute of Risk Management (IRM), ‘ARMS 2002: Risk Management Standards’, Institute of Risk Management (IRM), 2002. Accessed: Feb. 04, 2025. [Online]. Available: https://www.theirm.org/media/4709/arms_2002_irm.pdf
[220] National Institute of Standards and Technology (NIST), ‘Guide for Conducting Risk Assessments (SP 800-30 Rev. 1)’, National Institute of Standards and Technology, 2012. Accessed: Oct. 29, 2024. [Online]. Available: https://csrc.nist.gov/pubs/sp/800/30/r1/final
[221] ANAS, ‘Linee guida per la sicurezza nelle gallerie’, ANAS, 2009. Accessed: Oct. 29, 2024. [Online]. Available: https://www.stradeanas.it/sites/default/files/pdf/Linee_guida_sicurezza_gallerie_2009.pdf
[222] M. Guarascio, ‘As Low as Reasonably Practicable": How Does It Work in the Rail and Road Tunnels in Italian Rules. Risk Acceptability/Tolerability Criteria. The Gu@ larp Model’, *Safety and Security Engineering IX*, 2021.
[223] M. Guarascio, ‘Italian risk analysis for road tunnels. PIARC Technical Committee C3. 3 Road tunnel operation’, 2008.
[224] F. N. Laird, ‘The Decline of Deference: The Political Context of Risk Communication’, *Risk Analysis*, vol. 9, no. 4, pp. 543–550, Dec. 1989, doi: 10.1111/j.1539-6924.1989.tb01265.x.
[225] H. Spengler, ‘Kompensatorische Lohndifferenziale und der Wert eines statistischen Lebens in Deutschland’, *Zeitschrift für ArbeitsmarktForschung-Journal for Labour Market Research*, vol. 37, no. 3, pp. 269–305, 2004.
[226] D. N. D. Hartford, ‘Legal framework considerations in the development of risk acceptance criteria’, *Structural Safety*, vol. 31, no. 2, pp. 118–123, Mar. 2009, doi: 10.1016/j.strusafe.2008.06.011.
[227] J. K. Vrijling, W. van Hengel, and R. J. Houben, ‘Acceptable risk as a basis for design’, *Reliab Eng Syst Saf*, vol. 59, no. 1, pp. 141–150, Jan. 1998, doi: 10.1016/S0951-8320(97)00135-X.
[228] J. S. Nathwani, N. C. Lind, and M. D. Pandey, ‘Affordable safety by choice: the life quality method’, *INSTITUTE FOR RISK RESEARCH, WATERLOO, ON(CANADA). 245*, p. 1997, 1997.
[229] B. Fischhoff, ‘Risk Perception and Communication Unplugged: Twenty Years of Process’, *Risk Analysis*, vol. 15, no. 2, pp. 137–145, Apr. 1995, doi: 10.1111/j.1539-6924.1995.tb00308.x.
[230] P. Slovic, ‘Perception of Risk’, *Science (1979)*, vol. 236, no. 4799, pp. 280–285, Apr. 1987, doi: 10.1126/science.3563507.
[231] R. E. Kasperson *et al.*, ‘The Social Amplification of Risk: A Conceptual Framework’, *Risk Analysis*, vol. 8, no. 2, pp. 177–187, Jun. 1988, doi: 10.1111/j.1539-6924.1988.tb01168.x.
[232] C. Yoe, *Principles of Risk Analysis*. Second edition. | Boca Raton : Taylor and Francis, CRC Press, 2019.: CRC Press, 2019. doi: 10.1201/9780429021121.
[233] M. Rausand, *Risk assessment: theory, methods, and applications*, vol. 115. John Wiley & Sons, 2013.

[234] M. Rausand and A. Hoyland, *System reliability theory: models, statistical methods, and applications*, vol. 396. John Wiley & Sons, 2003.
[235] K. Mokhtari, J. Ren, C. Roberts, and J. Wang, 'Application of a generic bow-tie based risk analysis framework on risk management of sea ports and offshore terminals', *J Hazard Mater*, vol. 192, no. 2, pp. 465–475, Aug. 2011, doi: 10.1016/j.jhazmat.2011.05.035.
[236] N. Khakzad, F. Khan, and P. Amyotte, 'Dynamic risk analysis using bow-tie approach', *Reliab Eng Syst Saf*, vol. 104, pp. 36–44, Aug. 2012, doi: 10.1016/j.ress.2012.04.003.
[237] A. S. Markowski and A. Kotynia, '"Bow-tie" model in layer of protection analysis', *Process Safety and Environmental Protection*, vol. 89, no. 4, pp. 205–213, Jul. 2011, doi: 10.1016/j.psep.2011.04.005.
[238] R. Ferdous, F. Khan, R. Sadiq, P. Amyotte, and B. Veitch, 'Handling and updating uncertain information in bow-tie analysis', *J Loss Prev Process Ind*, vol. 25, no. 1, pp. 8–19, Jan. 2012, doi: 10.1016/j.jlp.2011.06.018.
[239] E. Ruijters and M. Stoelinga, 'Fault tree analysis: A survey of the state-of-the-art in modeling, analysis and tools', *Comput Sci Rev*, vol. 15–16, pp. 29–62, Feb. 2015, doi: 10.1016/j.cosrev.2015.03.001.
[240] W. E. Vesely, *Fault tree handbook*, vol. 88. Government Printing Office, 1981.
[241] P. Hopkin, *Fundamentals of risk management: understanding, evaluating and implementing effective risk management*. Kogan Page Publishers, 2018.
[242] British Standards Institution (BSI), 'BS 31100:2021 - Risk management - Code of practice and guidance for the implementation of BS ISO 31000 (Tracked Changes)', British Standards Institution, 2021. [Online]. Available: https://knowledge.bsigroup.com/products/risk-management-code-of-practice-and-guidance-for-the-implementation-of-bs-iso-31000-2018?version=tracked
[243] Committee of Sponsoring Organizations of the Treadway Commission (COSO), 'COSO Enterprise Risk Management Framework: Integrating with Strategy and Performance', Committee of Sponsoring Organizations of the Treadway Commission, 2017.
[244] Standards Australia/Standards New Zealand Standard Committee (AS/NZS), 'AS/NZS ISO 31000: 2009 Risk Management–Principles and Guidelines', *Standards Australia/Standards New Zealand Standard Committee, Sidney*, 2009.
[245] European Commission (EC), *Risk Assessment and Mapping Guidelines for Disaster Management*. Brussels: European Commission, 2010.
[246] United Nations Office for Disaster Risk Reduction (UNDRR), 'Hazard'. Accessed: Oct. 29, 2024. [Online]. Available: https://www.undrr.org/terminology/hazard
[247] United Nations Office for Disaster Risk Reduction (UNDRR) and United Nations General Assembly (UNGA), 'Report of the Open-Ended Intergovernmental Expert Working Group on Indicators and Terminology Relating to Disaster Risk Reduction', United Nations General Assembly, 2016. [Online]. Available: https://undocs.org/A/71/644
[248] United Nations Office for Disaster Risk Reduction (UNDRR), 'UNISDR terminology on disaster risk reduction', *United Nations Office for Disaster Risk Reduction, Report*, 2009, Accessed: Aug. 26, 2024. [Online]. Available: https://www.unisdr.org/files/7817_UNISDRTerminologyEnglish.pdf
[249] E. Keller, *Natural Hazards*. Routledge, 2016. doi: 10.4324/9781315269160.
[250] P. J. Crutzen and E. F. Stoermer, '"The "Anthropocene"' (2000)', in *The Future of Nature*, Yale University Press, 2017, pp. 479–490. doi: 10.12987/9780300188479-041.

[251] M. S. Kappes, M. Keiler, K. von Elverfeldt, and T. Glade, ‘Challenges of analyzing multi-hazard risk: a review’, *Natural Hazards*, vol. 64, no. 2, pp. 1925–1958, Nov. 2012, doi: 10.1007/s11069-012-0294-2.
[252] J. Zschau, ‘2.5 Where are we with multihazards, multirisks assessment capacities?’, 2017.
[253] J. Gill *et al.*, ‘MYRIAD-EUD1. 2 Handbook of Multi-Hazard, Multi-Risk Definitions and Concepts’, *H2020 MYRIAD-EU Project, grant agreement*, no. 101003276, p. 82, 2022, Accessed: Aug. 26, 2024. [Online]. Available: https://www.myriadproject.eu/wp-content/uploads/2022/11/D1_2_Handbook.pdf
[254] Z. Liu, F. Nadim, A. Garcia-Aristizabal, A. Mignan, K. Fleming, and B. Q. Luna, ‘A three-level framework for multi-risk assessment’, *Georisk: Assessment and Management of Risk for Engineered Systems and Geohazards*, vol. 9, no. 2, pp. 59–74, Apr. 2015, doi: 10.1080/17499518.2015.1041989.
[255] G. Delmonaco, C. Margottini, and D. Spizzichino, ‘ARMONIA methodology for multi-risk assessment and the harmonisation of different natural risk maps’, *Deliverable 3.1. 1, ARMONIA*, 2006.
[256] K. Hewitt and I. Burton, ‘The hazardousness of a place: a regional ecology of damaging events’, *(No Title)*, 1971.
[257] J. C. Gill and B. D. Malamud, ‘Reviewing and visualizing the interactions of natural hazards’, *Reviews of Geophysics*, vol. 52, no. 4, pp. 680–722, Dec. 2014, doi: 10.1002/2013RG000445.
[258] W. Marzocchi, A. Garcia-Aristizabal, P. Gasparini, M. L. Mastellone, and A. Di Ruocco, ‘Basic principles of multi-risk assessment: a case study in Italy’, *Natural Hazards*, vol. 62, no. 2, pp. 551–573, Jun. 2012, doi: 10.1007/s11069-012-0092-x.
[259] G. Pescaroli and D. Alexander, ‘A definition of cascading disasters and cascading effects: Going beyond the “toppling dominos” metaphor’, *Planet@ risk*, vol. 3, no. 1, pp. 58–67, 2015.
[260] G. Parisi, *In un volo di storni*. Rizzoli, 2021.
[261] P. Gardoni and J. M. LaFave, ‘Multi-hazard Approaches to Civil Infrastructure Engineering: Mitigating Risks and Promoting Resilence’, in *Multi-hazard Approaches to Civil Infrastructure Engineering*, Cham: Springer International Publishing, 2016, pp. 3–12. doi: 10.1007/978-3-319-29713-2_1.
[262] J. E. Padgett and S. Kameshwar, ‘Supporting Life Cycle Management of Bridges Through Multi-Hazard Reliability and Risk Assessment’, in *Multi-hazard Approaches to Civil Infrastructure Engineering*, Cham: Springer International Publishing, 2016, pp. 41–58. doi: 10.1007/978-3-319-29713-2_3.
[263] H. Guo, Y. Chen, Q. Feng, Q. Lin, and F. Wang, ‘Assessment of damage to buildings and farms during the 2011 M 9.0 earthquake and tsunami in Japan from remote sensing data’, *Chinese Science Bulletin*, vol. 56, no. 20, pp. 2138–2144, Jul. 2011, doi: 10.1007/s11434-011-4544-6.
[264] K. Soga, ‘Innovation in Instrumentation, Monitoring, and Condition Assessment of Infrastructure’, in *Multi-hazard Approaches to Civil Infrastructure Engineering*, Cham: Springer International Publishing, 2016, pp. 465–489. doi: 10.1007/978-3-319-29713-2_21.
[265] H. Mahmoud and A. Chulahwat, ‘Multi-Hazard Multi-Objective Optimization of Building Systems with Isolated Floors Under Seismic and Wind Demands’, in *Multi-hazard Approaches to Civil Infrastructure Engineering*, Cham: Springer International Publishing, 2016, pp. 141–164. doi: 10.1007/978-3-319-29713-2_8.
[266] B. Liu, Y. L. Siu, and G. Mitchell, ‘Hazard interaction analysis for multi-hazard risk assessment: a systematic classification based on hazard-forming

environment', *Natural Hazards and Earth System Sciences*, vol. 16, no. 2, pp. 629–642, Mar. 2016, doi: 10.5194/nhess-16-629-2016.
[267] A. Mignan, S. Wiemer, and D. Giardini, 'The quantification of low-probability–high-consequences events: part I. A generic multi-risk approach', *Natural Hazards*, vol. 73, no. 3, pp. 1999–2022, Sep. 2014, doi: 10.1007/s11069-014-1178-4.
[268] J. Schmidt *et al.*, 'Quantitative multi-risk analysis for natural hazards: a framework for multi-risk modelling', *Natural Hazards*, vol. 58, no. 3, pp. 1169–1192, Sep. 2011, doi: 10.1007/s11069-011-9721-z.
[269] E. Pantoli *et al.*, 'Full-Scale Structural and Nonstructural Building System Performance during Earthquakes: Part II – NCS Damage States', *Earthquake Spectra*, vol. 32, no. 2, pp. 771–794, May 2016, doi: 10.1193/012414eqs017m.
[270] M. C. Chen *et al.*, 'Full-Scale Structural and Nonstructural Building System Performance during Earthquakes: Part I – Specimen Description, Test Protocol, and Structural Response', *Earthquake Spectra*, vol. 32, no. 2, pp. 737–770, May 2016, doi: 10.1193/012414eqs016m.
[271] B. J. Meacham, 'Post-Earthquake Fire Performance of Buildings: Summary of a Large-Scale Experiment and Conceptual Framework for Integrated Performance-Based Seismic and Fire Design', *Fire Technol*, vol. 52, no. 4, pp. 1133–1157, Jul. 2016, doi: 10.1007/s10694-015-0523-9.
[272] A. I. Sekizawa, M. Ebihara, and H. Notake, 'Development of seismic-induced fire risk assessment method for a building', *system*, vol. 83, no. 20, pp. 21–24, 2000.
[273] C. Song *et al.*, 'Triggering and recovery of earthquake accelerated landslides in Central Italy revealed by satellite radar observations', *Nat Commun*, vol. 13, no. 1, p. 7278, Nov. 2022, doi: 10.1038/s41467-022-35035-5.
[274] T. Lou, W. Wang, and B. A. Izzuddin, 'A framework for performance-based assessment in post-earthquake fire: Methodology and case study', *Eng Struct*, vol. 294, p. 116766, Nov. 2023, doi: 10.1016/j.engstruct.2023.116766.
[275] D. P. Coppola, 'Hazards', in *Introduction to International Disaster Management*, Elsevier, 2015, pp. 40–149. doi: 10.1016/B978-0-12-801477-6.00002-2.
[276] J. Mohammadi, S. Alyasin, and D. N. Bak, *Investigation of cause and effects of fires following the Loma Prieta earthquake*. Illinois Institute of Technology, Department of Civil Engineering, Armour …, 1992.
[277] M. C. de Ruiter, A. Couasnon, M. J. C. van den Homberg, J. E. Daniell, J. C. Gill, and P. J. Ward, 'Why We Can No Longer Ignore Consecutive Disasters', *Earths Future*, vol. 8, no. 3, Mar. 2020, doi: 10.1029/2019EF001425.
[278] P. Gasparini and A. Garcia-Aristizabal, 'Seismic Risk Assessment, Cascading Effects', in *Encyclopedia of Earthquake Engineering*, Berlin, Heidelberg: Springer Berlin Heidelberg, 2014, pp. 1–20. doi: 10.1007/978-3-642-36197-5_260-1.
[279] S. L. Cutter *et al.*, 'Disaster Resilience: A National Imperative', *Environment: Science and Policy for Sustainable Development*, vol. 55, no. 2, pp. 25–29, Mar. 2013, doi: 10.1080/00139157.2013.768076.
[280] United Nations Office for Disaster Risk Reduction (UNDRR), 'Terminology - Understanding disaster risk'. Accessed: Oct. 29, 2024. [Online]. Available: https://www.undrr.org/drr-glossary/terminology
[281] R. Ciurean, J. Gill, H. J. Reeves, S. O'Grady, and T. Aldridge, 'Review of environmental multi-hazards research and risk assessments', *Br. Geol. Survey*, vol. 86, no. Apr, p. 13, 2018.

[282] European Commission (EC), ‘European Disaster Risk Management’. Accessed: Oct. 29, 2024. [Online]. Available: https://civil-protection-humanitarian-aid.ec.europa.eu/what/civil-protection/european-disaster-risk-management_en
[283] European Council, ‘Disaster Risk Reduction in EU external action - Council conclusions’, Council of the European Union, 2022. Accessed: Oct. 29, 2024. [Online]. Available: https://data.consilium.europa.eu/doc/document/ST-14463-2022-INIT/en/pdf
[284] P. J. Ward *et al.*, ‘Invited perspectives: A research agenda towards disaster risk management pathways in multi-(hazard-)risk assessment’, *Natural Hazards and Earth System Sciences*, vol. 22, no. 4, pp. 1487–1497, Apr. 2022, doi: 10.5194/nhess-22-1487-2022.
[285] L. Peek, S. S. Ryder, J. Moresco, and B. Tucker, ‘Disaster Risk Reduction Strategies in Earthquake-Prone Cities’, in *Multi-hazard Approaches to Civil Infrastructure Engineering*, Cham: Springer International Publishing, 2016, pp. 507–532. doi: 10.1007/978-3-319-29713-2_23.
[286] United Nations Office for Disaster Risk Reduction (UNDRR), ‘Hyogo Framework for Action 2005-2015: Mid-Term Review’, United Nations Office for Disaster Risk Reduction, 2011. [Online]. Available: https://www.undrr.org/publication/hyogo-framework-action-2005-2015-mid-term-review
[287] United Nations Office for Disaster Risk Reduction (UNDRR), ‘Sendai Framework for Disaster Risk Reduction 2015-2030’, United Nations Office for Disaster Risk Reduction, 2015. [Online]. Available: https://www.undrr.org/publication/sendai-framework-disaster-risk-reduction-2015-2030
[288] R. Ba, Q. Deng, Y. Liu, R. Yang, and H. Zhang, ‘Multi-hazard disaster scenario method and emergency management for urban resilience by integrating experiment–simulation–field data’, *Journal of Safety Science and Resilience*, vol. 2, no. 2, pp. 77–89, Jun. 2021, doi: 10.1016/j.jnlssr.2021.05.002.
[289] J. Kozák and V. Čermák, *The Illustrated History of Natural Disasters*. Dordrecht: Springer Netherlands, 2010. doi: 10.1007/978-90-481-3325-3.
[290] D. Fäh *et al.*, ‘The 1356 Basel earthquake: an interdisciplinary revision’, *Geophys J Int*, vol. 178, no. 1, pp. 351–374, Jul. 2009, doi: 10.1111/j.1365-246X.2009.04130.x.
[291] C. Scawthorn, ‘Fire following earthquake’, *Fire Safety Science*, vol. 1, pp. 971–979, 1986.
[292] C. Scawthorn, ‘Fire Losses from Earthquakes: State of the Art’, 1987, pp. 237–261. doi: 10.1016/B978-0-444-98955-0.50022-7.
[293] C. Scawthorn, T. D. O’Rourke, and F. T. Blackburn, ‘The 1906 San Francisco Earthquake and Fire—Enduring Lessons for Fire Protection and Water Supply’, *Earthquake Spectra*, vol. 22, no. 2_suppl, pp. 135–158, Apr. 2006, doi: 10.1193/1.2186678.
[294] K. Himoto, ‘Comparative Analysis of Post-Earthquake Fires in Japan from 1995 to 2017’, *Fire Technol*, vol. 55, no. 3, pp. 935–961, May 2019, doi: 10.1007/s10694-018-00813-5.
[295] J. Mohammadi, S. Alyasin, and D. N. Bak, *Investigation of cause and effects of fires following the Loma Prieta earthquake*. Illinois Institute of Technology, Department of Civil Engineering, Armour …, 1992.
[296] M. E. Durkin, ‘Improving earthquake casualty and loss estimation’, in *Proceedings of the Tenth*, 1992.

[297] R. Dobashi, ‘Fire and explosion disasters occurred due to the Great East Japan Earthquake (March 11, 2011)’, *J Loss Prev Process Ind*, vol. 31, pp. 121–126, Sep. 2014, doi: 10.1016/j.jlp.2014.03.001.
[298] M. E. Durkin, ‘Casualty patterns in the 1994 Northridge, California earthquake’, *Suicide*, vol. 1, p. 01, 1996.
[299] C. Scawthorn, J. M. Eidinger, and A. Schiff, *Fire following earthquake*, vol. 26. ASCE Publications, 2005.
[300] R. Okuwaki, Y. Yagi, A. Murakami, and Y. Fukahata, ‘A Multiplex Rupture Sequence Under Complex Fault Network Due To Preceding Earthquake Swarms During the 2024 Mw 7.5 Noto Peninsula, Japan, Earthquake’, *Geophys Res Lett*, vol. 51, no. 11, Jun. 2024, doi: 10.1029/2024GL109224.
[301] A. Suppasri, M. Kitamura, D. Alexander, S. Seto, and F. Imamura, ‘The 2024 Noto Peninsula earthquake: Preliminary observations and lessons to be learned’, *International Journal of Disaster Risk Reduction*, vol. 110, p. 104611, Aug. 2024, doi: 10.1016/j.ijdrr.2024.104611.
[302] E. Krausmann, A. M. Cruz, and E. Salzano, *Natech risk assessment and management: reducing the risk of natural-hazard impact on hazardous installations*. Elsevier, 2016.
[303] K. Smith, C. J. Fearnley, D. Dixon, D. K. Bird, and I. Kelman, *Environmental Hazards*. London: Routledge, 2023. doi: 10.4324/9781351261647.
[304] Joint Research Centre (JRC), ‘Natural hazard-triggered industrial accidents: Are they black swans?’ Accessed: Oct. 29, 2024. [Online]. Available: https://joint-research-centre.ec.europa.eu/jrc-news-and-updates/natural-hazard-triggered-industrial-accidents-are-they-black-swans-2021-05-04_en
[305] E. Krausmann and A. Necci, ‘Thinking the unthinkable: A perspective on Natech risks and Black Swans’, *Saf Sci*, vol. 139, p. 105255, Jul. 2021, doi: 10.1016/j.ssci.2021.105255.
[306] S. CHEN, M. XIAO, X. WANG, and J. CHEN, ‘Numerical analysis of seismic damage characteristics of an underground cavern intersected by a steeply dipped fault’, *Rock and Soil Mechanics*, vol. 42, no. 9, p. 9, 2021.
[307] H. Ritchie and P. Rosado, ‘Natural Disasters’, *Our World in Data*, 2022, Accessed: Aug. 28, 2024. [Online]. Available: https://ourworldindata.org/natural-disasters
[308] W. Pascaline and H. Rowena, ‘Economic Losses, Poverty and Disaster 1998-2017’, *United Nations Office for Disaster Risk Reduction*, 2018, [Online]. Available: https://www.undrr.org/publication/economic-losses-poverty-disasters-1998-2017#:~:text=
[309] A. Tilloy, B. D. Malamud, H. Winter, and A. Joly-Laugel, ‘A review of quantification methodologies for multi-hazard interrelationships’, *Earth Sci Rev*, vol. 196, p. 102881, Sep. 2019, doi: 10.1016/j.earscirev.2019.102881.
[310] C. S. Peirce, *Collected papers of charles sanders peirce*, vol. 5. Harvard University Press, 1974.
[311] R. J. Ormerod, ‘Rational inference: deductive, inductive and probabilistic thinking’, *Journal of the Operational Research Society*, vol. 61, no. 8, pp. 1207–1223, Aug. 2010, doi: 10.1057/jors.2009.96.
[312] F.-M. Arouet, *Candide ou l’Optimisme*. BoD-Books on Demand, 2019.
[313] S. Billingslea, ‘Echoes of Leibniz in Pope’s Essay on Man: Criticism and Cultural Shift in the Eighteenth Century’, *Pursuit-The Journal of Undergraduate Research at The University of Tennessee*, vol. 8, no. 1, p. 3, 2017.
[314] R. C. Stalnaker, ‘Probability and conditionals’, *Philos Sci*, vol. 37, no. 1, pp. 64–80, 1970.

[315] I. Opie and P. Opie, *The Oxford dictionary of nursery rhymes*. Oxford University Press, 1997.
[316] S. Kaplan, Y. Y. Haimes, and B. J. Garrick, 'Fitting Hierarchical Holographic Modeling into the Theory of Scenario Structuring and a Resulting Refinement to the Quantitative Definition of Risk', *Risk Analysis*, vol. 21, no. 5, pp. 807–807, Oct. 2001, doi: 10.1111/0272-4332.215153.
[317] T. Aven, *Foundations of risk analysis*. John Wiley & Sons, 2012.
[318] T. Aven, 'Ignoring scenarios in risk assessments: Understanding the issue and improving current practice', *Reliab Eng Syst Saf*, vol. 145, pp. 215–220, Jan. 2016, doi: 10.1016/J.RESS.2015.08.012.
[319] J. R. Hall and A. Sekizawa, 'Revisiting Our 1991 Paper on Fire Risk Assessment', *Fire Technol*, vol. 46, no. 4, pp. 789–801, Oct. 2010, doi: 10.1007/s10694-010-0146-0.
[320] International Organization for Standardization (ISO), 'ISO 23932-1:2018 Fire safety engineering — General principles — Part 1: General', ISO, Geneva, Switzerland, 2018. [Online]. Available: https://www.iso.org/standard/63933.html
[321] International Organization for Standardization (ISO), 'ISO 16732-1:2012 Fire safety engineering — Fire risk assessment Part 1: General', ISO, Geneva, Switzerland, 2012. [Online]. Available: https://www.iso.org/standard/51504.html
[322] R. Durrett, *Probability: theory and examples*, vol. 49. Cambridge university press, 2019.
[323] D. Bertsekas and J. N. Tsitsiklis, *Introduction to probability*, vol. 1. Athena Scientific, 2008.
[324] J. L. Weatherwax, 'A Solution Manual for: A First Course In Probability by Sheldon M. Ross', 2013.
[325] E. T. Jaynes, *Probability theory: The logic of science*. Cambridge university press, 2003.
[326] M. DeGroot and M. Schervish, *Probability and Statistics*, 4th ed. Pearson, 2012. [Online]. Available: https://www.amazon.com/Probability-Statistics-4th-Morris-DeGroot/dp/0321500466
[327] G. Koch, 'La matematica del probabile', Aracne, 1997.
[328] International Organization for Standardization (ISO), 'ISO 13822:2010 - Bases for design of structures - Assessment of existing structures', International Organization for Standardization, 2010. [Online]. Available: https://www.iso.org/standard/46556.html
[329] International Organization for Standardization (ISO), *ISO 2394:2015 - General principles on reliability for structures*. International Organization for Standardization, 2015. [Online]. Available: https://www.iso.org/standard/58036.html
[330] X.-H. Yu, K. Qian, D.-G. Lu, and B. Li, 'Progressive Collapse Behavior of Aging Reinforced Concrete Structures Considering Corrosion Effects', *Journal of Performance of Constructed Facilities*, vol. 31, no. 4, Aug. 2017, doi: 10.1061/(ASCE)CF.1943-5509.0001001.
[331] Y. Mori and B. R. Ellingwood, 'Reliability-Based Service-Life Assessment of Aging Concrete Structures', *Journal of Structural Engineering*, vol. 119, no. 5, pp. 1600–1621, May 1993, doi: 10.1061/(ASCE)0733-9445(1993)119:5(1600).
[332] R. Kacker, S. K. Singh, and A. A. Kasar, 'Understanding and Addressing Multi-faceted Failures in Building Structures', *Journal of Failure Analysis and Prevention*, vol. 24, no. 4, pp. 1542–1558, Aug. 2024, doi: 10.1007/s11668-024-01994-8.

[333] M. Morgese, F. Ansari, M. Domaneschi, and G. P. Cimellaro, ‘Post-collapse analysis of Morandi’s Polcevera viaduct in Genoa Italy’, *J Civ Struct Health Monit*, vol. 10, no. 1, pp. 69–85, Feb. 2020, doi: 10.1007/s13349-019-00370-7.
[334] G. M. Calvi *et al.*, ‘Once upon a Time in Italy: The Tale of the Morandi Bridge’, *Structural Engineering International*, vol. 29, no. 2, pp. 198–217, Apr. 2019, doi: 10.1080/10168664.2018.1558033.
[335] United States Geological Survey (USGS), ‘Aftershock Forecasting’. Accessed: Oct. 29, 2024. [Online]. Available: https://www.usgs.gov/publications/aftershock-forecasting
[336] X. Lu, Q. Cheng, Z. Xu, and C. Xiong, ‘Regional seismic-damage prediction of buildings under mainshock—aftershock sequence’, *Frontiers of Engineering Management*, vol. 8, no. 1, pp. 122–134, Mar. 2021, doi: 10.1007/s42524-019-0072-x.
[337] P. G. de Quevedo Iñarritu, N. Šipčić, and P. Bazzurro, ‘Engineering Demand Parameters for Cumulative Damage Estimation in URM and RC Buildings’, 2023, pp. 57–71. doi: 10.1007/978-3-031-36562-1_5.
[338] National Institute of Standards and Technology (NIST), ‘NIST WTC 7 Investigation Finds Building Fires Caused Collapse’. Accessed: Oct. 29, 2024. [Online]. Available: https://www.nist.gov/news-events/news/2008/08/nist-wtc-7-investigation-finds-building-fires-caused-collapse
[339] R. S. MacNeill and T. P. McAllister, ‘Global Structural Analysis of the Response of World Trade Center Building 7 to Fires and Debris Impact Damage, Federal Building and Fire Safety Investigation of the World Trade Center Disaster (NIST NCSTAR 1-9A)’, 2008.
[340] M. A. Orabi, L. Jiang, A. Usmani, and J. Torero, ‘The Collapse of World Trade Center 7: Revisited’, *Fire Technol*, vol. 60, no. 5, pp. 2963–2990, Sep. 2024, doi: 10.1007/s10694-022-01225-2.
[341] R. Gilsanz, ‘WTC 7’, 2002.
[342] A. A. Khan, R. V. V. Domada, X. Huang, M. A. Khan, and A. Usmani, ‘Modeling the collapse of the Plasco Building. Part I: Reconstruction of fire’, *Build Simul*, vol. 15, no. 4, pp. 583–596, Apr. 2022, doi: 10.1007/s12273-021-0825-4.
[343] A. A. Khan *et al.*, ‘Fire modelling framework for investigating tall building fire: A case study of the Plasco Building’, *Case Studies in Thermal Engineering*, vol. 45, p. 103018, May 2023, doi: 10.1016/j.csite.2023.103018.
[344] P. Ntzeremes and K. Kirytopoulos, ‘Applying a stochastic-based approach for developing a quantitative risk assessment method on the fire safety of underground road tunnels’, *Tunnelling and Underground Space Technology*, vol. 81, pp. 619–631, Nov. 2018, doi: 10.1016/j.tust.2018.08.020.
[345] M. Shirato, ‘Investigation of Tunnel Ceiling Collapse Accident’, 2014.
[346] V. Babrauskas, ‘Research on electrical fires: The state of the art’, *Fire Saf. Sci*, vol. 9, pp. 3–18, 2008.
[347] T. Vairo, M. Pontiggia, and B. Fabiano, ‘Critical aspects of natural gas pipelines risk assessments. A case-study application on buried layout’, *Process Safety and Environmental Protection*, vol. 149, pp. 258–268, May 2021, doi: 10.1016/j.psep.2020.10.050.
[348] R. K. Eckhoff, *Explosion hazards in the process industries*. Gulf Professional Publishing, 2016.
[349] N. Bariha, I. M. Mishra, and V. C. Srivastava, ‘Hazard analysis of failure of natural gas and petroleum gas pipelines’, *J Loss Prev Process Ind*, vol. 40, pp. 217–226, Mar. 2016, doi: 10.1016/j.jlp.2015.12.025.

[350] Z. Bilal, K. Mohammed, and H. Brahim, ‘Bayesian network and bow tie to analyze the risk of fire and explosion of pipelines’, *Process Safety Progress*, vol. 36, no. 2, pp. 202–212, Jun. 2017, doi: 10.1002/prs.11860.
[351] R. B. Campbell, *Fires in industrial and manufacturing properties*. National Fire Protection Association. Research, Data and Analytics Division, 2018.
[352] T. McGree, ‘Fire in Industrial or Manufacturing Properties’. Accessed: Oct. 29, 2024. [Online]. Available: https://www.nfpa.org/education-and-research/research/nfpa-research/fire-statistical-reports/fires-in-us-industrial-or-manufacturing-properties
[353] T.-T. Wang, O.-L. A. Kwok, and F.-S. Jeng, ‘Seismic response of tunnels revealed in two decades following the 1999 Chi-Chi earthquake (Mw 7.6) in Taiwan: A review’, *Eng Geol*, vol. 287, p. 106090, Jun. 2021, doi: 10.1016/j.enggeo.2021.106090.
[354] X. Fan *et al.*, ‘What we have learned from the 2008 Wenchuan Earthquake and its aftermath: A decade of research and challenges’, *Eng Geol*, vol. 241, pp. 25–32, Jul. 2018, doi: 10.1016/j.enggeo.2018.05.004.
[355] European Spallation Source (ESS), ‘ESS-0136479 RISE Seismic test of a sprinkler pump and its tank’, ESS, 2017.
[356] European Spallation Source (ESS), ‘ESS-0135316 Fire Water Supply - Seismic test of diesel pump at RISE in Borås’, ESS, 2017.
[357] European Spallation Source (ESS), ‘ESS-0096591 Seismic load for diesel pump laboratory test’, ESS, 2017.
[358] J.-K. Kim, B. J. Meacham, H. Park, T. Hutchinson, and E. Pantoli, ‘Fire performance of a full-scale building subjected to earthquake motions: test specimen, seismic motions and performance of fire protection systems’, 2014.
[359] P. Covi, N. Tondini, A. Sarreshtehdari, and N. Elhami-Khorasani, ‘Fires Following Earthquake Fragility Functions for Protected Steel Braced Frames’, *Fire Technol*, vol. 60, no. 4, pp. 2815–2844, Jul. 2024, doi: 10.1007/s10694-023-01526-0.
[360] L. Fiorino, V. Macillo, and R. Landolfo, ‘Shake table tests of a full-scale two-story sheathing-braced cold-formed steel building’, *Eng Struct*, vol. 151, pp. 633–647, Nov. 2017, doi: 10.1016/j.engstruct.2017.08.056.
[361] S. Zhang, B. Wang, L. Zhang, S. Lacasse, F. Nadim, and Y. Chen, ‘Increased human risk caused by cascading hazards – A framework’, *Science of The Total Environment*, vol. 857, p. 159308, Jan. 2023, doi: 10.1016/j.scitotenv.2022.159308.
[362] S. Kwag and A. Gupta, ‘Probabilistic risk assessment framework for structural systems under multiple hazards using Bayesian statistics’, *Nuclear Engineering and Design*, vol. 315, pp. 20–34, Apr. 2017, doi: 10.1016/j.nucengdes.2017.02.009.
[363] M. Jones-Lee and T. Aven, ‘ALARP—What does it really mean?’, *Reliab Eng Syst Saf*, vol. 96, no. 8, pp. 877–882, Aug. 2011, doi: 10.1016/j.ress.2011.02.006.
[364] Act HSW, ‘The Health and Safety at Work, Etc. Act’, 1974, *HMSO, London*. Accessed: Sep. 20, 2024. [Online]. Available: https://www.legislation.gov.uk/ukpga/1974/37/contents
[365] House of Lords (HL), *Marshall v Gotham Co Ltd*, vol. 300. 1954.
[366] B. Barrett, *Occupational Health & Safety Law Cases & Materials 2/e*. Routledge, 2000.
[367] M. Jones-Lee and T. Aven, ‘ALARP—What does it really mean?’, *Reliab Eng Syst Saf*, vol. 96, no. 8, pp. 877–882, Aug. 2011, doi: 10.1016/j.ress.2011.02.006.

[368] Court of Justice of the European Union (CJEU), ‘C-127/05 - Commission v United Kingdom’, 2007, *Court of Justice of the European Union*. [Online]. Available: https://curia.europa.eu/juris/liste.jsf?language=en&num=C-127/05
[369] Health and Safety Executive (HSE), ‘Legal Status of Guidance and ACOPs’. Accessed: Oct. 29, 2024. [Online]. Available: https://www.hse.gov.uk/legislation/legal-status.htm
[370] A. Dinariyana, K. Artana, D. Handani, F. Sarasvati, and P. Aprilia, ‘Societal risk assessment of terminal and oil refinery unit’, *IOP Conf Ser Mater Sci Eng*, vol. 1052, no. 1, p. 012025, Jan. 2021, doi: 10.1088/1757-899X/1052/1/012025.
[371] C. R. Timms, ‘Acheiving ALARP with Safety Instrumented Systems’, *Measurement and Control*, vol. 39, no. 10, pp. 298–303, Dec. 2006, doi: 10.1177/002029400603901001.
[372] Health and Safety Executive (HSE), ‘Guidance on ALARP Decisions in COMAH’, Health and Safety Executive, UK. Accessed: Oct. 29, 2024. [Online]. Available: https://www.hse.gov.uk/foi/internalops/hid_circs/permissioning/spc_perm_37/
[373] *Decreto Legislativo 05 ottobre 2006, n. 264: Attuazione della direttiva 2004/54/CE in materia di sicurezza per le gallerie della rete stradale transeuropea*. Normattiva, 2006. Accessed: Oct. 29, 2024. [Online]. Available: https://www.normattiva.it/uri-res/N2Ls?urn:nir:stato:decreto.legislativo:2006-10-05;264
[374] del S. pubblico e della D. civile Dipartimento dei Vigili del fuoco, *Testo Coordinato del D. Lgs 05 ottobre 2006, n. 264: Attuazione della direttiva 2004/54/CE in materia di sicurezza per le gallerie della rete stradale transeuropea*. Ministero dell’Interno, 2006. Accessed: Oct. 29, 2024. [Online]. Available: https://www.vigilfuoco.it/sites/default/files/coordinated-text/COORD_DLGS_05_10_2006_n_264.pdf
[375] M. Guarascio, ‘Italian risk analysis for road tunnels’, *PIARC Technical Committee C*, vol. 3, pp. 209–223, 2008.
[376] European Parliament (EP) and European Council, *Directive 2004/54/EC of the European Parliament and of the Council of 29 April 2004 on minimum safety requirements for tunnels in the Trans-European Road Network*. Official Journal of the European Union, 2004. Accessed: Oct. 29, 2024. [Online]. Available: https://eur-lex.europa.eu/legal-content/EN/TXT/?uri=celex%3A32004L0054
[377] S. Yasseri, ‘The ALARP argument’, *FABIG newsletter*, vol. 61, 2013.
[378] G. Maselli, M. Macchiaroli, and A. Nesticò, ‘ALARP Criteria to Estimate Acceptability and Tolerability Thresholds of the Investment Risk’, *Applied Sciences*, vol. 11, no. 19, p. 9086, Sep. 2021, doi: 10.3390/app11199086.
[379] S. N. Jonkman, P. H. A. J. M. van Gelder, and J. K. Vrijling, ‘An overview of quantitative risk measures for loss of life and economic damage’, *J Hazard Mater*, vol. 99, no. 1, pp. 1–30, Apr. 2003, doi: 10.1016/S0304-3894(02)00283-2.
[380] H. and S. E. HSE, *The Tolerability of Risk from Nuclear Power Stations*. London, UK: Her Majesty’s Stationery Office, 1992. Accessed: Oct. 25, 2024. [Online]. Available: https://www.hse.gov.uk/nuclear/tolerability.pdf
[381] B. Bhattacharya, ‘An appraisal of the LQI as an approach to setting target reliabilities in ISO 2394:2015’, *Structural Safety*, vol. 109, p. 102482, Jul. 2024, doi: 10.1016/j.strusafe.2024.102482.
[382] Y. Gong, Z. Niu, and T. Bai, ‘Societal risk acceptance criteria for gas distribution pipelines based on incident data from the United States’, *J Loss Prev Process Ind*, vol. 63, p. 104002, Jan. 2020, doi: 10.1016/j.jlp.2019.104002.

[383] B. J. M. Ale, ‘Tolerable or Acceptable: A Comparison of Risk Regulation in the United Kingdom and in the Netherlands’, *Risk Analysis*, vol. 25, no. 2, pp. 231–241, Apr. 2005, doi: 10.1111/j.1539-6924.2005.00585.x.
[384] R. Pitblado *et al.*, ‘International comparison on the application of societal risk criteria’, *Process Safety Progress*, vol. 31, no. 4, pp. 363–368, Dec. 2012, doi: 10.1002/prs.11525.
[385] L. Gucma, ‘Methods of ship-bridge collision safety evaluation’, *Reliability: Theory & Applications*, vol. 4, no. 2–1 (13), pp. 50–63, 2009.
[386] H.-H. Tsang, J. E. Daniell, F. Wenzel, and J. L. Wilson, ‘A universal approach for evaluating earthquake safety level based on societal fatality risk’, *Bulletin of Earthquake Engineering*, vol. 18, no. 1, pp. 273–296, Jan. 2020, doi: 10.1007/s10518-019-00727-9.
[387] Ministero delle Infrastrutture e dei Trasporti, *Decreto Ministeriale 28 ottobre 2005 – Sicurezza nelle gallerie ferroviarie*. Gazzetta Ufficiale della Repubblica Italiana, 2005. Accessed: Dec. 22, 2024. [Online]. Available: https://www.gazzettaufficiale.it/atto/serie_generale/caricaDettaglioAtto/originario?atto.dataPubblicazioneGazzetta=2006-04-08&atto.codiceRedazionale=06A03428
[388] G. Galilei, *Dialogues concerning two new sciences*. Dover, 1914.
[389] G. Galilei, *Il saggiatore*. BoD-Books on Demand, 2023.
[390] S. Drake, *Galileo: A Very Short Introduction*. Oxford University Press, 2001.
[391] M. A. Finocchiaro, *Galileo and the art of reasoning: Rhetorical foundation of logic and scientific method*, vol. 61. Springer Science & Business Media, 2012.
[392] T. C. Brickhouse, *Plato’s Socrates*. Oxford University Press, 1994.
[393] R. Weiss, *Socrates Dissatisfied: An Analysis of Plato’s Crito*. Oxford University Press, USA, 1998.
[394] P. T. Geach, ‘PLATO’S" EUTHYPHRO": An Analysis and Commentary’, *Monist*, pp. 369–382, 1966.
[395] C. D. C. Reeve, *Socrates in the Apology: an essay on Plato’s Apology of Socrates*. Hackett Publishing, 1989.
[396] A. Bloom, ‘The republic of Plato’, *Basic BooksInc., Ublishers*, 1968.
[397] F. Allhoff, ‘Philosophies of the Sciences’, *Philosophies of the Sciences: A Guide*, pp. 1–8, 2010.
[398] D. Kaplan, *Bayesian statistics for the social sciences*. Guilford Publications, 2023.
[399] S. J. Press, *Subjective and objective Bayesian statistics: principles, models, and applications*. John Wiley & Sons, 2009.
[400] E. T. Jaynes, *Probability theory: The logic of science*. Cambridge university press, 2003.
[401] А. Н. Колмогоров, ‘Основные понятия теории вероятностей’, 1974.
[402] A. Lyon, ‘Philosophy of probability’, *Philosophies of the Sciences: a guide*, pp. 92–125, 2010.
[403] A. T. Bharucha-Reid, *Foundations of the theory of probability: Second English Edition*. Courier Dover Publications, 2018.
[404] R. P. Feynman, ‘Negative probability’, PRE-27827, 1984.
[405] D. R. Cox, ‘The analysis of non-Markovian stochastic processes by the inclusion of supplementary variables’, in *Mathematical Proceedings of the Cambridge Philosophical Society*, Cambridge University Press, 1955, pp. 433–441.
[406] A. Rényi, *Foundations of probability*. Courier Corporation, 2007.
[407] A. P. Dempster, ‘Upper and lower probabilities induced by a multivalued mapping’, in *Classic works of the Dempster-Shafer theory of belief functions*, Springer, 2008, pp. 57–72.

[408] L. A. Zadeh, ‘Fuzzy sets’, *Information and control*, vol. 8, no. 3, pp. 338–353, 1965.
[409] L. A. Zadeh, ‘Fuzzy sets as a basis for a theory of possibility’, *Fuzzy Sets Syst*, vol. 1, no. 1, pp. 3–28, Jan. 1978, doi: 10.1016/0165-0114(78)90029-5.
[410] F. M. Dekking, C. Kraaikamp, H. P. Lopuhaä, and L. E. Meester, *A Modern Introduction to Probability and Statistics: Understanding why and how*. Springer Science & Business Media, 2006.
[411] T. Bayes, ‘An essay towards solving a problem in the doctrine of chances’, *Biometrika*, vol. 45, no. 3–4, pp. 296–315, 1958.
[412] P. S. Laplace, *Théorie analytique des probabilités*. Courcier, 1820.
[413] S. B. McGrayne, *The Theory That Would Not Die: How Bayes’ Rule Cracked the Enigma Code, Hunted Down Russian Submarines, & Emerged Triumphant from Two Centuries of C*. Yale University Press, 2011.
[414] E. Paté-Cornell, ‘On “Black Swans” and “Perfect Storms”: Risk Analysis and Management When Statistics Are Not Enough’, *Risk Analysis*, vol. 32, no. 11, pp. 1823–1833, Nov. 2012, doi: 10.1111/j.1539-6924.2011.01787.x.
[415] P. L. Clemens and R. J. Simmons, ‘System safety and risk management: NIOSH instructional module’, *US Department of Health and Human Services*, 1998.
[416] S. Lipschutz, *Schaum’s outline of probability*. McGraw Hill Professional, 2000.
[417] T. P. McAllister, ‘Community Resilience: The Role of the Built Environment’, in *Multi-hazard Approaches to Civil Infrastructure Engineering*, Cham: Springer International Publishing, 2016, pp. 533–548. doi: 10.1007/978-3-319-29713-2_24.
[418] R. B. Gilbert, M. Habibi, and F. Nadim, ‘Accounting for Unknown Unknowns in Managing Multi-hazard Risks’, in *Multi-hazard Approaches to Civil Infrastructure Engineering*, Cham: Springer International Publishing, 2016, pp. 383–412. doi: 10.1007/978-3-319-29713-2_18.
[419] M. Holický, ‘Risk analysis and optimization of road tunnels’, in *Risk Analysis V: Simulation and Hazard Mitigation*, Southampton, UK: WIT Press, Jun. 2006, pp. 57–66. doi: 10.2495/RISK060061.
[420] M. Holický, ‘Optimization of risk criteria for road tunnels’, in *Safety and Security Engineering II*, Southampton, UK: WIT Press, Jun. 2007, pp. 3–12. doi: 10.2495/SAFE070011.
[421] M. Holický, ‘Probabilistic risk optimization of road tunnels’, *Structural Safety*, vol. 31, no. 3, pp. 260–266, May 2009, doi: 10.1016/j.strusafe.2008.06.003.
[422] M. Holický, J. Smolík, and L. Šajtar, ‘Optimisation of road tunnel safety based on risk analysis’, Oct. 2023.
[423] Health and Safety Executive (HSE), ‘HSE, UK. Principles and guidelines to assist HSE in its judgements that duty-holders have reduced risk as low as reasonably practicable.’, Dec. 2001.
[424] S. Basu and A. K. Debnath, *Power plant instrumentation and control handbook: a guide to thermal power plants*. Academic Press, 2014.
[425] R. A. Freeze, J. Massmann, L. Smith, T. Sperling, and B. James, ‘Hydrogeological Decision Analysis: 1. A Framework’, *Groundwater*, vol. 28, no. 5, pp. 738–766, Sep. 1990, doi: 10.1111/j.1745-6584.1990.tb01989.x.
[426] J. Nash, ‘Non-Cooperative Games’, *The Annals of Mathematics*, vol. 54, no. 2, p. 286, Sep. 1951, doi: 10.2307/1969529.
[427] M.-C. Andreu, D. W. Michael, and R. G. Jerry, *Microeconomic theory*. Oxfors University Press, 1995.
[428] V. Pareto, *Manual of political economy: a critical and variorum edition*. OUP Oxford, 2014.

[429] J. Osborne, A. Tudora, and B. Swatton, ‘Tunnelling for Physics: Surveying the Geological, Environmental, and Technical Constraints of a Post-LHC Collider’, CERN, 2019. [Online]. Available: https://cds.cern.ch/record/2689203/files/CERNCourier2019SepOct-digitaledition.pdf
[430] A. Ouyang, V. Di Murro, M. Cull, R. Cunningham, J. A. Osborne, and Z. Li, ‘Automated pixel-level crack monitoring system for large-scale underground infrastructure – A case study at CERN’, *Tunnelling and Underground Space Technology*, vol. 140, p. 105310, Oct. 2023, doi: 10.1016/j.tust.2023.105310.
[431] CERN, ‘Member States and Governance of CERN’. Accessed: Oct. 29, 2024. [Online]. Available: https://home.cern/about/who-we-are/our-governance/member-states
[432] CERN, ‘CERN Annual Report 2023’, CERN, 2023. Accessed: Oct. 29, 2024. [Online]. Available: https://cds.cern.ch/record/2897082
[433] CERN, ‘Layout of the CERN complex’. Accessed: Oct. 29, 2024. [Online]. Available: https://maps.cern.ch/?cameraCenter=2494340.45,1115464.8,11478.2&heading=0.27&fov=55&tilt=39.01&basemap=plan&mode=3D&travelMode=Car&isVisitor=true
[434] CERN, ‘Super Proton Synchrotron’. Accessed: Oct. 29, 2024. [Online]. Available: https://home.cern/science/accelerators/super-proton-synchrotron
[435] C. Coman and L. Gatignon, ‘The North Area is Getting a Fresh Look’. Accessed: Oct. 29, 2024. [Online]. Available: https://home.cern/news/news/accelerators/north-area-getting-fresh-look
[436] E. Lopienska, ‘The CERN Accelerator Complex, Layout in 2022’, CERN, 2022. Accessed: Oct. 29, 2024. [Online]. Available: https://cds.cern.ch/record/2800984/?ln=en
[437] N. Doble, L. Gatignon, E. Wilson, and K. Hübner, ‘WSP: The Super Proton Synchrotron (SPS): A Tale of Two Lives’, *Adv. Ser. Direct. High Energy Phys.*, vol. 27, pp. 135–177, 2017.
[438] R. Alemany *et al.*, ‘Summary report of physics beyond colliders at CERN’, *arXiv preprint arXiv:1902.00260*, 2019.
[439] S. Evrard *et al.*, ‘How to Manage a Large Scale Beam Line Consolidation in a Highly Activated Area?’, 2016.
[440] CERN, ‘TT20 and North Area Consolidation’. Accessed: Oct. 29, 2024. [Online]. Available: https://section-mpc.web.cern.ch/content/tt20-and-north-area-consolidation
[441] CERN, ‘TCC2, the target hall of the SPS North Area’. Accessed: Jan. 13, 2025. [Online]. Available: http://cds.cern.ch/record/917351
[442] E. Harrouch, ‘Safety File TCC2-TDC2: Descriptive Part’, CERN, 2013. [Online]. Available: https://edms.cern.ch/document/1216951/0.2
[443] G. Zuccaro, D. De Gregorio, and M. F. Leone, ‘Theoretical model for cascading effects analyses’, *International Journal of Disaster Risk Reduction*, vol. 30, pp. 199–215, Sep. 2018, doi: 10.1016/j.ijdrr.2018.04.019.
[444] G. Capello, M. Guarascio, A. Liberta, L. Salvato, and G. Sanna, ‘Multipurpose Geostatistical Modelling of a Bauxite Orebody in Sardinia’, 1987, pp. 69–92. doi: 10.1007/978-94-009-3383-5_4.
[445] The ObsPy Development Team, ‘ObsPy 1.2.1’, Mar. 2020, *Zenodo*. doi: 10.5281/zenodo.3706479.
[446] ETH Zurich Strong Motion Portal, ‘Seismic Event Details: Event ID 472967348’. Accessed: Oct. 29, 2024. [Online]. Available:

https://strongmotionportal.seismo.ethz.ch/select-events/results/event-detail/index.html?eventid=472967348
[447] R. Camassi, M. Stucchi, and D. Molin, *NT4. 1 un catalogo parametrico di terremoti di area italiana al di sopra della soglia del danno*. Consiglio Nazionale delle Richerche, Gruppo Nazionale per la Difesa dai …, 1997.
[448] A. A. Gómez Capera, M. Santulin, M. Massa, M. Locati, and R. Puglia, 'Conversione tra parametri del moto del suolo e intensità macrosismica', 2019.
[449] E. Chapron, C. Beck, M. Pourchet, and J. Deconinck, '1822 earthquake-triggered homogenite in Lake Le Bourget (NW Alps)', *Terra Nova*, vol. 11, no. 2–3, pp. 86–92, Apr. 1999, doi: 10.1046/j.1365-3121.1999.00230.x.
[450] J. Chilès and P. Delfiner, *Geostatistics*. Wiley, 2012. doi: 10.1002/9781118136188.
[451] M. Guarascio, M. David, and C. Huijbregts, *Advanced Geostatistics in the Mining Industry*. Dordrecht: Springer Netherlands, 1976. doi: 10.1007/978-94-010-1470-0.
[452] P. Delfiner, 'Linear Estimation of non Stationary Spatial Phenomena', in *Advanced Geostatistics in the Mining Industry*, Dordrecht: Springer Netherlands, 1976, pp. 49–68. doi: 10.1007/978-94-010-1470-0_4.
[453] M. Guarascio, 'Improving the Uranium Deposits Estimations (The Novazza Case)', in *Advanced Geostatistics in the Mining Industry*, Dordrecht: Springer Netherlands, 1976, pp. 351–367. doi: 10.1007/978-94-010-1470-0_22.
[454] F. Thouvenot *et al.*, 'The M_L 5.3 Épagny (French Alps) earthquake of 1996 July 15: a long-awaited event on the Vuache Fault', *Geophys J Int*, vol. 135, no. 3, pp. 876–892, Dec. 1998, doi: 10.1046/j.1365-246X.1998.00662.x.
[455] G. Matheron, *Estimating and Choosing*. Berlin, Heidelberg: Springer Berlin Heidelberg, 1989. doi: 10.1007/978-3-642-48817-7.
[456] L. Sironi and M. Andreini, 'Seismic Risk Assessment of Configurations of Radiation Shielding Blocks', CERN, 2022. Accessed: Sep. 14, 2024. [Online]. Available: https://edms.cern.ch/document/2694636/1
[457] Z. Zhou *et al.*, 'Discrete Structural Systems Modeling: Benchmarking of LS-DEM and LMGC90 with Seismic Experiments', *J Eng Mech*, vol. 149, no. 12, Dec. 2023, doi: 10.1061/JENMDT.EMENG-7036.
[458] L. Sironi *et al.*, 'Shaking table tests for seismic stability of stacked concrete blocks used for radiation shielding', *Eng Struct*, vol. 283, p. 115895, May 2023, doi: 10.1016/j.engstruct.2023.115895.
[459] L. Sironi *et al.*, 'Seismic Vulnerability Assessment of Concrete Block Configurations for Radiation Shielding', 2023, pp. 5218–5228. doi: 10.7712/120123.10795.20712.
[460] EUCENTRE, 'Experimental Testing Campaign with CERN Blocks under Seismic Action', CERN, 2022. Accessed: Oct. 29, 2024. [Online]. Available: https://edms.cern.ch/document/2779772
[461] A. Navascues Cornago, 'Treatment of 3D CATIA Models of CERN Shielding Blocks for Seismic Study', CERN, 2022. Accessed: Oct. 29, 2024. [Online]. Available: https://edms.cern.ch/document/2779800
[462] European Strong-Motion Database (ESMD), 'Waveform Data for Event IT-2009-0009, Station AQK, Channel HN'. Accessed: Oct. 29, 2024. [Online]. Available: https://esm-db.eu/#/waveform/IT/AQK/00/IT-2009-0009/HN
[463] European Strong-Motion Database (ESMD), 'Waveform Data for Event EMSC-20160824_0000006, Station NOR, Channel HG'. Accessed: Oct. 29, 2024. [Online]. Available: https://esm-db.eu/#/waveform/IT/NOR/00/EMSC-20160824_0000006/HG

[464] European Strong-Motion Database (ESMD), ‘Waveform Data for Event EMSC-20161026_0000095, Station NOR, Channel HG’. Accessed: Oct. 29, 2024. [Online]. Available: https://esm-db.eu/#/waveform/IT/NOR/00/EMSC-20161026_0000095/HG
[465] European Strong-Motion Database (ESMD), ‘Waveform Data for Event EMSC-20140203_0000008, Station ARG2, Channel HN’. Accessed: Oct. 29, 2024. [Online]. Available: https://esm-db.eu/#/waveform/HI/ARG2//EMSC-20140203_0000008/HN
[466] European Strong-Motion Database (ESMD), ‘Waveform Data for Event EMSC-20161026_0000095, Station MMO, Channel HG’. Accessed: Oct. 29, 2024. [Online]. Available: https://esm-db.eu/#/waveform/IT/MMO/00/EMSC-20161026_0000095/HG
[467] European Strong-Motion Database (ESMD), ‘Waveform Data for Event EMSC-20161026_0000095, Station NRC, Channel HG’. Accessed: Oct. 29, 2024. [Online]. Available: https://esm-db.eu/#/waveform/IT/NRC/00/EMSC-20161026_0000095/HG
[468] European Strong-Motion Database (ESMD), ‘Waveform Data for Event IT-1976-0025, Station GMN, Channel HN’. Accessed: Oct. 29, 2024. [Online]. Available: https://esm-db.eu/#/waveform/EU/GMN/00/IT-1976-0025/HN
[469] Federal Emergency Management Agency (FEMA), ‘Prestandard and Commentary for the Seismic Rehabilitation of Buildings’, FEMA, 2000. [Online]. Available: https://www.nehrp.gov/pdf/fema356.pdf
[470] American Society of Civil Engineers (ASCE), ‘ASCE/SEI 41-17: Seismic Evaluation and Retrofit of Existing Buildings’, American Society of Civil Engineers, 2017.
[471] Federal Emergency Management Agency (FEMA), ‘FEMA P-58: Seismic Performance Assessment of Buildings’, FEMA, 2012. Accessed: Sep. 13, 2024. [Online]. Available: https://femap58.atcouncil.org/reports
[472] CERN, ‘Fire at CERN’, 1999. Accessed: Oct. 29, 2024. [Online]. Available: https://home.web.cern.ch/news/press-release/cern/fire-cern
[473] A. Harrison, ‘Risk analysis of the LHC underground area-Fire risk due to faulty electrical equipment’, 2007.
[474] G. Gai, ‘FIRIA Methodology’, CERN, 2021. Accessed: Oct. 29, 2024. [Online]. Available: https://edms.cern.ch/document/2426715/1
[475] CERN, ‘FIRIA: Fire Risk Assessment’. Accessed: Oct. 29, 2024. [Online]. Available: https://hse.cern/content/firia
[476] CERN, ‘Target Attenuator: Beam Equipment Documentation’. Accessed: Oct. 29, 2024. [Online]. Available: https://sba.web.cern.ch/sba/Documentations/Informations&Training/Beam_Equipments/target_attenuator/index.htm
[477] C. Ahdida *et al.*, ‘Findings of the Physics Beyond Colliders ECN3 Beam Delivery Task Force’, 2023. Accessed: Sep. 22, 2024. [Online]. Available: https://cds.cern.ch/record/2847433
[478] B. Debrouwere, ‘FIRIA 2.0 - TDC2-TCC2 - General Report’, CERN, 2024. Accessed: Oct. 29, 2024. [Online]. Available: https://edms.cern.ch/document/3054408/1
[479] K. B. McGrattan, A. J. Lock, N. D. Marsh, and M. R. Nyden, ‘Cable heat release, ignition, and spread in tray installations during fire (CHRISTIFIRE): phase 1-horizontal trays’, 2012.
[480] J. C. Lopez Santiago, ‘Combustibility study of resin for warm magnet coils used at CERN’, 2023. Accessed: Oct. 29, 2024. [Online]. Available: https://lup.lub.lu.se/student-papers/search/publication/9120242

[481] D. Madsen *et al.*, ‘Fire-Induced Radiological Integrated Assessment: Fire properties of selected materials and products’, 2019.
[482] L. Audouin and M. Coutin, ‘Experimental characterization of a forklift fire’, in *24th International Conference on Structural Mechanics in Reactor Technology (SMiRT 24), 15th International Post-Conference Seminar on Fire Safety in Nuclear Power Plants and Installations*, 2017.
[483] D. Funk, ‘DEVELOPMENT OF RISK INFORMED METHODS FOR ESTIMATING RADIATION RELEASE FROM CABLE FIRES AT HIGH ENERGY PHYSICS FACILITIES’, *LUTVDG/TVBB*, 2020.
[484] J. Heinz, ‘Modelling Cable Fire Frequencies for ATLAS and ISOLDE’, CERN, 2021. Accessed: Oct. 29, 2024. [Online]. Available: https://edms.cern.ch/document/2469803/1
[485] CERN, ‘GIS Portal - TCC2’. Accessed: Oct. 29, 2024. [Online]. Available: https://gis.cern.ch/gisportal/general.htm?no=[886]
[486] CERN, ‘TDC2-GIS Portal Racks’. Accessed: Oct. 10, 2024. [Online]. Available: https://gis.cern.ch/gisportal/Racks.htm?rna=[’44406719’]&share=b23d6f83fb400af30b80e01af729fc3bc937d0c8
[487] CERN, ‘TCC2-GIS Portal Racks’. Accessed: Oct. 10, 2024. [Online]. Available: https://gis.cern.ch/gisportal/Racks.htm?rna=[’44406719’]&share=bd47aefc64a9a84c6fd3583d611aa7631f5c707c
[488] E. Alakbarli, ‘Magnet Equipment Inventory for TDC2 and TCC2’, CERN, 2024. Accessed: Oct. 29, 2024. [Online]. Available: https://edms.cern.ch/document/3172665/1
[489] The Nuclear Regulatory Commission (U.S.NRC), ‘NUREG-2169:Nuclear Power Plant Fire Ignition Frequency and Non-Suppression Probability Estimation Using the Updated Fire Events Database’, 2015. [Online]. Available: https://www.nrc.gov/docs/ML1501/ML15016A069.pdf
[490] Nexans, ‘Nexans Website’. Accessed: Oct. 29, 2024. [Online]. Available: https://www.nexans.com
[491] Prysmian Group, ‘Prysmian Group Website’. Accessed: Oct. 29, 2024. [Online]. Available: https://www.prysmiangroup.com
[492] Eupen Cable, ‘Eupen Cable Website’. Accessed: Oct. 29, 2024. [Online]. Available: https://www.eupen.com
[493] Ducab, ‘Ducab Website’. Accessed: Oct. 29, 2024. [Online]. Available: https://www.ducab.com
[494] L. C. Cadwallader, ‘Fire protection system operating experience review for fusion applications’, *Fusion Technology*, vol. 30, no. 3P2B, pp. 1420–1423, 1996.
[495] E. Ronchi, S. Arias, S. La Mendola, and N. Johansson, ‘A fire safety assessment approach for evacuation analysis in underground physics research facilities’, *Fire Saf J*, vol. 108, p. 102839, Sep. 2019, doi: 10.1016/J.FIRESAF.2019.102839.
[496] D. Nilsson and R. Fahy, ‘Selecting Scenarios for Deterministic Fire Safety Engineering Analysis: Life Safety for Occupants’, in *SFPE Handbook of Fire Protection Engineering*, New York, NY: Springer New York, 2016, pp. 2047–2069. doi: 10.1007/978-1-4939-2565-0_57.
[497] G. V. Hadjisophocleous and J. R. Mehaffey, ‘Fire Scenarios’, in *SFPE Handbook of Fire Protection Engineering*, New York, NY: Springer New York, 2016, pp. 1262–1288. doi: 10.1007/978-1-4939-2565-0_38.
[498] T. Jin, ‘Studies on human behavior and tenability in fire smoke’, *Fire Safety Science*, vol. 5, pp. 3–21, 1997.

[499] J. R. Mawhinney, ‘Fixed Fire Protection Systems in Tunnels: Issues and Directions’, *Fire Technol*, vol. 49, no. 2, pp. 477–508, Apr. 2013, doi: 10.1007/s10694-011-0220-2.
[500] L. Benthorn and H. Frantzich, ‘Fire alarm in a public building: how do people evaluate information and choose an evacuation exit?’, *Fire Mater*, vol. 23, no. 6, pp. 311–315, Nov. 1999, doi: 10.1002/(SICI)1099-1018(199911/12)23:6<311::AID-FAM704>3.0.CO;2-J.
[501] G. Proulx, ‘Occupant behaviour and evacuation’, 2001.
[502] L. W. Menzemer, E. Ronchi, M. M. V. Karsten, S. Gwynne, and J. Frederiksen, ‘A scoping review and bibliometric analysis of methods for fire evacuation training in buildings’, *Fire Saf J*, vol. 136, p. 103742, Apr. 2023, doi: 10.1016/j.firesaf.2023.103742.
[503] D. Nilsson, M. Johansson, and H. Frantzich, ‘Evacuation experiment in a road tunnel: A study of human behaviour and technical installations’, *Fire Saf J*, vol. 44, no. 4, pp. 458–468, May 2009, doi: 10.1016/J.FIRESAF.2008.09.009.
[504] D. Purser, ‘How to determine toxic effects and human behaviour when exposed to fire smoke in underground facilities - challenges and possibilities’, Nov. 2018.
[505] D. Purser, ‘Application of human behaviour and toxic hazard analysis to the validation of CFD modelling for the Mont Blanc Tunnel fire incident’, Nov. 2009.
[506] M. Tsukahara, Y. Koshiba, and H. Ohtani, ‘Effectiveness of downward evacuation in a large-scale subway fire using Fire Dynamics Simulator’, *Tunnelling and Underground Space Technology*, vol. 26, no. 4, pp. 573–581, Jul. 2011, doi: 10.1016/j.tust.2011.02.002.
[507] H. K. Kim, A. Lönnermark, and H. Ingason, ‘Effective Firefighting Operations in Road Tunnels’, 2010.
[508] A. Voeltzel and A. Dix, ‘A comparative analysis of the Mont Blanc, Tauern and Gotthard tunnel fires’, *Routes/roads*, no. 324, 2004.
[509] J. H. Saleh and A. M. Cummings, ‘Safety in the mining industry and the unfinished legacy of mining accidents: Safety levers and defense-in-depth for addressing mining hazards’, *Saf Sci*, vol. 49, no. 6, pp. 764–777, Jul. 2011, doi: 10.1016/j.ssci.2011.02.017.
[510] E. Kuligowski, R. Peacock, and B. Hoskins, ‘A Review of Building Evacuation Models, 2nd Edition’, Feb. 2010, *Technical Note (NIST TN), National Institute of Standards and Technology, Gaithersburg, MD*. [Online]. Available: https://tsapps.nist.gov/publication/get_pdf.cfm?pub_id=906951
[511] G. V Hadjisophocleous and N. Benichou, ‘Performance criteria used in fire safety design’, *Autom Constr*, vol. 8, no. 4, pp. 489–501, Apr. 1999, doi: 10.1016/S0926-5805(98)00096-X.
[512] A. Cuesta, O. Abreu, and D. Alvear, ‘Future Challenges in Evacuation Modelling’, in *Evacuation Modeling Trends*, Cham: Springer International Publishing, 2016, pp. 103–129. doi: 10.1007/978-3-319-20708-7_5.
[513] S. M. V. Gwynne and E. D. Kuligowski, ‘Application Modes of Egress Simulation’, in *Pedestrian and Evacuation Dynamics 2008*, Berlin, Heidelberg: Springer Berlin Heidelberg, 2010, pp. 397–409. doi: 10.1007/978-3-642-04504-2_34.
[514] M. J. Hurley and E. R. Rosenbaum, ‘Performance-Based Design’, in *SFPE Handbook of Fire Protection Engineering*, New York, NY: Springer New York, 2016, pp. 1233–1261. doi: 10.1007/978-1-4939-2565-0_37.
[515] R. Lovreglio, D. Borri, L. dell’Olio, and A. Ibeas, ‘A discrete choice model based on random utilities for exit choice in emergency evacuations’, *Saf Sci*, vol. 62, pp. 418–426, Feb. 2014, doi: 10.1016/j.ssci.2013.10.004.

[516] E. Ronchi, P. Colonna, and N. Berloco, ‘Reviewing Italian Fire Safety Codes for the analysis of road tunnel evacuations: Advantages and limitations of using evacuation models’, *Saf Sci*, vol. 52, pp. 28–36, Feb. 2013, doi: 10.1016/j.ssci.2012.03.015.
[517] E. Ronchi and D. Nilsson, ‘Modelling total evacuation strategies for high-rise buildings’, *Build Simul*, vol. 7, no. 1, pp. 73–87, Feb. 2014, doi: 10.1007/s12273-013-0132-9.
[518] W. Sujatmiko, H. K. Dipojono, F. X. N. Soelami, and Soegijanto, ‘Performance-based Fire Safety Evacuation in High-rise Building Flats in Indonesia – A Case Study in Bandung’, *Procedia Environ Sci*, vol. 20, pp. 116–125, 2014, doi: 10.1016/j.proenv.2014.03.016.
[519] T. Wei-Wen, P. Kuo-Hsiung, and H. Che-Ming, ‘Performance-based Fire Safety Design for Existing Small-scale Hospitals’, *Procedia Eng*, vol. 11, pp. 514–521, 2011, doi: 10.1016/j.proeng.2011.04.690.
[520] A. Tinaburri, ‘Principles for Monte Carlo agent-based evacuation simulations including occupants who need assistance. From RSET to RiSET’, *Fire Saf J*, vol. 127, p. 103510, Jan. 2022, doi: 10.1016/J.FIRESAF.2021.103510.
[521] R. Rostami and M. Alaghmandan, ‘Performance-based design in emergency evacuation: From maneuver to simulation in school design’, *Journal of Building Engineering*, vol. 33, p. 101598, Jan. 2021, doi: 10.1016/j.jobe.2020.101598.
[522] Q. Xie, S. Guo, Y. Zhang, C. Wang, C. Ma, and Q. Li, ‘An integrated method for assessing passenger evacuation performance in ship fires’, *Ocean Engineering*, vol. 262, p. 112256, Oct. 2022, doi: 10.1016/j.oceaneng.2022.112256.
[523] F. Mirahadi, B. McCabe, and A. Shahi, ‘IFC-centric performance-based evaluation of building evacuations using fire dynamics simulation and agent-based modeling’, *Autom Constr*, vol. 101, pp. 1–16, May 2019, doi: 10.1016/j.autcon.2019.01.007.
[524] E. Ronchi *et al.*, ‘New approaches to evacuation modelling for fire safety engineering applications’, *Fire Saf J*, vol. 106, pp. 197–209, Jun. 2019, doi: 10.1016/J.FIRESAF.2019.05.002.
[525] E. Ronchi, P. A. Reneke, and R. D. Peacock, ‘A Method for the Analysis of Behavioural Uncertainty in Evacuation Modelling’, *Fire Technol*, vol. 50, no. 6, pp. 1545–1571, Nov. 2014, doi: 10.1007/s10694-013-0352-7.
[526] D. A. Purser, ‘ASET and RSET: addressing some issues in relation to occupant behaviour and tenability’, *Fire Safety Science*, vol. 7, pp. 91–102, 2003.
[527] D. A. Purser and M. Bensilum, ‘Quantification of behaviour for engineering design standards and escape time calculations’, *Saf Sci*, vol. 38, no. 2, pp. 157–182, Jul. 2001, doi: 10.1016/S0925-7535(00)00066-7.
[528] V. Babrauskas, J. M. Fleming, and B. Don Russell, ‘RSET/ASET, a flawed concept for fire safety assessment’, *Fire Mater*, vol. 34, no. 7, pp. 341–355, Nov. 2010, doi: 10.1002/fam.1025.
[529] M. Kobes, I. Helsloot, B. de Vries, and J. G. Post, ‘Building safety and human behaviour in fire: A literature review’, *Fire Saf J*, vol. 45, no. 1, pp. 1–11, Jan. 2010, doi: 10.1016/j.firesaf.2009.08.005.
[530] M. Haghani, R. Lovreglio, M. L. Button, E. Ronchi, and E. Kuligowski, ‘Human behaviour in fire: Knowledge foundation and temporal evolution’, *Fire Saf J*, vol. 144, p. 104085, Mar. 2024, doi: 10.1016/j.firesaf.2023.104085.
[531] S. W. Tweedie, J. R. Rowland, S. J. Walsh, R. P. Rhoten, and P. I. Hagle, ‘A methodology for estimating emergency evacuation times’, *Soc Sci J*, vol. 23, no. 2, pp. 189–204, Jun. 1986, doi: 10.1016/0362-3319(86)90035-2.

[532] M. Forssberg, J. Kjellström, H. Frantzich, A. Mossberg, and D. Nilsson, 'The Variation of Pre-movement Time in Building Evacuation', *Fire Technol*, vol. 55, no. 6, pp. 2491–2513, Nov. 2019, doi: 10.1007/s10694-019-00881-1.
[533] J. D. Averill, 'Five Grand Challenges in Pedestrian and Evacuation Dynamics', in *Pedestrian and Evacuation Dynamics*, Boston, MA: Springer US, 2011, pp. 1–11. doi: 10.1007/978-1-4419-9725-8_1.
[534] E. Ronchi, E. D. Kuligowski, R. D. Peacock, and P. A. Reneke, 'A probabilistic approach for the analysis of evacuation movement data', *Fire Saf J*, vol. 63, pp. 69–78, Jan. 2014, doi: 10.1016/J.FIRESAF.2013.11.012.
[535] D. R. Bish, E. Agca, and R. Glick, 'Decision support for hospital evacuation and emergency response', *Ann Oper Res*, vol. 221, no. 1, pp. 89–106, Oct. 2014, doi: 10.1007/s10479-011-0943-y.
[536] S. Bretschneider and A. Kimms, 'A basic mathematical model for evacuation problems in urban areas', *Transp Res Part A Policy Pract*, vol. 45, no. 6, pp. 523–539, Jul. 2011, doi: 10.1016/J.TRA.2011.03.008.
[537] E. Ronchi, 'Developing and validating evacuation models for fire safety engineering', *Fire Saf J*, vol. 120, p. 103020, Mar. 2021, doi: 10.1016/J.FIRESAF.2020.103020.
[538] И. С. Александров, 'Введение в теорию множеств и теорию функций.', 1948.
[539] B. J. Meacham, D. Charters, P. Johnson, and M. Salisbury, 'Building Fire Risk Analysis', in *SFPE Handbook of Fire Protection Engineering*, New York, NY: Springer New York, 2016, pp. 2941–2991. doi: 10.1007/978-1-4939-2565-0_75.
[540] C. Duarte, K. Van Den Wymelenberg, and C. Rieger, 'Revealing occupancy patterns in an office building through the use of occupancy sensor data', *Energy Build*, vol. 67, pp. 587–595, Dec. 2013, doi: 10.1016/J.ENBUILD.2013.08.062.
[541] S. Nejadshamsi, U. Eicker, C. Wang, and J. Bentahar, 'Data sources and approaches for building occupancy profiles at the urban scale – A review', *Build Environ*, vol. 238, p. 110375, Jun. 2023, doi: 10.1016/J.BUILDENV.2023.110375.
[542] R. D. Peacock, B. L. Hoskins, and E. D. Kuligowski, 'Overall and local movement speeds during fire drill evacuations in buildings up to 31 stories', *Saf Sci*, vol. 50, no. 8, pp. 1655–1664, Oct. 2012, doi: 10.1016/j.ssci.2012.01.003.
[543] T. Rinne, K. Tillander, and P. Grönberg, *Data collection and analysis of evacuation situations*, vol. 46. VTT Espoo, 2010.
[544] X. Zhang, X. Li, J. Mehaffey, and G. Hadjisophocleous, 'A probability-based Monte Carlo life-risk analysis model for fire emergencies', *Fire Saf J*, vol. 89, pp. 51–62, Apr. 2017, doi: 10.1016/j.firesaf.2017.02.003.
[545] Q. Xie, S. Lu, D. Kong, and J. Wang, 'The effect of uncertain parameters on evacuation time in commercial buildings', *J Fire Sci*, vol. 30, no. 1, pp. 55–67, 2012.
[546] S. Gwynne, E. R. Galea, P. J. Lawrence, and L. Filippidis, 'Modelling occupant interaction with fire conditions using the buildingEXODUS evacuation model', *Fire Saf J*, vol. 36, no. 4, pp. 327–357, Jun. 2001, doi: 10.1016/S0379-7112(00)00060-6.
[547] E. D. Kuligowski, 'Computer Evacuation Models for Buildings', in *SFPE Handbook of Fire Protection Engineering*, New York, NY: Springer New York, 2016, pp. 2152–2180. doi: 10.1007/978-1-4939-2565-0_60.
[548] S. M. V. Gwynne and K. E. Boyce, 'Engineering Data', in *SFPE Handbook of Fire Protection Engineering*, New York, NY: Springer New York, 2016, pp. 2429–2551. doi: 10.1007/978-1-4939-2565-0_64.

[549] K. Fridolf, E. Ronchi, D. Nilsson, and H. Frantzich, ‘The representation of evacuation movement in smoke-filled underground transportation systems’, *Tunnelling and Underground Space Technology*, vol. 90, pp. 28–41, Aug. 2019, doi: 10.1016/J.TUST.2019.04.016.
[550] X. Zhang, X. Li, and G. Hadjisophocleous, ‘A probabilistic occupant evacuation model for fire emergencies using Monte Carlo methods’, *Fire Saf J*, vol. 58, pp. 15–24, May 2013, doi: 10.1016/j.firesaf.2013.01.028.
[551] H. Hamacher and S. Tjandra, ‘Mathematical Modeling of Evacuation Problems: A State of The Art’, *Pedestrian and Evacuation Dynamics*, vol. 2002, Nov. 2002.
[552] S. M. V. Gwynne and E. R. Rosenbaum, ‘Employing the Hydraulic Model in Assessing Emergency Movement’, in *SFPE Handbook of Fire Protection Engineering*, New York, NY: Springer New York, 2016, pp. 2115–2151. doi: 10.1007/978-1-4939-2565-0_59.
[553] S. P. Hoogendoorn and W. Daamen, ‘Pedestrian Behavior at Bottlenecks’, *Transportation Science*, vol. 39, no. 2, pp. 147–159, 2005, [Online]. Available: http://www.jstor.org/stable/25769239
[554] K. Fridolf, K. Andrée, D. Nilsson, and H. Frantzich, ‘The impact of smoke on walking speed’, *Fire Mater*, vol. 38, no. 7, pp. 744–759, Nov. 2014, doi: 10.1002/fam.2217.
[555] H. Frantzich and D. Nilsson, ‘Evacuation experiments in a smoke filled tunnel’, Nov. 2004, pp. 229–238.
[556] K. Fujii, T. Sano, and Y. Ohmiya, ‘Influence of lit emergency signs and illuminated settings on walking speeds in smoky corridors’, *Fire Saf J*, vol. 120, p. 103026, Mar. 2021, doi: 10.1016/J.FIRESAF.2020.103026.
[557] G. Y. Jeon, J. Y. Kim, W. H. Hong, and G. Augenbroe, ‘Evacuation performance of individuals in different visibility conditions’, *Build Environ*, vol. 46, no. 5, pp. 1094–1103, May 2011, doi: 10.1016/J.BUILDENV.2010.11.010.
[558] G.-Y. Jeon, W.-J. Na, W.-H. Hong, and J.-K. Lee, ‘Influence of design and installation of emergency exit signs on evacuation speed’, *Journal of Asian Architecture and Building Engineering*, vol. 18, no. 2, pp. 104–111, Mar. 2019, doi: 10.1080/13467581.2019.1599897.
[559] T. Yamada and Y. Akizuki, ‘Visibility and Human Behavior in Fire Smoke’, in *SFPE Handbook of Fire Protection Engineering*, New York, NY: Springer New York, 2016, pp. 2181–2206. doi: 10.1007/978-1-4939-2565-0_61.
[560] R. R. M. Gershon, K. A. Qureshi, M. S. Rubin, and V. H. Raveis, ‘Factors Associated with High-Rise Evacuation: Qualitative Results from the World Trade Center Evacuation Study’, *Prehosp Disaster Med*, vol. 22, no. 3, pp. 165–173, Jun. 2007, doi: 10.1017/S1049023X0000460X.
[561] R. Lovreglio and E. Kuligowski, ‘A pre-evacuation study using data from evacuation drills and false alarm evacuations in a university library’, *Fire Saf J*, vol. 131, p. 103595, Jul. 2022, doi: 10.1016/J.FIRESAF.2022.103595.
[562] E. Ronchi, K. Fridolf, H. Frantzich, D. Nilsson, A. L. Walter, and H. Modig, ‘A tunnel evacuation experiment on movement speed and exit choice in smoke’, *Fire Saf J*, vol. 97, pp. 126–136, Apr. 2018, doi: 10.1016/j.firesaf.2017.06.002.
[563] International Organization for Standardization (ISO), ‘ISO/TS 16733-2:2021. Fire safety engineering Selection of design fire scenarios and design fires’, Geneva, 2021.
[564] E. Kuligowski, ‘Predicting Human Behavior During Fires’, *Fire Technol*, vol. 49, no. 1, pp. 101–120, Jan. 2013, doi: 10.1007/s10694-011-0245-6.
[565] R. Lovreglio, E. Kuligowski, S. Gwynne, and K. Boyce, ‘A pre-evacuation database for use in egress simulations’, *Fire Saf J*, vol. 105, pp. 107–128, Apr. 2019, doi: 10.1016/J.FIRESAF.2018.12.009.

[566] R. M. Tavares and E. Ronchi, ‘Uncertainties in evacuation modelling: Current flaws and future improvements’, in *6th international symposium: Human Behaviour in Fire*, 2015, pp. 185–196.
[567] A. Rahouti, R. Lovreglio, C. Dias, E. Kuligowski, G. Gai, and S. La Mendola, ‘Investigating office buildings evacuations using unannounced fire drills: The case study of CERN, Switzerland’, *Fire Saf J*, vol. 125, p. 103403, Oct. 2021, doi: 10.1016/J.FIRESAF.2021.103403.
[568] S. Arias, S. La Mendola, J. Wahlqvist, O. Rios, D. Nilsson, and E. Ronchi, ‘Virtual Reality Evacuation Experiments on Way-Finding Systems for the Future Circular Collider’, *Fire Technol*, vol. 55, no. 6, pp. 2319–2340, Nov. 2019, doi: 10.1007/s10694-019-00868-y.
[569] E. Cardellino *et al.*, ‘Fire Modelling and Structural Assessment of Concrete Linings of Underground Structures’, *ce/papers*, vol. 6, no. 5, pp. 205–212, Sep. 2023, doi: 10.1002/cepa.2206.
[570] D. Perović *et al.*, ‘Identification and characterization of design fires and particle emissions to be used in performance-based fire design of nuclear facilities’, *Fire Mater*, vol. 45, no. 8, pp. 1008–1024, Dec. 2021, doi: 10.1002/fam.2881.
[571] G. Gai, S. La Mendola, and E. Ronchi, ‘Evacuation Analysis of a Large Experimental Cavern of the CERN Accelerator Complex’, in *Fire and Evacuation Modeling Technical Conference (FEMTC)*, 2020.
[572] D. de Silva *et al.*, ‘Structural safety assessment of concrete tunnel lining subjected to fire’, *Fire Saf J*, vol. 134, p. 103697, Dec. 2022, doi: 10.1016/J.FIRESAF.2022.103697.
[573] E. Alakbarli, ‘Occupant Loads BA80 Logs (TDC2/TCC2)’. Accessed: Jan. 15, 2025. [Online]. Available: https://edms.cern.ch/document/3222105/1
[574] CERN, ‘Working on the CERN Site / Travailler sur le Site du CERN’, 2023. Accessed: Nov. 25, 2024. [Online]. Available: https://edms.cern.ch/ui/file/1155899/LAST_RELEASED/*.pdf
[575] CERN, ‘CERN Safety Rules’. Accessed: Nov. 25, 2024. [Online]. Available: https://hse.cern/content/safety-rules
[576] E. Ronchi, P. Colonna, J. Capote, D. Alvear, N. Berloco, and A. Cuesta, ‘The evaluation of different evacuation models for assessing road tunnel safety analysis’, *Tunnelling and Underground Space Technology*, vol. 30, pp. 74–84, Jul. 2012, doi: 10.1016/j.tust.2012.02.008.
[577] M. Seike, N. Kawabata, and M. Hasegawa, ‘Walking speed in completely darkened full-scale tunnel experiments’, *Tunnelling and Underground Space Technology*, vol. 106, p. 103621, Dec. 2020, doi: 10.1016/j.tust.2020.103621.
[578] T. Korhonen and S. Hostikka, ‘Fire dynamics simulator with evacuation: FDS+ Evac’, *Technical Reference and User’s Guide. VTT Technical Research Centre of Finland*, 2009.
[579] J. J. Bommer and A. Martínez-Pereira, ‘The effective duration of earthquake strong motion’, *Journal of earthquake engineering*, vol. 3, no. 02, pp. 127–172, 1999.
[580] Y. Kuwata and S. Takada, ‘Instantaneous instrumental seismic intensity and evacuation’, *Journal of Natural Disaster Science*, vol. 24, no. 1, pp. 35–42, 2002.
[581] United States Geological Survey (USGS), ‘What Was the Duration of the Earthquake? Why Don’t You Report Duration for Each Earthquake? How Does Duration Affect Earthquake Intensity?’ Accessed: Oct. 29, 2024. [Online]. Available: https://www.usgs.gov/faqs/what-was-duration-earthquake-why-dont-you-report-duration-each-earthquake-how-does-duration

[582] J. He, ‘Earthquake evacuation simulation of multi-story buildings during earthquakes’, *Earthquake Spectra*, vol. 37, no. 1, pp. 95–113, Feb. 2021, doi: 10.1177/8755293020957353.
[583] H. Frantzich and D. Nilsson, ‘Evacuation in Complex Environments-An Analysis of Evacuation Conditions at a Tunnel Construction Site’, in *Proceedings from the Fourth International Symposium on Tunnel Safety and Security, Frankfurt am Main, Germany, March 17-19, 2010*, 2010, p. 181.
[584] Thunderhead Engineering, ‘Pathfinder Monte Carlo User Manual’, 2020. Accessed: Nov. 20, 2024. [Online]. Available: https://support.thunderheadeng.com/docs/pathfinder/2020-1/monte-carlo-user-manual/
[585] R. Lovreglio, E. Ronchi, and D. Borri, ‘The validation of evacuation simulation models through the analysis of behavioural uncertainty’, *Reliab Eng Syst Saf*, vol. 131, pp. 166–174, Nov. 2014, doi: 10.1016/j.ress.2014.07.007.
[586] D. A. Purser, ‘Toxic product yields and hazard assessment for fully enclosed design fires’, *Polym Int*, vol. 49, no. 10, pp. 1232–1255, Oct. 2000, doi: 10.1002/1097-0126(200010)49:10<1232::AID-PI543>3.0.CO;2-T.
[587] K. Boyce, ‘Safe evacuation for all - Fact or Fantasy? Past experiences, current understanding and future challenges’, *Fire Saf J*, vol. 91, pp. 28–40, Jul. 2017, doi: 10.1016/j.firesaf.2017.05.004.
[588] C. Tingvall and N. Haworth, ‘Vision Zero-An ethical approach to safety and mobility’, in *6th ITE international conference road safety & traffic enforcement: Beyond 2000*, 1999.
[589] R. Johansson, ‘Vision Zero – Implementing a policy for traffic safety’, *Saf Sci*, vol. 47, no. 6, pp. 826–831, Jul. 2009, doi: 10.1016/j.ssci.2008.10.023.
[590] A. Alvarez, B. Meacham, N. Dembsey, and J. Thomas, ‘Twenty years of performance-based fire protection design: challenges faced and a look ahead’, *Journal of Fire Protection Engineering*, vol. 23, no. 4, pp. 249–276, Nov. 2013, doi: 10.1177/1042391513484911.
[591] D. Alvear, O. Abreu, A. Cuesta, and V. Alonso, ‘A new method for assessing the application of deterministic or stochastic modelling approach in evacuation scenarios’, *Fire Saf J*, vol. 65, pp. 11–18, Apr. 2014, doi: 10.1016/j.firesaf.2014.02.005.
[592] B. Kolen, M. Kok, I. Helsloot, and B. Maaskant, ‘EvacuAid: A Probabilistic Model to Determine the Expected Loss of Life for Different Mass Evacuation Strategies During Flood Threats’, *Risk Analysis*, vol. 33, no. 7, pp. 1312–1333, Jul. 2013, doi: 10.1111/j.1539-6924.2012.01932.x.
[593] G. Zhang, D. Huang, G. Zhu, and G. Yuan, ‘Probabilistic model for safe evacuation under the effect of uncertain factors in fire’, *Saf Sci*, vol. 93, pp. 222–229, Mar. 2017, doi: 10.1016/j.ssci.2016.12.008.
[594] A. Cuesta, O. Abreu, and D. Alvear, *Evacuation modeling trends*. Springer, 2015.
[595] J. D. Averill, P. A. Reneke, and R. D. Peacock, ‘Required safe egress time: data and modeling’, 2008.
[596] J. Lord, B. Meacham, A. Moore, R. Fahy, and G. Proulx, ‘Guide for evaluating the predictive capabilities of computer egress models’, *Nist Gcr*, vol. 6, p. 886, 2005.
[597] J. Giebułtowicz, M. Rużycka, P. Wroczyński, D. A. Purser, and A. A. Stec, ‘Analysis of fire deaths in Poland and influence of smoke toxicity’, *Forensic Sci Int*, vol. 277, pp. 77–87, Aug. 2017, doi: 10.1016/j.forsciint.2017.05.018.
[598] R. G. Gann, V. Babrauskas, R. D. Peacock, and J. R. Hall, ‘Fire conditions for smoke toxicity measurement’, *Fire Mater*, vol. 18, no. 3, pp. 193–199, May 1994, doi: 10.1002/fam.810180306.

[599] E. Ronchi and D. Nilsson, ‘Fire evacuation in high-rise buildings: a review of human behaviour and modelling research’, *Fire Sci Rev*, vol. 2, no. 1, p. 7, 2013, doi: 10.1186/2193-0414-2-7.
[600] W. R. Hendee and F. Marc Edwards, ‘ALARA and an integrated approach to radiation protection’, *Semin Nucl Med*, vol. 16, no. 2, pp. 142–150, Apr. 1986, doi: 10.1016/S0001-2998(86)80027-7.
[601] D. Forkel-Wirth *et al.*, ‘Radiation protection at CERN’, Mar. 2013, doi: 10.5170/CERN-2013-001.415.
[602] CERN, *Code F Rev. Radiation Protection - Radiation Protection Manual / Radioprotection - Manuel de radioprotection*. CERN, 2006. Accessed: Jan. 15, 2025. [Online]. Available: https://edms.cern.ch/document/335729/2
[603] H. Vincke, *ALARA rule applied to interventions at CERN*. CERN, 2017. [Online]. Available: https://edms.cern.ch/document/1751123/1.2
[604] G. Bibel, *Train Wreck*. Johns Hopkins University Press, 2012. doi: 10.56021/9781421405902.
[605] N. Zarboutis and N. Marmaras, ‘Searching efficient plans for emergency rescue through simulation: the case of a metro fire’, *Cognition, Technology & Work*, vol. 6, no. 2, pp. 117–126, May 2004, doi: 10.1007/s10111-004-0150-6.
[606] H.-C. Jang, Y.-N. Lien, and T.-C. Tsai, ‘Rescue information system for earthquake disasters based on MANET emergency communication platform’, in *Proceedings of the 2009 International Conference on Wireless Communications and Mobile Computing: Connecting the World Wirelessly*, New York, NY, USA: ACM, Jun. 2009, pp. 623–627. doi: 10.1145/1582379.1582514.
[607] J. B. Keller, ‘The Probability of Heads’, *The American Mathematical Monthly*, vol. 93, no. 3, pp. 191–197, Mar. 1986, doi: 10.1080/00029890.1986.11971784.